Investigations of the Transport, Sources, and Sinks of Atmospheric CO_2 Using a General Circulation Model

by
A. Scott Denning

Department of Atmospheric Science
Colorado State University
Fort Collins, Colorado

David A. Randall, Principal Investigator

Colorado State University

Department of Atmospheric Science

Paper No. 564

INVESTIGATIONS OF THE TRANSPORT, SOURCES, AND SINKS OF ATMOSPHERIC CO_2 USING A GENERAL CIRCULATION MODEL

by

A. Scott Denning

Research supported by the
National Aeronautics and Space Administration
under Contract number NAS5-31730
and a NASA Global Change Fellowship
Grant number NGT-30150

Department of Atmospheric Science
Colorado State University
Fort Collins, CO

November 1994

Atmospheric Science Paper No. 564

Abstract

Investigations of the Sources, Sinks, and Transport of Atmospheric CO_2 in a General Circulation Model

The mixing ratio of carbon dioxide (CO_2) in the atmosphere is increasing exponentially due to emissions from the combustion of fossil fuels. Only about half of the anthropogenic CO_2 emissions (about 6 kg of carbon per year, Gt C yr^{-1}) remains in the atmosphere, and the fate of the other half is not completely understood. The availability of high frequency observations of atmospheric CO_2 at a large number of widely distributed remote locations has made it possible to infer surface sources and sinks through the use of simulation models of atmospheric transport. Based on the observed difference of about 3 parts per million (ppm) between the mixing ratio of CO_2 in the high northern and high southern latitudes and relatively slow interhemispheric mixing, several studies using tracer transport models showed that a large sink must be present in the middle to high latitudes of the northern hemisphere. The sink was generally assumed to be in the ocean until 1990, when Tans, Fung, and Takahashi showed that the available oceanographic data were incompatible with such a large northern ocean sink. Their results suggested that terrestrial ecosystems in the northern temperate zone must be accumulating between 2 and 3.4 Gt C yr^{-1}, based on atmospheric observations of CO_2 and simulated transport using a tracer transport model driven by winds on a four hour time step and convective frequency saved as monthly means from a general circulation model (GCM).

This study repeats the calculations of Tans, Fung, and Takahashi (1990) to a large extent, but does so on-line in the Colorado State University (CSU) GCM with a six minute time step that (unlike previous studies) fully resolves the diurnal cycle of atmospheric circulation. Carbon dioxide is represented as a set of 16 passive atmospheric tracers that have been added as prognostic variables to the model. Each tracer represents the effect of a single source or sink of atmospheric CO_2 and all but one have unique maps of seasonally varying fluxes at the Earth's surface which are prescribed as boundary conditions in the simulation. One of the tracers, representing the effects of biologically driven CO_2 exchange at the land surface has boundary fluxes calculated on-line using the Simple Biosphere (SiB2) model. Two additional tracers representing radioactive trace gases are simulated to evaluate aspects of the simulated large-scale transport in the GCM. The con-

centration of each tracer was initialized to be globally uniform, and the tracer calculation was integrated for 14 simulated years.

Simulated annual mean meridional gradients of the mixing ratios of most of the tracers were somewhat weaker than as simulated in previous studies using off-line tracer transport models. This was due to slightly more vigorous interhemispheric exchange of tracers in the GCM relative to the off-line models. Tracers with purely seasonal sources and sinks (representing seasonal photosynthesis and respiration) exhibited much stronger meridional gradients than previously simulated, however, because of enhanced correlations between boundary fluxes and simulated vertical mixing due to the inclusion of a variable-depth, well mixed, planetary boundary layer in the CSU GCM.

The carbon budget of the atmosphere is expressed as a linear combination of the prescribed surface flux maps, with coefficients calculated by fitting the simulated tracer concentrations to observations. The best fit to observations was obtained for scenarios with a global ocean sink of about 0.9 Gt C yr^{-1} and a sink of between 2 and 3 Gt C yr^{-1} in the boreal forest. Tropical deforestation was calculated as a residual in this study because it has very little influence on the meridional concentration gradient, and was smaller than simulated in most previous studies (0 to 0.6 Gt C yr^{-1}).

The seasonal oscillation of atmospheric CO_2 was fairly well represented at locations for which observational data are available, although its amplitude was a bit stronger than previously simulated. The stronger seasonal amplitude was especially evident over the northern continents (where very few data have been gathered), and reflect the seasonality of turbulent mixing in the planetary boundary layer, which has not been previously simulated in global models of atmospheric CO_2.

The diurnal variability of CO_2 in the lower troposphere was much more realistic as simulated in the CSU GCM than in off-line tracer models because of the inclusion of the on-line calculation of photosynthesis and respiration at the model time step using SiB2. Simulated diurnal variations of tens of ppm in the boundary layer were highly correlated to the diurnal growth and decay of boundary layer turbulence and cumulus convection, and resulted in different spatial distributions from the other tracers, even in the annual mean.

Acknowledgments

I thank Professor David A. Randall, who has served as my advisor and principal mentor for the past four years, for his tremendous help and guidance in the work presented here. He has consistently provided me with just the right blend of academic independence and expert guidance to allow me to learn the creative process of doing research well. His ability to straddle the traditional divide between physical intuition and computational detail is incredible, and has been an inspiration to me.

Thanks also to my other committee members: Drs. Pieter Tans, Sonia Kreidenweis, Roger Pielke, David Schimel, and David Dandy. Dr. Pieter Tans spent many hours with me both on the telephone and in person, helping me to appreciate some of the most important aspects of the global carbon cycle and to fine tune this report. Dr. Sonia Kreidenweis provided important guidance regarding the interhemispheric transport of trace gases in the atmosphere. Dr. Roger Pielke, both in his classes and in informal discussions, pointed me to important parts of the problem at smaller scales than I have considered in this work, but which added greatly to my understanding. Dr. David Schimel engaged me in many fruitful discussions about the linkages between various components of the Earth system, and has always encouraged me to reach further in understanding them. Dr. David Dandy helped me to explain my work in the language of engineers, and reminded me anew that the same equations govern the largest and smallest scales of motion in the atmosphere.

My very special thanks go to my wife Jennifer Crane, whose patience and support during this very challenging time have been absolutely amazing. Especially since the birth of our son Nathaniel, she has provided the rock of stability and sanity in our chaotic lives.

I am indebted to Dr. Inez Y. Fung, now at the University of Victoria and formerly of the Goddard Institute for Space Studies, who started me on the path of modeling the global transport of atmospheric CO_2. She kindly provided data and, more importantly, the wise advice of someone who has done it all before.

Dr. Joe Berry at the Carnegie Institute of Washington and Stanford University and Dr. James Collatz at NASA Goddard Space Flight Center patiently explained the inner workings of SiB2 to me, and pointed me in all the right directions when I was at a loss to understand what was wrong. Thanks to Dr. Piers Sellers for his support, advice, and especially for his sense of humor regarding my work.

Don Dazlich is the undisputed guru of the CSU GCM. Without his expert help I would still be poring over Fortran code and would have nothing to show for my trouble

but sore eyes and error messages. Kelley Ann Wittmeyer kept the computers humming, and gave generously of her time and energy. The contributions of Cindy Carrick are invaluable to me, and to every member of Dave Randall's large research group. What would we ever do without her?

Dr. Jill Baron gave me the respect and responsibility to get a taste of what real academic research is all about. That opportunity gave me the motivation to pursue what followed, and I am very grateful to her for it.

Thanks to my parents, Margie Williams and Bob Denning, who believed me 30 years ago when I said I wanted to be a scientist, and then put up with everything I did afterward.

Finally, thanks to Nathaniel Stephen Denning for giving me the perspective not to take my defense too seriously – there is nothing like changing a dirty diaper before going to work to make one humble!

This work was supported by a NASA Global Change Fellowship, Grant NGT-30150, and by NASA Contract NAS5-31730. Computing resources were provided by the NASA Center for Computational Sciences.

Table of Contents

CHAPTER 1

Introduction

1.1 Motivation: Why Should We Care?

Carbon (C) is an element whose atoms contain six protons. Like all other elements heavier than helium, carbon is originally formed from lighter components by thermonuclear fusion in stars. It is the seventeenth most abundant element in the Earth's crust, comprising less than one tenth of one percent of the mass (Krauskopf, 1979). Forming somewhat more volatile compounds than other elements, carbon is better represented in the atmosphere than it is in the crust. Carbon dioxide (CO_2) is the fifth most abundant gas in the Earth's atmosphere, currently comprising about 355 parts per million (ppm) by volume (Wallace and Hobbs, 1977; Conway *et al.*, 1994). Carbon dioxide gas plays an important role chemically, in the oxidation state of the atmosphere (Holland, 1984) and in the acid-base status of waters (Drever, 1988), and physically in the atmosphere's radiant energy balance (Liou, 1980). Chemical properties associated with carbon's four valence electrons give its atoms the nearly unique ability to form an almost infinite variety of straight and branched chains (Chang, 1981), incorporating atoms of other elements into the framework as well and leading to the rich and complex organic chemistry which makes life possible (Stryer, 1981).

Chemical oxidation and reduction of carbon provides the means of exchange – the currency – of energy in the biosphere. Solar energy captured by plants is used to produce reduced organic compounds from atmospheric CO_2. This energy is then carried in the organic material from organism to organism, until it is eventually released when the compounds are oxidized back to CO_2. This biological economy is also a fundamental driver of human economics, in which organic materials and organically-derived energy are consumed to provide for human needs and comfort. As human economic activity has expanded, organic compounds have been oxidized – burned – more and more rapidly to release

their stored energy, which has led in the past two centuries to rising concentrations of CO_2 in the atmosphere. The current concentration of about 355 ppm represents an increase of about 27 percent since preindustrial times (Houghton *et al.*, 1990; see Fig. 1.1).

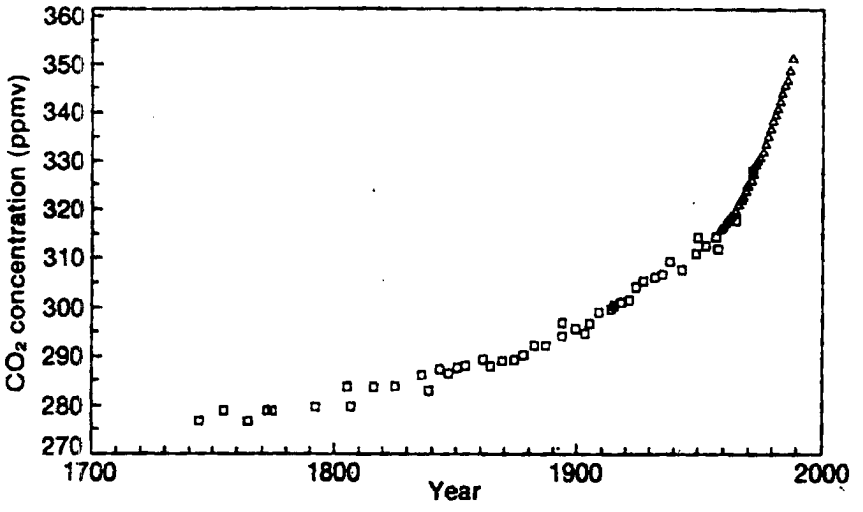

FIGURE 1.1: Time series of atmospheric CO_2 concentration over the past three centuries. Squares represent measurements of air trapped in ice cores, and triangles represent measurements at Mauna Loa, Hawaii (Houghton *et al.*, 1990).

The current increase in atmospheric CO_2 concentrations not the first such change that has occurred. Geological evidence suggests that during the early history of the Earth, CO_2 was very abundant, as it is today in gases emitted by volcanos (Worsley and Nance, 1989; Schlesinger, 1991). Analysis of air trapped in ice cores reveals that the concentration of CO_2 has undergone large shifts which have accompanied the growth and collapse of the great ice sheets over the past couple of hundred thousand years (Barnola *et al.*, 1987, see Fig. 1.2). These shifts in CO_2 and global climate inferred from paleontological evidence are closely correlated in time, although the mechanisms by which they are coupled is not well understood.

In the past century or so, it has become clear that CO_2 in the atmosphere plays an important role in the radiative balance of the Earth. Fourier (1827) first compared the atmosphere to a plate of glass, which transmits visible light from above but absorbs infrared

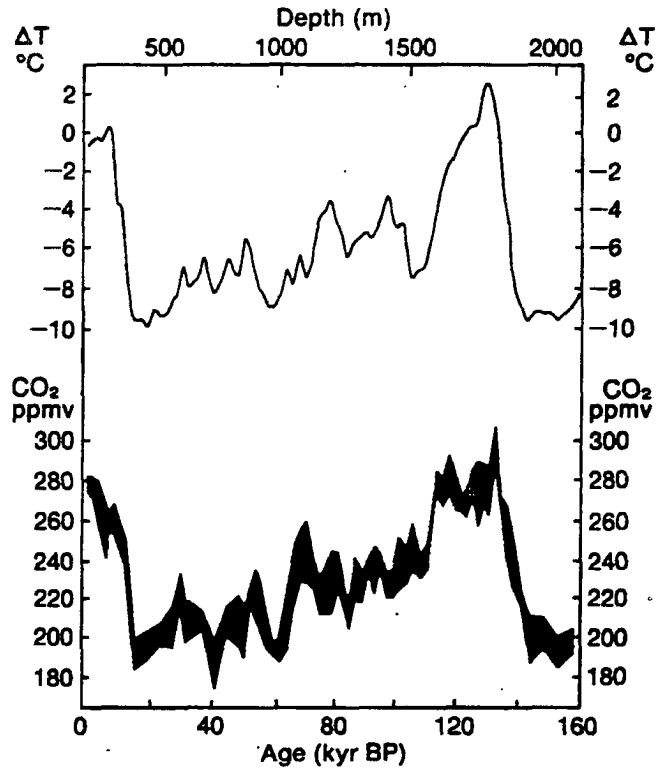

FIGURE 1.2: Variations of atmospheric CO_2 concentration and temperature inferred from analysis of air bubbles trapped in an Antarctic ice core (Houghton *et al.*, 1990).

energy emitted from below. When it was discovered in the nineteenth century that CO_2 absorbs most incident infrared radiation in the wavelengths of thermal radiation emitted at the Earth's surface, physicists speculated (Arrhenius, 1896; Chamberlain, 1897) that industrial combustion would lead to global warming. This concern was revived in the 1950's when it became clear that the rise in atmospheric abundance of CO_2 was real and global in extent. The advent of numerical simulation models of the Earth's climate in the 1960's and 1970's brought the concern into sharper focus and led to a rich literature in the atmospheric sciences regarding the prospect of CO_2-induced climate change. In recent years, this issue has exploded into the public eye and the popular press. Few people in the industrialized world have not now heard of the potential menace of the "greenhouse effect" due to atmospheric CO_2, and the possible prospect of dire consequences for the climate, their way of life, even "the survival of the planet." Others may doubt the "doomsday" scenarios, but feel it is prudent to consider major changes in the global in-

dustrial economy to forestall negative effects. Unprecedented gatherings of the world's political leaders have produced mountains of documents regarding strategies for preventing or dealing with global changes which many suspect are just around the corner.

This flurry of political activity, however, masks a profound lack of certainty in the scientific community regarding just what controls the abundance of atmospheric CO_2 in the first place. Scientists have generally regarded CO_2 as "well-mixed" in the atmosphere, but systematic variations on the order of 10 percent are now known to occur both region-

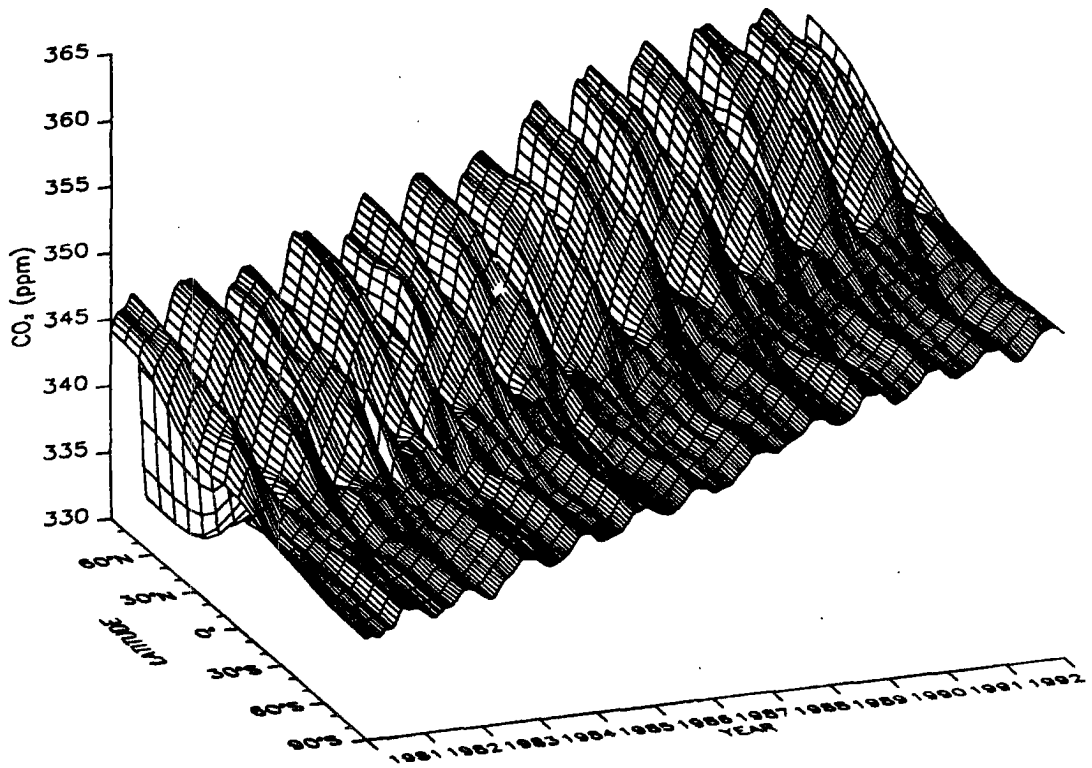

FIGURE 1.3: Variations of atmospheric CO_2 concentration by time and latitude for the period 1981 through 1992, based on samples collected by the NOAA flask network. From Conway *et al.* (1994).

ally and seasonally (Conway *et al.*, 1988; see Fig. 1.3). The pronounced seasonal cycle in the northern hemisphere is believed to be produced by seasonal growth and decay of terrestrial vegetation. Tropical ecosystems undergo much weaker seasonal variations, so the amplitude of the signal is much lower there. The southern hemisphere cycle is out of phase with that in the north, and much weaker because of the much larger areal fraction of ocean. These biological influences have long been suspected, but only recently have

there been observational data of sufficient quality and abundance to permit such a detailed examination.

While there is no question that human activity has caused concentrations to rise over the past century or so, the causes of the huge shifts of the geologic past are still mysterious. Only about half of the CO_2 released by industrial activities remains in the atmosphere, and the whereabouts of the other half are a matter of considerable debate. The so-called "missing carbon" is almost certainly stored in either the biosphere, the deep ocean, or some combination of the two, but ecologists and oceanographers cannot yet fully account for it (*e.g.*, Houghton *et al.*, 1990).

In the past two decades, scientific understanding of the changing global carbon cycle has been advanced by researchers willing to cross traditional boundaries of their disciplines. Any description of the carbon cycle must involve meteorologists, ecologists, chemists, oceanographers, and physicists. Through such interdisciplinary efforts, we have recently learned, for example, that large fluctuations in the carbon budget of the biosphere are produced during the large-scale fluctuations of the ocean-atmosphere system called El Niño (Keeling *et al.*, 1989*a*). Since much of the exchange between the Earth's large reservoirs of carbon is mediated by atmospheric transport, simulation models of the large-scale circulation of the atmosphere have been used to investigate these links in the global carbon cycle. This research has been very fruitful in the last ten years in elucidating processes which are difficult or impossible to observe, but has continued to pose as many questions as it has answered. Some of the apparent contradictions between observations of CO_2 concentration and theoretical aspects of the surface fluxes and atmospheric transport were highlighted in a study by Pieter Tans, Inez Fung, and Taro Takahashi published in the journal *Science* in 1990, (hereinafter referred to as TFT90), and in many subsequent papers in the literature.

The remainder of this chapter introduces the current understanding of the global carbon cycle. First, section 1.2 presents the major pools of carbon in the Earth system. To see how carbon is transferred between these major reservoirs, one must first understand some basic concepts of the chemistry and biochemistry of carbon in nature. These are discussed in 1.3. Next, section 1.4 discusses exchanges and storage of carbon in the world's oceans. With this background, section 1.5 presents current views of the inter-reservoir exchange of carbon on both geologic and interannual time scales. Section 1.6 presents key concepts and terminology involving the information available from study of the

various isotopes of carbon. Finally, in section 1.7 the objectives of the current study are presented.

1.2 Reservoirs of Carbon in the Earth System

As mentioned in section 1.1, carbon is a very active element in the Earth system, undergoing transformations from one form to another as living organisms fix it from nonliving CO_2 and then release it again. It is customary to treat global chemical cycles in terms of "reservoirs" or "pools," and the fluxes between these reservoirs. Because carbon is involved in biological and geological processes as well as simple chemical reactions, inter-reservoir exchanges of carbon are often referred to as "biogeochemical cycling." This section discusses the major reservoirs of carbon in the Earth system, but consideration of the fluxes between the various pools is postponed until section 1.5, following discussion of some of the exchange processes which control them.

Nearly all the carbon in the Earth system is contained in sedimentary rocks called carbonates (Press and Siever, 1978; see Fig. 1.4). This reservoir contains about 19 million gigatons (Gt, 1 Gt = 10^{12} kg) of carbon, or about 99.8 percent of the world's carbon (Wallace and Hobbs, 1977). These sediments are composed of calcium and magnesium carbonates ($CaCO_3$ and $MgCO_3$), and are mostly derived from the inorganic remains (*e.g.*, shells) of marine organisms. The shell materials accumulate on ocean floor when the organisms die, and the resulting calcareous mud hardens to rock over geologic time. A smaller amount of carbon is also contained other sedimentary rocks such as shales, and in the deeper crystalline rocks of the solid Earth (Olson *et al.*, 1985; Schlesinger, 1991).

The remaining carbon in the Earth system is much more active than that contained in the rock reservoir, and can be called *labile*, meaning "changeable." The labile carbon pool is dominated by the dissolved carbon of the deep oceans, which accounts for about 38,000 Gt (Schlesinger, 1991). Most of this is dissolved inorganic carbon (CO_2), but perhaps as much as 2000 Gt of the ocean carbon reservoir is composed of dissolved organic carbon compounds. Fossilized organic material comprises about 2000 Gt of carbon (Post *et al.*, 1990), much of it having been transformed into coal, oil, and natural gas which are currently being extracted rapidly and released into the atmosphere (see section 1.5.2). About 2000 Gt of organic carbon is stored on the land surface (Schlesinger, 1991) in the form of living biomass (about 500 Gt) and organic decay products in the soil (about 1500

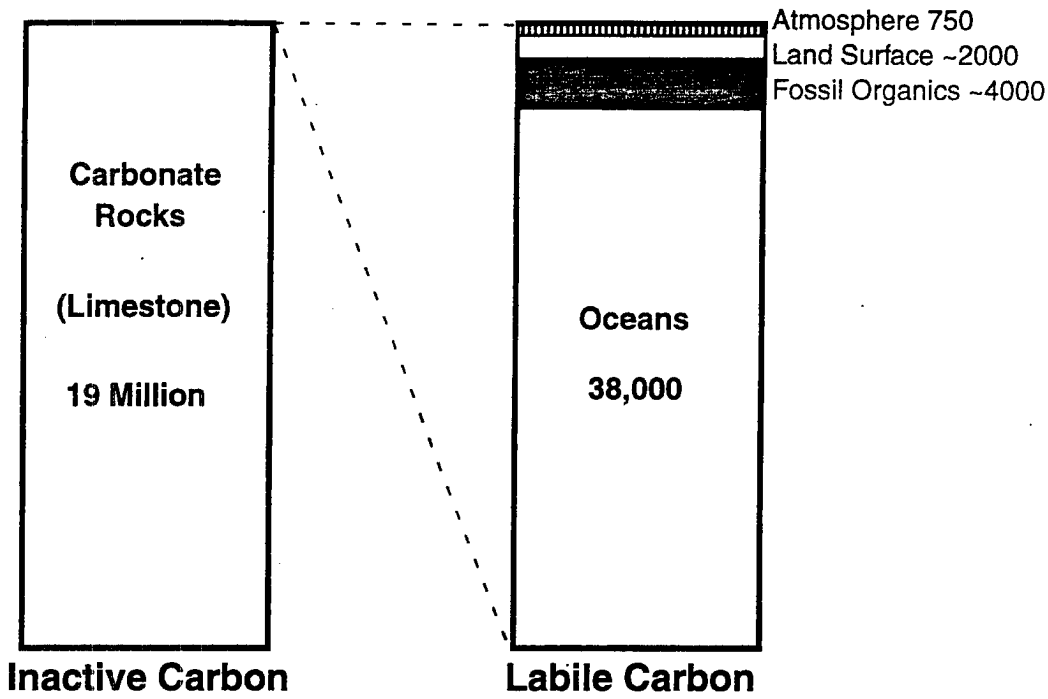

FIGURE 1.4: The major reservoirs of carbon in gigatons (Gt). One Gt = 10^{12} kg. Nearly all the carbon in the world is contained in the solid Earth. The entire column on the right would be thinner than the line at the top of the left-hand column if they were plotted at the same scale.

Gt). The atmosphere currently contains about 750 Gt of carbon, mostly in the form of CO_2, but also as methane (CH_4), carbon monoxide (CO), and various organic compounds.

Because the CO_2 in the atmosphere comprises such a small fraction of the total labile carbon, even relatively small fractional changes in the sizes of the other pools could be expected to have very significant effects on the atmospheric reservoir. An understanding of the mechanisms by which carbon is transferred between the major reservoirs is essential to our ability to assess the likely growth rate of atmospheric CO_2 in the future. Before discussing these exchanges in section 1.5, the next two sections review some important chemical, biological and physical processes by which these transfers are accomplished.

1.3 Background Chemistry of Carbon

Carbon dioxide is soluble in water. Virtually all water in contact with the atmosphere has some dissolved CO_2 present, and many important geochemical and biological processes are affected by CO_2 and related solutes. The organic chemistry of carbon is extremely complex, and is beyond the scope of this report. (The interested reader may wish to consult a textbook such as Solomons, 1980.) I present here the relevant inorganic chemistry and sketch the qualitative aspects of organic reactions which affect the global carbon budget.

1.3.1 Aqueous Carbonate Equilibria

The discussion of carbonate equilibrium chemistry in this section is primarily derived from Drever (1988). When CO_2 gas is dissolved into water, it hydrates to form carbonic acid

$$CO_2(g) + H_2O \rightleftharpoons H_2CO_3(aq)\,. \tag{1.1}$$

The solubility of CO_2 in water is defined by the Henry's law coefficient

$$K_H \equiv \frac{[H_2CO_3]}{p_{CO2}}, \tag{1.2}$$

where the square brackets refer to the concentration[1] in the solution, and p_{CO2} indicates the partial pressure of CO_2 in the overlying air. This notation is standard, and will be used throughout this report. Equation (1.2) states a one-to-one relationship between dissolved CO_2 and the partial pressure p_{CO2} in the overlying air (under conditions of chemical equilibrium at standard temperature, pressure, and salinity). This relationship is commonly used to refer to the p_{CO2} of *water*, (regardless of the actual p_{CO2} of the overlying air) meaning the partial pressure of CO_2 in air that is *in equilibrium* with water containing a given concentration of H_2CO_3.

1. The relevant parameter is actually the *activity* of the dissolved species, which is always slightly less than its concentration. In relatively dilute solutions, these quantities are nearly identical, and it is common practice to use aqueous concentration rather than activity.

The weak acid H_2CO_3 partially dissociates to form hydrogen ions and bicarbonate ions according to

$$H_2CO_3 \rightleftharpoons H^+ + HCO_3^- \ , \tag{1.3}$$

with the dissociation constant

$$K_1 \equiv \frac{[\ H^+\ ]\ [HCO_3^-\ ]}{[H_2CO_3]} . \tag{1.4}$$

The bicarbonate further dissociates into hydrogen ions and carbonate ions

$$HCO_3^- \rightleftharpoons H^+ + CO_3^{2-} \ , \tag{1.5}$$

with the second dissociation constant

$$K_2 \equiv \frac{[\ H^+\ ]\ [CO_3^{2-}\ ]}{[HCO_3^-\ ]} . \tag{1.6}$$

The values of the equilibrium "constants" K_H, K_1, and K_2 defined in (1.2), (1.4), and (1.6) are actually functions of temperature, pressure, and salinity or total ionic strength of the solution. The values of these ratios are most sensitive to temperature, with higher temperature generally leading to smaller values so that cold water can dissolve more CO_2 than warm water. The overall solubility of CO_2 in water is about twice as high at 0°C as it is at 20°C.

Note that the equilibrium relations (1.4) and (1.6) each contain the factor $[H^+]$, which represents the concentration of hydrogen ions in the solution. This concentration, by definition, quantifies the degree to which the solution is acidic. "Acid" solutions contain a lot of free hydrogen ions, and "basic" solutions contain almost none. Because hydrogen ion concentration varies by many orders of magnitude in natural waters, the notation

$$pH \equiv -\log_{10}[\ H^+\ ] \tag{1.7}$$

has been adopted to describe it. Very acidic solutions like vinegar have a pH near 1, and very basic solutions like lye have pH near 14. Pure distilled water in equilibrium with atmospheric CO_2 has a pH of 5.6, due to the reactions (1.3) and (1.5).

Other dissolved constituents (solutes) in water include positively-charged "cations" and negatively charged "anions." The concentrations of most dissolved solutes do not depend on the temperature, pressure, or salinity of the solution. These solutes are termed "conservative species." When the total concentration of the conservative anions is subtracted from the sum of the conservative cations (weighted by the charge on the ions of each solute), the remaining solutes determine the "total alkalinity" of the solution. In most natural waters, this quantity is dominated by the ions in the carbonate system, so that many writers refer to "carbonate alkalinity" interchangeably with "total alkalinity." The carbonate alkalinity is defined by

$$\mathrm{Alk} = 2[\ CO_3^{2-}\ ] + [\ HCO_3^-\ ] - [\ H^+\ ] + [B(OH)_4^-\ ] + [OH^-\ ], \qquad (1.8)$$

where $[B(OH)_4^-\ ]$ is the concentration of the "borate" ion and $[OH^-\ ]$ is the concentration of the "hydroxyl" ion. Both of these are small in ocean water, but the borate chemistry plays an important role in controlling the solubility of CO_2 because of its contribution to the total alkalinity (Tans, 1994). Since borate concentration in the ocean simply reflects the overall salinity of a given water sample, salinity can be used as a surrogate variable to reduce the degrees of freedom in the calculation of the p_{CO2} of ocean water.

The factor of two on the carbonate ion concentration reflects the fact that each carbonate ion carries two negative charges. Alkalinity is a measure of the ability of the solution to neutralize acids, and is sometimes called "acid neutralizing capacity." Note that alkalinity is not a function of p_{CO2}, since each mole of CO_2 dissolved produces stoichiometrically balanced quantities of HCO_3^-, CO_3^{2-}, and H^+.

Another frequently used quantity describing carbon dioxide in water is the total dissolved inorganic carbon, DIC or ΣCO_2. This is defined as

$$\Sigma CO_2 = [H_2CO_3] + [\ HCO_3^-\ ] + [\ CO_3^{2-}\ ]. \qquad (1.9)$$

Usually, the concentrations of H^+, H_2CO_3, HCO_3^-, and CO_3^{2-} are not measured directly. In practice, the only quantities in the carbonate system that can easily be measured are pH, p_{CO2}, Alk, and ΣCO_2. Given any two of these four quantities, the equilibrium constants K_H, K_1, and K_2, and the concentrations of any conservative solutes, all the other species can be calculated from the equilibrium relations (1.2), (1.4), (1.6), (1.8), and (1.9).

1.3.2 Calcium Carbonate Formation and Chemical Weathering

If the doubly-charged cation Ca^{2+} is added in sufficient concentration to the carbonate system described in the previous section, a mineral precipitate,

$$Ca^{2+} + 2\ HCO_3^- \rightleftharpoons CaCO_3(s) + H^+ + HCO_3^-, \tag{1.10}$$

is formed, where the (s) indicates the solid phase. The carbonic acid produced and bicarbonate ion consumed in this reaction are subject to the other equilibria already discussed. The solid calcium carbonate ($CaCO_3$, calcite) formed would precipitate and settle out of the solution. Such pure crystalline calcite formed from chemical precipitation is rare in nature, because biological processes driven by the expenditure of energy are more efficient at extracting $CaCO_3$ from the water column than the simple chemical equilibrium presented here. Calcite is used by many marine organisms to form their shells or other hard body parts (Press and Siever, 1978).

Reaction (1.10) represents an equilibrium between the solid and dissolved phases of calcium carbonate. In the reverse reaction, it represents the dissolution of the solid phase into an acidic solution. Such reactions are referred to as chemical weathering. From the equilibrium in (1.10), the solubility of calcite is given by

$$K_C = \frac{[\,Ca^{2+}\,]\,[\,HCO_3^-\,]}{[\,H^+\,]}. \tag{1.11}$$

From the equilibria (1.4) and (1.6), it can be seen that this reaction is favored by lower pH, and from (1.2), that it is also favored by high p_{CO2}. This result turns out to be quite general for most chemical weathering processes.

There are thousands of silicate minerals which form the rocks of the surface of the Earth, but in terms of the effect of silicate weathering on atmospheric CO_2, an idealized reaction can be written

$$H_2O + CO_2 + CaSiO_3 \rightleftharpoons Ca^{2+} + 2\,HCO_3^- + SiO_2. \qquad (1.12)$$

This reaction consumes CO_2, producing alkalinity and dissolved calcium in surface waters, and leaving silica (SiO_2) behind as quartz sand and silt. The presence of dissolved carbonic acid in rainwater reduces its pH. Biological processes in soils also add to the concentration of dissolved CO_2 in groundwater, so that soil solution pH is often less than 5. The acidity of surface and ground waters greatly increases the solubility of rock materials with which they come into contact, and therefore the rate of chemical weathering.

Chemical weathering is a small net sink for atmospheric CO_2, the result of which is high concentrations of HCO_3^- and dissolved cations in rivers. When this high-alkalinity water reaches the oceans, the forward reaction (1.10) dominates, resulting in biologically-enhanced precipitation of $CaCO_3$ on the sea-floor. One mole of carbon is converted back to dissolved CO_2 for each mole of solid $CaCO_3$ formed in reaction (1.10), with the net result being the removal of one mole carbon from the atmosphere. Calcium carbonate accumulates in marine sediments, but is sometimes destroyed by metamorphic reactions if the sediments become buried to great depths. In this case, the reverse of reaction (1.12) occurs, forming new silicate minerals like $CaSiO_3$ and releasing volatile H_2O and CO_2 into interstitial fluids in the rocks.

1.3.3 Biochemical Cycling of Carbon

The discussion in this section is derived mainly from Schlesinger (1991). Photosynthesis is the process by which plants use sunlight to manufacture simple carbohydrates from atmospheric CO_2 and water. It is actually a very complicated process involving many biochemical steps, but for the sake of the present discussion it can be represented by the simple reaction

$$H_2O + CO_2 \rightarrow CH_2O + O_2. \qquad (1.13)$$

In this idealized representation, CH_2O represents any simple carbohydrate such as glucose ($C_6H_{12}O_6$). Organic molecules produced by photosynthesis have much less bond energy than is contained in the CO_2 molecule, and so reaction (1.13) is endothermic, requiring energy input to proceed. This energy is derived directly from sunlight by chlorophyll molecules in specialized plant cell parts called chloroplasts. The relatively weak bonds in the reduced organic molecules produced in this way can be easily broken and rearranged in further reactions to provide the plant with energy to live and also with the building blocks for all of its tissues. The rate at which plants convert inorganic CO_2 into organic compounds is called *gross primary productivity*, and the total amount of carbon fixed annually is called *gross primary production* (GPP). This quantity is usually expressed in units of mass of carbon per unit area per year.

The rate of photosynthetic carbon fixation can be estimated by enclosing a leaf in an experimental vessel and measuring the rate of decrease of CO_2 concentration. This rate is usually determined by the rate at which CO_2 molecules can diffuse into plant cells where they can be fixed by chloroplasts. Gas diffusion at leaf surfaces is regulated by openings in plant leaves called *stomata*, which can be closed to prevent rapid loss of water from the plant tissues. When moisture is abundant, both in the soil around the plant's roots and in the air in the form of vapor, the stomata open as much as possible and photosynthetic carbon fixation is rapid. In this case, the rate of photosynthesis can be limited by the availability of certain enzyme complexes which participate in the reactions. The supply of these enzymes is dependent on the availability of nitrogen and other nutrients, so that the ability to fix carbon in a plant with sufficient water may be limited by nutrient supply.

The processes by which living organisms rearrange organic compounds to extract energy and build tissues are collectively known as metabolism. Metabolic energy is derived from carbohydrate molecules by reactions which can be thought of as the reverse of reaction (1.13) above. This energy extraction reaction is called respiration. Plants respire carbon which they have previously fixed to provide the energy they need in order to grow, reproduce, and generally sustain life. Plant respiration occurs all the time, and dominates over photosynthesis at night and during other times (like winter) when plants need more metabolic energy than they can produce. Integrated over a year, the net amount of carbon fixed from CO_2 by plants is called the *net primary production* (NPP), which is defined as

$$NPP = GPP - R_P \tag{1.14}$$

where R_P is the annual total plant respiration. Annual NPP is estimated by "harvest" methods, whereby plants are killed and dried, and then weighed to see how much organic matter was created. This is difficult because much of the biomass of many plant species is below ground, in the roots. Annual NPP is about half of GPP in most ecosystems.

When plants or parts of plants (like leaves and branches) die, organic material they have manufactured through photosynthesis and metabolic activity is usually deposited on the ground. There it is broken down in a process of decomposition by bacteria and other microorganisms in a process called *heterotrophic*[1] respiration. The reactions involved are again essentially the reverse of reaction (1.13), and energy is released in the process of decomposition. In mature ecosystems at steady state, the annual total of heterotrophic respiration is approximately equal to the annual NPP. This means that the annual growth increment of the average plant in the ecosystem is matched by falling "litter" from the plants, so that the total biomass of the ecosystem remains constant. The term *net ecosystem production* (NEP) is used to refer to the annual increase in the biomass of an ecosystem, and is expressed

$$NEP = NPP - R_H = GPP - R_T. \tag{1.15}$$

where $R_T = R_P + R_H$ is the total respiration in the ecosystem. This quantity is generally positive after a major disturbance (like a forest fire or harvest) which removes biomass from an ecosystem. In forests, NEP reaches a maximum several decades after disturbance, and declines to nearly zero after a century or two (Houghton *et al.*, 1987).

It should be noted that the above remarks on NEP are meant to apply only on large spatial scales, over which actual measurement of NPP and R_T are nearly impossible. On the scale of experimental plots on the order of a few thousand square meters, measured NEP is nearly always positive in undisturbed ecosystems (David Schimel, personal communication). On regional scales, significant disturbances due to fire, weather, or human activities are believed to balance the biomass accumulated by undisturbed parts of the ecosystem.

1. The term *heterotrophic* means that these organisms derive their energy from outside themselves. It distinguishes all organisms that do not photosynthesize from those that do, which are called *autotrophic*.

1.4 Carbon in the Oceans

The discussion in this section is derived mainly from material in Broecker (1974) and Baes *et al.* (1985).

1.4.1 Air-Sea Exchange at the Ocean Surface

As discussed in section 1.3.1, carbon dioxide gas dissolves into water according to Henry's law (1.1). This equation relates the partial pressure of the gas to the aqueous concentration of its dissolved ions at equilibrium. Unfortunately, the entire ocean-atmosphere system is not in equilibrium with respect to CO_2, and locally may be quite far from equilibrium. This is primarily due to biological activity in the relatively thin layer (no more than 100 m) through which light penetrates – the *photic zone*. Over large areas of the oceans, photosynthesis in the photic zone depletes dissolved inorganic carbon species to build reduced organic compounds, as discussed in section 1.3.3. This commonly leaves the ocean surface undersaturated with respect to CO_2, and the gas then dissolves into the upper ocean from the air by diffusion. In other areas, the surface ocean carries more ΣCO_2 than predicted by the equilibria in section 1.3.1, leaving the water supersaturated and causing CO_2 gas to diffuse from the water into the air. This occurs most frequently in the equatorial upwelling zones, for reasons which will become clear in section 1.4.2.

The temperature dependence of the carbonate equilibria discussed in section 1.3.1 also act to change the p_{CO2} of surface ocean water when temperature changes occur faster than the CO_2 can equilibrate across the air-sea interface. At 15°C, for example, the equilibrium p_{CO2} of seawater decreases by about four percent for each degree of cooling if alkalinity and ΣCO_2 remain constant (Baes *et al.*, 1985). Rapid cooling is associated with winter weather and rapid warming occurs when cold water from the deep ocean is brought to the warmer surface in upwelling regions, as discussed in section 1.4.2.

The diffusive flux of CO_2 across the air-sea interface from the ocean to the atmosphere can be written as

$$F_{CO2} = c_T(p_{CO2,\,sea} - p_{CO2,\,air}) = c_T \Delta p_{CO2} \qquad (1.16)$$

which is just a definition of a transfer coefficient c_T (Broecker, 1974; TFT90). Here $p_{CO2,sea}$ is the theoretical partial pressure of CO_2 which would be in equilibrium with the dissolved CO_2 in the water according to equation (1.1). This bulk formula envisions the exchange of CO_2 between the ocean and atmosphere as driven by the disequilibrium between the gas and aqueous phases, and limited by the exchange coefficient c_T. Because the partitioning of CO_2 between the various dissolved carbon species in the water is determined by the many equilibria discussed in section 1.3.1, the value of c_T depends on the values of the various equilibrium constants K_H, K_1, K_2, and K_C. As discussed on page 9, these values depend strongly on temperature, and somewhat less strongly on pressure and salinity. Therefore the transfer coefficient c_T depends on temperature and to some extent salinity (the atmospheric pressure at the sea surface being essentially constant for the purposes of calculating c_T). The value of c_T is also sensitively dependent on wind speed in the overlying atmosphere, both directly due to turbulence in the air, and indirectly due to the generation of waves by sea-surface winds.

In practice, the functional dependence of c_T on sea-surface temperature and atmospheric wind is determined empirically. Wind tunnel and field experiments have been used to investigate the behavior of this parameter under various environmental conditions (see Fig. 1.5). It seems clear that under very low wind conditions, gas transfer is extremely slow because a thin layer of water develops which is nearly in equilibrium with atmospheric concentration (Liss and Merlivat, 1986). Surface exchange increases gradually with wind speed until certain thresholds are crossed (such as the development of a rough surface and breaking waves), at which point the slope of the relationship with wind speed becomes much steeper. Unfortunately, globally integrated fluxes calculated using these laboratory results are not consistent with observations of the penetration of radioactive ^{14}C and other radioisotopes into the world oceans (Peng and Takahashi, 1989; TFT90). Theoretical considerations indicate that the exchange coefficient must also be a function of static stability in the atmosphere (Erickson, 1993).

Because of the presence of solid $CaCO_3$ suspended in the water column and in marine sediments, the inorganic reactions outlined in section 1.3 act to hold the pH of ocean water nearly constant at about 8.0 (Drever, 1988; Schlesinger, 1991). This process, known as *buffering*, is accomplished by shifting the equilibrium of reaction (1.10) to the right when some process removes hydrogen ions from the water, and to the left when hydrogen ions are added. Another consequence of this buffer effect is that the carbonate equilibria discussed in section 1.3 tend to resist changes in the total concentration of car-

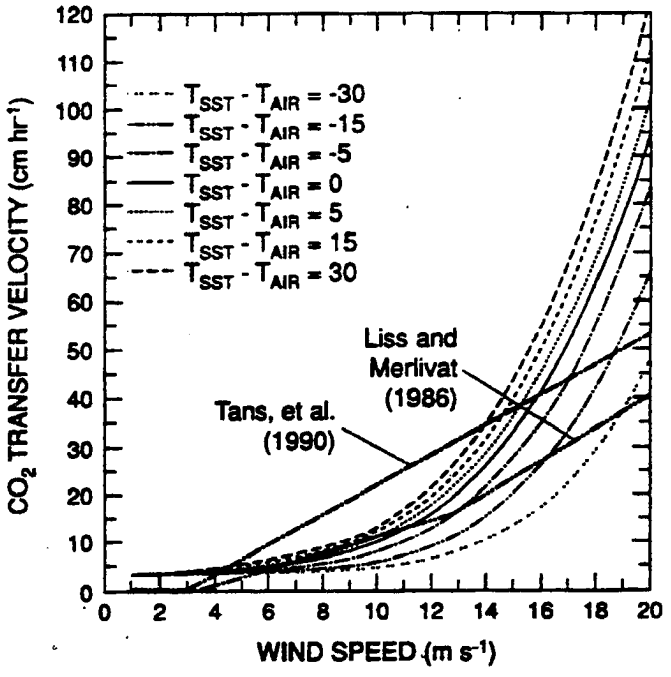

FIGURE 1.5: Dependence of the air-sea gas transfer coefficient C_T on wind speed as determined in three separate studies (Erickson, 1993).

bon dissolved in the water. A carbon "buffer factor" has been defined (Baes *et al.*, 1985) as

$$\beta \equiv \frac{\delta \ln p_{CO2}}{\delta \ln \Sigma CO_2}. \tag{1.17}$$

The value of this buffer factor (also known as the *Revelle factor*; Takahashi, 1979) in the surface oceans is about 10, meaning that doubling the concentration of atmospheric p_{CO2} would result in an increase of only 10 percent in the total concentration of carbon in the surface ocean.

1.4.2 Deep-Sea Circulation and Storage of Carbon

Having penetrated the air-sea interface, the question remains as to how CO_2 reaches the deep ocean. Because the ocean is warmed at its surface by solar heating, the water column is in most cases stably stratified, with a well-defined surface mixed-layer 30 to

100 meters thick overlying the main thermocline, and water in the deep ocean is essentially isolated from contact with the atmosphere for many decades or even centuries (Baes *et al.*, 1985; see Fig. 1.6).

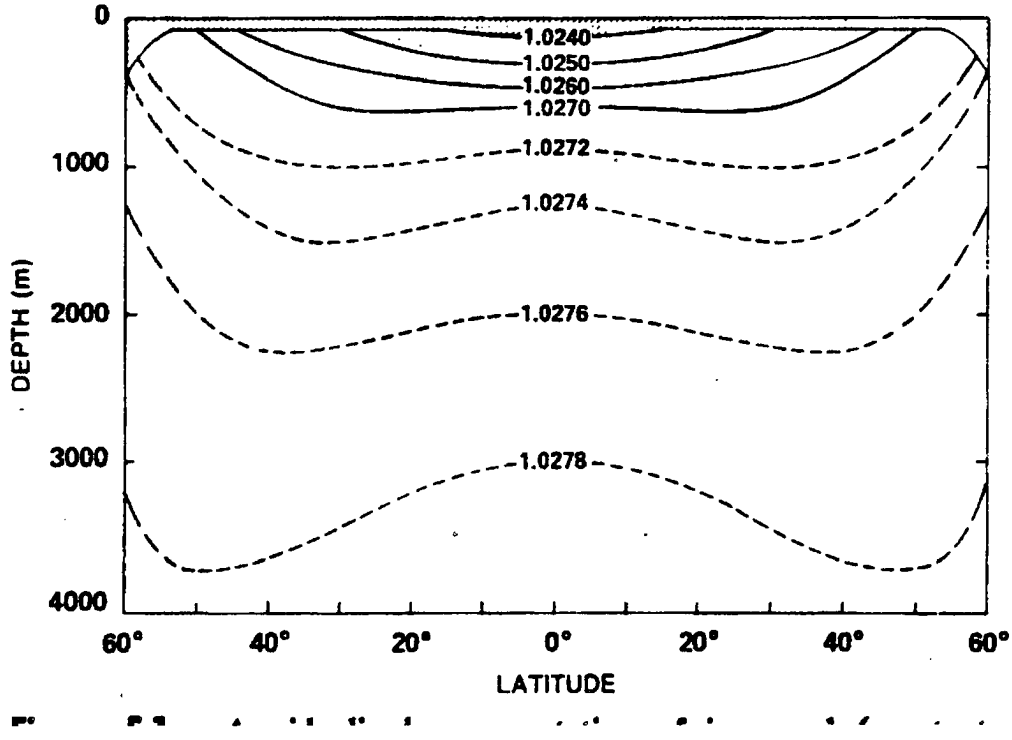

FIGURE 1.6: Idealized representation of the variation of density (in thousands of kg m^{-3}) with latitude and depth in the oceans (Baes *et al.*, 1985).

Some diffusion of CO_2 from the surface mixed layer through the thermocline and into the deep ocean occurs, but this process is extremely slow since turbulent transfer against the density gradient is very inefficient. There are at least three mechanisms by which CO_2 derived from the atmosphere can reach the deep ocean much more effectively. These are referred to as the "biological pump," the "solubility pump," and deep water formation in the high latitudes.

The biological pump consists of the transport of carbon downward by gravitational settling of particulate organic matter fixed by photosynthesis in the photic zone (Baes *et al.*, 1985; Archer, 1990; Rintoul, 1992). Marine microflora collectively known as phytoplankton create organic matter from dissolved CO_2 and other nutrients through photosynthesis (see section 1.3.3). When these organisms die, they begin to sink and

decompose, and the carbon, nitrogen, phosphorus, and other nutrients they contain are re-oxidized and returned to the dissolved nutrient pool of the mixed layer. Most of this material is rapidly recycled into organic compounds by biological uptake, but a small fraction (about 10 percent according to Archer, 1990) escapes through the base of the mixed layer into water too dark to support photosynthesis. Nearly all of the sinking organic particles are consumed by bacterial decomposition ("remineralized") in the deep ocean, so that ΣCO_2 in the deep ocean is about 10 percent higher than in the mixed layer (Rintoul, 1992), but a small fraction reach the bottom and are buried in the sediment (Schlesinger, 1991).

The term "solubility pump" describes the process by which CO_2 dissolves in the cold surface waters of the high-latitude oceans, and then moves along constant-density (*"isopycnal"*) surfaces to deeper water at lower latitudes (Baes *et al.*, 1985; see Fig. 1.6). Because of the much colder surface temperatures of the high latitude oceans, isopycnal surfaces exposed in those regions are those which are located much deeper in the midlatitudes and tropics. This phenomenon, in which the thermocline is located at the surface and exposed to the air in high latitudes is called "thermocline ventilation." Since cold water can dissolve much more CO_2 than warm water (see page 9, and the discussion in the previous section), CO_2 tends to penetrate the ocean surface in the high latitudes and then can diffuse downward from the base of the thermocline in lower latitudes after isopycnal mixing.

During winter, extremely cold air temperatures in the Arctic and Antarctic regions often cause sea-surface temperatures to drop to the freezing point. Under these conditions, the entire water column can become statically unstable, and deep convection can take place. This phenomenon is enhanced by the formation of sea ice, which excludes dissolved salts and thereby increases the salinity of the remaining water, making it even more dense. Sinking in high-latitude regions of deep convection is believed to be the principal source for the deep water of the world's oceans (Brown *et al.*, 1989), and because of the high solubility of CO_2 in very cold water, also represents an important mechanism for deep penetration of atmospheric CO_2. Regions of the oceans which are convectively neutral or unstable to great depths are often referred to as "polar outcrops" of deep ocean water (Siegenthaler and Oeschger, 1987; Post *et al.*, 1990).

Near the equator, on the other hand, climatological wind patterns produce divergent transport patterns in the ocean's mixed layer (Brown *et al.*, 1989). This surface divergence causes upwelling of cold deep water which was previously enriched in ΣCO_2 by

both sinking organic matter and the high-latitude processes discussed above. As this water warms near the surface, it becomes supersaturated with respect to CO_2. The equatorial oceans are therefore characterized by large-scale degassing of CO_2 into the air. In the absence of other sources and sinks, the oceans would therefore impose pole-to-equator gradient in atmospheric CO_2, and transport in the atmosphere would close the loop, carrying CO_2 from the outgassing areas in the tropics to the undersaturated waters in the high latitudes.

1.5 The Global Carbon Cycle

Since the atmosphere is the smallest major reservoir of carbon in the Earth system (see section 1.2), relatively minor fluxes between the other reservoirs could have a large impact on the atmospheric concentration of CO_2. Such inter-reservoir exchanges of carbon are large, but difficult to measure. Fluxes that are important on long time scales have essentially determined the basic partitioning of carbon into the major reservoirs discussed in section 1.2 above, but are not thought to vary significantly on the human time scale. These fluxes are discussed in section 1.5.1. Other fluxes are important on the interannual time scale, and are discussed in section 1.5.2.

1.5.1 Inter-reservoir Exchanges Over Geologic Time

Early in the history of the Earth, heat released by radioactive decay of elements in the interior caused a large-scale differentiation of the planet (Krauskopf, 1979), with the heaviest materials settling into a dense metallic core, and the lightest materials rising to form a thin crust of rock. At the same time, volatile compounds (mostly water vapor and CO_2) were released to form the early atmosphere. The early atmosphere was probably similar to gases that are today vented from the Earth's interior by volcanos, which are more than 90 percent water vapor, with 1 to 5 percent CO_2, and the remainder SO_2, H_2S, HCl, and N_2 (Schlesinger, 1991). When the atmosphere cooled below 100°C, the water must have condensed to form the oceans, into which the acidic sulfur and chlorine compounds would have readily dissolved. Some of the CO_2 would also have dissolved, according to the equilibrium in equation (1.1). As chemical weathering added soluble cations from the continents to the ocean (see section 1.3.2), carbonate sedimentation removed more and more dissolved carbon from the water. This process allowed the ocean to continue to remove atmospheric CO_2 over geologic time, probably more quickly after

the evolution of marine organisms which form $CaCO_3$ more efficiently than by chemical precipitation. The burial in marine sediments of organic matter formed by photosynthetic organisms has also progressively removed CO_2 from the atmosphere throughout the past several billion years.

During the early history of the Earth, the sun was less radiant by as much as 30 percent than it is today (Gough, 1981). Judging from calculations of radiant energy balance and the ice-albedo feedback (Budyko, 1969), this should have led to extremely cold surface temperatures and the freezing of all the water on the planet. There is clear geologic evidence, however, that liquid water has been present continuously since it first appeared about 3.8 billion years ago (Schlesinger, 1991). These apparently inconsistent observations have been called the "faint young sun paradox" (Sagan and Mullen, 1972). It has been suggested that enhanced downward infrared radiation from the early atmosphere with its very high CO_2 concentration was responsible for the relatively warm surface temperature of the early Earth, and that drawdown of CO_2 by carbonate sedimentation and biological processes has compensated for the increasing brightness of the sun throughout geologic history (Kasting *et al.*, 1988; Worsley and Nance, 1989).

On time scales of millions of years, the cycle of carbon in the Earth system is dominated by emissions of CO_2 from volcanic eruptions and vents, and the steady drawdown by formation of carbonate sediments (Fig. 1.7). Some of the carbon locked up in sedimentary rocks is released when ocean crust is subsumed back into the deeper Earth in a process known as "subduction," along some margins of the ocean basins. Some of the CO_2 in volcanic gases is derived from primordial volatiles in the Earth's interior, but much of it is thought to be "recycled" by the melting of sedimentary material which has been subducted.

1.5.2 Inter-reservoir Exchange on the Interannual Time Scale

On interannual to decadal time scales, the global carbon cycle is dominated by exchanges between the atmosphere and the ocean by the mechanisms described in section 1.4, with the impact of anthropogenic emissions seen in the secular trend (Fig. 1.1). Seasonally, the most significant fluxes are those driven by photosynthesis and respiration of the terrestrial biosphere as discussed in section 1.3.3. These fluxes are responsible for the observed seasonal cycle of CO_2 concentration in the northern hemisphere (Fig. 1.3).

The Carbon Cycle on the Geologic Time Scale

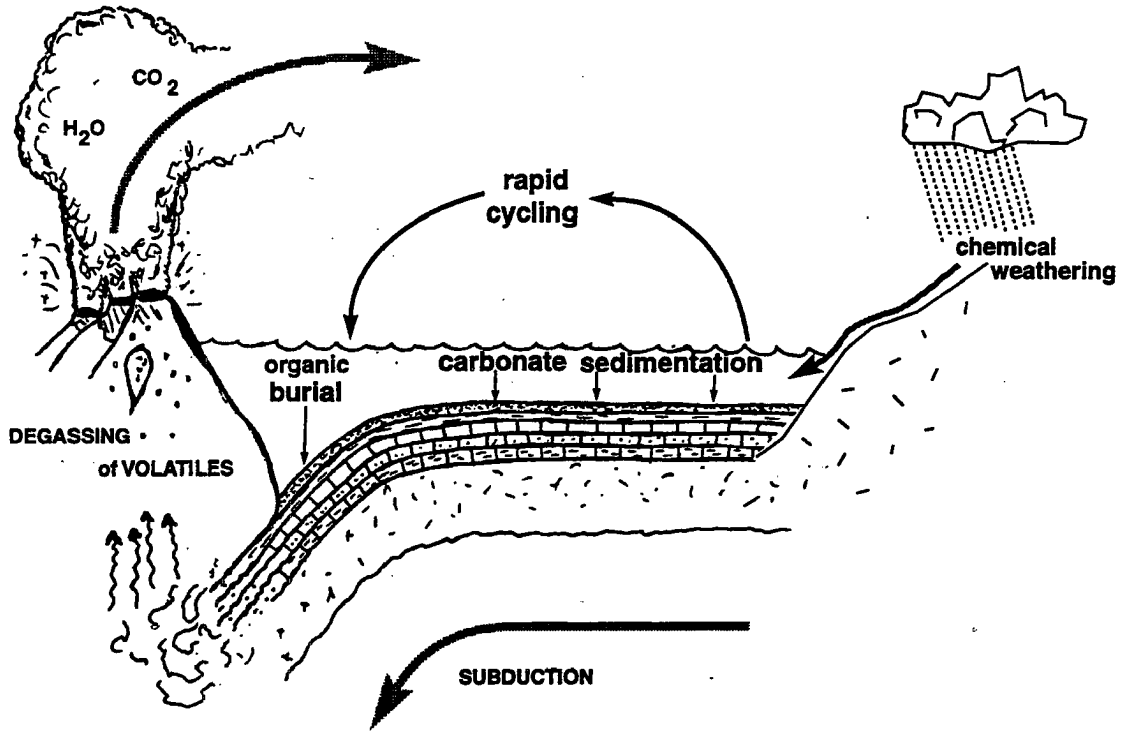

FIGURE 1.7: Over geologic time, the carbon cycle is a balance between sequestration in sedimentary rocks and degassing by volcanos.

Estimates of the pool sizes and fluxes which make up the global carbon cycle were reviewed by the Intergovernmental Panel on Climate Change (IPCC) of the World Meteorological Organization and the United Nations Environment Programme (Houghton *et al.*, 1990). This "consensus" view of these fluxes is presented in Fig. 1.8, but it should be emphasized that several key aspects of the carbon cycle are subject to significant disagreement in the scientific community. These disagreements are discussed in detail in sections 2.2 and 2.5 of Chapter 2.

Because it can be calculated from carefully-tabulated economic data, the flux of anthropogenic CO_2 due to industrial combustion and cement manufacture is the best-known exchange in the global carbon budget (*e.g.* Marland, 1989). This flux amounts to between about 6 Gt C yr^{-1}, with only minor seasonal variations. The atmospheric inventory of CO_2 annually increases by about 3 Gt, based on widely dispersed observations of background concentration (*e.g.*, Conway *et al.*, 1988), although the rate of increase is subject to significant interannual variability (Conway *et al.*, 1994).

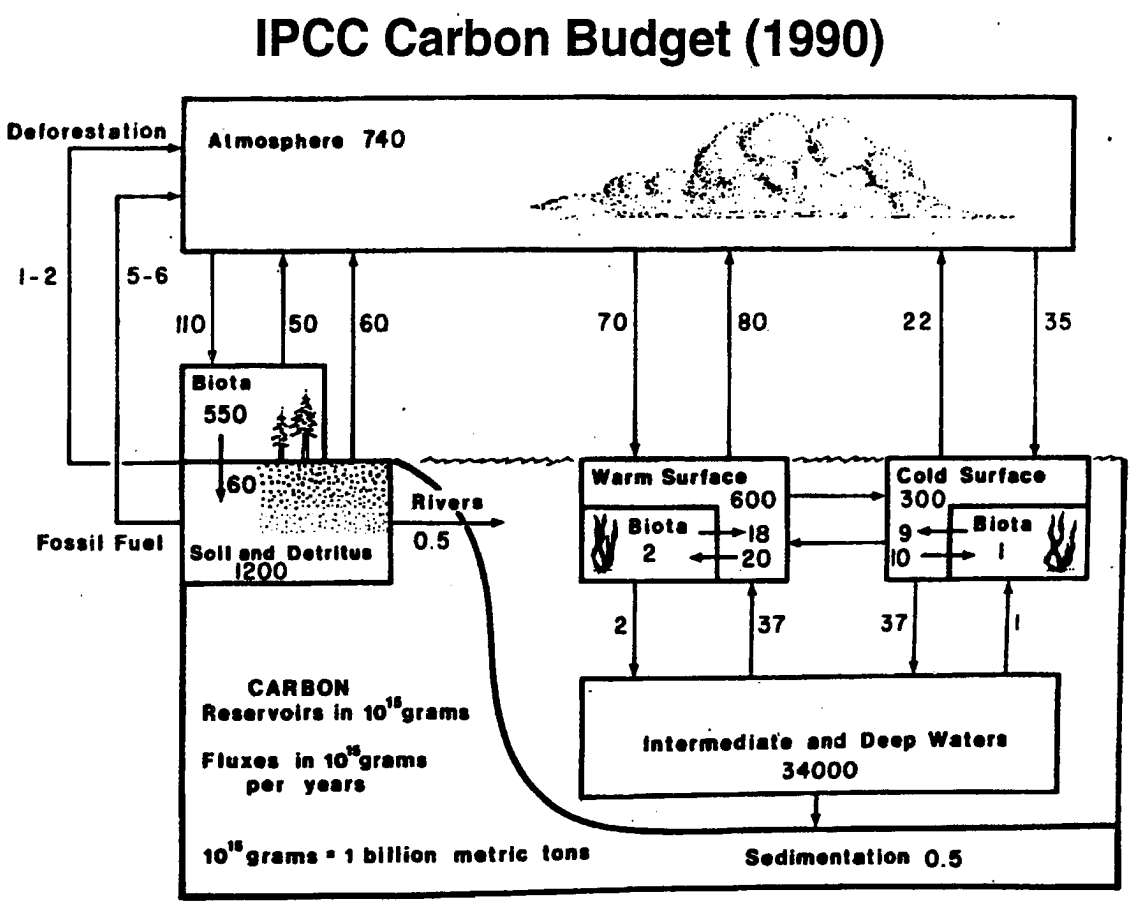

FIGURE 1.8: A "consensus" view of the global carbon budget on the interannual to decadal time scale. Reservoirs indicated in Gt of carbon, with fluxes in Gt C yr^{-1} indicated by arrows (Houghton *et al.*, 1990).

Estimates of GPP, NPP, and respiration made by ecologists have been extrapolated from field plots to ecosystems (*e.g.* Whittaker and Likens, 1975), and then to the globe using remote sensing and geographical information systems (Matthews, 1983). Each of these fluxes is more than an order of magnitude greater than the annual anthropogenic emissions, but largely cancel each other over the course of a year. Net primary productivity and heterotrophic respiration are each in the neighborhood of 60 Gt C yr^{-1}, but the uncertainty in these numbers is on the order of 10 Gt C yr^{-1} (Bolin and Fung, 1992), so a net gain or loss of carbon from the biosphere of the same order of magnitude as the industrial emissions is not ruled out. In fact, the IPCC budget includes an annual loss of one to two Gt C yr^{-1} from the terrestrial biosphere due to tropical deforestation which releases biospheric carbon faster than it can be replaced by growing forests. Some studies have found, however, that the terrestrial biosphere is currently acting as a net sink for as

much as 2 Gt C yr^{-1} (Keeling *et al.*, 1989*a*; TFT90), possibly due to increased photosynthesis in response to elevated atmospheric CO_2 concentration.

The IPCC budget calls for a net flux of 3.5 Gt C yr^{-1} into the ocean. Of this amount, 3 Gt is envisioned as dissolving in the surface ocean from the atmosphere and 0.5 Gt is added as dissolved carbon in river discharge. A loss of 0.5 Gt C yr^{-1} is calculated due to sedimentation. In the "warm" regions of the tropics and midlatitudes, an estimated annual uptake of 70 Gt is exceeded by estimated losses of 80 Gt due to equatorial upwelling. In the high-latitude oceans, the uptake of 35 Gt C yr^{-1} exceeds the annual efflux of 22 Gt because of the enhanced solubility of CO_2 at low temperatures and because of transport by bottom water formation, as discussed on page 19. All of these estimates are subject to uncertainties which are considerably larger than the difference between the estimated uptake and release of CO_2 (Bolin and Fung, 1992). The IPCC budget calls for a net accumulation of 3 Gt C yr^{-1} in the ocean, with 2.5 Gt added to the mixed layer and 0.5 Gt added to the deep ocean each year. These numbers are also subject to substantial disagreement among different researchers. Ocean modelers have calculated that at least 2 Gt C yr^{-1} is being transferred from the atmosphere to the ocean (Sarmiento *et al.*, 1992), but annual flux estimates based on observed p_{CO2} measured on oceanographic cruises are as low as 0.8 Gt C yr^{-1} (TFT90).

In summary, the only components of the annual carbon budget which are relatively well known are the anthropogenic emissions and the actual atmospheric increment. The IPCC budget shown in Fig. 1.8 gives a plausible picture of the general features of the inter-reservoir fluxes based on current estimates by various workers, but these are subject to large uncertainties. The uncertainties are a serious problem because the important parameters for understanding or estimating the future of atmospheric CO_2 concentrations are the relatively small net differences between the very large annual fluxes into and out of the atmosphere. It is interesting to note that the budget presented in Fig. 1.8 does not match the observed annual increment of about 3 Gt C yr^{-1}.

1.6 Isotope Biogeochemistry of Carbon

Carbon has two stable isotopes, carbon-12 (^{12}C) with six neutrons, which comprises about 98.89 percent of natural carbon, and carbon-13 (^{13}C) with seven neutrons. Carbon-14 (^{14}C) is a radioactive isotope which is naturally produced by cosmic rays from nitrogen in the upper atmosphere, and also by nuclear explosions (Degens, 1969; Faure,

1977). In the atmosphere, about 1.11 percent of the carbon atoms are ^{13}C, and 98.89 percent are ^{12}C. The unstable radioisotope ^{14}C comprises a negligible fraction of the total carbon, but is important because its radioactive decay with a half-life of 5730 yr (Faure, 1977) allows the age of organic material to be determined.

During photosynthesis, CO_2 molecules which contain the lighter ^{12}C atoms diffuse more readily into leaf cells containing chloroplasts. Also, the enzymes which facilitate the processing of CO_2 into organic carbohydrates have a greater affinity for the lighter $^{12}CO_2$ (Schlesinger, 1991). These two factors cause carbon which has undergone photosynthetic conversion from inorganic to organic to be depleted in ^{13}C relative to the atmosphere and to other carbon (Degens, 1969). Similarly, the reaction (1.10) by which $CaCO_3$ is formed from dissolved CO_2 in water discriminates between the two stable carbon isotopes, favoring the heavier ^{13}C.

By convention, the isotopic composition of any carbon sample is expressed as

$$\delta^{13}C \equiv \frac{(^{13}C/^{12}C)_{sample} - (^{13}C/^{12}C)_{standard}}{(^{13}C/^{12}C)_{standard}} (1000 \text{ per mil}), \qquad (1.18)$$

where the ratios are measured on the sample, and the standard most commonly used is referred to as "PDB," a fossil carbonate for which many measurements are available. The mean $\delta^{13}C$ ratio in terrestrial vegetation is about -27 per mil (Degens, 1969), because of the photosynthetic fractionation mentioned above. Ocean water has a $\delta^{13}C$ value of about 2 per mil (Keeling *et al.*, 1989*a*). Because the carbon contained in fossil fuels was derived by plants from atmospheric CO_2, its $\delta^{13}C$ value is very similar to that of vegetation. The atmosphere currently has a $\delta^{13}C$ ratio of about -7.8 per mil, and is decreasing at about 0.2 per mil per decade due to the addition of ^{13}C-depleted CO_2 from the combustion of fossil fuels and the destruction of terrestrial vegetation (Keeling *et al.*, 1989*a*).

1.7 Objectives of this Study

This study is intended to serve two fundamental purposes:

1) to investigate the surface fluxes and atmospheric transport of CO_2 in order to better understand the global carbon cycle, and

2) to serve as a building block for the integration of models of the atmosphere and the terrestrial biosphere, which will facilitate future work in elucidating the linkages between these components of the Earth system.

A central question in carbon cycle research involves the relative strengths of the various sinks of anthropogenic CO_2 in the Earth system. If the sinks are primarily in the oceans, then they can be expected to continue to sequester about the same fraction of emissions for centuries, due to the slow turnover of the deep ocean. On the other hand, some recent studies (Keeling *et al.*, 1989*a*; TFT90) have suggested that a large sink exists in the terrestrial biosphere. This idea – posed by global modelers seeking to balance the carbon budget – is controversial, with many biologists and ecologists skeptical that such a large sink can exist. It is quite uncertain where the sink is, how it works, or for how long it should be expected to function. If such a large biological sink exists and were to stop working (for instance, if enhanced plant productivity due to CO_2 fertilization were to stop upon encountering other limitations such as water or nutrients), the atmospheric CO_2 concentration would be expected to rise much more quickly than it is rising today.

Several approaches have been taken to solving this problem. Direct measurements of CO_2 flux at the Earth's surface have been made at many locations over many types of ecosystems and over the ocean. Unfortunately, surface CO_2 flux is extremely variable in both space and time, limiting the direct applicability of such measurements in balancing the global carbon budget. Monitoring programs now routinely collect and analyze samples of air from remote areas around the world for CO_2 concentration and stable isotope ratio (see section 2.3). Such studies offer the possibility of distinguishing between oceanic and terrestrial influences on concentration, and such analyses are underway. In order to avoid biasing the measurements by local contamination, however, nearly all the measurement sites are located on remote islands or in rural coastal areas and so sample only marine air. The terrestrial signal is still present in such data, but is quite dilute after thousands of kilometers of atmospheric transport. In recent years, several groups have used numerical

models of atmospheric transport to investigate the surface fluxes of CO_2. These studies are reviewed in considerable detail in section 2.4. By prescribing sources and sinks at the Earth's surface and then using the atmospheric model to simulate transport of the gas, different scenarios can be tested against observations.

Other studies have attempted to directly compute the distribution of sources and sinks from the atmospheric CO_2 observations by using "inverse" modeling techniques (Enting, 1985; Enting and Mansbridge, 1987*b*; Tans *et al.*, 1989; Enting and Mansbridge, 1989). Here the CO_2 concentration and the atmospheric transport are prescribed, and the surface fluxes are computed using an iterative technique that enforces consistency between the simulated transport and the time-varying surface concentrations. This technique is only practical for application in a two-dimensional representation of the global atmosphere. It cannot distinguish the nature of a source or sink, but rather deduces only the magnitude of the fluxes in different latitude zones.

In the present study, a hybrid of the two modeling approaches will be used. Starting from a globally uniform CO_2 distribution, prescribed distributions of sources and sinks will be applied, and atmospheric transport of CO_2 will be simulated using a full three-dimensional atmospheric general circulation model (GCM). After the simulation has reached equilibrium with the surface fluxes, some of the most problematic aspects of the surface flux distributions will be calculated by comparison with observations.

The use of the full GCM (see section 3.4.2), with its short time step and detailed representation of vertical transports due to cumulus convection (see section 3.4.5) allows a more detailed examination of geographic and temporal changes in CO_2 than has been previously performed. By applying methods similar to those used by TFT90, estimates of the geographic and seasonal distributions of the surface fluxes will be constrained by the circulation simulated by the GCM.

The simulation performed in this study will require the implementation of CO_2 as a prognostic variable in the GCM. This will pave the way for future studies in which surface fluxes of CO_2 can be directly modeled at the land surface, using the new parameterization of Sellers *et al.* (1993). The disadvantage of performing such an "inversion" study with the full GCM is of course that the model is computationally expensive to run. Unlike TFT90, I was unable to perform multiple simulations to test different scenarios of sources and sinks, but carefully chose distributions of the surface fluxes before the simulation to maximize the amount of information that could be obtained from the results.

CHAPTER 2

A Review of Previous Work in Carbon Cycle Research

This chapter presents a chronological review of the development of our present understanding of the carbon cycle. Section 2.1 reviews some of the early studies of the carbon cycle. Speculations on the role of carbon dioxide in determining the Earth's climate date back to the middle of the 19th century (Tyndall, 1861). There were attempts to document the concentration of atmospheric CO_2 over the following century, but the modern era of carbon cycle research began with the advent of continuous measurement of CO_2 concentration at several sites during the International Geophysical Year (1957) by C. D. Keeling. These observations quickly led to the discovery and documentation of the secular trend, seasonal cycle, geographic patterns, and interannual variability in CO_2 concentration as frequent and reliable data became available from a growing network of stations around the world. Some early attempts to construct a global budget of atmospheric carbon predate the first regular measurement programs in the late 1950's, but this work really took off in the 1960's and early 1970's as one-dimensional box models of atmospheric mixing and carbon uptake by the oceans were applied to the observational data.

In the mid-1970's, a growing controversy developed in the literature as geochemists and oceanographers were unable to account for the large amounts of carbon which ecologists believed were being released from the biosphere as a result of changing land use patterns. This controversy raged for more than a decade, and is the subject of section 2.2. Ecologists used "bookkeeping" models of carbon allocation following major landscape disturbance, driven with historical data, to reconstruct a history of large releases of carbon from the biosphere during the past two centuries. Geochemists continued to refine the one-dimensional models of carbon diffusion into the ocean, but could not reconcile their results with those of the ecological modelers and balance the global budget. This round of the controversy was largely settled in the mid-1980's when reliable data on the history of atmospheric CO_2 concentrations became available through the analysis of air

trapped in bubbles in Antarctic ice, but the debate about the role of the biosphere has heated up again in the last few years.

Starting with the continuous measuring stations started by Keeling in the 1950's, regular, high-precision measurement programs were instituted at a growing number of sites around the world. By the 1980's at least three groups were maintaining networks of such observational sites with good latitudinal coverage of the globe. Section 2.3 discusses these observational networks, their methods, geographic distributions, and some of their results.

The high quality, global distribution, and easy availability of measurements of the concentration and isotopic composition of atmospheric CO_2 allowed them to be used to quantitatively constrain the sources and sinks in time and space, given a knowledge of the detailed behavior of atmospheric transport. Section 2.4 outlines the development of two-dimensional and three-dimensional transport models which were used for this purpose. Since these studies form the direct intellectual background of my work, I review several of these papers in depth, presenting the model formulations and surface flux data used to drive the simulated carbon cycle. In particular, my review focuses on the work of Dr. Inez Fung and her colleagues at the Goddard Institute for Space Studies (GISS) of the National Aeronautic and Space Administration (NASA), since they provided direct guidance and surface flux data for the present study.

In the last few years, the relative roles of the biosphere and ocean in the global carbon budget have again been the subject of intense disagreement, which has reopened the earlier controversy to some extent. This current debate is reviewed in section 2.5. Observational and modeling work in the late 1980's suggested the existence of a terrestrial sink for atmospheric CO_2 in the middle and high latitudes of the northern hemisphere. TFT90 invigorated the debate by suggesting on the basis of shipboard observations that the ocean uptake must be much smaller than had been estimated by earlier studies. This meant that the terrestrial sink in the northern hemisphere must be much larger than previously estimated in order to match the observed interhemispheric concentration gradient and annual increase in global mean concentration. Since that time, a lively discussion of these issues has dominated the carbon cycle literature, with biologists, ecologists, geochemists, oceanographers, and meteorologists contributing to an exciting and interdisciplinary debate. The present study is meant to enter into this debate, and the central questions raised by TFT90 are those which I most want to address.

2.1 Early Observations and Interpretations

Attempts to measure the concentration of CO_2 in the atmosphere go back more than 100 years, but much of the early work suffered from a lack of standardized analytical techniques and geographically unrepresentative samples. It has been known for centuries that CO_2 is released into the atmosphere by nearly all combustion, and by biological respiration. On the basis of laboratory measurements of absorption of radiation by gases, Tyndall (1861) suggested that CO_2 must act as a greenhouse gas (the greenhouse analogy was first used by Fourier, 1827), and that variations in atmospheric CO_2 and water vapor could explain the climate changes associated with the ice ages. Others focused on the dominant effect of absorption by water vapor, but interest in CO_2-induced climate change persisted in the late 19th century, especially in the work of Arrhenius (1896) and Chamberlain (1897). This interest motivated much of the early work in measuring the concentration of atmospheric CO_2. Some of these early measurements were reviewed by Callendar (1940, 1958), and have been recently reevaluated by Fraser *et al.* (1986).

Early measurements of CO_2 concentration in air were made by acidimetric titration of water through which air had been bubbled. Most of the early measurement programs were conducted in Europe. Callendar (1940) states that the earliest attempts to measure the partial pressure of CO_2 in air were made in the mid-18th century, but that the earliest accurate measurements were made by Thorpe (1867). Schultze (1871) measured CO_2 concentration near Rostok, Germany, and reported some dependence of concentration on wind direction. Reiset (1882) documented differences in concentration according to the wind direction and the diurnal cycle, and speculated about a seasonal cycle and secular trend. Muntz and Aubin (1886) developed a new method by which CO_2 was absorbed onto pumice containing potassium hydroxide. This technique was more accurate than the earlier method (the authors claimed 1% accuracy), and the sampling apparatus was portable. This allowed estimates of CO_2 concentration to be made for Central and South America, as well as many locations in Europe. Petermann and Graftiau (1892) made more than 500 measurements of CO_2 in Belgium between 1889 and 1891. Letts and Blake (1900) measured CO_2 concentrations in northern Ireland. They also reviewed most of the previous work in this field, including descriptions of the experimental apparatus and analytical techniques used by others (their paper contains over 300 references). Brown and Escombe (1905) used an improved wet titration technique to measure CO_2 concentrations to the west of London between 1898 and 1901, and found that concentrations were significantly higher when the wind blew from the east, reflecting the urban influence.

Callendar (1938) reviewed some of these the early observations, choosing those which he considered most "reliable" and, by comparing them to the contemporary measurements of Haldane (1936), argued that a secular trend was present in the data. He suggested that the increase was due to the combustion of fossil fuels. He analyzed temperature records from stations around the globe, and concluded that the CO_2-induced warming was already underway. He further documented (Callendar, 1940) the secular trend by a more thorough analysis of earlier measurements, and by a comparison to the measurement program reported by Buch (1939). He attributed the seasonal variability of CO_2 concentrations to the activity of the terrestrial biota, and suggested that the lower concentrations in polar regions were evidence of temperature-dependent uptake of CO_2 by the surface of the ocean (see section 1.4.1). On the basis of temperature records from sixteen rural weather stations, he calculated that fossil fuel CO_2 was responsible for a rise in the global-mean surface temperature of 0.2 K, and suggested on the basis of radiative flux calculations that a doubling of atmospheric CO_2 would lead to a mean global warming of 1.5 K. He estimated that 75 percent of the CO_2 emitted by fossil fuel combustion remained in the atmosphere, with the remainder dissolved in the oceans.

Analytical methods for the determination of the isotopic composition of carbon were developed by Nier and Gulbransen (1939) and Nier (1947). By the mid-1950's, the isotopic fractionation of carbon by various physical and biological processes (see section 1.6) had been documented by Craig (1953), and the use of ^{14}C activity to determine the age of organic materials had been established by Libby (1955). This work laid the foundations for the later use of carbon isotope geochemistry to elucidate various aspects of the global carbon cycle.

In the mid-1950's, some work on the global cycle of carbon had already begun, although very few reliable data were available on concentrations at that time. Plass (1953, 1956) speculated on the details of CO_2-induced climate change, and elucidated the mechanisms for carbon exchange between the atmosphere and ocean. Eriksson and Welander (1956) developed a simple box model of the carbon cycle involving exchanges between the atmosphere, ocean, and biosphere (through photosynthesis, respiration, and decay), and explored various scenarios which could lead to large shifts in the concentration of atmospheric CO_2. Craig (1957) and Revelle and Suess (1957) used the apparent ^{14}C age of dissolved carbon and organic material in the oceans to estimate the rate of exchange of carbon between the atmosphere and the sea. They calculated by two independent methods that the average residence time of a molecule of CO_2 in the atmosphere is about seven years. They estimated the average rate of ocean uptake of CO_2 to be about 2×10^{-3}

moles cm^{-2} yr^{-1} (about 90 Gt C yr^{-1}, which is consistent with the best current estimates of gross carbon flux into the world oceans, although this figure is mostly balanced by degassing in upwelling regions, as discussed in section 1.4.1). These authors also estimated that the average lifetime of carbon in the deep ocean was not more than 500 years.

New analytical techniques were developed in the mid-1950's for the determination of atmospheric CO_2 concentration with enough precision for detailed analysis of temporal trends and geographic patterns. Earlier measurements were subject to rather large analytical uncertainty and poor standardization. The new technique measured the CO_2 in the air directly with an infrared gas analyzer (Smith, 1953), which could be calibrated with a reference gas used for many samples. Continuous monitoring of atmospheric CO_2 using the new technique was begun by Keeling (1958, 1960) in 1957 at the South Pole and in 1958 at Mauna Loa, Hawaii, as part of the International Geophysical Year (IGY) research program. This marked the beginning of the modern era of carbon cycle research, since concentration data were collected by standardized methods and could be rigorously compared in both time and space.

By the early 1960's, the secular trend, seasonal cycle, and meridional gradient in both the concentration and isotopic composition of atmospheric CO_2 were well established. Keeling (1960) documented the year-to-year increase in concentration in Hawaii and Antarctica. He also reported on the seasonal cycle of CO_2 concentration and isotopic composition, noted the greater amplitude and shift in phase of this oscillation from south to north, and attributed the oscillation to the seasonal growth and decay of the terrestrial biosphere. Bolin and Keeling (1963) used measurements of CO_2 in air collected in flasks on ocean cruises in the Pacific to investigate the meridional transport of the gas by large-scale atmospheric eddies. Their data firmly established the meridional profile of CO_2 concentration, and the changes in seasonality from north to south. Using a simple interhemispheric mixing model, they estimated the overall eddy diffusivity of the atmosphere, and the seasonal drawdown of CO_2 by the terrestrial biosphere in the northern hemisphere. Analysis of air samples collected by airplane flights established the vertical profiles of CO_2 concentration and the action of the tropopause as a barrier to vertical mixing (Bischof, 1965; Bischof and Bolin, 1966). Airplane sampling also documented the general horizontal homogeneity of CO_2 concentration along latitude circles above the planetary boundary layer (PBL), and the role of transient weather systems in meridional mixing (Keeling *et al.*, 1968).

About this time, serious attempts at estimating the surface fluxes responsible for the observed seasonal fluctuations and secular trend in atmospheric CO_2 constituted the first observationally-constrained global carbon budgets. Junge and Czeplak (1968) analyzed the seasonal and meridional patterns of atmospheric concentration and transport of CO_2, and made quantitative estimates of the contributions of anthropogenic emissions, seasonality in the rate of ocean uptake, and the terrestrial biosphere to the observed seasonal and meridional patterns. They concluded that the seasonal cycle was driven almost entirely by the biosphere, and that the inverse problem of diagnosing the latitude-dependent eddy diffusivity of the atmosphere from CO_2 observations was intractable. Bolin and Bischof (1970) estimated that only about one third of the CO_2 released as industrial emissions remained in the atmosphere, with about half of the emissions being absorbed by the oceans, and the remainder being sequestered in the terrestrial biosphere as a result of the CO_2 "fertilization" effect. They noted that their estimates suggested very rapid transfer of CO_2 across the surface of the ocean, and that the slow rate of transfer between the surface layers and deeper ocean represents the most significant barrier to carbon storage.

Better estimates of the fossil fuel emission rate were made by Keeling (1973*a*) and Rotty (1973), who used economic data collected by the United Nations. Using these new estimates, Keeling (1973*b*) calculated that the terrestrial biosphere must have increased in mass by about 4% since preindustrial times. The question of the rate of carbon penetration into the deep ocean was investigated by Oeschger *et al.* (1975), who developed a one-dimensional box-diffusion model of the world ocean. In contrast to previous models, they did not treat the deep ocean as a single, well-mixed box, but rather as a series of boxes through which the penetration of CO_2 was determined by eddy diffusion.Their model was calibrated by the observed profiles of natural radiocarbon and verified using observed penetration of ^{14}C produced during the atmospheric nuclear weapons tests in the 1950's and 1960's. Their results supported a somewhat more efficient oceanic uptake than in previous studies, but they still argued for a small sink of atmospheric carbon in the terrestrial biosphere to balance the global budget.

In the mid-1970's interannual variability in the seasonal oscillation and annual increase of CO_2 was investigated by several studies. Hall *et al.* (1975) subtracted the secular trend from the Keeling's Mauna Loa record, and derived annual net hemispheric photosynthesis and net hemispheric respiration curves from the residual. These curves, they argued, provided an index of the metabolic activity of the global terrestrial biosphere. These authors argued that the small interannual variations in the record did not support either a large source or sink for atmospheric carbon in the terrestrial vegetation.

Bacastow (1976) showed that interannual variability in the observed CO_2 record was correlated with the southern oscillation index (SOI), and argued that perturbations to the upwelling of deep water in the equatorial Pacific during El Niño events caused significant reductions in the rate of uptake of CO_2 by the oceans. Keeling *et al.* (1976 *a*, *b*) also reported interannual variability in concentrations at both Mauna Loa and the South Pole, which they also ascribed to changes in the rate of oceanic uptake.

2.2 Geochemists *vs.* Ecologists: Controversy Regarding Biospheric Carbon Emissions

The concept of the global carbon budget that had emerged by the mid-1970's was one in which fossil fuel emissions of CO_2 to the atmosphere were about halfway compensated by absorption into the oceans, with a small amount of carbon also being sequestered in the terrestrial biosphere. This concept was challenged by Bolin (1977). He proposed that rather than being a sink for anthropogenic carbon, the biosphere was actually losing carbon at a rate comparable to the burning of fossil fuels as forests were cut and natural ecosystems were converted to agricultural production. Thus began a period of lively controversy which dominated the carbon cycle literature for the next decade and has been resurrected in the past few years. Broecker *et al.* (1979) refuted Bolin's proposed biospheric carbon loss by analyzing the uncertainty of model estimates of oceanic uptake. They concluded that the estimates were sufficiently firm that large emissions of CO_2 from the biosphere could not be accounted for in either the atmosphere or the ocean. The debate between the ecologists and geochemical modelers was summarized by Hobbie *et al.* (1984).

Ecologists attempted to resolve this question using "bookkeeping" models of carbon reservoirs in which emissions due to changing land use patterns could be reconstructed from historical records (Houghton *et al.*, 1983; Schlesinger, 1984; Emanuel *et al.*, 1984; Houghton *et al.*, 1987). In the pioneering study of this type by Houghton *et al.* (1983), the land areas of the world were divided into 69 regional ecosystems. This was done using a classification scheme including 14 "biomes" or vegetation classes (*e.g.*, tropical moist forest, temperate grassland, boreal forest, desert scrub, *etc.*). Literature values were used to estimate the total carbon storage per unit area in each biome. A response function

was developed to predict the time-history of the change in carbon storage when a given biome was converted to another through land use changes (for instance, conversion of tropical forest to grassland had a certain response curve, and conversion of temperate grassland to irrigated cropland had another). These response curves described changes in carbon storage of both vegetation and soils. Some of the changes (*e.g.*, irrigation of desert scrub for agriculture) involved a net increase in carbon storage, and some changes were only temporary (*e.g.*, harvest and regrowth of temperate forests for timber production).

The land area of each biome in 1700 was estimated from literature values and historical sources as an initial condition for the model, assuming that the world's terrestrial ecosystems were at steady state with respect to carbon storage at that time. Historical, economic, and agricultural records were then used to "time-step" through the changes in land use and resulting changes in global carbon storage of the world's terrestrial ecosystems over the following 280 years. The model was thus actually a historical reconstruction of carbon storage, rather than a process-based explicit calculation of carbon changes due to respiration and photosynthesis.

The model was run using three different scenarios of land-use change derived from historical records. A "low estimate," based on a data compilation by the United Nations' Food and Agricultural Organization, calculated a total release of 184 Gt of carbon since 1860. Using these input data, the model estimated releases of about 1 Gt C yr^{-1} in the 19th and early 20th century, followed by a peak in emissions of about 3.5 Gt C yr^{-1} around 1950, and then a slow decline to about 1.8 Gt C yr^{-1} in 1980. A "high estimate" of carbon release included more recent estimates of tropical deforestation rates (Myers, 1980) in the input data. This run produced almost the same total long-term carbon release (184 Gt) as the run driven by the FAO data, but the recent emissions were very different. Using these deforestation rates, the authors estimated a release of 4.7 Gt C yr^{-1} from the terrestrial biosphere in 1980, nearly as much as the global emissions from fuel combustion. In the third scenario, the authors assumed that since 1950, conversion of tropical forests to agricultural lands has been proportional to the population of the tropical regions of the world. In this scenario, the total release of biospheric carbon since 1860 was 180 Gt, with 2.6 Gt C yr^{-1} released in 1980.

In all three scenarios, these authors found that forests in the middle and high latitudes of the northern hemisphere have been accumulating carbon in recent decades, but not fast enough to offset the enormous losses from the tropics. The total net losses from the

biosphere since the industrial revolution was estimated to be equal to or greater than the accumulated emissions of fossil carbon due to industrial activity. The authors acknowledged the discrepancy between their results and those of ocean modelers, suggesting that perhaps their low estimates might be reconciled with the highest estimates of ocean uptake then in use. They noted that their results were quite sensitive to the characterization of the "undisturbed" ecosystems being replaced by agricultural lands, and that the historical records contained significant uncertainty in this respect. They also pointed out that much of the area which underwent land use change in the past two centuries was very heterogeneous, and that their model had unrealistically treated these areas as large homogeneous blocks. Since the carbon storage estimates and response functions they used in the model were developed for small field plots, there is some question as to the applicability of these data to regional and global scales.

Siegenthaler (1983) developed a modified model of oceanic carbon uptake, based on the work of Oeschger *et al.* (1975), but which included faster penetration into a high-latitude "outcrop" of cold thermocline waters. Ventilation of the thermocline allows faster penetration of CO_2 into the deep ocean because of the enhanced solubility at low temperatures, and because transport is rapid along constant-density (isopycnal) surfaces (see section 1.4.2). Even the faster uptake of anthropogenic CO_2 by this new "outcrop-diffusion" model could not account for the large biospheric releases proposed by the ecologists, however.

The question of large emissions of carbon from the biosphere was largely settled by the publication of data on CO_2 concentrations in air trapped in Antarctic ice cores (Neftel, 1985; Pearman *et al.*, 1986), which showed that the preindustrial concentration of CO_2 was about 280 ppm. The history of CO_2 concentrations in the atmosphere as preserved in the ice cores could be directly compared with the concentrations predicted by the ecological reconstructions of Houghton *et al.* (1983) and others.

Siegenthaler and Oeschger (1987) used box-diffusion and outcrop-diffusion models of ocean uptake to reconstruct the past 200 years of emissions of CO_2 from the biosphere by "deconvolution" of the ice-core CO_2 record. Ocean uptake as predicted by the ocean model was subtracted from the observed time series of CO_2 concentration in the ice core data, resulting in independent estimates of biospheric release. They concluded that although significant biospheric carbon loss had indeed taken place during the 19th and early 20th centuries, the global biosphere was currently either a very small source or even a net sink for atmospheric CO_2.

Using the ice core data of Neftel *et al.* (1986), Enting and Mansbridge (1987) showed that the estimates of biospheric carbon release made by the bookkeeping methods of Houghton *et al.* (1983) were incompatible with any linear, time-invariant model of ocean uptake. Enting and Pearman (1987) used a one-dimensional carbon cycle model calibrated by constrained inversion of observations (see section 2.4) to estimate the contribution of CO_2 from the biosphere. They concluded that the net release was currently small or even negative.

2.3 Observational Monitoring of Atmospheric CO_2 Concentration

Continuous monitoring of CO_2 concentration in air using a nondispersive infrared gas analyzer was begun by C. D. Keeling at the South Pole in 1957 and at the Mauna Loa Observatory, Hawaii in 1958 (Keeling, 1960; see section 2.1). The analytical technique involves comparison of the sample gas to a reference gas (usually CO_2 in pure nitrogen) in which the concentration (mole fraction) of CO_2 is supposedly well known. The reference gases used by Keeling and his colleagues were calibrated repeatedly against "semi-permanent" reference gases at Scripps Institute of Oceanography (SIO) of the University of California. The mole fraction of CO_2 in these semi-permanent gases was determined at regular intervals by a "manometric" technique in which the CO_2 was extracted from the carrier gas (again, usually nitrogen) by freezing, and then the pressure of the pure CO_2 was measured. Over the years, the reference gases were used up, and new standard mixtures were made, always with exhaustive intercomparisons between the two reference gases to establish the standard mole fraction. These procedures have been described in detail by Pales and Keeling (1965) and Keeling *et al.* (1976*a*, *b*).

By the mid-1980's there were at least three long-term monitoring programs in place in which high-frequency (approximately weekly) samples of air were analyzed for CO_2 concentration by standardized methods on infrared analyzers calibrated with reference gases traceable to the SIO standards. These programs included the original SIO program, expanded to about ten sites in the Pacific; a flask sampling program administered by the Commonwealth Scientific and Industrial Research Organization (CSIRO) in Australia, with five sites in the southern hemisphere; and the flask sampling network of the U.S. National Oceanic and Atmospheric Administration (NOAA) Geophysical Monitoring for

Climatic Change (GMCC) program, with more than 20 stations around the world. All these programs selected sampling sites with the intention that air collected for analysis represent "background" conditions, free from local "contamination" due to industrial or urban influences, biological activity or volcanic activity. Most of the sites were therefore located on remote islands, mountain tops, or windward coasts in rural areas. Flask sampling protocol required the operator to hold his or her breath while sampling, and to collect the sample when the wind was onshore. Comparability of the data was assured by using a limited number of instruments to analyze all the flask samples, calibrating the instruments using the SIO standard gases, and frequent laboratory intercomparison studies. Since the CO_2 concentration in rural air was known to decrease systematically from north to south, an effort was made to place sampling stations at as many latitudes as possible, within the constraints mentioned above. Concentration data were made available by all three laboratories, and were the subject of many analyses in the 1980's.

Several groups tried to use the observational record to sort out the relative roles of fossil fuel emissions, land use change, ocean uptake, and biospheric fertilization in the carbon budget. Pearman and Hyson (1981) showed that the amplitude of the seasonal cycle of CO_2 concentration at several measuring sites had increased significantly during the period of record, and speculated that this might indicate the terrestrial biosphere of the northern hemisphere was growing. The increasing amplitude of the seasonal cycle was also noted by Cleveland *et al.* (1983), Komhyr *et al.* (1985), Bacastow *et al.* (1985), and Thompson *et al.* (1986). The latter paper also found that the interannual variations in the growth rate of atmospheric CO_2, although closely correlated with the El Niño-Southern Oscillation phenomenon, could not be explained solely on the basis of sea surface temperature anomalies in the Pacific. They suggested that a related perturbation of tropical terrestrial biosphere (possibly due to altered precipitation patterns) was responsible for the interannual variability in the CO_2 concentrations.

Hall *et al.* (1993) noted that the change in amplitude of the seasonal cycle has not been constant through time, but was particularly strong in the 1970's and particularly weak in the 1980's. They also estimated that the changes in the global rate of photosynthesis have been nearly exactly compensated by changes in global respiration, so that a net change in the mass of the biosphere is not indicated by the changing amplitude of the seasonal cycle of atmospheric CO_2.

Keeling and Heimann (1986) compared the meridional distribution of mean annual atmospheric CO_2 concentration in 1962 to that in 1980, and analyzed the difference with a

one-dimensional meridional eddy diffusion model. They concluded that the difference was almost entirely due to the combustion of fossil fuels. Subtracting this effect, they suggested that the residual indicated a source of carbon to the atmosphere in the deep tropics (due to deforestation, the tropical ocean, or some combination), coupled through poleward transport to a sink of the same magnitude in the middle latitudes.

An analysis by Conway *et al.* (1988) of the data collected at 22 NOAA-GMCC flask stations confirmed that the annual mean concentrations both globally and station-by-station exhibited interannual variability related to the El Niño-Southern Oscillation phenomenon. They also found that, in contrast to earlier work, there was no statistically significant trend or interannual variability in the phase or amplitude of the seasonal cycle.

In the most exhaustive analysis of observational CO_2 data to date, Keeling *et al.* (1989*a*) analyzed records of concentration and stable isotopic composition of CO_2 from ten SIO stations spanning the north-south extent of the Pacific over more than 30 years. They decomposed each record into an annually fluctuating period, longer term variations, and remaining "noise," and examined trends, geographic patterns, and interannual variability.

The stable isotope ratio, $\delta^{13}C$ (see section 1.6) was found to exhibit a seasonal oscillation in phase with that of CO_2 concentration, as had been reported in earlier studies. These seasonal fluctuations in $\delta^{13}C$ were analyzed in terms of mixing of two components of different isotopic compositions, and the seasonal component was found to have $\delta^{13}C$ consistent with biological exchange. This relationship was strongest in the middle to high latitudes of the northern hemisphere, with some of the seasonal variation in CO_2 concentration in the tropics and southern hemisphere probably not due to biological activity. Since $\delta^{13}C$ is very little affected when CO_2 is exchanged between the air and the ocean, seasonal air-sea exchange was hypothesized to cause much of the seasonal behavior in those regions. A weak seasonal cycle in $\delta^{13}C$ in Antarctica was documented, with the most negative values in the austral spring, suggesting that the seasonal variations in CO_2 concentration at high southern latitudes were driven by the seasonal southern biosphere rather than representing transport of the northern hemisphere signal. The increasing amplitude of the seasonal cycle was confirmed, but was found to have stabilized since reaching a maximum in the early 1980's.

After subtracting the seasonal cycle from the station data, meridional profiles were constructed for each year for which data were available (see Fig. 2.1). A peak in concen-

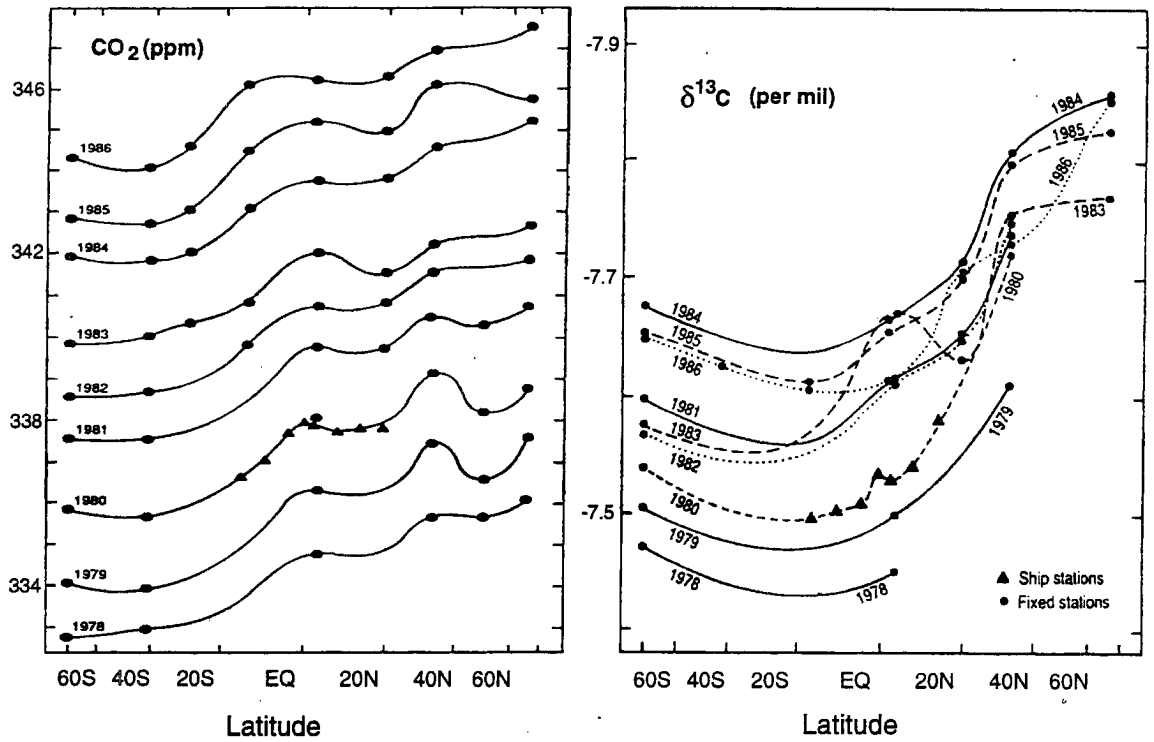

FIGURE 2.1: Meridional profiles of concentration and stable isotope ratio of atmospheric CO_2, 1978 through 1986 (Keeling *et al.*, 1989*a*).

tration in the tropics was superimposed upon the general north-south gradient in every year, but this peak was not present in the isotope profiles except in 1983. The concentration profiles increased smoothly by about 1.5 ppm yr^{-1}, presumably due to emissions from fossil fuel combustion, but the $\delta^{13}C$ profiles show nearly constant values from 1981 to 1983 except for the aforementioned anomaly in the tropics in 1983. After 1983, concentrations and $\delta^{13}C$ rose synchronously again. The authors attributed these anomalies in $\delta^{13}C$ to perturbations of the global carbon cycle associated with the strong El Niño event in 1982-83. The interannual variability in the rate of decrease of $\delta^{13}C$ was greater than could be accounted for by variable consumption of fossil fuels, and strongly suggested a large release of carbon from the tropical terrestrial biosphere. The seasonal cycle and fossil fuel contributions were subtracted from the CO_2 concentration records, and the resulting time series of "anomaly" CO_2 were compared to the southern oscillation index. Peaks in anomaly CO_2 at Mauna Loa were found to correlate very well with weak Indian summer monsoons during or immediately after the onset of every El Niño warm event since 1957. Based on the isotope results, the authors attributed the anomalous fluxes of CO_2 to reduced photosynthetic activity in southeast Asia during weak summer monsoons. In the 1982-83 El Niño, however, the magnitude of the concentration in

crease was not consistent with the change in $\delta^{13}C$, and suggested reduced CO_2 flux out of the tropical ocean at the same time. Oceanographic records indicate that equatorial upwelling in the eastern Pacific was nearly shut down during this strong event, and that p_{CO2} in these surface waters was far below normal. The authors argued that the response of the global carbon cycle to the 1982-83 El Niño involved large opposing perturbations – reduced photosynthetic uptake in drought-stricken Asia, partly compensated by a reduced flux out of the tropical oceans.

Although the combined time series of $\delta^{13}C$ and CO_2 provides tantalizing clues about large compensating effects in the marine and terrestrial components of the carbon cycle, other authors have not drawn these conclusions (Francey, 1985; Francey *et al.*, 1990; P. Tans, personal communication). Because the interannual differences in $\delta^{13}C$ are close to the overall measurement precision of the data (Francey (1985) reports a standard deviation between paired flasks of 0.04 per mil, while the secular trend is only -0.025 per mil yr^{-1}), it is difficult to establish the El Niño "signal" from the measurement "noise."

Meridional profiles of seasonally-adjusted CO_2 concentrations from 1962, 1968, 1980, and 1984 (see Fig. 2.2) indicated that the interhemispheric gradient has changed significantly over the period, with CO_2 slowly "piling up" in the middle to high latitudes of the northern hemisphere. The 1962 profile had a maximum concentration in the tropics, with a only a secondary maximum at higher latitudes. The north-pole-to-south-pole difference in concentration at that time was only about 1 ppm. By 1984, the pole-to-pole difference was about 3 ppm, and the tropical maximum was almost masked by the steep interhemispheric gradient. The authors suggest that the increase in the gradient reflects a larger "airborne fraction" of industrial CO_2 in the north than the south, and that such an effect is to be expected whenever the emissions of fossil fuel CO_2 are accelerating. The acceleration in emissions has subsided significantly since the mid-1970's due to economic factors, which the authors note is consistent with the fact that the interhemispheric concentration difference changed most dramatically between 1962 and 1984, and seemed to be leveling off in the 1980's. Using historical estimates of the rate of fossil fuel emissions, the interhemispheric gradient was extrapolated backward in time, and it was calculated that the preindustrial gradient consisted of southern hemisphere concentrations about 0.8 ppm *higher* than northern hemisphere concentrations. The authors used a three-dimensional tracer model (see section 2.4.2.5) to investigate possible reasons for this reverse gradient, and concluded that it was due to interhemispheric transport by the deep water of the Atlantic Ocean.

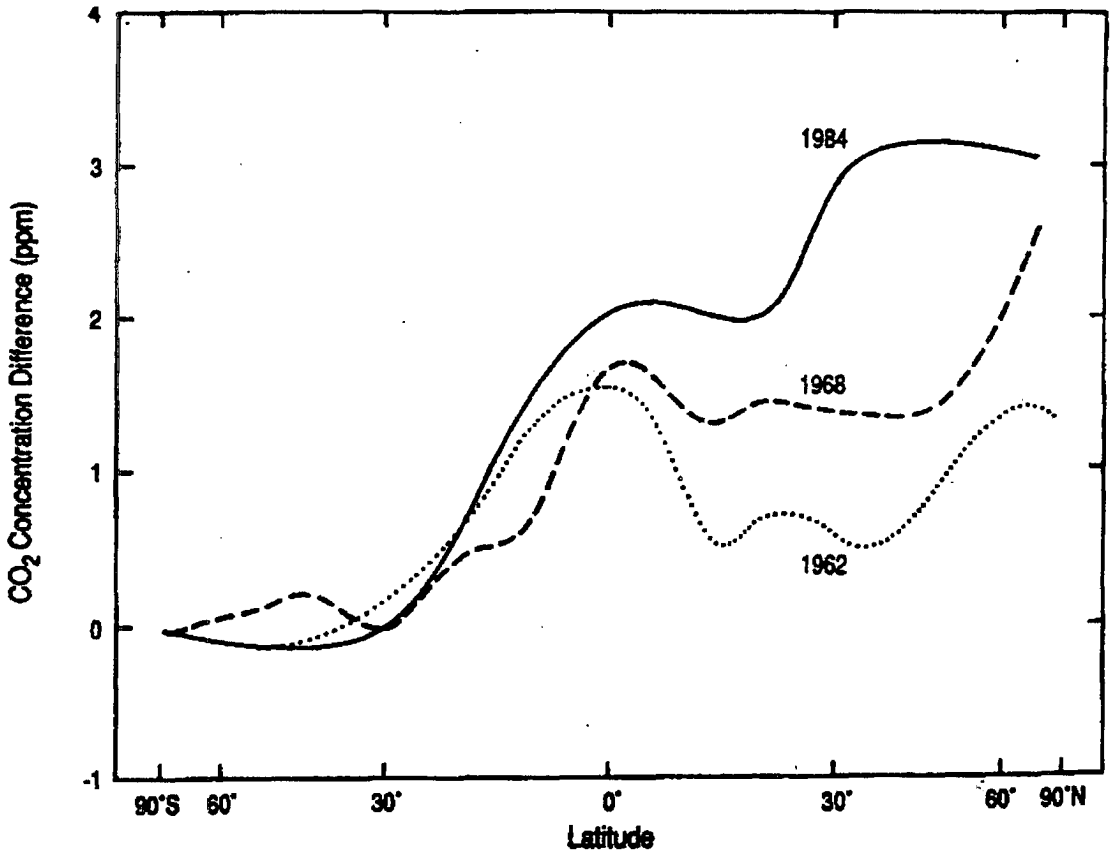

FIGURE 2.2: Meridional profiles of seasonally-adjusted CO_2 concentration in 1962, 1968, and 1984 (Keeling *et al.*, 1989*a*).

2.4 Modeling the Atmospheric Transport of CO_2

Easily available, frequent measurements of CO_2 around the world and improvements in atmospheric transport models during the 1980's allowed the carbon budget to be studied by an "inverse" approach in which observations were combined with simulated transport to deduce surface fluxes. This approach was employed by a group at the Commonwealth Scientific and Industrial Research Organization (CSIRO) in Australia (Hyson *et al.*, 1980; Pearman and Hyson, 1980; Pearman *et al.*, 1983; Pearman and Hyson, 1986) using a two-dimensional model. A three-dimensional tracer model was developed at NASA GISS (Fung *et al.*, 1983; Fung, 1986; Heimann *et al.*, 1986; Fung *et al.*, 1987; TFT90), using wind fields produced by a GCM. Another group at CSIRO (Enting, 1985; Enting and Pearman, 1987; Enting and Mansbridge, 1989; Enting and Mansbridge, 1991) formalized the concept of the inverse calculation, calculating the surface fluxes of CO_2 directly from the observational data. A fourth group, at the University of Califor-

nia's Scripps Institute of Oceanography (SIO) (Keeling *et al.*, 1989*a*; Heimann and Keeling, 1989; Heimann *et al.*, 1989; Keeling *et al.*, 1989*b*) used a three-dimensional transport model derived from observed wind fields to deduce features of the global carbon cycle from observations. This section outlines the development of each of these models, and briefly summarizes the results obtained by each.

The concept of *interhemispheric exchange time* is used in most of the modeling studies of atmospheric transport of CO_2 reviewed in this section, and to compare the rates of meridional mixing of tracers between different models. Unfortunately, this quantity is defined and calculated differently by different authors. Section 2.4.3 compares some of the definitions, values, and methods of calculation of this parameter found in the papers reviewed in sections 2.4.1 and 2.4.2.

2.4.1 Two-Dimensional Modeling

2.4.1.1 The CSIRO Model

A two-dimensional (latitude and height) transport model developed at the CSIRO (Hyson *et al.*, 1980) divided the atmosphere into 20 equal-area columns from pole to pole, with each column subdivided in the vertical into eight layers (four in the troposphere and four more in the stratosphere). Transport simulated by the model involved advection by monthly mean winds and diffusion. Meridional winds were derived from observational analyses, adjusted to produce no vertically-integrated mass transport across latitude circles. Data on mean meridional winds were not available south of 10°S latitude, so southern hemisphere monthly mean winds were prescribed from northern hemisphere data shifted by six months. Mean vertical winds were derived from the meridional winds by continuity. Diffusion coefficients in both dimensions were prescribed from earlier studies, but initial simulations of the meridional profiles of chlorofluorocarbons (CFCs) using economic data for CFC emissions resulted in interhemispheric gradients which were too strong. The meridional diffusion coefficients were then increased in the equatorial zones by a factor of four to five, and by lesser amounts at higher latitudes in both hemispheres. The model was then able to simulate the observed meridional distribution of CFC concentration at the Earth's surface to an acceptable degree of accuracy. The simulated interhemispheric exchange time was about 0.75 years, in rough agreement with the 1 year exchange time obtained by an earlier study (Czeplak and Junge, 1974; see section 2.4.3 for a discussion of interhemispheric exchange times).

This model was applied to the study of the seasonal exchange of CO_2 between the atmosphere and the terrestrial biota by Pearman and Hyson (1980). They forced the model with surface fluxes of CO_2 derived from Lieth's (1965) estimates of zonal mean net ecosystem production (see section 1.3.3) as reported by Machta (1974). These estimates were defined for six broad latitude belts for each month of the year. No surface fluxes due to fossil fuel emissions or exchange with the surface ocean were included in this study, so only seasonal variations were simulated. Initial simulations of the seasonal cycle did not reproduce the observed amplitude and phase of CO_2 concentrations, so the surface flux distributions were adjusted and another simulation was performed. This procedure was repeated iteratively until a satisfactory match with the observed seasonal cycle was obtained. The best agreement with observations was for surface flux distributions which were unreasonable (the growing season in the high latitudes had to start earlier than at lower latitudes). The authors attributed this problem to either another source or sink (*e.g.*, seasonal exchange with the ocean surface) or to a failure of the surface observations to be zonally representative. The model also produced an accumulation of CO_2 in the southern hemisphere due to seasonal properties of the simulated Hadley circulation, which is not unreasonable given that there were no emissions from fossil fuel in the simulation. The simulated damping of the seasonal oscillation with height and the seasonal cycle of $\delta^{13}C$ agreed fairly well with contemporary observations.

The two-dimensional CSIRO model was used by Pearman *et al.* (1983) to investigate exchanges of CO_2 between the atmosphere, ocean, and terrestrial biosphere. Surface fluxes of CO_2 at the ocean surface were calculated using a bulk aerodynamic formula from published estimates of p_{CO2}. The calculated fluxes were temperature dependent, both in terms of the solubility of CO_2 and the air-to-sea transfer coefficient, so the air-sea fluxes varied seasonally. The meridional profile of wind speeds used in the aerodynamic formula was based on observations, but was adjusted to agree with published estimates of oceanic uptake of bomb-produced ^{14}C. Exchanges of CO_2 between the atmosphere and the seasonal biosphere as derived by Pearman and Hyson (1980) were adjusted to compensate for the "extra" seasonality introduced by the seasonal component of the ocean exchange. The meridional distribution of fossil fuel emissions was prescribed from economic data.

Global oceanic uptake was calculated to be about 3.1 Gt C yr^{-1} in 1980, with the tropical oceans releasing about 1.3 Gt C yr^{-1} and the high latitude oceans absorbing 4.4 Gt C yr^{-1}. The simulated North Pole-to-South Pole gradient in atmospheric CO_2 concentration increased from -1 ppm in preindustrial times to about 5 ppm in 1980. The authors

stated that this value was reasonable given the "provisional" observations then available, but later studies (*e.g.*, Komhyr *et al.*, 1985; Pearman and Hyson, 1986; Conway *et al.*, 1988; Keeling *et al.*, 1989*a*) have shown that the actual pole-to-pole gradient is currently closer to 3 ppm, so their simulated gradient was too strong. They investigated various scenarios of equatorial carbon sources (such as tropical deforestation) combined with ocean or terrestrial sinks, and compared the resulting meridional CO_2 profiles with observations. They concluded that tropical deforestation could not amount to more than about 2 Gt C yr^{-1} flux into the atmosphere.

Pearman and Hyson (1986) used the CSIRO model to simulate the seasonal cycle of the zonal means of both the concentration and isotopic composition of CO_2, and study the relative contributions of the ocean and terrestrial biosphere to the global carbon budget. Air-sea exchanges of carbon were prescribed in the same way as used by Pearman *et al.* (1983), but (minor) isotopic fractionation was calculated according to published fractionation constants for air-sea exchange. The changing isotopic composition of the ocean's mixed layer was calculated according to the air-to-sea fluxes as described above and parameterized diffusion into the deep ocean. Fossil fuel emissions were prescribed as in the earlier study by Pearman *et al.* (1983), with time-varying $\delta^{13}C$ specified from published estimates.

This study used a much more complicated scheme to represent the terrestrial biosphere than that used in the earlier work of the CSIRO group. This was necessary in order to calculate the isotopic fractionation associated with photosynthesis and respiration (see section 1.6). A 1° by 1° map of the world's vegetation (Matthews, 1983) was used to derive a meridional profile of fractional composition of each biome in the zonal mean vegetation cover at the coarse latitudinal grid of the model. Within each biome, published estimates of total biomass were divided into three carbon reservoirs. A "fast" carbon pool representing non-woody vegetation was assumed to have a residence time for carbon assimilated by gross primary productivity (GPP, see section 1.3.3 for a discussion of the differences between GPP, NPP, and NEP) of 2.6 yr. An intermediate reservoir represented woody parts of trees, with a residence time of 25 yr, and a "slow" pool represented soil carbon with a residence time of 100 yr. The GPP was assumed to be twice the net primary productivity (NPP), following an ecological rule of thumb, with annual NPP prescribed for each biome from published estimates. Seasonal variations of the NPP were prescribed to follow a simple function of climatological monthly mean temperatures at each latitude. The total respiration flux of CO_2 to the atmosphere was then set to be that required to match observations, by repeated runs of the model and iterative adjustments

to the respiration. The contribution of each of the reservoirs described above to the total respiratory flux was distributed as required to give the residence times listed. Isotopic fractionation during photosynthesis (GPP) was calculated using published estimates, and the $\delta^{13}C$ of CO_2 released from each terrestrial carbon pool during respiration was calculated by keeping track of changes in the isotopic composition of each pool at each latitude through time.

The simulated amplitude and phase of the seasonal cycle of concentration and isotopic composition of atmospheric CO_2 agreed well with observations, including the attenuation of the oscillation with altitude. These authors concluded that the seasonal cycle in CO_2 concentration generated by the terrestrial biosphere in the northern hemisphere was transported southwards, but that the weaker cycle (of opposite phase) generated in the southern midlatitudes damps the oscillation in the southern tropics. The weak cycle observed (and simulated by their model) at high latitudes of the southern hemisphere is in phase with biological activity in the southern hemisphere, probably reflecting this more local influence. Analysis of the observed and simulated isotopic variations, showed that the seasonal cycle in the northern hemisphere reflected the net effect of opposing exchanges with the terrestrial biota and the ocean. During the growing season, when photosynthetic uptake is greatest, the warmer surface ocean takes up less atmospheric CO_2, and the opposite occurs during the winter. The anomalies in simulated $\delta^{13}C$ were quite small due to the "dilution" of the isotopically fractionated CO_2 into the large pools of terrestrial and marine carbon. The authors suggest that the current observational network does not establish geographic and temporal variations of $\delta^{13}C$ with sufficient precision for meaningful conclusions to be drawn based strictly on observations.

As in the earlier simulations by Pearman *et al.* (1983), the mean annual Arctic-to-Antarctic difference in CO_2 concentration was about 5 ppm, as compared to the observed difference of about 3 ppm. Although the authors used more recent data which showed their gradient to be too strong, they questioned the observational data rather than the simulation. They performed experiments in which a tropical CO_2 source (such as deforestation) was added, coupled with a sink of the same magnitude to balance the budget. Ocean sinks were prescribed by uniformly reducing the p_{CO2} of the mixed layer everywhere, and these experiments only made the excess pole-to-pole concentration difference worse. When the tropical source was balanced by a sink in the temperate forests of the northern hemisphere, the interhemispheric gradient improved, with the best fit to observations in an experiment with a 2 Gt C yr^{-1} tropical source balanced by the terrestrial midlatitude sink. Larger tropical sources led to tropical maxima in CO_2 concentration, which

are not observed. The observational isotopic data available at that time were not sufficiently precise to determine the validity of the coupled tropical source - midlatitude sink scenarios.

2.4.1.2 Modeling Surface CO_2 Fluxes by Constrained Inversion

In the studies discussed in sections 2.4.1 and 2.4.2, the problem of simulating the atmospheric CO_2 concentration field was approached by making certain assumptions about the surface fluxes and then integrating the model to see if the results were in reasonable agreement with observations. This "forward" approach was then used again with improved estimates of the surface fluxes after careful analysis of the results, and so forth. Another approach, pioneered by Enting (1985) and his colleagues at CSIRO is a "backward" approach in which surface fluxes or other carbon cycle parameters are deduced directly from the observational data on CO_2, using inverse modeling by linear programming methods.

Enting and Pearman (1987) used the constrained inversion technique to calibrate a one-dimensional box model of the global carbon cycle which included fossil fuel emissions and exchanges between the atmosphere and both the ocean and the biosphere. The observational record of CO_2 concentration and stable isotopic composition over the past two centuries (as derived from the ice core data) was used to constrain the inversion. Their results suggested that the global biosphere was a net sink of about 1 Gt C yr^{-1} in 1980. Enting and Mansbridge (1989) performed a similar calculation using a two-dimensional atmospheric transport model based on eddy diffusion coefficients derived from the GFDL GCM by Plumb and Mahlman (1987). This study confirmed their earlier one-dimensional results regarding a significant net sink in the northern hemisphere midlatitudes which they attributed to net accumulation of carbon in the terrestrial biosphere. This sink more than compensated for a seasonal source in the tropics which probably represents tropical deforestation and associated biomass burning. Southern hemisphere ocean uptake of atmospheric CO_2 was found to be quite seasonal, and was most intense in the middle rather than high latitudes.

Using a similar model and technique to that of Enting and Mansbridge (1989), Tans *et al.* (1989) independently inverted the observational data to calculate the latitudinal distribution of sources and sinks. They deduced a net sink of about 3 Gt C yr^{-1} between 30° N and 65° N, but argued that longitudinal variability in the observational data precludes

reliable estimates of such a sink by inversion with a zonally uniform (two-dimensional) model.

2.4.2 Three-Dimensional Modeling

Fung *et al.* (1983) developed a three-dimensional atmospheric tracer model to study the atmospheric transport of CO_2, and the seasonal surface fluxes associated with the terrestrial biota. The model used as input the wind field and convective mass exchanges produced by the GISS GCM (Model II of Hansen *et al.*, 1983). Mean winds were saved every eight hours for an annual cycle simulation, and convective mass fluxes between each pair of layers were saved as monthly means. Both the GCM and the tracer model were integrated on a very coarse $8° \times 10°$ global grid, with nine layers in the vertical (two in the stratosphere and seven in the troposphere). The tracer model calculated the change in tracer (CO_2) concentration at each eight-hour time step due to advection, convection, and surface fluxes. Advective changes were calculated by a highly conservative finite differencing scheme (Russell and Lerner, 1981), from winds generated by the "parent" GCM which used second-order finite differencing. No subgrid-scale diffusion was included in the tracer model.

Convection in the GISS GCM II was represented on a one-hour time step by assuming a gaussian distribution for subgrid-scale variations in temperatures based on extrapolation from the large-scale temperature gradient (Hansen *et al.*, 1983). Cumulus convection was then assumed to occur, originating in any model layer which was statically unstable, with a parcel penetrating upward until it reached a layer with respect to which it was stable. The rising parcels were assumed to retain the properties of the layer in which they originated, that is, entrainment was assumed not to occur during convective ascent. Fractional areas of each grid column transporting mass from each layer to each higher layer in this manner were calculated from the subgrid-scale temperature variance. The model then calculated downward mass flux between each pair of layers due to compensating subsidence, and the net transfer of mass between each pair of layers in each grid column for was saved in a 9×9 matrix. This process was repeated for clouds originating in each model layer and terminating in each higher model layer, so that a total of thirty-six 9×9 mass flux matrices were computed for each time step at each grid column. The product of these 36 matrices, representing the total mass flux from each layer to each other layer due to all convective overturning, was saved onto history tapes as monthly means for

each month of the annual cycle simulation. These monthly mean convective mass fluxes were used to drive the off-line tracer model.

Fung *et al.* (1983) noted that the simulated transport of CO_2 in their tracer model is subject to discrepancies in the parent GCM's atmospheric transport processes. They pointed out that the Hadley circulation simulated by the GCM was too weak by about 10-20%, and that the Ferrel cell was too weak by about two-thirds. The simulated ITCZ in the model was too wide due to the coarse horizontal resolution, and is too far north in July. Synoptic-scale weather systems were not adequately resolved by the model. All of these deficiencies of the parent GCM would be expected to limit the meridional transport of CO_2 in the tracer model.

2.4.2.1 Seasonal Exchange with the Terrestrial Biota (Fung *et al.*,1983)

Three experiments were performed with the tracer model, using different representations of surface exchanges of carbon between the atmosphere and terrestrial ecosystems. The first used the seasonal exchange estimates of Lieth (1965), reported by Machta (1972) as was done by Pearman and Hyson (1980), but after performing an area-weighted interpolation to the 8° × 10° grid of the tracer model. The second experiment used the revised surface fluxes of Pearman and Hyson (1980), which they produced by iteratively adjusting Machta's (1972) estimates through repeated simulations to give the best agreement with observations. These fluxes were distributed evenly over the land areas in latitude zones after interpolating from the equal-area zones of Pearman and Hyson (1983). The third experiment used the 1° × 1° vegetation map of Matthews (1983) combined with published estimates of annual net primary productivity (NPP) for each biome to produce a global map of annual NPP at the 8° × 10° model grid. The biomass at each grid point was assumed to be at steady state, so that the annually-integrated net flux of CO_2 at each location was zero. This constraint meant that the NPP assigned to each grid cell during the growing season was exactly matched by a loss of carbon from the land surface due to respiration during the rest of the year. The positive and negative fluxes from each grid point were then distributed seasonally using estimates of seasonal uptake and release of biospheric CO_2 constructed by Azevedo (1982). These were defined over broad latitude zones: 10°N–40°N and 40°N–70°N, with more seasonal variation at the higher latitudes. Between 10°N and 10°S, uptake and release of carbon were assumed to exactly balance throughout the year, so that the surface flux of CO_2 was always zero in the deep

tropics. In the southern hemisphere, the northern hemisphere estimates of the seasonal uptake and release were used, shifted in phase by six months.

After integrating the tracer model for 25 simulated months, the results for the final year were analyzed. The first two experiments were found to underestimate the amplitude of the seasonal cycle of CO_2 concentration at five observational sites. The third experiment using the more recent biological productivity estimates matched the observations better, although the seasonal cycle was still too weak in some regions. The seasonal cycle was found to exhibit large variability within a latitude zone, with peak-to-peak station amplitudes differing from the simulated zonal mean by as much as 5 ppm (35%) even in experiment 3 for which the simulation agreed well with the observations. The simulated seasonal amplitude over the oceans was less than half of that over the continents. The time scale for zonal mixing in the middle latitudes was found to be several times longer than the time scale for changes due to the surface fluxes, and that therefore zonal homogeneity of CO_2 concentration would never occur.

Zonal means were calculated for concentration and for each of the processes which affect concentration (vertical and horizontal convergence by the mean flow and by eddies, convection, and surface fluxes), and zonal mean balances were computed for the lower troposphere. Meridional eddy transport was found to dominate the CO_2 balance in the middle latitudes throughout the year. This transport was diffusive, transporting CO_2 into the middle latitudes during the growing season and out of the middle latitudes during times of large respirations fluxes. The down-gradient diffusive transport by the eddies opposed the biological exchange so that changes in CO_2 in the midlatitudes were never more than about half of what would be expected based on the area-integrated surface flux. Mean meridional transport of CO_2 was inhibited by the ITCZ, which proved to be an effective barrier against interhemispheric exchange. Convection was important in determining the overall CO_2 balance only in the tropics, but horizontal convergence was always greater than vertical convergence. The simulated transport exerted sufficient influence on the simulated concentration field that the authors suggested that interannual variability in measured CO_2 could be the result of interannual variability in atmospheric circulation. They acknowledged that the failure of the model to reproduce the seasonal cycle at some of the sampling sites could have resulted either from model deficiencies or from surface fluxes associated with seasonal changes in the ocean, which were not represented in their model.

2.4.2.2 Seasonal and Interannual Influence of the Air-Sea Exchange

(Fung, 1986)

Using the same tracer model described above, Fung (1986) simulated the influence of seasonal changes in the p_{CO2} of the surface ocean on the amplitude and phase of the seasonal cycle. Seasonally-varying surface exchanges of CO_2 were prescribed as input to the tracer model by calculating p_{CO2} in the ocean mixed layer using monthly mean climatological SSTs from literature values. No other surface fluxes were included in this simulation. The oceanic p_{CO2} values varied by as much as 100 ppm in the northern midlatitudes where SST seasonality is greatest. The simulated seasonal cycle of atmospheric CO_2 was about 3 ppm in these regions, and less elsewhere. In the southern hemisphere, however, the amplitude of the seasonal oscillation produced by the SST effect alone was about as large as that produced by the seasonal exchange with the terrestrial biosphere as simulated by Fung *et al.* (1983). In the northern hemisphere, the seasonal cycle produced by SST variations was out of phase with those produced by biological activity in the earlier study, resulting in a slightly reduced amplitude but little shift in phase when both effects were combined.

Fung (1986) also investigated the potential effects of anomalous atmospheric circulations produced by changes in SSTs in a warm El Niño event on the seasonal and geographic distribution of CO_2. The tracer model was run with the same surface fluxes derived by Fung *et al.* (1983) using the seasonal variations constructed by Azevedo (1982), but with atmospheric winds and convection produced by running the GISS GCM with SSTs adjusted according to observations of Rasmussen and Carpenter (1982) for a "composite" El Niño warm event. This represented the transport of CO_2 during an El Niño year, and the results were compared to those for experiment three of Fung *et al.* (1983). Changes in the amplitude and phase of the seasonal cycle of CO_2 due to the anomalous atmospheric transport were minor, representing about 10-20% of the amplitude of the cycle. The changes were due to advection of CO_2 into or out of a given region by the anomalous winds, and were of a magnitude consistent with interannual variability reported at observing stations.

2.4.2.3 Seasonal and Meridional Patterns of Atmospheric Transport (Heimann *et al.*,1986)

Heimann *et al.* (1986) used the GISS tracer model to explore contributions of the terrestrial exchange, ocean surface fluxes, industrial emissions, and atmospheric transport

to the seasonality and meridional gradients of atmospheric CO_2 concentration. In this study, the tracer model was run four times with different sets of surface fluxes representing four distinct surface exchange processes. The results of the four simulations were analyzed separately to study the effects of each process, and then combined to study the annual mean distribution of total CO_2. The four surface processes represented were the terrestrial biosphere, fossil fuel emissions, and preindustrial air-sea exchange, which was divided into annual mean and seasonally varying components. Surface fluxes due to biological exchange were prescribed as in experiment three of Fung *et al.* (1983), with the exception that the simple step-function behavior of the seasonal phasing of uptake and release was smoothed, using one annual harmonic in the low latitudes and two in the higher latitudes. Emissions from fossil fuel combustion, with a global total of 5.29 Gt C yr^{-1}, were prescribed from published economic data. A steady sink of 1.76 Gt C yr^{-1} was distributed uniformly over the global ocean in the fossil fuel simulation, so that the annual increase of this tracer in the model was 3.53 Gt C yr^{-1}.

The annual mean component of air-sea exchange (essentially a function of the vertical motion field of the ocean, see section 1.4.2) was calculated by a bulk aerodynamic formula driven by differences in the amount of dissolved CO_2 in the ocean mixed layer. Using sparsely distributed shipboard measurements from the literature, the authors constructed a crude map of the stationary difference in p_{CO2} between the ocean and atmosphere to drive this flux. They assumed that the net global total of this flux was zero, and so prescribed uniform net sinks at the ocean surfaces poleward of 16° latitude in both hemispheres to match the net sources due to equatorial upwelling. The tracer experiments suggested that interhemispheric exchange by the model atmosphere was insufficient to account for the observed meridional CO_2 distribution, so a net interhemispheric transport by the deep ocean was added to the annual mean ocean fluxes. This was accomplished by adding a sink of 1.2 Gt C yr^{-1} in the Atlantic north of 24°N and a source of the same magnitude in the southern ocean to the distribution described above. Seasonal variations in the air-sea exchange were assumed to be driven by changes in the solubility of CO_2 in the surface ocean (a function of temperature and biological activity in the ocean mixed layer). Sources and sinks in this tracer run were prescribed according to climatological SSTs, with the dependence of p_{CO2} on temperature reduced in high latitudes where decreased biological activity in winter partly cancels the effect of lower SSTs. Further adjustments were applied in the tropical upwelling areas where substantial changes in the total amount of dissolved carbon in the water accompany seasonal changes in SSTs (see section 1.4.2).

These authors found that a seasonal signal was present in the tracer concentrations at the surface even in the simulations in which sources and sinks were constant in time (the annual mean ocean flux and fossil fuel emission runs). The seasonality in these terms was due to the time-dependent transport in the atmosphere. The inclusion of these "stationary" sources in the total CO_2 (calculated as the sum of the tracers in the four simulations) resulted in a better fit of the seasonal cycle to observations than the seasonal surface fluxes alone. This was especially true in the monsoon regions where the atmospheric transport has a strong seasonal component. Conversely, the seasonal biospheric source led to a mean annual concentration field which was not geographically uniform even though the surface fluxes integrated to zero at all grid points over the course of a year. This was also due to correlations of concentration and circulation anomalies during the year. Since the flow in the lower branch of the Hadley cell is always more intense in the winter hemisphere, for example, and the prescribed seasonal uptake of CO_2 was greatest in the summer hemisphere, the Hadley circulation caused CO_2 to "pile up" in the tropics. Also, because convective activity is more intense over the continents in summer than in winter, the wintertime respiration flux was less diluted in the vertical than the summer uptake, leading to low-level concentration maxima over the boreal regions.

In the annual mean, the total simulated CO_2 showed a pole-to-pole concentration gradient of about 7 ppm, more than twice that observed. This was attributed by the authors to result from underdeveloped interhemispheric mixing in the GISS tracer model. The interhemispheric exchange time determined in this study was 1.87 years, which is nearly twice as long as most other estimates for this parameter (see section 2.4.3).

2.4.2.4 Simulation of the Biological Exchange Using Remotely Sensed Vegetation Data: (Fung *et al.*, 1987)

One of the major shortcomings of the modeling studies discussed in this section was that the very large seasonal surface fluxes of CO_2 associated with terrestrial photosynthesis and respiration were parameterized by overly simplistic functions of latitude. Although field measurements of NPP are relatively uniform within biomes, the seasonal variations depend strongly on regional and local factors such as availability of nutrients and moisture, soil properties, and land use history. Developments in remote sensing in the 1980's allowed a more objective analysis of these processes on the global scale.

It had long been recognized (*e.g.*, Monteith, 1972) that as a direct consequence of radiative interactions during photosynthesis, growing plants preferentially absorb radiation in the visible range of the spectrum as compared to the near-infrared range. This property was used (*e.g.*, Colwell, 1974; Richardson and Wiegand, 1977; Tucker, 1979) to infer information about the state of plant canopies from differences in their spectral reflectance. To standardize the radiative response of plant canopies over many species, the normalized difference vegetation index (NDVI) was defined by Tucker (1980) as $\frac{I_{NIR} - I_{VIS}}{I_{NIR} + I_{VIS}}$, where I_{NIR} is the reflected irradiance in the near infrared wavelengths (0.7 to 1.1 μm) and I_{VIS} is the irradiance in the visible wavelengths (0.4 to 0.7 μm). This index has been shown by Sellers (1985) to vary linearly with the absorbed fraction of incident photosynthetically-active radiation over the diurnal cycle in many biomes, and therefore to provide a direct measurement of photosynthetic capacity. Tucker *et al.* (1986) computed NDVI from data collected by the advanced very high resolution radiometer (AVHRR) aboard the NOAA-7 weather satellite, and showed that this parameter was an excellent predictor of month-to-month drawdown of atmospheric CO_2. A linear relationship was found between monthly zonal means of detrended atmospheric CO_2 concentrations and the zonal mean NDVI, although in some cases the relationship was strongest when a lag was applied to account for atmospheric transport.

The relationship derived by Tucker *et al.* (1986) between NDVI and photosynthetic drawdown of CO_2 was used by Fung *et al.* (1987) to simulate the seasonal exchange of atmospheric CO_2 with the global biosphere in the GISS tracer model, updated to run on a finer 4°×5° grid. They calculated NDVI from daily data collected by the AVHRR at 4 km spacing, and selected the maximum value of the NDVI for each grid point for each week, to correct for the effects of sun angle, viewing angle, clouds, atmospheric aerosols, and path length, all of which reduce the NDVI. The weekly values were then aggregated to form monthly means on the 4°×5° global grid used for the tracer model.

Uptake of CO_2 by the terrestrial biota was then specified as follows. The total annual uptake of CO_2 by terrestrial ecosystems was specified on a 1°×1° global grid from the vegetation map of Matthews (1983) and published values of NPP for 32 different vegetation types. The biosphere was assumed to be in steady state (i.e. no net change in total carbon storage over a period of one year), so the annual totals of both the photosynthetic flux and the respiration flux were set equal to the NPP. The phase of the seasonally-varying uptake of atmospheric CO_2 was calculated from the monthly mean NDVI maps by assuming that above a lower "threshold" value, photosynthetic activity was a simple function of the NDVI. Both a linear function

$$\begin{aligned} f_1(t, NDVI) &= NDVI - V_C \quad , \quad (NDVI > V_C) \\ f_1(t, NDVI) &= 0 \quad , \quad (NDVI < V_C) \end{aligned} \tag{2.1}$$

and a simple exponential function

$$\begin{aligned} f_2(t, NDVI) &= exp\,[a\,(NDVI - V_C)\,] \quad , \quad (NDVI > V_C) \\ f_2(t, NDVI) &= 0 \quad , \quad (NDVI < V_C) \end{aligned} \tag{2.2}$$

were tried, where V_C indicates a "critical value" below which photosynthetic activity does not occur. The values of V_C were specified from wintertime NDVI observations, and the coefficient a in (2.2) was simply set to $1/V_C$. For each month, the carbon uptake was prescribed as the value of the function f_1 or f_2 times the area-weighted NPP for the 4°×5° model grid cell, divided by the annual integral of the NDVI function.

The seasonal phase of carbon release due to respiration and decomposition was specified as a linear function of climatological mean temperature. These functions were derived empirically by linear regression for four broad groups of ecosystems from published data on CO_2 fluxes, based on field studies. The four functions were then applied to the 4°×5° area-weighted NPP map in the same manner as the uptake functions f_1 and f_2, so that the total annual uptake and release of carbon from the terrestrial surface was zero at all grid points. Net surface flux of CO_2 from the land to the atmosphere was defined at each grid point to be the respiratory release minus the photosynthetic uptake.

The tracer model was integrated for 25 months with each CO_2 uptake function f_1 and f_2, using the winds and convection generated by the GISS Model II. The amplitude of the simulated seasonal cycle of atmospheric CO_2 was less than observed in the run with carbon uptake specified by (2.1), but was within 1 ppm of the observed amplitude in the run using (2.2). The simulated amplitude decreased with height as observed and as simulated by the previous studies of Fung *et al.* (1983), Fung (1986) and Heimann *et al.* (1986). The seasonal cycle in the middle and upper troposphere of the southern hemisphere reflected transport of the seasonal anomalies from the north in the upper branch of the Hadley circulation. Longitudinal variations of simulated CO_2 concentration near the surface led these authors to suggest that attempts to deduce the surface fluxes from observations using two-dimensional models would always underestimate the fluxes because of the assumption of zonal homogeneity.

2.4.2.5 Use of the Tracer Model Driven by Observed Winds

(Heimann and Keeling, 1989; Heimann *et al.*, 1989; Keeling *et al.*, 1989)

As part of an exhaustive study of the carbon cycle from both observational and modeling perspectives, Heimann and Keeling (1989) simulated the transport of atmospheric CO_2 with the GISS tracer model driven by observed winds rather than GCM output. Some of the surface fluxes were prescribed by new methods, and both the concentration and isotopic composition of CO_2 were simulated. The observational data used in this study are described by Keeling *et al.* (1989*a*) (see the discussion on page 40). Simulation of the seasonal cycle is discussed by Heimann *et al.* (1989), and simulation of the annual mean carbon cycle and its interannual variability is discussed by Keeling *et al.* (1989*b*).

Because of the slow interhemispheric exchange simulated by the GISS tracer model as noted by Heimann *et al.* (1986), the model was modified by Heimann and Keeling (1989) to use observed winds compiled during the Global Weather Experiment (December 1978 through November 1979) and processed by the four-dimensional data assimilation system at the European Center for Medium-Range Weather Forecasting (ECMWF). The coarse resolution version of the GISS tracer model was used, with a horizontal grid of about 8°×10° and nine layers. Winds were averaged from the ECMWF grid to the tracer model grid, and then adjusted to assure mass conservation according to the surface pressure tendency from the ECMWF data. Winds were specified from the ECMWF data every twelve hours, and the model used a four-hour computational time step. The vertical mixing of CO_2 by cumulus convection was still calculated from the monthly mean frequencies of convection saved on GCM history tapes as in the earlier studies described above, which may have resulted in horizontal winds and vertical transports being inconsistent with one another, as noted by the authors. All convective frequencies from the GCM output were decreased by half because the simulated attenuation of the seasonal cycle of CO_2 concentration with height was weaker than observed. The new formulation had a Hadley circulation that was about 20 percent weaker than the original GISS tracer model, but mean meridional transport by the Ferrel cells in midlatitudes was somewhat stronger.

Tracer simulations of ^{85}Kr and radon-222 (^{222}Rn) were used to evaluate the meridional and vertical transport, respectively, of the hybrid tracer model. In the case of ^{85}Kr, the model was initialized with a globally uniform field corresponding to the global mean concentration for 1975, and then integrated for eight years, using estimates of the source

distribution from a previous study. The simulated interhemispheric concentration difference at the end of the run was about 10 to 20 percent too high, and the interhemispheric exchange time (see section 2.4.3) of about 1.3 yr was longer than a previous estimate (Prather *et al.*, 1987) of about 1.1 yr. Still, the interhemispheric mixing was more rapid than in the original tracer model which used the full GCM-simulated convective fluxes. The ^{85}Kr experiment was repeated using convective mixing prescribed at just 25 percent of the GCM monthly mean values, and the exchange time was further reduced to 1.2 yr. The authors concluded that overly vigorous convective transport simulated in the tropics was the most significant barrier to interhemispheric transport. They reasoned that when simulated convection in the intertropical convergence zone (ITCZ) is too strong, interhemispheric mixing is inhibited by air parcels from the lower levels returning into their hemisphere of origin in the upper branch of the Hadley cell.

Radon-222 is a fairly short-lived (order days) radioactive noble gas produced at the ground surface by the decay of naturally-occurring uranium in rocks. Its vertical distribution is therefore an indication of the degree of vertical mixing of the atmosphere over any given region. A uniform source of this gas was specified at the Earth's surface in the tracer model, and the vertical profiles of concentration were then examined for summer and winter conditions over North America. A comparison of these results with limited field observations showed that the simulated concentration was close to that observed in the lower and middle troposphere, but was too high by a factor of three in the upper troposphere, indicating that the simulated tracer transport by deep convection was still too vigorous. Based partly on the good agreement at the lower levels, the authors decided to use the half-strength vertical exchanges rather than complicate the model by introducing a height-dependent scaling for the convective fluxes.

Emissions of CO_2 due to industrial combustion (F_{IND}) were specified from seasonally-varying published maps. Surface fluxes due to biological activity were divided into four parts: seasonally-varying fluxes due to photosynthesis and respiration, and constant fluxes due to deforestation and CO_2 "fertilization" (the "missing sink"). Similarly, exchange of CO_2 between the atmosphere and the ocean surface was divided into four parts: a seasonally-varying component driven by SST seasonality, and stationary fluxes due to equatorial upwelling (balanced by sinks in the midlatitude gyres) and north-to-south transport of CO_2 in deep water of the Atlantic Ocean. Fractionation of the stable carbon isotopes was calculated for each type of exchange.

Photosynthetic uptake (F_{NPP}) was calculated for each month from the same monthly maximum-value composited NDVI data used by Fung *et al.* (1987). Rather than simply using the NDVI to specify the phase of a previously-defined NPP as was done in that study, however, these authors attempted to calculate monthly mean uptake directly from climatological insolation data in combination with the vegetation index. The monthly mean NPP at each location was assumed represented as the climatological visible solar radiation for the month (using a simple cloud fraction estimate) times the fraction of the radiation intercepted by the plant canopy (derived from the NDVI) scaled by a global "efficiency" constant. No account was taken of different values of the efficiency parameter across different biomes. The grid-point values of NPP determined in this way were in rough agreement with but somewhat higher than those used by Fung *et al.* (1983, 1987), which were in turn derived from the map of Matthews (1983). Seasonal release of CO_2 from the land surface due to respiration and decomposition (F_{RES}) was specified as a linear combination of a constant value and a simple exponential function of climatological surface temperature. The annual integral of F_{RES} was forced to equal F_{NPP} at each grid point. This left one free parameter (the ratio of the exponential term and the constant background flux), which was determined at each model grid point *a posteriori* from a least-squares fit of the simulated seasonal cycle to observations. Again, no variation of the form of this function according to vegetation type was attempted.

Surface fluxes due to deforestation (F_{DES}, for "biosphere destruction") were prescribed according to the estimates of Houghton *et al.* (1987) from historical reconstructions of land use change. The magnitude of the flux in each of twelve regions was distributed according to the NPP estimates described above. The sink of CO_2 due to "fertilization" of the terrestrial biosphere (F_{FER}) was prescribed according to the one-dimensional box model derived by Keeling *et al.* (1989*a*) from the observational data (see section 2.3, page 40). The sink was distributed according to the annual total NPP as described above. No seasonal variations were prescribed for either the deforestation source or the fertilization sink.

Atmosphere-ocean exchange of CO_2 was prescribed in much the same manner as was done by Heimann *et al.* (1986). The flux of CO_2 across the air-sea interface was described by a bulk aerodynamic formula, with an exchange coefficient derived empirically from the box-diffusion calculations of Siegenthaler (1983) for preindustrial ^{14}C. A seasonal component of air-sea exchange due to p_{CO2} variability (F_{TDE}, for "time-dependent exchange") was calculated according to climatological SST by carbonate equilibrium chemistry (see section 1.3). The dependence of p_{CO2} on temperature was reduced

smoothly with increasing latitude (to zero poleward of 51°) due to the compensating effect of marine biota, which draw down dissolved CO_2 during summer when the water is warmest and the light is greatest. The temperature dependence was also adjusted in the tropical upwelling regions because p_{CO2} is more closely related to vertical motion than SST there (see sections 1.4.1 and 1.4.2). Based on very sparse observational data from oceanographic cruises, annual mean p_{CO2} in the equatorial regions was used to construct a nonseasonal flux distribution (F_{EQU}). Emissions of CO_2 from the tropical oceans were assumed to exactly balance sinks in the midlatitude gyres poleward of about 16° latitude. In addition, a strong sink (F_{ATL}) was prescribed in the north Atlantic (north of 23.5°N) on the basis of a few observations and because the model-simulated interhemispheric concentration difference was too strong. This sink represented interhemispheric transport by North Atlantic deep water, and was exactly balanced by a source in the southern ocean (south of 39°S). Both stationary source-sink pairs (F_{EQU} and F_{ATL}) were scaled by arbitrary constants which were determined *a posteriori* by least squares fits of the simulation to observational data, as was done for the respiration fluxes. An additional globally-uniform ocean sink (F_{UOS}) was prescribed which represented the penetration of "perturbation" CO_2 (generated by anthropogenic activity – both fossil fuel combustion and land use changes). The global value of this flux was determined from the annual mean observed concentrations using the one-dimensional box model of Keeling *et al.* (1989*a*, see section 2.3, page 40).

The effect of each of the nine types of surface fluxes on the stable isotopic composition of atmospheric CO_2 was calculated by multiplying each flux by an isotope ratio appropriate for the year 1980. Temperature-dependent fractionation associated with air-sea exchange of CO_2 was determined by a separate simulation.

It should be emphasized that the overall global carbon budget in this model was set *a priori*. In this budget $F_{IND} = 5.3$ Gt C yr^{-1}, using the data of Marland *et al.* (1985) and $F_{DES} = 1.8$ Gt C yr^{-1} from the estimate of Houghton *et al.* (1987). The budget was balanced by setting the CO_2 fertilization and global ocean uptake sinks following the results of Keeling *et al.* (1989*a*, see section 2.3, page 40). Using their one-dimensional box model constrained by observational concentration and isotope data and ice core deconvolution, $F_{FER} = -2.1$ Gt C yr^{-1} and $F_{UOS} = 2.2$ Gt C yr^{-1}. The *a posteriori* adjustments to the three free parameters involved in F_{RES}, F_{EQU}, and F_{ATL} improved the simulated seasonal variations and meridional gradients, but had no effect on the global annual budget, since both F_{EQU} and F_{ATL} have zero global integrals and F_{RES} was balanced by F_{NPP}. After finding the best values of the three free parameters in the model, a series of sensitiv-

ity experiments were performed in which these parameters and other aspects of the model were changed, and the simulated distributions of CO_2 and $\delta^{13}C$ were again compared to observations.

Seasonal variations of the simulated CO_2 were analyzed by Heimann *et al.* (1989). The amplitude of the seasonal cycle at four northern hemisphere stations was used to fit a best value for the respiration parameter, and the resulting simulated seasonal cycle of CO_2 concentration at those four stations was extremely close to the observed cycle. Simulated seasonal cycles at four other stations in the middle to high northern latitudes also showed good agreement with observations, even though these data were not used in the calibration. The simulated concentrations were less accurate at tropical stations, especially in the southern hemisphere. In the southern midlatitudes, the amplitude of the seasonal cycle was overestimated by as much as 100 percent, but the agreement was good at the South Pole. Seasonal variations in simulated isotopic composition were in good agreement with limited observations, but like Pearman and Hyson (1986), the authors caution that current measurement programs fail to establish geographic and seasonal variability of this parameter with enough precision. In general, the simulated seasonal variations in CO_2 concentration at all of the stations were in much better agreement with observations (especially in the higher harmonics) than in any previous modeling study of the global carbon cycle.

The simulated seasonal cycle was dominated by the signal from the terrestrial biosphere, as expected, with the seasonal fluxes from the ocean surface generally acting to oppose the biological signal. Some contribution to the seasonality was present in the industrial emissions, because of the seasonal variations in atmospheric transport. This feature was considerably weaker than in the previous results of Heimann *et al.* (1986), presumably due to the use of the observed winds to drive this model as compared to the GISS GCM output used in the earlier study. The vertical structure of the amplitude and phase of the seasonal cycle were compared to regular sampling sites at mountainous locations and to the airplane sampling observations of Tanaka *et al.* (1987). The amplitude was well represented at the mountain sites, with phase errors on the order of a few weeks. The aircraft observations were best simulated in the middle troposphere, with significant errors in both amplitude and phase above about eight km and especially below two km. The authors attributed these errors to the problems with the simulated convective transports noted above, and the lack of an explicitly represented boundary layer in the model. Vertical structure in the zonal mean seasonal variations clearly illustrated the

transport of the biological signal from the northern to southern hemispheres in the middle and upper levels of the model atmosphere.

Meridional gradients in the annual mean fields, and interannual variability of the simulated CO_2 were analyzed by Keeling *et al.* (1989*b*). Both of the globally-balanced, stationary air-sea flux pairs (F_{EQU} and F_{ATL}, see page 60) were adjusted to match the meridional gradients in the observed annual mean concentration data. After adjusting these parameters, the cross-equatorial flux in Atlantic deep water (F_{ATL}) was found to be 1.1 Gt C yr^{-1}, and the equatorial upwelling source (F_{EQU}) was 2.0 Gt C yr^{-1} (recall that this source was exactly balanced by midlatitude sinks). The simulated meridional distributions of concentration and stable isotope ratio ($\delta^{13}C$) produced with these adjusted fluxes (referred to by the authors as the "standard model") compared very favorably to those observed. The interhemispheric exchange time (see section 2.4.3) of CO_2 was found to be 1.37 yr – shorter than the exchange time of 1.86 yr when the same model was run with the GCM-simulated winds by Heimann *et al.* (1986), but still longer than the generally-accepted value of about 1 yr. The pole-to-pole difference in concentration was about 3 ppm, and the difference in $\delta^{13}C$ was about 0.25 per mil. No adjustments in model parameters were made to improve the fit of the isotope simulations to observations, so these were regarded as independent checks of the validity of the flux adjustments.

The standard model value of F_{EQU} was combined with observed values of p_{CO2} from shipboard measurements in the tropical Pacific to calculate a value for the air-sea exchange coefficient. The value determined in this way was only 64 percent as large as the globally-uniform prescribed value calculated from ^{14}C studies and used in the simulation. This discrepancy was attributed to the lack of a wind speed dependence in the model formulation, and/or the poor representation of tropical convection.

Sensitivity experiments strongly supported the authors' contention that the interhemispheric gradient in CO_2 concentration is kept relatively small by a large sink in the north Atlantic, with associated interhemispheric transport in the deep ocean and balancing source in the southern ocean. This sink (F_{ATL}) was replaced by a biospheric sink by adding 1.1 Gt C yr^{-1} to F_{FER}. Because of the strong influence isotopic fractionation associated with biological exchange, the meridional profile of $\delta^{13}C$ simulated in this experiment was significantly less accurate than in the standard model. It was noted that the large air-to-sea flux required in the north Atlantic can only be produced if very large transfer coefficients or very small values of p_{CO2} are used in that region, and that existing data do not

support such extreme values. The authors suggested that such a sink might be present in the higher latitudes of both the Atlantic and Pacific Oceans, but since available oceanographic evidence in both regions was insufficient to establish such fluxes, they chose to model the Atlantic flux because of the known role of that region in deep water formation.

The sensitivity experiments were unable to provide much new information regarding the flux from tropical deforestation (F_{DES}), because the location of this source in the deep tropics minimized its effect on the meridional profile of CO_2 or $\delta^{13}C$. The large-scale biospheric sink (F_{FER}), on the other hand, had a large impact on the simulated patterns of CO_2 and $\delta^{13}C$, and attempts to replace this sink with increased ocean uptake led to significantly degraded agreement with observations, especially with respect to $\delta^{13}C$. In fact, *increasing* both F_{FER} and F_{DES} by a factor of two improved the simulated meridional profile of $\delta^{13}C$, and also reduced the required p_{CO2} deficit in the waters of the north Atlantic to a range more acceptable in light of oceanographic observations. The best fit to observations was obtained by applying a variable air-sea transfer coefficient driven by surface wind speed and also introducing subgrid-scale diffusion of CO_2 to reduce the interhemispheric exchange time (see section 2.4.3) to 1.1 yr.

2.4.3 "Interhemispheric Exchange Times"

As used in the discussion in the previous sections, the concept of *interhemispheric exchange time*, τ, is a measure of the rate at which a tracer with predominantly northern hemisphere sources is mixed by air motions into the southern hemisphere. Implicit in the concept is the idea that differences in the concentration of chemical tracers *within* a hemisphere are less than differences in concentration *between* hemispheres, and that meridional tracer transport can therefore be treated to a first approximation as a simple two-component mixing problem. Such an approximation is motivated by the fact that the intertropical convergence zone provides a significant barrier to interhemispheric transport of mass (Czeplak and Junge, 1974), although of course this "barrier" is not fixed with respect to either time or place and so is rather "permeable." The use of the simple two-box conceptual model of tracer transport is attractive because τ provides a simple parameter by which tracer transport models of varying structure and complexity can be compared.

Unfortunately, there has been some confusion in the literature about the precise definition (and meaning) of this simple parameter. Czeplak and Junge (1974) reviewed nine previous studies of interhemispheric exchange time of the atmosphere, ranging from 0.9

yr to 4.4 yr. Most of these studies involved estimation of the difference in mean concentration of some anthropogenic tracer between the hemispheres (with larger values of τ being computed for larger concentration differences), although at least one study attempted to calculate τ directly from meteorological data (mean cross-equatorial winds – Newell, *et al.*, 1969).

Following Czeplak and Junge (1974), a two-box mixing model of interhemispheric tracer exchange can be expressed as

$$\frac{dq_N}{dt} = S_N - k(q_N - q_S) - \lambda q_N$$
$$\frac{dq_S}{dt} = S_S + k(q_N - q_S) - \lambda q_S \qquad (2.3)$$

where q is the hemispheric mean mixing ratio of the tracer (total hemispheric mass of the tracer divided by the mass of air in that hemisphere), S is the source (emission) rate of the tracer (in mixing ratio units per year), k is the rate of cross-equatorial mixing (yr^{-1}), λ is the radioactive decay constant for the tracer, and the subscripts N and S designate a quantity to refer to the northern and southern hemisphere, respectively. The tracer is assumed to be chemically inactive in the atmosphere, with surface emissions being the only source, and radioactive decay being the only sink. This assumption is quite reasonable for ^{85}Kr, and with λ=0 is also appropriate for CO_2 and for tropospheric transport of CFCs (whose only significant sink is photochemical destruction in the stratosphere).

The rate of change of the mean difference in hemispheric concentrations is obtained by subtracting the two equations in (2.3)

$$\frac{d}{dt}(\Delta q) = (S_N - S_S) - 2k\Delta q - \lambda\Delta q \qquad (2.4)$$

where $\Delta q \equiv q_N - q_S$ is the interhemispheric concentration difference. If the emission rates of the tracer are relatively steady, the meridional gradient of concentration reaches a steady state determined by cross-equatorial transport. In this case, $\frac{d}{dt}(\Delta q) = 0$ and the interhemispheric exchange time τ can be determined from estimates of the hemispheric

concentration difference, the emission rates, and the radioactive decay constant according to

$$\tau \equiv k^{-1} = \frac{2\Delta q}{(S_N - S_S) - \lambda \Delta q}. \qquad (2.5)$$

Czeplak and Junge (1974) arrived at this expression (from their equations 9 and 10), but muddied the waters by using a different definition for τ based on current CO_2 concentration data. Using an estimates of 0.65 ppm for Δq, and 0.70 ppm yr^{-1} for the secular trend of CO_2, they calculated τ = (0.65 ppm) / (0.70 ppm yr^{-1}) = 0.9 yr (p. 60). Assuming that they intended the secular trend to represent S_N (they pointed out that for CO_2, $S_N \gg S_S$, and of course the radioactive decay term in (2.5) does not apply to CO_2), this value is half of what they should have calculated from (2.5). Interestingly, they estimated τ from shipboard observations of ^{85}Kr and obtained 1.8 yr (see Table 2.1:).

If the tracer emissions were to be "turned off" at a time t_0, interhemispheric exchange would immediately begin to reduce the magnitude of Δq. From (2.4), Δq decays according to

$$\Delta q(t) = \Delta q(t_0)\, exp\,[-(2k+\lambda)\, t]\,. \qquad (2.6)$$

For a tracer with $k \gg \lambda$ (such as CO_2 with $\lambda = 0$ or ^{85}Kr with $k \approx 20\lambda$), (2.6) implies that the interhemispheric gradient decays with an *e*-folding time of $\tau_e = \tau/2$.

Another definition for τ was used by Weiss *et al.* (1983), who measured surface concentrations of ^{85}Kr along several north-south cruises in the Atlantic Ocean. They considered the interhemispheric difference in terms of the radiometric "age" of southern hemisphere ^{85}Kr, by assuming the hemispheric concentrations to be well mixed and applying the radioactive decay equation to calculate τ (which they called the "residence time" of the tracer in the northern hemisphere). Their measurements were made at a time when Δq was increasing by about 2.5% yr^{-1}, so (2.5) was not strictly applicable. For a meridional profile measured in March and April, they obtained τ = 1.7 yr, and for a second cruise in October and November, they obtained τ = 1.0 yr.

Many authors have referred to the "interhemispheric exchange time" as if it were an independent property of the atmosphere, regardless of the tracer considered. Plumb and

McConalogue (1988) used a two-dimensional advective-diffusive model of the atmosphere to investigate the vertical and meridional structure of chemical tracers in general, without reference to a specific gas species. They pointed out that there is really no unique value for τ, but that the rate of interhemispheric exchange depends strongly on the geographic distribution of the emissions of a tracer. This stands to reason – common sense would suggest that a tracer with northern tropical sources would show a smaller Δq than one emitted only in the Arctic. These authors defined a "gross interhemispheric exchange time" which is exactly half that defined by (2.5), and which therefore corresponds to the *e*-folding time of the decay of the interhemispheric concentration gradient following the cessation of emissions. For a tracer with a northern hemisphere source that peaks at 30 latitude, they calculated an exchange time of 0.73 yr.

Heimann *et al.* (1986, see section 2.4.2.3 above) found that for their simulations of atmospheric CO_2 transport, the GISS tracer model gave $\tau = 1.87$ yr, which is substantially longer than most other estimates. Subsequent studies using the same model therefore introduced a subgrid-scale tracer diffusion scheme to increase the rate of meridional mixing (Jacob *et al.*, 1987; Prather *et al.*, 1987; Heimann and Keeling, 1989; TFT90). The diffusion was parameterized to maximize the agreement between model calculations of ^{85}Kr concentrations with the observational data of Weiss *et al.* (1983). In the simulation model, the full three-dimensional structure of the tracer concentration and the model winds is known, so yet another definition of τ was possible: the exchange was expressed as $(\Delta q) / F_{N \rightarrow S}$, where $F_{N \rightarrow S}$ is the net cross-equatorial flux of tracer. At steady-state, this value is numerically equal to that defined by (2.5).

The various definitions and values of the interhemispheric exchange time are summarized in Table 2.1. Three basic definitions are present in the table. Most modeling studies have used a definition compatible with (2.5). These include Heimann *et al.* (1986), Jacob *et al.* (1987), Prather *et al.* (1987), Heimann and Keeling (1989), and TFT90, so the exchange times determined for each of those studies can be directly compared. These numbers cluster around 1.0 yr, the exceptions being the estimate of about 1.9 yr for CO_2 found by Heimann *et al.* (1986) and the estimate of about 0.7 yr for CFCs determined by Prather *et al.* (1987). The slow interhemispheric exchange in the GISS model was recognized by Heimann *et al.* (1986) to be unrealistic, so subgrid-scale diffusion was used in

Table 2.1: Interhemispheric Exchange Times

Tracer Species	Study	Definition	τ (years)
CO_2	Czeplak and Junge (1974)	$\frac{\Delta q}{dq/dt}$	0.9
	Heimann *et al.* (1986)	$\frac{2\Delta q}{S_N - S_S}$	1.87
	TFT90	$\frac{2\Delta q}{S_N - S_S}$	1.0
^{85}Kr	Czeplak and Junge (1974)	$\frac{2\Delta q}{S_N + k\Delta q}$	1.8
	Weiss *et al.* (1983)	$\frac{ln\,(q_N/q_S)}{k + 2.5\%}$	1.0, 1.7[a]
	Jacob *et al.* (1987)	$\frac{\Delta q}{F_{N \to S}}$	1.1
	Heimann and Keeling (1989)	$\frac{M_N - M_S}{F_{N \to S}}$	1.3
CFC-11, CFC-12	Prather *et al.* (1987)	$\frac{M_N - M_S}{F_{N \to S}}$	.74, .68
General	Plumb and McConalogue (1988)	$\Delta q / S_N$	.73[b]

a. The two values were derived from separate Atlantic Ocean cruises; the larger value was derived from measured concentrations in March and April, and the smaller value for October and November data.

b. This value was derived for a tracer with a source maximum at 30° N latitude.

all the other studies in this group, resulting in the lower values for τ that they all share. Czeplak and Junge (1974) derived an equivalent expression to (2.5) for ^{85}Kr, but used a different formulation for their estimate of $\tau = 0.9$ yr for CO_2 (equivalent to the definition later used by Plumb and McConalogue, 1988, for a generalized tracer). The missing factor of 2 in the numerator of Czeplak and Junge's (1974) expression for the exchange time of CO_2 accounts for the factor of two difference in their estimates for CO_2 and ^{85}Kr, and the slower exchange they estimated must be due to the earlier concentration data

which they used as compared to the other studies cited here. The definition used by Weiss *et al.* (1983) is based on the difference in the radiometric "age" of ^{85}Kr between the hemispheres, and is not really compatible with the other estimates. In the present study, I will use the formulation in (2.5), which is compatible with the definition used in the more recent modeling studies. The important issue of interhemispheric exchange is further explored in sections 5.3 and 6.1.

2.5 Carbon Cycle Research Since 1990: The Search for the "Missing Sink"

2.5.1 Oceans *vs.* Land Ecosystems Revisited (Tans *et al.*, 1990)

All the modeling studies discussed in section 2.4 prescribed broad geographical distributions of CO_2 fluxes at the ocean surface from limited equatorial observations, using carbonate chemistry and known patterns of sea-surface temperatures to estimate the flux over most of the world oceans. In contrast, TFT90 used nearly all of the existing oceanographic data on p_{CO2} published over the previous 20 years to attempt to constrain these fluxes observationally. They then used the GISS three-dimensional tracer model to explore various carbon budget scenarios under these constraints. Their results painted a very different picture of the global carbon cycle from that sketched by earlier modeling studies. They found that the relatively weak interhemispheric gradient in atmospheric CO_2 concentrations precluded a strong sink in the southern oceans, and that sufficient direct measurements were available in the northern oceans to preclude a very strong sink there either. Their conclusion was that the global oceans take up less than 1 Gt C yr^{-1}, only half of the previous "consensus" value. To balance the global carbon budget and match the observed geographic patterns of CO_2 concentrations, they said, the terrestrial biosphere must be taking up between 2.0 and 2.7 Gt C yr^{-1} in the northern temperate zone.

Sea surface measurements of p_{CO2} made during ocean cruises of the Transient Tracers in the Ocean (TTO) and the Geochemical Sections (GEOSECS) programs were tabulated and averaged onto a $2° \times 2°$ grid for January through April and July through October seasons. Regression equations were developed for p_{CO2} *vs.* SST for each of four

ocean regions, and these coefficients were then used to estimate p_{CO2} in areas with no observational data from climatological SSTs. The global distribution of air-sea exchange of CO_2 was then computed from the p_{CO2} distribution using a bulk aerodynamic formula similar to (1.16). The transfer coefficient was assumed to be a function of climatological wind speed only, since the authors argued that the temperature dependence of the "piston velocity" and solubility of CO_2 nearly cancel each other. The wind-speed relationship they adopted was adjusted empirically to match the estimated global uptake rate of ^{14}C by the oceans. The global air-to-sea flux of CO_2 estimated by this method was 1.6 Gt C yr^{-1}, which is at the low end of previous estimates of the ocean uptake made by the one-dimensional box-diffusion models (about 1.4 to 2.6 Gt C yr^{-1}, Houghton *et al.*, 1990).

Surface exchange with the terrestrial biosphere was prescribed using the NDVI-based estimates of photosynthesis and temperature-based estimates of respiration developed by Fung *et al.* (1987), and fossil fuel emissions were prescribed from economic data (Marland, 1989). Tropical deforestation was prescribed as a source of atmospheric CO_2 following the maps produced by Houghton *et al.* (1987), but scaled to give a global total flux of only 0.3 Gt C yr^{-1}. The GISS tracer model was used as in the Fung *et al.* (1987) study, but subgrid-scale diffusion was added to adjust the interhemispheric exchange time for fossil-fuel CO_2 to 1.0 years. The model was integrated for three years for each set of sources and sinks (*e.g.*, fossil fuel emissions, ocean surface fluxes, etc.), and linear combinations of the various source/sink functions were constructed to investigate many scenarios of global carbon budgets. Each scenario was compared to the observed meridional pattern of annual mean concentration as represented by the NOAA flask observations for 1987 (see section 2.3). Scenarios constructed from the various source functions were considered unrealistic if there was any statistically significant meridional structure to the residuals when the observed meridional gradient was subtracted from the simulated one. Also, the simulated scenarios were constrained to match the observed increase in the total atmospheric inventory of 3.0 Gt of carbon.

Several scenarios based on *a priori* assumptions about the global carbon budget were explored first. These included the observationally-based ocean fluxes described above; another set of ocean fluxes based on the same p_{CO2} estimates, but using experimentally-derived transfer coefficients rather than the empirical approach outlined above; and an earlier, model-based estimate of global ocean uptake much larger than the other two (Broecker *et al.*, 1986). In the first two cases, terrestrial sinks were required to balance the global budget since ocean uptake was not sufficient. The experimentally-based transfer

coefficients led to a smaller ocean sink than the empirically-derived ones, so a larger terrestrial sink was required for the former scenario. The third case (with global ocean uptake of 2.6 Gt C yr^{-1}) was balanced without a terrestrial sink. All of the scenarios tested produced mean annual atmospheric concentration fields with pole-to-pole differences much larger than the observed 3 ppm for 1987.

To investigate the source of the discrepancy between the results of the initial scenarios and the observed meridional gradient in atmospheric CO_2, the authors constructed a series of "basis functions" of sources and sinks which they then adjusted *a posteriori* to produce realistic atmospheric gradients. The world oceans were divided into five independently variable regions plus the equatorial upwelling region (which was assumed to be well constrained by observations). The terrestrial biosphere was assumed to contribute to the global annual carbon budget by four independently variable processes: tropical deforestation, scaled from the Houghton *et al.* (1987) estimates; net uptake by temperate ecosystems, applied across the world's deciduous forests; net uptake by boreal ecosystems applied uniformly to coniferous forests and tundra ecosystems; and globally enhanced photosynthetic flux due to increased CO_2 concentration ("CO_2 fertilization"), which was assumed to be proportional to NPP, as was done by Keeling *et al.* (1989*b*).

Several scenarios of terrestrial basis functions were tested, with the five ocean basis functions adjusted a posteriori to produce the maximum agreement between the simulated and observed annual mean meridional gradient of CO_2 concentration. These scenarios differed in the amount of tropical deforestation, and in the amount of net terrestrial uptake in each region. Adjustments to the ocean fluxes were made within the constraint that the total annual increment of atmospheric carbon was 3.0 Gt. Good agreement with observations was achieved for all the scenarios tested by significant adjustments to the regional ocean sources and sinks. Available field data were insufficient to discriminate between the various scenarios of terrestrial uptake in terms of realism. In all of these cases, the adjustments to the ocean fluxes were considered by the authors to be unrealistic, however, requiring changes to sea surface p_{CO2} which were outside the possible range defined by the observational data. The relatively well-measured p_{CO2} values in the northern hemisphere oceans were the most significant constraint in this respect, and the adjustments required to fit the observed meridional patterns were in all cases much greater than the uncertainty in these measurements.

Another series of experiments involved prescribing several scenarios of ocean fluxes which were plausible within the limits of the oceanographic data, and then performing a

posteriori "best-fit" adjustment to the terrestrial sources and the southern oceans (for which observational data are quite sparse). These experiments were again successful in reproducing the observed meridional gradient, resulting in an under-determined global carbon budget due to lack of enough observational data on the continents to discriminate between various successful scenarios. In all cases, however, a large terrestrial sink was required in the northern hemisphere to balance the fossil fuel source without violating the observational constraints on ocean uptake. The authors were not able to distinguish precisely how much of this sink was in the temperate deciduous forest as opposed to the boreal coniferous forest and tundra, but ruled out a sink of more than a few tenths of a gigaton in the highest latitudes. Some scenarios required a small net source of CO_2 in the tundra regions to bring concentrations at the northernmost stations up to observed values. The total terrestrial sink in the northern hemisphere was estimated to be between 2.0 and 2.7 Gt C yr^{-1}. The global budget could *not* be balanced by CO_2 fertilization as modeled in this study, because this sink is concentrated in the tropics where NPP is highest, and cannot exert enough influence on the pole-to-pole gradient. Equatorial concentrations were below observed values in that scenario, unless tropical deforestation was adjusted upward to 2.5 Gt C yr^{-1}. Such large tropical deforestation fluxes could only be balanced by requiring a northern hemisphere terrestrial sink to match the meridional gradient, leading to a total terrestrial sink of about 3.4 Gt C yr^{-1}. The authors concluded that the global annual ocean uptake of CO_2 was not more than 1 Gt C yr^{-1}, less than half of the "consensus" estimate of ocean modelers (see Fig. 1.8, section 1.5.2). They stressed that the budget is under-determined given the data currently available, and pointed out the importance of obtaining information on the CO_2 concentration on the continents to better constrain estimates of the terrestrial fluxes.

2.5.2 "It's in the Water!" – Oceanographers Respond to Tans *et al.*

Since the publication of the TFT90 paper the literature has been buzzing with discussions of the "missing sink" in the northern hemisphere, and with discussions about whether the oceans are a large sink (absorbing almost half of the fossil fuel emissions) as had been thought previously, or a small sink (absorbing less than one fourth of the fossil fuel emissions) as proposed by TFT90.

Earlier estimates of the rate of uptake of anthropogenic CO_2 by the oceans were based on the one dimensional box-diffusion and outcrop-diffusion models (Oeschger *et*

al., 1975; Siegenthaler, 1983; see section 2.2) in which mixing coefficients were calibrated to produce the observed rate of penetration of natural and bomb-produced radiocarbon. These models consistently showed a net uptake of about two Gt C yr^{-1} by the global oceans. Since these models are not based on the actual physics of ocean transport, their credibility depends on the penetration rates of radiocarbon and fossil fuel carbon being exactly analogous. Because the penetration rate of ^{14}C is determined almost exclusively by the air-sea gas exchange process, however, it is reasonable to think it might be somewhat different than the penetration rate of anthropogenic CO_2, which also depends on the carbonate equilibria discussed in section 1.3.1 (Broecker and Peng, 1982). The smaller estimates of global ocean uptake presented by TFT90 were based on actual observations of p_{CO2}, and were constrained by the atmospheric observations as well, so they pose a serious challenge to the one-dimensional ocean model estimates.

The ocean carbon cycle has also been investigated with more sophisticated three-dimensional ocean general circulation models (Maier-Reimer and Hasselmann, 1987; Bacastow and Maier-Reimer, 1990; Sarmiento *et al.*, 1992; Maier-Reimer, 1993). Of these studies, only the work of Sarmiento *et al.* (1992) attempted to directly estimate the global uptake of anthropogenic CO_2 by the oceans. They found that at least 1.9 Gt C yr^{-1} is being absorbed by the oceans, confirming the earlier estimates from one-dimensional simulations and providing the most compelling evidence that the ocean sink is greater than the 0.8 Gt C yr^{-1} estimated by TFT90.

In the Sarmiento *et al.* (1992) study, an off-line tracer transport model was developed using the calculated currents and convective frequencies produced by a 3500 year ocean general circulation model simulation (Toggweiler *et al.*, 1989*a*). The original simulation was "spun up" from rest to reach equilibrium using annual mean atmospheric forcing (fluxes of momentum, energy, and fresh water, specified from climatology). The finite-difference grid of the model was 4.5° in latitude by 3.75° in longitude, with 12 levels in the vertical, and the time step was 1/300 yr. The "distorted physics" technique of Bryan (1984) was used to lengthen the effective time step in the deep ocean and accelerate the approach to equilibrium. A time-mean velocity field and convective frequency map was saved from this calculation and used to drive the off-line tracer model of Sarmiento *et al.* (1992).

The ocean carbon cycle was assumed by Sarmiento *et al.* (1992) to be in equilibrium with atmospheric CO_2. They simulated the *perturbation* CO_2 ($\delta\Sigma CO_2$) added to the oceans by anthropogenic activity since preindustrial times. This was accomplished by ini-

tializing the model with zero concentration of $\delta\Sigma CO_2$ everywhere, and then forcing the simulation with the time history of atmospheric CO_2 from 1750 to 1990 from the ice core records of Neftel *et al.* (1985) and the Mauna Loa record of Keeling *et al.* (1989*a*). Uptake of CO_2 at the ocean surface was calculated according to a bulk aerodynamic formula (see equation 1.16), with the transfer coefficient depending only on the annual mean wind speed at each model grid point. The complex carbonate equilibria described in section 1.3.1 were linearized so that a $\delta\Sigma CO_2$ was simply proportional to the perturbation partial pressure of CO_2 (δp_{CO2}), with the proportionality constant dependent on the water temperature. This simplification reduced the computational expense of the simulation while still capturing most of the behavior of the "solubility pump" of the marine carbon cycle as described in section 1.4. No attempt was made to represent the "biological pump," although the authors noted that earlier work by Knox and McElroy (1984), Siegenthaler and Wenk (1984), Peng and Broecker (1991) and others had explored changes in biological cycling of carbon due to anthropogenic effects. Riebesell *et al.* (1993) have shown that certain algae important to the ocean's "biological pump" respond in the laboratory to elevated CO_2 concentrations.On the other hand, Falkowski and Wilson (1992) analyzed historical records of ocean photic zone transparency between 1900 and 1981 and concluded that no significant change had occurred in phytoplankton productivity over that period.

In the final 10 years of the tracer simulation (1980-1990), the model ocean absorbed an average of 1.9 Gt of perturbation carbon per year, roughly in agreement with the earlier one-dimensional calculations for the same period, and more than twice as much as the 0.8 Gt C yr^{-1} maximum estimate of TFT90. Unfortunately, it is very difficult to compare the geographic distributions of the surface carbon fluxes between the data-based estimates of Tans *et al.* and the Sarmiento *et al.* simulation. The latter simulation reflects only the *perturbation* flux, but since there is no map of the preindustrial fluxes, and the observational data represent the sum of these two, a direct comparison in any given region is meaningless. The observational data show the tropical Pacific to be a strong source of CO_2 to the atmosphere, for example, due to the upwelling of cold CO_2-rich water there. The Sarmiento *et al.* simulation, however, shows that this area is a strong *sink* for perturbation CO_2 since the upwelling water comes from the deep ocean and was last exposed to the atmosphere when the p_{CO2} was much lower. Nevertheless, given that the preindustrial ocean was neither a source nor a sink for atmospheric CO_2 on a global scale, the two estimates of ocean uptake are incompatible with one another.

The TFT90 estimate of 0.8 Gt C yr^{-1} global ocean uptake was based on the fact that the atmospheric tracer transport model produced an interhemispheric concentration gradient that was too steep when the poorly constrained observationally-based estimate of 2.6 Gt C yr^{-1} uptake south of 15°S latitude was used (see section 2.5.1). Since data coverage was extremely poor in this region, TFT90 ignored the limited observational data and fit the southern hemisphere fluxes from the atmospheric observations, obtaining a much lower rate of uptake. Sarmiento *et al.* (1992) point out that this value would be higher if the interhemispheric transport from the northern source regions was more vigorous in the real atmosphere than in the GISS tracer model, but since this parameter was verified against observed meridional profiles of other anthropogenic tracers and is in agreement with other transport models, they concede this is not the most likely cause for the disagreement. They also considered the possibility that the data-based estimates of Tans *et al.* for net carbon uptake in the northern oceans might be much too low, but found this to be implausible because of the good observational coverage in those regions.

An intriguing revision to the TFT90 fluxes was proposed by Robertson and Watson (1992). They pointed out that the actual skin temperature of the sea surface is on average somewhat lower than that of the bulk mixed layer, and that the air-sea gas exchange process is controlled by the solubility of the gas in this surface skin. The cooler skin temperature is only about 0.3 K cooler than the mixed layer on average, and may only affect a layer of water perhaps 50 μm thick, due to sensible and radiative heat fluxes from the ocean to the overlying atmosphere. Because the solubility of CO_2 is very sensitive to temperature (see section 1.4.1), this skin temperature effect leads to greater flux of CO_2 from the atmosphere to the oceans than would be the case if the mixed layer temperature limited gas solubility. Robertson and Watson (1992) noted that the flux estimates of TFT90 were made from p_{CO2} measured on samples of bulk mixed layer water and that they were therefore generally overestimates of the p_{CO2} of the surface skin layer at the interface. Since TFT90 had used the data-based fluxes only north of 15° S latitude, Robertson and Watson (1992) applied their skin temperature correction only to these regions and concluded that the TFT90 fluxes should be increased by 0.44 Gt C yr^{-1}.

Sarmiento and Sundquist (1992) considered Robertson and Watson's (1992) skin temperature correction and other possible reasons for the discrepancy between the observationally-constrained estimates of TFT90 and the uptake simulated by ocean models. They stated that the minimum global uptake that was consistent with the ocean models was 1.7 Gt C yr^{-1} and considered three processes which might allow the TFT90 value of 0.3 to 0.8 Gt C yr^{-1} to approach this value. They assigned the skin temperature correction

a value of between 0.1 and 0.6 Gt C yr^{-1} based on uncertainties in the Robertson and Watson analysis. A second "correction" to the Tans *et al.* fluxes, they argued, was to add 0.4 to 0.7 Gt yr^{-1} uptake of carbon delivered to the oceans in river discharge. This flux in the preindustrial world must have been balanced by efflux from the oceans to the atmosphere to maintain the steady-state partitioning of carbon between the two reservoirs. Thus the observed uptake would be larger if it were not for these compensating fluxes. Finally, because some of the carbon released to the atmosphere form the combustion of fossil fuels is only oxidized to carbon monoxide (CO) rather than to CO_2, Sarmiento and Sundquist (1992) argued that some interhemispheric transport of atmospheric carbon must take place in this form. They estimated that between 0.25 and 0.29 Gt C yr^{-1} should be added to the Tans *et al.* ocean uptake in the southern hemisphere to account for CO that is transported across the equator and subsequently oxidizes to CO_2 and is absorbed by the southern oceans. Considering these three processes, these authors argued that 0.8 to 1.6 Gt C yr^{-1} should be added to the Tans *et al.* estimates, bringing them up to a total of 1.1 to 2.4 Gt C yr^{-1} and into agreement with the ocean models.

It is important to note that although the processes noted by Sarmiento and Sundquist (1992) which "add" to the uptake estimates of TFT90 can reconcile the differences in the two estimates, some of the differences are more semantic than substantive. Because the Sarmiento *et al.* (1992) model calculates the uptake of *perturbation* carbon and the observationally-based flux estimates of Tans *et al.* represent the flux of *total* carbon, one might just as well subtract the preindustrial efflux that balanced the river fluxes from the model fluxes as add them to the observations. In any case, from the point of view of the atmosphere as modeled by TFT90, the uptake of this carbon occurs on the *land* due to both organic processes and inorganic weathering. These fluxes are not added to the oceans by the process of air-sea gas exchange but rather by river discharge which was not included in either model. Also, the skin-temperature effect of Robertson and Watson (1992) acts to modify the p_{CO2} of the ocean surface, but the fluxes are estimated by multiplying the air-sea difference in p_{CO2} by a gas transfer coefficient which was determined empirically from observations of the penetration of ^{14}C into the oceans. Changing the maps of p_{CO2} to include the skin-temperature effect would presumably also change the value of the transfer coefficient needed to produce the observed depth profiles of ^{14}C and therefore the estimated flux would not change nearly as much as one might think. Finally, it is important to remember that the proposed revisions to the TFT90 uptake estimates are to be applied to the global annual total and there is no way to specify their geographic variations (except perhaps for the skin temperature correction). These revisions reduce the dis-

crepancy between the global total uptake of CO_2 by the oceans as calculated by the two methods, but do not alleviate the difficulty of the too-steep interhemispheric gradient in atmospheric CO_2 concentrations that results if the southern oceans are a strong sink.

Another approach to resolving the question of the smaller-than-expected interhemispheric gradient in the atmosphere was proposed by Broecker and Peng (1992). They showed that a significant amount of atmospherically-derived carbon is transported from the northern to the southern hemisphere in the oceans. They used observations of PO_4, NO_3, salinity, and alkalinity to separate total ocean CO_2 into that associated with biological processes and the remainder, associated with air-sea exchange of CO_2. They found that the atmospherically-derived carbon was significantly more concentrated in the southward-flowing deep water of the Atlantic Ocean than the northward-flowing upper layers. This difference leads to a net transport of about 0.6 Gt C yr^{-1} of atmospherically-derived dissolved carbon from the northern to the southern hemisphere, providing an alternative to the northern terrestrial sink proposed by TFT90 as a means to reduce the interhemispheric concentration gradient.

Quay *et al.* (1992) addressed the question of oceanic carbon uptake by comparing the depth profiles of the stable isotopic composition of dissolved CO_2 in the Pacific as sampled in 1970 and in 1990. Using the changes in atmospheric CO_2 concentration and $\delta^{13}C$ and ocean $\delta^{13}C$, they calculated that the oceans absorb 2.1 Gt C yr^{-1}, in agreement with the ocean models and contrary to the results of TFT90. This study has been criticized, however, by Broecker and Peng (1993) who pointed out that although changes in atmospheric CO_2 concentration are driven by the *net* flux between the atmosphere and the oceanic and biospheric reservoirs, the isotopic fractionation is a function of the total or *gross* fluxes, which are larger by more than an order of magnitude. Although Quay *et al.* (1992) have claimed a net oceanic uptake of about 2 Gt C yr^{-1}, the total exchange of carbon between these reservoirs is more than 80 Gt C yr^{-1} (see Chapter 1). These large inter-reservoir exchanges greatly dilute the signal represented by anomalies in the isotopic composition, and Broecker and Peng (1993) contend that the uncertainty in estimates of the gross surface exchanges is too great to support the results of Quay *et al.* (1992).

Using the assumptions of Quay *et al.* (1992), Tans *et al.* (1993) also obtained an estimate of 2.1 Gt C yr^{-1} ocean uptake from the apparent change in the depth profiles of $\delta^{13}C$. However, using the same data to estimate the net flux from the air-sea surface isotope disequilibrium, they obtained a much smaller global flux (only a few tenths of a Gt C yr^{-1}) They concluded therefore, that the isotope data is not of sufficient quality to

fix the global uptake of CO_2 by the oceans any more precisely than has already been done by analyzing the p_{CO2} observations.

Another promising new technique for distinguishing the carbon uptake by the oceans from that of the terrestrial biosphere involves changes in atmospheric oxygen which accompany combustion of fossil fuels and biological metabolism (Keeling *et al.*, 1993). Because changes in CO_2 and O_2 are stoichiometrically related when carbon is burned or exchanged between the atmosphere and biosphere, but not when inorganic CO_2 gas is exchanged across the air-sea interface, a comparison of time series of CO_2 and O_2 in air can be used to distinguish ocean exchange from other processes.These changes are extremely difficult to detect because of the large background concentration of oxygen (a change in atmospheric CO_2 of 1 ppm due to combustion is accompanied by a change in the O_2 content by only 4.8×10^{-6} of its background value). Keeling (1988) developed a new analytical technique which is capable of detecting such tiny differences. Keeling and Shertz (1992) measured the seasonal cycle of the ratio of atmospheric oxygen to nitrogen at three flask sampling stations which are also part of the regular CO_2 measurement program. This analysis confirmed that variations in CO_2 and O_2 were negatively correlated at all three sites, and these authors concluded that the global oceans were a sink of 3 ± 2Gt C yr^{-1} for the three years studied. Analyses of the O_2/N_2 ratio are now being performed routinely on flask samples of air from many stations around the world, and in several years will be able to add substantially to the available information about the nature of the global carbon sink.

2.5.3 Presence and Nature of a Terrestrial Carbon Sink

Early recognition by carbon cycle modelers that the global carbon cycle did not balance without a "missing sink" led to speculation that the global biosphere was growing (see section 2.2). Terrestrial ecologists countered, though, that because of widespread deforestation and conversion of native ecosystems to agricultural lands, the biosphere was more likely acting as a source of CO_2 to the atmosphere than as a sink. Although this controversy was largely laid to rest by the deconvolution of the ice core carbon records in the mid-1980's, the TFT90 paper has led to a reexamination of the hypothesis of "global greening," because their results suggest the "missing terrestrial sink" must be even stronger than was implied by the ice core records. Research in this area has concentrated in the past on two primary issues: direct enhancement of ecosystem production due to increased levels of atmospheric CO_2 (the "CO_2 fertilization" effect) and changes in the dis-

tribution of ecosystems in various stages of ecological "succession" (regeneration following a disturbance). More recently, some workers have been investigating the effects of climate change on the balance between primary production and respiration and the effects of increased deposition of nutrients such as nitrogen to terrestrial ecosystems.

Plant physiologists have long known that many plants grow more vigorously in air with elevated concentrations of CO_2, especially in environments with ample nutrients and water (*e.g.*, see the reviews by Kimball, 1983 and Mooney *et al.*, 1991). The biochemical reaction in which plants fix inorganic CO_2 into organic molecules is mediated by an enzyme, *Ribulose bis-phosphate carboxylase-oxygenase* (usually abbreviated Rubisco) which also acts to release CO_2 from leaves in a biologically wasteful process known as photorespiration (Farquhar, 1979; Lorimer, 1981). The balance between the useful carbon fixation reaction and photorespiration is determined by the ratio of CO_2 to O_2 in the leaf environment, with higher CO_2 concentrations favoring the useful production of energy. Also, it appears that the biochemistry of soil respiration is affected by CO_2 levels, such that respiration and decomposition of soil organic matter slow down in elevated CO_2 relative to control experiments (Drake, 1992; Idso and Kimball, 1993). The decreased soil respiration may result from a higher carbon to nitrogen ratio in the litter of plants grown in elevated CO_2 (Williams *et al.*, 1986). Both increased photosynthesis and decreased respiration tend to enhance the sequestration of carbon by ecosystems exposed to elevated CO_2. Another important physiological response to elevated CO_2 involves the way many plants balance their need to take in carbon with the concurrent loss of water from their cells through the same openings (stomata) in their leaves (see section 1.3.3). The stomata of plants growing under water stress close to restrict water loss, and so are limited in the amount of carbon they can absorb (Nobel, 1974). When grown in air with elevated CO_2, the effective gradient in partial pressure of the gas across the stomata is increased, and hence diffusion of carbon into the stomata is more efficient, with more carbon assimilated per unit of water lost to transpiration (Goudriaan and Atjay, 1977; Conroy *et al.*, 1986; Mooney *et al.*, 1991; Drake, 1992).

Although many laboratory and field studies have demonstrated these physiological responses to elevated CO_2 (Idso, 1992 analyzed 342 published studies that found an average growth enhancement of 52%), terrestrial ecologists have been reluctant to ascribe the missing sink in the global carbon budget to this "CO_2 fertilization effect" (*e.g.*, Goudriaan and Ajtay, 1977; Houghton and Woodwell, 1983;Woodwell *et al.*, 1983; Jarvis, 1989). Laboratory experiments have shown that plants' response to elevated CO_2 is greatly reduced when other resources (light, nutrients, and water) are limited, which is usually

the case in natural ecosystems (Goudriaan and Atjay, 1977; Kramer, 1981; Peterson and Melillo, 1985; Norby *et al.*, 1992). Many plant species also appear to exhibit a "saturation" response to elevated CO_2 in laboratory and field experiments due to a buildup of starch in their leaves which inhibits photosynthesis (Arp, 1991; Bazazz and Fajer, 1992; Körner and Arnone, 1992). In addition, the responses of natural ecosystems to enhanced CO_2 are complicated by changes in competitive dynamics between plant species and herbivory by insects (Bazazz and Fajer, 1992).

Despite the above-mentioned difficulties in extrapolating laboratory or field plot-scale measures of CO_2 fertilization to natural ecosystems, evidence is accumulating that this effect is occurring. Many of the reduced responses to elevated CO_2 seen in controlled experiments have been shown to result from the inability of plants grown in pots to gather enough nutrients from the soil to "keep up" with their enhanced potential to sequester carbon (Arp, 1991; Thomas and Strain, 1991). When plants are exposed to slowly increasing CO_2, and their roots are allowed grow without artificial restrictions, they may be able to enlarge their nutrient-gathering capacity in proportion to the incremental rise in CO_2 (Rogers, 1992; Drake, 1992). Multi-year experiments on natural plants in native soils have shown major enhancements to growth in salt-marsh ecosystems (Curtis *et al.*, 1990; Long and Drake, 1991; Drake, 1992) and in sour orange trees (Idso and Kimball, 1993). Graybill and Idso (1993) analyzed tree-ring chronologies from the southwestern United States and found increases in growth rates of naturally growing trees of several species dating back over 100 years, after attempting to statistically correct for climate effects.

One problem with the concept of direct CO_2 fertilization as a mechanism to explain the "missing" sink for atmospheric carbon is that it is often assumed to be proportional to the overall productivity of ecosystems (Keeling, 1973; Heimann and Keeling, 1989; TFT90). Since NPP is a maximum in tropical ecosystems (Whittaker and Likens, 1975; Fung *et al.*, 1987), the inclusion of the CO_2 fertilization effect in global carbon cycle models leads to a tropical sink which tends to balance the deforestation source (Keeling *et al.*, 1989*b*). However, as shown by TFT90, a terrestrial sink is required in the northern temperate zone to match the observational CO_2 gradient. Because of the much greater area of land in the northern than the southern temperate zone, modeling CO_2 fertilization as proportional to NPP does reduce the north-south gradient in atmospheric CO_2, but leads to unrealistically large offsetting estimates of both deforestation and fertilization in the tropics (Keeling *et al.*, 1989*b*).

Even if it could be conclusively demonstrated that natural ecosystems are experiencing increased primary productivity due to enhanced atmospheric CO_2, the question of terrestrial carbon sequestration would not be closed. The issue involved is not gross plant growth, but rather changes in the net storage of carbon in the ecosystem, including changes in root respiration and decomposition of soil organic matter. It is extremely difficult to directly measure carbon accumulation or loss on the ecosystem scale, because of heterogeneity of plant communities and soil properties at all spatial scales, and because much of the stored carbon is below ground in roots and soil organic material (Drake, 1992; Norby, *et al.*, 1992). Given the hypothesis that primary productivity is enhanced by CO_2 fertilization, a key parameter for evaluating the change in ecosystem storage is the residence time of carbon in the soil. In practice, simulation models have been used to account for the flows of N, P, and C in soil organic matter (Parton *et al.*, 1987, 1993), and yield a spectrum of residence times. Organic carbon in soils can be divided into a "fast pool," which decomposes rapidly in a year or so and several "slower" pools composed of refractory compounds that decay more slowly over periods ranging from years to centuries. If recent increases in NPP due to CO_2 fertilization lead to greater production of these refractory fractions then net storage would be expected to be enhanced much more than if the increased production was apportioned into the fast-decaying pool. Harrison *et al.* (1993) measured bomb-produced radiocarbon in soil organic matter to constrain the possible residence-time spectrum of soil carbon. They estimated that if CO_2 fertilization enhances plant growth rates by 35% as suggested by earlier work, that about 1.1 Gt C yr^{-1} is currently being sequestered in terrestrial ecosystems.

One approach to measuring total ecosystem carbon flux is to use the micrometeorological technique of eddy correlation. This expensive and labor-intensive method cannot be applied at very large spatial scales, but nevertheless can give valuable information. Because of the strong seasonality of ecosystem metabolism, the measurements must be continued throughout the year. Wofsy *et al.* (1993) performed such a study at the Harvard Forest in Massachusetts. They found that the forest, which is fairly typical of temperate deciduous forests, was a net annual sink of 3.7 ± 0.7 metric tons of carbon per hectare. If this single site is extrapolated to the entire temperate forest biome worldwide, the authors calculate it would represent a sink of over 2 Gt C yr^{-1}. Of course, there is no way of knowing just how representative the Harvard Forest is on a global basis, but this study demonstrates that temperate deciduous forests can be sequester a significant amount of atmospherically derived carbon, at least on small spatial scales and over a year's time.

The concept of succession in terrestrial ecology (Odum, 1969) suggests that entire ecosystems, including the plant community, soil organic matter, and the microorganisms which decompose it, evolve toward an equilibrium state in which net ecosystem production approaches zero as time passes after a disturbance such as fire or harvest. Major disturbances such as fires and logging release carbon into the atmosphere, but are followed by a period of recovery during which time NPP far outstrips ecosystem respiration (Vitousek and Reiners, 1975, see Fig. 2.3). The geographic patterns of successional stages

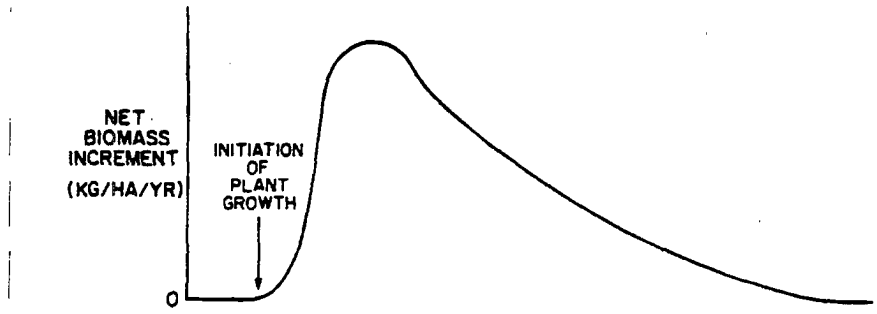

FIGURE 2.3: Schematic illustration of changes in biomass during ecosystem succession following a disturbance (Vitousek and Reiners, 1975).

are always changing as natural disturbances and human land use alter the landscape. Early attempts to quantify the effects of these changes on net carbon exchange between the terrestrial biosphere and the atmosphere (see section 2.2) found that the predominant effect was the release of large amounts of carbon, especially in the tropics (Bolin, 1977; Houghton, *et al.*, 1983; Houghton *et al.*, 1987). More recently, several studies (cited below) have considered the effects of changing patterns of human land use in the temperate zone, and have come to different conclusions.

In many regions of the northern temperate zone, changes in the agroeconomics have led to reversion of agricultural lands to forest. This phenomenon of "reforestation" was documented in the southeastern United States by Schiffman and Johnson (1989), who found that old fields that had since been planted with commercial trees stored about 22% more carbon than natural forests. Kauppi *et al.* (1992) examined forest inventory data collected over the past two decades in Europe and found that biomass had accumulated since 1970. They estimated that European forests were accumulating about 0.1 Gt C yr^{-1}, and attributed this to expansion of commercial forestry and the fertilization of forest ecosystems by atmospheric pollutants, especially nitrogen. Sedjo (1992) performed a similar

analysis for the entire northern temperate zone, and calculated that about 0.7 Gt C yr^{-1} was accumulating in these forests. These studies have been criticized by Houghton (1993), who wrote "The search for 'missing' carbon may be getting out of hand." He suggested that the Kauppi *et al.* (1992) and Sedjo (1992) calculations failed to account properly for the carbon released from these forests following harvests, a matter also addressed by Harmon *et al.* (1990). A more detailed analysis of carbon fluxes from forests of the former Soviet Union by Kolchugina and Vinson (1993) also showed a strong sink, however (about 0.5 Gt C yr^{-1} for Asia alone). Dixon *et al.* (1994) performed an exhaustive survey of available data on forest biomass estimates around the world. They concluded that tropical forests were a net source of carbon to the atmosphere, emitting 1.6 ± 0.4 Gt C yr^{-1}, while temperate and boreal forests were a net sink of 0.7 ± 0.2 Gt C yr^{-1}. Their estimates for the Asian sink (0.3 to 0.5 Gt C yr^{-1}) were in line with those of Kolchugina and Vinson (1993), and their estimate of about 0.1 Gt C yr^{-1} net uptake for Europe is about the same as that of Kauppi *et al.* (1992) even though R. A. Houghton was one of the authors!

Even mature forest ecosystems which would be expected to be in steady state may be accumulating carbon. Bonan (1991) used an ecophysiological model to simulate nutrient and carbon cycling dynamics and carbon isotope fractionation in 23 mature forest plots in Alaska, and compared his results to field measurements. He found that all but one of the forest plots was a net sink of carbon on the annual time scale, and speculated that since the various plots spanned the range of productivity found in the boreal forest, his results might be applied to boreal ecosystems around the world. As Bonan correctly pointed out however, extrapolation of his results to regional scale would require a knowledge of the distribution of undisturbed plots like the ones he studied and areas of disturbance due to forest fires, storms, and logging.

One way to account for increased carbon uptake by temperate and boreal ecosystems was explored by Schindler and Bayley (1993). They note that deposition of atmospheric nitrogen compounds both in precipitation and as dry deposition has increased several fold in recent decades (Malanchuk and Nilsson, 1989; Duce *et al.*, 1991). Because many terrestrial ecosystems are nitrogen limited, nearly all of the increased nitrogen deposition is retained – it cannot be accounted for in river runoff, for example. These authors also note that dry deposition of nitrogen oxides and ammonia is enhanced by "edge effects" in patchy or aggrading forests such as those found in large areas in the populous northern temperate zone. They also show that phytoplankton in coastal oceans should have been stimulated by this increased nitrogen deposition. Using published estimates of carbon:ni-

trogen ratios in various terrestrial ecosystems, they calculate that between 1.0 and 2.3 Gt C yr^{-1} is currently being sequestered as a result of wet and dry nitrogen deposition, with 64 to 80% of the uptake occurring on the northern continents.

Dai and Fung (1993) examined the possibility that perturbations in climate can account for much of the "missing" carbon due to the differences between the responses of NPP and soil respiration to such changes. They used simple empirical regression equations to represent the effect of precipitation and temperature on NPP (Friedlingstein *et al.*, 1992) and soil respiration (Raich and Schlesinger, 1992). Climatological data sets of precipitation and temperature anomalies since the turn of the century were interpolated to a 2.5 by 2.5 global grid, and the re gression equations were applied to each grid point for a "steady state" period (rather arbitrarily defined as 1920-1949). They then estimated the perturbation in net ecosystem production at each grid point for the years 1940-1988 using the regression equations and the assumption of a mean steady state for the earlier period. Temperature anomalies were greatest in the high latitudes during the period, while precipitation anomalies were more important in the tropics and subtropics due to the influence of the Southern Oscillation. Because of the different sensitivities of NPP and soil respiration to anomalies in temperature and precipitation, grid point estimates of net ecosystem production were positive in some months and negative in others.

Dai and Fung (1993) stressed that their estimates of NEP based on the simple regression of temperature and precipitation anomalies are very rough. Nevertheless, their results showed intriguing similarities to earlier estimates using other methods. During the mid-1950's and again in the mid-1970's unusually wet weather led to higher NPP than soil respiration over much of the world, so that the terrestrial biosphere acted as a net sink for those periods. The regression equations are more sensitive to perturbations in climate at low temperatures, so the variability in the simulated NEP was greatest in the higher latitudes than the tropics. For the period 1980-1987, the authors estimate that the middle latitudes of the northern hemisphere acted as a net sink of about 0.2 Gt C yr^{-1}, simply due to perturbations in climate. For the entire period simulated, the global total uptake due to climate fluctuations was 20 ± 5 Gt C, as compared to an estimate of 30-35 Gt from deconvolution of the ice core record (Houghton, 1989). Indeed the year-to-year variations of the global NEP calculated in this study were strongly correlated with the deconvolution estimates of Houghton (1989), although smaller in magnitude. The authors suggested that the extra uptake inferred from the ice-core record might be due to enhanced NPP as a result of CO_2 or N fertilization.

2.6 Modeling Atmosphere-Biosphere Interactions – A Convergence of Technologies

It should be clear from the preceding discussion that the carbon cycle brings together processes that have traditionally been the domain of many disciplines. Seasonal uptake and release of carbon at the land surface are controlled by the biochemical and physiological processes of photosynthesis and respiration, but also by larger-scale ecosystem-level processes such as nutrient cycling in the soil and local climate (see section 1.3.3). Uptake and efflux at the air-sea interface are controlled by physical and chemical processes, biological productivity and nutrient cycling, and the large-scale motion field of the deep ocean (see section 1.4). Atmospheric transport and mixing play an important role in the geographic and seasonal patterns of CO_2 concentration (see sections 2.4 and 2.5.1). Over the longer term, ecological considerations may control the responses of terrestrial ecosystems to rising CO_2 concentrations which lead to sequestration or release of large amounts of carbon (see section 2.5.3). Finally, all of these processes interact with climate on time scales from minutes to decades. In the past decade or so, major progress in understanding the interactions between climate, terrestrial ecology, and atmospheric transport of CO_2 has been made by simulation modelers working at a variety of scales from individual plant cells to the global atmosphere.

Terrestrial ecologists have generalized models developed by plant physiologists to represent experimental plots (Running, 1992; Parton, *et al.*, 1992), and by simplifying their logic were able to extend these models upward in spatial scale to encompass, landscapes, watersheds, and regions. Hydrology and primary productivity were simulated for forested watersheds by Knight *et al.* (1985), and later at regional scale by Running and Coughlan (1988) and Running *et al.* (1989). Running's model (now called BIOME-BGC) has since evolved (Running, 1992) to include the ability to simulate other biomes, including grasslands, tundra, and tropical forests (Running and Hunt, 1993). Parton *et al.* (1987) developed the CENTURY model (see Fig. 2.4) to simulate the decomposition of soil organic matter and related nutrient cycling processes in grasslands; CENTURY and similar models have since been extended to temperate forests (Aber, *et al.*, 1991) and to tropical forests (Sanford *et al.*, 1991). Another group of ecologists built a regional-scale model called the Terrestrial Ecosystem Model (TEM) and used it to simulate water balance and NPP over all of South America (Raich *et al.*, 1991), and even the entire global terrestrial biosphere (Melillo *et al.*, 1993). A similar global calculation was performed re-

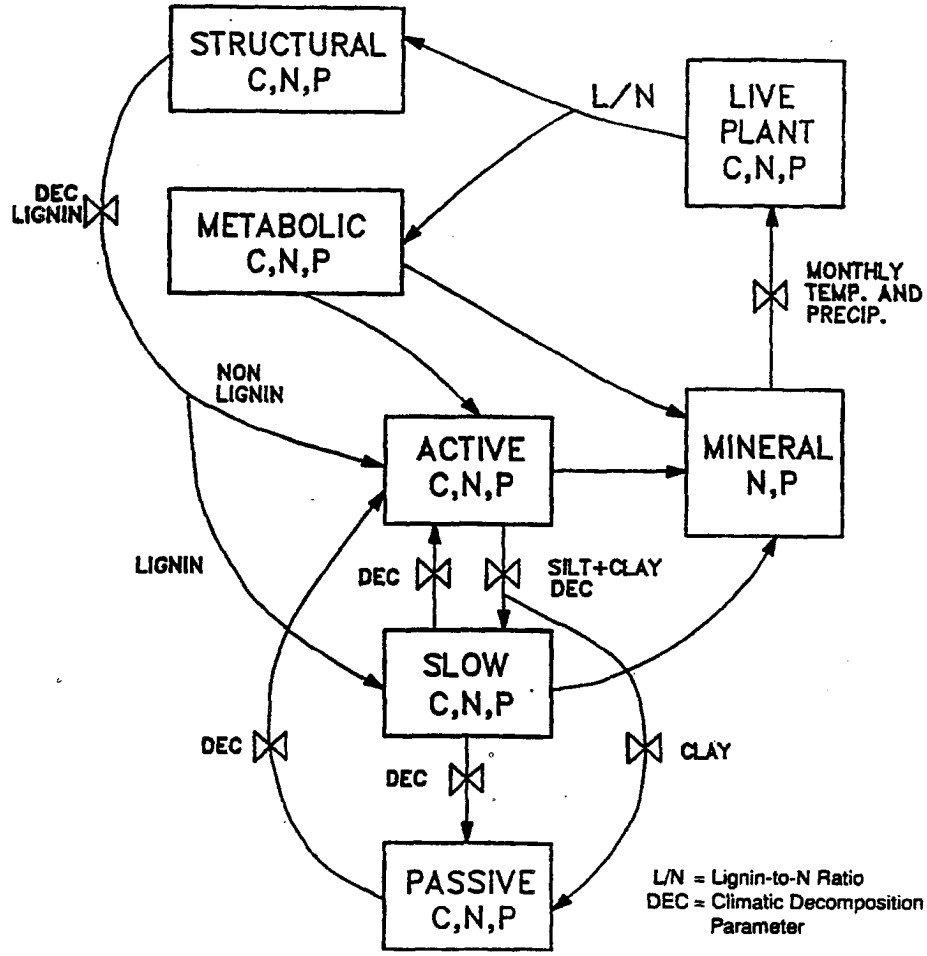

Figure 1. Flow diagram for the Century model.

FIGURE 2.4: Structure of the CENTURY model after Parton (1992). The model predicts changes in organic matter quantity and composition in seven plant and soil reservoirs. The rate of turnover between reservoirs is controlled by climatological factors, soil texture, and nutrient content.

cently by Potter *et al.* (1993), using a model derived from CENTURY. All of these models require information about climate at the land surface on the model grid; these data have been supplied from climatological summaries and satellite data.

As terrestrial ecologists have simplified their models and extended them to ever larger spatial domains, atmospheric modelers have begun to incorporate more detailed submodels of the land surface into their calculations, primarily to provide better boundary conditions to the atmosphere. Atmospheric models require information about surface fluxes of sensible and latent heat, radiative energy, water, and momentum at the model time step (generally seconds to minutes), and interactions between these parameters are

controlled by the physiology of vegetation and land surface hydrology. Earlier models prescribed surface properties such as albedo and roughness length from various maps derived independently of one another. Hydrologic processes like percolation of rainfall, surface runoff, and evapotranspiration from the vegetated land surface were calculated from simple conceptual models bearing little resemblance to the actual physical processes involved (Manabe, 1969). Biophysically based models such as the Simple Biosphere (SiB) model (Sellers *et al.*, 1986) and the Biosphere-Atmosphere Transfer Scheme (BATS; Dickinson *et al.*, 1986) represented a major departure from these earlier schemes. Vegetation was explicitly represented for the first time, and the partition of surface energy budgets into sensible and latent heat fluxes was done by considering physiological responses of simulated leaves, stems, and bare ground to incoming radiation. SiB represented vegetation in two-layers, an upper canopy and lower-growing ground cover (see Fig. 2.5), while BATS used a single layer to calculate its energy budget and fluxes. (A newer version of SiB uses a single vegetation canopy; Sellers *et al.*, 1994*a*). Water fluxes from the

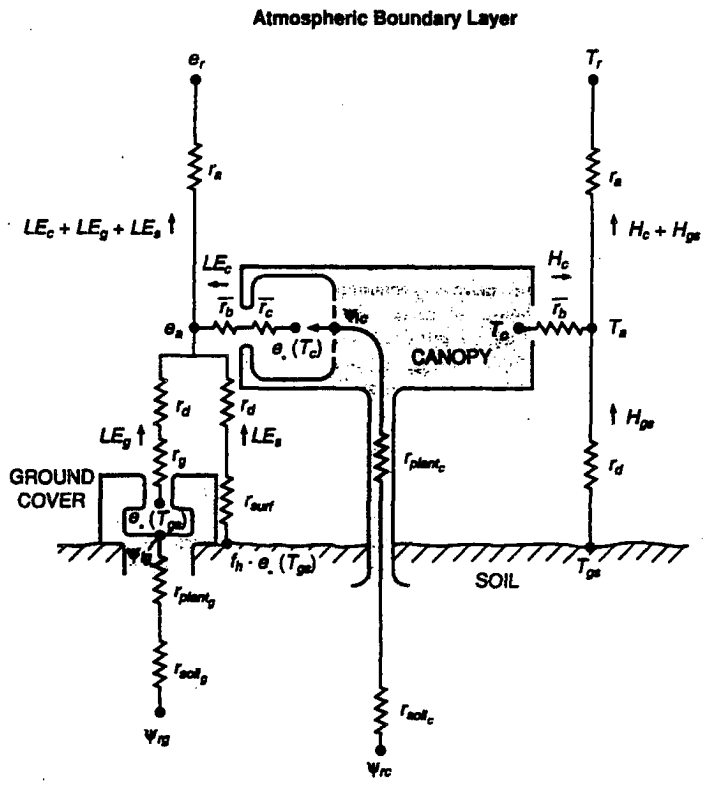

FIGURE 2.5: Structure of the SiB model after Sellers *et al.* (1986). Fluxes are indicated by arrows (H is sensible heat flux and λE is latent heat flux) and are calculated as the gradient of the scalar quantities (T for temperature, e for vapor pressure, ψ for water potential) divided by empirically defined resistances.

land to the atmosphere were divided into direct evaporation from the soil surface, transpiration from the root zone of the soil (limited by stomatal conductance in the leaves), and evaporation of intercepted water on canopy surfaces. Sato, *et al.* (1989) showed that for most biomes the diurnal cycle of the surface fluxes and especially surface temperatures were more realistic using SiB than using the earlier "bucket" surface hydrology.

As atmospheric models incorporated biophysically based land surface parameterizations, unexpected problems sometimes arose from the coupling because of the feedbacks between biological and atmospheric processes. Some experiments with SiB, for example, showed that when the simulated turbulent planetary boundary layer (PBL) became very hot and dry, the stomatal conductance of the plant canopy approached zero, leading to even hotter and drier air due to increased sensible and decreased latent heat flux from the surface (Piers Sellers, personal communication). This unrealistically strong positive feedback between the vegetation and the atmosphere could lead to persistent drought in a GCM, and probably resulted from the fact that the equations used to prescribe the response of stomatal conductance to atmospheric heat and water stress were derived from laboratory and plot-scale experiments in which the plants had little direct effect on the properties of the air.

The problems of unrealistic feedback loops between the canopy and the PBL have been alleviated by a reconsideration of the factors that actually regulate stomatal aperture in plant canopies. Rather than the more traditional description of stomatal conductance in terms of empirically-derived response curves to environmental stress, Ball (1988) (see also Ball, *et al.*, 1986 and Ball, 1987) showed that stomatal behavior could be described in terms of demand for CO_2 at the cellular level in the leaves. He applied a biochemical model of the kinetics of the carboxylating enzyme Rubisco (Farquhar *et al.*, 1980) to calculate the changes in stomatal conductance in intact leaves of various plants in terms of the changes in concentration gradients across the stomatal opening resulting from the metabolism of CO_2 in chloroplasts. Collatz *et al.* (1991) extended this logic to the plant and canopy level by incorporating the effects of a leaf boundary layer through which gases must diffuse when entering or exiting stomata (see Fig. 2.6).

Sellers *et al.* (1992*a*) used an innovative canopy integration scheme to incorporate this biochemical mechanism into SiB (the updated model is hereinafter referred to as SiB2). They argued that because the biochemical machinery of photosynthetic carbon assimilation is obtained by plant leaves at a cost of scarce organic nitrogen (a key constituent of the enzyme Rubisco), plant canopies must partition their Rubisco resources

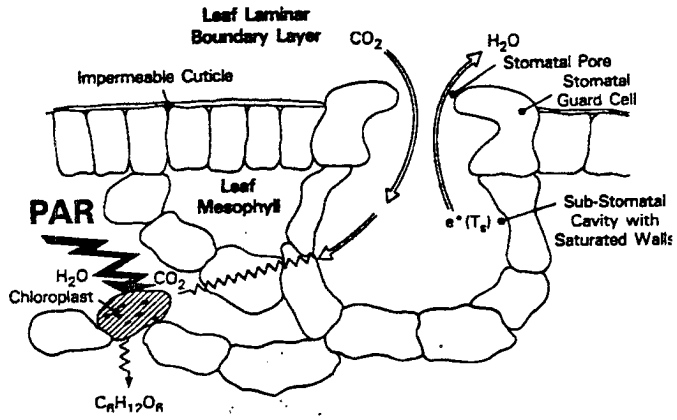

FIGURE 2.6: Schematic showing stomatal structure in a plant leaf as simulated by Collatz *et al.*, 1991 and illustrated by Sellers, *et al.*, 1992*b*. Photosynthetically-active radiation (PAR) drives the carboxylation reaction in chloroplasts, reducing the internal CO_2 concentration. The resulting gradient in p_{CO2} across the stomatal pore causes CO_2 uptake by diffusion. Water vapor loss (transpiration) is a consequence because the air in the stomatal cavity is saturated with respect to water. The guard cells act to regulate stomatal opening for optimum CO_2 gain while minimizing water loss.

according to the available incident light, where their nitrogen investment will "pay off" in terms of gains in carbon (Field and Mooney, 1986). They assumed an exponential decrease in Rubisco concentration downward through plant canopies in response to the exponential decrease in incident radiation due to shading by upper leaves. This simplification allowed the variation of stomatal conductance in the canopy to be integrated in closed form, leading to a relatively simple parameterization of the overall canopy resistance to water and heat flux. Sellers *et al.*, 1992*c*) showed that this level of biological realism and detail produced excellent agreement with micrometeorologically measured fluxes over a natural grassland, and scaled very well from small experimental plots to large heterogeneous areas. (The updated model, referred to in this study as SiB2, also has a simplified single-layer canopy structure. The new formulation is described in detail by Sellers *et al.* (1994*a*), and is summarized in section 3.3.2 of this report).

Besides providing atmospheric models with more accurate and robust estimates of surface fluxes of energy, water, and momentum, SiB2 predicts the photosynthetic uptake of carbon based on biochemically realistic methods. Thus a level of coupling between climate and carbon uptake is achieved in this model which has not been possible before. Whereas modeling of terrestrial NPP has in the past involved prescribing climatological data from sparse observations, SiB2 can be coupled directly to an atmospheric GCM, providing surface boundary conditions to the atmosphere and receiving meteorological forc-

ing in return. A major advantage of coupling biophysically and biochemically realistic terrestrial vegetation models and hydrologically realistic soil models with atmospheric models is that all the components receive information from each other which is internally consistent. This allows both a meaningful examination of the feedbacks and interactions among the various systems and simulation of responses to conditions outside the realm of experimental observations.

Addressing the questions involving the CO_2 fertilization effect (Mooney *et al.*, 1991) and the "missing" terrestrial sink (TFT90) will require coupling among at least three systems (soils, vegetation, and atmosphere), including a parameterization of organic matter decomposition in the soil which is not currently available in SiB2. There are serious problems to overcome in coupling these systems in models. One of the biggest difficulties is the difference in both spatial and temporal scales which need to be resolved in the various submodels (Bretherton *et al.*, 1992). Another is specification of land surface properties such as leaf area index (LAI), soil hydraulic conductivity and rooting depth at fine spatial resolution over the entire land surface of the Earth. Many properties of vegetation can now be determined from satellite data (Justice *et al.*, 1985; Goward *et al.*, 1985; 1987; Sellers, 1985, 1987). Unfortunately, this is not true of important soil parameters, which must be estimated from sparse published data which were not designed to drive ecosystem models (Running, 1992).

The modeling efforts of terrestrial ecologists and atmospheric scientists are converging in an environment of unprecedented computer power at a time when understanding the coupling between these systems is crucial for our understanding of the global carbon cycle. Cooperation among scientists in disciplines that have traditionally been unfamiliar with each others' literature and jargon is required to construct the coupled models that will be needed to address the "missing sink" issue. It seems certain that the rest of this decade will be a time of rapid progress in this area. I hope that the current study can contribute in some way to these efforts.

2.7 Summary

Research in quantifying the amount of CO_2 in the air and the mechanisms controlling it began more than 100 years ago, but suffered from inadequate instrumentation until the 1950's. Beginning in 1957, reliable and precise concentration measurements became available at a large number of remote sites around the world, which quickly led to the realization that CO_2 concentration was increasing rapidly (section 2.1).

By comparing the rising concentration of CO_2 in the air with economic inventories of fuel consumption, it became clear that a large sink was consuming about half of the carbon emitted by anthropogenic fossil fuel combustion. Box-diffusion models of the ocean were developed to account for sequestration of atmospheric CO_2 in the oceans, and they were apparently able to account for most of the difference between fuel consumption and atmospheric increase, so the global budget seemed to be balanced. Observations of the penetration of bomb-produced ^{14}C were used to refine the box-diffusion models of the ocean, and by the mid-1970's some workers suggested that a small terrestrial sink was necessary to close the budget.

Bolin (1977) challenged this view of the global carbon budget by pointing out that changes in land use patterns were almost certainly releasing large quantities of CO_2 into the atmosphere, particularly in the tropics. He estimated that this source amounted to nearly as much annual flux as the fossil fuel emissions, and suggested that the ocean models were significantly underestimating the amount of annual uptake. Geochemical ocean modelers and terrestrial ecologists argued this point in the literature, leading to some groundbreaking studies of terrestrial carbon flux and much-refined versions of the ocean models (section 2.2). In the mid-1980's, when Antarctic ice cores were analyzed for CO_2 concentrations in gas bubbles, a reliable history of changes in atmospheric concentration became available for the first time. Analysis of these data suggested that although the terrestrial biosphere had been a large source of CO_2 to the atmosphere over time, large releases of biospheric carbon were no longer occurring, and that the biosphere might even be a small net sink.

Another class of studies used the improving global observational data on geographic and temporal variability in atmospheric CO_2 (section 2.3) to try to unravel the patterns of sources and sinks at the Earth's surface using simulation models of atmospheric transport (section 2.4). These studies showed that the although the secular trend in CO_2 was due to

fossil fuel emissions, the seasonal variations were driven primarily by the seasonal growth and decay of terrestrial plants. In addition, they suggested that although the ocean was certainly absorbing a large amount of CO_2, a "missing" sink must also exist in the northern terrestrial biosphere to account for the relatively small meridional gradient in annual mean concentration.

Tans *et al.* (1990) used a compilation of available observations of air-sea gas fluxes to suggest that the uptake of CO_2 by northern hemisphere oceans was much less than had been assumed in earlier studies. By using a global, three-dimensional tracer transport model in conjunction with available observations of atmospheric CO_2 they also showed that a large sink in the northern middle latitudes was necessary to explain the meridional gradient (as had also been demonstrated before). Their conclusion was that this northern sink must be in the terrestrial biosphere rather than the northern oceans.

The TFT90 paper set off a fresh wave of controversy in the literature (section 2.5). A new generation of three-dimensional ocean models had been developed which supported a much sink for anthropogenic CO_2 than argued for by Tans *et al.* Also, the concept of the terrestrial biosphere as a large sink for CO_2 ran counter to the sensibilities of the terrestrial ecologists, who had been arguing for a large source due to land use perturbations. Some of the conflict with the ocean modelers appears to be a matter of different definitions of flux into the ocean, and of separating gross carbon uptake into natural and anthropogenic components (Sarmiento and Sunquist, 1992), but a real reconciliation of model results and surface observations of carbon flux will have to await further work.

Terrestrial ecologists have risen to the challenge of explaining how the biosphere can simultaneously lose carbon from large areas of anthropogenic disturbance (like tropical deforestation) and yet be a large sink for anthropogenic carbon on the global scale. It now seems clear that direct fertilization of terrestrial ecosystems by increased atmospheric CO_2 or by nutrient deposition, temperate zone reforestation, differential response of photosynthesis and respiration to changing climate, or some combination of these factors can account for at least most of the "missing" terrestrial sink. A new class of terrestrial ecosystem models has emerged (section 2.6) which can be used in conjunction with climate models to provide more insight into this problem.

CHAPTER 3

Methods

This chapter contains five sections. The basic strategy used is discussed in section 3.1, in terms of the overall objectives listed in section 1.7. Section 3.2 briefly discusses the theory of modeling a passive atmospheric tracer, then presents the rationale for the choice of the 18 tracers used in this study to investigate atmospheric transport and surface fluxes of CO_2. The tracers are defined and briefly described in section 3.2.2, but a full accounting of how they were coded and the input data used to define their surface fluxes is deferred until section 3.4.

Section 3.3 describes the Colorado State University (CSU) general circulation model (GCM), which I modified to study the behavior of CO_2 in the atmosphere. This discussion includes a brief review of the history of the CSU GCM, its structure, and previous results obtained with the model, followed by a detailed description of those algorithms used to simulate the transport of CO_2 in the model, and how my modifications were coded.

The surface flux data used to drive the atmospheric model are presented in Section 3.4. Finally, Section 3.5 discusses the computational aspects of the simulations I performed.

3.1 Basic Strategy

As discussed in section 1.7, this study is intended to serve two main purposes (repeated here for convenience):

1) to investigate the surface fluxes and atmospheric transport of CO_2 in order to better understand the global carbon cycle, and

2) to serve as a building block for the integration of models of the atmosphere and the terrestrial biosphere, which will facilitate future work in elucidating the linkages between these components of the Earth system.

The first objective stems from the current controversy in the carbon cycle research community (see section 2.5). Although Tans *et al.* (1990, herein TFT90) estimated that the oceans take up less than 1 Gt yr^{-1} of carbon from the atmosphere, Sarmiento *et al.* (1992) calculated that at least 1.9 Gt yr^{-1} of anthropogenic carbon is being added to the oceans. Although Sarmiento and Sundquist (1992) showed that the discrepancy between these estimates may not be as great as it seemed at first, the problem of simultaneously balancing the global carbon budget and accounting for the weaker-than-expected meridional gradient in CO_2 concentration remains vexing. Sarmiento *et al.* (1992) considered the possibility that the simulated meridional mixing in the GISS tracer model used by TFT90 might be too weak, but concluded that since the interhemispheric mixing properties had been calibrated against the observed meridional profile of krypton-85, this was not likely to be the cause of the problem.

Although the representation of atmospheric transport in models of the carbon cycle has been progressively more detailed in the past two decades, even the state-of-the-science calculation by TFT90 used a highly simplified model by the standards of meteorologists and climate modelers. The off-line tracer transport was determined from GCM-simulated winds saved only once every four hours, and the vertical mixing by cumulus convection was driven by a matrix of "mixing frequency" between each pair of levels saved from the GCM as a monthly mean. Heimann and Keeling (1989) found that the interhemispheric mixing of the GISS tracer model was extremely sensitive to the intensity of this monthly convective frequency. Surface fluxes of CO_2 were also prescribed as monthly means. Such a coarse temporal representation of tracer fluxes and transport cannot capture such processes as correlations between surface wind fields and the diurnal cycle of cumulus convection, or the "pumping" of CO_2 into the free troposphere that could result from diurnal growth and decay of the turbulent PBL (Randall *et al.*, 1991).

In order to address the possibility that a more detailed representation of atmospheric transport might result in different results from those obtained by TFT90, this study repeats their calculations to a large degree, but the tracer simulation is performed *on-line* in the CSU GCM. Tracer transport by advective processes is calculated at the model time step of six minutes, and convective transports are calculated every hour. The possible effects of diurnal correlations among tracer fluxes, cumulus convection, and PBL evolution

are investigated in detail. Many of the tracers I used were driven by the same surface flux maps used by TFT90, so a direct comparison of the results can be made. Tracers are chosen to allow the same *a posteriori* analysis of meridional gradients performed by TFT90, so that many scenarios of global carbon budgets may be tested against the NOAA flask observations. The vertical and interhemispheric mixing properties of the CSU GCM are examined by simulating the transport of ^{222}Rn and ^{85}Kr, as has been done for the off-line tracer models by Keeling *et al.* (1989) and TFT90.

Almost all current estimates of global fluxes suggest a large terrestrial sink in the northern hemisphere. Such a sink may be due to the direct effect of CO_2 fertilization (Mooney *et al.*, 1991), indirect fertilization effects of nitrogen deposition (Schindler *et al.*, 1993), an imbalance of primary production and decomposition resulting from climate fluctuations (Dai and Fung, 1993), or some combination of these effects. In any case, even a sink of 3 or 4 Gt C yr^{-1} represents only a small perturbation (about 5% of global NPP) to the huge seasonal fluxes into and out of the terrestrial biosphere. It seems unlikely that such a small signal will be discernible by direct measurement anytime in the near future, so investigation of this phenomenon is likely to depend on realistic coupling between atmospheric and ecological models for some time to come.

Physiologically based simulation modeling of vegetation has progressed to the point that the first global calculations have recently been published (Melillo *et al.*, 1993; Potter *et al.*,1993). At the same time, recent advances in land surface parameterization for GCMs make truly coupled simulations of the atmosphere and terrestrial biosphere a tantalizing possibility (Sellers *et al.*, 1992*a*; 1994*a*, *b*; Randall *et al.*, 1994). Before such models can be successfully used to investigate the "missing" terrestrial sink, at least two ingredients will need to be added: atmospheric transport of the important chemical constituents that affect the behavior of the biosphere, and a parameterization of the decomposition of soil organic matter. This study takes several steps toward those ends, by adding passive trace gases as prognostic variables to the CSU GCM, building some of the logical and numerical "hooks" needed to allow interactive coupling between these trace gases and SiB2, and testing two new representations of seasonal exchange of CO_2 at the land surface (SiB2 and the Carnegie-Ames-Stanford (CASA) model of Potter *et al.*, 1993) against CO_2 flask station observations.

3.2 Tracer Modeling

3.2.1 Modeling of a passive atmospheric tracer

In general, the local time rate of change in any passive atmospheric quantity q is given by

$$\frac{\partial}{\partial t}(\rho q) = -\nabla\bullet(\bar{\rho}\bar{q}\bar{V}) - \nabla\bullet(\rho'\overline{q'V'}) + S_q \qquad (3.1)$$

ρ is the density of the air, V is the three-dimensional wind vector, and S_q is a volumetric source or sink. The overbar indicates grid cell averaged quantities and the primes indicate subgrid-scale deviations from these averages. The adjective "passive" in this context means that the wind V is not affected in any way (even indirectly) by the concentration of the tracer.

The first term on the right-hand side of (3.1) refers to explicitly resolved tracer transport (advection) by the mean flow, and the second term to parameterized processes affecting the concentration that occur at spatial scales too small to be explicitly resolved by the model. Sub-grid scale fluxes represented in the model include turbulent diffusion in a well mixed planetary boundary layer, vertical mixing due to dry convection, and vertical transport by penetrative cumulus convection. The formulation of each of these processes in the GCM is discussed in section 3.3. Convection resulting from instability in higher layers is parameterized by a moist adjustment process (Manabe *et al.*, 1965; see section 3.3), but I have not attempted to represent vertical transport of CO_2 by this process. Exchanges of mass between the PBL and the free troposphere also occur in the model in the presence of boundary layer clouds. This process is referred to as "layer cloud instability" (Suarez *et al.*, 1983). For simplicity I have neglected its effect on the simulated tracer concentrations.

Volumetric sources and sinks of CO_2 due to the oxidation of reduced carbon compounds such as CH_4 and CO in the atmosphere constitute a source of perhaps 1 Gt C yr^{-1} (Tans *et al.*, 1994). This source is one to two orders of magnitude smaller than the boundary fluxes due to biological activity at the land surface and air-sea exchange, and is neglected in this study for computational convenience. Radioactive decay of two of the simulated tracers (see section 3.4.6) is included as part of the S_q term in (3.1).

In the case of CO_2 then, the only represented sources and sinks are at the Earth's surface, and so are included as boundary conditions. The boundary flux is assumed to be homogeneous across the horizontal area represented by a grid cell, and to mix instantaneously throughout the vertical extent of the planetary boundary layer by turbulent diffusion, and so is included in the second term on the right-hand side of (3.1).

So long as the boundary fluxes of a tracer do not depend nonlinearly on the concentration of the tracer, equation (3.1) is linear in q. This makes it possible to divide the problem into convenient parts by defining an arbitrary number of passive tracers whose concentrations sum to the total CO_2 concentration. Each tracer can have unique source and sink distributions at the lower boundary, and linear combinations can be constructed to study various aspects of the transport of atmospheric CO_2. I have taken advantage of this property of linear systems by simulating a number of tracer concentrations simultaneously. Since the tracers are independent of one another, the results are identical to those that would result from performing many experiments with different boundary fluxes (computationally expensive because the tracers are simulated on-line in the full GCM). Since tracer transport is determined by the atmosphere and not by the nature of the tracer (it is not dependent, for example, on the molecular weight or chemical properties of the tracer), only the boundary fluxes must be specified separately for each tracer. In implementing prognostic CO_2 in the CSU GCM, I have represented these as of prescribed, seasonally- and geographically-varying surface fluxes (see section 3.4).

3.2.2 Choice of Tracers

Simulation of a number of tracers was required to address the objectives outlined in section 3.1. This section defines the 18 tracers to represent CO_2 in the CSU GCM, and describes the rationale for choosing them. Detailed maps of the surface fluxes of the tracers as well as the sources for these data and the methods used to prescribe them to the model are presented later (in section 3.4).

Evaluation of the effect of the more detailed atmospheric transport in the CSU GCM as compared to the GISS tracer model required that most of the experiment of TFT90 be repeated. Comparison with their results required a minimum of five types of tracers be included in the calculation:

1) Anthropogenic emissions of CO_2 due to fuel combustion and cement manufacture;

2) Releases of CO_2 from the terrestrial biosphere due to land use changes (primarily tropical deforestation);

3) Exchange of CO_2 at the surface of the oceans;

4) Seasonal exchange of CO_2 between the atmosphere and terrestrial biosphere;

5) Some representation of the "missing" terrestrial sink.

Eighteen tracers were implemented in the CSU GCM to represent these five basic processes and to evaluate the simulated transport; they are summarized in Table 3.1. Items 1 and 2 in the above list require one tracer each (T_1 and T_2), and were implemented exactly as done by TFT90. I chose to use six different tracers ($T_3 - T_8$) to represent the air-sea exchange, again using a representation as similar as possible to that of TFT90. In addition, three different tracers (T_9, T_{15}, and T_{18}) were used to evaluate different parameterizations of seasonal exchange with the terrestrial biosphere; five possible scenarios (T_{10} - T_{14}) were simulated for a terrestrial missing sink; and two more (T_{16} and T_{17}) were implemented to evaluate the transport characteristics of the CSU GCM. The numbers of the tracers are unimportant and reflect programming considerations rather than qualitative similarities between consecutively numbered tracers. The rationale for choosing these particular tracers is described in Table 3.1.

3.2.2.1 Air-Sea Gas Exchange

In order to assess the geographic distribution of the air-sea exchange, several different tracers must be defined with sources and sinks prescribed over different regions of the oceans. Therefore item (3) in the list above must be divided into a number of separate tracers. It seems reasonable to do this based on similarities of the surface fluxes over ocean regions; TFT90 specified six such regions in their calculation (their table 2), which were later combined into their various "basis functions" to test global budget scenarios. In order to allow a detailed comparison with their study, I defined six tracers ($T_3 - T_8$) to represent air-sea exchange of CO_2 based on the regional divisions in TFT90 (see Table 3.1). The specific latitudes and longitudes used to define boundaries between the regions of influence of the tracers are slightly different than the TFTFT90 boundaries shown in the table because of the different grid cell boundaries used in the CSU GCM (see section 3.4.3).

Table 3.1: Tracers Used in this Study

	Anthropogenic Emissions	
T_1	Industrial Emissions	after Marland (1989)
T_2	Tropical Deforestation	after Houghton *et al.* (1987)
	Regional Ocean Fluxes	
T_3	Subarctic Atlantic	north of 50°N
T_4	North Atlantic Gyre	15°N to 50°N
T_5	North Pacific Ocean	north of 15°N
T_6	Equatorial Oceans	15°S to 15°N
T_7	Combined Southern Gyres	15°S to 50°S
T_8	Antarctic Oceans	south of 50°S
	Seasonal Terrestrial Biosphere	
T_9	NDVI driven	Fung *et al.* (1987)
T_{15}	CASA NEP Model	Potter *et al.* (1993)
T_{18}	SiB2 (Prognostic) Flux	On-line calculation
	Net Terrestrial Sinks	
T_{10}	CO_2 Fertilization (NPP based)	Strongest in tropics
T_{11}	CO_2 Fertilization (drought stress and NPP based)	Strongest in subtropics
T_{12}	Temperate Forests	biome-specific
T_{13}	Boreal Forests	biome-specific
T_{14}	Tundra	biome-specific
	Radioactive Trace Gases	
T_{16}	Krypton-85	Interhemispheric mixing
T_{17}	Radon-222	Vertical Mixing

3.2.2.2 Seasonal Exchange with the Terrestrial Biosphere

The seasonal biosphere was represented by TFT90 using a scheme derived and tested by Fung *et al.* (1987) in which published estimates of NPP were spread out over the year according to a satellite vegetation index (NDVI) to represent photosynthetic uptake, and an equal amount of carbon was released over a simulated year according to monthly mean temperature, representing ecosystem respiration (see section 2.4.2.4). I have included this representation in the present study (T_9) to allow a direct comparison with earlier work. Even though the sources and sinks of this tracer are purely seasonal, with annual net flux equal zero at all grid points, correlations between atmospheric transport and the surface flux lead to an annual mean meridional gradient in concentration (Heimann and Keeling, 1986; Fung *et al.*, 1987). Therefore a global budget scenario calculated by matching linear combinations of tracers against observed concentrations may be affected by the representation of the seasonal fluxes even though they have no net contribution to the global budget. To evaluate this possibility, and to test new ideas about modeling the seasonal fluxes, I included two additional tracers (T_{15} and T_{18}) representing seasonal exchange with the terrestrial biosphere. The new seasonal fluxes are driven by new models of terrestrial ecosystem function.

Surface fluxes of tracer T_{15} were calculated by the Carnegie-Ames-Stanford (CASA) model (Potter *et al.*,1993). The CASA model uses satellite-based NDVI and climatological data to drive a model of NPP, a soil hydrology submodel, and a nutrient-cycling - soil decomposition submodel based on CENTURY (Parton *et al.*, 1992). The resulting seasonal fluxes of CO_2 to the atmosphere as published by Potter *et al.* (1993) were quite different from those of Fung *et al.* (1987), so an experiment using these fluxes to drive an atmospheric simulation could be very enlightening. The fluxes used in this study were obtained using a slightly different formulation for soil decomposition than the published version of the model; these changes are discussed in section 3.4.4.

Surface exchange of tracer T_{18} was determined on-line in SiB2. This was a departure from all the other tracers which were prescribed from monthly maps derived separately from the GCM. The fluxes of T_{18} represent photosynthetic uptake and release of CO_2 from plant respiration and soil decomposition. Uptake is determined directly by SiB2 using the enzyme kinetics models of Collatz *et al.* (1991, 1992) integrated to the canopy scale by the method of Sellers *et al.* (1992*a*), as discussed in section 2.6 and explained in detail in section 3.3.2. The model uses this information to calculate the stomatal conductance and related energy and water fluxes; it was relatively simple to add code to apply

the calculated carbon assimilation to the atmospheric tracer. The rate of decomposition of soil organic matter is calculated only diagnostically in SiB2, and is parameterized following Raich *et al.* (1991) as a function of soil temperature and moisture (which are prognostic variables in SiB2, see section 3.3.2). This diagnostic variable was used in concert with the calculated assimilation rate to determine the net uptake of CO_2 at the land surface on the model time step of six minutes (the equations used are described in section 3.4.4). Tracer T_{18} was therefore the only one with surface fluxes that responded to the diurnal cycle in the model, with photosynthesis dominating respiration during the growing season in the daytime, and respiration dominating at night.

Besides providing an additional view of seasonal exchange with the terrestrial biota to compare with the behavior of the fluxes (of tracer T_9) derived by Fung *et al.* (1987), the inclusion of tracers T_{15} and T_{18} provide a framework for future work in coupling biological and atmospheric processes in the CSU GCM. As simple as the representation of gas exchange is in the code for surface flux of the SiB2 tracer (T_{18}), this is a crucial link between the biochemical model in SiB2 and the simulated atmosphere. The inclusion of a fully prognostic CO_2 variable is a first step toward possible future simulations of isotope fractionation, CO_2 fertilization, or other atmosphere-biosphere interactions. In the present study, the interaction is restricted to one direction only: SiB2 can change the local atmospheric concentration of CO_2, but the information does not feed back to SiB. The assimilation calculation is done assuming a constant and uniform concentration of 350 ppm. This precludes any immediate conclusions about the effects of increased CO_2 on the simulated ecosystems, but prevents the kind of pathological behavior of runaway positive feedbacks sometimes encountered when new interactions are allowed in a simulation model (*e.g.*, climate drift in coupled ocean-atmosphere GCMs, see Meehl, 1989). A more realistic calculation of the direct effects of increased CO_2 on the global biosphere will require a somewhat more sophisticated parameterization of soil decomposition than is now possible using the simple diagnostic equation of soil temperature and moisture content. Some progress in this area is expected from a collaboration of the CASA authors with the SiB authors over the next few years as part of NASA's Mission to Planet Earth program (Piers Sellers and Christopher Potter, personal communication). The inclusion of the CASA fluxes in the present study is therefore a way both to test the resulting geographic and seasonal patterns against the flask observations and to evaluate key parts of the model logic in preparation for integrating some of these principles in SiB.

3.2.2.3 The "Missing" Terrestrial Sink

The direct calculation of the net ecosystem production of the terrestrial biosphere and its role in and response to the rising CO_2 concentration of the atmosphere is an intriguing possibility for a future experiment with some descendant of a coupled SiB-GCM-CASA model, but is beyond the scope of this study. Nevertheless, some representation of a large terrestrial sink will most likely be necessary to close the global carbon budget unless the GCM transport leads to dramatically different results from those of earlier studies. I chose to represent five scenarios for such a "missing" sink with tracers $T_{10} - T_{14}$.

The first two of these tracers represent a sink due to direct CO_2 fertilization. Annual total fluxes of tracer T_{10} are proportional to NPP at each terrestrial grid point, following earlier studies (*e.g.*, Keeling, 1973; Heimann and Keeling, 1989, TFT90) which assumed the effect of elevated CO_2 on ecosystems is to increase NPP by a certain fraction without a compensating increase in ecosystem respiration. Many field studies have found that the direct CO_2 fertilization effect is much stronger in plants that are water-limited, due to the increased water use efficiency of stomatal function under enhanced CO_2 conditions (Mooney *et al.*, 1991). This effect is simulated by setting the total annual sink of tracer T_{11} proportional to both NPP and annual mean water stress, as measured by a diagnostic parameter calculated in SiB2 (the equations used are presented in section 3.4.5).

Considerable uncertainty exists regarding the nature of the "missing" sink (see section 2.5.3), which may not be due to the direct effects of CO_2 fertilization at all, but rather to enhanced atmospheric deposition of nutrients (Duce *et al.*, 1991; Schindler *et al.*, 1993), perturbations in the balance between NPP and ecosystem respiration due to climate fluctuations (Dai and Fung, 1993), some combination of these processes, or some other process not yet understood. Moreover, the results of TFT90 and Keeling *et al.* (1989) suggest that this sink is strongest in the middle to high latitudes of the northern hemisphere, yet tracer T_{10} has its maximum sink in the tropics (where NPP is greatest) and T_{11} has a maximum sink in the subtropics (where drought stress is strongest). Although these tracers have sinks which are based on some understanding of biological responses to increased atmospheric CO_2, their geographic distributions make them unlikely to provide the necessary influence on the meridional profile of simulated CO_2. Tracers $T_{12} - T_{14}$ are therefore defined as biome-specific sinks of an unspecified nature in the temperate forest, the boreal forest, and the tundra regions, respectively. All of the "missing sink" tracers $T_{10} - T_{14}$ have surface fluxes which vary seasonally according to NDVI.

3.2.2.4 Radioactive Tracers for Model Validation

Tracers T_{16} and T_{17} do not represent CO_2 at all, but rather simulate the behavior of the radioisotopes ^{85}Kr and ^{222}Rn, which can be used to evaluate the simulated interhemispheric mixing and vertical mixing of the GCM, respectively (Jacob *et al.*, 1987; Heimann and Keeling, 1989). Krypton-85 has a half-life of 10.8 yr (Jacob *et al.*, 1987), and is produced as a by-product of nuclear fuels reprocessing. Because all of its sources are in the northern hemisphere, the rate of penetration of the tracer into the southern hemisphere can be used to measure the rate of interhemispheric mixing. Heimann and Keeling (1989) evaluated the intensity of vertical overturning in their model by simulating the concentration of Radon-222 (^{222}Rn). This radioisotope is an unreactive noble gas with a half-life of only 3.82 days, and is produced naturally in rocks and soils as an intermediate product in the decay chain of Uranium-238 to Lead-206 (Faure, 1977). Because of its short half-life, the concentration of ^{222}Rn diminishes rapidly with height; by comparing the vertical profile of the simulated tracer with that observed in several experiments, a measure of the accuracy of the vertical mixing of the model atmosphere can be obtained.

3.3 The Atmospheric Model

3.3.1 Brief Description of the CSU GCM

The CSU GCM has been derived from the UCLA GCM, which was developed at UCLA, over a period of 20 years, by Prof. A. Arakawa and collaborators. A copy of the model was brought to the Goddard Laboratory for Atmospheres in 1982, and from there to CSU in 1988. Many changes have been made since the model left UCLA, including revised parameterizations of solar and terrestrial radiation (Harshvardhan *et al.*, 1987), the PBL (Randall *et al.*, 1992), and cumulus convection (Randall and Pan, 1993), and new parameterizations of land-surface processes (Sellers *et al.*, 1986, 1989, 1992*a*, *b*, *c*, 1994*a*, *b*), and cloud microphysical processes (Fowler *et al.*, 1994). Some recent results are presented by Harshvardhan *et al.* (1989), Randall *et al.* (1989, 1991, 1994), Stephens *et al.* (1993), and Fowler and Randall (1994).

The prognostic variables of the CSU GCM are: potential temperature; the mixing ratios of water vapor; the horizontal wind components; the pressure thicknesses of the free troposphere and the PBL; the turbulence kinetic energy of the PBL, the temperature of

the plant canopy, the ground surface, and the "deep" soil at land points and the ice temperature at land ice and sea ice points; the depth of both snow and intercepted surface liquid water and the stomatal conductance at land points; the kinetic energy associated with cumulus convection; and the 18 tracers implemented in this study. The governing equations are finite-differenced, using highly conservative schemes (Arakawa and Lamb, 1977, 1981). Fourier filtering of the mass flux and pressure gradient vectors is used to maintain computational stability near the poles (Arakawa and Lamb, 1977). The model has been programmed so that the horizontal and vertical resolutions and the pressure of the model top are easily varied. The code is portable enough to run on a variety of computers.

A key feature of the CSU GCM is its formulation in terms of a modified sigma coordinate, in which the PBL top is a coordinate surface, and the PBL itself is the lowest model layer (Suarez *et al.*, 1983). This vertical coordinate is defined as

$$\sigma = \begin{cases} \dfrac{p - p_I}{p_I - p_T} & , \quad (p_I \geq p \geq p_T) \\ \dfrac{p - p_I}{p_B - p_I} & , \quad (p_B \geq p \geq p_I) \\ 1 + \left(\dfrac{p - p_B}{p_S - p_B} \right) & , \quad (p_S \geq p \geq p_B) \end{cases} \tag{3.2}$$

where p_T, p_I, p_B, and p_S represent the pressure at the top of the model, the tropopause, the top of the PBL, and the surface, respectively.

The PBL depth is calculated prognostically from

$$\frac{\partial}{\partial t}(\pi_M) + \nabla \cdot \left(\int_1^2 \pi_M V d\sigma \right) = g\,(E - M_B) \tag{3.3}$$

where $\pi_M \equiv p_S - p_B$ is the pressure thickness of the PBL, E is the rate of turbulent entrainment at the PBL top, and M_B is the mass flux into the base of cumulus clouds, which is calculated by the cumulus parameterization. Thus the mass sources and sinks for the PBL consist of large-scale convergence or divergence, turbulent entrainment, and the cumulus mass flux. The turbulence kinetic energy (TKE, e_M) of the PBL has recently been introduced as a new prognostic variable, simplifying the entrainment calculation

(Randall *et al.*, 1992). Turbulent entrainment can be driven by positive buoyancy fluxes, or by shear of the mean wind in the surface layer or at the PBL top, and is derived from the prognostic equation for the TKE,

$$g^{-1}\pi_M \frac{\partial e_M}{\partial t} + E e_M = B + S - D \tag{3.4}$$

where B and S represent TKE production by buoyancy fluxes and shear, respectively, and D represents dissipation of TKE.

The cumulus mass flux and the warming and drying of the free atmosphere due to cumulus convection are determined through the cumulus parameterization of Arakawa and Schubert (1974; see also Lord *et al.*, 1982), as recently revised to include the ice phase and a prognostic equation for the turbulence kinetic energy associated with cumulus convection (Randall and Pan, 1993). Cumulus friction is included.

The Arakawa-Schubert parameterization currently applies only to clouds that draw their mass from the PBL. There are also moist convective motions that originate above the PBL, which are parameterized through a conventional moist convective adjustment scheme (Suarez *et al.*, 1983). Dry convection is also simulated in the model whenever adjacent layers become statically unstable ($\partial\theta/\partial\sigma > 0$). If at least one superadiabatic pair of layers is found in a column, the column is examined to find the upper and lower bounds of the unstable layer(s). In each unstable region, potential temperature and moisture are homogenized, and the process is repeated iteratively until the column is statically stable.

The radiation parameterization of the model has been revised by Harshvardhan *et al.* (1987). The terrestrial radiation parameterization includes radiative flux divergence due to water vapor, carbon dioxide, and ozone. The solar radiation parameterization includes Rayleigh scattering and absorption by water vapor and ozone, and simulates both the diurnal and seasonal cycles. A complete (solar and terrestrial) radiation calculation is done once per simulated hour, in order to resolve adequately the diurnal cycle and the effects of transient cloudiness (Wilson and Mitchell, 1986). For the present study, a zonally uniform ozone distribution was prescribed as a function of latitude and height from the observations of McPeters *et al.* (1984).

Stratiform clouds and precipitation are simulated by a new parameterization (EAULIQ) of liquid and ice cloud microphysics (Fowler *et al.*, 1994; Fowler and Randall, 1994; see Fig. 3.1). Five prognostic variables are used to track the mixing ratios of water

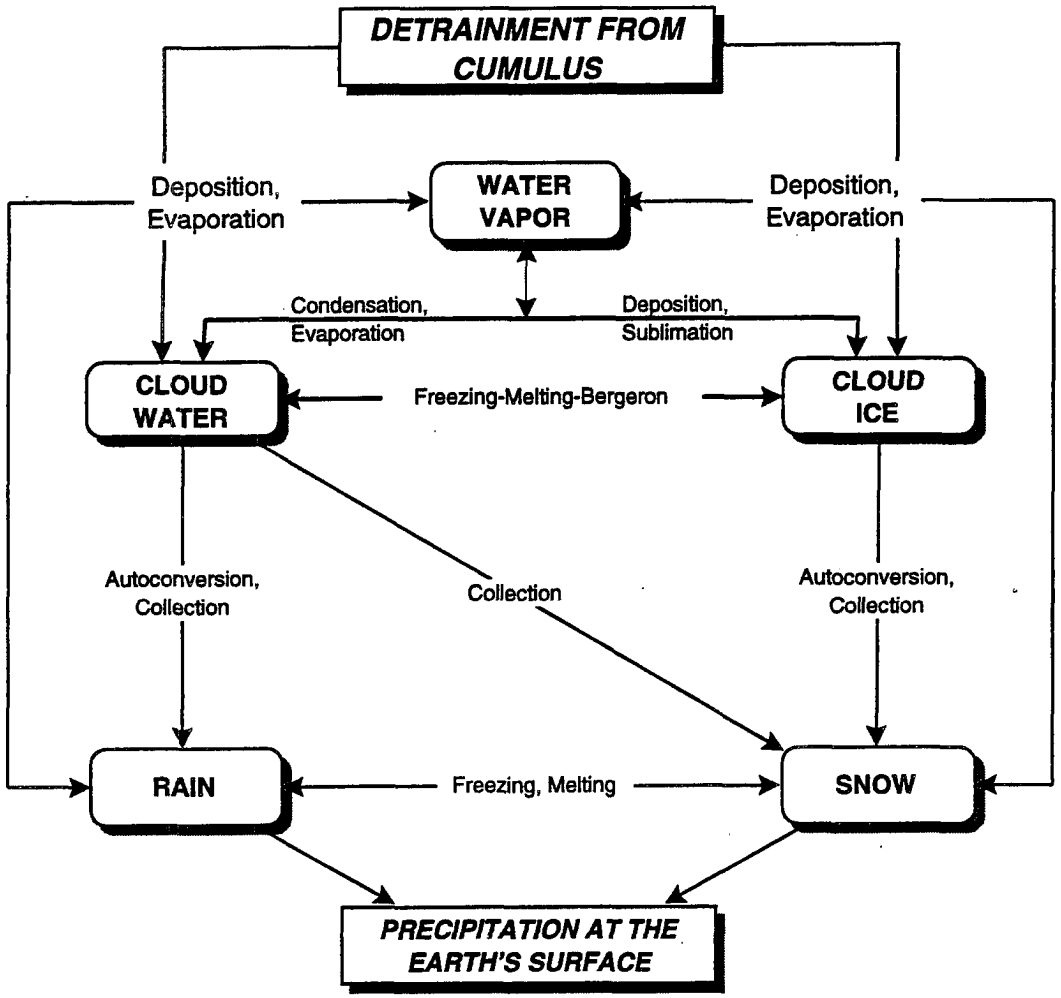

FIGURE 3.1: Structure of EAULIQ, the cloud microphysics parameterization used by the CSU GCM. After Fowler *et al.*, 1994.

vapor, cloud water, cloud ice, and falling rain and snow in the model, with transformation between phases representing condensation, freezing, melting, ice deposition, evaporation, sublimation, and mixed-phase physical processes (graupel and hail are neglected). Large-scale saturation at the grid scale can lead to formation of cloud water and ice, and the cumulus parameterization also provides detrained water and ice as inputs to EAULIQ. In order to allow microphysical transformations among the five phases of water substance simulated in the model, rain and snow particles do not fall instantly to the ground

but rather are time-stepped explicitly, with collection, evaporation, melting, and freezing occurring during their descent. Optical and infrared radiative properties of the clouds are parameterized according to the cloud water, cloud ice, and snow paths for grid cells in which the condensate mixing ratio exceeds 10^{-5} kg kg^{-1} (less dense condensate is assumed to be radiatively inactive). No clouds may form in the model above the 100 mb level, and no parameterization of fractional cloudiness is used in the free troposphere.

Stratocumulus clouds are assumed to be present in the PBL whenever the temperature and mixing ratio at the PBL top (as determined by a mixed-layer assumption) correspond to supersaturation, provided that cloud-top entrainment instability does not occur. The cloud fraction in the PBL is set to 1 when such clouds are more than 12.5 mb deep, and decreases linearly to zero as their depth decreases. The presence of the stratocumulus clouds is felt through both the radiation and entrainment parameterizations. The latter takes into account the generation of turbulence kinetic energy through increased buoyancy fluxes associated with phase changes and highly concentrated cloud-top radiative cooling (Randall 1980, 1984). As a result of these cloud-enhanced buoyancy fluxes, the presence of a stratocumulus layer in the PBL tends to favor more rapid entrainment and, therefore, a deeper PBL.

When cloud-top entrainment instability occurs, the PBL is assumed to exchange mass with the free atmosphere. The amount of mass exchanged is that required to remove the supersaturation, or to restore stability, whichever is less. The PBL depth is assumed to remain unchanged during this process, which is referred to as "layer cloud instability" (LCI).

The prescribed boundary conditions of the GCM include realistic topography, and the observed climatological seasonally varying global distributions of sea-surface temperature, sea-ice thickness, surface albedo, and surface roughness, as well as seasonally varying morphological and physiological parameters for the land-surface vegetation. The surface albedo of the ocean is zenith-angle dependent, following Briegleb *et al.* (1986), who used the data of Payne (1972).

The albedo of the vegetated land surface is determined according to the method of Sellers *et al.* (1986, Appendix B), which includes the effects of snow cover. The fraction of the ground covered by snow is not permitted to exceed 0.8. The albedo of sea ice is 0.8 in the visible, and 0.4 in the near infrared, except that when the temperature of the

sea ice is within 0.05 K of the melting point, these values are replaced by 0.48 and 0.24, respectively. The albedo of land ice is 0.8 in the visible and 0.5 in the near infrared.

3.3.2 The Simple Biosphere Model (SiB2)

For vegetated land points, the surface fluxes of sensible and latent heat are determined using the Simple Biosphere (SiB) parameterization developed by Sellers *et al.* (1986). SiB has recently undergone substantial modification (Sellers *et al.*, 1994*a*, *b*; Randall *et al.*, 1994), and is now referred to as SiB2. The second vegetation layer (ground cover) that was present in the original model as described by Sellers *et al.* (1986) has been removed, but the model otherwise has a similar structure to that shown in Fig. 2.5 (Chapter 2). The other major change is in the calculation of stomatal and canopy conductance as discussed in section 2.6; since this parameterization is used to determine the surface fluxes of tracer T_{18}, it is described in detail here.

Vegetation is represented in SiB by one of nine cover types or "biomes." Some of the twelve biomes defined in the earlier SiB model have been combined and others have been redefined (*cf.* Dorman and Sellers, 1989; see Table 3.2). Individual vegetation elements are considered to be evenly spaced, and their root systems are assumed to extend uniformly throughout the entire grid-area. The depth and density of the root systems determine the amount of soil moisture available for evapotranspiration. Since the soil under a dense vegetation canopy intercepts less radiation and may be aerodynamically sheltered, the energy available to the covered soil is small, and the component terms of the soil energy budget (evaporation, sensible heat flux and ground heat flux) are correspondingly reduced. There is a thin upper soil layer from which there can be a significant rate of withdrawal of water by direct evaporation into the air when the pores of the soil are at or near saturation. Beneath the root zone, there is an underlying recharge layer within which the transfer of water is governed only by gravitational drainage and hydraulic diffusion. The morphological parameters used in SiB are given in Table 1a of Sellers *et al.* (1986).

Vegetative canopies also intercept precipitation, and can store the equivalent of several mm of water on the leaf surfaces. The evaporation of this intercepted water reduces the precipitation input into the soil and reduces the local Bowen ratio, sometimes to negative values.

Table 3.2: Cover Types (Biomes) Represented in SiB and SiB2

SiB1		SiB2	
Type	Name	Type	Name
1	Broadleaf evergreen trees	1	Broadleaf evergreen trees
2	Broadleaf deciduous trees	2	Broadleaf deciduous tree
3	Broadleaf & needleleaf trees	3	Broadleaf & needleleaf trees
4	Needleleaf evergreen trees	4	Needleleaf evergreen trees
5	Needleleaf-deciduous trees	5	Needleleaf-deciduous trees
6	Broadleaf trees with groundcover	6	Short vegetation / C_4 Grassland
7	Perennial grasslands	6	
8	Broadleaf shrubs with grass	6	
9	Broadleaf shrubs with bare soil	7	Broadleaf shrubs with bare soil
10	Tundra	8	Tundra
11	Bare Soil and Desert	6	Short vegetation / C_4 Grassland
12	Cultivation	9	Cultivation / C_3 Grassland

Vegetative canopies strongly absorb photosynthetically active radiation (PAR), in the wavelength interval 0.4 - 0.72 micrometers (μm), and are moderately reflective in the near-infrared region (0.72 μm - 4.0 μm). In contrast, bare ground generally exhibits a gradual increase in reflectivity with wavelength over the interval of 0.4 - 4.0 μm. The incoming short-wave radiation is partitioned into diffuse and direct-beam components, because the absorption and scattering coefficients of canopies are highly dependent upon the angle of the incident flux. Following Dickinson (1983), the two-stream approximation is used to determine the surface albedo and the radiation absorption by the canopy and the surface, as functions of the spectral properties and angular orientation of the stems and leaves. The boundary conditions are provided by the incoming radiative flux above the canopy and the reflective properties of the soil beneath it.

Stomatal conductance is predicted in the CSU GCM by a new method (Collatz *et al.*, 1991, 1992; Sellers *et al.*, 1992*a*, *b*; Sellers *et al.*, 1994*a*) that includes explicit treatment of the carbon assimilation rate by photosynthesis. The regulation of stomatal conduc-

tance by plants can be seen as an optimization problem: they seek to maximize their ability to import atmospheric CO_2 while at the same time minimizing water losses. Since both uptake of CO_2 and loss of water by transpiration are regulated by the stomatal conductance, they are calculated together in SiB2 using biochemical models of photosynthesis based on the work of Farquhar *et al.* (1980) and Berry and Farquhar (1978). The links between photosynthetic carbon assimilation and stomatal conductance are represented in SiB2 following the models of Collatz *et al.* (1991, 1992; see Fig. 3.2). An extra set of

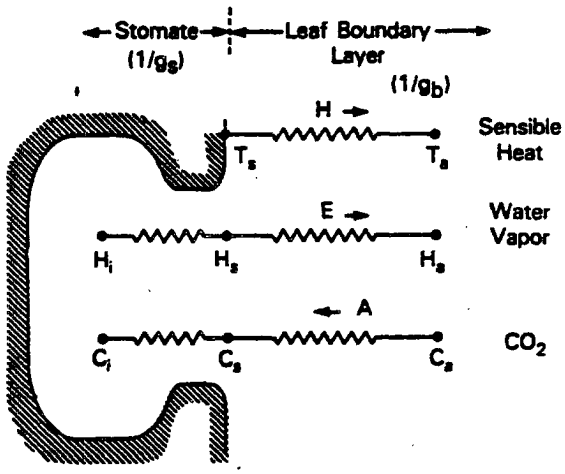

FIGURE 3.2: Detail of stomatal structure in SiB2 as described by Collatz *et al.* (1991) and illustrated by Sellers *et al.* (1992a). Compare to Fig. 2.5 in Chapter 2. Symbols are defined in the text.

variables has been added to the stomatal model: the CO_2 concentration is defined in the interior of the plant (C_i), at the surface of the leaves (C_s, inside the laminar leaf boundary layer), and outside the leaf boundary layer in the canopy air space (expressed as partial pressure in Pa). Fluxes of water vapor, sensible heat, and CO_2 are expressed as differences in potentials divided by resistances. The sensible heat flux, H is given by

$$H = \frac{(T_s - T_a)}{r_b} = g_b (T_s - T_a), \tag{3.5}$$

where T_s and T_a are the temperature at the leaf surface and in the canopy air space, respectively, and g_b=1/r_b is the leaf boundary layer conductance. For water vapor,

$$E = g_s(H_i - H_s) = g_s(H_s - H_a), \tag{3.6}$$

where H_i, H_s, and H_a are the water vapor concentration (mol mol^{-1}) in the leaf interior, at the leaf surface, and in the canopy air space, respectively, and $g_s=1/r_s$ is the stomatal conductance. The leaf interior is assumed always to be saturated with respect to water vapor, so that $H_s/H_i = h_s$, the relative humidity at the leaf surface.

The diffusive flow of CO_2 into the stomata (net assimilation, A_n) is similarly expressed as

$$A_n = \frac{g_s}{1.6}\frac{(C_i - C_s)}{p_s} = \frac{g_b}{1.4}\frac{(C_s - C_a)}{p_s}, \tag{3.7}$$

where A_n is expressed in mol CO_2 m^{-2} s^{-1}, p_s is the surface pressure in Pa, and the constant factors 1.4 and 1.6 account for the different molecular diffusivities of CO_2 and water vapor in the leaf boundary layer and the stomatal pores, respectively. The partial pressure of CO_2 in the canopy air space is assumed to be a uniform constant of 355 ppm times p_s.

The concentration of CO_2 in the leaf interior is calculated from the leaf surface concentration and the assimilation rate

$$C_i = C_s - \frac{1.6A_n}{g_s}p_s. \tag{3.8}$$

Following Collatz *et al.* (1991, 1992) and Ball (1988), stomatal conductance, the carbon assimilation rate, and the CO_2 concentration at the leaf surfaces are assumed to be related by

$$g_s = m\frac{A_n h_s}{C_s}p + b. \tag{3.9}$$

The coefficients m and b are empirically-derived slope and intercept of the (assumed linear) relationship between $(A_n h_s/C_s)\ p$ and g_s. The intercept b represents the resistance when the stomata are completely closed (also called the *cuticle resistance*).

The units of both g_s and b in (3.9) are μmol m^{-2} s^{-1}. The slope m is nondimensional. Collatz *et al.* (1991) used an iterative procedure to simultaneously solve for g_s, A_n, and C_i. For computational efficiency, g_s is updated as a prognostic variable in SiB2, using a scheme which relaxes the new value of g_s toward that predicted from (3.9), while using the "old" value to calculate A_n and C_i.

The net assimilation rate A_n is modeled as limited by the kinetics of the carboxylation enzyme Rubisco, by *electron transport* (a series of reactions that take place when green plant cells are illuminated with visible radiation), and by buildup of the sugars and starches that are the end products of photosynthesis[1].

Farquhar *et al.* (1980) used a simple minimum of the three limits to calculate the assimilation rate

$$A_n = min\,(\omega_C, \omega_e, \omega_s) - R_d \qquad \textbf{(3.10)}$$

where ω_c is the carbon-limited rate of photosynthesis (often referred to as Rubisco-limited, since the rate is determined by Rubisco enzyme kinetics), ω_e is the rate limited by electron transport (light-limited), ω_s is the end product-limited (or sink-limited) rate, and R_d is the rate of carbon loss due to "dark" respiration. SiB2 uses a smoothed function to avoid abrupt transitions from one limitation to another (Collatz *et al.*, 1991) by expressing the rate limitations in terms of simultaneous quadratics:

$$\begin{aligned} \beta_{Ce}\omega_p^2 - \omega_p\,(\omega_C + \omega_e) + \omega_e\omega_C &= 0 \\ \beta_{ps}A^2 - A\,(\omega_p + \omega_s) + \omega_p\omega_s &= 0 \end{aligned} \qquad \textbf{(3.11)}$$

where ω_p is the "smoothed" minimum (found by choosing the smallest root of (3.11)), and β_{Ce} and β_{ps} are "coupling coefficients" which can range from 0 to 1 (typical values are 0.8 to 0.99).

The Rubisco limited assimilation rate, ω_c is calculated from

1. The discussion here refers to C_3 photosynthesis (see section 2.4.2.4). A somewhat different formulation is used for C_4 plants (such as tropical and subtropical grasses of SiB2 biome 7). The links between photosynthesis and canopy conductance are identical, but the specific equations used are not presented here. The interested reader is referred to Collatz *et al.* (1992).

$$\omega_C = V_m \left[\frac{c_i - \Gamma}{c_i + K_C(1 + O_2/K_O)} \right] \tag{3.12}$$

where K_c and K_o are kinetic rate constants for the carboxylation and oxidation reactions, respectively (see section 2.5.3, page 78), O_2 is the partial pressure of oxygen in the plant cells, and V_m is the maximum carboxylation rate. The parameter Γ is called the "CO_2 compensation point", which is the concentration of CO_2 below which carboxylation is slower than the competing oxygenation reaction. The maximum possible rate of the carboxylation reaction V_m is scaled from the "optimum" rate to reflect changes in environmental conditions. The carboxylation rate is given by

$$V_m = V_{max} f_{Hi}(T_C) f_\Psi(w_2), \tag{3.13}$$

where V_{max} is the unstressed maximum reaction rat (essentially a measure of the Rubisco concentration). The rate is reduced by the environmental stress inhibition functions $f_\Psi(w_2)$, representing moisture stress and $f_{Hi}(T_C)$, representing high temperature stress. These inhibition functions are given by

$$\begin{aligned} f_{Hi}(T_C) &= 2^{Q_t}/(1 + exp[m_{HT}(T_C - H_{HT})]) \\ f_\Psi(w_2) &= \{1 + exp[(\Psi_c - \Psi_{root})/50]\}^{-1} \end{aligned} \tag{3.14}$$

where T_c is the canopy temperature, $Q_t = (T_C - 298)/10$, and Ψ_{root} is the water potential in the root zone of the soil (w_2 is the volumetric water content of the second soil layer). The biome-specific parameters m_{HT} and H_{HT} define the slopes and half-heights of $f_{Hi}(T_C)$, and Ψ_c is a "critical" value for root-zone water potential. The value of $f(\Psi)$ is constrained to lie between 10^{-4} (for very dry soils) and 1.0 (for very moist soils).

The light-limited assimilation rate ω_e is computed as

$$\omega_e = (F \bullet n)\,\varepsilon\,(1 - \omega_v) \left[\frac{c_i - \Gamma}{c_i + 2\Gamma} \right] \tag{3.15}$$

where $\boldsymbol{F} \bullet \boldsymbol{n}$ is the intensity of the incident photosynthetically-active radiation normal to the leaf surface, ε is the quantum efficiency for CO_2 uptake (the number of moles of CO_2 fixed per mole of photons absorbed by chlorophyll molecules, another biome-specific parameter), and ω_v is the shortwave albedo of the leaf.

Finally, the end product inhibition limited assimilation rate ω_s is computed as

$$\omega_s = \frac{V_{max}}{2} f_\Psi(T_C) \; f_{Low}(T_C) \,. \tag{3.16}$$

Conceptually, this expression reflects the assumption that the capacity to utilize the immediate products of photosynthesis scales linearly with the Rubisco concentration in the leaf (which is not unreasonable since both represent leaf nitrogen allocation). The assimilation rate is reduced by a moisture stress factor as defined above and by a low-temperature inhibition factor defined by

$$f_{Low}(T_C) = \frac{1.8^{Q_t}}{1 + exp\,[m_{LT}(H_{LT} - T_C)\,]} \tag{3.17}$$

where m_{LT} *and* H_{LT} are biome-specific parameters defining the slope and half-height of $f_{Low}(T_C)$.

The net assimilation must also reflect the loss of CO_2 due to leaf respiration, R_d. This is not to be confused with the wasteful photorespiration which results from competitive inhibition of the carboxylation activity of Rubisco, but is a necessary part of plant metabolism. In SiB2, the rate of autotrophic "dark" respiration is given as

$$R_d = \frac{a_{RD} V_{max0} f(\Psi)\, 2.0^{Q_t}}{1 + exp\,(T_{RDA}\,(T_C - T_{RDM}))}, \tag{3.18}$$

where a_{RD}, T_{RDA}, and T_{RDM} are biome-specific parameters.

The equations presented here are based on considerations of local conditions (internal CO_2 concentration, Rubisco activity, light intensity, *etc.*) at the scale of a single chloroplast or at most a single leaf. Sellers *et al.* (1992*a*) extended the applicability of the

model by performing an integration through the full plant canopy. This was made possible by assuming that the distribution of Rubisco activity (*i.e.* V_m) in the canopy reflects the time-mean distribution of PAR. This assumption is justified based on studies of the economics of nitrogen allocation in plants (*e.g.* Field and Mooney, 1986; Cowan, 1986; Givnish, 1986), which suggest exactly such a partition to maximize the return in energy for a given investment in scarce nitrogen. Nitrogen is allocated by plants to construct Rubisco where it will "do the most good" by allowing the plant to assimilate the most carbon. This means the "sun leaves" at the top of the canopy have the greatest photosynthetic capacity (Rubisco content), and that Rubisco levels decline in the canopy with the degree of shading by upper leaves.

Sellers *et al.* (1992*a*) applied Beer's Law for interception and absorption of PAR to express the net assimilation and stomatal conductance for the entire canopy as closed-form integrals which are solved analytically. They showed that the quantities defined by equations (3.8) through (3.18) can be converted from "top leaf" values to canopy-integrated values simply by multiplying by the "canopy PAR use parameter,"

$$\Pi = \frac{1 - exp\,(-\bar{k}\,\mathrm{LAI})}{\bar{k}} = \frac{\overline{\mathrm{FPAR}}}{\bar{k}}. \qquad (3.19)$$

In (3.19), k is the extinction coefficient for PAR flux in the canopy, LAI is the total leaf area index (leaf area per unit ground surface area), FPAR is the fraction of PAR absorbed in the canopy, and the overbars indicate time-mean values of these quantities. All three quantities in this expression can be estimated from spectral vegetation indices (such as NDVI). In SiB2, these parameters (and many others) are calculated as described by Sellers *et al.* (1994) using NDVI data on a $1^\circ \times 1^\circ$ global grid recently generated from NOAA Advanced Very High Resolution Radiometer data as described by Los *et al.* (1994).

3.3.3 Model Parameters for this Study

Two finite difference grids were used in this study: "standard" experiments used a horizontal grid of 4° latitude by 5° longitude with 17 levels in the vertical and a time step of 6 minutes; and "low-resolution" experiments used a horizontal grid of 7.2° latitude by 9° longitude, with 9 levels in the vertical and a time step of 10 minutes (Fig. 3.3, see also section 3.5). The prognostic variables of the CSU GCM are staggered with respect to this

Horizontal Grids Used in this Study

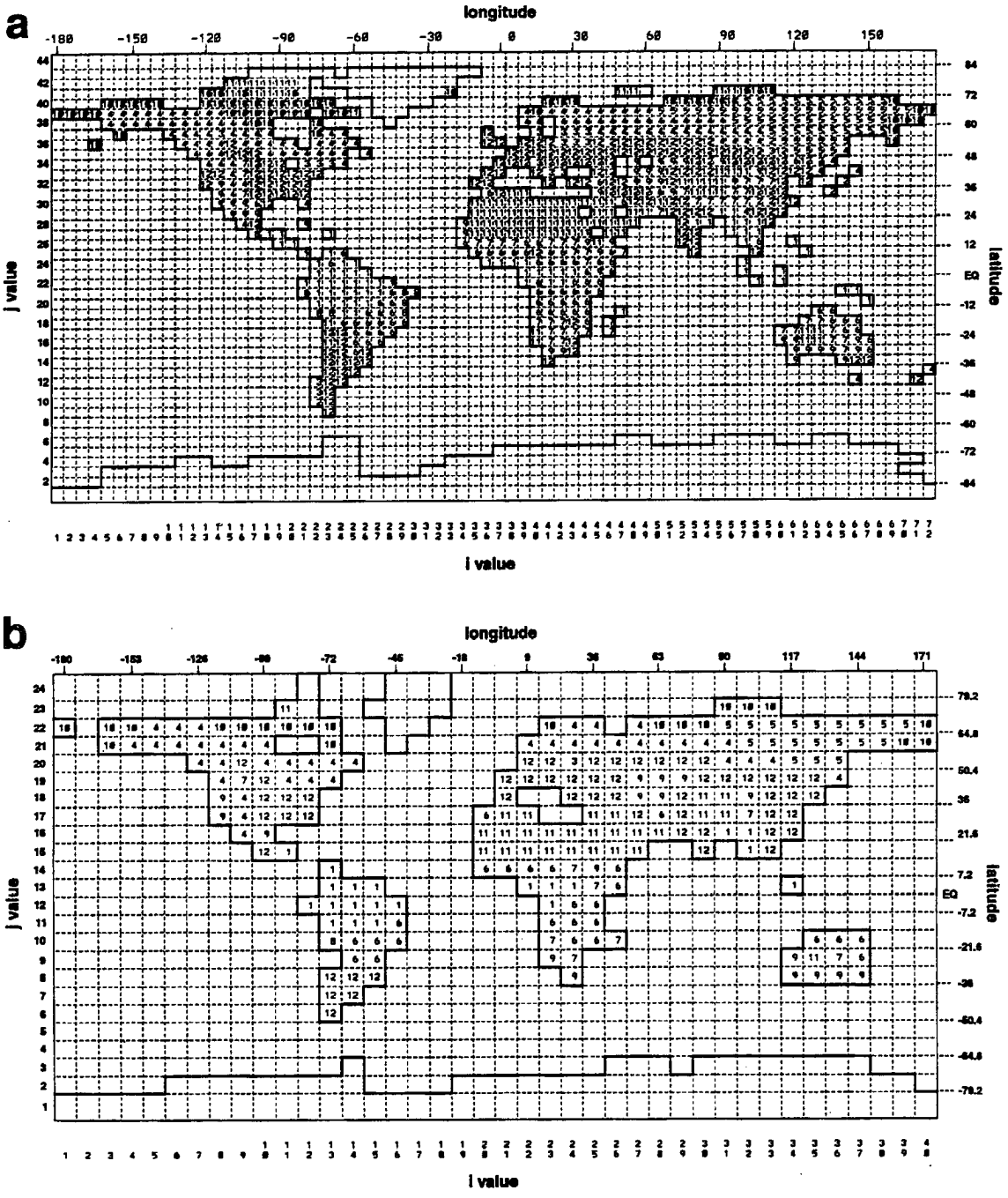

FIGURE 3.3: Horizontal grids used in the CSU GCM for this study. (a) The standard (4° × 5°) grid; (b) the low-resolution (7.2° × 9°) grid. Numbers along the left and bottom margins are indices used in the model. The land-sea mask of the GCM is indicated by the heavy lines, and the numbers in each grid cell indicate the SiB2 biome (vegetation type, see Table 3.2). Unlabeled land points are covered by perpetual ice.

grid in such a way that "mass" type variables (pressure, temperature, moisture, CO_2, *etc.*) are defined in the centers of the grid cells in Fig. 3.3, zonal wind is defined one half grid cell to the east, and meridional wind is defined one half grid cell to the south (Arakawa and Lamb, 1977, Grid "C"). For reasons explained by Arakawa and Lamb (1981), the row of grid cells closest to each pole span six degrees of latitude instead of the four degrees occupied by all the "internal" grid cells in the standard run; the polar grid cells in the low-resolution model span 10.8° of latitude. In both the low-resolution and the standard simulations, the top of the model atmosphere at 51.3 mb.

Both experiments used a one hour time step for the "physics" (radiation, cumulus convection, moist adjustment, large scale precipitation, LCI, PBL processes and surface fluxes). The increments calculated by the "physics" each hour are divided into equal fractions (the number of dynamics time steps per physics time step) and added incrementally in "eyedropper" fashion every dynamics time step (six or ten minutes). The model uses leapfrog time differencing for the dynamics time steps, with a Matsuno time step once per hour.

The vertical structure of the low-resolution model is shown in Fig. 3.4. One additional level is included in the standard model's "stratosphere" and seven additional levels are included in the standard model's free troposphere. Both versions use a single, variable-depth bulk boundary layer as their lowest atmospheric level.

3.3.4 Horizontal Advection

Horizontal advection of all 18 of the CO_2 tracers was by a second-order, centered-in-space, leapfrog-in-time scheme. It is recognized that this scheme is prone to dispersion errors in the presence of strong gradients (Rood, 1987), but since the CO_2 tracers were integrated from a globally uniform initial condition and the surface fluxes of most tracers are orders of magnitude smaller than the "background" concentrations, this was generally not a problem. The only significant exceptions were the radioactive tracers T_{16} and T_{17}. Because all of the sources of ^{85}Kr are point sources (nine nuclear fuels reprocessing plants) and ^{222}Rn is emitted only on land, very strong gradients in the concentration of T_{16} were produced in the PBL in the vicinity of the point sources and in the concentration of T_{17} near most coastlines. In these cases, negative concentrations frequently developed in the model due to more tracer being removed from a given grid cell than its total inventory of the tracer. Because this problem only occurred for the radioactive tracers

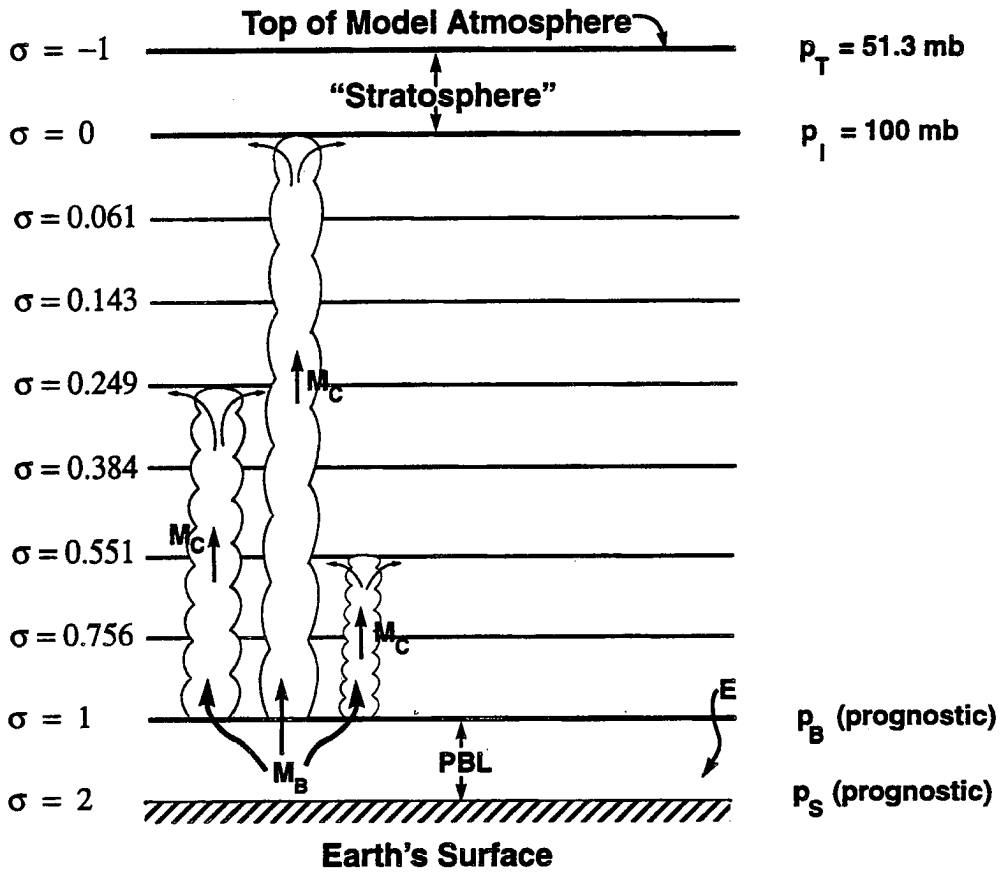

FIGURE 3.4: Vertical Structure of the low-resolution version of the model atmosphere in this study. M_B and M_C are the cumulus mass flux at the base of and in the interior of each cloud type, respectively, and E is the rate of turbulent entrainment at the top of the PBL. Other symbols are defined in the text.

and not the CO_2 tracers, I chose to simply fill the "holes" (negative concentrations) in the fields of these two tracers by adding enough tracer to bring the concentration to zero and then applying a multiplicative scaling to every other atmospheric value such that the global total mass of each tracer was conserved at each time step.

I recognize that this procedure causes computational "diffusion" of the radioactive tracers; this is particularly unfortunate because these tracers are intended to measure the realism of the simulated mixing in the GCM. Nevertheless, since the hole-filling algorithm was not applied to the simulated CO_2, the conclusions regarding the global carbon budget and atmospheric transport of CO_2 are unaffected. Every grid cell in the model atmosphere was checked for negative concentration of all 18 tracers in every dynamical time step; aside from the radioactive tracers, no hole was ever found.

3.3.5 Vertical Advection

Above the top of the PBL, vertical advection of CO_2 was accomplished by a second order, centered-in-space, leapfrog-in-time scheme. The vertical fluxes were based on layer-edge values which were simply the average of the layer center values above and below. At the PBL top, a first-order upstream scheme was applied separately for turbulent entrainment and loss of tracer mass from the PBL due to cumulus mass flux. This is also the method used for vertical advection of all the other "mass-like" variables in the GCM.

3.3.6 Cumulus Convection

In the cumulus parameterization, an ensemble of clouds of multiple heights are considered to exist in those model columns in which cumulus convection occurs (Arakawa and Schubert, 1974; Lord, 1978; Lord and Arakawa, 1980; Lord, 1982, Lord *et al.*, 1982). The clouds all originate at the top of the PBL and extend to some (or even all) of the other layer-tops in the model atmosphere. The model calculates the amount of cumulus available potential energy in a grid column, and then apportions the release of this energy into one or more "types" of clouds defined by the fractional amount of entrainment of environmental air into the cloud as it passes through each layer. The fractional entrainment rate is not considered to vary with height. In-cloud air in each type of cloud has the properties of the PBL at cloud base, but is altered by entrainment in each layer through which it passes. The top of each cloud type is determined by the level at which the in-cloud air (now diluted by entrainment) becomes neutrally buoyant with respect to the environment. The mass flux M_C, due to each cloud type at the base of each layer in each grid column (see Fig. 3.4) is calculated by the Arakawa-Schubert parameterization. The availability of this flux makes calculation of the vertical transport of atmospheric tracers quite straightforward, and is one of the strengths of this cumulus parameterization.

The in-cloud air at the top of the PBL was assumed to have the tracer concentration of the PBL, since all the cloud air is drawn from the PBL. At each successive layer base above the PBL top, the in-cloud tracer concentration was calculated for each cloud type as

$$C_C(L) = \frac{C_C(L+1) + C(L+1)\,\lambda\delta z}{1+\lambda\delta z} \tag{3.20}$$

where C_C(L) is the in-cloud concentration C(L) is the environmental concentration of the tracer at level L, and

$$\lambda \delta z \equiv \frac{M_C(L) - M_C(L+1)}{M_C(L+1)} \tag{3.21}$$

is the fractional entrainment rate of the cloud. The flux of each tracer into each model layer due to cumulus convection is simply $M_C(C_C - C)$, the product of the cumulus mass flux into the layer and the difference in tracer concentration between the in-cloud air and the ambient or "environmental" air at that level. This calculation was performed for each level up to the top of each cloud, and the fluxes were summed over all types (top-heights) of cloud present in the given grid column. The change in tracer concentration due to cumulus convection was then calculated as the divergence of the total tracer flux due to all cloud types. This calculation was performed only once per simulated hour, and one tenth of the change in concentration was applied incrementally in "eyedropper" fashion every six minutes (one sixth every ten minutes for the low-resolution simulations).

Moist convection originating above the PBL is parameterized in the model as simple vertical overturning of the air with moisture condensed when a layer becomes supersaturated (Manabe *et al.*, 1965). I did not calculate vertical transport of the tracers by this process.

3.3.7 Dry Convective Adjustment

The subroutine which controls dry convection in pairs of superadiabatic layers was modified to include vertical mixing of CO_2. After horizontal and vertical advection has been performed in the dynamics routine (every six minutes), each column of air in the model is checked for unstable pairs of layers. If at least one pair of unstable layers ($\theta_L < \theta_{L+1}$) is found in a column, the column is examined in detail to find the upper and lower bounds of the unstable layer(s). In each unstable region, the total mass of the region and of each tracer was determined. The concentration of each tracer at each model level in the unstable region was then set to the mass of the tracer in the unstable region divided by the mass of the region. This process was repeated until the entire column was statically stable. This process is important over arid land areas (such as the Sahara) where surface heating is strong but there is little water vapor in the PBL to allow cumulus convection. This situation is essentially an extension of the PBL, but the lowest mod-

el layer is not allowed to occupy more than 20% of the depth of the troposphere to prevent excessive loss of vertical resolution.

3.3.8 Radioactive Decay

The concentrations of tracers T_{16} and T_{17} are also updated due to radioactive decay, using the equation

$$C^{n+1} = C^n - \lambda_D C^n \Delta t, \tag{3.22}$$

where C^n is the "old" concentration and C^{n+1} is the "new" concentration, and λ_D is the radioactive decay constant (2.042×10^{-9} s^{-1} for T_{16} and 2.097×10^{-6} s^{-1} for T_{17}). Equation (3.22) is numerically unstable under leapfrog time differencing (Haltiner and Williams, 1980), so the radioactive decay is performed only once per hour in the "physics" part of the model calculation, using a simple forward time step.

3.4 Input Data for the Atmospheric Model: Surface Fluxes of CO_2

The surface flux data used to construct the scenarios evaluated in the TFT90 study were obtained from NASA GISS (Inez Fung, personal communication). These data consisted of:

1) A map of emissions of CO_2 from fossil fuel combustion and cement manufacturing in 1987;

2) A map of estimated emissions of CO_2 to the atmosphere due to changes in land use (deforestation);

3) Twelve maps of monthly mean estimates of uptake and release of CO_2 from the terrestrial biosphere due to photosynthesis and ecosystem respiration.

In the following subsections, I present maps of the surface flux of each tracer for each month of the year. I also describe the sources for these data, and the calculations I performed to convert them to the $4° \times 5°$ grid used by the CSU GCM. The data used to

drive the low-resolution experiments were derived from the standard resolution data; the procedures used to generate these fields are described in section 3.4.7

A word on the color schemes used in the color-filled contour maps in this document is in order. All of the color maps in this thesis use a 19 color "rainbow," with the smallest values represented by dark purple and the largest values represented by bright red. I have consistently chosen the colors so that the "middle" color (light green) represents a "special," meaningful value: either zero, where appropriate, or the global (area-weighted) mean of the field. In the case of surface fluxes presented in this section, blue and purple values represent net loss of CO_2 from the atmosphere and yellows, oranges, and reds represent a net gain of CO_2 by the atmosphere. The contour values are the same among all the surface flux maps in this section, so that the same colors represent fluxes of the same magnitude across all of the surface flux maps. The unit of surface flux in these maps is 10^{-9} kg m^{-2} s^{-1}, which is equivalent to μg m^{-2} s^{-1}. Note that the contour interval is not linear in these maps, but is much finer at low values to show the geographic structure of fluxes which are relatively weak.

3.4.1 Tracer T_1: Industrial Emissions of CO_2

Surface fluxes of carbon to the atmosphere due to fossil fuel combustion and cement manufacture were derived from the data of Marland (1989), and were assumed not to vary seasonally. These data were used to define the sources for tracer T_1 and are presented in Fig. 3.5. These estimates were obtained by Marland (1989) from economic data by country. The global annual flux of carbon from anthropogenic sources in these estimates is 5.3 Gt. Marland (1989) suggests that this total is accurate to within ± 10%. TFT90 distributed Marland's country by country data by population density on a 1° × 1° grid. I converted these data to the 4° × 5° grid of the CSU GCM by averaging all the 1° × 1° grid cells contained in each of the larger CSU GCM grid cells.

The emissions map shows that the source of this tracer is primarily in three regions of the world: North America, Europe, and eastern Asia. The greatest rate of grid-cell averaged emissions is about 27.3 μg m^{-2} s^{-1} over western Europe. Secondary source regions in the southern hemisphere, smaller both in the magnitude of the flux and the area of elevated emissions, are located along the east coast of South America, South Africa, and southeast Australia. Some areas of the figure appear to show emissions in the ocean (*e.g.*, off the southeast coast of North America and northeast of Japan). These anomalous

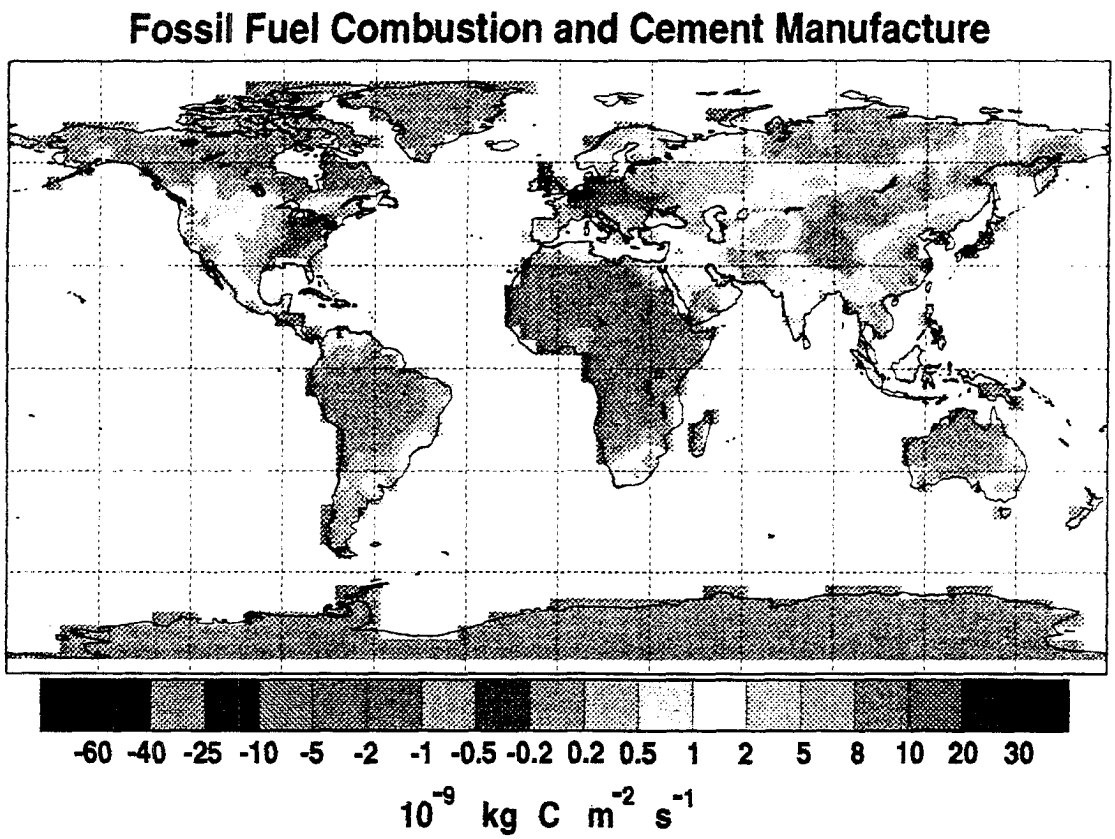

FIGURE 3.5: Flux of carbon to the atmosphere due to anthropogenic emissions.

fluxes result from the relatively coarse resolution of the GCM, and the slightly different coastline as represented in the model and the plotting package. The fluxes of this tracer are zero at all points defined to be in the ocean by the model.

3.4.2 Tracer T_2: Emissions Due to Changes in Land Use (Tropical Deforestation)

Fluxes of carbon from the land surface to the atmosphere in each country as a result of changes in land use were compiled by Houghton *et al.* (1987) (see section 2.2). TFT90 distributed the per-country fluxes uniformly on the same $1° \times 1°$ grid as they used for anthropogenic emissions. Houghton *et al.* (1987) estimate the global annual net flux from this source to be between 1.0 and 2.6 Gt of C. The preferred scenario of TFT90 used a scaled down deforestation flux of only 0.3 Gt C yr^{-1}, but they distributed the flux exactly as was done by Houghton *et al.* (1987). To simplify the later analysis of the results, I scaled the global flux to be a source of exactly 1.0 Gt C yr^{-1}. Having obtained the

gridded data set used by TFT90, I averaged the 1° × 1° data onto the coarser 4° × 5° grid of the CSU GCM and multiplied each point value by a constant to bring the total flux up to 1.0 Gt. The resulting map of surface fluxes (which I have again assumed not to vary seasonally) is shown in Fig. 3.5.

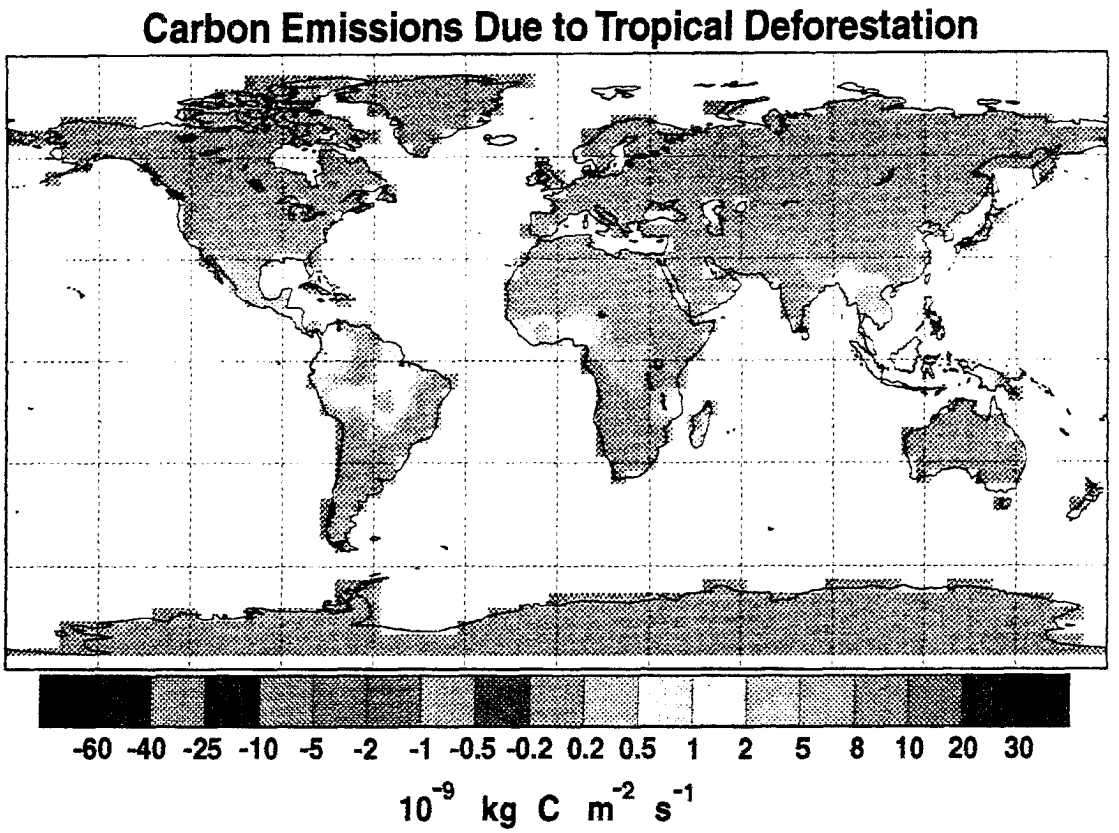

FIGURE 3.6: Flux of carbon to the atmosphere due to land use changes (after Houghton *et al.*, 1987)

3.4.3 Tracers T_3 - T_8: Exchange Between the Atmosphere and the Ocean Surface

Because the tracer transport problem is linear in the tracer concentrations (see section 3.2), the magnitude of the total source or sink of any of the regional ocean tracers can be scaled *a posteriori* to test any hypothesis about air-sea exchange of CO_2, as was done by TFT90. To construct the flux data for the tracers $T_3 - T_8$, the oceans were divided by region, following the boundaries used by TFT90 as closely as the grid allowed (Fig. 3.7). The sea-to-air flux of CO_2 at each grid point was set such that the total annual source or

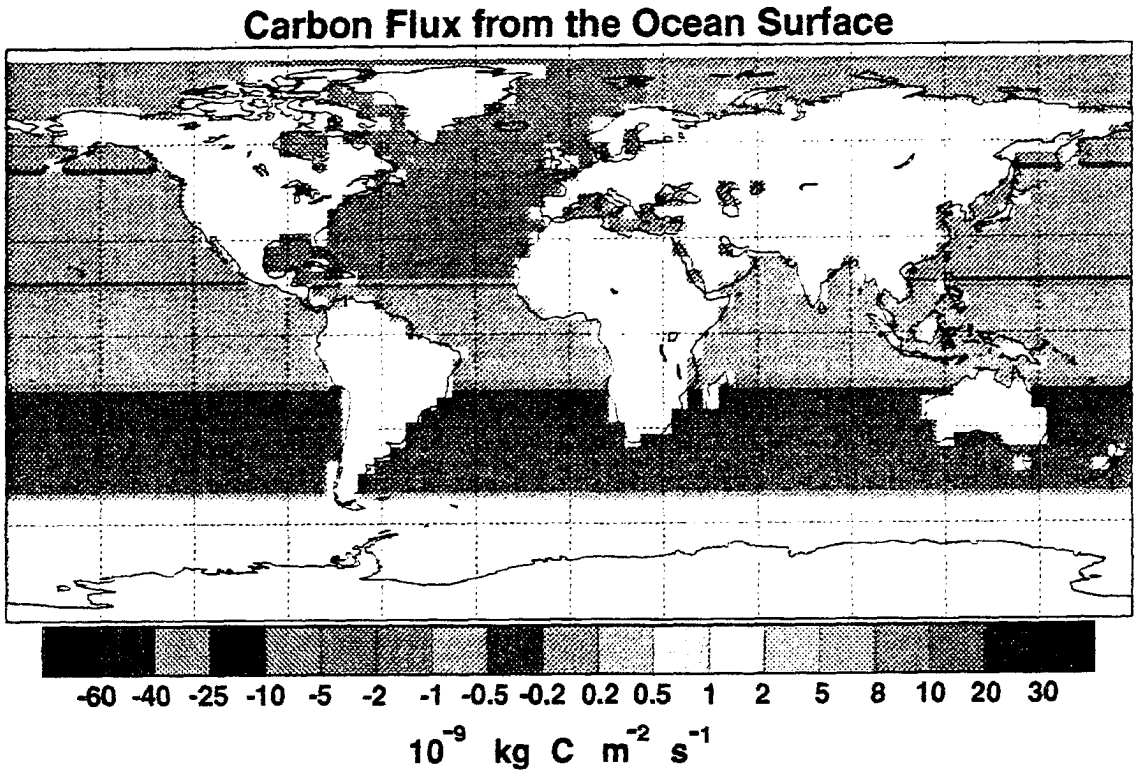

FIGURE 3.7: Surface fluxes of tracers T_3 through T_8, shown here for the standard model. The regional boundaries were slightly different in the low-resolution model.

sink of each tracer was exactly 1 Gt C yr^{-1}. When ice was present at a given grid point, the flux was set to zero there until the ice melted.

3.4.4 Seasonal Exchange with the Terrestrial Biosphere

Three tracers (T_9, T_{15}, and T_{18}) were defined to represent seasonal exchanges with the terrestrial biosphere. Tracer T_9 was driven by the monthly flux maps of Fung *et al.* (1987), as used by TFT90. The monthly estimates of net ecosystem flux made by the revised CASA model (Potter *et al.*, 1993) were used to drive tracer T_{15}. The fluxes of tracer T_{18} were not prescribed from maps, but rather calculated at the dynamical time step of the GCM.

3.4.4.1 Tracer T_9: Flux Maps of Fung *et al.* (1987)

TFT90 used net fluxes from the terrestrial biosphere to the atmosphere which were derived by Fung *et al.* (1987). That study (see section 2.4) used maximum-value compos-

ited monthly NDVI to estimate the seasonal phase of changes in net primary production. This seasonal pattern was then applied to estimates of annual net primary productivity derived from field measurements published by other authors, according to a vegetation group (biome) classification. They used a simple function of temperature to estimate respiration fluxes from each biome. The global annual net flux from this source is nearly zero. I obtained these data on a 4° × 5° grid from NASA GISS. The only adjustments to these data were in the polar latitude strips, where the CSU GCM uses special 6° × 5° grid cells. The data vary seasonally. Twelve monthly maps of these fluxes are presented on the following pages (Figs. 3.8 through 3.8).

Although these fluxes are purely seasonal (with no net source or sink in the annual mean), Fung *et al.* (1983, 1987) showed that they have an effect on the annual mean meridional gradient of atmospheric CO_2 because of correlations between the fluxes and atmospheric transport. In order to examine this behavior in the CSU GCM, I enforced the condition that the net annual flux equals zero by summing the twelve monthly fluxes at each grid point and then subtracting one-twelfth of the sum from each monthly value.

Even though they have no net effect on the global carbon budget in the annual mean, regional extrema of monthly surface fluxes into and out of the terrestrial biosphere are the most intense of all the tracers considered. In the winter months, surface fluxes in the high latitudes of northern hemisphere are near zero because the soils are frozen and there is little or no photosynthetic activity (Fig. 3.8). Further south, CO_2 is released from soils in warmer regions where respiration exceeds photosynthesis during the season of minimum productivity. The African Sahel is a net source of CO_2 to the atmosphere at this time because carbon fixed during the rainy season is being released. Carbon uptake in the southern hemisphere tropics is a maximum at that time, however, as seasonal rains stimulate plant growth. As the spring progresses, soils thaw in the northern temperate latitudes, and CO_2 is released by respiration.

Emissions of biospheric CO_2 reach a maximum in May as boreal soils begin to thaw (Fig. 3.8), with large areas of Asia and North America releasing more than 10 $\mu g\ C\ m^{-2}\ s^{-1}$ (the most intense grid cell average emission rate is 33.8 $\mu g\ m^{-2}\ s^{-1}$ in Alaska in June). By June, the seasonal rains in the southern tropics have stopped, and respiration overtakes photosynthesis in these regions, which then become a net source of atmospheric CO_2. As the growing season progresses in the northern midlatitudes, very strong uptake of CO_2 occurs, exceeding 10 $\mu g\ m^{-2}\ s^{-1}$ over most of the northern hemisphere landmasses. The greatest uptake rate is 76.2 $\mu g\ m^{-2}\ s^{-1}$ in Alaska in August. Boreal re-

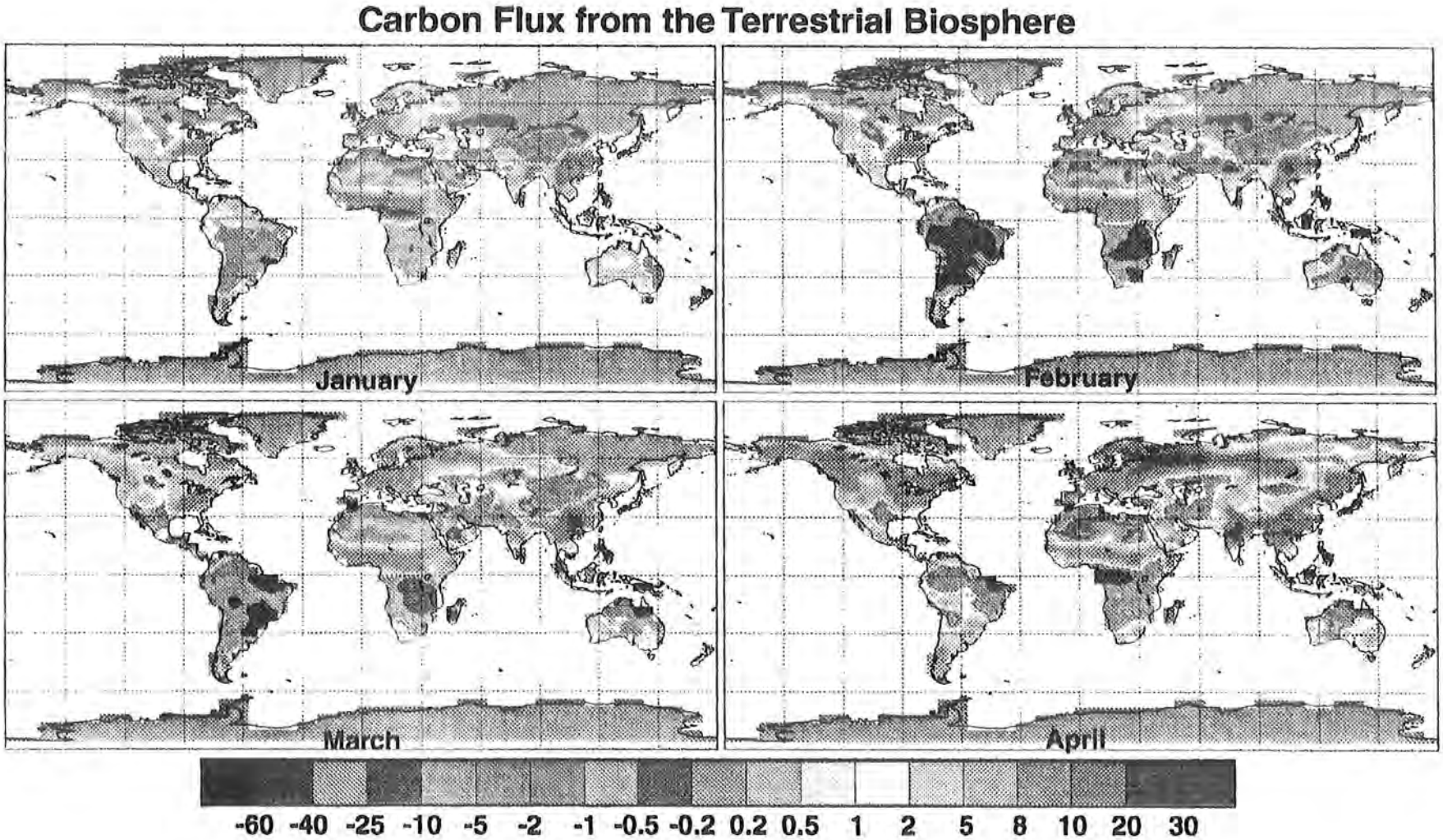

FIGURE 3.8: Carbon flux (10^{-9} kg m^{-2} s^{-1}) from the terrestrial biosphere for January through April

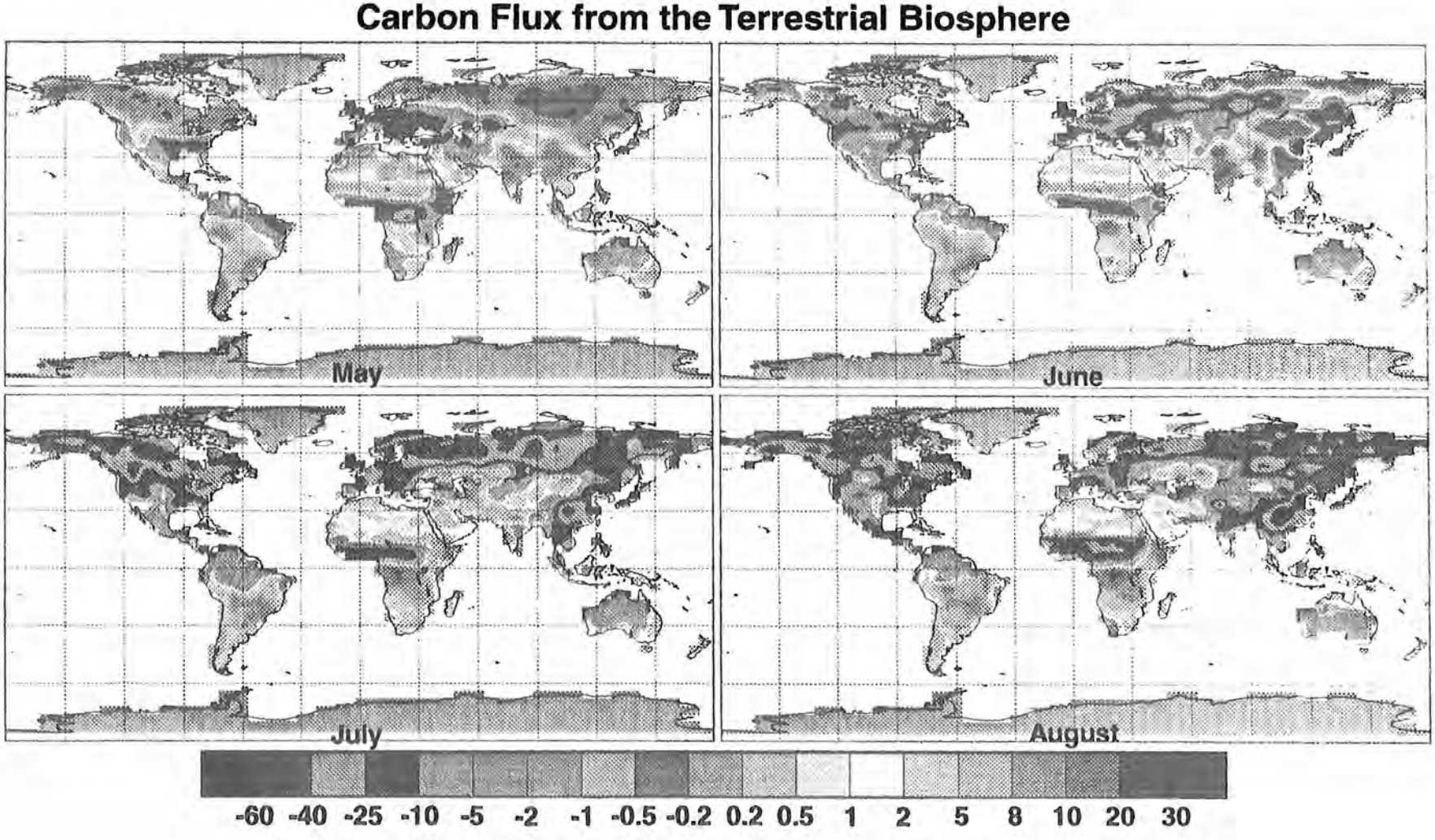

FIGURE 3.9: Carbon flux (10^{-9} kg m^{-2} s^{-1}) from the terrestrial biosphere for May through August

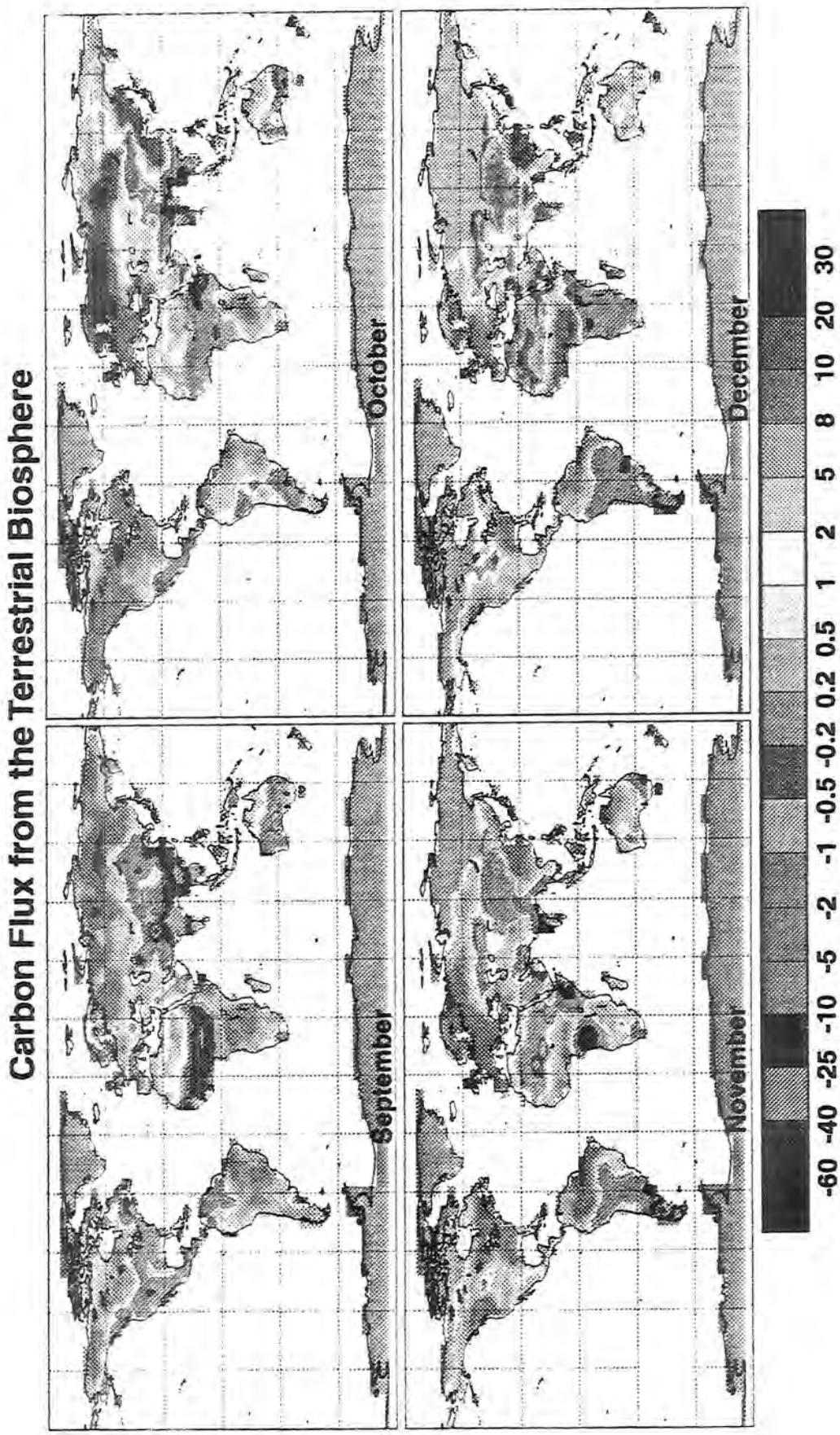

FIGURE 3.10: Carbon flux (10^{-9} kg m^{-2} s^{-1}) from the terrestrial biosphere for September through December

gions change from strong net sources to strong net sinks in just a couple of months. Strong uptake of CO_2 by vegetation in the tropics of the northern hemisphere also occurs during this time as monsoon rains stimulate primary production in southern Asia and the African Sahel.

At the end of the summer, respiration releases much of the carbon that was fixed during the growing season in the boreal and northern regions (Fig. 3.8). As the seasonal rains once again retreat southward through central Africa and out of Asia, these areas once again become net CO_2 sources as well. By December, frozen boreal soils have once again become neutral in terms of CO_2 fluxes, and uptake exceeds respiratory fluxes in the southern tropics.

3.4.4.2 Tracer T_{15}: Revised CASA NEP Fluxes

Potter *et al.* (1993) used global data sets of NDVI, incident solar radiation, and soil texture and organic matter content to drive a new model of Net Ecosystem Production (see section 2.6). Their approach was to construct simple models of NPP and soil moisture based on published data and satellite imagery, and then use these models to drive a biochemical model of organic carbon and nitrogen cycling in the litter and soil. Estimates of NPP were based on incident solar radiation, scaled by a photosynthetic efficiency factor and reduced to account for effects of water limitation and temperature stress. The efficiency factor was assumed to be globally uniform (not biome dependent), and was determined by calibrating the NPP submodel against published values of NPP at 17 sites in various biomes. The incident radiation was prescribed from satellite data and climatological maps of cloudiness.

A "bucket" type soil moisture submodel was used to keep track of the total soil moisture content at each (monthly) time step. The capacity of the "bucket" was varied according to soil texture data prescribed from published data. Climatological data were used to update the soil moisture at each month, with precipitation added to the soil up to the field capacity, and losses to evapotranspiration estimated based on the equations of Thronthwaite (1948), with a reduced drying rate in drier soils as derived by Saxton *et al.* (1986).

Each year's new plant production was passed into the soil carbon submodel by prescribing "litterfall" to occur according to month-to-month changes in LAI as determined from the satellite-derived NDVI data. Fluxes between the various carbon pools were calculated according to temperature, soil moisture, soil texture, and the carbon-to-nitrogen

(C:N) ratio of the material. Litter was represented as three separate components (leaves, roots, and woody material, see Fig. 3.11), with the leaf and root components having both

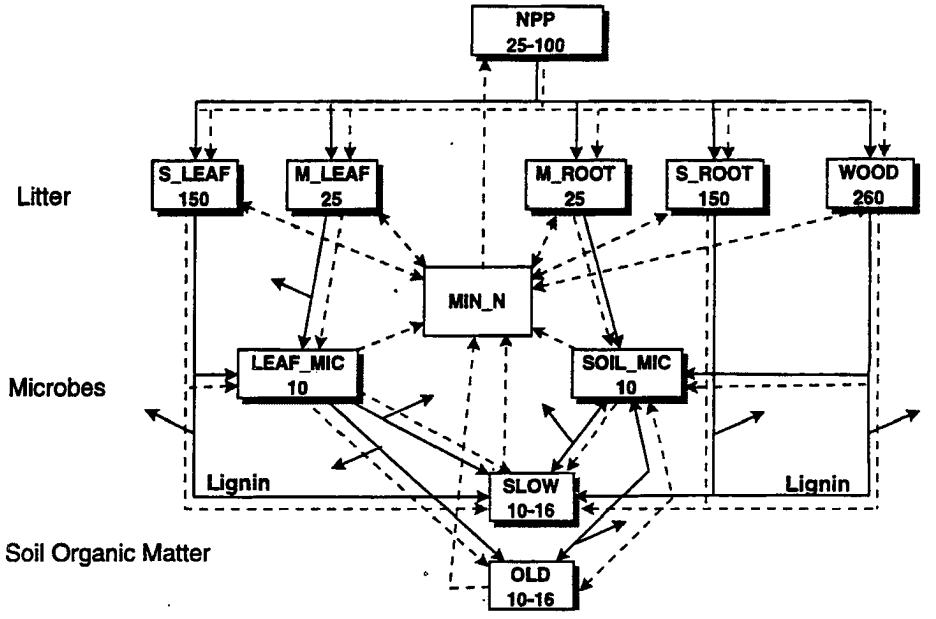

FIGURE 3.11: Compartmental structure of the soil carbon and nitrogen cycling submodel of CASA. The litter layer is divided into leaf, root, and woody pools. These are further divided into "structural (S_)" and "metabolic (M_)" components. The dashed arrows indicate fluxes of nitrogen which accompany carbon fluxes (indicated by the solid arrows). MIN_N is the mineral nitrogen pool. Numbers indicate the C:N ratios of the various pools. Arrows branching off from the various flux pathways indicate evolution of CO_2 gas, which is released to the atmosphere. After Potter *et al.* (1993).

structural (higher C:N ratio) and metabolic (lower C:N ratio) fractions. All decomposition was represented as being mediated by microbial activity, with microbial carbon pools having a much lower C:N content than the litter pools. Microbial decomposition then passed the organic material into two different soil pools, a "slow" pool which stored more easily decomposed material and an "old" pool which received more resistant material (higher lignin content).

Fluxes between each carbon pool were represented as accompanied by companion fluxes of nitrogen. Plant production was allocated such that the plant tissue (as represented in the model by the litter produced) had the highest "quality" (lowest C:N ratio) appropriate for the biome. Plant production thus depleted a pool of available nitrogen that could be replenished by decomposition in the litter and soil. When insufficient nitrogen was available to maintain the optimum C:N ratio in the living plant material, litter C:N ratios increased, reducing the efficiency of microbial decomposition. Fluxes between the

various reservoirs in the litter, microbes, and soils resulted in addition or removal of nitrogen from the available N pool, and could also lead to the release of carbon as CO_2. The monthly mean flux of CO_2 to the atmosphere was calculated as the difference between this microbial respiration and the monthly NPP.

The CASA model was integrated for 300 simulated years, after which time the sizes of the various carbon and nitrogen pools had stabilized. The resulting monthly NEP values showed stronger seasonality in the tropics than in the middle and high latitudes of the northern hemisphere (Potter *et al.*, 1993, their plate 3), which is unexpected given the much stronger seasonal amplitude of the CO_2 concentrations observed at those latitudes (Conway *et al.*, 1988), and is very different from the fluxes estimated by Fung *et al.* (1987) and used for my tracer T_9.

The unexpectedly weak seasonality in the estimated CO_2 fluxes in the CASA model has been attributed to an overestimated sensitivity of soil respiration to soil temperature (Christopher Potter, personal communication). Decomposition rates in the published model were adjusted for the effects of temperature according to

$$T_s = Q_{10}^{(T-30)/10}, \tag{3.23}$$

where T_s is a scalar which was multiplied by the "optimum" decomposition rate, T is the monthly mean air temperature in Celsius, and $Q_{10} = 2.0$ is an empirical constant which represents the multiplicative increase in microbial decomposition rates for a 10° increase in temperature. In months when the prescribed climatological air temperature was very low, the simulated decomposition rate would be nearly zero. Since the annual integral of the soil decomposition must be near zero at equilibrium, this forced more of the respiration flux of CO_2 into the warmer months of the year, when it "cancels out" the uptake by photosynthesis.

To address this unrealistic result, the CASA model was run again using $Q_{10} = 1.5$, to reduce the temperature sensitivity and shift some of the respiration into the colder months (Christopher Potter, personal communication). The new monthly NEP fluxes were provided to me by James Randerson at Stanford University. I averaged the $1° \times 1°$ data onto the $4° \times 5°$ grid of the CSU GCM. The revised CASA fluxes did not give a purely seasonal effect on atmospheric CO_2, but rather amounted to a small but significant net sink in the global annual integral. This may result from a slower approach of the soil car-

bon pools to equilibrium using the lower temperature sensitivity factor (Christopher Potter, personal communication). Since I want to compare the seasonal and geographic influence of these fluxes with those of Fung *et al.* (1987) in this study, I subtracted a fraction of the annual integral from the monthly fluxes at each grid point, such that the annual total flux at each $1° \times 1°$ grid cell is exactly zero.

3.4.4.3 Tracer T_{18}: On-line Prognostic CO_2 Exchange

Unlike all the other tracers, the flux of tracer T_{18} was not prescribed *a priori* as a boundary condition but was determined diagnostically on-line in the GCM calculation. Such a calculation is unprecedented in a global model. The flux of this tracer is calculated as

$$F(T_{18}) = R - A_n \tag{3.24}$$

where R is the release of CO_2 from the ecosystem due to respiration and A_n is the assimilation due to photosynthesis. Since SiB2 already calculates the rate of CO_2 assimilation due to photosynthesis (see section 3.3.2), the second term on the right-hand side of (3.24) was easy to include in my calculation. The relative intensity of soil respiration is also calculated on a monthly mean basis as a diagnostic output of the SiB2 model (here designated R^*, the SiB2 variable name is `soilscale`), following the method used in the TEM model (Raich *et al.*, 1991). To estimate an actual flux of CO_2 due to soil respiration, I scaled the `soilscale` diagnostic by the annual sum of net assimilation at each grid point, then calculated the flux of CO_2 to the atmosphere as the difference between this estimated respiration flux and the net assimilation calculated by SiB2.

The soil respiration diagnostic R^* is simply a measure of the relative effects of soil temperature and moisture on soil respiration. It is defined as

$$R^* = 2.0^{Q_1} f(M), \tag{3.25}$$

where

$$f(M) = 0.2 + w_{sat}^{B} \tag{3.26}$$

$$B = \left[\frac{w^{zm} - w_{opt}^{zm}}{w_{opt}^{zm} - 100^{zm}} \right]^2$$

The temperature response function uses the same $Q_t = (T - 298)/10$ as is used elsewhere in SiB2 (see Fig. 3.12). This is a departure from the method of Raich *et al.*

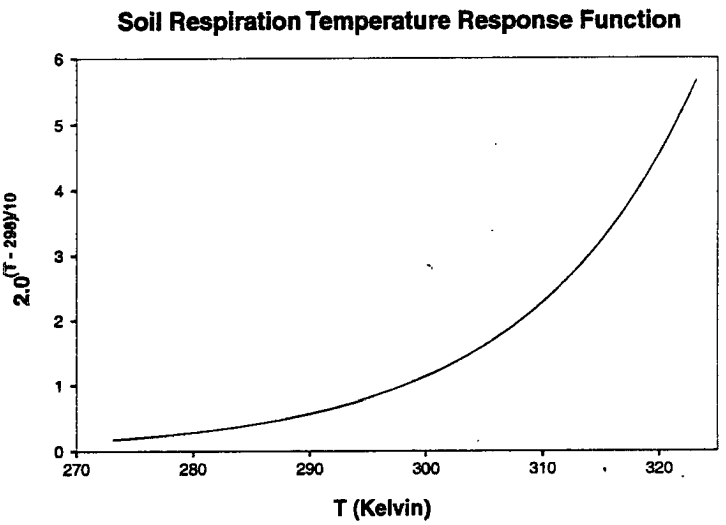

FIGURE 3.12: Temperature response function for soil respiration in equation (3.25).

(1991), who used 273 K. The temperature used to define Q_t in (3.24) is the mean of the surface soil temperature and the deep soil temperature. When the mean temperature in the soil column is below 273 K, the value of R^* is set to zero.

The soil moisture response function is exactly as defined by Raich *et al.* (1991). The variable w in (3.26) is the fraction of the pore space occupied by water in the root zone (middle layer) of the soil. The parameters w_{sat}, w_{opt}, and zm are functions of soil texture prescribed from a lookup table using the values suggested by Raich *et al.* (1991). The curves produced by this equation for a variety of soil textures are shown in Fig. 3.13. Note that soil respiration is a maximum for some value w_{opt} of soil moisture, and that respiration is less efficient under very dry or very wet conditions. The parameter zm determines the skewness of the curves in Fig. 3.13; it is higher for well-drained coarse-textured soils and lower (negative) for clay soils. The parameter w_{sat} determines the val-

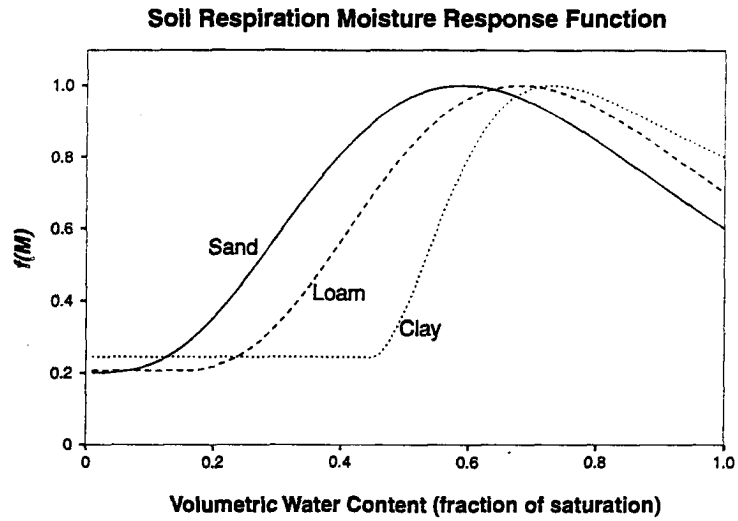

FIGURE 3.13: Effect of root zone soil moisture content on relative rate of soil respiration according to equation Fig. 3.26. After Raich *et al.* (1991).

ue of $f(M)$ when the soil is completely saturated. The value of $f(M)$ is always between 0.2 and 1.0, so that the value of R^* is usually between 0.0 and 1.0 for realistic soil conditions (it is never greater than 2.0 because of the negative correlation between soil temperature and soil moisture in hot climates). Raich *et al.* (1991) applied this function to heterotrophic (that is microbial) respiration only, but in SiB2 it is applied to the total soil respiration including root respiration. No attempt is made to represent litter decomposition directly.

Over the course of one year, the flux of CO_2 from the atmosphere into the terrestrial biosphere at each model grid point is

$$GPP = \sum_{1year} A_n(t)\,\Delta t \tag{3.27}$$

where $A_n(t)$ is the net assimilation at each model time step as defined by (3.11). The local GPP as defined here is the total photosynthesis minus leaf respiration, whereas the conventional definition of this quantity would not subtract the leaf respiration. The flux of CO_2 from the ecosystem due to respiration is calculated from R^* according to

$$R(t) = GPP \frac{R^*(t)}{\sum_{1year} R^*(t)\,\Delta t}, \tag{3.28}$$

so that the net flux of CO_2 from every grid point is zero. In practice, the annual sums used in (3.27) and (3.28) are derived from the model output for the *previous* year and applied to the flux calculation at each time step in the *current* year. This means that if a multi-year trend is present in either GPP or the annual sum of R^* there will be an imbalance between total uptake and release of carbon by the terrestrial biosphere at a given grid point. Such a trend might be expected due to slow adjustment of soil moisture to the model climate, or to changing climate in the GCM. I used the end of a previous simulation with SiB2 to initialize my simulation to avoid such a problem (I used the end of a 30-year simulation to initialize my low-resolution experiments and the end of a 10-year simulation to initialize my standard resolution experiments; see section 3.5). As long as no such trend is present, the long-term mean of the calculated CO_2 flux at each grid point should be nearly zero.

3.4.4.4 Comparison of the Three Seasonal Flux Estimates

Because the surface flux of tracer T_{18} is calculated on-line in the GCM, it is not possible to know in advance exactly what the seasonal and geographic distribution of the flux will be as it is for the other tracers. By using monthly mean values of the fields used in the calculation of the flux, however, it is possible to estimate what these maps will look like from previous experiments with SiB2. Using monthly mean diagnostic output files for $\overline{A_n}$ and $\overline{R^*}$ from such a previous run, I used (3.24), (3.27), and (3.28) to generate monthly mean estimates of the flux of T_{18}, recognizing that the numbers are somewhat different than those that would be determined on-line by using instantaneous values of A_n and R^* and performing the averaging on the fluxes directly.

Fig. 3.14 compares the seasonal patterns of uptake and release of CO_2 by the terrestrial biosphere summed over the 4° latitude zones of the CSU GCM, as represented in tracers T_9, T_{15}, and T_{18}. The three formulations of the seasonal fluxes show the most striking differences in the middle latitudes of the northern hemisphere. Tracer T_9 has much greater seasonal amplitude in this region than either of the other two tracers, and has a double-peaked structure to its annual cycle. Emissions due to respiration in the biosphere exceed 150×10^9 kg month^{-1} in the northern spring and fall, with rapid transitions in June and

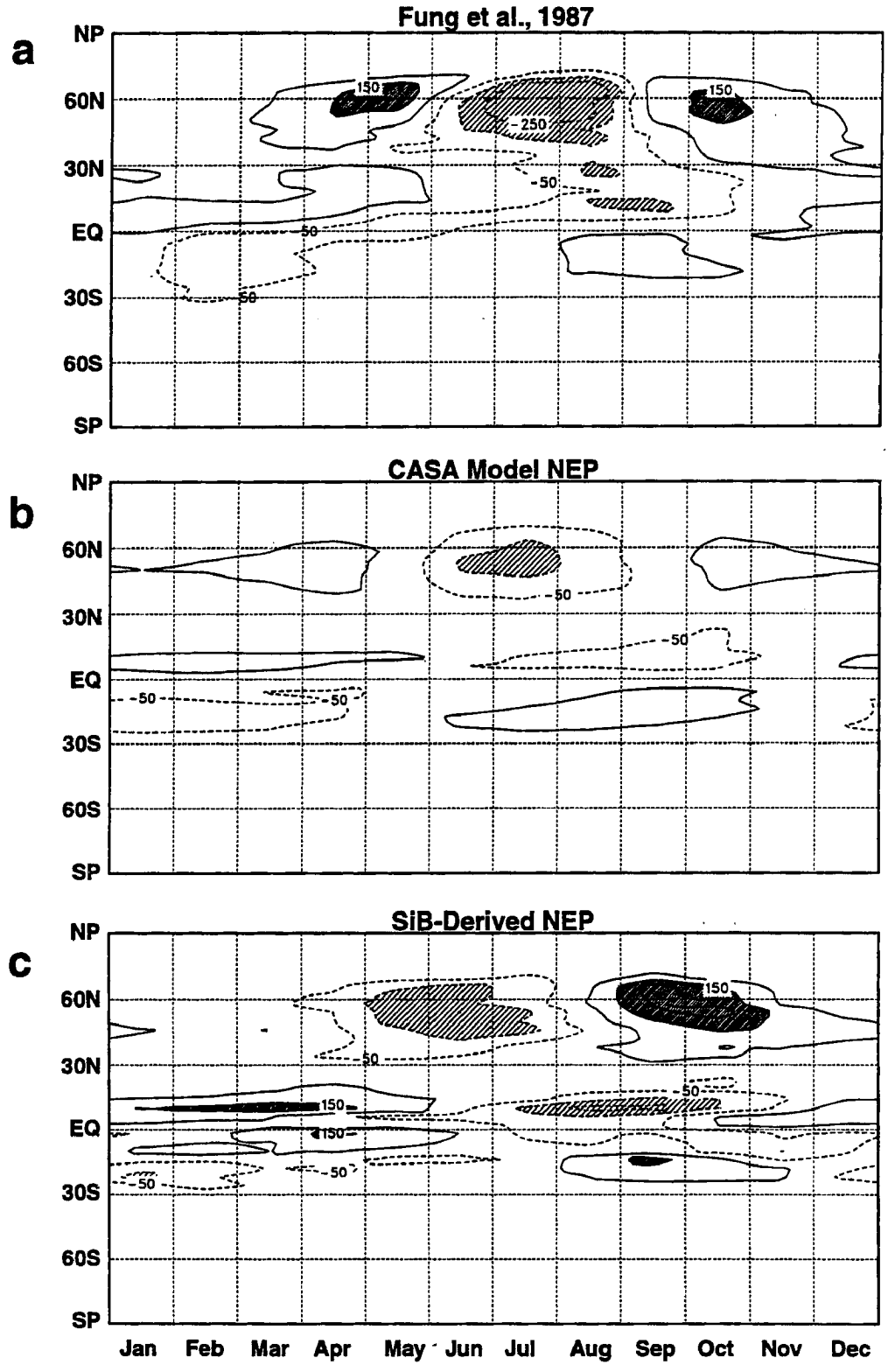

FIGURE 3.14: Zonal total flux of carbon from the terrestrial biosphere to the atmosphere for (a) tracer T_9, (b) tracer T_{15}, and (c) tracer T_{18}. The contour interval is 100×10^9 kg C per 4° latitude zone per month. Absolute values greater or less than 150×10^9 kg mo^{-1} have been shaded in all three plots.

September between net sources and sinks (compare to Fig. 3.8 through Fig. 3.8). Tracer T_{15} also shows this double-peak structure in the northern midlatitudes, but the amplitude is much smaller, with respiration emissions spread out into the northern winter as well as the spring and fall. This may be due to sensitivity of the decomposition rate to temperature, as discussed in section 3.4.4.2 above; the fluxes used here show considerably higher seasonal amplitude than those in the original Potter *et al.* (1993) paper (see their Plate 3a). Tracer T_{18} (fluxes estimated off-line from a previous simulation) shows much weaker emissions from the biosphere in the northern spring than either of the other two formulations, but instead places most of the annual respiration in the northern autumn, at which time the fluxes are higher even than those of tracer T_9. The annual cycle of the SiB2 fluxes is also somewhat shifted in phase as compared to the other two tracers, with the springtime drawdown and the fall decomposition "seasons" beginning about a month earlier than for T_9 and T_{15}.

In the tropics, it is tracer T_{18} which shows the greatest seasonal amplitude, nearly three times as intense as the annual cycle in tracers T_9 and T_{15}. Much of the difference between the tropical fluxes of the three tracers occurs in Africa, although this cannot be seen in Fig. 3.14 because the fluxes were zonally averaged to show the seasonal variations.

3.4.5 The "Missing" Terrestrial Sink

Five scenarios were explored for geographic and seasonal distributions of a terrestrial "missing sink." The annual global flux of each of these tracers was set arbitrarily to –1.0 Gt C yr^{-1} and can be scaled *a posteriori* to explore various global carbon budgets.

3.4.5.1 Tracer T_{10}: NPP-based CO_2 Fertilization

To define the fluxes of tracer T_{10}, a 1.0 Gt C yr^{-1} sink was distributed over land grid points in proportion to estimated NPP, with a seasonal phase prescribed according to the function f_2 of Fung *et al.* (1987) which they found to produce the best fit to seasonal CO_2 time series. The monthly flux at each grid point was proportional to

$$f(\mathrm{NDVI}) = \frac{exp\,(\mathrm{NDVI} - \mathrm{NDVI}_{crit})}{\mathrm{NDVI}_{crit}} - 1, \qquad (3.29)$$

with the monthly NDVI values specified from the NDVI data of Los *et al.* (1994). The function in (3.29) was set to zero when NDVI < $NDVI_{crit}$, with this "critical" value of NDVI prescribed by biome following the values given by Fung *et al.* (1987) (Table 3.3).

Table 3.3: Parameters used to define fluxes of tracer T_{10}

Biome	NPP ($g\ m^{-2}\ yr^{-1}$)	$NDVI_{crit}$	Biome	NPP ($g\ m^{-2}\ yr^{-1}$)	$NDVI_{crit}$
1	945	0.1	7	300	0.02
2	540	0.1	8	300	0.02
3	540	0.1	9	261	0.02
4	585	0.1	10	100	0.02
5	585	0.1	11	20	0.02
6	300	0.1	12	270	0.02

NPP was assumed to be uniform in each of the 12 biomes recognized by SiB2 (see Table 3.2), with annual NPP in each type specified according to the compilation of Fung *et al.* (1987; their table 1). The monthly gridded values of this flux were scaled such that total annual sink of this tracer was exactly 1.0 Gt C yr^{-1}. Because the highest NPP values are in the tropical forests, the fluxes of this tracer are maximum in the tropics in the annual mean. Because of the seasonal nature of NPP in temperate ecosystems, however, this tracer is also drawn down in the northern growing season (Fig. 3.16) with the greatest sink intensity occurring at that time. The uptake of CO_2 by these fluxes is more than an order of magnitude weaker than that of the seasonal NEP tracers (T_9, T_{15}, and T_{18}, compare to Fig. 3.14).

3.4.5.2 Tracer T_{11}: Drought-Stress-Based CO_2 Fertilization

The SiB2 water stress inhibition function $f(\Psi)$, as defined in (3.14), was used to scale the prescribed gridded flux values of tracer T_{11}. The annual mean value of this diagnostic was multiplied by the annual NPP value for each grid point, as listed in Table 3.3, and the result was also multiplied by the function f(NDVI) as defined in (3.29) to specify seasonal variations. The resulting fluxes were scaled to give a 1.0 Gt C yr^{-1} global sink, which is locally proportional to both NPP and water stress in the root zone.

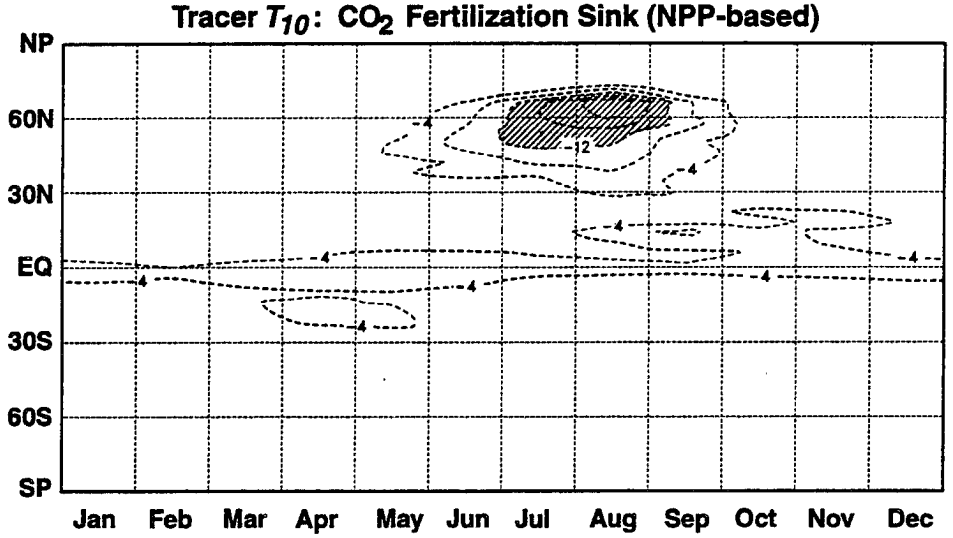

FIGURE 3.15: Zonal total flux of tracer T_{10} to the atmosphere. Contour interval is 4×10^9 kg C mo^{-1} over each 4° latitude zone in the GCM. Uptake rates of greater than 12×10^9 kg C mo^{-1} have been shaded.

The sink of this tracer is greatest in the subtropics, and is only weakly seasonal (Fig. 3.16). The intensity of this sink is somewhat weaker than that of tracer T_{10}, because the drought stress and NPP fields are negatively correlated. As in the former case, this tracer has a significant amount of drawdown in the northern growing season, but the local sink strength is much less than the seasonal NEP tracers (compare to Fig. 3.14).

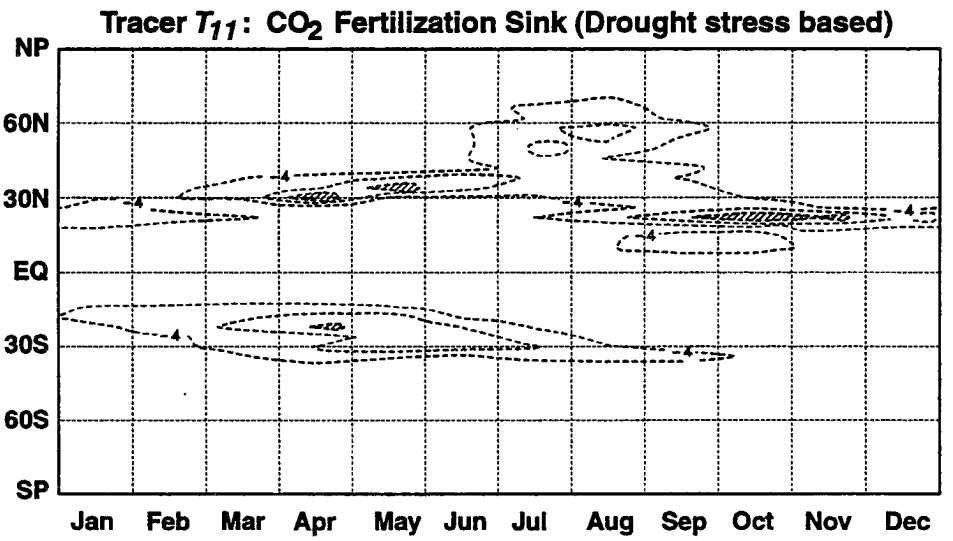

FIGURE 3.16: Zonal total flux of tracer T_{11} to the atmosphere. Contour interval and shading are exactly as in Fig. 3.16.

3.4.5.3 Tracers $T_{12} - T_{14}$: Biome-Specific Terrestrial Sinks

Gridded monthly values of the fluxes of tracers $T_{12} - T_{14}$ were also prescribed to be vary seasonally according to f(NDVI) in (3.29). Each tracer was scaled to give a 1.0 Gt C yr^{-1} sink, and was nonzero only at grid points defined to represent a particular biome (Fig. 3.17). Tracer T_{12}, representing a sink in the temperate forest, was defined for

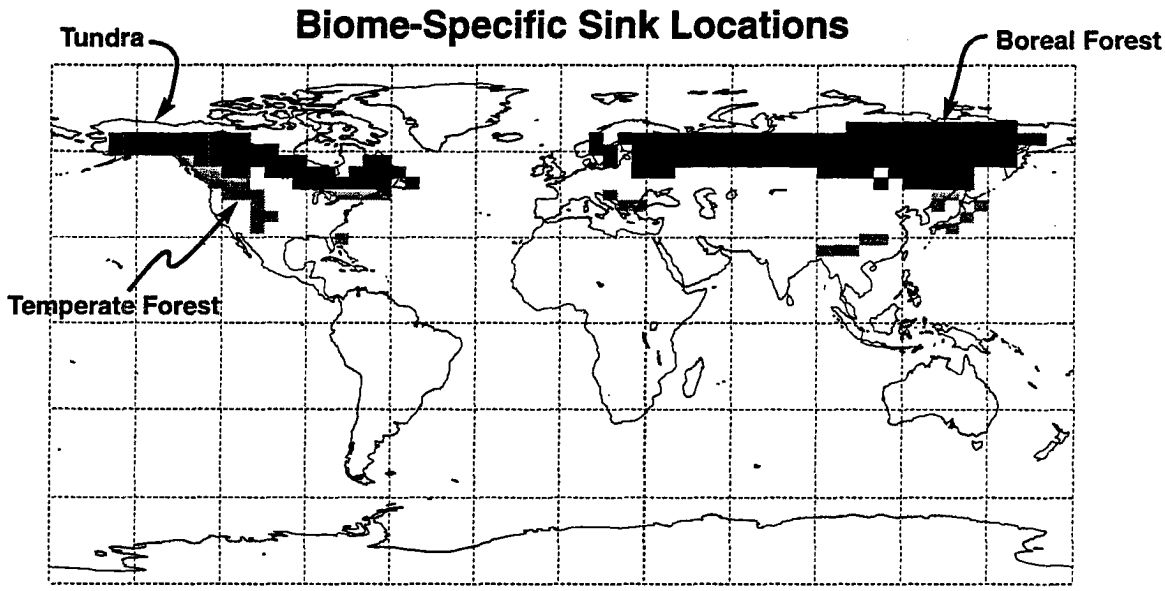

FIGURE 3.17: Standard resolution grid cells with nonzero fluxes of tracers T_{12} (temperate forests, dark gray), T_{13} (boreal forests, black), and T_{14} (tundra, light gray).

SiB2 surface types 2 – 4 at latitudes between 24° N and 48° N. Six standard resolution grid cells in western Canada which are north of 48° N were also classified as temperate forest. Tracer T_{13}, representing a boreal forest sink, was defined at all grid points with SiB2 surface types of 4 and 5 north of 48° N, except for the six grid points mentioned above. Tracer T_{14} was defined at all grid points which have SiB2 classification of 10.

3.4.6 Radioactive tracers

Tracers T_{16} and T_{17} represent the radioisotopes ^{85}Kr and ^{222}Rn, respectively. I have followed the methods of Heimann and Keeling (1989) in prescribing the surface fluxes of these tracers in the CSU GCM.

Krypton-85 is emitted from only nine nuclear fuels reprocessing plants, all in the northern hemisphere. Nine years of estimated emissions were published by Heimann and Keeling (1989, their Table 3), based on the earlier tracer studies of Jacob *et al.* (1987). I used these data to prescribe the surface fluxes of tracer T_{16} (Table 3.4). Because the fluxes at Karlsruhe, Germany and Idaho, USA are too weak to be well-resolved in 32-bit arithmetic, they were combined with neighboring sources in France and Hanford, USA in the tracer simulations. Also, the GCM grid cell containing the latitude and longitude of the La Hague plant is defined as ocean in the model (the English Channel). The emissions from this plant were implemented in the GCM one grid point to the east, and included with the emissions from the plant in Germany.

No global or regional scale data are available for emission rates of natural ^{222}Rn (tracer T_{17}) from soils. I followed Heimann and Keeling (1989) by prescribing a uniform source of 1.32 atoms cm^{-2} s^{-1} at all land grid points not covered by permanent ice. This flux was not varied by season.

3.4.7 Tracer Flux Boundary Condition for the Low-Resolution Model

The monthly gridded flux data described above were generated on the standard 4° x 5° grid of the CSU GCM. In many cases, the surface flux data for the low-resolution (7.2° x 9°) experiments were linearly interpolated from these maps. The exceptions were the ocean tracers ($T_3 - T_8$) and the radioactive tracers (T_{16} and T_{17}), which are defined based on specific geographic locations.

In generating the low-resolution boundary fluxes from the standard maps, care was taken to preserve the meridional structure of the fluxes as closely as possible while at the same time enforcing the condition that fluxes defined for terrestrial processes be zero at all ocean grid points. This was accomplished by performing the interpolation from the standard to low resolution grid (which resulted in some nonzero fluxes at ocean points), then applying the land-sea mask and scaling the values to preserve the total flux in each of the 24 zonal bands on the low resolution grid. Thus the global and hemispheric totals of the flux of every tracer are the same as the standard resolution fluxes in every month.

Table 3.4: Krypton-85 Emissions 1975-1983 (after Heimann and Keeling,1989)

Plant			Annual Emissions (10^3 Ci yr^{-1})								
Location	Lat	Lon	75	76	77	78	79	80	81	82	83
Hanford, USA	46.6 N	114.7 W	294	250	108	291	283	276	212	95	214
Idaho, USA	43.4 N	112.1 W	24	33	111	101	0	92	59	9	3
Savannah, USA	33.3 N	81.7 W	520	711	448	530	480	580	840	515	698
Windscale, UK	54.6 N	3.6 W	1200	1200	800	700	940	840	1400	1190	1129
Marcoule, France	44.4 N	4.5 E	100	92	117	308	280	535	310	310	620
La Hague, France	49.0 N	0.9 W	657	343	669	786	642	825	969	1220	1356
Karlsruhe, Germany	49.0 N	8.4 E	43	86	115	34	51	32	70	16	76
Tokai Mura, Japan	36.5 N	140.6 E	0	0	0	60	0	280	110	190	90
Kyshtym, Russia	55.7 N	60.6 E	1559	2067	2893	2955	3535	3064	2691	3103	2442

3.4.8 Annual Totals of Tracer Fluxes

The prescribed surface fluxes of tracer T_9 and T_{15} are purely seasonal, with the annual total flux at each grid point nearly equal to zero. The annual totals of the SiB2 on-line fluxes (tracer T_{18}) should be close to zero as well, but there is no way to know before running the model. The meridional structure of the annual total flux of all the other tracers is presented in Fig. 3.18. The figure shows the meridional profiles of the fluxes as they are defined on the standard resolution grid, but there is almost no difference between these profiles and the ones defined on the low-resolution grid.

Almost 95% of the emissions of fossil fuel CO_2 (tracer T_1) are in the northern hemisphere, and the annually integrated net fluxes of this tracer are the strongest of all the tracers. This tracer is therefore expected to have the strongest meridional gradient in concentration in the annual mean. Conversely, because the fluxes of tracer T_2 are nearly normally distributed across the equator, this tracer is expected to show very little annual mean meridional gradient. The ocean fluxes are arbitrarily defined, so that they can be scaled to appropriate values *a posteriori*, but it is clear from Fig. 3.18 that all but the equatorial oceans (tracer T_6) will show strong meridional gradients.

The "missing sink" tracers ($T_{10} - T_{14}$) are intended to allow linear combinations to be constructed that simultaneously satisfy the constraints of the global budget and the meridional gradient. The biome-specific sinks ($T_{12} - T_{14}$) will obviously work well for this, because they are defined at relatively high latitudes. The meridional profiles of annual total fluxes of tracers T_{10} and T_{11} are more complicated. Although about 73% of the uptake of tracer T_{10} is in the northern hemisphere, the tropics are a strong sink as well, due to the high NPP of the tropical forests. The sink of tracer T_{11} is even more smoothly distributed in latitude. About 67% of its uptake is in the northern hemisphere but the strongest sink is in the subtropics of each hemisphere, where the climate is driest.

3.5 Experimental Details

The tracer calculation using the low-resolution version of the CSU GCM was integrated for a period of 10 years. Tracers T_{16} (representing ^{85}Kr) and tracer T_{17} (representing ^{222}Rn) were initialized to globally uniform concentrations of 13.5 pCi m^{-3} STP and 20 pCi m^{-3} STP, respectively (Heimann and Keeling, 1989); all other tracers (representing CO_2) were initialized to a globally uniform concentration of 350 ppm by volume. The

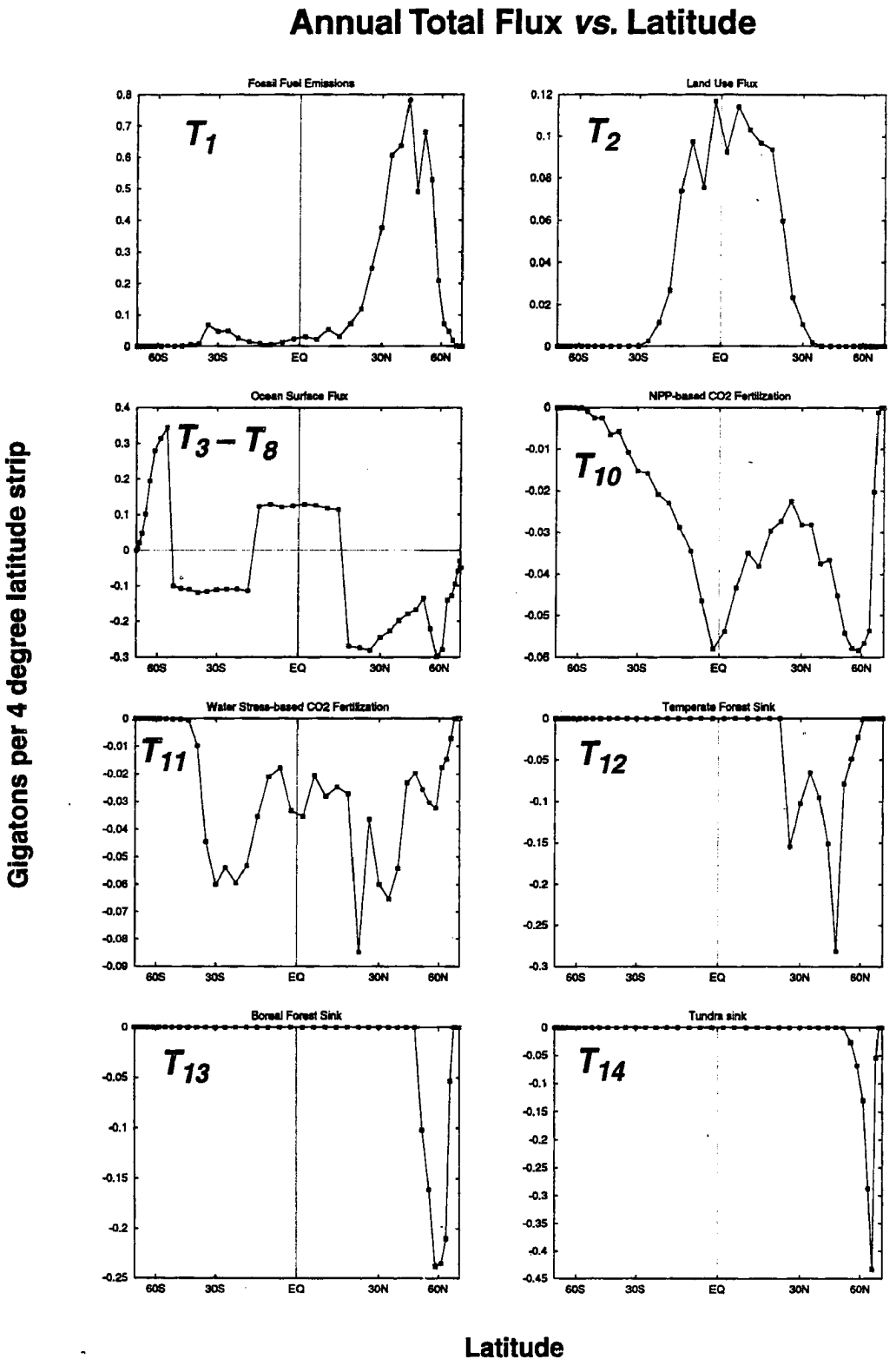

FIGURE 3.18: Meridional profile of annual total flux of 15 of the 18 tracers to the atmosphere in the standard resolution version. Ocean fluxes (tracers $T_3 - T_8$) have been combined onto a single plot.

other prognostic variables in the GCM were initialized from a previous climate simulation using SiB2, but without the new cloud microphysics parameterization (EAULIQ, see section 3.3.1). Because the use of this parameterization has a significant effect on the simulated climate of the GCM, variables with a long physical "memory" in the climate system (especially soil moisture in SiB) required a long "spin-up" period to adjust to the new model climate. Therefore I have not used data in the first five years of this run in constructing multiyear means presented in the later chapters of this report. This run is referred to as the "LOWRES" experiment.

At the end of the tenth year of the low-resolution simulation, tracer concentrations were interpolated onto the $4° \times 5°$, 17 level grid and a new simulation was started using the standard version of the GCM. Initial conditions were specified for all prognostic variables other than the tracers from the end of a two-year simulation using both SiB2 and EAULIQ in the standard model. Because the 18 tracers had been "spun up" in the low-resolution simulation, they adjusted much more quickly to the somewhat different circulation of the standard model than they would have if they had been initialized as globally uniform again (see Chapter 5). This simulation was therefore only integrated for four years, and multiyear means were saved from the final three years of the run. The tracer concentrations had fully adjusted to the change in circulation by the end of the second year at the higher resolution, as is demonstrated in section 6.1. I shall refer to this experiment as the "standard" experiment; most of the analysis in the chapters to follow focuses on the results obtained from it.

In addition to these two simulations two "sensitivity experiments" were performed using the low resolution model. In an experiment I shall call "NOCUTRAN," tracer T_1 (the fossil fuel CO_2) was simulated as described above, but all transport by cumulus convection was "turned off." Comparison of the results of this experiment with the standard runs is intended to allow an evaluation of the effects of cumulus transport on the final tracer distributions. Also, in an experiment I will call "2BOX," a tracer was simulated with no surface fluxes at all. This experiment was initialized with a concentration of 350 ppm everywhere in the northern hemisphere, and zero at all points in the southern hemisphere. The motivation behind this experiment is to evaluate the expressions derived in section 2.4.3 concerning interhemispheric exchange time. The NOCUTRAN and 2BOX experiments were each integrated for three years.

The complete set of model prognostic variables was written to files at the end of every calendar month in all experiments, to allow the model to be restarted at any of those

points if desired. Diagnostic model output (both tracer concentrations and meteorological fields) was interpolated hourly onto constant-pressure surfaces and monthly means of these data were calculated and written to files every month. A time series of hourly values of selected variables was written to "point-by-point" diagnostic files for several grid points in July of year 4 of the standard experiment. These hourly time series are used to examine the diurnal and other high frequency variability of some of the tracers (section 7.2).

The standard and LOWRES experiments were run on the Cray Y-MP C98/6256 at NASA Goddard Space Flight Center. For these experiments, the model was compiled on the Cray using Cray Fortran 77 version 6.0 and run under Unicos 7.C.3. The other experiments were run at the CSU Department of Atmospheric Science on a Hewlett Packard (HP) Series 9000 model 715 workstation. The tracer calculation added 14.4% CPU overhead to the standard resolution CSU GCM on the Cray C98. This figure scales approximately linearly with the number of tracers simulated (less than 1% computational overhead is required per simulated tracer). With 18 tracers, the model used 32% more memory than the same version of the GCM requires without prognostic trace gases. About 6 MB of diagnostic output per simulated month was produced by the tracer calculation in addition to the output files already generated by the GCM.

3.6 Summary

The prognostic calculation of trace gas concentrations has been added to the CSU GCM in order to investigate the atmospheric transport and surface fluxes of CO_2. Eighteen separate tracers are defined for the present set of experiments, representing the response of atmospheric CO_2 to emissions from fossil fuel combustion (T_1) and tropical deforestation (T_2), air-sea exchange ($T_3 - T_8$), and surface exchange with the terrestrial biosphere ($T_9 - T_{15}$ and T_{18}). In addition, two radioactive trace gases, ^{85}Kr (T_{16}) and ^{222}Rn (T_{17}) are simulated to allow the tracer transport characteristics of the model to be compared to observations. Five of the tracers ($T_{10} - T_{14}$) represent net terrestrial sinks of arbitrary strength, and are intended to test various hypotheses regarding the global carbon budget.

Three of the tracers represent the seasonal fluxes of CO_2 due to photosynthesis and respiration by land plants and soils. Two of these (T_9 and T_{15}) are purely seasonal by design, with a net flux of exactly zero at every grid point when integrated over an annual

cycle. The surface fluxes of these tracers are prescribed according to previously published estimates (after Fung *et al.*, 1987 for T_9 and using a significantly revised version of the CASA model as described by Potter *et al.*, 1993 for T_{15}). The third seasonal tracer (T_{18}) is calculated on-line by SiB2 in the GCM, according to local environmental conditions at each model time step. The net annual flux of this tracer at each grid point is unknown, but the formulation is designed to minimize the net source or sink over a period of several years. The on-line calculation of surface carbon flux at the land surface has never before been performed in a global atmospheric model.

Tracer transport due to advection by the mean flow, vertical mixing by dry convection, and vertical transport by cumulus convection are included in the simulations. Horizontal advection is by a simple second order, centered-in-space, leapfrog-in-time algorithm. Several experiments are performed: the standard experiment uses a $4° \times 5°$ (latitude by longitude) grid with 17 levels and a six minute time step. The LOWRES another experiment (and two sensitivity experiments) uses a $7.2° \times 9°$ grid with 9 levels and are integrated with a 10 minute time step. The LOWRES experiment was run for 10 years from an initial condition in which the 18 tracers were each set to arbitrary globally uniform concentrations. The standard experiment used the end of the LOWRES run as its initial condition. All experiments included full seasonal and diurnal cycles, but boundary conditions (such as sea surface temperatures) were prescribed without interannual variability.

CHAPTER 4

Analysis of Flask Sample CO_2 Data

In this chapter, the NOAA/CMDL flask air sample data are analyzed to develop a data set with which to compare the results of the GCM experiments described in chapter 3. Section 4.1 briefly describes the sampling program, the flask sample locations, and the procedures used to select and assure the quality of the concentration data. Section 4.2 describes the time series of the data for each station used in this study, and the derivation of simple functions to represent those data. Finally, section 4.3 describes the global patterns of CO_2 concentration for an "average" year, as derived from the fitted curves, which will be compared with the GCM results in chapters 5 and 6.

4.1 NOAA/CMDL Flask Sampling Program

Since 1968, the NOAA/CMDL flask sampling program has collected quality-assured data on the concentration of atmospheric CO_2 approximately weekly at a growing number of stations in remote areas around the world (Conway *et al.*, 1988, 1994; also see the review in Chapter 2). Remote sites have been selected in an attempt to sample air which is "regionally representative," that is, air which is free from local contamination by anthropogenic or natural sources or sinks. Duplicate samples are collected at all sites by a standardized protocol (Komhyr *et al.*, 1985, Conway *et al.*, 1994) in glass flasks, and are then shipped for analysis to a central laboratory in Boulder, Colorado, where they are analyzed by nondispersive infrared gas analyzers (Khomyr *et al.*, 1983, Thoning *et al.*, 1994) calibrated to a set of standards maintained by the Scripps Institute of Oceanography (Thoning *et al.*, 1987). Some recent results of the flask sampling program are presented by Conway *et al.* (1994).

I obtained the data via anonymous ftp from NOAA (Pieter Tans, personal communication). The numeric data package contains analyses of all the individual samples before any quality assurance screening was applied, but the files also contain flags to indicate quality assurance selection status by the methods of Khomyr *et al.* (1985) and Conway *et al.* (1988). Sample data were flagged for several reasons:

1) The concentration was more than three standard deviations (3σ) from the fitted curve for the site (Conway *et al.*, 1988), and so was believed not to be representative of background conditions (local contamination was suspected);

2) The flask was cracked or broken, or an error occurred in sample collection or instrumental analysis;

3) Concentrations of CO_2 from the two flasks differ by more than 0.5 ppm;

4) Only a single flask was collected at the site, or one of the flasks was not analyzed due to breakage, contamination, or analytical error.

In earlier studies (Komhyr *et al.*, 1985; Conway *et al.*, 1988), the "good" member of a bad pair of samples (which was flagged under criterion 3 above) was retained if its concentration fell within 3σ of the fitted curve. This allowed some sites more recently added to the sampling network to be used which otherwise would not have had enough data. As data continued to accumulate, this became less of a concern, and since 1989, both members of a bad pair have been rejected by the NOAA/CMDL group (Tans *et al.*, 1989; Conway *et al.*, 1994). I chose to follow this latter practice, and have only used data from "good pairs" (concentrations differ by less than 0.5 ppm) and single flask samples which were retained by the NOAA group (concentrations within 3σ of the fitted curve).

The data set provided by the CMDL contains data for a total of 34 sampling sites on land, and for data collected by three shipboard sampling programs in the Pacific. The shipboard data were collected at intervals of approximately 5° in latitude on regular container ship cruises between the west coast of the U.S. and New Zealand, and at 3° latitude intervals in the South China Sea between Hong Kong and Singapore. The shipboard data are grouped into "bins" 5° of latitude wide. The land stations are summarized in Table 4.1.

Altogether, concentration records for 77 sites are present in the NOAA data set, including both the land and shipboard data. For the purpose of comparison with the GCM

simulation, some site selection was necessary. Time series were fitted to the data (as described below in section 4.2) and monthly means were extracted for a single "average" year. It was therefore important to have data available for the same time period across most of the stations used. Since more stations were added to the network as time went on, I chose not to use data from stations with data records ending before 1985. Stations located higher than 1000 m in elevation were also excluded since the model topography at the coarse horizontal resolution of the GCM is unrealistically smooth leading to a poor match in elevation between mountainous locations and the analogous grid point in the model. The South Pole station was retained in the analysis as an exception to this rule because it helps constrain the meridional profiles, because of its excellent data record, and because the terrain is so smooth in that region. I also excluded stations with fewer than 20 total samples, and with fewer than five samples per year on the average, since the time series for these data would be poorly constrained. Because the two sampling stations on the island of Bermuda (BME and BMW) are in the same GCM grid cell, I combined their data to form a single station, to which I will refer as "BER." A preponderance of "bad" sample pairs collected at South Georgia Island have led the NOAA group to believe the data from that station are not reliable (P. Tans, personal communication, and so they have not been included in this analysis. Excluding these sites left 25 land sites (the locations of which are indicated in Fig. 4.1) and 15 shipboard sites, for a total of 40 flask stations.

4.2 Time Series of Station CO_2 Concentration

Conway *et al.* (1994) have shown that significant interannual variability is present in the global and hemispheric trends and meridional distribution of concentration from the flask network. The source of this variability is not entirely clear, but much of it appears to be related to interannual climate perturbations such as the Southern Oscillation and the Mount Pinatubo volcanic eruption of 1991 (Bacastow, 1976; Thompson *et al.*, 1986; Keeling *et al.*, 1989*a*). Although there may be interannual variability in the climate simulated by the GCM, such major "forcing" as the Southern Oscillation (sea-surface temperatures were prescribed from climatological data and repeated the same "seasons" year after year) and volcanic eruptions are not present, so it is likely to be minor compared to the real climate. Furthermore, the prescribed surface fluxes of the simulated tracers were not varied over the duration of the experiments. For the purpose of comparing the ob-

Table 4.1: NOAA/CMDL Flask Sampling Sites

Code	Site	Country	Lat	Long	Elev (m)
ALT	Alert, N.W.T.	Canada	82 27' N	62 31' W	210
AMS	Amsterdam Island	France	37 57' S	77 32' E	150
ASC	Ascension Island	U.K.	7 55' S	14 25' W	54
AVI	St. Croix, Virgin Islands	U.S.	17 45' N	64 45' W	3
AZR	Azores	Portugal	38 45' N	27 05' W	30
BME	Bermuda (east)	Bermuda	32 22' N	64 39' W	30
BMW	Bermuda (west)	Bermuda	32 16' N	65 53' W	30
BRW	Point Barrow, Alaska	U.S.	71 19' N	156 36' W	11
CBA	Cold Bay, Alaska	U.S.	55 12' N	162 43' W	25
CGO	Cape Grim, Tasmania	Australia	40 41' S	144 41' E	94
CHR	Christmas Island	Kiribati	2 00' N	157 19' W	3
CMO	Cape Meares, Oregon	U.S.	45 29' N	124 00' W	30
GMI	Guam	U.S.	13 26' N	144 47' E	2
HBA	Halley Bay	Antarctica	75 40' S	25 30' W	10
IZO	Tenerife, Canary Islands	Spain	28 18' N	16 29' W	2300
KEY	Key Biscayne, Florida	U.S.	24 40' N	80 12' W	3
KUM	Cape Kumukahi, Hawaii	U.S.	19 31' N	154 49' W	3
MBC	Mould Bay, N.W.T.	Canada	76 14' N	119 20' W	15
MHT	Mace Head	Ireland	53 26' N	9 44' W	5
MID	Sand Island, Midway	U.S.	28 13' N	177 22' W	4
MLO	Mauna Loa, Hawaii	U.S.	19 32' N	155 35' W	3397
NWR	Niwot Ridge, Colorado	U.S.	40 03' N	105 38' W	3749
PSA	Palmer Station	Antarctica	64 55' S	64 00' W	10
QPC	Qinghai Province	China	36 16' N	100 55' E	3810
RPB	Ragged Point	Barbados	13 10' N	59 26' W	3
SEY	Seychelles (Mahe Is.)	Seychelles	4 40' S	55 10' E	3
SGI	South Georgia Island	U.K.	54 00' S	38 00' W	30
SHM	Shemya Island	U.S.	52 43' N	174 06' E	40
SMO	American Samoa	U.S.	14 15' S	170 34' W	30
SPO	South Pole	Antarctica	89 59' S	24 48' W	2810
STC	Ocean Station "C"	U.S.	54 00' N	35 00' W	6
STM	Ocean Station "M"	Norway	66 00' N	2 00' E	6
SYO	Syowa Station	Antarctica	69 00' N	39 35' E	11
TAP	Tae-ahn Peninsula	36 44'N	36 44' N	126 08' E	20

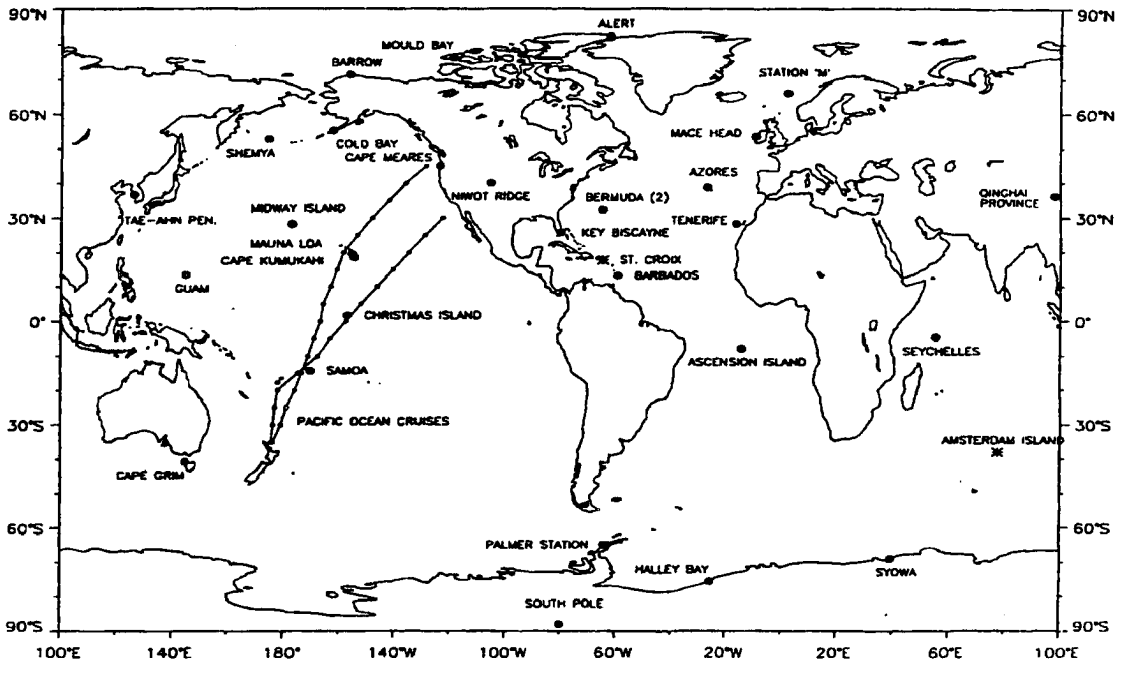

FIGURE 4.1: Locations of the NOAA flask sampling stations described in Table 4.1 and the routes of the container ships also used for sampling. Conway *et al.* (1994)

served flask concentration data to the GCM results, therefore, an "average" year of flask data is a better choice than any "real" year.

To obtain such an "average" year, the quality-assured data described in section 4.1 were fitted to functions of the form

$$a + bt + \sum_{k=-4}^{4} c_k e^{i(2\pi kt)} \tag{4.1}$$

where t is time in years, and a, b, and all the c_k's are coefficients determined by a least-squares fit to the selected data. The function (4.1) represents the temporal variations in CO_2 concentration as a linear trend plus the annual cycle and its first three harmonics. The time series for the 40 stations are presented in alphabetical order in Fig. 4.2. The shipboard observations are represented by the station prefix "PAC" followed by the latitude at which the 5° bin is centered (*e.g.*, PACs20 means shipboard samples collected between 22.5° S and 17.5° S).

In general, the functions fit the data quite well. The seasonal variations at most stations were fairly well represented with just a single annual mode, but some stations ex-

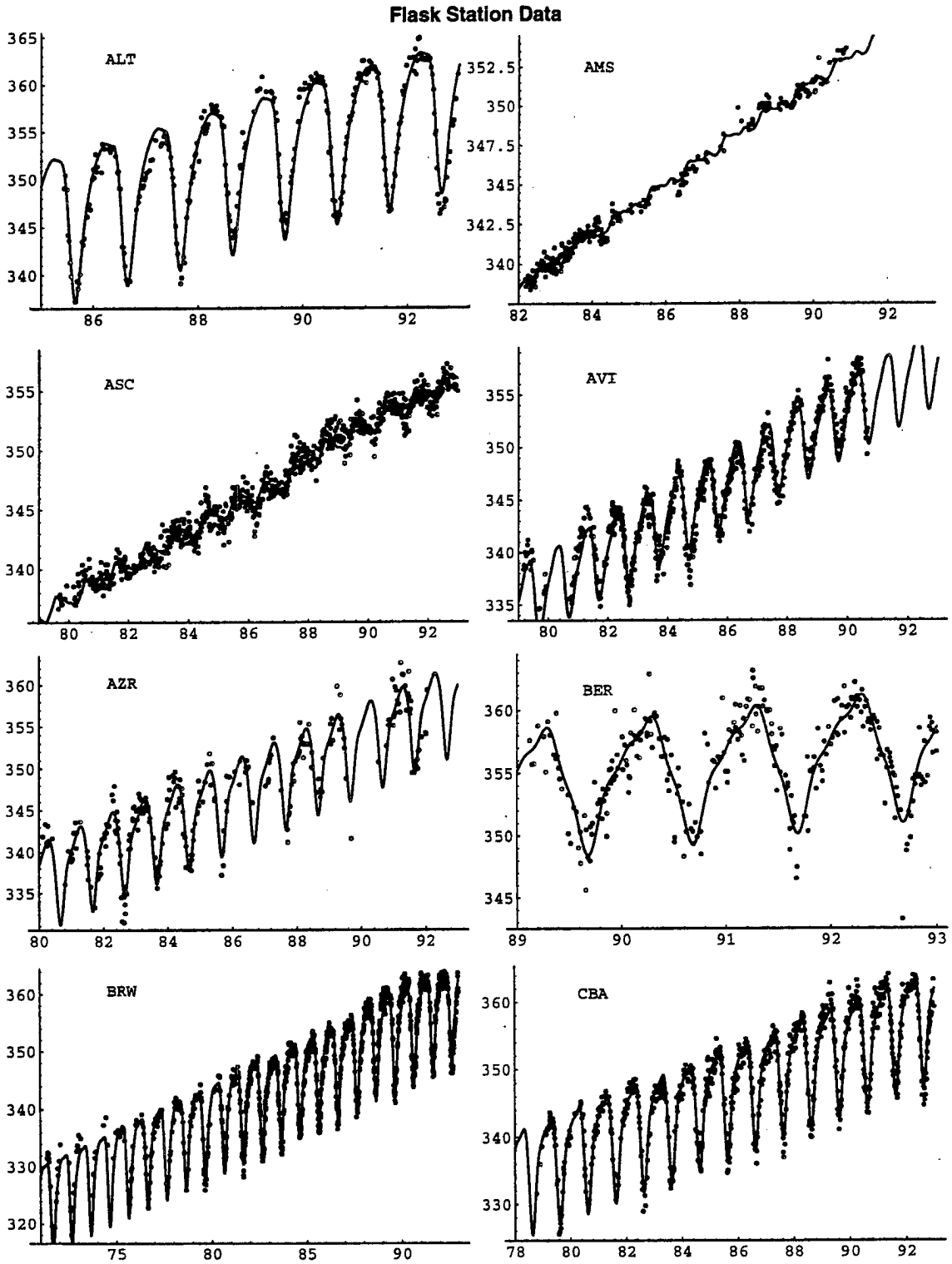

FIGURE 4.2: Time series of CO_2 concentration fitted to flask station observations (dots). The vertical axis is concentration in ppm. The horizontal axis is the year (after 1900).

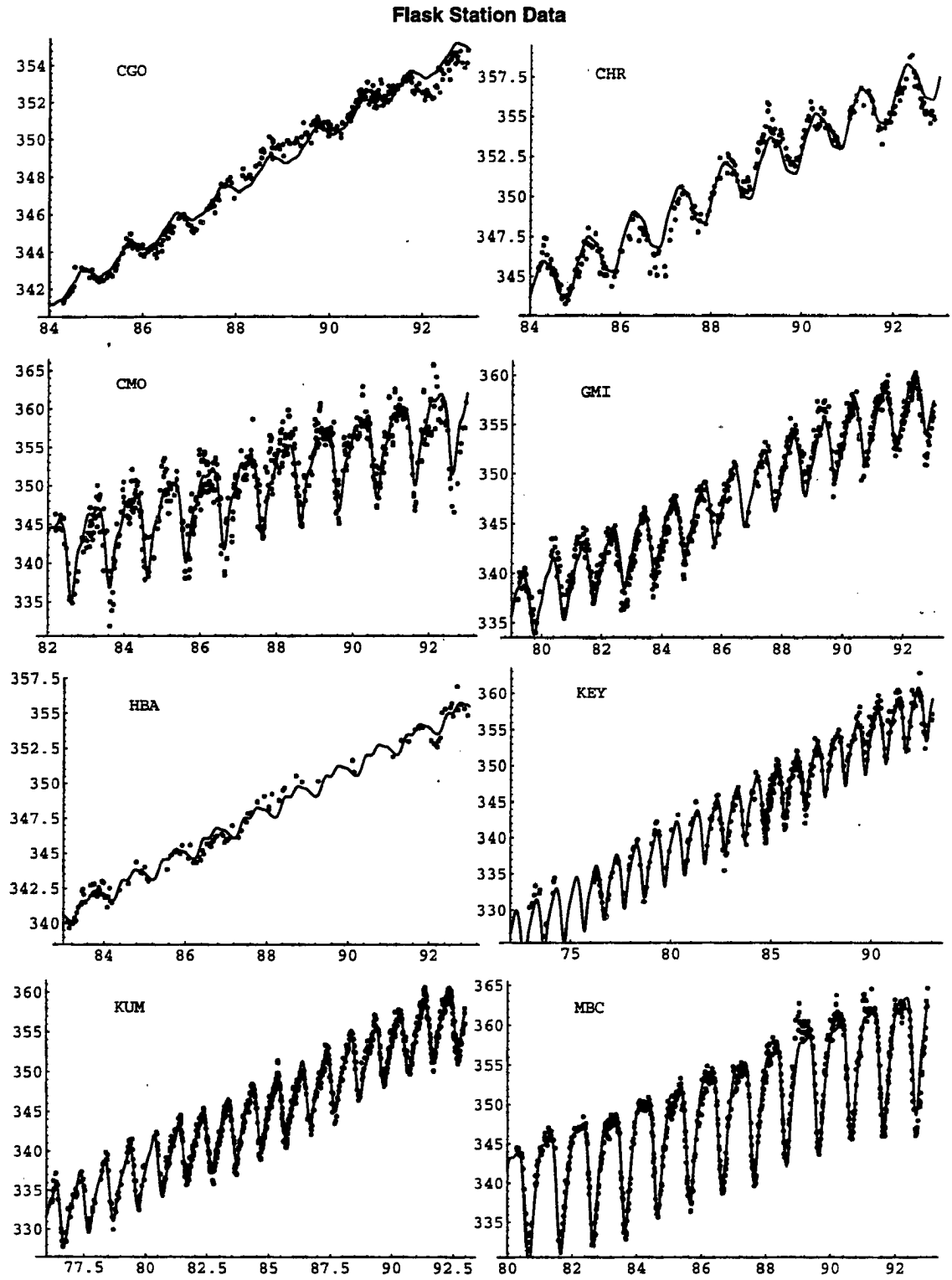

FIGURE 4.2 (cont'd): Time series of CO_2 concentration fitted to flask station observations (dots). The vertical axis is concentration in ppm. The horizontal axis is the year (after 1900).

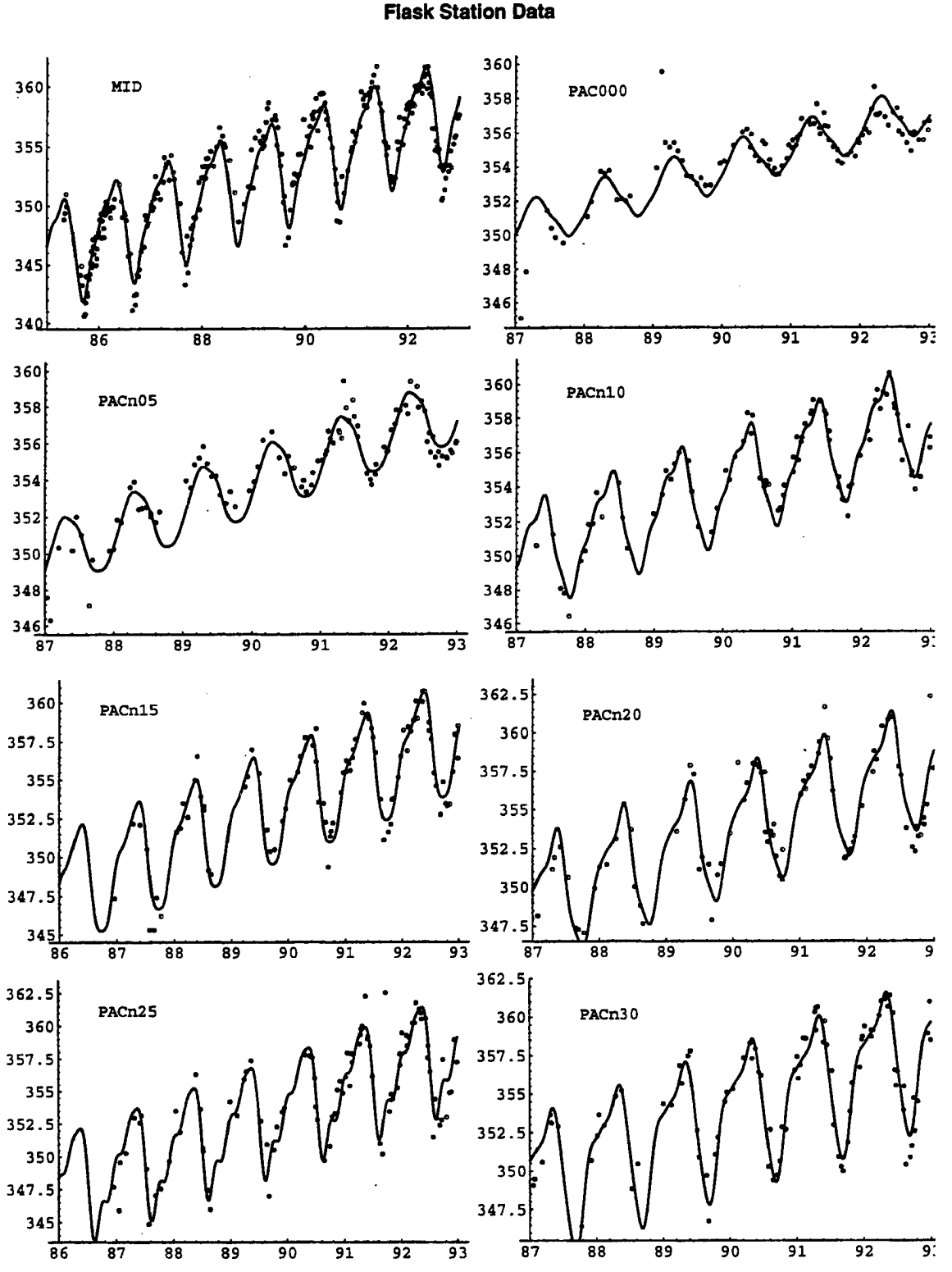

FIGURE 4.2 (cont'd): Time series of CO_2 concentration fitted to flask station observations (dots). The vertical axis is concentration in ppm. The horizontal axis is the year (after 1900).

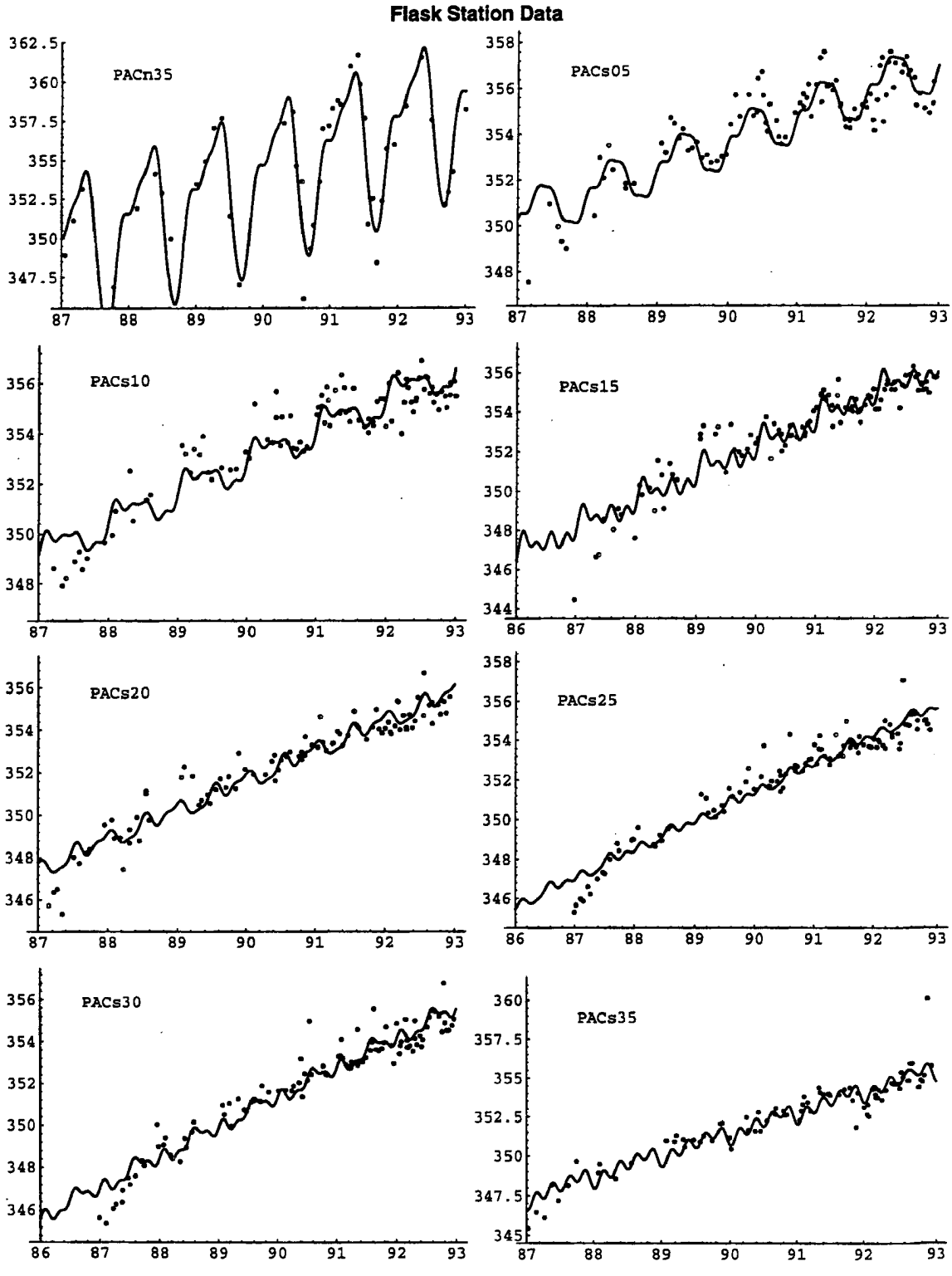

FIGURE 4.2 (cont'd): Time series of CO_2 concentration fitted to flask station observations (dots). The vertical axis is concentration in ppm. The horizontal axis is the year (after 1900).

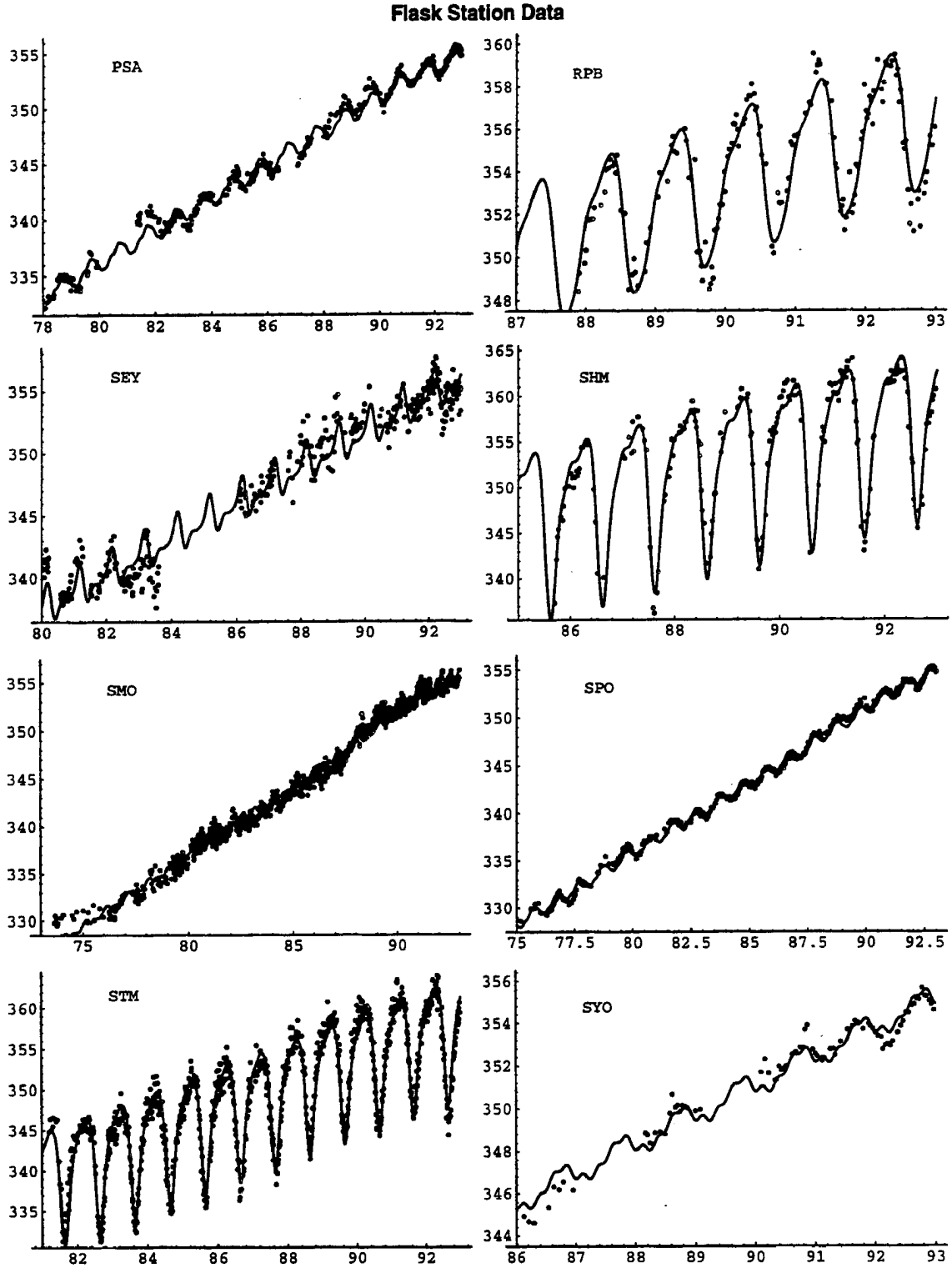

FIGURE 4.2 (cont'd): Time series of CO_2 concentration fitted to flask station observations (dots). The vertical axis is concentration in ppm. The horizontal axis is the year (after 1900).

hibited a strong concentration spike in the spring. This feature is particularly obvious for stations at the higher latitudes of the northern hemisphere (*e.g.*, ALT, BRW, CBA, MBC), and may correspond to respiration flux from boreal soils as they thaw (compare to Fig. 3.8 and the discussion in section 3.4.4). This feature has also been noted by previous studies (Conway *et al.*, 1988; Keeling *et al.*, 1989*a*). The amplitude of the seasonal cycle in concentration decreases rapidly from north to south, as expected. The annual pattern at some southern hemisphere stations is complicated and noisy (SMO and SPO), so that the small-amplitude annual cycle is obscured by variability on shorter time scales.

The harmonic functions seem to miss concentration extrema at some of the stations (AZR, CMO, CHR, KEY, MID, SEY, SHM). In the case of SEY, an extended period of values below the fitted curve in 1982-83 may be related to the strong El Niño event of that time (Khomyr *et al.*, 1985; Keeling *et al.*, 1989a). Two stations have an "outlier" data point which falls well away from the fitted curve (PAC000, SGI). Examination of the individual flask analyses for these stations confirm that these data were in fact consistent between the two members of the flask pairs, and that contamination was not noted in the sample record.

4.3 Mean Concentrations for an "Average" Year

To obtain monthly data for comparison with the GCM simulations, the functions derived from the flask data in section 4.2 were integrated over each month of 1990, and an annual mean for each station was obtained by integrating the appropriate function over all of 1990. These concentrations are presented in Table 4.2. They are not meant to represent actual station concentrations in 1990, but rather what station concentrations would have been in 1990 if they had behaved exactly as represented by (4.1).

The meridional structure of the annual mean concentrations from Table 4.2 is presented in Fig. 4.3. The difference between the annual mean concentration at ALT (82° 27' N) and SPO (90° S) is 3.84 ppm, which is higher than the 3.0 ppm observed pole-to-pole difference (based on 1987 data) which T90 used to constrain their model results. The functions presented in section 4.2 include linear trends in concentration which are different from one flask station to another. The pole-to-pole difference in concentration as represented by these functions is increasing by a little more than 0.1 ppm yr^{-1} (as measured by the difference between the functions fitted to the data from ALT and SPO). Pre-

Table 4.2: Station Concentrations for an "Average" Year (Scaled to 1990)

Station	Monthly Mean Concentration (ppm)												Ann. Mean
	Jan	Feb	Mar	Apr	May	Jun	Jul	Aug	Sep	Oct	Nov	Dec	
ALT	357.99	359.21	359.96	360.02	359.80	357.94	352.10	346.25	346.57	351.11	355.10	357.73	355.29
AMS	351.57	351.81	351.82	351.70	351.75	352.06	352.56	352.92	352.95	352.98	353.04	353.03	352.35
ASC	351.68	351.59	351.41	351.63	352.19	352.83	353.48	353.60	353.30	353.30	353.34	353.16	352.63
AVI	353.96	355.01	356.14	356.83	357.03	356.40	354.10	351.33	350.33	351.15	352.79	354.42	354.12
AZR	355.46	356.49	357.48	358.01	357.46	355.58	352.02	348.43	348.48	351.87	354.81	356.12	354.33
BER	356.75	357.60	358.48	359.35	357.89	355.43	353.43	350.58	349.66	352.44	354.96	356.17	355.21
BRW	358.53	359.33	359.69	359.96	360.10	357.98	351.43	345.31	346.37	351.78	355.91	358.38	355.37
CBA	357.82	358.61	359.22	360.00	359.74	356.02	349.17	344.80	347.29	352.90	356.52	358.16	354.99
CGO	350.28	350.34	350.48	350.60	350.87	351.20	351.49	351.87	352.14	352.12	352.04	351.92	351.29
CHR	353.40	354.13	354.78	355.19	355.06	354.82	354.32	353.51	353.11	353.01	353.06	353.84	354.02
CMO	357.57	357.78	358.04	358.52	358.10	355.73	351.16	348.66	351.26	354.44	355.72	357.52	355.36
GMI	353.44	354.80	355.49	356.20	356.97	356.60	355.32	353.39	351.37	351.19	352.63	353.77	354.26
HBA	350.90	350.66	350.55	350.79	351.46	351.96	351.99	352.17	352.60	352.73	352.64	352.57	351.76
KEY	355.07	356.06	357.03	357.66	357.37	356.28	354.30	351.59	350.41	351.90	354.10	355.54	354.77
KUM	353.79	354.71	355.47	356.64	357.43	356.29	353.49	350.73	349.71	350.81	352.67	354.11	353.81
MBC	358.90	359.39	359.53	359.94	360.11	358.25	352.37	346.47	346.81	351.31	355.27	358.39	355.54
MID	355.18	356.28	356.92	357.96	358.24	356.79	354.13	351.03	349.86	351.61	353.73	355.13	354.73
PAC000	353.84	354.64	355.35	355.72	355.56	355.02	354.56	354.19	353.69	353.49	353.83	354.36	354.52
PACN05	353.64	354.66	355.59	356.04	355.93	355.60	354.87	353.81	353.20	353.11	353.33	353.99	354.48
PACN10	353.95	355.22	356.02	356.47	357.47	357.11	355.06	353.53	352.40	351.84	353.04	354.45	354.71

Table 4.2: Station Concentrations for an "Average" Year (Scaled to 1990)

Station	Monthly Mean Concentration (ppm)												Ann. Mean
	Jan	Feb	Mar	Apr	May	Jun	Jul	Aug	Sep	Oct	Nov	Dec	
PACN15	354.50	355.14	356.01	357.02	357.77	357.18	354.45	351.79	351.01	351.16	352.32	354.48	354.40
PACN20	354.71	355.40	355.99	357.23	358.22	356.55	353.60	351.88	350.89	351.01	353.05	355.12	354.46
PACN25	354.77	355.27	356.76	357.92	358.28	356.83	352.45	349.98	351.69	352.76	353.18	355.14	354.5
PACN30	355.46	356.02	356.75	358.07	358.23	355.92	352.86	350.30	349.51	351.83	354.99	356.38	354.68
PACN35	354.95	356.08	357.00	358.05	358.84	356.84	352.82	349.75	349.12	351.62	355.05	356.21	354.68
PACS05	353.87	353.95	354.38	355.01	355.13	355.06	354.69	353.92	353.59	353.56	353.61	354.33	354.26
PACS10	353.39	353.80	353.50	353.53	353.67	353.67	353.75	353.43	353.07	353.28	353.38	353.66	353.51
PACS15	352.60	353.37	352.87	352.73	352.81	352.54	353.04	353.25	352.67	352.97	353.26	353.04	352.93
PACS20	352.05	351.88	351.55	351.63	351.82	352.25	352.83	352.68	352.35	352.67	352.97	353.16	352.32
PACS25	351.45	351.73	351.62	351.54	351.71	351.97	352.42	352.60	352.37	352.47	352.71	352.69	352.11
PACS30	351.56	351.60	351.29	351.47	351.66	351.86	352.46	352.68	352.51	352.56	352.42	352.43	352.04
PACS35	350.82	351.60	351.60	351.54	352.25	352.13	352.01	352.70	352.64	352.63	353.10	352.48	352.13
PSA	350.50	350.40	350.50	350.78	351.31	351.68	351.96	352.50	352.84	352.79	352.70	352.41	351.71
RPB	354.51	355.21	355.93	356.72	357.09	356.37	354.03	351.51	350.73	351.23	352.40	354.20	354.15
SEY	352.47	353.52	353.75	352.63	351.30	351.08	351.73	352.24	352.35	352.43	352.64	353.04	352.43
SHM	358.56	358.90	359.84	360.96	360.63	356.35	347.95	343.31	347.36	353.27	356.42	358.69	355.16
SMO	351.99	352.23	352.33	352.14	351.98	352.19	352.41	352.43	352.45	352.51	352.70	353.11	352.37
SPO	350.55	350.45	350.45	350.68	350.97	351.20	351.63	352.10	352.31	352.41	352.40	352.22	351.45
STM	357.07	357.96	358.87	359.19	358.52	355.99	350.39	345.52	346.64	351.40	355.12	357.30	354.47
SYO	350.87	351.04	350.87	350.94	351.37	351.55	351.89	352.41	352.54	352.71	352.78	352.36	351.78

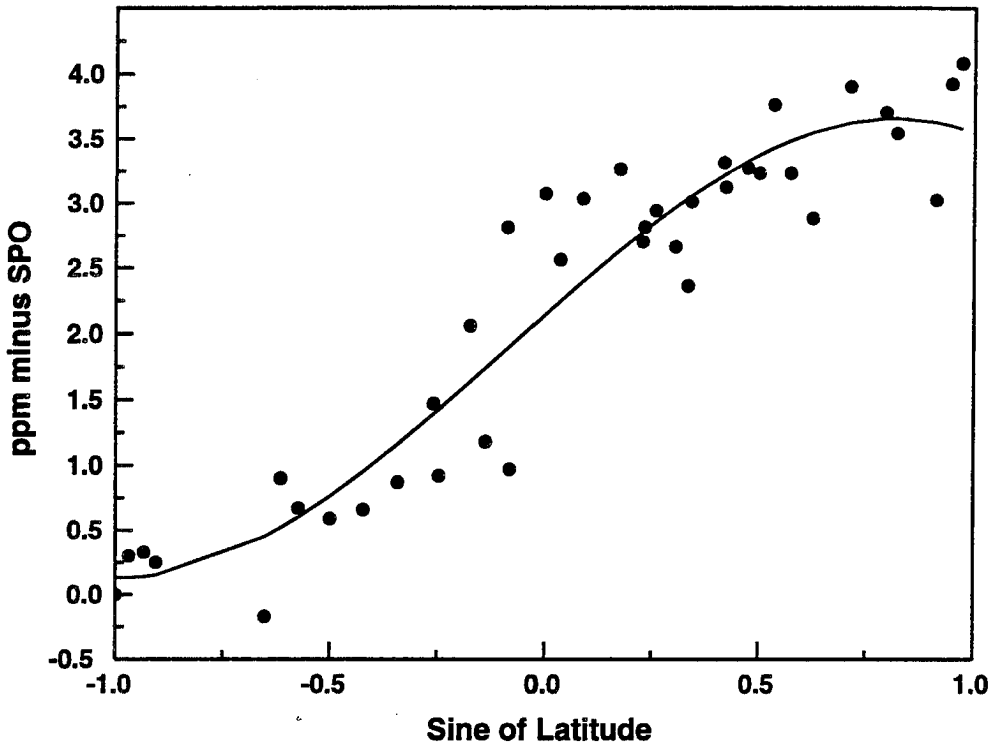

FIGURE 4.3: Meridional profiles of the annual mean CO_2 concentration at each of the 40 NOAA flask stations used in this chapter. The annual mean concentration at the South Pole has been subtracted from each value. The curve is a third order polynomial fit to the station values

vious studies have also reported that the pole-to-pole difference in annual mean CO_2 is increasing (see Fig. 2.2 in section 2.3).

Conway *et al.* (1994) showed that the growth of this difference have not been as regular as the progression in the fitted functions shown here, but that after a period from 1981-87 when the gradient was about 3.0 ppm with little variation, it grew to about 4.0 ppm in 1988-91 and then fell to 3.0 ppm in 1992. They found that the interannual variability in this gradient was related to changes in the natural carbon cycle rather than year-to-year changes in fossil fuel emissions. The more regular increase in pole-to-pole CO_2 difference as deduced from the fitted curves in Fig. 4.2 *is* closely related to the time trend of global fossil fuel emissions, however (Fig. 4.4).

Since the GCM experiments performed in this study used fossil fuel emissions prescribed from an older estimate (Marland, 1989) of 5.3 Gt C yr^{-1}, comparison of the simulated tracer concentrations to the monthly and annual means derived in this chapter will

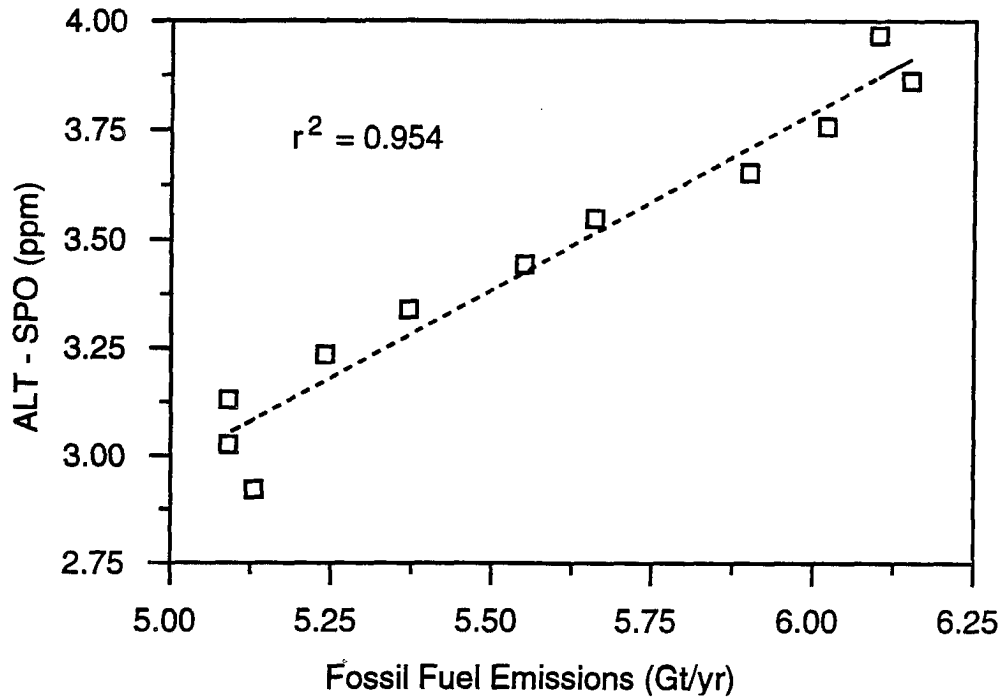

FIGURE 4.4: Pole-to-pole difference in the fitted curves of Fig. 4.2 vs. fossil fuel emissions from 1981-91. Emission data from 1981-89 are from Marland and Boden (1991). Preliminary estimates of global emissions in 1990-91 are from Conway *et al.* (1994).

require scaling tracer T_1 to by an appropriate factor to account for the increase in emissions, such that global emissions equal 6.0 Gt C yr^{-1}, the rate for 1990.

The linear growth coefficient b in (4.1) varies from about 0.85 ppm yr^{-1} to over 1.6 ppm yr^{-1} (Fig. 4.5). Both stations on the island of Bermuda show much slower growth in CO_2 concentration than is indicated for the other stations (compare to Fig. 4.2). To estimate the globally averaged rate of increase in atmospheric CO_2 for the "average" year derived in this chapter, I fitted a cubic polynomial to the growth rate data presented in Fig. 4.5, and integrated from pole to pole. The global mean rate of increase found in this way is 1.45 ppm yr^{-1}, which is close to the average for the past decade, but slightly higher than the actual growth rate observed in 1990 (Conway *et al.*, 1994). Assuming that this rate is representative of the entire atmosphere, and using a global mean surface pressure of 985.8 mb (Peixoto and Oort, 1992), the changes in CO_2 concentration amount to an annual addition of 3.09 Gt C yr^{-1} for the "average" conditions described here. This is in line with previous estimates of 3.0 to 3.2 Gt C yr^{-1} (TFT90, Houghton *et al.*, 1990), and

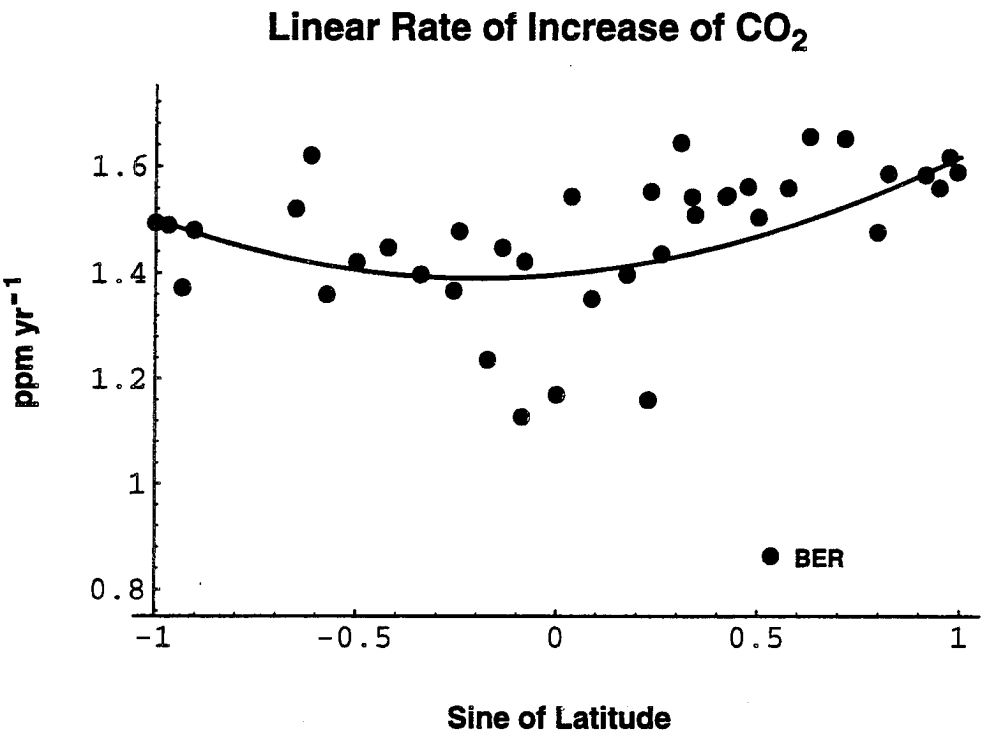

FIGURE 4.5: Meridional profile of the linear growth rate of CO_2 concentration at the 40 NOAA flask stations used in this study. The curve indicated is a third-degree polynomial fit by a least-squares technique.

is the figure I will use in calculating the global carbon budget from the results of this study in Chapter 6.

CHAPTER 5

Comparison of the Simulated Climate to Observational Data

In this chapter, the simulated climate of the CSU GCM is compared to observational data to evaluate the realism of the circulation used to transport the tracers. Section 5.1 considers surface climate features (temperature, precipitation, and atmospheric pressure). The three-dimensional circulation of the atmosphere is evaluated in section 5.2 by examining the vertical structure of temperature and winds in the zonal mean. The simulated large-scale mixing of the atmosphere is evaluated in section 5.3 by analyzing the simulated concentration fields of ^{85}Kr (tracer T_{16}), and the simulated vertical mixing is evaluated in section 5.4 in terms of vertical profiles of ^{222}Rn (tracer T_{17}) concentration.

Climatologies of surface air temperature and precipitation compiled by Legates and Willmott (1990*a*, *b*; hereafter referred to as LW90) are compared with GCM simulations of those fields in sections 5.1.1 and 5.1.2. LW90 produced estimates of climatological temperature and precipitation (without reference to a specific time period) on a 0.5° × 0.5° grid by analyzing station records from 24,635 precipitation gauges and 17,986 temperature shelters on land and 6,955 oceanic grid point temperature records. Oceanic precipitation data at island weather stations was augmented by estimates calculated from precipitation frequency in shipboard observations using a statistical relationship between precipitation frequency and precipitation amount developed from regional island measurements. Precipitation gauge reports were corrected for undercatch due to high winds and evaporation. A spherical interpolation scheme was used to produce the gridded data from the point observations. I obtained the gridded data from National Center for Atmospheric Research (NCAR)'s Data Support Section.

The rest of the simulated climatological fields in sections 5.1 and 5.2 are compared to mean global data derived from meteorological analyses performed by the European Center for Medium-Range Weather Forecasts (ECMWF). The data were collected four times daily (at midnight, 6:00, noon, and 18:00 Greenwich Mean Time) by the global radio-

sonde network and satellite remote sensing and analyzed on a global grid using a "first guess" field generated from a six-hour forecast by the ECMWF model. The data assimilation and analysis system is described by Lorenc (1981) and evaluated by Hollingsworth *et al.* (1986). I obtained the data on a 2.5° × 2.5° grid from NCAR. The data presented here were obtained by simply averaging over all the days in a given month over the years 1985 through 1988, and combining both the noon and midnight data, and then interpolating onto the coarser grids of the CSU GCM.

The GCM data used for comparison in sections 5.1 and 5.2 are three-year means from the standard experiment (see section 3.5), and five-year means from LOWRES experiment. To calculate difference maps presented in some of the figures, I first interpolated the observational data onto both the standard 4° × 5° and the low-resolution 7.2° × 9° grids of the CSU GCM, and then subtracted the observational data from the GCM fields for each month.

Each of the figures in sections 5.1 and 5.2 contain six plots comparing output from both the standard resolution GCM and the low-resolution GCM to observational data in both January and July. I realize that the individual plots in the figures are rather small, but this format is desirable since it allows easy intercomparison on a single page. The observational data are in all cases displayed at the top of the figure, followed by the standard resolution GCM in the middle, and the low-resolution GCM results at the bottom. Also, in all cases January data are presented in the left column and July data in the right column. Contour intervals and shading thresholds are the same for January and July in all plots, and are also consistent for all the difference plots of a given field. In some cases differences are not computed, in which case all six plots on a page have the same contour interval and shading thresholds. In all black and white contour plots in this report, dashed contours indicate negative values.

5.1 Horizontal Structure of the Atmosphere

The climate at the Earth's surface is familiar to all of us because we experience it in our daily lives, and so it is useful to compare the surface climate simulated by the GCM with the observed climate. Temperature and precipitation are the primary climatological factors which might affect the carbon exchange dynamics of SiB2 (see Chapter 3); they are examined in this section. Sea level pressure can not directly affect the tracer distributions, but it integrates much of the atmospheric circulation and physics, so it is also com-

pared to observational data. The simulated wind field in both the upper and lower troposphere is also presented in this section, because it has a direct bearing on the transport of the simulated tracers.

5.1.1 Surface Air Temperature

Fig. 5.1 compares the surface air temperature simulated by the CSU GCM with the LW90 climatology. The LW90 data are for air temperature at 2 m above the ground, and the CSU GCM results are for the air temperature of the PBL just above the plant canopy, calculated from the PBL potential temperature using the assumption of an adiabatic mixed layer. Note that the GCM results are presented in terms of *difference* maps; the LW90 data have been subtracted from the simulated mean fields in the four lower panels of the figure.

The general geographic distribution of temperature is captured quite well by both the low-resolution and standard simulations, but in both January and July, the simulated temperature fields are somewhat "flatter" than the observations (regional variations are weaker). The difference is more pronounced in January than July, and is greater in the low-resolution simulation than in the standard resolution one. In the global (area-weighted) mean, the standard model agrees quite well with observations, being about 0.6 K too warm in January and only 0.1 K too cold in July. Surface air temperatures in the LOWRES simulation are too warm in both seasons (by 1.7 K in January and 1.2 K in July).

The temperature differences are most pronounced over cold land areas, especially in Antarctica. As compared to the LW90 climatology, the simulated temperatures over Antarctica are too warm in summer (January) and too cold in winter (July) by more than 6 K in both simulations in both seasons over the entire continent. This difference is probably due in part to the representation of the high Antarctic topography at the coarse resolution of the GCM. Wintertime temperatures over the Arctic oceans as simulated in the standard model (and over a smaller region in the LOWRES run) are too cold by as much as 10 K, but are close to observed in summer. This is probably due to inadequate heat flux from the ice-covered ocean in the GCM. In the real world, substantial heat flux through openings in the ice called leads warms the lower atmosphere; this effect is not represented in the GCM, so the air can become extremely cold over sea ice.

Surface Air Temperature

(Kelvin)

January

July

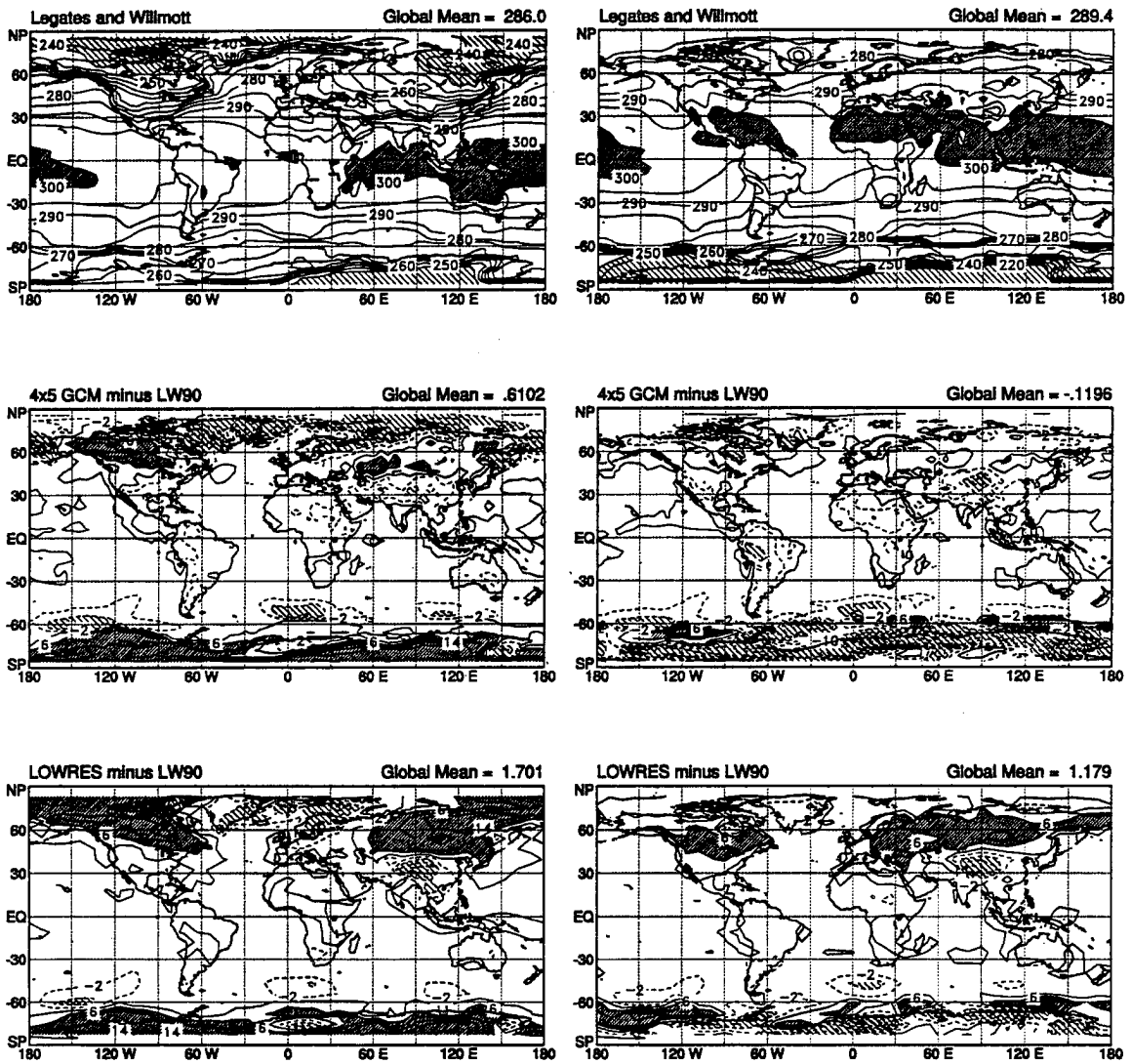

FIGURE 5.1: Comparison of the surface air temperature as analyzed by Legates and Willmott (1990*a*, top pair of panels) and as simulated by the CSU GCM (bottom four panels). The GCM results are presented as difference maps (observational data are subtracted before plotting). Contour interval for the LW90 data is 5 K, with dark shading above 300 K and light shading below 245 K. Contour interval for the GCM difference maps is 4 K, with dark shading above +6 K and light shading below -6 K. Dashed contours indicate negative values.

Over the northern continents, the differences are generally smaller and positive. In the standard resolution simulation, a large area of northwestern North America is warmer than the LW90 data by more than 6 K in January, and an even larger area of eastern Asia is quite warm in the low resolution simulation. The situation is much improved in the standard resolution simulation in summer, with much smaller, more randomly distributed areas cooler than observed by more than 6 K. The low-resolution results are still too warm in middle latitude continental interiors even in summer. The Tibetan Plateau appears to be a problem area in both seasons and in both simulations, with temperatures too cold by as much as 14 K in summer in the low-resolution run. This may also be related to coarse resolution of the steep topography in that region as discussed above for Antarctica, but also is probably due in part to excessive snowfall in that region, as discussed in the next section.

5.1.2 Precipitation

The global distribution of precipitation is presented in Fig. 5.7. As in the temperature data presented above, the GCM results are presented as difference maps for the lower four panels. Here the top panels show the climatological data compiled by LW90 for January and July; these data have been subtracted from the simulated precipitation in the other panels.

The global total precipitation is quite well captured by the GCM: annual precipitation (not shown here) is estimated to be 3.12 mm day^{-1} by LW90, whereas the standard GCM predicts 3.05 mm day^{-1} and the LOWRES model predicts 2.90 mm day^{-1}. This is a much greater degree of agreement than in earlier simulations without EAULIQ (Fowler *et al.*, 1994; Fowler and Randall, 1994; see section 3.3.1). In both the standard and LOWRES simulations, there is more global precipitation in January than the LW90 estimates and less in July.

A peculiar feature of the LW90 climatology is the large maximum (almost 15 mm day^{-1} in the annual mean) in the eastern Pacific near 150° W longitude. This is the wettest location in the world according to the observational data set, and is drier in the GCM in both simulations and in both seasons. This feature is likely related to occasionally very heavy rains associated with El Niño, and is not present in most years but still shows up in the long-term climatology. Because the GCM does not simulate El Niños (the sea surface

Precipitation

(millimeters per day)

January

July

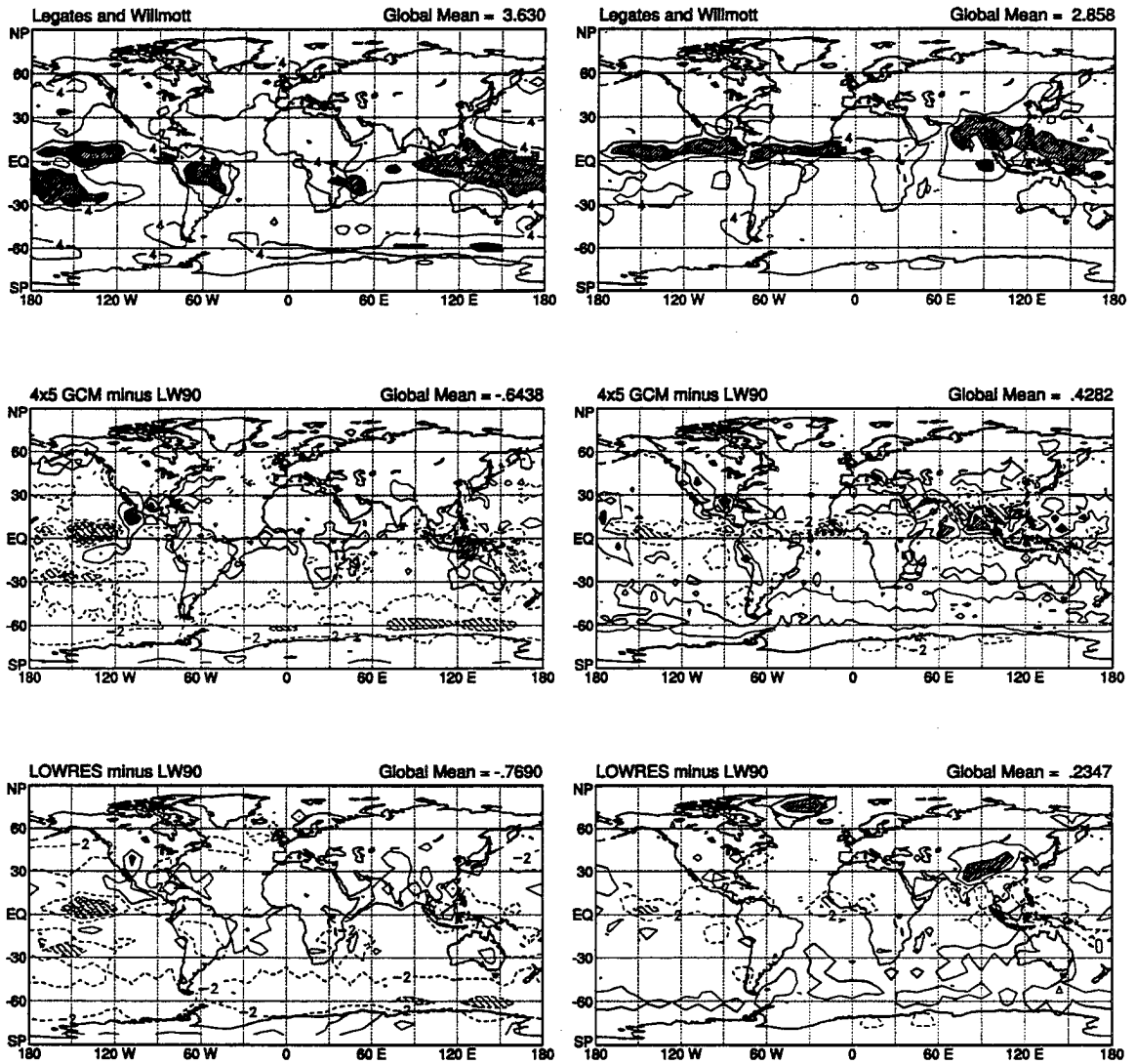

FIGURE 5.2: Comparison of the total precipitation as analyzed by Legates and Willmott (1990*b*) (top pair of panels) and as simulated by the CSU GCM (bottom four panels). The GCM results are presented as difference maps (observational data are subtracted before plotting). Contour interval for the observational data is 4 mm day^{-1}, with dark shading above 8 mm day^{-1}. Contour interval for the GCM difference maps is 4 mm day^{-1}, with dark shading above +6 mm day^{-1} and light shading below -6 mm day^{-1}. Dashed contours indicate negative values.

temperature is a fixed, seasonally varying boundary condition in these experiments), such a feature is not expected, and has not developed.

The band of maximum rainfall in the intertropical convergence zone (ITCZ) is slightly too weak in the standard simulation. Precipitation associated with the Indian summer monsoon is under-represented by more than 6 mm day^{-1} in the standard model over the land areas of southern and southeast Asia, but the model actually over-represents seasonal rainfall over the adjacent ocean areas of the Arabian Sea and Bay of Bengal, as compared to the LW90 estimates. The monsoon rains over southern Asia are better simulated than in earlier simulations without EAULIQ – very dry conditions in that region were noted by Randall *et al.* (1994) as a potential problem area for SiB because of incompatibilities between the prescribed vegetation and the simulated climate. These problems are less apparent in the LOWRES simulation.

The LOWRES simulation is too wet over both Greenland and the Tibetan Plateau in July. Diagnostic output from EAULIQ (not shown here) shows that these anomalies are due to snow. Monthly mean snowfall amounts are as high as 13 mm day^{-1} (water equivalent) in both regions. The standard model also simulates some July snowfall in these regions, but the amounts are much lower (less than 4 mm day^{-1}). The grid cell in Tibet receiving the greatest snowfall in July has snow on the ground during all months of the year, which reaches a maximum accumulation of 1.3 m of water equivalent in May, and has only decreased to about 0.7 m by July. Surface air temperatures at this location are consistently more than 10 K below the LW90 climatology (see section 5.1.1), which may explain the accumulation of so much snow, or conversely may be caused by the persistent snowpack.

Precipitation in other regions of the world is relatively well simulated by the GCM at both standard and low resolution, with less than 2 mm day^{-1} difference over much of the world. The summer precipitation maximum over the Antarctic Ocean is under-represented in both simulations as compared to the LW90 estimates (although there are of course almost no observations in that region).

5.1.3 Sea Level Pressure

Fig. 5.7 presents the observed sea level pressure as calculated by the ECMWF and the difference between the simulations and the observations. Four-year means of the ECMWF data are presented in the upper pair of panels for January and July, and these

Sealevel Pressure

(millibars)

January

July

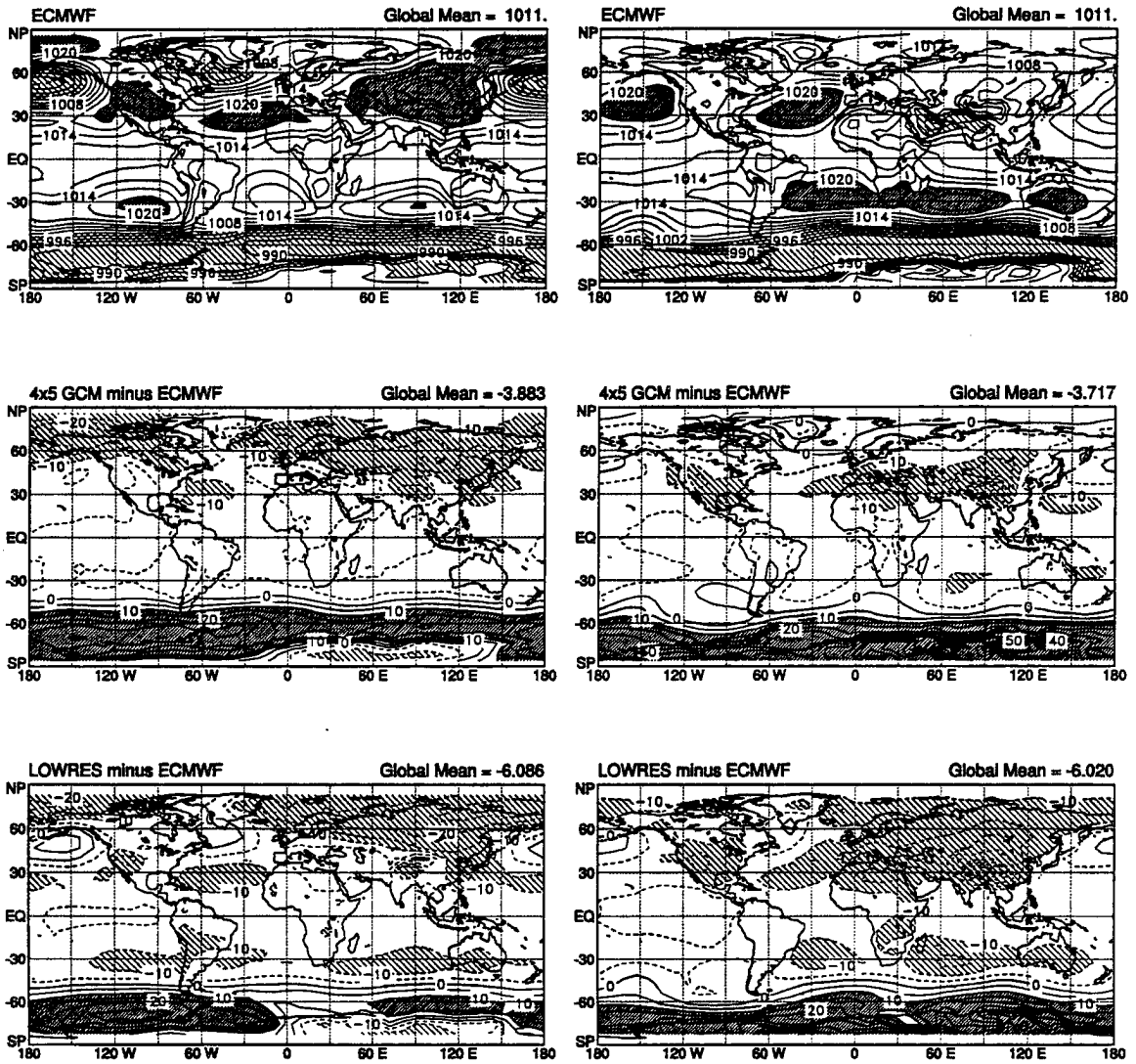

FIGURE 5.3: Comparison of the sea level pressure as calculated from the ECMWF data (top pair of panels) and as simulated by the CSU GCM (bottom four panels). The GCM results are presented as difference maps (ECMWF data are subtracted before plotting). Contour interval for the ECMWF data is 3 mb, with dark shading above1020 mb and light shading below 1002 mb. Contour interval for the GCM difference maps is 5 mb, with dark shading above +10 mb and light shading below -10 mb. Dashed contours indicate negative values.

data have been subtracted from the GCM results in the lower panels.In both seasons and at both resolutions, the global mean sea level pressure as calculated from the GCM results is lower than from the ECMWF data. The difference in the global means is more pronounced for the low resolution simulation than for the standard simulation.

By far, the largest differences between the simulated sea level pressure and that calculated from the observations is over Antarctica in July, with the GCM result as much as 102 mb higher than the ECMWF data. Because of the elevated terrain over most of the continental ice sheet, sea level pressure is a "fictitious" variable there, and is sensitive to the assumed temperature structure of the "missing" atmosphere below the ice surface. Trenberth and Olson (1988) have pointed out that the ECMWF analyses are extremely error-prone over Antarctica, and have changed dramatically whenever the model was updated, so the large differences in that region may not be significant. The sea level pressure as simulated in the low resolution run was also much higher there than the ECMWF analyses, but by only half as much as in the standard experiment. The deep region of very low sea level pressure over the Antarctic Ocean in January in the ECMWF analyses is also under-represented in the GCM, with differences greater than 20 mb in both simulations.

In middle latitudes, the simulated sea level pressure is lower than the ECMWF analyses over most regions, but the geographic pattern of highs and lows is generally as observed. Some of the differences tend to amplify the observed longwave patterns (*e.g.*, the Aleutian and Icelandic lows in January and the Asian monsoon in July), whereas others tend to damp them (*e.g.*, the Siberian and Canadian highs in January and the subtropical highs in both seasons in the LOWRES experiment). The differences are generally larger in the low resolution than the standard simulation. The sea level pressure over the northern continents is lower than observed in both simulations in both seasons.

The differences in sea level pressure over the continents in the LOWRES simulation tend to reflect the temperature differences in both seasons (compare Fig. 5.7 with Fig. 5.1). The Siberian high in January is associated with very cold temperatures (the monthly mean is less than 235 K over a large area in the ECMWF data) which are not as extreme in the GCM results. Similarly, the deep and extensive continental low pressure over most of Asia in the simulation results for July are associated with temperatures that are generally higher than observed (see Fig. 5.7).

The causal relationships between these features are difficult to sort out, since temperature, precipitation, cloudiness, and sea level pressure are intimately related. The zonal pattern of high temperature and low pressure over the northern midlatitudes may be related to the fact that no parameterization of gravity wave drag has been used in the GCM simulations. Topographically forced waves tend to decelerate the zonal winds near the tropopause in the real atmosphere, and are therefore associated with a weaker meridional temperature gradient in this region by thermal wind balance (Palmer *et al.*, 1986).

5.1.4 Tropospheric Wind Field

Streamline plots of the wind field at 850 mb are presented in Fig. 5.4. The general pattern of middle latitude westerlies, tropical easterlies, and subtropical highs is well represented in the GCM in both simulations. The region of cross-equatorial flow from north to south associated with the Australian monsoon in January is somewhat further east in the GCM than in the ECMWF data, and the corresponding south to north cross-equatorial flow over the Indian Ocean in July seems to be a bit too wide. Simulated winds over western equatorial Africa are more onshore (westerly) in January than they are in the observationally based data, indicating a slightly different response to monsoon heating in that region, but temperature and precipitation are well-simulated (see Fig. 5.1 and Fig. 5.7).

Wind streamlines at 200 mb are presented in Fig. 5.5. As was the case in the 850 mb results, the GCM captures the general pattern of midlatitude westerlies and tropical divergence, but there are more significant differences at this level. The GCM tends to produce more westerlies in the tropics than represented by the ECMWF data, especially in the LOWRES simulation. In January, the observationally based data show cross-equatorial flow from south to north in a basically easterly regime throughout most of the Eastern Hemisphere. By contrast, the flow in the GCM is dominated by westerlies around the world, with little cross-equatorial flow from the south except over the central Pacific. The flow in the standard experiment in July is closer to the ECMWF representation, but the tropical flow in the LOWRES model is still heavily dominated by westerlies, and cross-equatorial winds cover a much smaller range of longitudes than in the observationally based data. Since seasonally-reversing cross-equatorial wind currents are potentially the most significant agents for interhemispheric mixing of trace gases (see section 2.4.3), these differences may be quite significant. This issue is explored in more detail in Chapters 6 and 7.

Winds at 850 mb

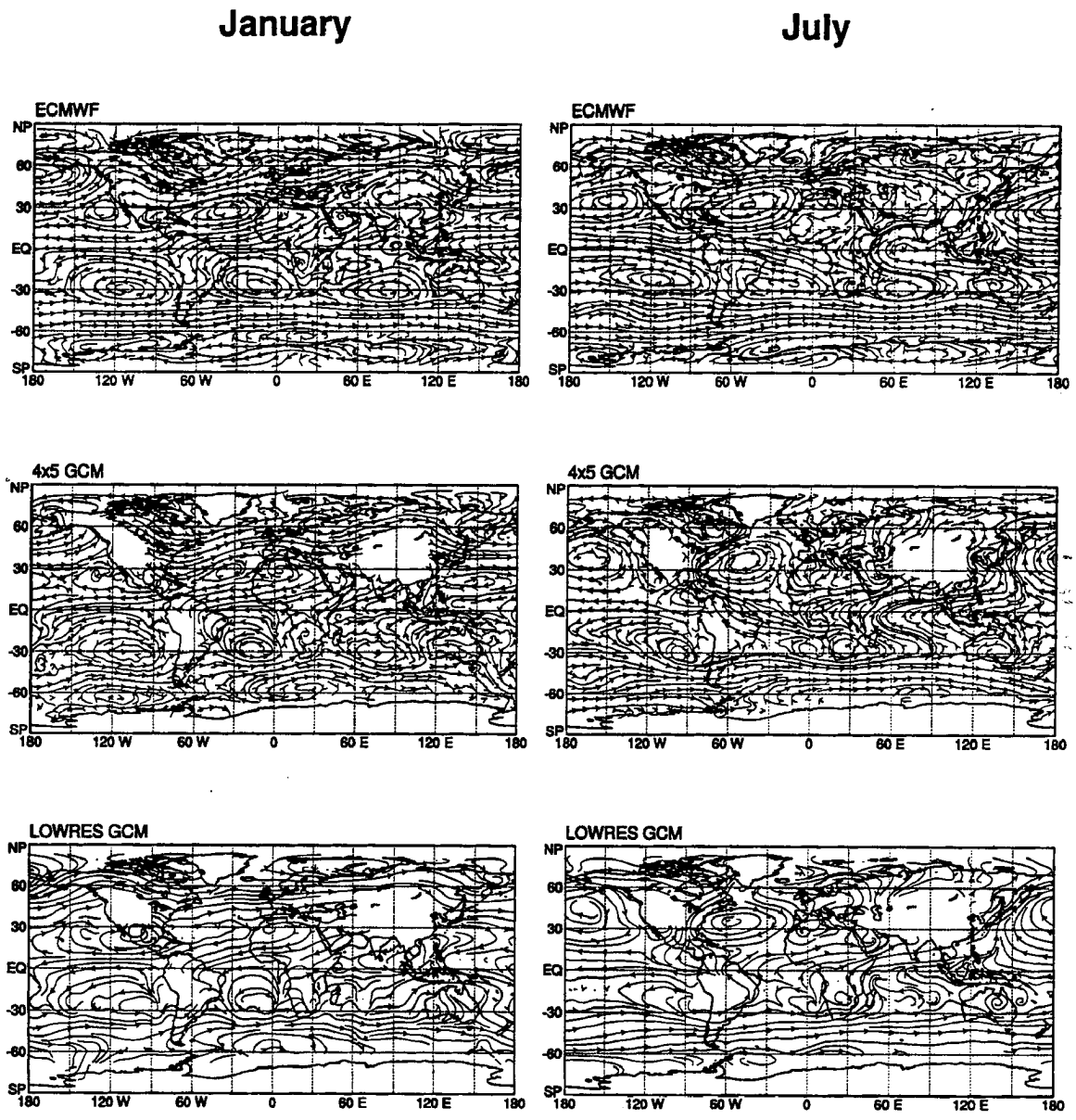

FIGURE 5.4: Comparison of the horizontal wind at 850 mb as calculated by the ECMWF (top two panels) and by the CSU GCM (bottom four panels). These streamline plots are constructed to indicate the tangent of the wind direction at each point, but no information is provided about the magnitude of the wind. Blank areas in the CSU GCM plots indicate that monthly mean surface pressure was less than 850 mb, due to elevated terrain (the ECMWF provides data at such points by extrapolation from higher levels).

Winds at 200 mb

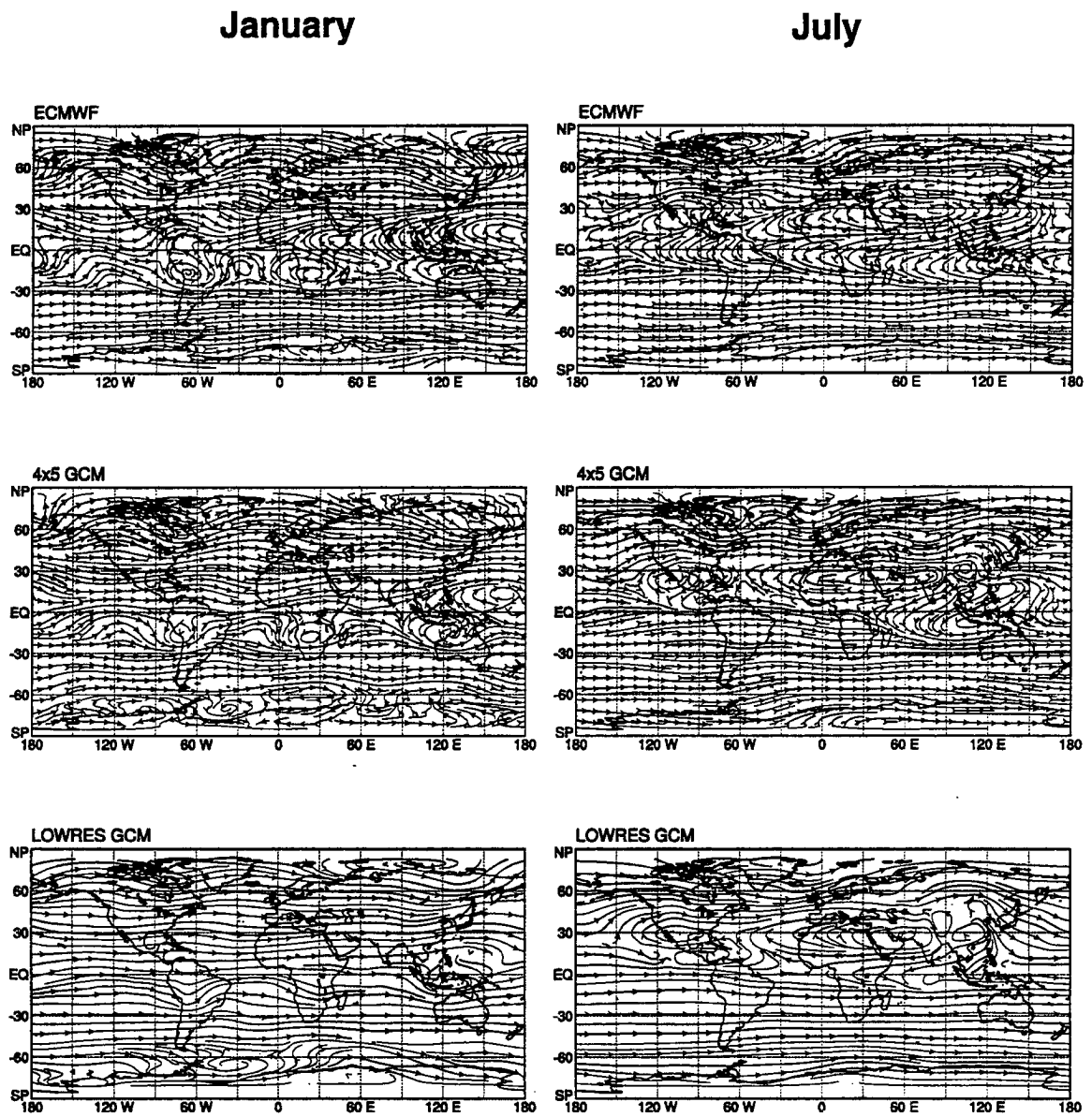

FIGURE 5.5: Comparison of the horizontal wind at 200 mb as calculated by the ECMWF (top two panels) and by the CSU GCM (bottom four panels). These streamline plots are constructed to indicate the tangent of the wind direction at each point, but no information is provided about the magnitude of the wind.

5.2 Vertical and Meridional Structure

Having examined the horizontal structure of the temperature, moisture, and circulation features in section 5.1, we now turn to the vertical structure of the simulated atmosphere. In this section, the results of both standard and low resolution GCM simulations are compared with the ECMWF analyses, but the data have been averaged around each latitude band of the CSU GCM (see section 3.3.3), and are presented as latitude-pressure "cross sections" of the zonal means. The y-axis of these plots is pressure, which can be thought of as a log-height axis because of the exponential decrease in pressure with altitude. Diagnostic data were saved in both simulations at seven constant-pressure levels: 100, 200, 300, 500, 700, 850, and 1000 mb. Because the surface pressure is commonly below 1000 mb over elevated terrain, the 1000 mb surface is "underground" in many cases. This leads to missing data for the lower troposphere in the plots presented here; areas of missing data are simply left blank. To construct the plots of ECMWF data for comparison, I used only the data from the same pressure levels as was saved for the GCM simulations. Unlike the GCM results, the data from the ECMWF have been extrapolated to 1000 mb in all cases, so there are no areas of missing data in the plots of "observed" data even though the 1000 mb surface (and in some cases the 850 and 700 mb surfaces) are below the Earth's surface. In all the plots in this section, the x-axis is latitude, with the South Pole on the left, and the North Pole on the right.

5.2.1 Temperature Structure

The vertical and meridional structure of the zonal mean temperature for the ECMWF data is presented in Fig. 5.7; these data have been subtracted from the analogous results of the GCM experiments to form the difference plots in the lower four panels. The basic pattern is quite simple, with high temperatures over the tropics in both January and July, and temperatures decreasing with both latitude and height, although of course the gradient is somewhat more steep in the winter hemisphere.

The most obvious difference between the ECMWF data and the simulated thermal structure is the region of very warm temperatures in the GCM's upper troposphere. This feature is much more pronounced in the LOWRES experiment than in the standard run, and stronger in July than in January, with a large area of more than 15 K difference for the LOWRES experiment in July. Simulated temperatures in the lower troposphere are much closer to the ECMWF values, so the warm region near 200 mb in the tropics indi-

Zonal Mean Temperature

(Kelvin)

January

July

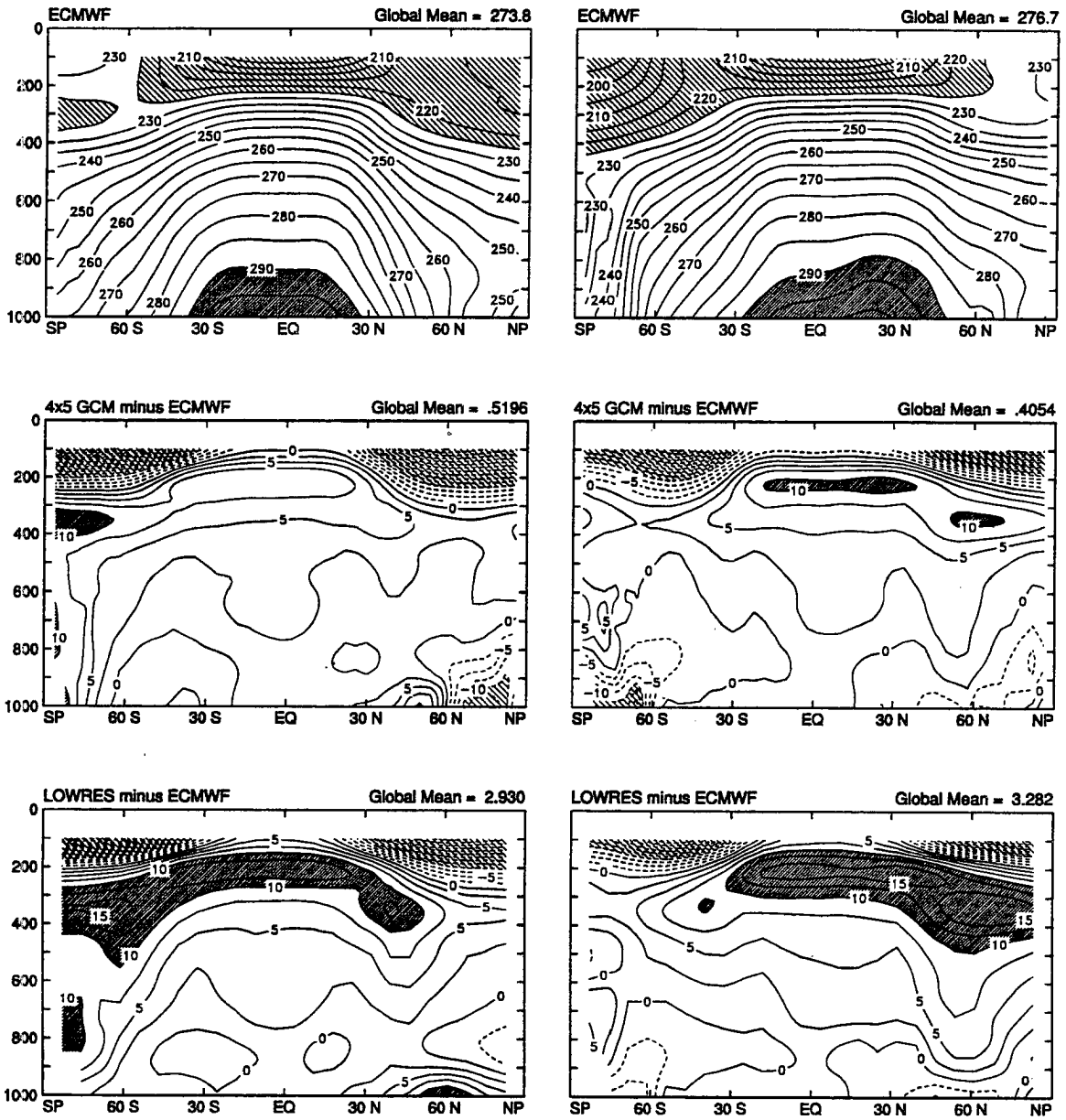

FIGURE 5.6: The zonal mean temperature as calculated from the ECMWF data (top pair of panels) and as simulated by the CSU GCM (bottom four panels). The horizontal axis is latitude and the vertical axis is pressure. The GCM results are presented as difference plots (ECMWF data are subtracted before plotting. Contour interval for the ECMWF data is 5 K, with dark shading above 290 K and light shading below 225 K. The difference plots have a contour interval of 2.5 K, with light shading below -10 K and dark shading above 10 K. Dashed contours indicate negative values.

cates that the model atmosphere is much more statically stable in the tropics than indicated by the ECMWF data. This is expected to lead to a reduced mean meridional circulation (Hadley cell) due to the enhanced static stability (this idea is further explored in section 5.2.3).

It is interesting to note that in earlier simulations without the new cloud microphysics parameterization, the tropical upper troposphere was *colder* than observed, and the Hadley cell was much too strong, with more cumulus precipitation in the ITCZ than observed (Fowler and Randall, 1994). Before the inclusion of EAULIQ in the CSU GCM, cloud albedo and infrared emissivity were parameterized according to cloud temperature only. The availability of the mixing ratios of the various condensate phases in EAULIQ has made possible a more sophisticated representation of cloud radiative properties according to liquid and ice water paths. (Fowler *et al.*, 1994, see section 3.3.1). The new parameterization has resulted in more absorption of solar radiation by upper tropospheric clouds than in previous simulations, giving a more realistic simulation of the Earth's radiation budget and tropical precipitation (Fowler and Randall, 1994), but it appears from the results in Fig. 5.7 that this problem has been "fixed" a little too well, especially for the low resolution version of the GCM. The single scattering albedo used to calculate the interactions of shortwave radiation with ice crystals in the model was 0.97, which may be too low, leading to excessive solar heating in the tropical upper troposphere.

The simulated temperatures are also warmer than observed above the summer polar regions in both January and July. In January, the effect is not confined to the upper troposphere but is felt throughout the depth of the troposphere, leading to a considerably weaker meridional temperature gradient in the southern summer than is observed. This is associated with weaker than observed westerly winds through the thermal wind balance (see Fig. 5.7 and the discussion in the next section).

Near the surface, the difference plots of thermal structure are qualitatively different between the standard and LOWRES simulations in the lower troposphere in winter. The standard model is considerably cooler than observed (by more than 10 K) at 70° N in January and at 70° S in July, whereas the LOWRES model is nearly 10 K *warmer* than observed in the northern Arctic winter.

Simulated temperatures in the "stratosphere" (above about 200 mb in middle latitudes) are systematically colder than in the ECMWF data. The "top" of the GCM is at 51.3 mb, and there are only two model levels above 100 mb (just one in the LOWRES cal-

culation), so the stratosphere is not resolved. Thus it is not surprising that the temperature structure simulated in these experiments differs significantly from observations of the real stratosphere in which both radiative and dynamical processes are active. Because the region of colder than observed temperatures near the top of the model is confined to the extratropics in both simulations in both months, the reverse temperature gradient seen in the ECMWF data is much weaker in the GCM. This is probably the reason for the lack of simulated easterly winds at 200 mb (see Fig. 5.5).

5.2.2 Zonal Wind

As noted in the previous sections, the vertical and meridional distribution of the zonal wind is directly related to the temperature field according to the thermal wind balance. The zonal mean cross section of zonal wind presented in Fig. 5.7 reflects this relationship. The general structure of the zonal wind field is quite similar between the ECMWF data and the simulation results, showing a strong westerly jet in the winter hemisphere and a somewhat weaker jet at higher latitude in the summer hemisphere in both January and July.

The simulated midlatitude jet streams in the winter hemisphere are quite well represented in the standard experiment in both January and July, but are considerably weaker than observed in the LOWRES run. As noted in the previous section, the simulated westerly winds in the southern hemisphere are much weaker than observed, especially in January. This is related to the fact that the meridional temperature gradient in the summer hemisphere is so much weaker than observed.

The observational data show deep easterly winds in the tropics, reaching all the way to 100 mb over the equator in both January and July; the tropical easterlies are much shallower as simulated by the GCM. As noted above, this is a consequence of the colder than observed extratropical "stratosphere" in the GCM. Weak polar easterly winds are present in both the ECMWF data and the GCM results, although because of the elevated terrain much of these areas are masked out as missing values in the figure.

From the data considered here, it is impossible to discern the cause of the differences between the vertical structure simulated by the GCM and that represented by the ECMWF data. The thermal wind balance dictates that the warm temperatures in the simulated upper troposphere and the cold extratropical "stratosphere" are intimately timed to the weaker than observed midlatitude westerlies and the lack of deep tropical easterlies

Zonal Mean Zonal Wind

(meters per second)

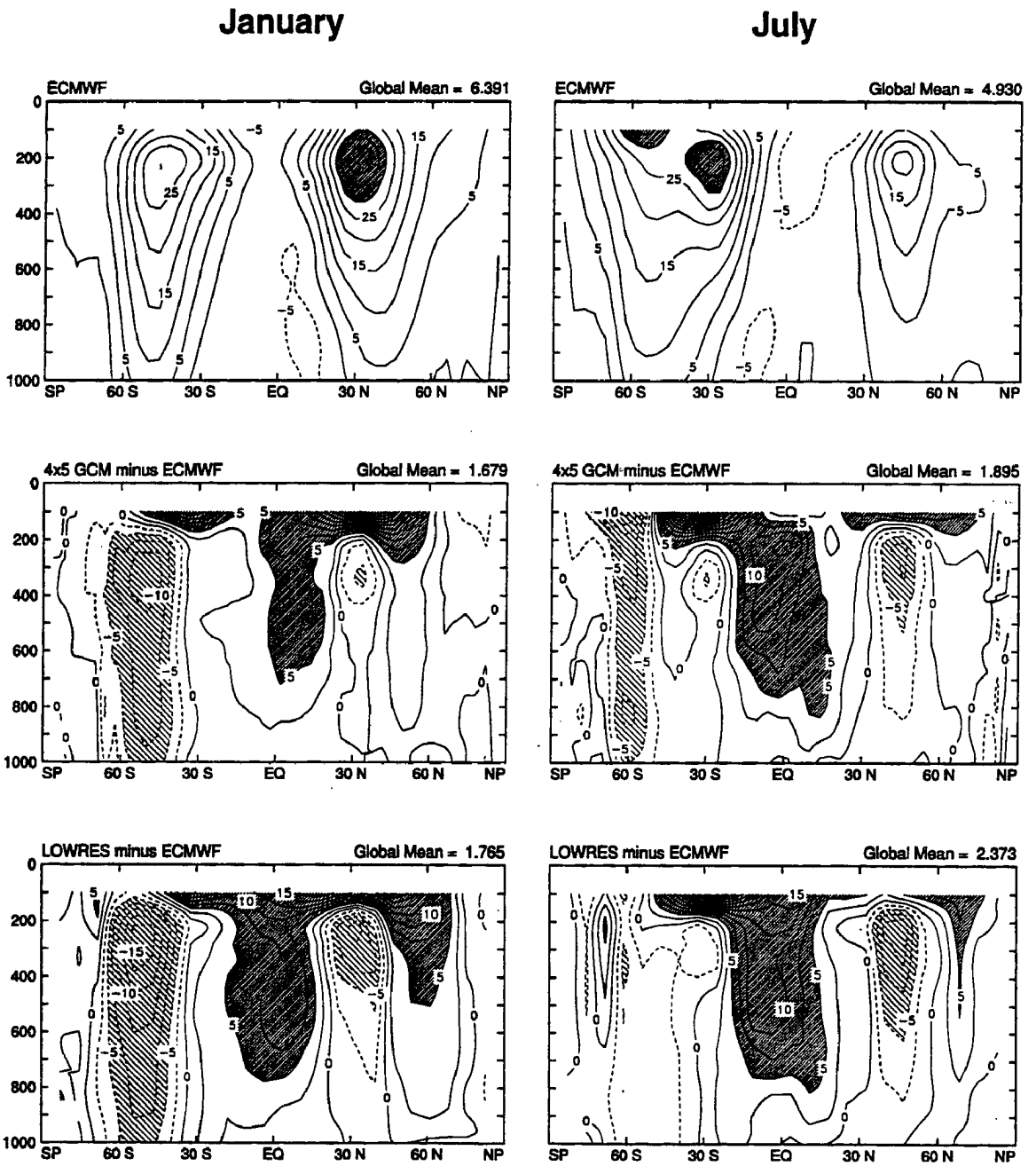

FIGURE 5.7: The zonal mean zonal wind as calculated from the ECMWF data (top pair of panels) and as simulated by the CSU GCM (bottom four panels). The horizontal axis is latitude and the vertical axis is pressure. The GCM results are presented as difference plots (ECMWF data are subtracted before plotting). Contour interval for the ECMWF data is 5 m s^{-1}, with dark shading above 30 m s^{-1}. The difference plots have a contour interval of 2.5 m s^{-1}, with dark shading above 5 m s^{-1} and light shading below -5 m s^{-1}. Dashed contours indicate negative

in the GCM. Whether this is caused by dynamical factors affecting the simulation of the winds or by physical factors affecting the thermal structure is unknown, however. Certainly the enhanced radiative heating associated with EAULIQ may play a role.

5.2.3 Mean Meridional Circulation

The streamfunction of the mean meridional circulation (MMC) is presented in Fig. 5.7 as derived from the zonal mean meridional wind component from the ECMWF data and both GCM simulations. Contours of the streamfunction represent mass transport in the zonal mean, with the intensity of the vertical and meridional transport shown by the gradient of the streamfunction. Specifically, the streamfunction is defined from

$$[v]\,2\pi a\cos\varphi = g\frac{\partial\Psi}{\partial p}$$
$$[\omega]\,2\pi a^2\cos\varphi = -g\frac{\partial\Psi}{\partial\varphi} \qquad (5.1)$$

where Ψ is the streamfunction of the MMC, $[v]$ is the zonal mean meridional (southerly) wind component, $[\omega]$ is the zonal mean vertical velocity in pressure coordinates ($\omega \equiv \frac{dp}{dt}$) p is pressure, φ is latitude, a is the radius of the Earth, and g is the acceleration of gravity. The streamfunction Ψ is obtained by integrating (5.1), and an arbitrary constant of integration defines the units of Ψ. To construct Fig. 5.7, the zonal mean meridional wind $[v]$ was used to calculate $[\omega]$ by mass continuity, and the streamfunction was calculated by integrating upward using the boundary condition that no mass crosses the Earth's surface (thus the streamfunction is defined to be zero at 1000 mb).

Mass transport along the contours of the streamfunction in Fig. 5.7 is clockwise around positive values and counterclockwise around negative values. By far the strongest circulation cell is the winter Hadley cell, which is represented by the strong positive values of Ψ in January and by the strong negative values in July. A much weaker Hadley cell is evident in the summer hemisphere in both months, and is represented in the figure by values of opposite sign from the main cell. Even weaker circulations in the opposite sense are present poleward of the Hadley cells in both hemispheres; these are the Ferrel cells.

Mean Meridional Circulation

(10^9 kg s^{-1})

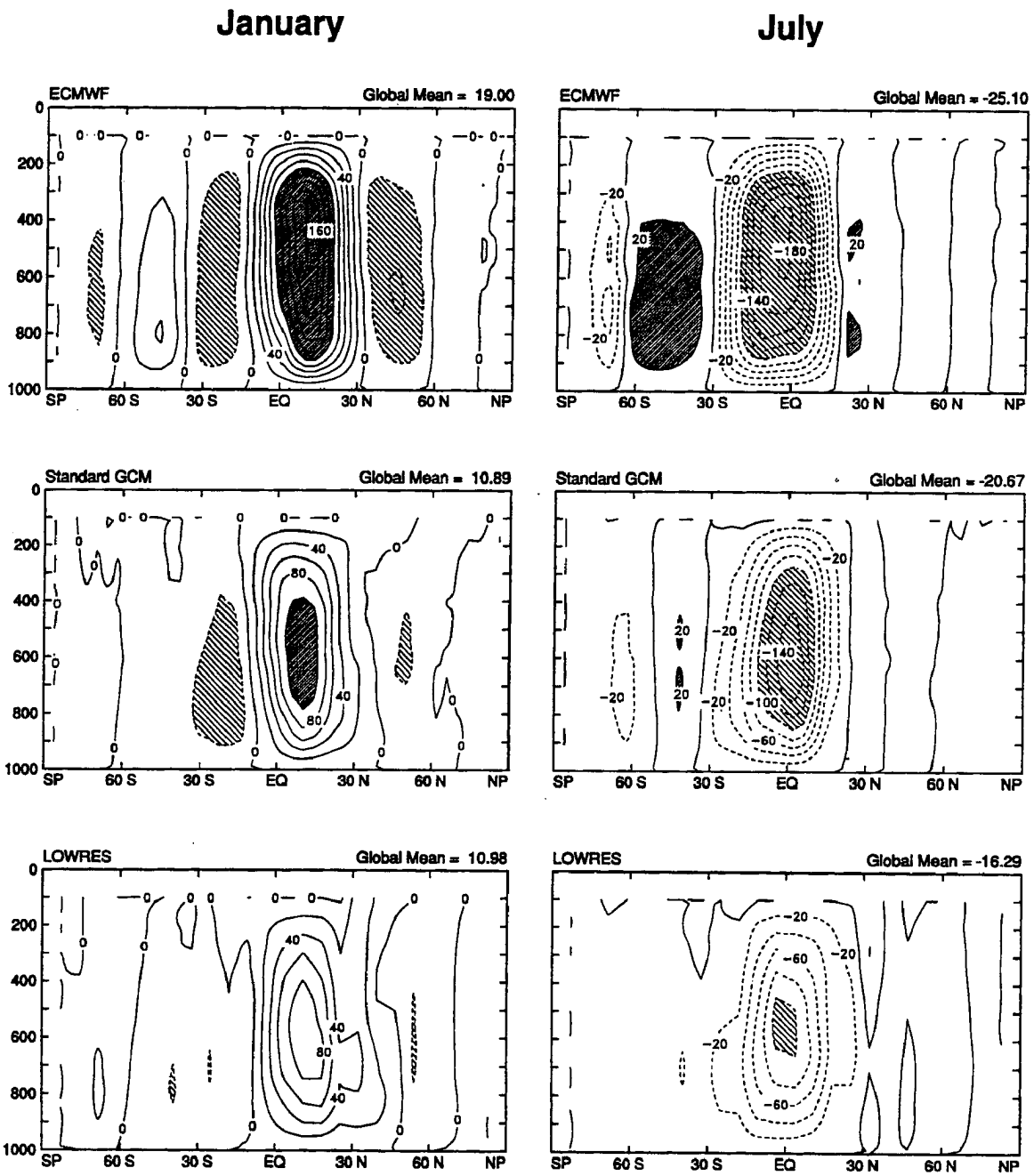

FIGURE 5.8: The streamfunction of the zonal mean meridional circulation as calculated from the ECMWF data (top pair of panels) and as simulated by the CSU GCM (bottom four panels). The horizontal axis is latitude and the vertical axis is pressure. Contour interval for all six panels is 20×10^9 kg s^{-1}. Dark shading is used for values greater than 100×10^9 kg s^{-1} in January and greater than 20×10^9 kg s^{-1} in July. Light shading indicates values less than -20×10^9 kg s^{-1} in January and less than -100×10^9 kg s^{-1} in July. Dashed contours indicate negative values.

Upward motion is indicated by positive $\frac{\partial \Psi}{\partial \varphi}$ (see (5.1)), and is strongest in the ECMWF data just south of the Equator in January and at about 15° N in July; this is the rising limb of the Hadley cell. Sinking motion in the subsiding branch of the Hadley cell is indicated by strong gradients of the opposite sign, and is strongest at about 20° latitude in the winter hemisphere in the ECMWF data.

The location of the Hadley cell in the standard GCM is quite well simulated in both January and July, although the intensity of meridional overturning is somewhat weaker than indicated by the ECMWF data. This is particularly true in January, where the maximum value near 10° N in the middle troposphere is only about 110 in the GCM, compared to about 180 as derived from the ECMWF data. The strength of the Hadley cell as represented by the LOWRES model is even weaker still, with central maxima of the streamfunction less than half that of the ECMWF in January and about 70% as strong in July.

To the extent that meridional transport of the simulated tracers is accomplished by the mean meridional circulation, these results suggest that it will be rather weak in the experiments performed here, and that it will be stronger in the standard than the LOWRES run. Meridional mixing is evaluated in the next section by a comparison of the simulated concentrations of ^{85}Kr (tracer T_{16}) with observations and with a previous simulation.

5.3 Large-scale Mixing of Krypton-85

Because ^{85}Kr is produced only in the northern middle latitudes (as a by-product of nuclear fuel processing, see the discussions of ^{85}Kr in sections 2.4 and 3.4.6), it is useful as a tracer for evaluating the large-scale mixing properties of the atmospheric circulation. In this section the simulated concentrations of this tracer are compared to both observations and a previous simulation by Heimann and Keeling (1989; hereafter referred to as HK89) to provide information about the realism of the meridional transport of tracers in the CSU GCM. From the results of the previous section (Fig. 5.7) with respect to mean meridional circulation of atmospheric mass, we expect that the meridional mixing of tracers might be slightly weaker than observed.

Weiss *et al.* (1983) reported on measurements of ^{85}Kr concentration in samples collected along several ship cruises along the Atlantic Ocean. These data (and some supplemental data not previously reported) were used by HK89 to evaluate large scale mixing

of tracers in the GISS tracer model. The comparison presented by HK89 is repeated here (Fig. 5.9), and a similar plot is made for the given months using the simulated concentrations of tracer T_{16} from the standard experiment in the present study.

In the shipboard measurements and in both the simulation by HK89 and the standard GCM, the difference in concentration between the northern and southern high latitudes is about 4 pCi m^{-3} STP in all four months shown in the figure. The HK89 concentrations are a bit too high in January of both 1982 and 1983 in the northern middle latitudes, and also in the lower northern latitudes in March of 1983. The CSU GCM results are closer to the observations during these months.

The simulated concentrations from the GCM experiment show more variability in the northern middle latitudes than the HK89 concentrations. This is due to dispersion error in the numerical scheme used to advect the tracer in the GCM (see section 3.3.4), which is expected in the simple second order scheme used in this experiment (Rood, 1987). This issue is explored in more detail below.

The HK89 simulations show a sharp break in concentration near the equator in all four months; this is also evident (although slightly weaker) in the Weiss *et al.* (1983) observations. This steep tropical gradient has been interpreted as the result of deep tropical convection in the ITCZ, which forms the most significant barrier to interhemispheric exchange of mass (see section 2.4.3). The tropical gradient in the GCM results is considerably weaker than in the HK89 results, and slightly weaker than in the observational data. This suggests that interhemispheric exchange of ^{85}Kr in the CSU GCM is too strong, contrary to the analysis of simulated winds shown above in section 5.2.3.

In section 2.4.3, an expression was derived for calculating the "interhemispheric exchange time" of a tracer from hemispheric mean concentrations and total hemispheric surface emissions; it is repeated here for convenience:

$$\tau = \frac{2\Delta q}{(S_N - S_S) - \lambda \Delta q} \qquad (5.2)$$

where Δq is the difference in hemispheric mean concentration between north and south, S_N is the total rate of tracer emission in the northern hemisphere (S_S is zero for ^{85}Kr), and λ is the decay constant for the tracer. Substituting annual mean values of Δq and S_N into (5.2), τ = 0.87 yr for ^{85}Kr in the standard experiment. This is less than the value of

Meridional Concentration Profiles of Krypton-85

Surface Values at 30° W

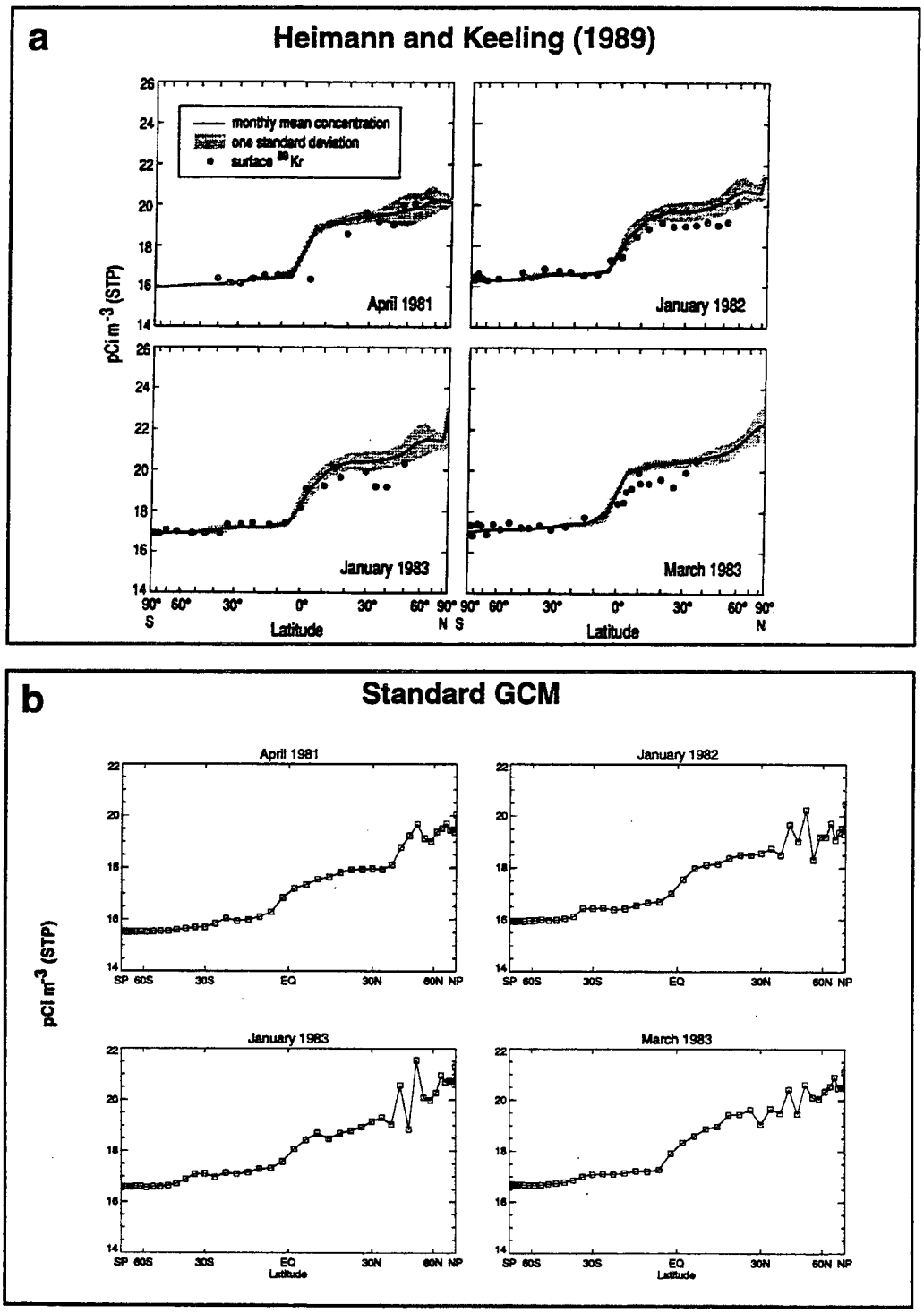

FIGURE 5.9: Simulated concentration ^{85}Kr over the Atlantic Ocean at 30° W longitude for four months in which observational data are also available. (a) Results of Heimann and Keeling (1989) using the GISS tracer model; (b) Results of the present study using the standard GCM.

1.3 yr determined by HK89, which is consistent with the weaker tropical gradient in Fig. 5.9. Weiss *et al.* (1983) estimated t to be between 1.0 yr and 1.7 yr using a different definition strictly from their observational data (other estimates of τ for ^{85}Kr are reviewed in section 2.4.3).

Maps of the simulated concentration field at the surface of the Earth from HK89 and the standard GCM are compared in Fig. 5.9 for January 1982 and in Fig. 5.11 for July, 1982. Both maps are for the concentration in the lowest model layer, but while the CSU GCM uses a bulk boundary layer parameterization to represent this variable depth layer the GISS tracer model uses a fixed layer of 50 mb depth. Note that the contour intervals are not uniform in either the HK89 results of the GCM results. The GCM results have been smoothed by computing each value as a weighted mean of the gridded concentration and its nearest neighbors in each direction.

The general shape of the concentration field is very similar between the HK89 results and the GCM simulation. Regional "hot spots" of high concentration surround each of the point sources (see Table 3.4 in 3.2.2.4); these are superimposed on a roughly zonal pattern of isolines showing a north to south gradient of about 4 pCi m^{-3} at standard temperature and pressure (STP). In both simulations the background meridional gradient is noticeably "distorted" by the atmospheric circulation in the North Atlantic and near the east coast of Asia. The meridional gradient is also concentrated in the tropics in both simulations, although not quite as strongly in the GCM experiment as in the HK89 results.

The biggest difference between simulated concentration fields in the HK89 study and the present results is that the concentration maxima near the point sources are much stronger in the GCM simulation. The maximum concentration (in the unsmoothed data) in the GCM was 270 pCi m^{-3} STP in January and 116 pCi m^{-3} STP in July (in western Russia near what is by far the largest emission source in the world, see Table 3.4). It is difficult to tell exactly what the highest contour values are in the HK89 plots, but they appear to be about 45 pCi m^{-3} STP in January and 26 pCi m^{-3} STP in July. Regional concentrations are also much higher western Europe and in the vicinity of Hanford, WA and Savannah River, GA in the GCM than they are in the HK89 study. Not only are the concentrations very high in the vicinity of the emission sources, but there are also extremely low concentrations immediately upwind of the grid cells containing the point sources.

Monthly mean concentrations reach lows of 6.6 pCi m^{-3} STP in July and *negative* 6.1 pCi m^{-3} STP in January immediately upwind of the Kyshtym, Russia site (Fig. 5.12).

Simulated Surface Concentration of Krypton-85

January, 1982

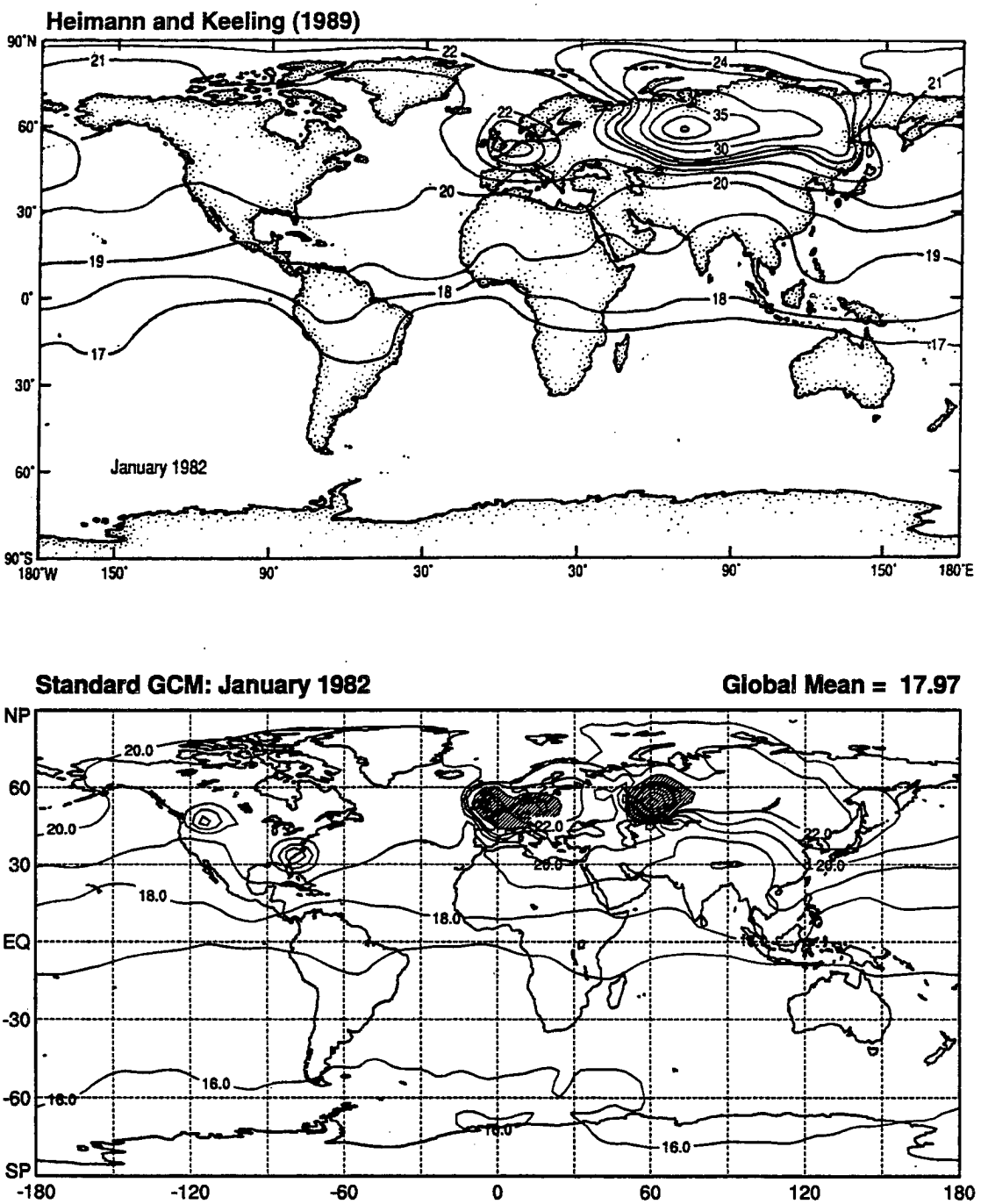

FIGURE 5.10: Comparison of the simulated concentration (pCi m^{-3} STP) for January, 1982 between an earlier study (Heimann and Keeling, 1989, upper panel) and the standard GCM in the present study (lower panel). Contour interval varies in both figures. Contours in the lower panel are drawn at 16-21 by ones, 25-40 by 5, and 40-80 by 10. Shaded regions in the lower panel are above 25 pCi m^{-3} STP

Simulated Surface Concentration of Krypton-85

July, 1982

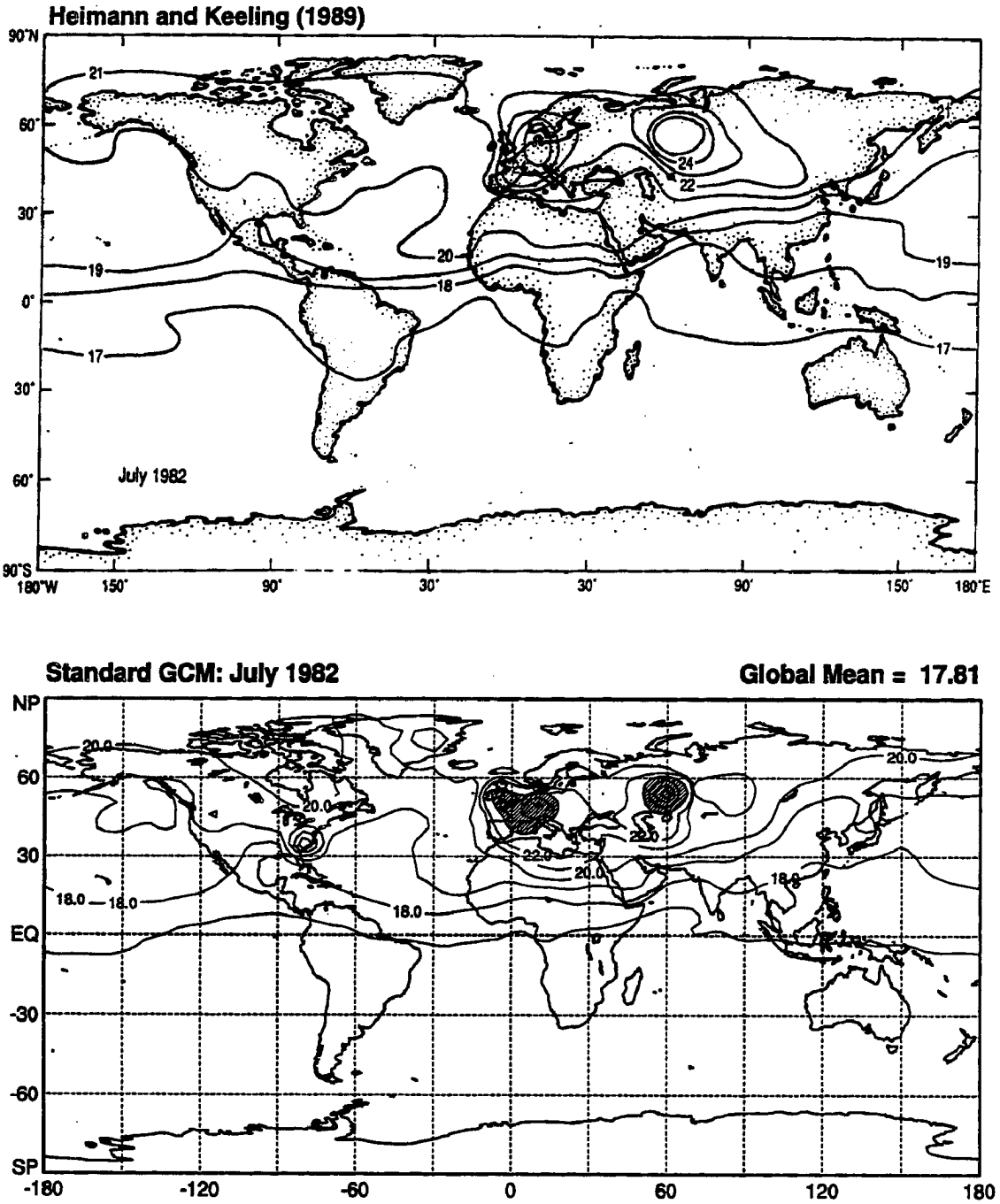

FIGURE 5.11: Comparison of the simulated concentration (pCi m^{-3} STP) for January, 1982 between an earlier study (Heimann and Keeling, 1989, upper panel) and the standard GCM in the present study (lower panel). Contour interval varies in both figures. Contours in the lower panel are drawn at 16-21 by ones, 25-40 by 5, and 40-80 by 10. Shaded regions in the lower panel are above 25 pCi m^{-3} STP

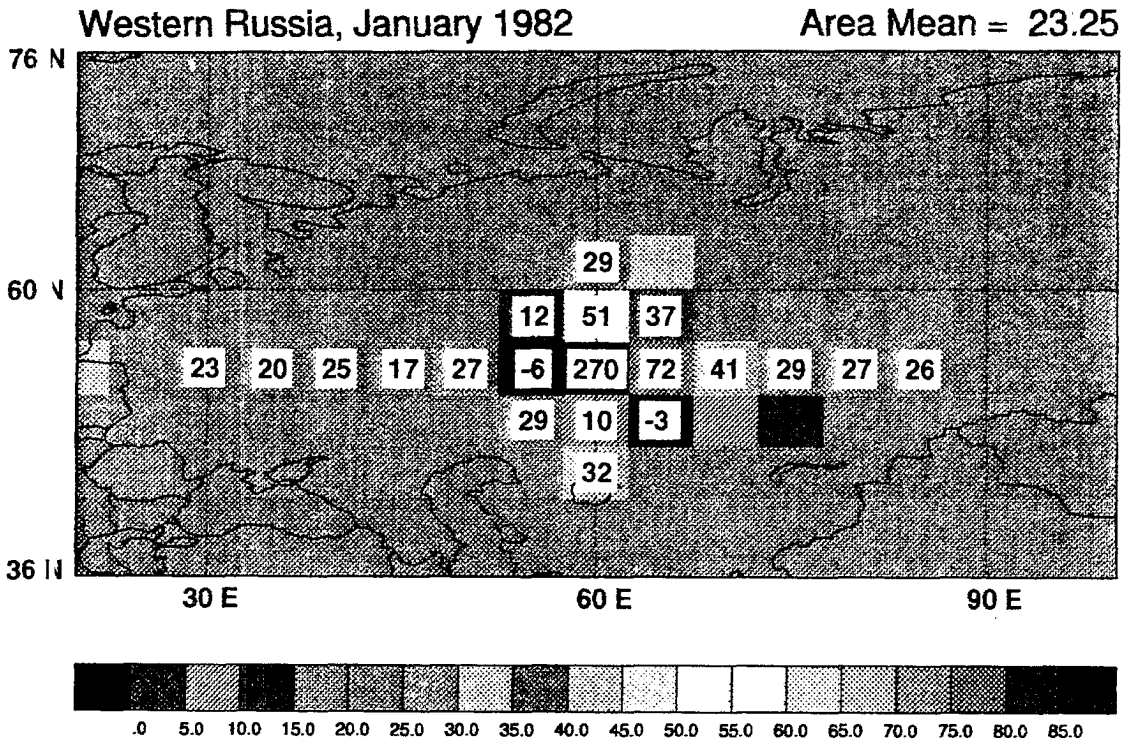

FIGURE 5.12: Gridded values of monthly mean concentration (pCi m^{-3} STP) of ^{85}Kr (tracer T_{16}) over Western Russia in January, 1982. The Khyshtym nuclear fuel plant (55.7° N, 60.6° E) is located in the grid cell with 270 pCi m^{-3} STP concentration.

Also note the pattern of high and low concentrations simulated west of the emission site. The strong periodicity of the concentration field at the $2\Delta x$ wavelength in the zonal direction shows that this feature results from dispersion error in the advection of the tracer in the presence of the extremely strong gradient in concentration near the emission sources, as expected for the simple second order advection scheme used in this experiment.

Point sources have Fourier components in many wavelengths, and the centered, second-order scheme advects these components with different phase speeds (Rood, 1987). The scheme fails completely with $2\Delta x$ wavelength, and it is this "trapped" $2\Delta x$ component that leads to the "ripples" of that wavelength upstream of the source. The reason the problem is so much more pronounced in the January than the July results is that the model's prognostic PBL is much shallower at that season (due to cold and statically stable winter conditions), so the emissions are felt in a very shallow layer. This causes the local gradient in concentration to be greater, resulting in stronger dispersion error than in the summer months. The $2\Delta y$ fluctuations in the meridional profiles discussed above (Fig.

5.9) are due to the same numerical problem, with advection "ripples" propagating upstream (westward) from the several point sources in Western Europe.

Although the numerical problems noted here preclude interpretation of the details of the tracer concentration field in the regions of emission sites, the model does quite well in reproducing the overall meridional gradient of ^{85}Kr concentration, the interhemispheric exchange time, and many of the more subtle features in the previous simulation by HK89. Numerical modeling of a tracer such as ^{85}Kr with several very strong point sources is much more challenging than the numerical modeling of CO_2, because the sources of CO_2 are very small compared to its background concentration. Therefore the simulated meridional gradients of the other tracers can be interpreted with confidence, based on the results shown here for ^{85}Kr.

5.4 Vertical Mixing of Radon-222

Because ^{222}Rn has such a short radioactive half-life (3.83 days), it never gets far from its sources (radioactive decay of mineral material in rocks and soils). It has therefore been used to evaluate the vertical mixing of the atmosphere. Liu *et al.* (1984) reviewed existing observational data of vertical profiles of ^{222}Rn, and this compilation was used by HK89 to evaluate the vertical mixing simulated by the GISS model.

Meridional cross-sections of the zonal mean concentration of ^{222}Rn as simulated by the standard GCM are presented in Fig. 5.13. The general pattern of concentration reflects the fact that the (uniform, invariant) source is located on the ice-free continents, which are of course concentrated in the northern hemisphere. The maximum concentration is slightly elevated (around 850 mb) because the concentration is much lower over the oceans, and because 1000 mb data are missing over land much of the time due to low surface pressure. Concentration diminishes rapidly with height due to radioactive decay, as expected. Note the secondary maximum near 200 mb at about 15° S in January and about 20 °N in July. This is due to penetrative cumulus convection, which transports the tracer directly from the PBL to the level at which the cloud detrains (its level of neutral buoyancy).

Most of the available observational data are for summer conditions, and Liu *et al.* (1984) compiled an "average" profile for summertime conditions over the central United States. To compare vertical profiles of ^{222}Rn with these observational data, I combined

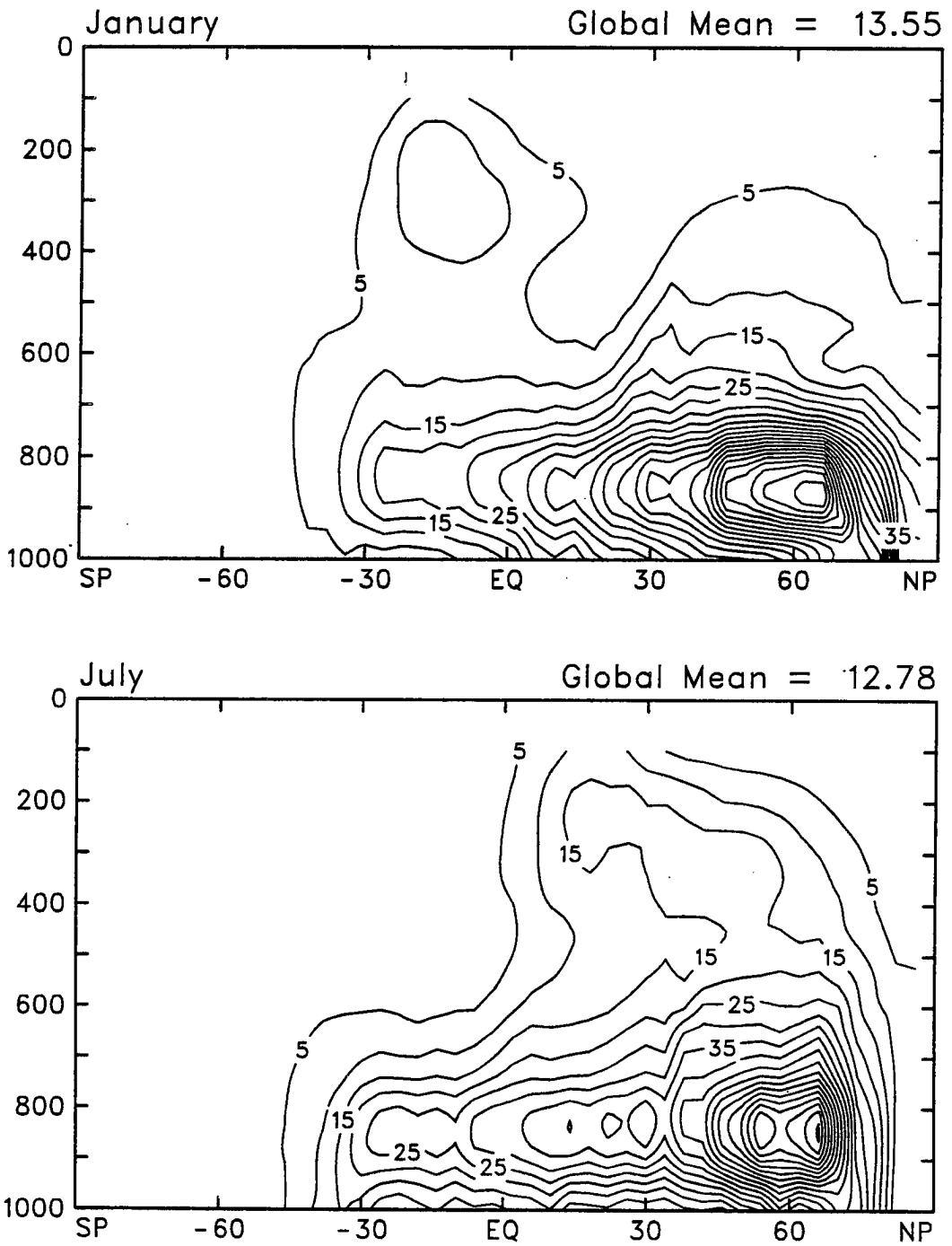

FIGURE 5.13: Meridional cross sections of ^{222}Rn as simulated in the standard GCM experiment. The horizontal axis is latitude and the vertical axis is pressure. Data are multiyear means for January and July. The contour interval is 5 pCi m^{-3} STP in both panels.

monthly mean data from the last three years of the standard experiment at 16 grid cells representing the Rocky Mountain region and central Great Plains of the US in June, July, and August. This data set amounted to 981 individual concentrations, but because the data were saved on constant pressure levels, the corresponding heights were not consistent across all the data. The data were therefore grouped into height ranges, and analyzed according to the mean height of the data within each category. Following HK89, I scaled the concentration data so that the concentration at 2 km above the ground matched the Liu *et al.* (1984) summertime profile (HK89 used a constant source of 1.32 atoms m^{-2} s^{-1}; my scaling corresponds to a smaller emission rate of only 0.82 atoms m^{-2} s^{-1}).

The resulting "average" vertical profile of ^{222}Rn over the central US during summer is presented in Fig. 5.14. Also included in the figure are the observational compilation of Liu *et al.* (1984) and the simulated profile presented by HK89. The error bars in the upper panel were obtained by computing the standard deviation of the approximately 50 individual GCM concentrations in each height bin, and the error bars in the lower panel represent the standard deviation of the observational data as computed by Liu *et al.* (1984). Note that the vertical scale of Fig. 5.14a extends further than that of Fig. 5.14b. This is because observations of ^{222}Rn are unavailable in the upper troposphere and stratosphere.

The ^{222}Rn simulated by the GCM agrees very well with the observational data in the lower and middle troposphere. Above about 8 km, the GCM tends to estimate a higher concentration than is observed; this trend was also noted by HK89 for the GISS model. The CSU GCM is closer to the observationally derived profile than the GISS model in the upper troposphere, and the error bars of the GCM simulation and the Liu *et al.* profile overlap. Above 12 km, the concentration simulated by the GCM drops off sharply, presumably because of inhibited vertical transport into the stable "stratosphere" at the highest model levels. There are no observational data at this height, however, so the realism of this feature is impossible to evaluate.

Wintertime concentrations of ^{222}Rn are expected to decrease even more rapidly with height than in summer due to increased static stability, but there are not many observational data available for winter. Liu *et al.* (1984) present four such profiles in their compilation, all of which were collected by Larson (1974) over the Yukon Valley (Alaska) in February, 1972. HK89 compared their simulated concentrations over Alaska with the wintertime "average" shown by Liu *et al.* (1984). Fig. 5.15a presents the monthly mean concentrations simulated by the GCM at a single grid point over central Alaska during

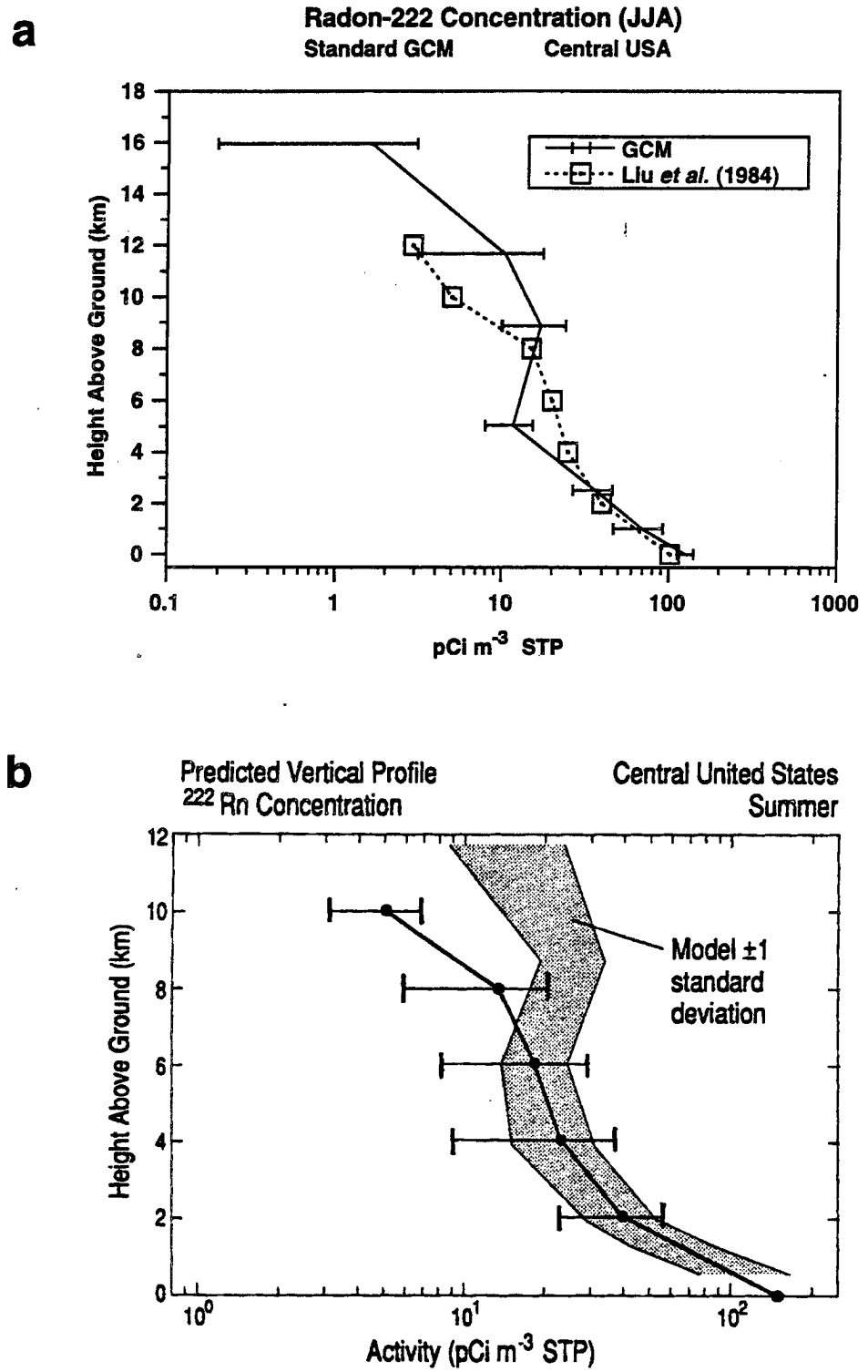

FIGURE 5.14: Vertical profiles of ^{222}Rn (pCi m^{-3} STP) over the central United States as simulated by (a) the standard GCM and (b) HK89. Both panels also include the observational data compiled by Liu *et al.* (1984). In (a), the error bars indicate one standard deviation of the GCM data. In (b) the error bars indicate one standard deviation of the observational data.

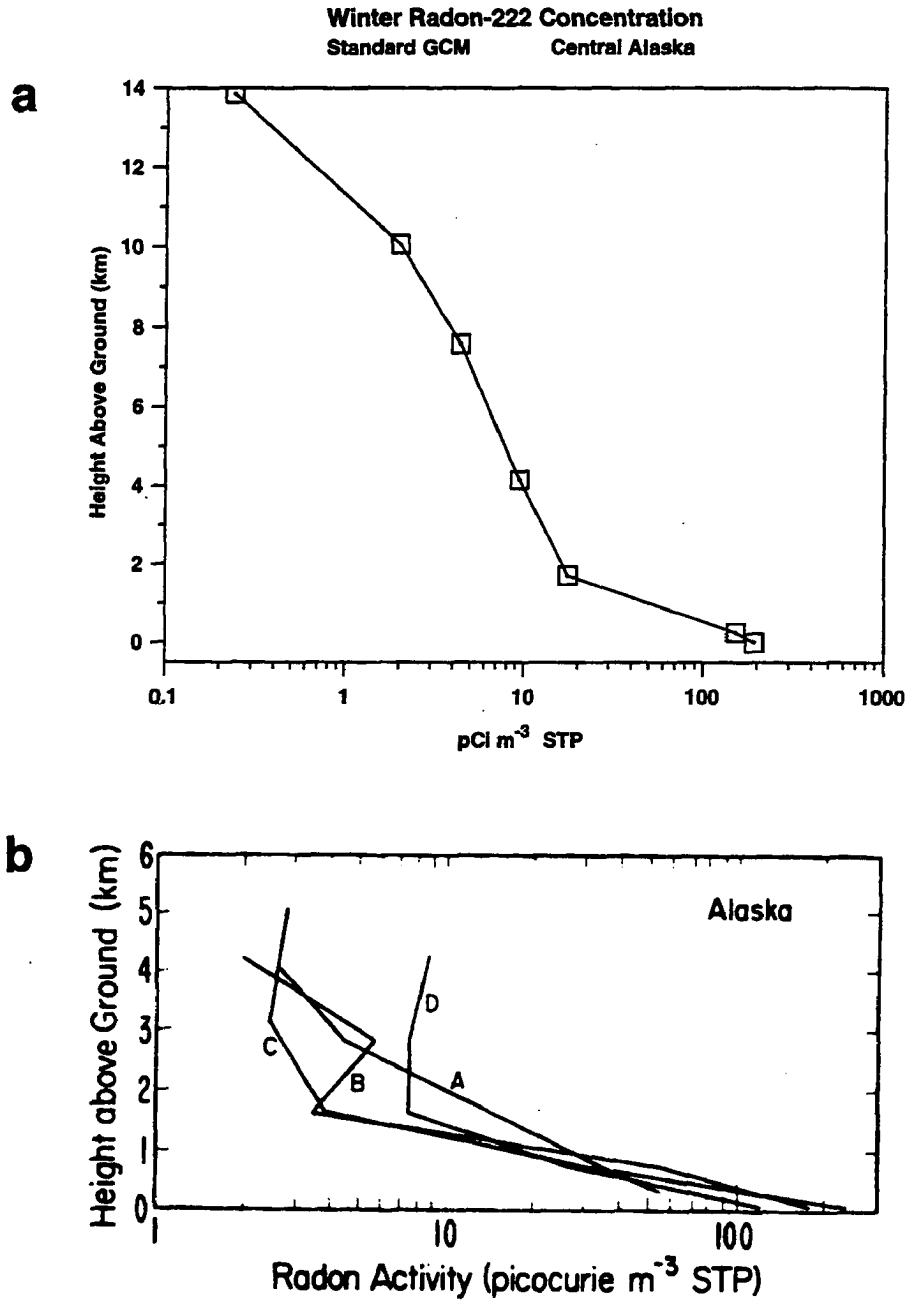

FIGURE 5.15: Vertical profiles of wintertime ^{222}Rn concentration over central Alaska (a) as simulated by the standard GCM and (b) as measured by Larson (1974, presented by Liu *et al.*, 1984).

the final three Februaries of the standard experiment. Fig. 5.15b shows the measured profiles presented by Liu *et al.* (1984) for comparison. Because the GCM data comprise just three numbers for each data point, I have not computed standard deviations of these means.

As expected, the vertical gradient in concentration is steeper in the wintertime case than in summer, for both the simulation and the observations. The simulated concentrations do not decrease quite as rapidly as the observed ones in the lower troposphere, and no observational data are available above 5 km. It is not clear how representative these data are, however, so robust conclusions about the wintertime vertical mixing in the CSU GCM are impossible from this comparison. HK89 also noted that the GISS model predicted slightly weaker vertical gradients in ^{222}Rn in winter than presented by Liu *et al.* (1984).

5.5 Summary

The climate as simulated by the CSU GCM successfully reproduces that of the Earth in many respects, but has a number of significant deficiencies. From the point of view of the tracer calculation in the present study these are of most concern in the LOWRES experiment. Serious deviations from the expected circulation are:

- The Hadley cell in the LOWRES model is much weaker than calculated from the ECMWF data. This was expected to lead to insufficient meridional mixing of the tracers from the north to south, but in fact the LOWRES experiment was characterized by very rapid interhemispheric tracer exchange (section 6.1).
- The midlatitude westerly winds in the LOWRES model are much too weak, especially in the southern hemisphere. This problem is much less serious in the northern hemisphere in the standard model.
- Rainfall over India associated with the summer monsoon is weaker than observed, especially in the standard model. This is not a problem for the tracer calculation *per se*, but could lead to anomalous behavior by SiB2 due to unrealistic drought stress, which could have repercussions for the calculation of the surface CO_2 flux. The Tibetan plateau is much too cold and wet in July in the LOWRES model (because of deep snow!).

On the other hand, the results of the tracer simulations of ^{85}Kr and ^{222}Rn are very satisfying, and suggest that at least the standard model does an acceptable job of distributing trace gases for which we have a good idea of the real distribution. Because of the aforementioned problems with the circulation in the LOWRES model, I will focus primarily on the results of the standard model in my analysis of the CO_2 tracers in Chapters 6 and 7.

CHAPTER 6

Annual Mean Tracer Distributions and the Global Carbon Budget

This chapter discusses the spatial distributions of the simulated tracers in the annual mean. Annual mean differences in mass-weighted mean concentration between the northern and southern hemisphere are the broadest measure of the effect of atmospheric tracer transport given the distribution of surface fluxes prescribed as a boundary condition. The interhemispheric gradient in concentration is determined by the rate of interhemispheric mixing, which is expressed in terms of the interhemispheric exchange time τ, as discussed in section 2.4.3 and briefly considered in section 5.3. This parameter is important because meridional mixing largely determines the gradients in concentration of the tracers that are used to calculate the global carbon budget by fitting simulated to observed concentrations at the NOAA flask stations. In section 6.1, the evolution of the interhemispheric gradient during the experiments is considered. This analysis provides important insights into the processes involved in meridional mixing and interhemispheric exchange of the tracers.

As noted in previous studies (Fung *et al.*, 1983; Heimann *et al.*, 1986; Heimann and keeling, 1989; TFT90), tracers with purely seasonal surface fluxes (*e.g.* tracer T_9 in this study) show spatial gradients in annual mean concentration due to seasonal correlations between surface fluxes and the atmospheric circulation. Conversely, tracers with steady surface fluxes (e.g. tracer T_1 in this study) can show pronounced seasonality in concentration due to seasonal fluctuations of the winds. The annual mean spatial distribution of each tracer is examined in section 6.2, both at the Earth's surface, and in terms of its vertical and meridional structure in the free troposphere.

The seasonal cycle of photosynthesis and respiration in the northern hemisphere dominates the variability of global CO_2 concentrations (see Fig. 1.3 in Chapter 1 and the discussion in Chapter 4). Some of the most significant elements (*e.g.* fossil fuel emissions) of the global carbon budget have very little seasonal variation, however. In attempting to

deduce the strengths of the various sources and sinks by fitting the simulated tracer concentrations in this study to the observed variations of atmospheric CO_2, it is important to keep the "signal to noise ratio" as high as possible. Fitting the monthly concentration time series at each station would result in a fit dominated by the seasonal "breathing" of the terrestrial biosphere, so the calculation is done instead in terms of the annual mean concentration at each station. This approach has also been used by Keeling *et al.* (1989a) and TFT90. The global carbon budget is analyzed in section 6.3.

6.1 Interhemispheric Exchange of the Tracers

After initializing the tracer calculation with globally uniform concentrations of each tracer in the LOWRES experiment, the difference in concentration between the northern and southern hemispheres grew rapidly, and equilibrium became established after several years (Fig. 6.1). As expected (Plumb and McConalogue, 1988), tracers with emissions concentrated far from the equator (T_3, T_4, T_8, and T_{16}) develop a steeper gradient than those of with sources of equal magnitude concentrated in the tropics (*e.g.* T_2 and T_6). The seasonal cycle is prominent in the plots shown here. The only tracer whose surface fluxes can experience any interannual variability is T_{18}, the SiB2 terrestrial CO_2 flux. Interannual variability in the interhemispheric concentration difference in other tracers is due to interannual variability in the model circulation.

At the end of the tenth year, the tracer concentration fields were passed from the LOWRES model to the standard GCM, which was then integrated for another four years. This transition is easy to see in Fig. 6.1 as a jump in the "equilibrium" interhemispheric gradient of many of the tracers. The changes in gradient are not uniform across the different tracers; those with purely seasonal fluxes (T_9, T_{15}, and T_{18}) barely show any effect for example, and the tracers with tropical sources (T_2 and T_6) respond mainly by showing less high-frequency "noise." Most important for the carbon budget calculation is that the gradients tend to be *stronger* in the standard than in the LOWRES experiment. This is surprising, because the interhemispheric exchange of mass is actually much *weaker* in the LOWRES model, as discussed in section 5.3 (see Fig. 5.7).

Interhemispheric exchange times for ^{85}Kr and fossil fuel CO_2 (tracer T_1) were calculated for years 6 – 10 of the LOWRES experiment and for years 2 – 4 of the standard experiment, using the definition derived in section 2.4.3. For comparison with earlier estimates of this parameter, the values are presented in Table 6.1 along with the others

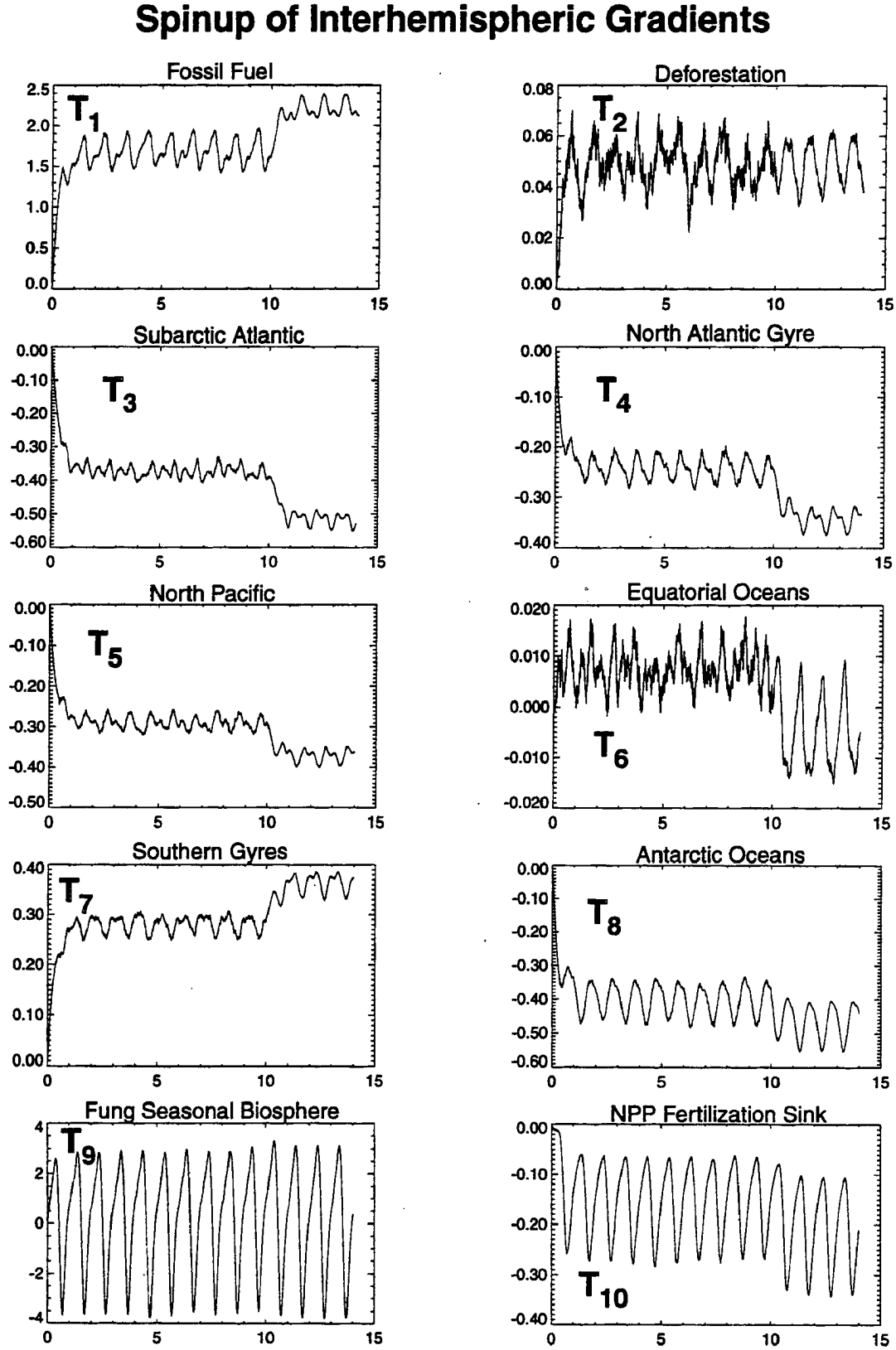

FIGURE 6.1: Interhemispheric concentration difference (Northern Hemisphere mean minus Northern Hemisphere mean) in parts per million, *vs.* elapsed time in years.

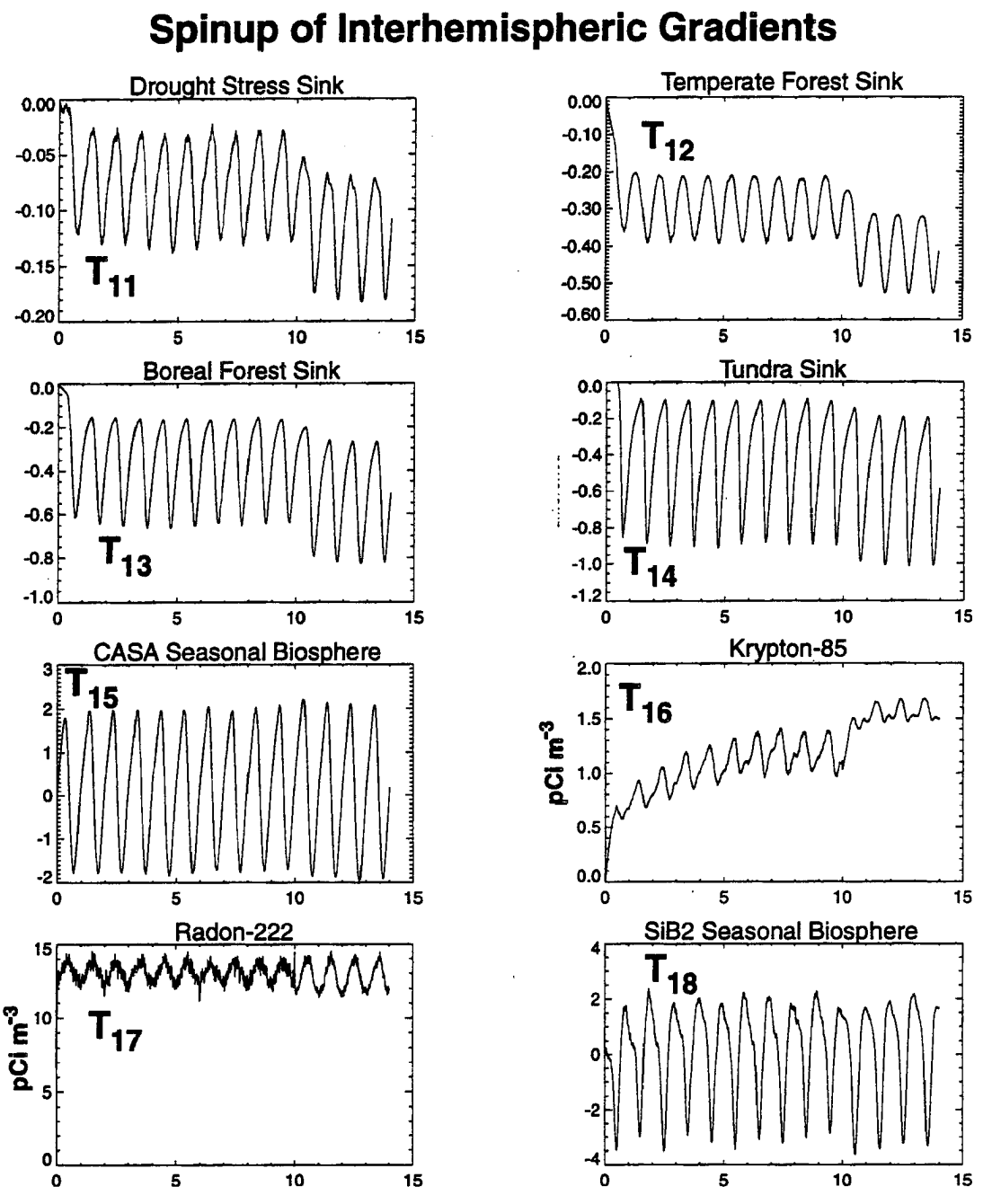

FIGURE 6.1 (cont'd): Interhemispheric concentration difference (Northern Hemisphere mean minus Northern Hemisphere mean) in parts per million, *vs.* elapsed time in years.

discussed in Chapter 2. For the LOWRES experiment, $\tau < 0.7$ yr for both tracers, which is much shorter than previous estimates using the same definition of the exchange time. As discussed in Chapter 5, the exchange time for the standard model is close to that derived by others, but is a bit shorter than most. Why should the LOWRES model give such a short exchange time, considering that the mean meridional circulation is so much weaker than it is in the standard model?

Table 6.1: Interhemispheric Exchange Times

Tracer Species	Study	Definition	τ (years)
CO_2	This study (LOWRES)	$\frac{2\Delta q}{S_N - S_S}$	0.62
	This study (standard model)	$\frac{2\Delta q}{S_N - S_S}$	0.82
	Czeplak and Junge (1974)	$\frac{\Delta q}{dq/dt}$	0.9
	Heimann *et al.* (1986)	$\frac{2\Delta q}{S_N - S_S}$	1.87
	TFT90	$\frac{2\Delta q}{S_N - S_S}$	1.0
^{85}Kr	This study (LOWRES)	$\frac{2\Delta q}{S_N - S_S}$	0.67
	This study (standard model)	$\frac{2\Delta q}{S_N - S_S}$	0.89
	Czeplak and Junge (1974)	$\frac{2\Delta q}{S_N + k\Delta q}$	1.8
	Weiss *et al.* (1983)	$\frac{ln\,(q_N/q_S)}{k + 2.5\%}$	1.0, 1.7
	Jacob *et al.* (1987)	$\frac{\Delta q}{F_{N \to S}}$	1.1
	Heimann and Keeling (1989)	$\frac{M_N - M_S}{F_{N \to S}}$	1.3
CFC-11, CFC-12	Prather *et al.* (1987)	$\frac{M_N - M_S}{F_{N \to S}}$	.74, .68
General	Plumb and McConalogue (1988)	$\Delta q / S_N$	.73

The answer lies in the fact that the *vertical* gradient of tracer concentration is steeper in the LOWRES experiment than in the standard run (Fig. 6.2). In the annual mean, the

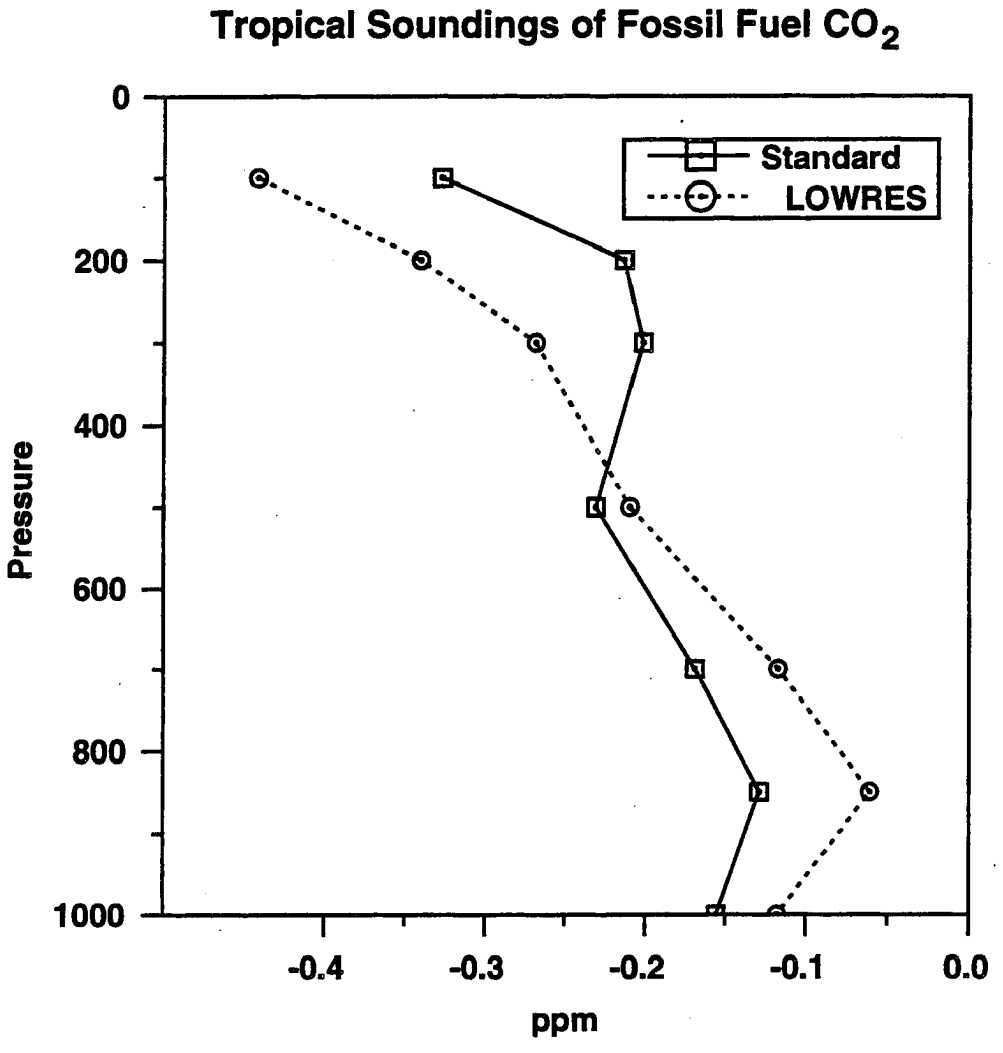

FIGURE 6.2: Vertical profile of simulated annual mean concentration of fossil fuel CO_2 in the tropics (20° S to 20° N latitude) in both the LOWRES and standard experiments. The global mean concentration was subtracted from each value before averaging.

mean concentration of tracer T_1 in the tropics in the LOWRES model decreases nearly twice as fast from the surface to the top of the model as it does in the standard experiment. This means that although the Hadley cell is much stronger in the standard run, the concentration of CO_2 in the upper and lower branches are more nearly equal, so the net flux of tracer across the equator is slower than in the LOWRES experiment.

The reason for the stronger vertical gradient in the LOWRES run is apparent from Fig. 6.4, which compares the zonal mean detrainment rate from cumulus convection in

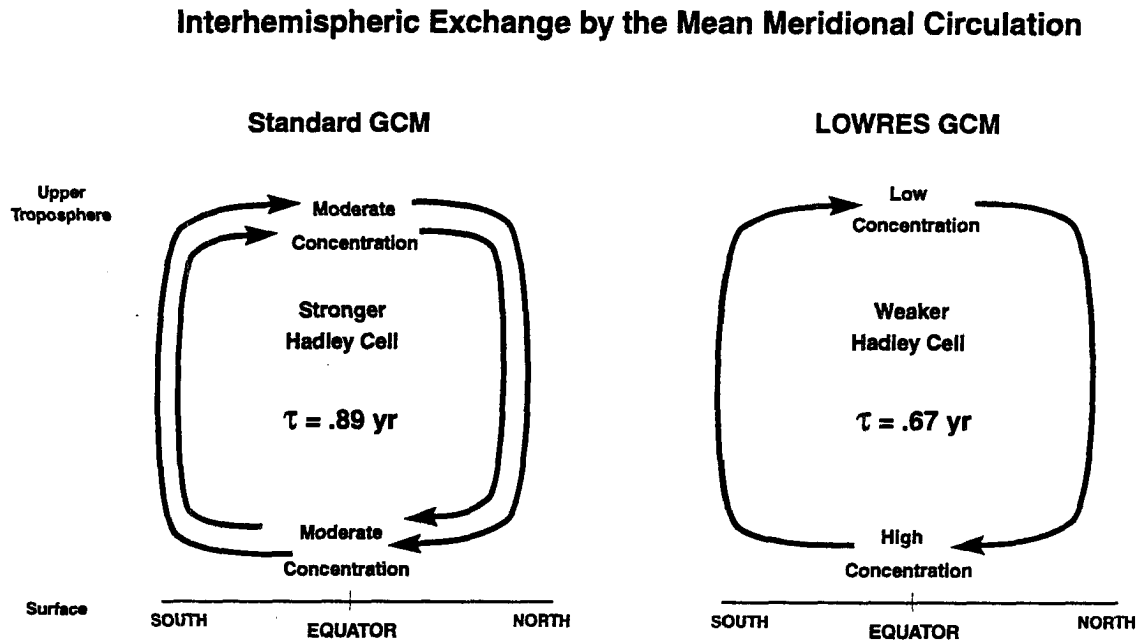

FIGURE 6.3: Schematic of the reason why a stronger mean meridional circulation in the tropics can lead to weaker interhemispheric mixing of a tracer. The weaker vertical tracer concentration gradient in the standard experiment produces an interhemispheric exchange time that is significantly longer than in the LOWRES

the two experiments. The detrainment mass flux in the standard run is nearly twice as intense as it is in the LOWRES experiment, resulting in the homogenization of tracers in the vertical in the tropics. The reasons for the weak convective activity in the LOWRES experiment are unknown, but probably result from the general "dilution" of large scale inhomogeneities in moist static energy at the coarse resolution of the LOWRES grid.

The inhibitory effect of vertical mixing by cumulus convection on the interhemispheric exchange of tracers was confirmed by the NOCUTRAN experiment. Recall that the tracer simulated in this sensitivity test was identical to the LOWRES tracer T_1 (driven by the same fossil fuel emission data, and using the same atmospheric circulation), but with tracer transport by cumulus convection disabled. Cumulus convection and EAULIQ still operated in the same way as in the LOWRES run, but had no effect on the tracer concentration. The interhemispheric mixing time determined from this experiment was only 0.56 yr – even shorter than the 0.62 value obtained for the LOWRES run.

The use of the interhemispheric exchange time τ implies a conceptual model of the atmosphere as a pair of boxes, with mixing across the interface between them much slower than mixing within the boxes. To investigate the realism of this conceptual model, the 2BOX experiment simulated a tracer with no source or sinks at all that was initially con-

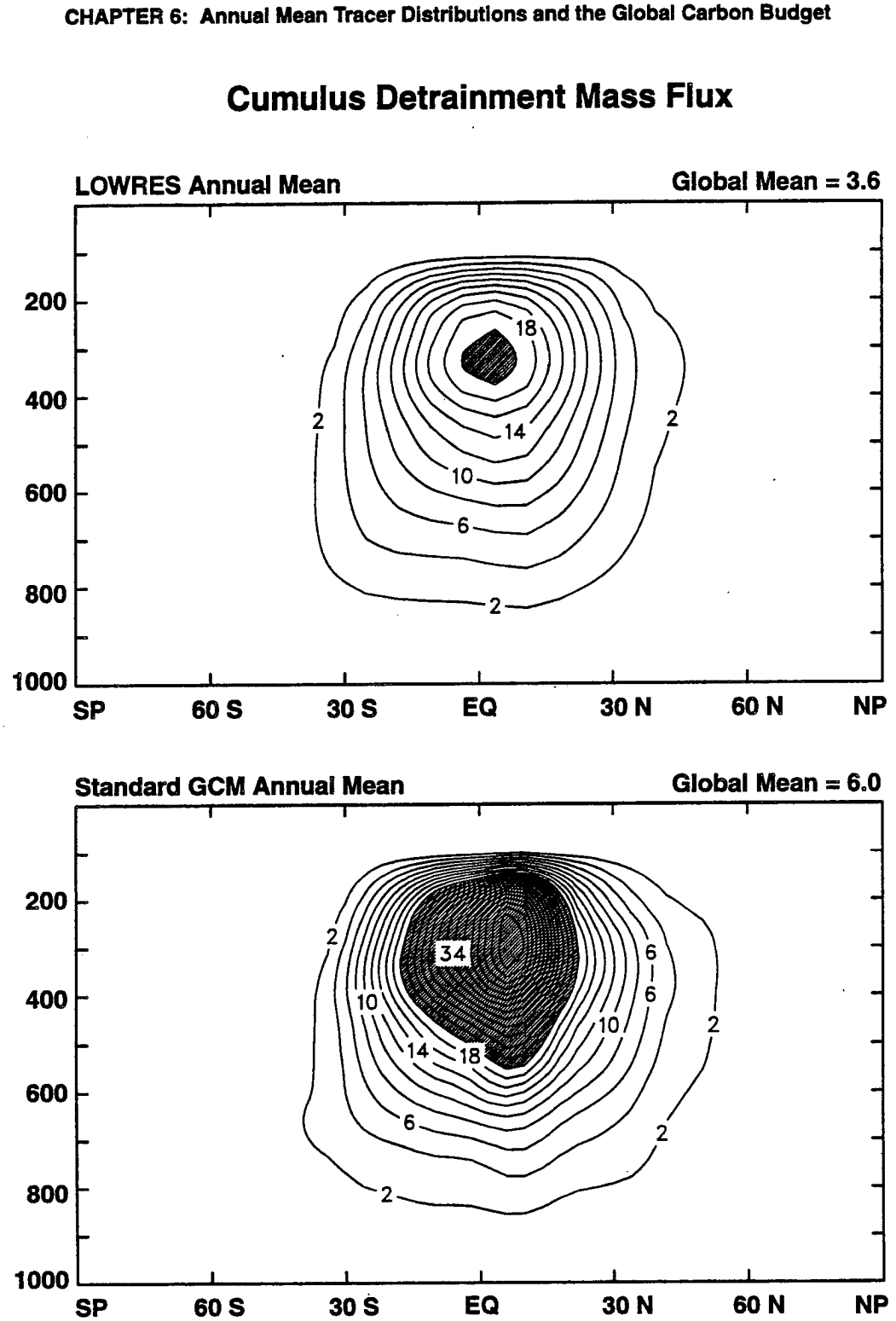

FIGURE 6.4: Latitude-pressure cross sections of the zonal mean cumulus detrainment mass flux (month^{-1}), as simulated in the LOWRES experiment (upper panel) and the standard GCM (lower panel). Contour interval in both plots is 2 month^{-1}. Values over 20 month^{-1} are shaded. The ordinate in both panels is pressure in mb, and the abscissae are latitude.

fined to the northern hemisphere and allowed to mix freely into the southern hemisphere with time. As shown by Plumb and McConalogue (1988), τ as defined in section 2.4.3 is a function of the source distribution of a tracer; the mixing time deduced from the 2BOX experiment is truer to the concept of a simple mixing model. In the 2BOX experiment, the *e*-folding time of the interhemispheric concentration difference is only 0.21 yr (Fig.

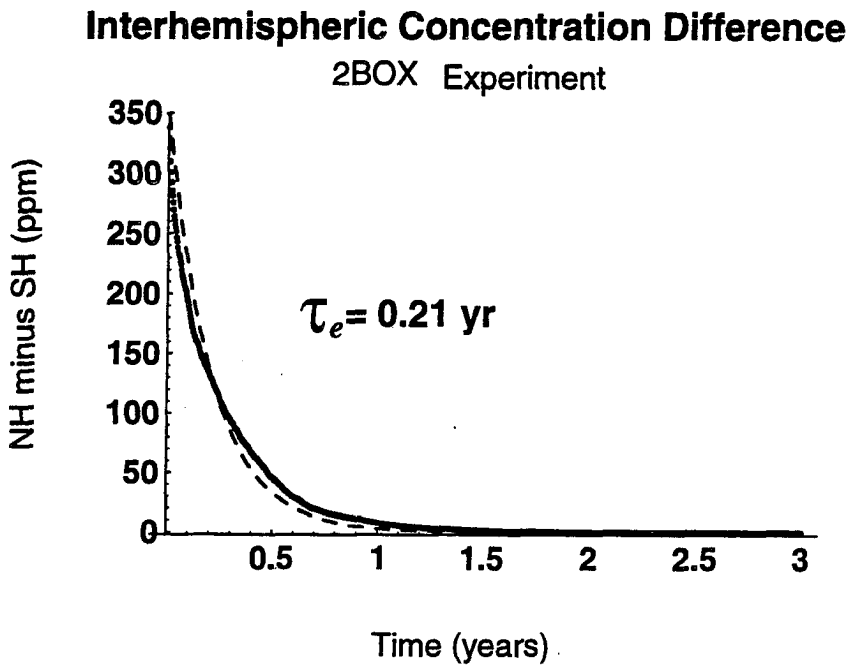

FIGURE 6.5: Time series of the difference in mass-weighted mean concentration between the northern and southern hemispheres in the HEMIS experiment. The tracer has no sources or sinks. The solid curve shows actual daily values of the simulated tracer, and the dashed curve is an exponential fit from which τ_e is derived.

6.5). Recall from section 2.4.3 that τ is supposed to represent *twice* the *e*-folding time of mean interhemispheric concentration difference of a tracer after the surface fluxes are "shut off" as they have been here (although the definition of t used above is meaningless in the case of no sources or sinks). Using $\tau = 2\tau_e$, the interhemispheric exchange time for the 2BOX experiment is significantly shorter than calculated for any other experiment performed in this study. This difference highlights the dependence of τ on the tracer being simulated and calls into some question the applicability of the two-box concept of interhemispheric mixing.

6.2 Annual Mean Concentration Fields

The concentrations of the tracers are simulated by the model throughout the depth of the troposphere, but since nearly all the observational data are available only for the surface of the Earth, maps of the simulated concentration are only shown below (section 6.2.1) for the planetary boundary layer (PBL). Above the PBL, the concentration field becomes more zonal as mixing by stronger winds dilutes regional gradients imposed by surface fluxes below. Thus the vertical structure is fairly well captured by latitude-pressure cross sections of the zonal mean concentrations, which are shown in section 6.2.2.

All of the data presented in this section are multiyear annual means calculated from monthly means of years 2 through 4 of the standard experiment. To avoid weighting the concentration data toward the later years in the presence of secular trends, the concentration at the South Pole in January was subtracted from each monthly concentration field of a given year. After the multiyear means were calculated, the multiyear mean at the South Pole was subtracted from the overall average field as well, so that all the data here a relative to the surface concentration at the South Pole. Dark shading is always used to indicate high concentrations, and light shading to indicate low concentrations. Specific thresholds used to define the shaded regions vary from plot to plot, as does the contour interval; these parameters are indicated in the caption of each figure.

6.2.1 PBL Maps

6.2.1.1 Anthropogenic Tracers

The concentrations of the two tracers representing the response to anthropogenic emissions (T_1 and T_2) have very different geographic patterns in the annual mean (Fig. 6.6). The global emissions from fossil fuel combustion (T_1) are prescribed to be 6 times as great as those from tropical deforestation (T_2), but the global mean difference from the South Pole concentration is nearly 16 times as high. This is because the deforestation source is located in the tropics, straddling the Equator and so is able to penetrate much more easily to high southern latitudes than the fossil fuel tracer. The pole-to-pole difference in concentration of T_1 is more than 5 ppm, but there is almost no difference between Arctic and Antarctic concentrations of T_2 because of its ability to penetrate equally into both hemispheres.

PBL Concentration (ppm)

Anthropogenic Emission Tracers

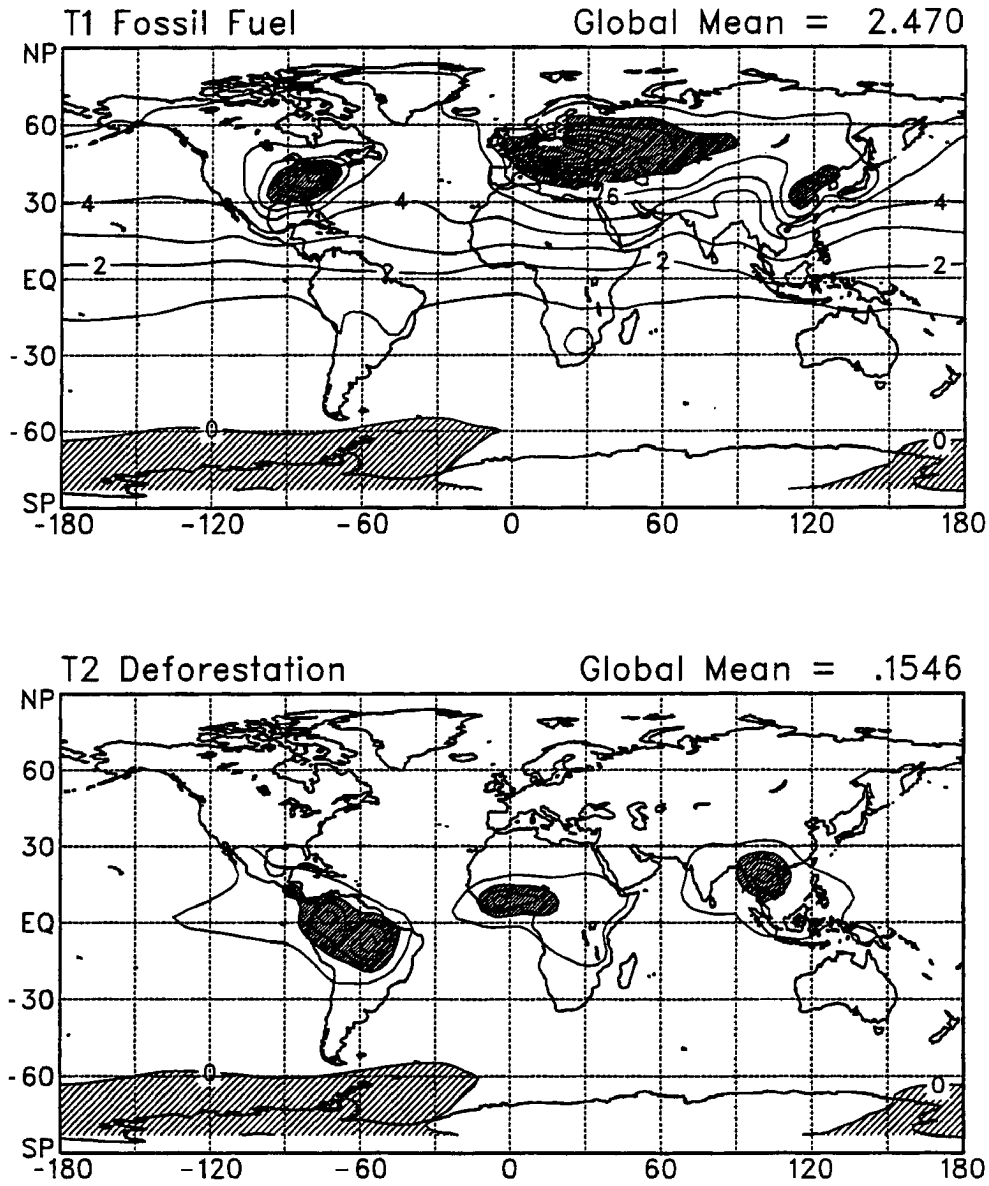

FIGURE 6.6: Annual mean concentration of the anthropogenic tracers T_1 and T_2 (ppm difference from the South Pole).

Contour interval is 1.0 ppm for T_1 and 0.25 for T_2.

Dark shading indicates values above 7.0 ppm for T_1 and 0.5 ppm for T_2.

Light shading indicates values below 0.0 ppm fin both panels.

Both tracers show regional "hot spots" of high concentration near their sources, but these are much more intense in the case of fossil fuel emissions than for tropical deforestation. Maximum concentrations of T_1 in western Europe are over 14 ppm, but T_1 never reaches more than about 1.25 ppm in the annual mean. This is likely due to the fact that fossil fuel is burned in regions that are subject to very stable air masses during at least part of the year, whereas tropical deforestation occurs in a region dominated by a deep turbulent PBL and deep cumulus convection which mixes the tracer vertically into the higher levels where long-range transport by strong winds is more likely.

Some downwind transport of T_2 in the trade wind zone is evident, but outside the tropics the concentration field is nearly flat. By contrast, the concentration field of T_1 outside the source regions shows a distinct meridional gradient that is concentrated in the tropics because of relatively sluggish interhemispheric transport as discussed in section 6.1 above. The PBL concentration field of T_1 is notably flat in the southern hemisphere.

6.2.1.2 Ocean tracers

The concentration fields of the regional ocean tracers ($T_3 - T_8$, see Fig. 6.7) exhibit some of the same features discussed above for the anthropogenic tracers. Total annual surface fluxes for all six regions are the same (1 Gt C yr^{-1}), with the Equatorial and Antarctic regions acting as sources and the other four regions acting as sinks. The global mean concentration difference from the South Pole increases with latitude (both north and south) because of the barrier posed by deep tropical convection. Each tracer has a maximum (or minimum, according to the sign of its surface fluxes) in its source region, with nearly zonal isopleths outside this region. The meridional gradients of all six tracers are concentrated in the tropics, and are relatively flat in the opposite hemisphere from the source area.

Note that the concentration field of tracer T_8 (due to a 1 Gt C yr^{-1} source in the Antarctic) is negative everywhere north of about 45° S, relative to the concentration at the South Pole. From the point of view of the meridional gradient at observing stations, this source is equivalent to a strong northern hemisphere sink. Also, note that the concentration field of tracer T_6 (due to a 1 Gt C yr^{-1} source in the Equatorial oceans) is very flat; the contours are chosen to exaggerate its gradients and show spatial patterns. Like the tropical deforestation tracer, this source has almost no influence on the meridional gradient because it is efficiently mixed upward and poleward from its source region.

PBL Concentration (ppm)

Regional Ocean Tracers

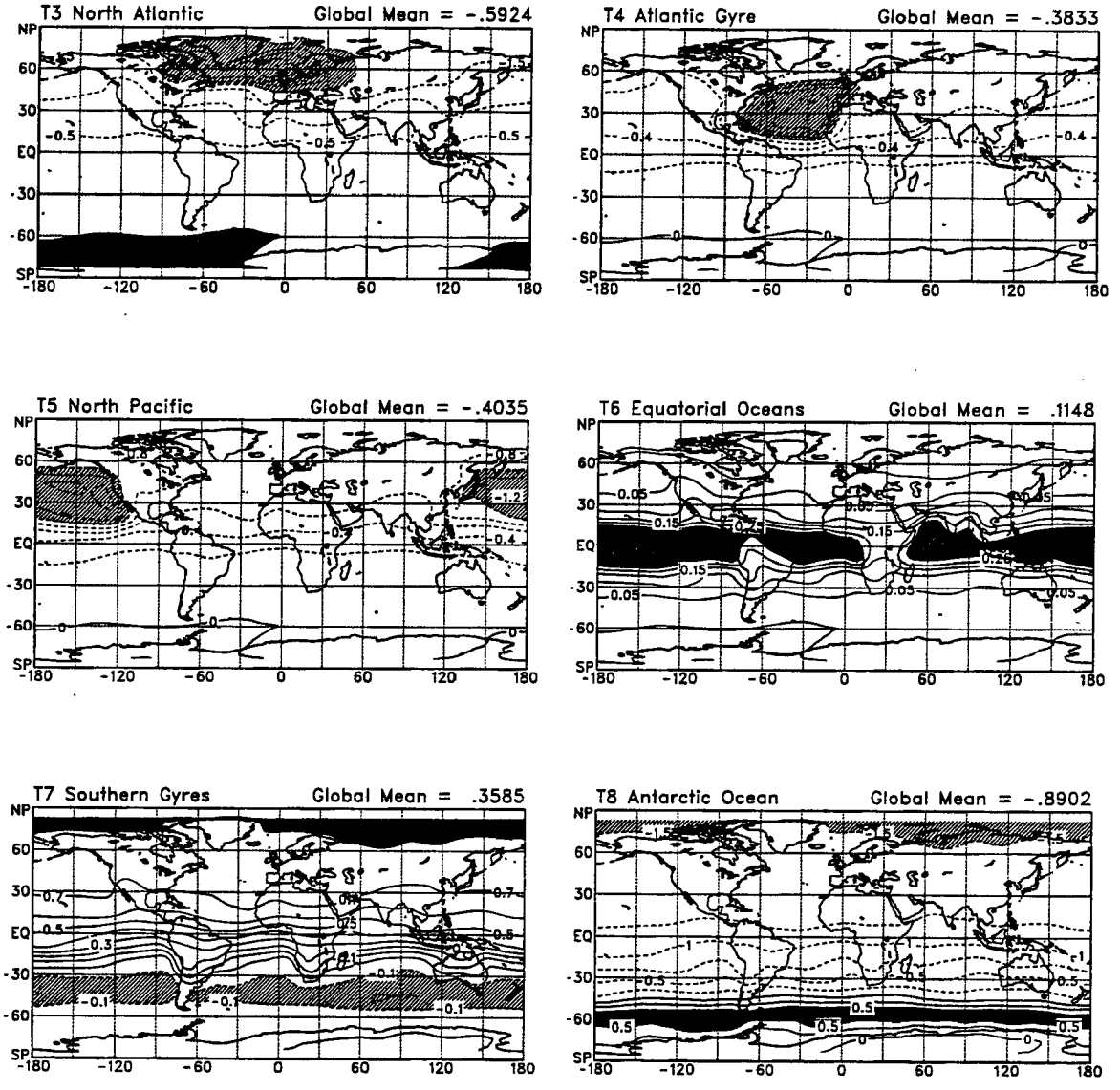

FIGURE 6.7: Annual mean concentration of the regional ocean tracers $T_3 - T_8$ (ppm difference from the South Pole).

Contour intervals in ppm for each tracer are as follows:
$T_3 = 0.5$, $T_4 = 0.2$, $T_5 = 0.2$, $T_6 = 0.05$, $T_7 = 0.1$, $T_8 = 0.25$.

Dark shading is used for values above the following thresholds in ppm:
$T_3 = 0$, $T_6 = 0.25$, $T_7 = 0.8$, $T_8 = 0.25$.

Light shading is used for values below the following thresholds in ppm:
$T_3 = -2$, $T_4 = -1.0$, $T_5 = -1.0$, $T_7 = -0.1$, $T_8 = -1.5$.

6.2.1.3 Net Terrestrial Sinks

The concentration fields due to the net terrestrial sinks (tracers $T_{10} - T_{14}$, see Fig. 6.8) display the now-familiar pattern of concentration minima in the sink region, zonal isopleths elsewhere, a concentrated meridional gradient in the tropics, and a weak gradient in the opposite hemisphere noted above. As expected, the further north the sink area is located, the more intense its effect on the meridional gradient outside the source region.

The geographic distribution of tracer T_{10} (due to CO_2 fertilization proportional to annual NPP) is somewhat surprising. The sink of this tracer is strongest in the tropics, where NPP is highest (see Fig. 3.18 in section 3.4), yet the concentration is lowest in the boreal forests of Canada and Russia. This could be due to the larger areal extent over which the sink is active in the northern forests as compared to the tropics; air masses which spend a long time in contact with the surface sink will be depleted more than air masses which simply "pass through" the region quickly. More likely this is due to the more efficient convective mixing in the tropics as noted above for tracers with tropical sources. A further complication is that the intensity of these sinks varies seasonally according to monthly NDVI, so they are only active in the boreal region during the summer months when the PBL is deeper and more turbulent. Had they been constant throughout the year, steeper gradients would likely have resulted in the annual mean because of the long residence time of air parcels in the PBL during stable wintertime conditions.

The concentration field of tracer T_{11} (due to CO_2 fertilization proportional to both NPP and water stress) is the flattest of all these tracers. This is partly because some of the sink is located in the southern hemisphere (so the tracer reaches the south pole more easily than the others), and partly because a significant part of the sink is active in the tropics where convective mixing destroys the surface gradients. The sink strength is particularly strong in southern Asia, which is probably due to the fact that the GCM underpredicts the monsoon rainfall over India in July. This leads to significant water stress as predicted by SiB2, which was used to define the sink strength of this tracer. This feature is probably not very realistic, since drought stress in an "average" year in that region is probably not significant.

6.2.1.4 Seasonal Terrestrial Biosphere

Finally, in the concentration fields of the tracers representing seasonal exchange of CO_2 with the terrestrial biosphere (T_9, T_{15}, and T_{18}, see Fig. 6.9), we see geographic pat-

PBL Concentration (ppm)

Net Terrestrial Sinks

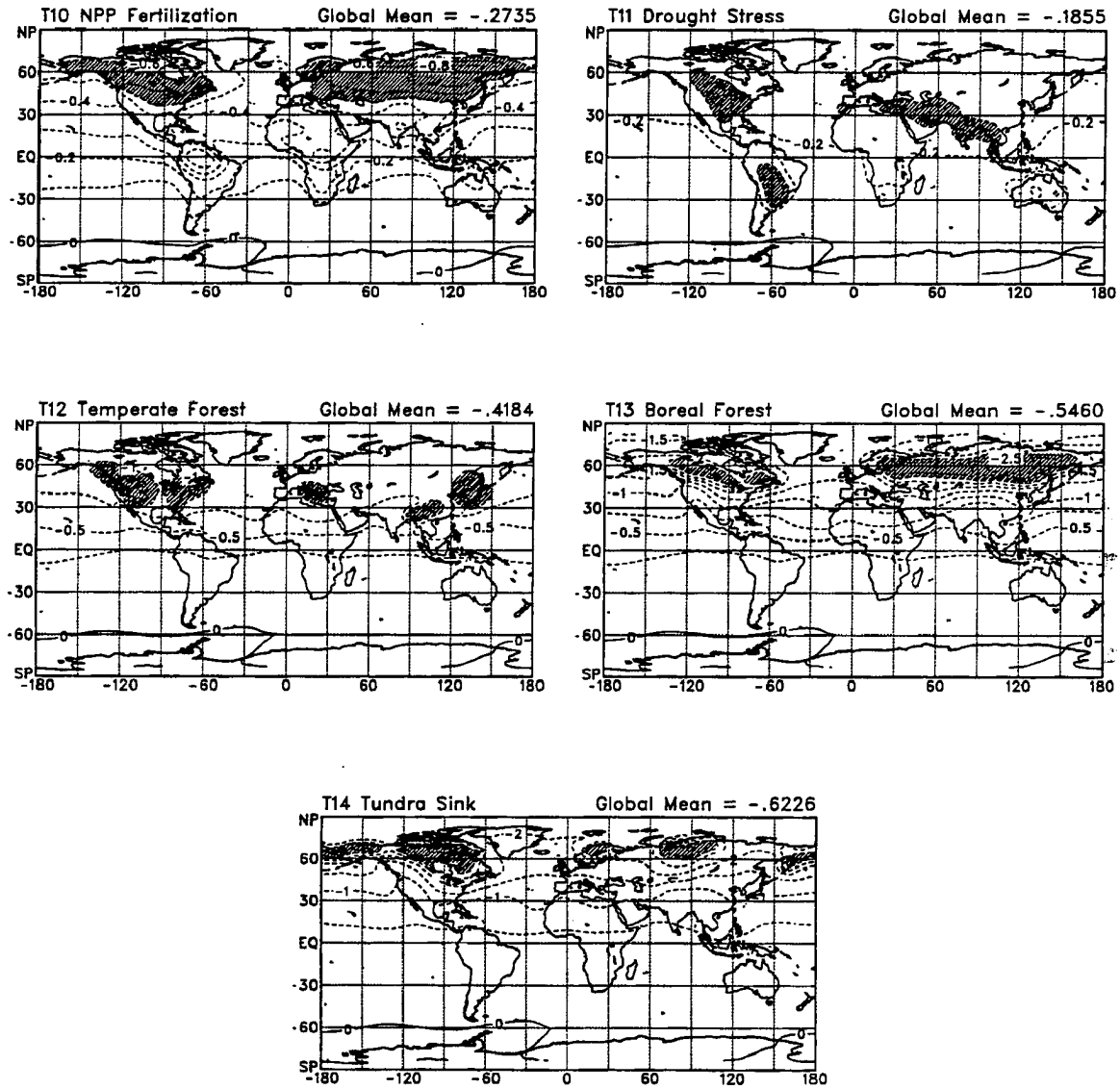

FIGURE 6.8: Annual mean concentration of the net terrestrial sink tracers $T_{10} - T_{14}$ (ppm difference from the South Pole).

Contour intervals in ppm for each tracer are as follows:
$T_{10} = 0.1$, $T_{11} = 0.2$, $T_{12} = 0.25$, $T_{13} = 0.25$, $T_{14} = 0.5$.

Light shading is used for values below the following thresholds in ppm:
$T_{10} = -0.6$, $T_{11} = -0.4$, $T_{12} = -1.0$, $T_{13} = -2.0$, $T_{14} = -3.0$.

PBL Concentration (ppm)

Seasonal Terrestrial Biosphere

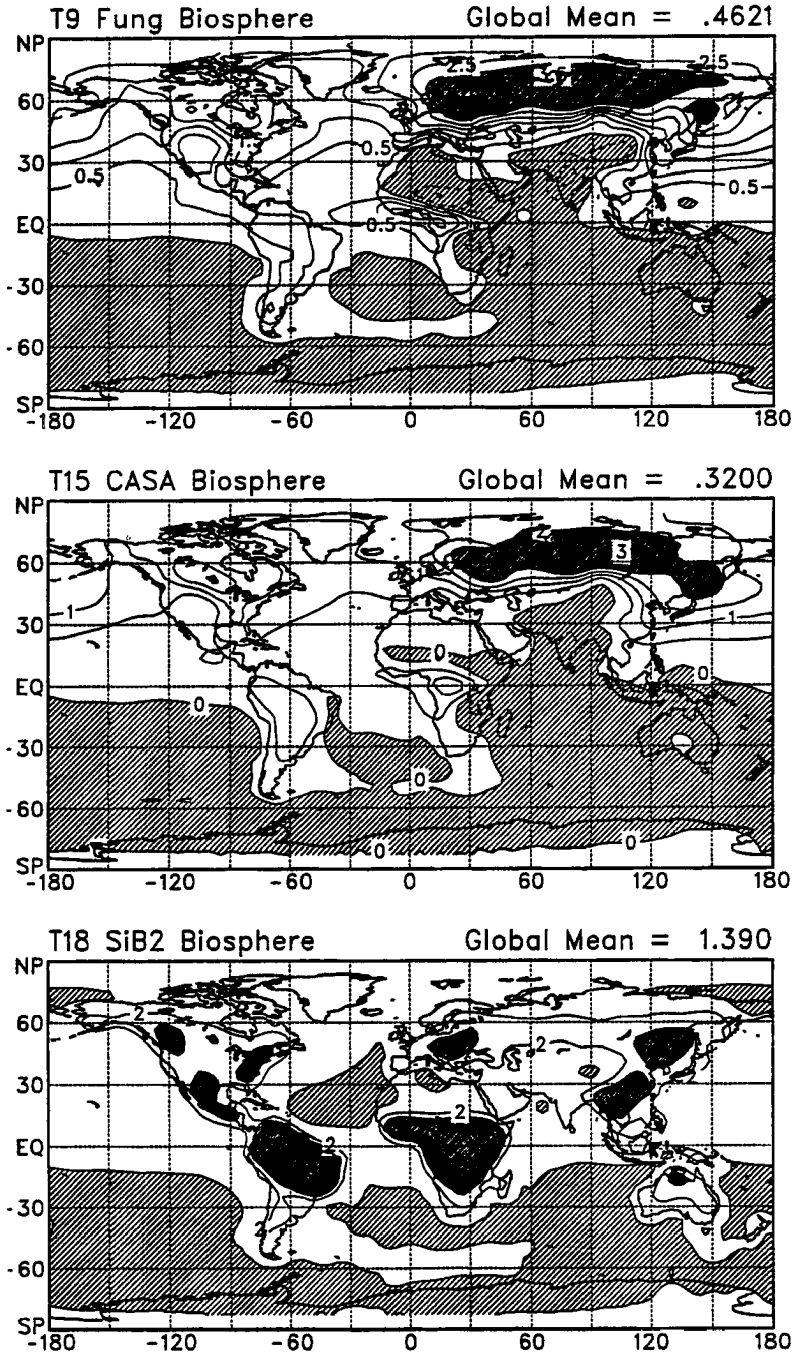

FIGURE 6.9: Annual mean concentration of the tracers which represent the exchange with the seasonal terrestrial biosphere (ppm difference from the South Pole).

Contour intervals for T_9 and T_{15} are 0.5 ppm, and for T_{18} is 2.0 ppm.

Dark shading indicates values above 3 ppm for T_9, 2 ppm for T_{15}, and 4 ppm for T_{18}.

Light shading indicates values below 0.0 in all three panels.

terns that are very different from the ones considered above. Recall that the fluxes of tracers T_9 (prescribed according to Fung *et al.*, 1987 and TFT90) and T_{15} (using the CASA model of Potter *et al.*, 1993) are exactly zero at all grid points in the annual mean by definition, reflecting an annual balance between NPP and soil respiration at the grid cell scale. The annual total of soil respiration in SiB2 is constrained to equal last year's NPP and so should be close to zero as well, but was impossible to predict *a priori*.

The global annual fluxes of tracer T_{18}, representing the seasonal exchange due to SiB2, varied from year to year as the model adjusted (Fig. 6.10). The soil moisture field

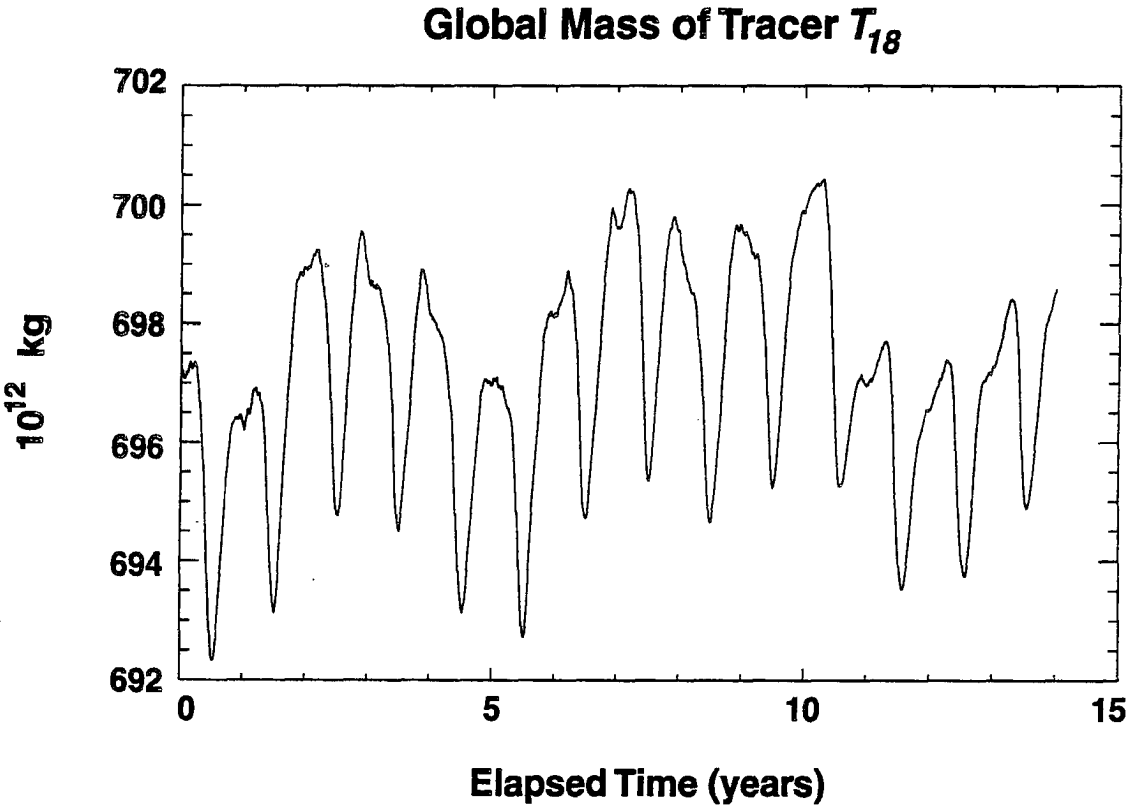

FIGURE 6.10: Time series of the global mass of tracer T_{18} representing the exchange of CO_2 between the atmosphere and terrestrial biosphere as simulated by SiB2. The first 10 years are from the LOWRES experiment, and the final four years are from the standard experiment. Annual means considered in the this chapter refer only to the final three years of the standard experiment.

in SiB2 required several years to reach equilibrium with the climate of the GCM because of the new cloud microphysics parameterization (EAULIQ) imposed at the start-up of the LOWRES experiment (see section 3.5), and the CO_2 fluxes due to SiB2 reflect these changes. After about five years, the flux became steady, but then showed a significant

fluctuation again at the beginning of the standard experiment. The soil moisture required less "spin-up" time in this experiment because the initial condition was specified from the end of another two year run with EAULIQ and SiB2. For the final three years of the standard experiment, the CO_2 flux due to SiB2 was relatively stable, and amounted to a net source of about 0.2 Gt C yr^{-1}. Most of the net flux in the annual mean of tracer T_{18} was concentrated at a few grid points where significant interannual variability in NPP resulted in a mismatch between uptake and release of CO_2 by the biosphere (Fig. 6.11).

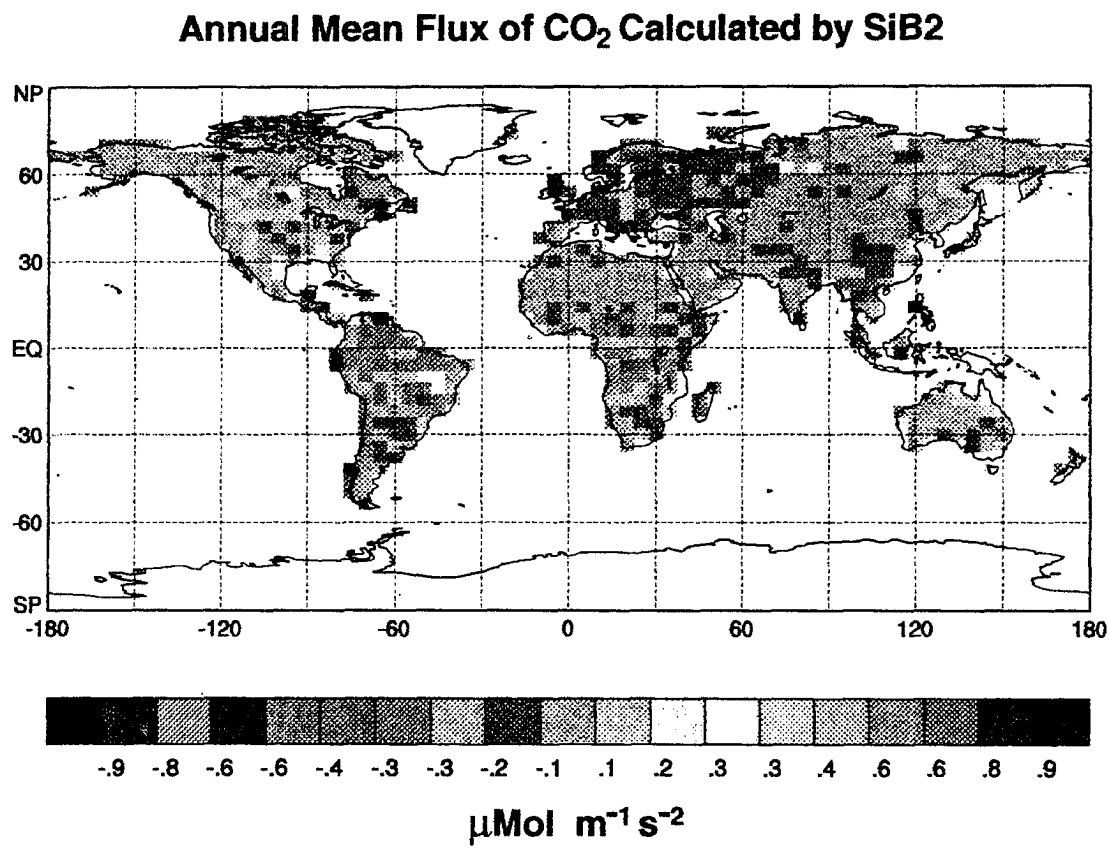

FIGURE 6.11: Gridded values of the annual mean net flux of CO_2 to the atmosphere as calculated by SiB2 for tracer T_{18} in years 2 – 4 of the standard experiment. The color scheme is centered on zero net flux.

All three tracers exhibit significant meridional concentration gradients in the annual mean due to correlations between the seasonal fluxes and the atmospheric circulation although their annual fluxes are zero or nearly so at every grid point. At middle and high latitudes, photosynthesis dominates the net flux in the summer growing season when the PBL is deep and the atmosphere is more convective than it is during the "respiration" season in spring and fall. Thus the signal from photosynthetic drawdown of CO_2 is "mixed away" much more efficiently than the signal from soil respiration. All three tracers have

nearly flat concentration fields over the southern oceans; they are all slightly negative over most of the southern hemisphere relative to the South Pole.

Both the Fung tracer and the CASA tracer show strong maxima in concentration (Fig. 6.9) over the boreal forests of Europe and Asia (tracer T_9 has a maximum concentration just over 6 ppm in northern Europe whereas tracer T_{15} has a maximum concentration of about 3.5 ppm in Siberia). The concentration field of the SiB2 tracer (T_{18}) is dramatically different, however. Like the other two tracers it is positive over most of the northern continents, but over the tropical rainforest regions it is an order of magnitude more concentrated, with a maximum of over 20 ppm over Brazil. Why does tracer T_{18} behave so much differently than the other two seasonal biosphere tracers?

Of the 18 tracers simulated in this study, only tracer T_{18} has fluxes which are calculated on-line by the GCM. The fluxes due to SiB2 represent not only the *seasonal* oscillation between photosynthesis and respiration, but also the *diurnal* cycle in which photosynthesis is active during daylight but soil respiration continues through the night as well. The atmospheric transport of trace gases has strong diurnal components as well: surface heating by the sun drives PBL growth by turbulent entrainment during daylight hours, and cumulus convection (at least over land) shows a daytime maximum in most regions. Because photosynthetic drawdown of CO_2 is positively correlated with active PBL turbulence, it acts on a deeper layer of air than nighttime respiratory fluxes. Furthermore, the CO_2-depleted air in the daytime PBL is much more likely to be carried aloft by cumulus convection than is the CO_2-enriched air at night. This pattern is more realistic than the case for tracers T_9 and T_{15}, which go right on depleting the nighttime PBL of CO_2 as if the sun were shining 24 hours a day during the growing season. Similarly, in the fall when daily soil respiration exceeds daily NPP, CASA and the Fung *et al.* (1987) fluxes behave as if photosynthesis is completely absent whereas SiB2 continues to deplete CO_2 from the deep PBL in the daytime and enrich the more stable autumn PBL at night.

The diurnal cycle of photosynthesis and respiration in a variable-depth turbulent PBL is active throughout most of the year in the tropics, where seasonality in rainfall rather than temperature determines the "growing season." By contrast the winter months in the boreal forest exhibit almost no net flux of any of the three seasonally driven tracers. This year-long correlation between PBL structure, cumulus activity, and CO_2 flux may explain the very strong T_{18} concentration maxima in South America and Equatorial Africa. Diurnal and seasonal variability of tracer fluxes, concentrations, and transport is the subject

of Chapter 7. A detailed examination of the hypothesis advanced here is deferred until then.

Unfortunately, very few observational data on CO_2 concentrations are available with which to compare the simulated tracer distributions presented in Fig. 6.9. The annual means in this study represent measurements taken at each grid point once per hour, 24 hours a day, 365 days a year. The NOAA flask stations sample only the remote marine PBL, and care is taken to avoid significant local sources. The diurnal cycle has been well documented by intensive field sampling campaigns like the Amazon Boundary Layer Experiment (ABLE, Wofsy, *et al.*, 1988) and the First ISLSCP Field Experiment (FIFE, Sellers, *et al.*, 1992*a*), but never over very large spatial scales or throughout the year, so the realism of the annual mean fields in Fig. 6.9 is unknown. The effects of the diurnal correlations and the much stronger concentration maxima as simulated by SiB2 over the tropical rainforests are investigated in more detail in section Fig. 7.2.

6.2.2 L-P cross sections

The three-dimensional structure of the annual mean simulated tracer concentrations throughout the troposphere is examined in this section in terms of zonally averaged deviations from the surface concentration at the South Pole. In all the plots in this section, the horizontal axis is latitude, with the South Pole on the left and the North Pole on the right, and the vertical axis is pressure, with the Earth's surface at the bottom, and the top of the model at the top of the plot.

As seen in Fig. 6.12, the spatial distributions of the anthropogenic tracers T_1 (from fossil fuel combustion) and T_2 (from tropical deforestation) are very different from one another and serve as "archetypes" for most of the other tracers because of the transport processes that define them.

Fossil fuel emissions are concentrated in the middle latitudes of the northern hemisphere, which of course is where the highest concentrations are simulated. From the source region, tracer T_1 is transported both upward and southward, so that there is a strong concentration gradient in both directions toward about 45° N at the surface. The gradient is concentrated in the northern tropics (due to the barrier posed by tropical convection as discussed above), and near the tropopause because of the barrier to vertical mixing posed by the strong static stability there. Above the tropics, the vertical gradient is almost eliminated by deep cumulus convection, and convective detrainment is evident

Meridional Cross Sections

Anthropogenic Emission Tracers

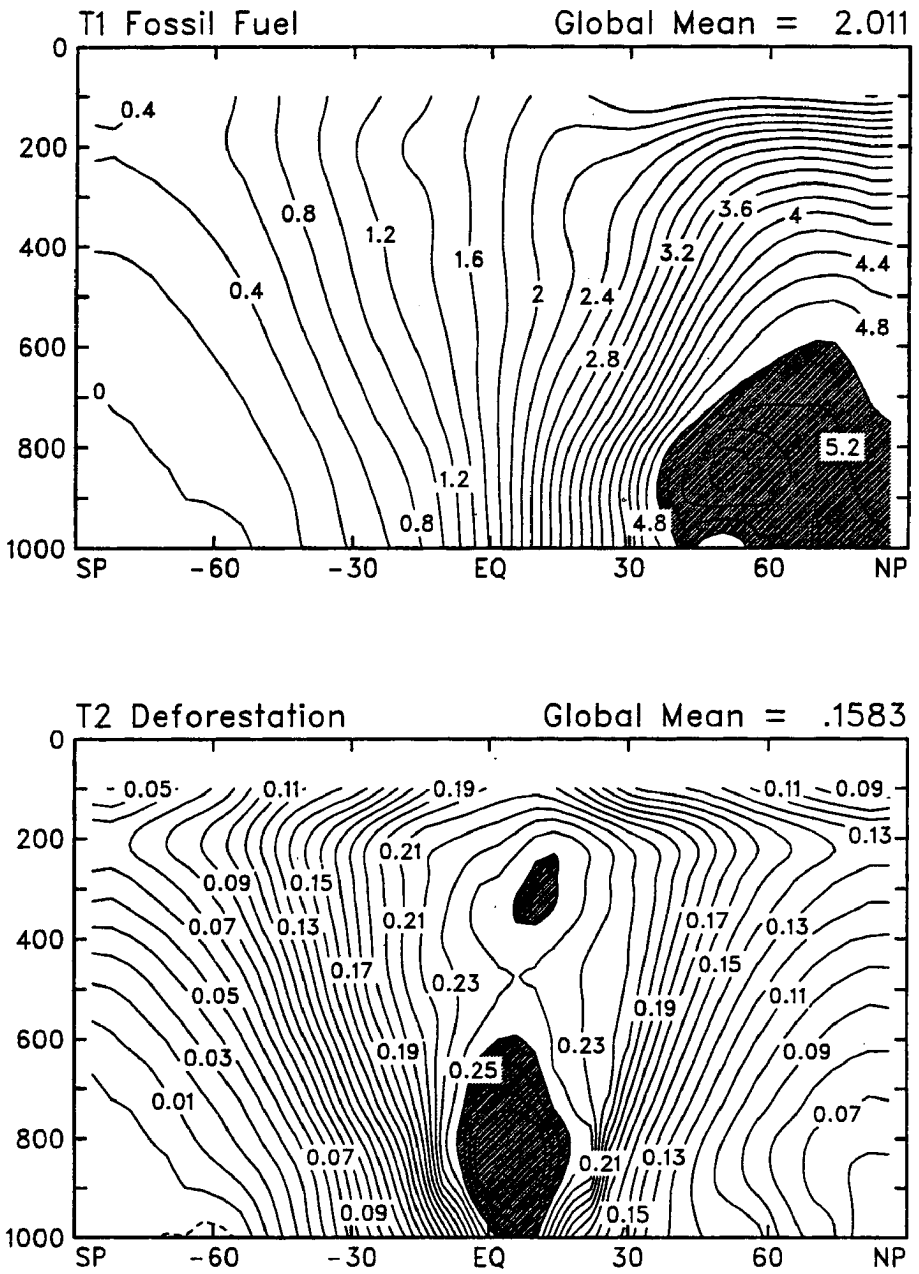

FIGURE 6.12: Annual mean concentration of the anthropogenic tracers T_1 and T_2 (ppm difference from the South Pole). Ordinates are latitude and abscissae are pressure.

Contour interval is 0.2 ppm for T_1 and 0.01 for T_2.

Dark shading indicates values above 5.0 ppm for T_1 and 0.25 ppm for T_2.

Light shading indicates values below 0.0 ppm fin both panels.

as a source of the tracer in the upper troposphere (near 200 mb) by the slight "bulge" in the isopleths there. The vertical gradient in the southern hemisphere is reversed in sign (concentration increases upward), because the primary source of tracer in the southern hemisphere is detrainment from deep tropical convection. Tracer transport in the southern hemisphere is downward and poleward, resulting in a weak meridional gradient. Because the South Pole is elevated (it is 2.8 km above sea level, with an annual mean surface pressure of less than 750 mb in the GCM), tracer concentrations are slightly higher there than they are on the Antarctic coast. This explains the anomalies in concentration at high southern latitudes seen in many of the maps in the previous section.

The concentration of T_2 is much more uniform than that of T_1, with a total range of less than 0.3 ppm throughout the troposphere. The source of this tracer is near the equator, and the highest concentrations are located below about 700 mb in the vicinity of the emissions. Vertical structure in the tropics is dominated by a midtropospheric minimum in concentration, with a secondary maximum located at the level of detrainment of deep convection (200 to 300 mb). This double maximum structure is not seen in similar plots made from two-dimensional tracer simulations (e.g., Plumb and McConalogue, 1988). It is due to the penetrative effects of deep cumulus convection, in which the tracer is transported directly from the PBL to the level at which the cloud detrains. Entrainment along the way diluted the surface tracer concentration with environmental air, but the in-cloud tracer concentrations have no influence on the environmental air below the level of neutral buoyancy.

The tropical upper troposphere is the primary source of tracer for the rest of the model, as can be seen by the reverse vertical gradient (concentration increases with height) in almost the entire troposphere and the way the isopleths bulge poleward near the tropopause. There is a hint of slow diffusion of tracer upward into the stratosphere, but as discussed in Chapter 5, this process is not well represented in the CSU GCM because only two model levels are used to represent the entire atmosphere above 100 mb. Tracer transport is almost just as efficient into the higher latitudes of both the northern and southern hemispheres, with only weak gradients in concentration near the surface except in the tropics. Subtropical and tropical convergence at the lower levels results in a much steeper gradient there. Note that in the southern hemisphere, the spatial patterns of T_1 and T_2 are not dissimilar. This is because for both tracers, the tropical upper troposphere is the main source in the southern hemisphere, whereas the northern hemisphere feels the fossil fuel emissions primarily at the surface.

6.2.2.1 Regional Ocean Tracers

In Fig. 6.13, the tracers representing exchange at the air-sea interface ($T_3 - T_8$) show the familiar pattern of stronger gradients with higher latitude sources, reversed vertical gradients in the hemisphere without the source, and concentration of the low-level gradient with divergence aloft in the tropics.

Tracer T_6 (due to the equatorial oceans) has a distribution that looks very much like that of tracer T_2 (due to tropical deforestation), with a tropical source in the lower levels, a midtropospheric minimum, and an upper tropospheric maximum associated with strong cumulus detrainment.

Tracers T_7 (with a sink in the southern middle latitudes), and T_8 (with an Antarctic source) show that the spatial distribution of tracers with strong northern sources has a very similar "mirror image" in the southern hemisphere. These tracers are felt most strongly in the high southern latitudes, with transport upward in the south, outward at the tropopause, and downward in the north. The resulting pattern in the northern hemisphere reflects the downward and poleward transport from the tropical upper tropospheric maximum, and is not unlike the northern hemisphere pattern of tracers like T_2 and T_6 with tropical sources.

6.2.2.2 Net terrestrial sinks

The simulated three-dimensional structure of the concentration fields of the tracers representing net terrestrial sinks ($T_{10} - T_{14}$) resembles that of tracer T_1 (fossil fuel combustion), because the sinks are mostly concentrated in the middle to high northern latitudes (Fig. 6.14) The further north the sink region is located, the less the tracer tends to be transported away. This reflects the general decrease in atmospheric convection with latitude, and the more stable PBL, as discussed above.

The concentration field of tracer T_{11} (reflecting increased water use efficiency of plants in a high CO_2 environment) shows the influence of a secondary surface sink in the subtropics of the southern hemisphere. Near 20° S, the concentration is significantly lower (the sink is stronger) at the surface than the other tracers, and there is almost no vertical gradient below the tropopause. This "extra" sink in the southern hemisphere accounts for the very small deviation from the South Pole concentration exhibited anywhere in the troposphere.

Meridional Cross Sections

Regional Ocean Tracers

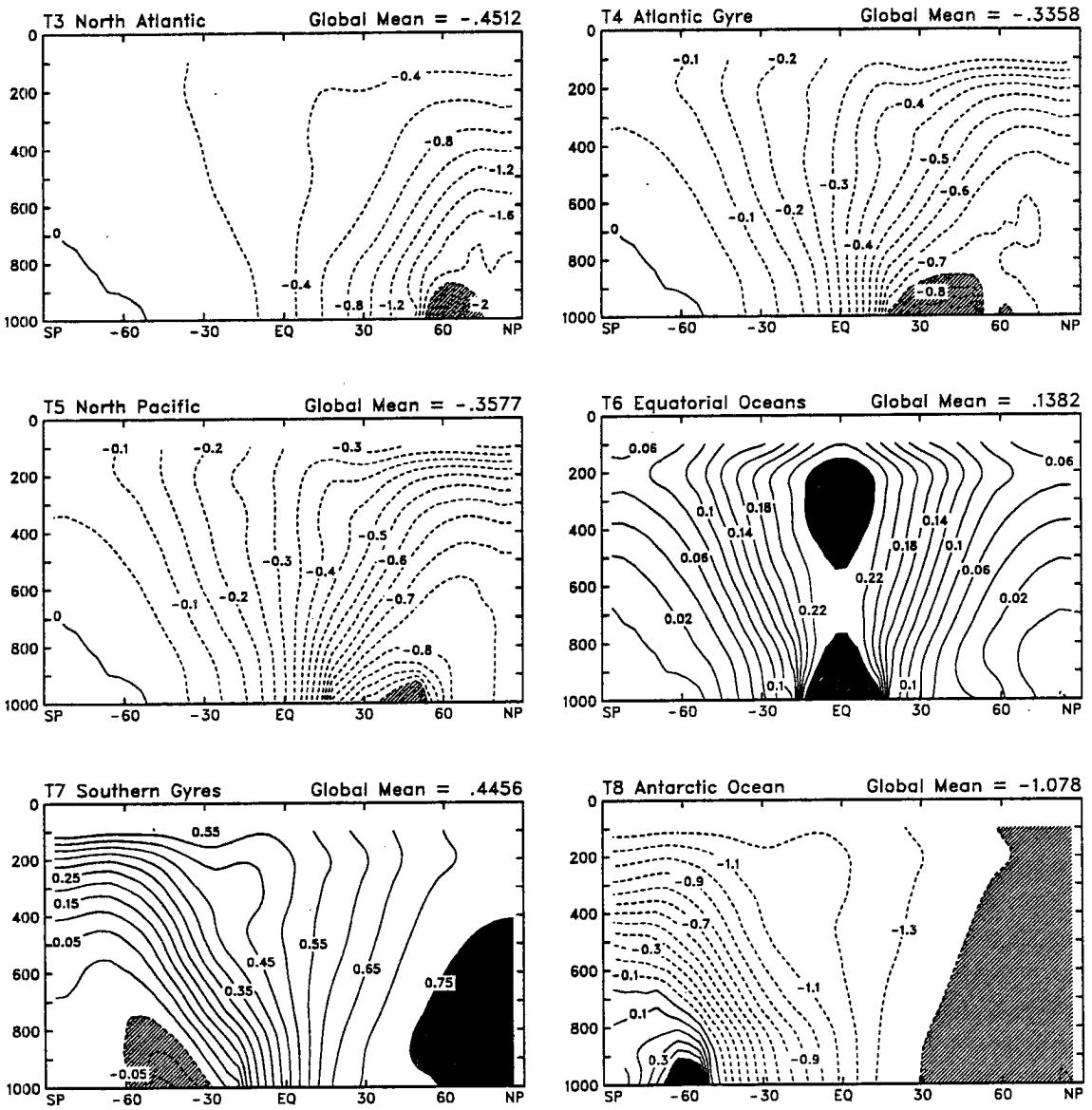

FIGURE 6.13: Annual mean concentration of the anthropogenic tracers T_1 and T_2 (ppm difference from the South Pole). Ordinates are latitude and abscissae are pressure.

Contour intervals in ppm for each tracer are as follows:
$T_3 = 0.2$, $T_4 = 0.05$, $T_5 = 0.05$, $T_6 = 0.02$, $T_7 = 0.05$, $T_8 = 0.1$.

Dark shading is used for values above the following thresholds in ppm:
$T_6 = 0.24$, $T_7 = 0.75$, and $T_8 = 0.5$.

Light shading is used for values below the following thresholds in ppm:
$T_3 = -2$, $T_4 = -0.75$, $T_5 = -1.0$, $T_7 = -0.05$, $T_8 = -1.4$.

Meridional Cross Sections

Net Terrestrial Sinks

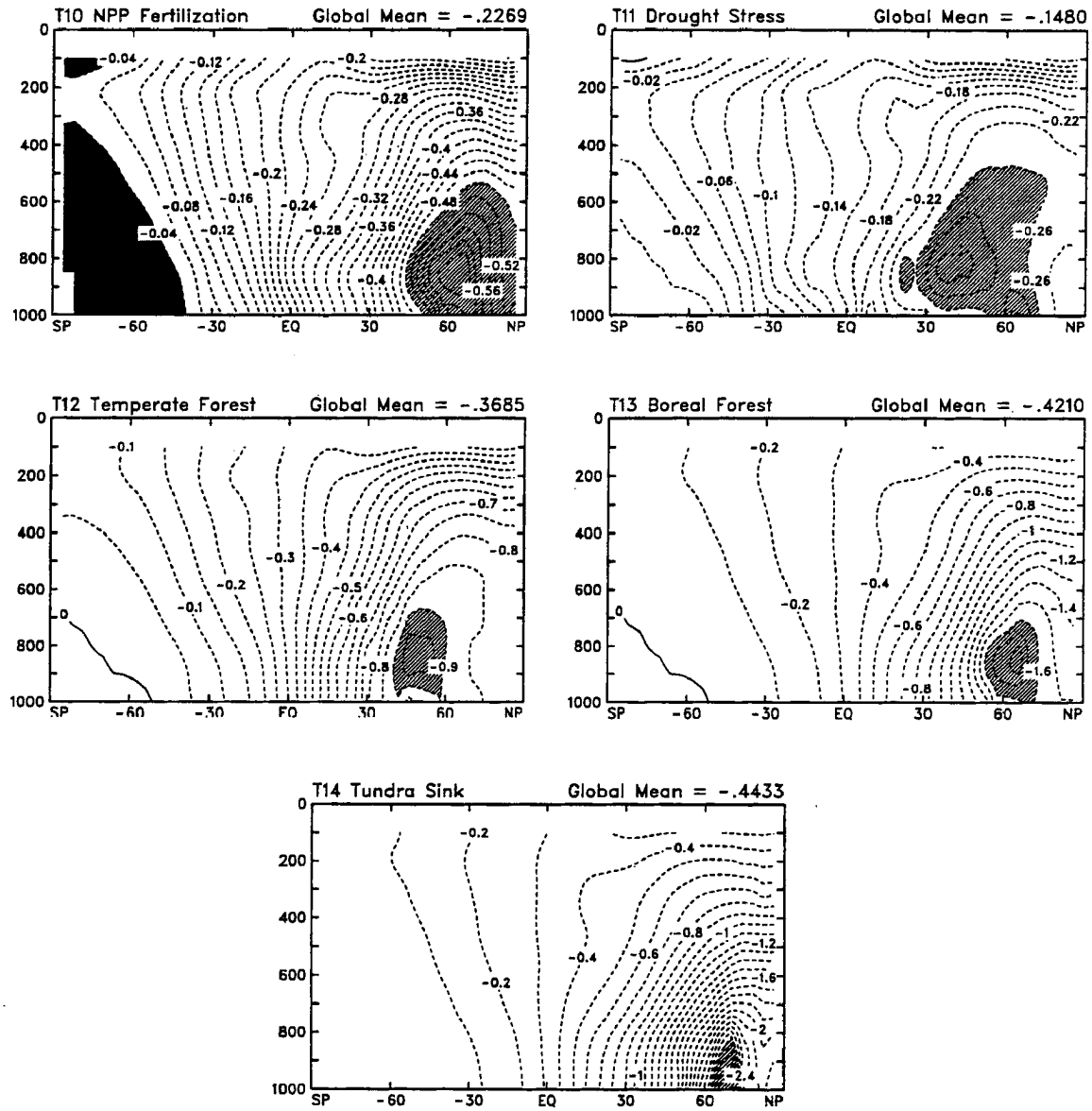

FIGURE 6.14: Annual mean concentration of the net terrestrial sink tracers $T_{10} - T_{14}$ (ppm difference from the South Pole). Ordinates are latitude and abscissae are pressure.

Contour intervals in ppm for each tracer are as follows:
$T_{10} = 0.02$, $T_{11} = 0.02$, $T_{12} = 0.05$, $T_{13} = 0.1$, $T_{14} = 0.1$.

Dark shading indicates values greater than -0.04 for T_{10}

Light shading is used for values below the following thresholds in ppm:
$T_{10} = -0.5$, $T_{11} = -0.26$, $T_{12} = -0.9$, $T_{13} = -1.6$, $T_{14} = -2.5$.

6.2.2.3 Seasonal Terrestrial Biosphere

As we saw in the maps of PBL concentration in the previous section, the three-dimensional distributions of the tracers representing seasonal exchange with the terrestrial biosphere are different from those previously considered, and fail to fall into either of the "archetypes" defined by the two anthropogenic tracers (Fig. 6.15).

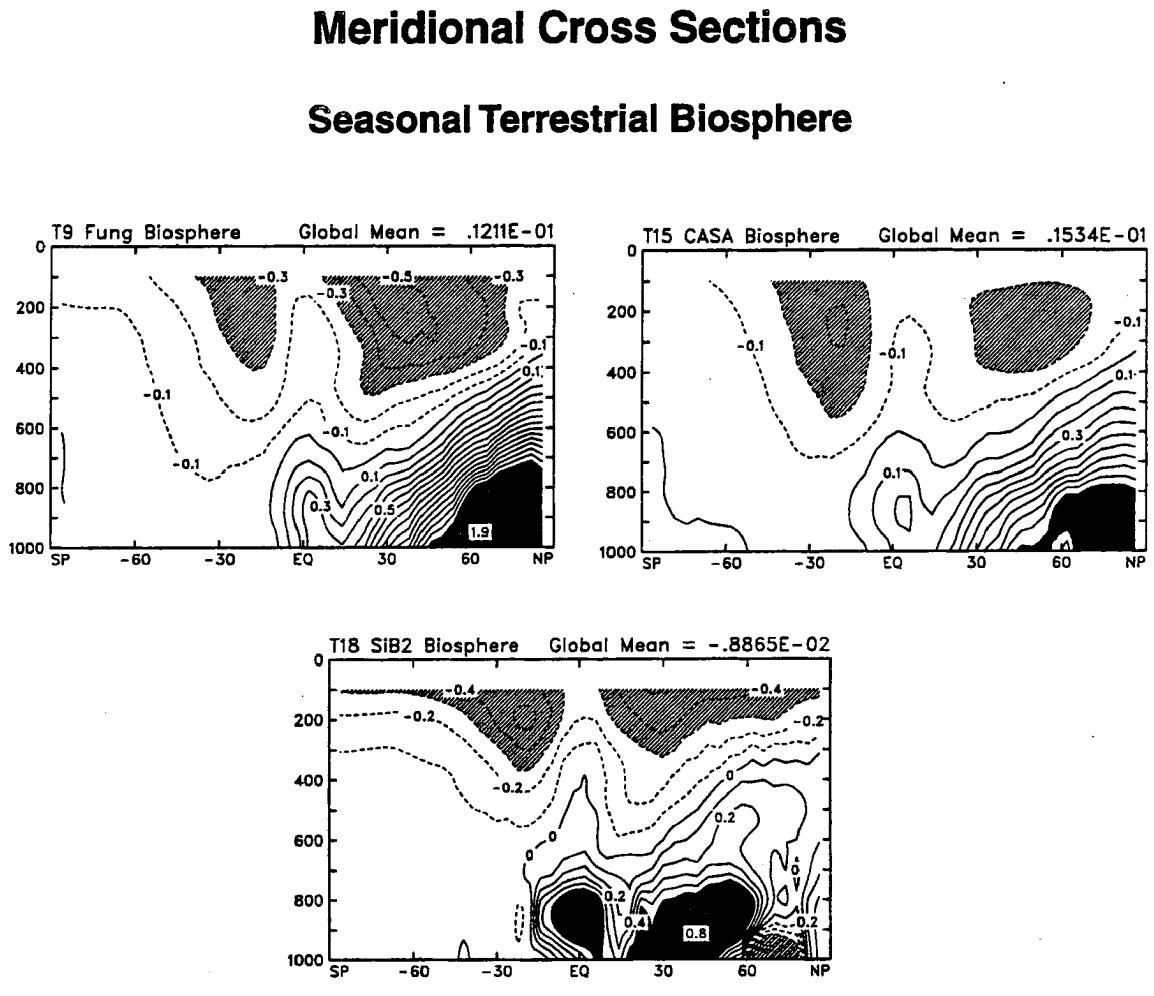

FIGURE 6.15: Annual mean concentration of the tracers which represent the exchange with the seasonal terrestrial biosphere (ppm difference from the South Pole). Ordinates are latitude and abscissae are pressure.

Contour intervals in all three panels are 0.1 ppm.

Dark shading indicates values above 1.5 ppm for T_9, 1 ppm for T_{15}, and 0.5 ppm for T_{18}.

Light shading indicates values below -0.3 for T_9 and T_{18}, and below -0.2 for T_{15}.

All three tracers have strong maxima confined to the lower troposphere in the regions where biological activity occurs (recall that none have a strong source or sink in the annual mean), and strong minima in the subtropical upper troposphere of both hemispheres. In addition, all three tracers show some evidence of a weak secondary maximum in the tropical upper troposphere, although this feature is much more subtle than it was in the distributions of tracers T_2 and T_6. The concentrations in the lower southern troposphere are remarkably uniform. Another surprise is how similar the distribution of T_{18} is to that of tracers T_9 and T_{15}, in light of the very different response in the PBL discussed in the previous section.

The strong vertical gradients over areas of biological activity seen in all three tracers are consistent with the explanation advanced above that photosynthesis dominates during the convective season and respiration occurs during periods of greater atmospheric stability. The depletion of tracer by photosynthesis is carried aloft, leading to minima in the upper troposphere in the annual mean. The positive fluxes due to soil respiration, on the other hand preferentially remain in the source regions, and show up as concentration maxima. Since the surface fluxes change signs (on a seasonal basis for all three tracers and on a daily basis for SiB2), transport of both the drawdown and the release of CO_2 must occur simultaneously. As the signal is advected further from the source region, mixing occurs, so that by the time a tracer-enriched parcel of air originating in say, the stable PBL of the subarctic Autumn, reaches the South Pole it has mixed with tracer-depleted parcels that last were in contact with the biosphere in the tropical rainy season. This may explain the relatively flat concentration field in the southern high latitudes. A similar argument would suggest that the very strong surface maxima in tracer T_{18} (SiB2) in the tropical rainforests is essentially a local feature and is lost almost immediately as air moves upward or outward from those regions and mixes with air that last contacted the surface at a different time of day. These interesting features will be further explored in Chapter 7.

6.3 Constrained Global Carbon Budgets

TFT90 considered many scenarios of sources and sinks, testing them against the observed distribution of annual mean CO_2 concentration at the NOAA flask stations. In this section a similar analysis is performed using the simulated concentration fields presented

in section 6.2.1 above and the annual mean flask concentrations as derived in Chapter 4. The station data used are described in section 6.3.1.

Rather than just try scenarios that seemed plausible, I attempted to select the "best" scenario by formally fitting linear combinations of the simulated tracers to the observed flask concentrations. This exercise was less useful than had been hoped, and is described in section 6.3.2.

To compare the results of the present study to those of TFT90, I evaluated all eight of their scenarios, each of which provided an acceptable fit to observations using the GISS tracer model. The results of this comparison point out the differences in atmospheric tracer transport between the GISS model and the CSU GCM, and are presented in section 6.3.3.

Using the lessons learned from fitting the TFT90 scenarios, new scenarios were tested, using a hybrid approach in which some of the components of the carbon budget were prescribed and others are calculated by the methods described in section 6.3.2. These results lead to a "preferred" set of carbon budget scenarios, described in section 6.3.4. Unfortunately, a unique carbon budget solution is not possible from the results of this study.

6.3.1 Simulated Concentration at the NOAA flask Stations

To generate a data set with which to compare the observed CO_2 data, the annual mean simulated concentration of each tracer was extracted from the fields shown in section 6.2.1 for each GCM grid cell representing the coordinates of each NOAA flask station. Only data from the standard experiment was used.

The locations of each flask station are shown in Fig. 4.1, repeated here for convenience (Fig. 6.16). Recall that samples are also collected from commercial container ships on regular tracks between the west coast of North America and New Zealand. The NOAA flask sampling network is designed to sample only remote marine air, free of local terrestrial influence, so most stations are located on remote islands or coastlines. The initial GCM grid coordinates selected to represent the flask stations included three grid points (representing stations CGO, CBA, and BRW) that are defined as land rather than ocean. Each of these "simulated flask stations" was "moved" one grid point off shore so that the simulated concentrations extracted from the GCM record would reflect a marine rather than terrestrial environment.

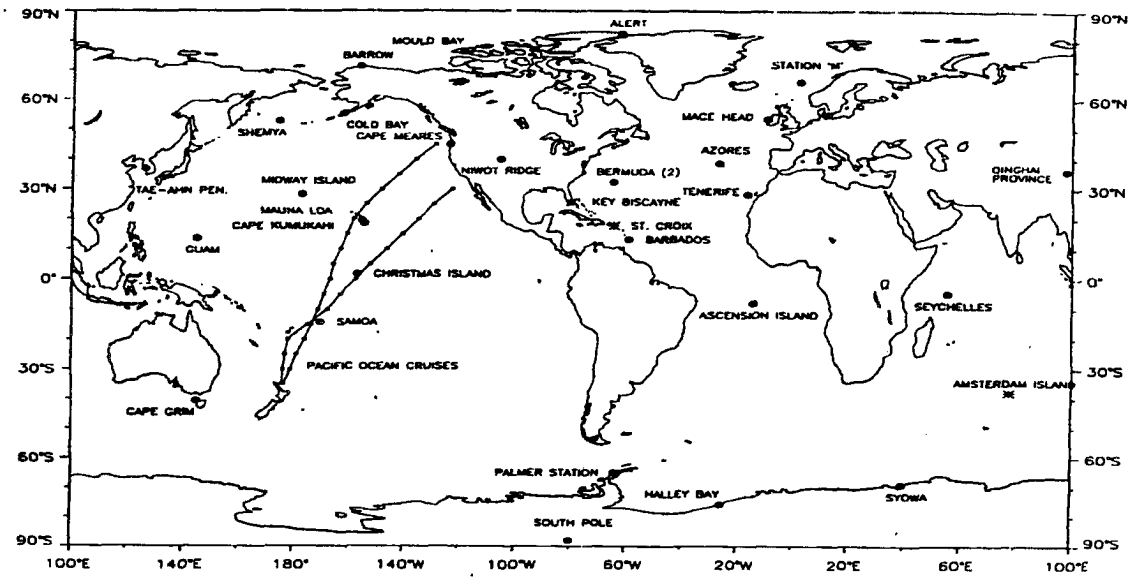

FIGURE 6.16: Sampling sites in the NOAA flask network for which concentration data were analyzed in Chapter 4.

Multiyear annual means for each station were derived from the NOAA sampling record in Chapter 4. They are also repeated here for convenience (Fig. 6.17). The simulated annual mean concentration of each tracer at each flask station is displayed in Fig. 6.18. These are the data that will be "fitted" to the flask data in Fig. 6.17 to make inferences about the global carbon budget. The meridional gradients produced at the flask stations by the purely seasonal tracers (T_9 and T_{15}) are much stronger than simulated in previous studies. TFT90 used the same surface fluxes as used here for T_9, and found a difference of only 0.25 ppm between the annual mean concentrations at the flask stations in the northern hemisphere versus the southern hemisphere. In the data presented here, the difference is 0.87 ppm. This is expected to lead to the need for a larger northern hemisphere sink to counter the effect of the seasonal tracers on the annual mean meridional gradient.

6.3.2 The Naïve Approach – Let's Just Fit *All* the Tracers!

Having simulated so many tracers covering so many hypotheses regarding the sources and sinks of CO_2 at the Earth's surface, and having assembled a set of observational data to which they can be properly compared, it is enticing to think that by pure effort of numerical algebra we should now be able to arrive at a definitive linear combination of these tracers which "best" fits the observations. This set might not give the "true" global

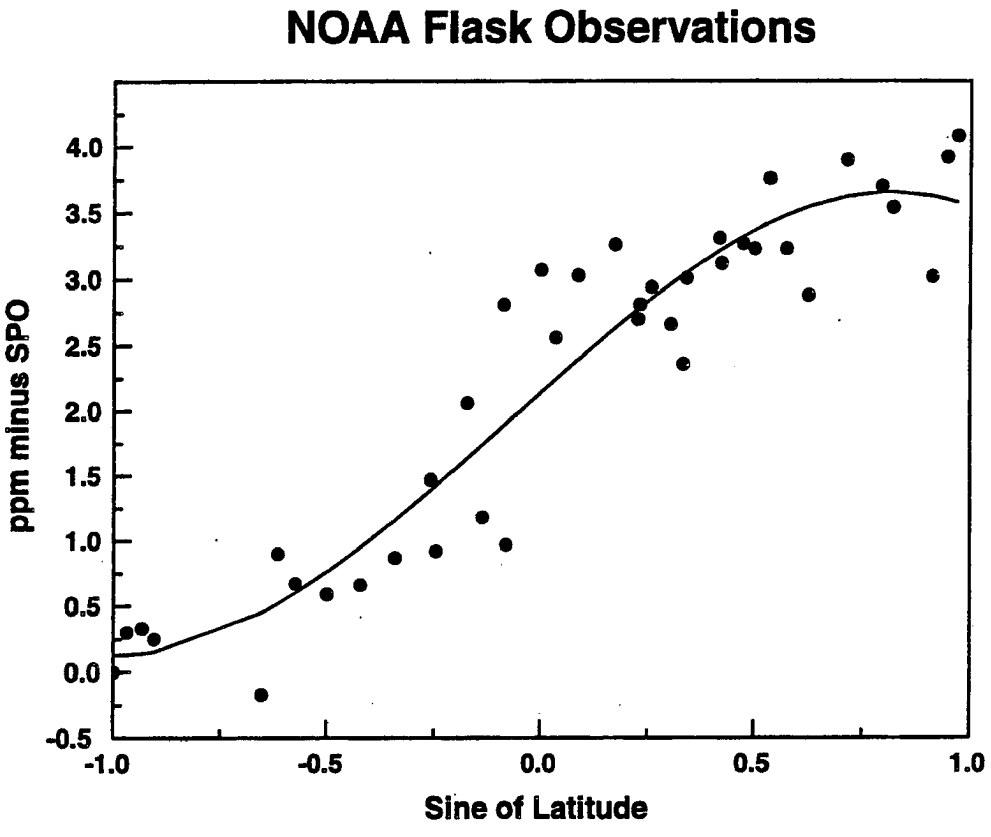

FIGURE 6.17: Meridional profile of the multiyear annual mean CO_2 concentration at each of the 40 NOAA flask stations derived in Chapter 4. The annual mean concentration at the South Pole has been subtracted from each value. The solid curve is a least-squares cubic polynomial fit to the data.

carbon budget, but should at least be the one which is most consistent with the set of assumptions implicit in the formulation of the problem, the transport characteristics of the GCM, and the placement of the flask stations.

The problem is to derive an expression which can be solved for the coefficients α_i such that the linear combination of tracer concentrations

$$C_{Tn} = \sum_{i=1}^{N_T} \alpha_i C_{in} \tag{6.1}$$

best fits the observed concentrations obs_n. In (A.1), C_{in} represents the concentration of tracer T_i at station n ($i = 1, \ldots, M$), and C_{Tn} is the "total" CO_2 concentration at station n,

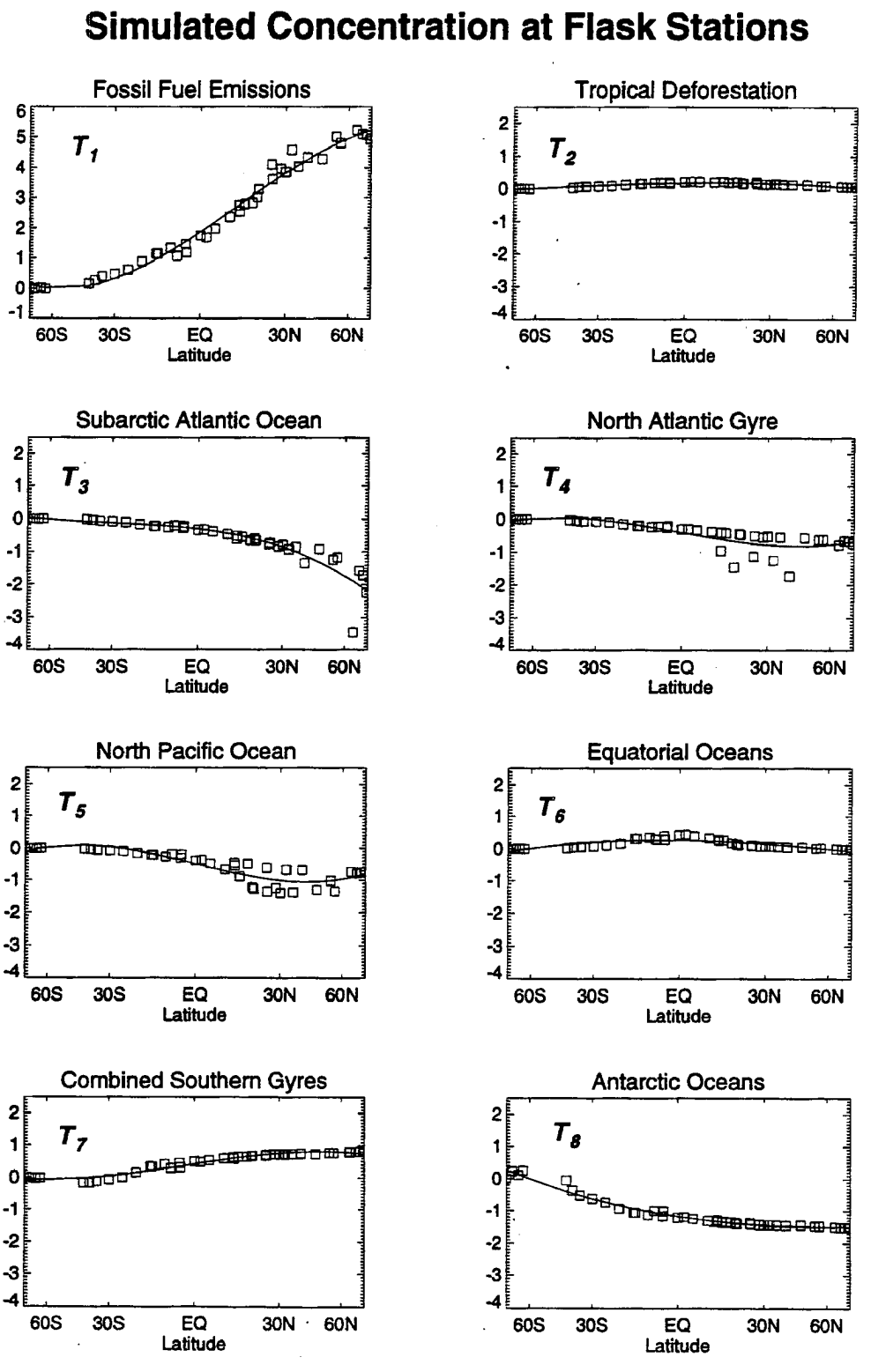

FIGURE 6.18: Annual mean simulated concentration (ppm, difference from the South Pole) of each tracer at the 40 NOAA flask sampling stations. The vertical scale of tracer T_1 is expanded because it has such a strong gradient. All other tracers are plotted on the same scale. Individual station values are plotted as open squares. The solid curves are cubic polynomials of concentration as functions of the sine of latitude, fit by least squares.

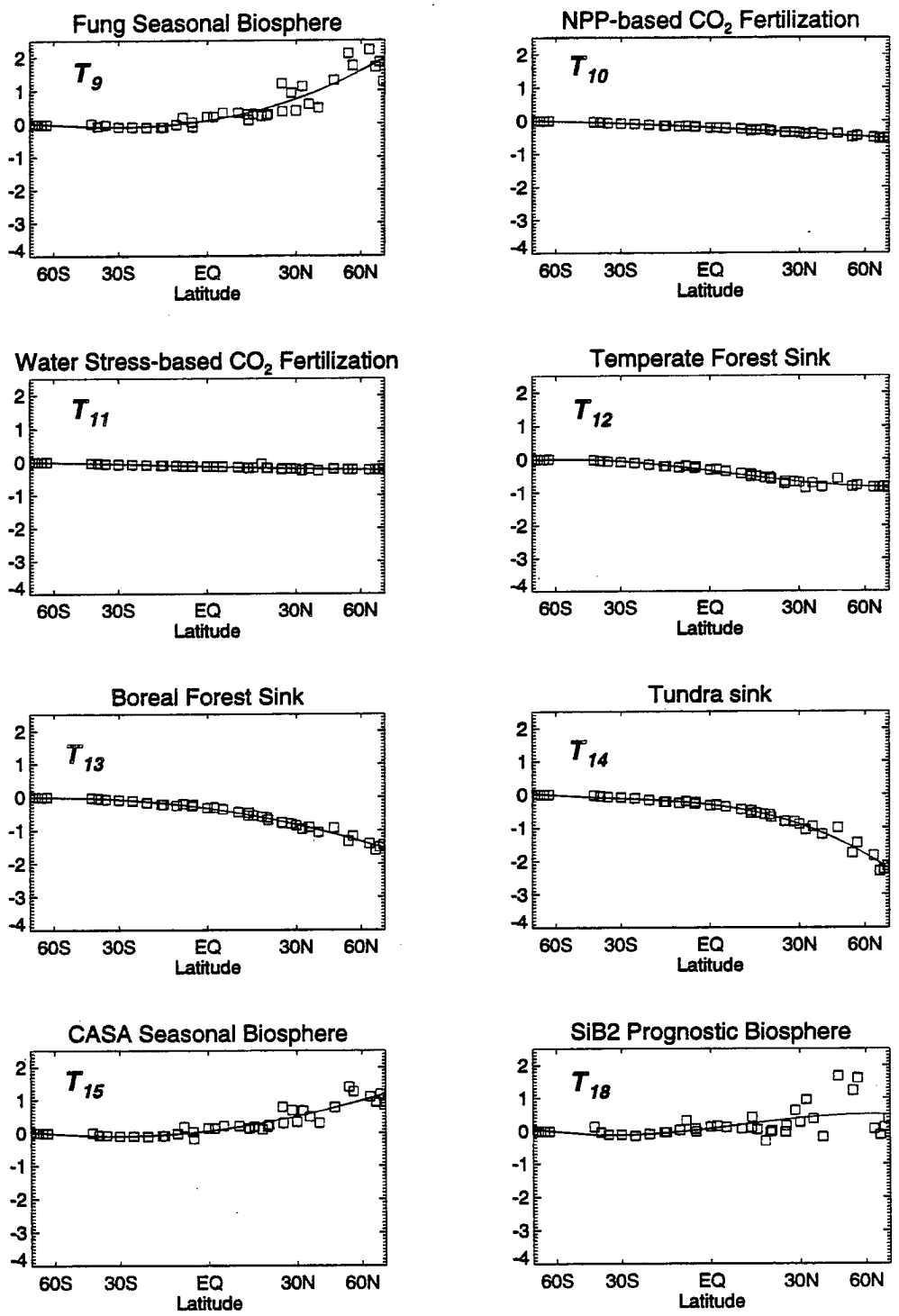

FIGURE 6.18 (cont'd): Annual mean simulated concentration (ppm, difference from the South Pole) of each tracer at the 40 NOAA flask sampling stations. Individual station values are plotted as open squares. The solid curves are cubic polynomials of concentration as functions of the sine of latitude, fit by least squares.

which is to be compared with the observed annual mean concentration at the same station obs_n ($n = 1, \ldots, N$). Because of the linear nature of the tracer calculation (see the discussion in section 3.2), determination of the coefficients α_i for the best fit of tracer *concentrations* (C_i) is equivalent to finding the best map of the tracer *fluxes* (F_i) which describe the CO_2 budget of the Earth's atmosphere in a manner consistent with both the observed annual mean concentration field and the simulated transport. The total surface flux of CO_2 at each grid point x on the planet is therefore given by

$$F(x) = \sum_{i=1}^{N_T} \alpha_i F_i(x) . \qquad (6.2)$$

Before solving for such a "best" carbon budget, it is appropriate to introduce several simplifications that make the problem easier to solve and also seek to preserve a degree of realism in the final solution. These simplifications, like so much else in this report, are guided by the previous study of TFT90.

1) The uncertainties in the global fluxes of CO_2 at the ocean surface and the "missing sink" fluxes are much greater than the uncertainties in the fossil fuel emissions (see Chapter 2). Therefore, for the purpose of this calculation, the fossil fuel fluxes will be held fixed. Similarly, the air-sea fluxes in the equatorial oceans are known much more precisely than those in other regions because of the high correlation between sea-surface temperature and vertical motion in the tropical oceans. Fluxes of tracer T_6 are therefore held constant at 1.62 Gt C yr^{-1} in this analysis (the value arrived at from the observational compilation of TFT90).

2) Only one of the estimates of the seasonal exchange of CO_2 between the atmosphere and the terrestrial biosphere (tracers T_9, T_{15}, and T_{18}) is appropriate to consider at a time, since all three represent the same process. Furthermore, the flux maps of both Fung *et al.* (1987) (tracer T_9) and the CASA model (tracer T_{15}) integrate to zero net flux at each grid point over a year, and so have no influence on the global carbon budget. Therefore only one of these tracers will be included.

3) The annual increase in the global mass of atmospheric carbon is known quite well from the time series of the NOAA flask observations (see Chapter 4).

For the multiyear means derived in section 4.3, the annual change in atmospheric carbon storage is 3.09 Gt C yr^{-1}.

4) Because tracer T_2 mixes so rapidly into both hemispheres in the GCM, resulting in very little meridional structure in the annual mean tracer concentrations (Fig. 6.18), this tracer is therefore used to enforce the condition that the global total annual increase in atmospheric carbon is 3.09 Gt C yr^{-1}. The flux due to tropical deforestation is then not determined from the fit, but rather calculated as a residual after the other tracers have been fit.

Using a simple least squares approach, a method is derived in the Appendix to calculate the coefficients a_i from the flask data and the simulated annual mean tracer concentrations, subject to the above constraints. A system of 10 equations in 10 unknowns is solved for the coefficients on the extratropical ocean fluxes and the "missing sink" fluxes of tracers $T_{10} - T_{14}$. The flux due to tropical deforestation is then determined as a residual.

Unfortunately, attempting to obtain a numerical solution to the system derived in the Appendix led to a nearly singular coefficient matrix, with mathematically meaningless results. An examination of the meridional profiles in Fig. 6.18 shows that several of the tracers have very similar profiles (e.g., the terrestrial "missing sinks" are very nearly simple multiples of one another). This means that the rows of the coefficient matrix are not independent of one another, and that in essence we have more variables than equations in the problem. The problem is numerically "ill conditioned," in the parlance of linear algebra.

The numerical difficulties associated with the ill-conditioned coefficient matrix can be overcome by a technique called Singular Value Decomposition (SVD, Press *et al.*, 1992). The matrix is decomposed into orthogonal vectors and the redundant combinations are removed. A new matrix is then constructed which is numerically more tractable but has not lost meaningful information, since the equation that was discarded is essentially just a "repeat" of the ones still present.

Using SVD, I performed the calculation outlined above, and solved simultaneously for the ocean fluxes, the terrestrial sinks, and the tropical deforestation source. The results are presented in Table 6.2. for each of the hypotheses regarding seasonal exchange

with the terrestrial biosphere. The fit between the simulated and observed concentrations obtained by each of these three budgets is excellent (Fig. 6.19).

Table 6.2: "Best Fit" Global Fluxes of Each Tracer[a]

Tracer	Description	Seasonal Terrestrial Biosphere		
		Fung	CASA	SiB2
T_3	Subarctic Atlantic	-0.40	-0.30	+0.05
T_4	North Atlantic Gyre	+0.69	+0.37	+0.57
T_5	North Pacific	+1.26	+0.64	+0.80
T_6	Equatorial Oceans	+1.62	+1.62	+1.62
T_7	Southern Gyres	-0.11	+0.15	+1.56
T_8	Antarctic Oceans	-0.50	-0.43	-0.30
Total Ocean Flux		+2.56	+2.06	+4.31
T_2	Tropical Deforestation	4.75	+6.04	12.98
T_{10}	NPP-based CO_2 Fertilization	-4.22	-4.41	-9.56
T_{11}	Water stress CO_2 Fertilization	-2.69	-5.62	-14.41
T_{12}	Temperate Forest Sink	+0.39	+0.14	+3.83
T_{13}	Boreal Forest Sink	-8.29	-3.68	-4.45
T_{14}	Tundra Sink	+4.59	+2.55	+4.19
Total Terrestrial Flux		-5.47	-4.97	-7.22
r.m.s. error (ppm)		0.39	0.35	0.41

a. Annual global fluxes in Gt C yr^{-1}. All three scenarios include 6.0 Gt C yr^{-1}. due to fossil fuel emissions, and a net increase of 3.09 Gt C yr^{-1} in the atmosphere.

Unfortunately, the budgets obtained by this approach are extremely unreasonable! In all three scenarios, the oceans are strong *sources* of CO_2 to the atmosphere, which is incompatible with observational evidence to the contrary. While the overall flux from the terrestrial biosphere is appropriately negative in all three cases, individual components act in very unexpected ways, with large positive and negative fluxes nearly canceling one another. Using the Fung seasonal fluxes, for example, the boreal forest is a sink of more than 8 Gt C yr^{-1}, but is paired with almost 4.6 Gt C yr^{-1} *source* in the nearby tundra. The regional sinks are even more bizarre using the SiB2 seasonal data, with a 13 Gt C yr^{-1}

"Best Fit" Carbon Budgets

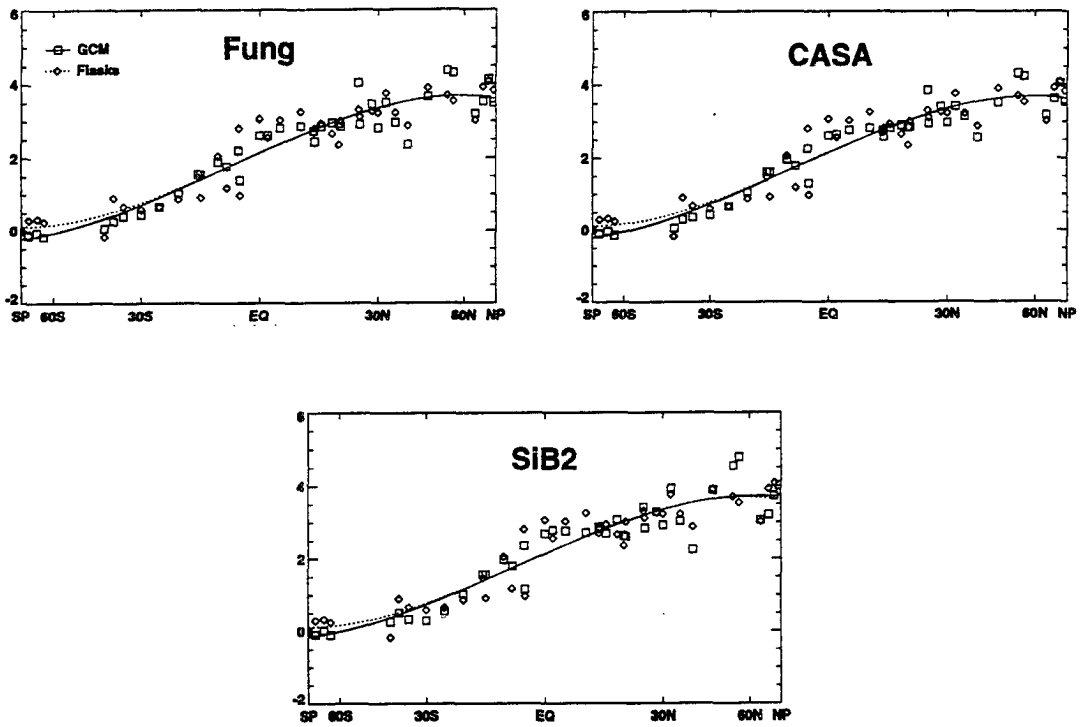

FIGURE 6.19: Simulated and observed CO_2 concentrations (ppm, difference from South Pole) at each of the NOAA flask stations using the "best fit" linear combinations of tracers (Table 6.2) derived from the data. Flask data are plotted as diamonds, and GCM data as squares. The solid curve (representing the GCM data) and the dotted curve (representing the observations) are cubic polynomials of the sine of latitude fitted to the station data.

source due to tropical deforestation coupled with a 14.4 Gt C yr^{-1} sink due to CO_2 fertilization (water stress based).

Evidently, the "goodness of fit" between the observed and simulated concentrations is a necessary, but not sufficient condition for a plausible carbon budget. This is a direct consequence of the similarity between the shapes of the curves in Fig. 6.18 – the use of SVD allowed a numerical solution, but the problem is still fundamentally underdetermined, meaning there is no unique solution. Excellent fits to the observed concentrations can be "concocted" using huge and opposing combinations of tracers that act in opposite ways on the meridional distribution of the simulated concentrations.

This result should not be very surprising. Previous studies (Keeling *et al.*, 1989*a*; TFT90) have specified "scenarios" of the global budget *a priori* and then used tracer

transport models to evaluate them. The fact that the atmospheric transport acts on the tracers in much the same way, and that only a couple of "typical" patterns of tracer concentration were able to represent all but a few of the distributions examined in section 6.2 implies that many of the tracer distributions will not be linearly independent.

A few features that are common to all three "best fit" budgets in Table 6.2 may hold clues to requirements of successful carbon budget scenarios given the data in this study. Although the individual components vary wildly, all three have a net sink of 5 – 7 Gt C yr^{-1} on the northern hemisphere continents. This is consistent with nearly all previous tracer modeling studies, and arises from the need to balance the steeper than observed meridional gradient imposed by the huge emissions from fossil fuel combustion.

The fluxes due to tropical deforestation and CO_2 fertilization (T_2, T_{10}, and T_{11}) have a tendency to partially balance each other, leaving a weak sink in the Fung and CASA budgets and a strong one in the SiB2 budget. These tracers have very weak meridional gradients at the flask stations, and so require large coefficients to have a significant effect on the overall fit.

None of the scenarios has a sink in the temperate forests of the middle latitudes, which actually act as a strong source in the SiB2 case. All have a strong sink in the boreal forest and a strong source in the tundra. This is a consequence of the higher concentrations at the three highest latitude flask stations (ALT, MBC, and BRW, all north of 70°) than at STM (66° N) (Fig. 6.17), and the fact that the meridional profiles of T_{13} (the boreal forest sink) and T_{14} (the tundra sink) are so similar (Fig. 6.18). Fitting the gradient in the Arctic requires that these fluxes be strong and of opposite signs.

All three scenarios have sinks rather than sources in the Antarctic oceans, even though the observed concentrations along the coast of Antarctica are higher than that at the South Pole. This is somewhat surprising considering that most of the global oceans are acting as sources in these scenarios, but is consistent with the scenarios explored in section 6.3.4 below.

6.3.3 TFT90 Scenarios

The carbon budget scenarios used by TFT90 were not intended to be "best fits," but rather were chosen to explore the realism of various current assumptions and hypotheses about the global carbon budget given the constraints of the available observations of at-

mospheric CO_2 concentration and sea-surface p_{CO2}. Eight scenarios were considered (summarized in Table 6.2), all of which were deemed "successful" by TFT90, meaning

Table 6.3: Carbon Budget Scenarios of Tans *et al.* (1990)[a]

Source or Sink	Scenario (Net Flux in Gt C yr^{-1})							
	1	2	3	4	5	6	7	8
Subarctic Atlantic	-0.7	-0.5	-0.7	-0.5	-.23	-.23	-.23	-.23
North Atlantic Gyre	-1.0	-0.8	-1.4	-1.0	-.30	-.30	-.30	-.30
North Pacific	-1.0	-0.7	-1.4	-1.0	-.06	-.06	-.06	-.06
Equatorial Oceans	1.0	1.0	1.0	1.0	1.3	1.3	1.3	1.3
Southern Gyres	-1.4	-1.1	-2.3	-2.3	-1.5	-1.9	-1.6	-1.8
Antarctic Oceans	0.5	0.5	0.5	0.5	0.5	0.5	0.5	0.5
Total Oceans	-2.6	-1.6	-4.3	-3.3	-0.3	-0.7	-0.4	-0.6
Tropical Deforestation	0.3	0.3	2.0	2.0	0.0	1.0	1.0	2.5
CO_2 Fertilization	0.0	-1.0	0.0	0.0	0.0	0.0	-1.0	-3.0
Temperate Sink	0.0	0.0	0.0	-1.0	-2.0	-3.0	-2.3	-1.9
Boreal *Source*[b]	0.0	0.0	0.0	0.0	0.0	0.4	0.4	0.7
Total Terrestrial	0.3	-0.7	2.0	1.0	-2.0	-1.6	-1.9	-1.7

a. All scenarios also used a global fossil fuel source of 5.3 Gt C yr^{-1} and the same seasonal fluxes due to photosynthesis and respiration as those used to drive tracer T_9 in the present study.
b. The "boreal" source used by TFT90 was distributed over the boreal forest and tundra biomes.

that the differences between the simulated and observed flask station concentrations (the "residuals") had no statistically significant meridional structure. In this section, these eight scenarios are evaluated using the simulated and observed concentrations from the present study.

The strategy used by TFT90 to construct these scenarios was to specify either a set of terrestrial fluxes (in scenarios 1 – 4), or a set of ocean fluxes (in scenarios 5 – 8) and adjust the other fluxes to obtain an acceptable fit between the simulated and observed concentrations. The ocean fluxes used for the northern hemisphere in scenarios 5 – 8 were calculated from p_{CO2} data, but the fluxes south of 15° S were deemed too uncertain to

specify in this way. Simulated concentrations using all the scenarios "fit the atmospheric data equally well," according to TFT90.

When the tracer concentrations from the present study are compared to the observed concentration data using the scenarios which worked for TFT90, the fit is consistently bad (Fig. 6.20). In all eight scenarios, the GCM concentrations are systematically low compared to the flask observations. The fit is worst in the tropics and subtropics. The agreement at the South Pole is meaningless because the concentration there has been subtracted from all other points before plotting, so it is identically zero in all cases. The fit in the Arctic is not too bad for scenarios 1 – 4, but the GCM consistently simulates concentrations that are too high in that region using scenarios 5 – 8 (in which the northern ocean fluxes are specified from observed p_{CO2}).

The poor fit using TFT90's scenarios is not surprising. Both the simulations and the observational data differ in several important respects:

1) The observational data set used in the present study includes more stations (40 vs. 21), for a different time period. TFT90 considered only data from 1981 through 1987, whereas the concentrations used here include the entire period of record for every station, some going back more than 25 years and many including data as recent as 1992. The pole-to-pole difference determined in the present study is 3.83 ppm vs. 3.0 for TFT90.

2) The fossil fuel emissions used to drive my tracer T_1 amount to 6.0 Gt C yr^{-1}, vs. only 5.3 Gt C yr^{-1} for TFT90.

3) The net terrestrial sinks considered in this study are seasonally varying, whereas those modeled by TFT90 were steady throughout the year (Inez Fung, personal communication).

The newer flask station data used here (but not by TFT90) includes the shipboard sampling program in the Pacific, which produces systematically higher concentrations than the earlier flask record in the tropics. Without these stations, the discrepancies between the simulated and observed concentrations in every scenario shown in Fig. 6.20 are much smaller in the tropics.

Following the logic of TFT90, I prescribed the fluxes they used in their scenarios and adjusted the remaining fluxes to evaluate various hypotheses. My "revisions" of some of

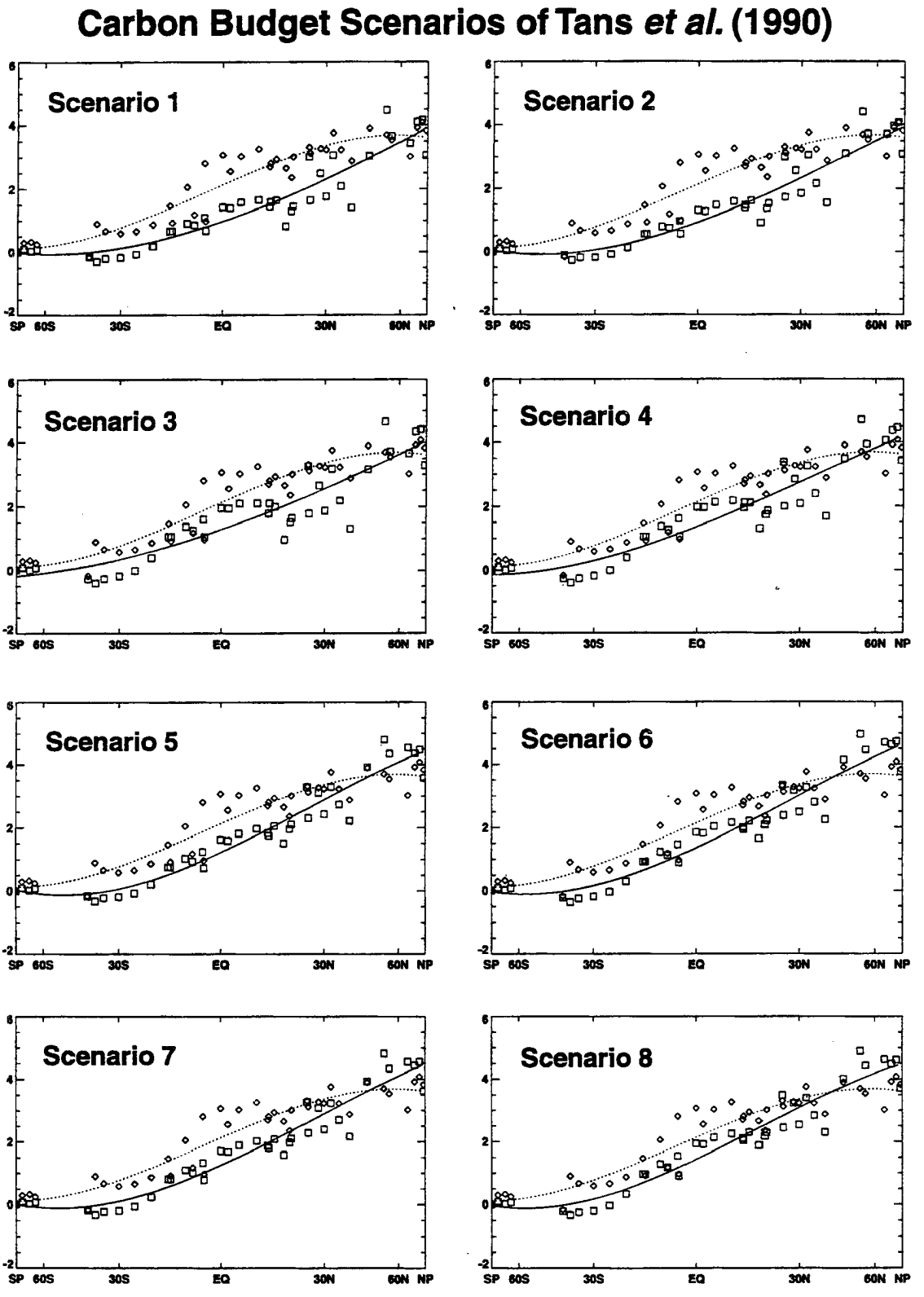

FIGURE 6.20: Simulated and observed CO_2 concentrations at the NOAA flask stations using the scenarios derived by TFT90. Flask observations are plotted as diamonds, and the GCM data are plotted as squares. solid and dashed curves are cubic polynomials fit to the data for the GCM and the observations, respectively.

TFT90's scenarios are presented in Table 6.2. In all cases, the Fung seasonal fluxes (tracer T_9) were used, annual fossil fuel emissions were 6.0 Gt C yr^{-1}, and the annual change in total atmospheric CO_2 was fixed at 3.09 Gt C yr^{-1}.

Table 6.4: Revised Carbon Budget Scenarios after TFT90

Source or Sink	Scenario				
	1	2	3	4	8
Subarctic Atlantic	-1.5	-1.3	-1.5	-1.3	-.23
North Atlantic Gyre	-0.5	-1.0	-1.3	-1.0	-.30
North Pacific	-1.3	-0.5	-1.5	-1.0	-.06
Equatorial Oceans	1.4	1.6	1.3	1.3	1.3
Southern Gyres	-0.8	-0.5	-1.4	-1.4	-1.0
Antarctic Oceans	-0.5	-0.5	-0.5	-0.5	-0.7
Total Oceans	-3.2	-2.2	-4.9	-3.9	-1.0
Tropical Deforestation	0.3	0.3	2.0	2.0	4.1
CO_2 Fertilization	0.0	-1.0	0.0	0.0	-2.0
Temperate Sink	0.0	0.0	0.0	-1.0	-4.0
Boreal *Source*	0.0	0.0	0.0	0.0	0.0
Total Terrestrial	0.3	-0.7	2.0	1.0	-1.9
r.m.s. Error	0.55	0.54	0.59	0.53	0.49

In scenarios 1 – 4, exactly the same terrestrial fluxes used by TFT90 were assumed, and ocean fluxes were adjusted to produce a good fit. As expected based on the results in 6.20, the most difficult aspect of the observations to fit using these scenarios is the relatively high concentrations in the tropics, relative to the high latitude southern hemisphere. Even using a flux of 1.62 Gt C yr^{-1} for tracer T_6 (the equatorial efflux estimated from the p_{CO2} data by TFT90), the simulated CO_2 was systematically too low there, and the simulated gradient in the southern hemisphere subtropics is too weak. The only way to match these features in the flask data was to reverse the sign on the Antarctic air-sea exchange used by TFT90, and assume a moderate sink of about 0.5 Gt C yr^{-1} there. This region was also a sink in all of the numerically determined "best fit" budget scenarios derived in section 6.3.2.

Because the CO_2 source due to tropical deforestation is fixed in scenarios 1 – 4, balancing the overall budget while preserving the observed meridional gradient is difficult, and requires even larger regional ocean fluxes than were used by TFT90. The northern hemisphere regional ocean sinks required to fit the atmospheric observations are in every case much larger than is compatible with the observed sea surface p_{CO2}.

In scenarios 5 – 8 of TFT90, a temperate forest sink and the southern oceans (and in some cases a tundra and boreal forest source) were used to fit the observed gradient, and the tropical deforestation was used to balance the global budget, while holding the air-sea fluxes north of 15° S constant. In trying to adjust these scenarios using the results of the present study, the temperate forests turned out to be a poor choice of sink to use to manipulate the simulated meridional gradient. In order to achieve enough reduction in the high latitudes of the northern hemisphere, the temperate sink must be made so strong that the concentrations in the low latitudes are too low, leading to a distinct minimum in the residuals in the tropics. This problem is even worse when a high latitude *source* is prescribed, as was done by TFT90 in scenarios 6 – 8. Although such a source improves the fit north of 66° N, it is impossible to adjust the other tracers to produce an acceptable fit in this scenario.

Table 6.2 shows a modified version of scenario 8, but the budget used actually bears only superficial resemblance to that scenario. Scenarios 5 – 7 were even more difficult to modify, and are not included here. Because both the CO_2 fertilization sink (T_{10}) and the deforestation source (T_2) have very little meridional structure, they are free to vary in opposite directions to balance one another with strong opposing fluxes. My modified scenario 8 uses no high latitude source, and the southern ocean is a much stronger sink than TFT90 used for this scenario.

6.3.4 "Preferred" Carbon Budget Scenarios

From the results presented in the previous two sections, it is clear that estimates of the components of the global carbon budget deduced by direct numerical solution (as in section 6.3.2) and balancing temperate terrestrial uptake, tropical deforestation, and boreal sources (as in section 6.3.3) are unsatisfying. In both approaches we are led to scenarios with large opposing fluxes from various sources whose concentration fields are spatially correlated. In this section we will take a fresh look at the components of the bud-

get and attempt to construct scenarios that match the observations acceptably while consciously minimizing the use of spatially correlated fluxes of opposite sign.

The observational p_{CO2} data presented by TFT90 are a powerful constraint on the ocean fluxes north of 15° S. It is clear from the previous section that large ocean fluxes cannot be used to produce a reasonable agreement with the observed atmospheric CO_2 concentration without seriously violating this constraint. Even the ocean modelers have conceded this point (Sarmiento and Sundquist, 1992). Only the southern oceans and the northern terrestrial ecosystems can be varied enough to construct scenarios that are believable given the observational constraints.

The "revisions" proposed by Sarmiento and Sundquist (1992) to the ocean flux estimates of TFT90 (see section 2.5.2) include three processes that add carbon to the oceans: 1) the geochemical flux of dissolved in rivers; 2) the southern hemisphere uptake of CO_2 produced by interhemispheric transport and subsequent oxidation of CO by OH radicals; and 3) the increased solubility of CO_2 at the ocean surface due to radiational cooling of a thin layer of water (the "skin temperature" effect of Robertson and Watson, 1992). From the point of view of an atmospheric model, the river flux is actually a *terrestrial* sink, since CO_2 is first removed from the atmosphere on land and then transported overland to the oceans by rivers. The interhemispheric transport of CO was estimated by Sarmiento and Sundquist (1992) to add less than 0.3 Gt C yr^{-1} to the uptake by the southern oceans, which is well within the uncertainty in the southern hemisphere ocean sink estimates of TFT90, and will not in any case have much effect on the simulated meridional gradient. Of these revisions, only the skin temperature effect can make much difference to the present calculation. Sarmiento and Sundquist (1992) estimate this effect to add between 0.1 and 0.6 Gt C yr^{-1} to the oceanic uptake north of 15° S that is calculated from the observational data presented by TFT90.

Taking the upper bound of the skin temperature correction, suppose that 0.6 Gt C yr^{-1} should be added to the annual net uptake of tracers $T_3 - T_6$ (representing all ocean areas north of 15° S). How should this "extra" uptake be distributed? Making the simple assumption that the sources should be weakened (in the equatorial oceans) and the sinks strengthened (everywhere else) by an equal fractional amount, we arrive at the "revised"

fluxes shown in Table 6.5. Each of the sink strengths has been increased by 27%, and the

Table 6.5: Annual Flux (Gt C yr^{-1}) of Ocean Tracers North of 15° S Latitude

Tracer	Description	TFT90	Revised
T_3	Subarctic Atlantic	-0.23	-0.29
T_4	North Atlantic Gyre	-0.30	-0.38
T_5	North Pacific	-0.06	-0.08
T_6	Equatorial Oceans	1.62	1.18

equatorial source has been weakened by 27%. These fluxes should be regarded as an upper limit for northern hemisphere uptake by the oceans.

Taking the fossil fuel emissions to be "well known," and assuming that tracer $T_3 - T_6$ have the flux distribution shown above, the data which must be matched are shown in

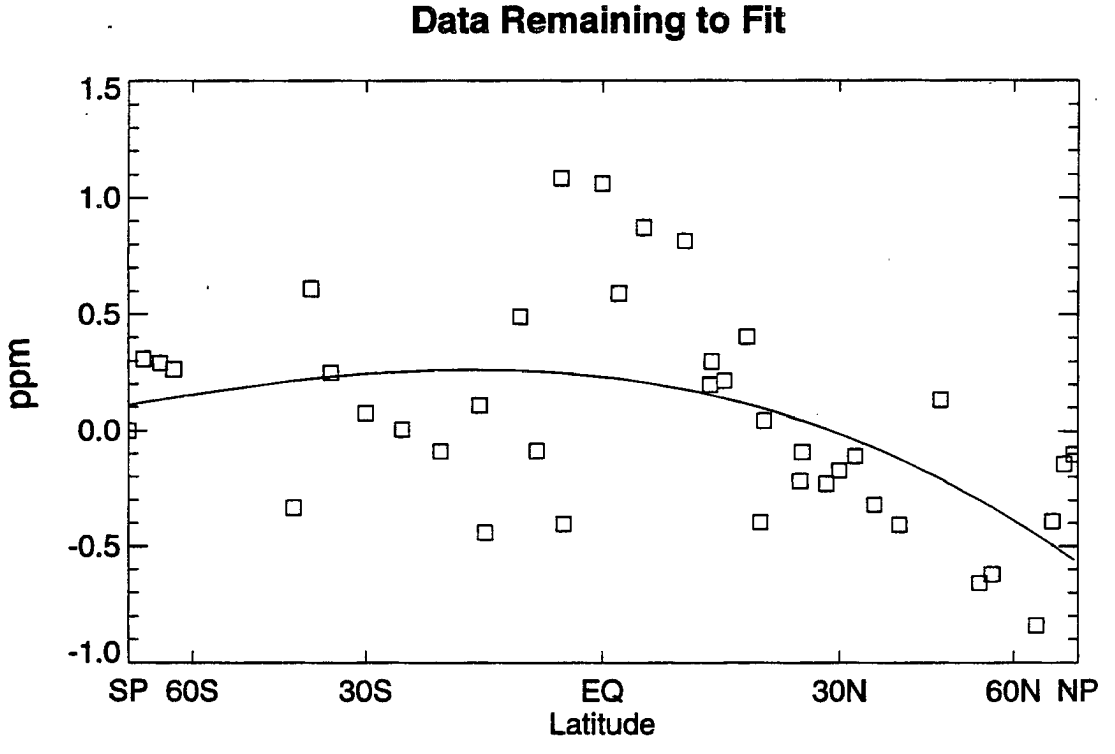

FIGURE 6.21: Observational CO_2 data remaining to fit with simulated tracers after subtracting fossil fuel CO_2 (T_1) and the fixed ocean tracers ($T_3 - T_6$) as defined in Table 6.5.

Fig. 6.21. The salient features of the remaining atmospheric CO_2 data which must be approximated by the remaining tracers in a successful simulation are:

1) The weak meridional gradient in the southern hemisphere;

2) The tropical concentration maximum; and

3) The stronger negative meridional gradient in the northern hemisphere.

Recall that all three hypotheses regarding seasonal exchange with the terrestrial biosphere impose a positive meridional gradient in the northern hemisphere (Fig. 6.18). Tracer T_9 (using the fluxes of Fung *et al.*, 1987) has the highest relative concentrations in the high northern latitudes (about 2 ppm above the South Pole). The gradients of T_{15} (the CASA fluxes) and T_{18} (the SiB2 tracer) are weaker in that order. Because the gradients of the seasonal tracers are stronger than the negative gradient in Fig. 6.21, each require an additional sink to be imposed in the northern hemisphere.

The meridional structure of the simulated tracers representing CO_2 fertilization is very weak (Fig. 6.18). In order to have any significant effect on the degree of realism of the simulated CO_2 at the flask stations, the sinks of these tracers must be quite strong. Strong terrestrial sinks require a large tropical deforestation source to balance the budget (the southern oceans can not be used in this way because they have a strong effect on the meridional gradient). This is exactly the kind of strong source/sink dipole of spatially correlated fluxes I want to avoid, so in constructing the carbon budgets in this section these two tracers will not be used.

Using only the tracers representing air-sea exchange in the southern oceans (T_7 and T_8), tropical deforestation (T_2), the biome-specific net sinks at the land surface (T_{12}, T_{13}, and T_{14}), and the seasonal terrestrial biosphere (T_9, T_{15}, and T_{18}) new budgets were constructed that approximated the residuals in Fig. 6.21 while being careful to avoid large opposing source/sink dipoles. Each of the three seasonal biosphere tracers was fit separately.

In all three cases, the temperate forest sink was found to depress the tropical maximum too much when applied at sufficient strength to reproduce a significant negative gradient in the higher northern latitudes. Increasing tropical deforestation to counter this effect is not useful, because tracer T_2 is so well mixed (see section 6.2.1), and because of the constraint imposed by the observed annual change in atmospheric CO_2.

The steep jump in observed concentration between STM (at 66° N) and the three northernmost stations suggests a high-latitude source. None of the seasonal tracers (T_9, T_{15}, or T_{18}) show this pattern (the SiB2 tracer shows just the opposite), so there is a temptation to apply a tundra source to increase the simulated concentration at these three stations, as was done by TFT90. This of course increases the overall northern hemisphere gradient and must then be offset by a stronger boreal forest sink, which introduces the sort of "runaway" opposing fluxes that we wish to avoid. This is most problematic with the Fung fluxes (T_9), which has the steepest high latitude gradient of the three seasonal biosphere tracers. Only with very large boreal uptake was an Arctic source compatible with the simulated T_9 concentrations and the observations, so a budget using T_9 was constructed without a tundra source. The high latitude gradient due to the CASA fluxes (T_{15}) is weaker by almost half than that of T_9, so a small source in the highest latitudes can be accommodated. In the case of T_{18}, the concentration at stations CMO, SHM, and

Table 6.6: "Preferred" Global Carbon Budgets

Tracer	Description	Seasonal Terrestrial Biosphere		
		Fung	CASA	SiB2
T_3	Subarctic Atlantic	-0.29	-0.29	-0.29
T_4	North Atlantic Gyre	-.38	-.38	-.38
T_5	North Pacific	-.08	-.08	-.08
T_6	Equatorial Oceans	+1.18	+1.18	+1.18
T_7	Southern Gyres	-0.77	-0.68	-0.80
T_8	Antarctic Oceans	-0.52	-0.54	-0.50
Total Ocean Flux		-0.86	-0.79	-0.86
T_2	Tropical Deforestation	+0.55	+0.06	-0.16
T_{13}	Boreal Forest Sink	-2.60	-2.43	-3.08
T_{14}	Tundra *Source*	0.0	+0.25	1.00
Total Terrestrial Flux		-2.05	-2.12	-2.05
r.m.s. error (ppm)		0.46	0.40	0.53

CBA (45° N, 53° N, and 55° N) is more than 1.2 ppm higher than at the stations further north, so a high latitude source is necessary to produce an acceptable level of agreement.

The budgets presented in Table 6.2 do not produce the "best" fit to the observational data, but are "preferred" because they do not rely on ridiculously strong sources and sinks that nearly balance each other in order to reduce the root mean square error by the last tenth of a ppm. The overall fit is almost as good as the "best fit" budgets derived in section 6.3.2, and there is very little meridional structure to the error (Fig. 6.19). The simulated concentrations at the stations on the coast of Antarctica are lower than observed, but the difference is not great enough to allow an Antarctic source as TFT90 did. Perhaps such a source exists in nature but is localized in the coastal waters, or perhaps the CSU GCM transport is too vigorous in that region, allowing the Antarctic tracer to be felt far away from the source area.

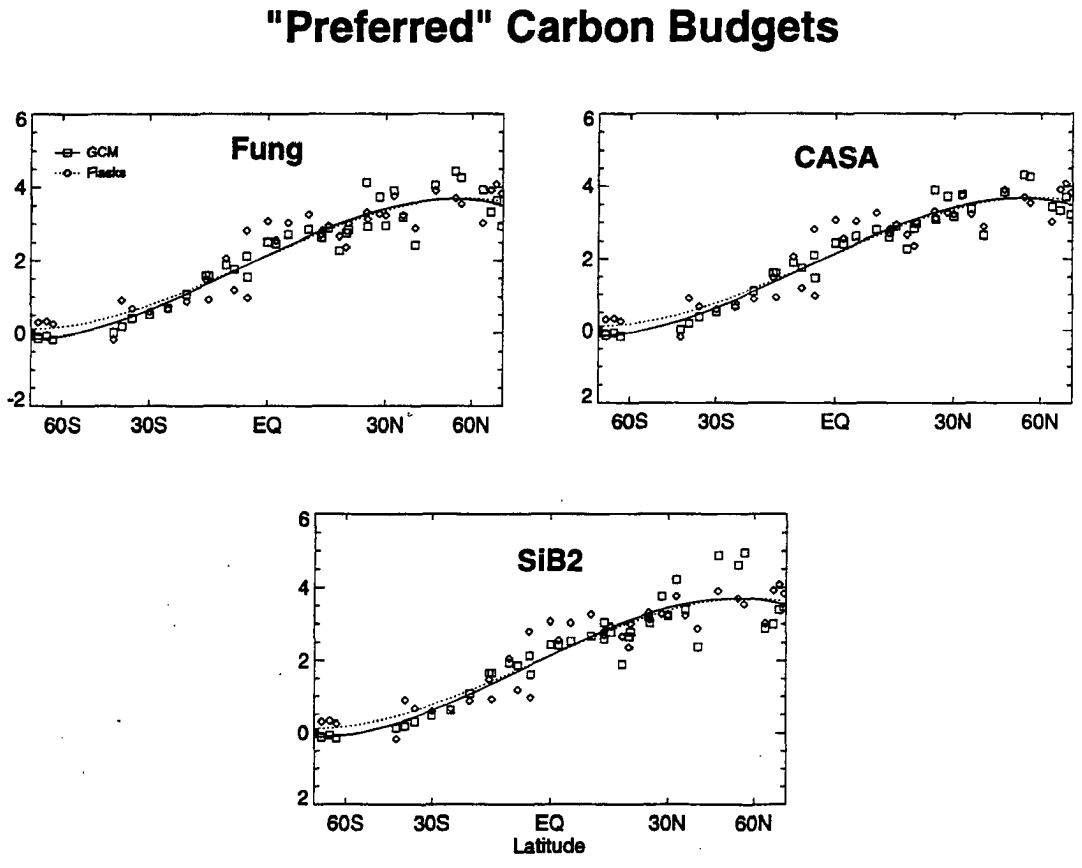

FIGURE 6.22: Simulated and observed CO_2 concentrations (ppm, difference from South Pole) at each of the NOAA flask stations using the "preferred" linear combinations of tracers (Table 6.2) derived from the data. Flask data are plotted as diamonds, and GCM data as squares. The solid curve (representing the GCM data) and the dotted curve (representing the observations) are cubic polynomials of the sine of latitude fitted to the station data.

All three of the budgets presented here invoke global ocean uptake at the high end of the TFT90-estimates of 0.3 to 0.8 Gt C yr^{-1}. This is partly due to the application of the skin temperature "correction" of Robertson and Watson (1992), and partly due to the change in sign of the Antarctic air-sea fluxes. The global ocean sink is still less than the ocean modelers would like to see. Global uptake by the terrestrial biosphere is about 2 Gt C yr^{-1} in all three scenarios, with very little tropical deforestation. Recall that the latter tracer was used to balance the global budget so the value assigned is not particularly meaningful. It is not inconsistent with these results to assume a larger deforestation flux that is partly compensated by tropical terrestrial uptake (by CO_2 fertilization or some other unknown process). The budgets presented here are not very different from the "consensus" view of Houghton *et al.* (1990), except perhaps in the relatively small global ocean sink.

6.4 Summary

The interhemispheric exchange time for the tracer calculations in the standard experiment is in line with that calculated in earlier studies, although perhaps a bit shorter (about 0.9 yr for ^{85}Kr and 0.8 yr for fossil fuel CO_2). This fact, and the time series of interhemispheric tracer gradients show that tracer concentrations in both experiments reached equilibrium with the prescribed surface fluxes quickly. Interhemispheric exchange in the LOWRES experiment was more vigorous, with $\tau = 0.62$ yr for CO_2. This was associated with more rapid tracer transport across the equator by the mean meridional circulation due to the steeper vertical gradient of tracer concentration in the tropics, which was in turn caused by the weaker tropical cumulus convection in the LOWRES than the standard experiment. Shutting off cumulus tracer transport completely in the NOCUTRAN experiment led to even weaker interhemispheric gradients and a shorter exchange time ($\tau = 0.56$ yr). The interhemispheric gradient decays even more rapidly than this, however ($\tau \approx 0.4$ yr) for a simple mixing experiment (2BOX) in which the tracer has no sources or sinks.

Simulated annual mean concentrations of each tracer in the PBL reflect the surface fluxes in the source or sink regions, and impose meridional gradients with nearly zonal isopleths away from the source regions (section 6.2.1). Three somewhat "generic" geographic patterns were defined: 1) tracers with sources in the middle and high latitudes (like fossil fuel CO_2) have relatively steep meridional gradients that are concentrated in

the tropics due to relatively slow interhemispheric exchange, and relatively weak meridional gradients in the hemisphere opposite from the source or sink; 2) tracers with low-latitude sources (like tropical deforestation) have very weak meridional gradients away from the source region because they are transported in nearly equal measure into both the northern and southern hemispheres; and 3) the tracers representing the seasonal exchange of CO_2 between the atmosphere and the terrestrial biosphere (Fung, CASA, and SiB2) have concentration fields that reflect correlations between the intensity of vertical mixing in the source regions and the sign of the surface fluxes. The simulated annual mean meridional gradients in surface concentration of these type 3 tracers is significantly stronger than has been simulated in off-line tracer modeling studies in which a fixed-depth lowest layer is used. This reflects the stronger correlation between surface fluxes and vertical mixing in the CSU GCM due to the inclusion of the variable-depth mixed layer as a lowest model layer.

The classification of the tracers into these three "archetypes" is reinforced by considering the three-dimensional distributions of tracer concentration as expressed by latitude-pressure cross sections of their zonal means (section 6.2.2). Tracer transport inferred from concentration gradients is upward and equatorward in the source region for tracers of the first type (like T_1). Tropical tracer transport is dominated by deep penetrative cumulus convection. Tracers of the second type (like T_2) have distinct midtropospheric minima in concentration because deep convection links the PBL with the upper troposphere. In higher latitudes, transport of tracers like T_2 is poleward in the tropical upper troposphere, which is also the inferred transport mechanism for tracers of type 1 in the hemisphere opposite from their source region. Transport of type 3 tracers (with seasonal sources and sinks) weakens the gradients imposed in the PBL by correlations between surface fluxes and transport, and tends to lead to upper tropospheric minima in all three cases. This reflects the positive correlation at both the seasonal and diurnal time scale between vertical mixing and photosynthesis, as discussed in Chapter 7.

The annual mean concentration of tracer T_{18} (due to carbon exchange with the land surface as calculated on-line by SiB2) shows strong maxima over the tropical forests (Fig. 6.9) that are not simulated for the other tracers. This appears to be an effect produced by the diurnal cycle of photosynthesis and respiration, and has not been simulated in previous studies. Long-term observations of CO_2 concentration are not available on the diurnal timescale over the tropical continents, but such a feature seems reasonable based on an understanding of the diurnal cycle of photosynthesis and boundary layer meteorology. This feature is explored in more detail in section 7.2.

The results of formally calculating the components of the global carbon budget by fitting simulated tracer concentrations to the observed distribution of annual mean CO_2 concentration at the NOAA flask stations are not very useful (section 6.3.2). An excellent degree of agreement can be produced by numerical linear algebra, but strong correlations between the spatial distributions of the simulated tracers lead to strong source/sink pairs that nearly cancel each other at most stations. This is a direct consequence of the "generic" responses of tracer concentrations to the atmospheric transport discussed in section 6.2.

The results of this study are not consistent with the carbon budget scenarios of TFT90 (section 6.3.3). This is partly due to the different observational data set used, and partly to differences in the tracer formulations and of course the model transport. Specifically, the spatial distributions of tracer concentrations in the present study are inconsistent with a spatially extensive CO_2 source in the Antarctic oceans or strong uptake of CO_2 in the temperate forest.

There are too many degrees of freedom in the tracer calculation to arrive at a unique interpretation of the global carbon budget from the results of this experiment. If strong source/sink dipoles of spatially correlated tracers are consciously excluded, balancing the carbon budget and meridional gradient using broadly defined CO_2 fertilization (tracers T_{10} and T_{11}) does not appear to be consistent with the simulated and observed concentrations. Net sequestration of CO_2 in the boreal forest is the most likely candidate for the "missing" carbon sink as derived from the tracers simulated here. A small source of CO_2 in the Arctic is also plausible, and is suggested by the observed concentrations at the highest latitudes. The results of the tracer calculation performed here support a global ocean sink for CO_2 that is at the high end of the range suggested by TFT90 (about 0.8 Gt C yr^{-1}), but is still somewhat lower than the sink proposed by ocean modelers (about 2 Gt C yr^{-1}).

CHAPTER 7

Temporal Variations of Simulated Tracer Concentrations

In this chapter, the temporal variations of the simulated CO_2 are examined, both on the seasonal to annual time scale, and on the diurnal time scale. The global carbon budgets derived in Chapter 6 were obtained by fitting linear combinations of the simulated tracers to the CO_2 concentrations observed at the NOAA flask stations in the annual mean. Therefore all three of the "preferred" budgets derived in section 6.3.4 fit the annual mean flask observations very well, and it is impossible to choose between the three scenarios (using the Fung, CASA, and SiB2 seasonal carbon flux estimates). Seasonal variations provide an "independent test" against the flask data, by which the relative merits of the three scenarios can be evaluated.

Seasonal variations in surface tracer fluxes are in some cases correlated with important features of the atmospheric transport of the tracers. Such correlations lead to features in the annual mean concentration fields that cannot be explained in terms of the annual mean surface fluxes or the annual mean tracer transport alone. Some of these effects are explored in section 7.1.1.

The amplitude of the seasonal cycle of CO_2 is a useful diagnostic with which to evaluate the simulated CO_2 scenarios because it integrates information about the seasonal behavior of the tracers into a single number which can be checked against other data at individual observing stations, along geographic gradients, and in the vertical. The amplitude of the seasonal cycle of each of the three scenarios of total CO_2 is compared to available observational data and previous model results in sections 7.1.2 and 7.1.3.

The seasonal fluxes of CO_2 at the land surface due to the annual growth and decay of biological material was simulated prognostically in SiB2 for the first time in this study. As shown in Chapter 6, some features of the annual mean concentration field produced by SiB2 were notably different the concentrations of other tracers used to simulate the

same processes (T_9 and T_{15}). This is even more true of the seasonal amplitude and phase examined in this chapter. The simulated surface fluxes of CO_2 due to SiB2 are examined in detail in section 7.1.4, and some of the reasons for the differences are explored.

The simulation of surface carbon fluxes in SiB2 fully resolve the diurnal cycle of photosynthesis and respiration, and its correlation with the diurnal cycle of atmospheric phenomena in the planetary boundary layer (PBL). Such a simulation has not been performed on a global scale before. In section 7.2, some of the unique aspects of the diurnal evolution of CO_2 concentration, surface fluxes, and vertical transport and mixing are explored, and compared to the limited observations of these processes in field studies.

7.1 The Seasonal Cycle

7.1.1 Interactions Between Seasonality and Annual Mean Spatial Gradients

As discussed in section 6.2.1, annual mean spatial gradients in tracer concentrations are affected by correlations between atmospheric circulations and surface fluxes of the tracers, even for tracers whose annual net flux is zero at every grid point. Conversely, seasonal variations in concentration can be produced for tracers whose surface fluxes do not vary in time.

It was suggested in section 6.2.1 that high annual mean concentrations of the tracers driven by seasonal exchange of CO_2 between the atmosphere and the terrestrial biosphere were the result of correlations between strong vertical mixing during periods of net CO_2 uptake and weaker vertical mixing during periods of strong net CO_2 release.

To investigate this hypothesis, I calculated correlations between the seasonally varying surface fluxes of each tracer in Fig. 7.3 and two variables which measure vertical transport of the tracers, the depth of the PBL and the flux of mass out of the PBL into cumulus clouds (M_B). Because both cumulus convection and deep turbulent boundary layers are associated with strong solar heating (at least over land), these two variables tend

to have higher values during the summer, when photosynthesis dominates over respiration and CO_2 is sequestered on the land surface. Fig. 7.1 shows the product of these two correlation coefficients, calculated from the multiyear monthly mean values of each variable at all land grid points.

For the tracers with purely seasonal surface fluxes (T_9 and T_{15}) there is a strong spatial relationship between these correlation coefficients and the annual mean tracer concentrations displayed in Fig. 6.9. The regions in which fluxes and both indices of vertical mixing (PBL depth and M_B) are strongly *negatively* correlated have a strong *positive* value of the product of the correlation coefficients. In these regions CO_2 depleted air is rapidly mixed in the vertical but CO_2 enriched air is held close to the ground, resulting in strong regional concentration maxima in the annual mean (Fig. 6.9). The predictive strength of the product of the correlations shown in Fig. 7.1 is not perfect, of course, because of other factors such as horizontal transport by the winds. The correlation is more effective in Eurasia than in North America, for example, possibly because of the longer "fetch" which provides for longer contact between air masses and the biosphere in Eurasia.

Seasonal correlations between surface fluxes and vertical mixing are much less useful in explaining the spatial distribution of the annual mean concentration of tracer T_{18} (due to the on-line CO_2 flux in SiB2). Western Europe and the southeastern United States appear as "hot spots" in both concentration and seasonal correlations, but in other areas the relationship breaks down. Most notably, the tropical rainforests are areas of very high annual mean concentration, but have weak or negative values of the product of the correlation coefficients in Fig. 7.1. Other regions in which surface fluxes and vertical mixing are weakly or positively correlated but which appear as concentration maxima are western Canada and eastern Asia.

The failure of the simple statistical index presented in Fig. 7.1 to predict the basic features of the spatial distribution of tracer T_{18} in the PBL highlights the difference between this tracer and the others representing seasonal exchange with the terrestrial biosphere. It was suggested in section 6.2 that *diurnal* correlations between tracer fluxes and vertical mixing might be important for this tracer. The results presented here support that hypothesis in that the spatial patterns are not easily explained in terms of seasonal correlations. This hypothesis will be further examined in terms of hourly tracer concentrations and transport processes in section 7.2.

Correlations Between Fluxes and Vertical Mixing

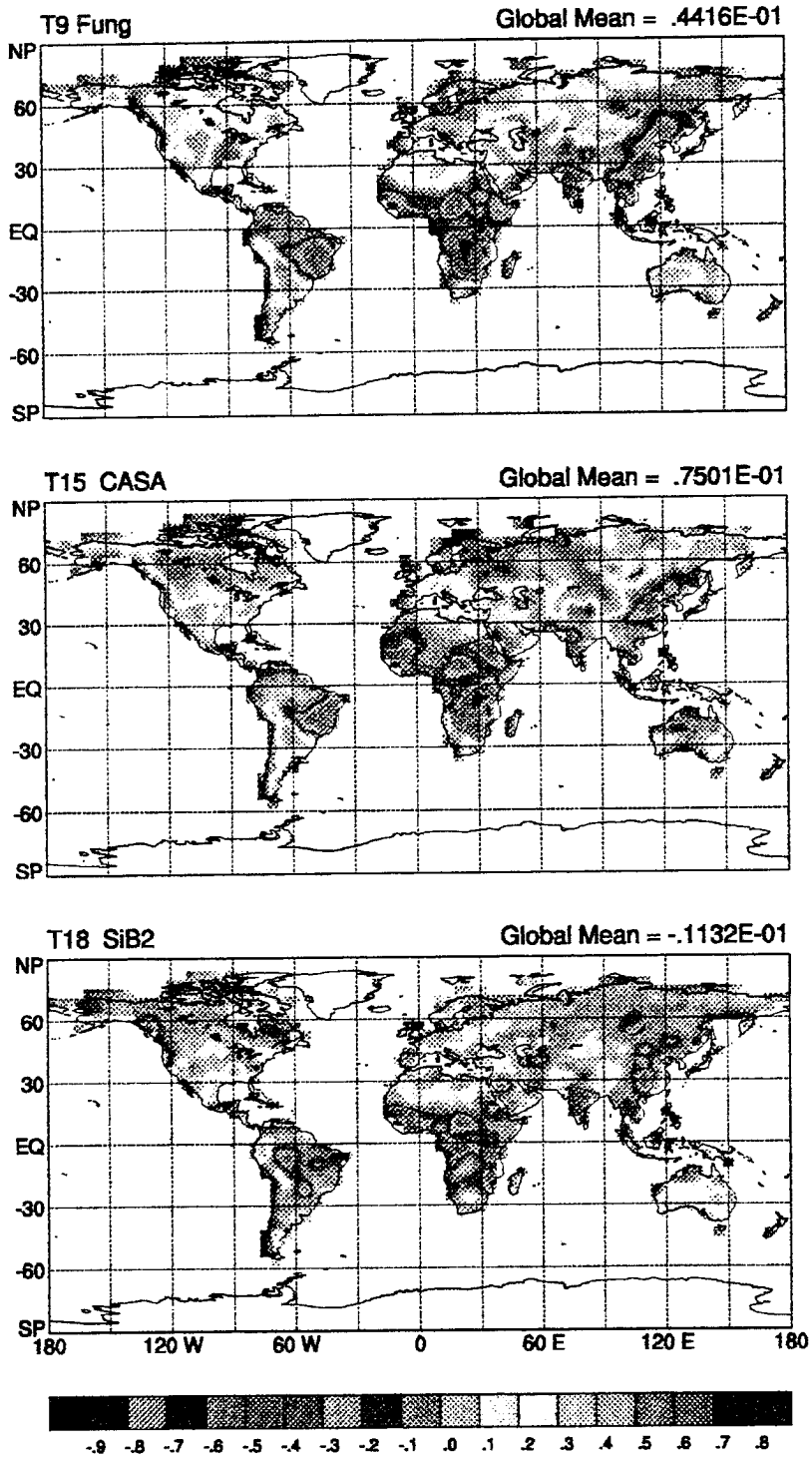

FIGURE 7.1: Product of the correlation coefficient between monthly mean surface CO_2 flux from the terrestrial biosphere and PBL depth and between CO_2 flux and cumulus mass flux M_B at each land grid cell. The contour interval is 0.1

7.1.2 Amplitude of the Seasonal Cycle

The amplitude of the seasonal cycle could be defined in a number of ways. One might simply take the amplitude of the annual harmonic of concentration as the amplitude. Previous studies, however, have used the "peak-to-peak" amplitude of some fit of the time series of concentration using numeric filtering techniques (Fung, *et al.*, 1983; Heimann *et al.*, 1986; Keeling *et al.*, 1989*a*). For computational convenience, and to maintain comparability with these previous studies I have chosen to define the amplitude of the seasonal cycle as the difference between the maximum and minimum concentration of monthly mean CO_2 over the course of a year.

7.1.2.1 Seasonal Amplitude in the PBL

The prescribed surface fluxes of tracer T_1 (due to fossil fuel emissions) were not seasonal (see section 3.4.1). Nevertheless, simulated surface (PBL) concentrations of this tracer underwent a strong seasonal oscillation in many regions of the world (Fig. 7.2).

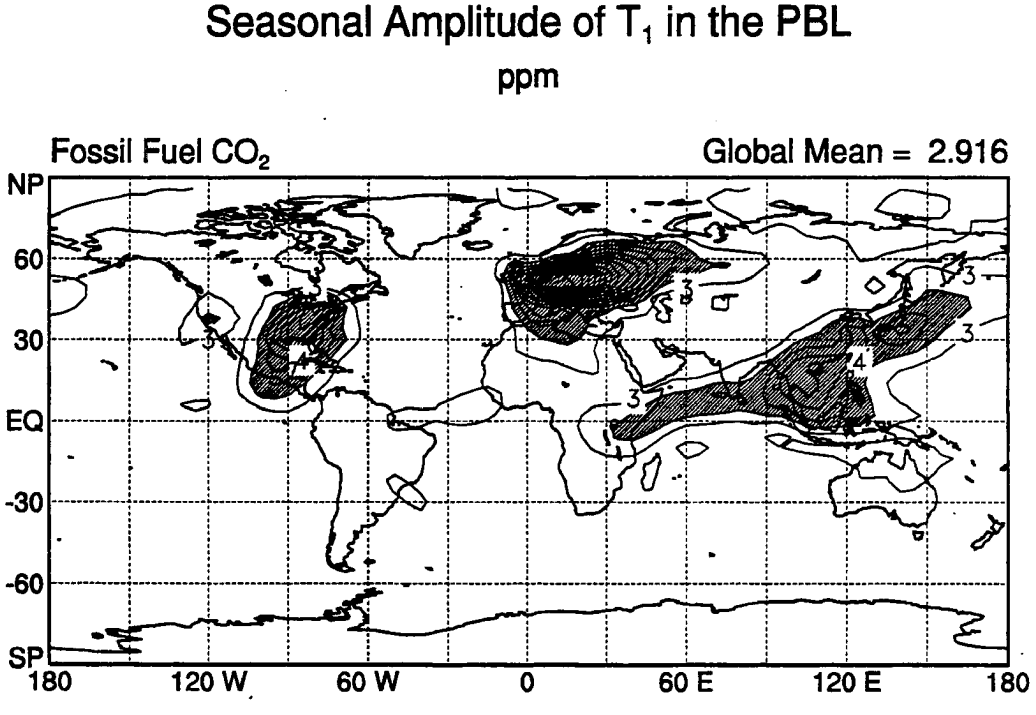

FIGURE 7.2: Peak-to-peak amplitude (ppm) of the seasonal cycle of tracer T_1 in the PBL in the standard experiment. Contour interval is 0.5 ppm. Shaded areas indicate regions of greater than 3.5 ppm seasonal amplitude.

Seasonality is most pronounced in the emission regions, but a broad secondary maximum in seasonal amplitude is also noted in the tropics of the Eastern Hemisphere. The source region maxima are associated with strongly seasonal vertical transport processes in the GCM. During summer months, the constant fossil fuel flux is applied (on average) to a deeper and more convective PBL than in winter, so its influence on the PBL concentration is "diluted." This pattern is also prevalent in the other tracers with middle and high latitude sources (the ocean tracers and the biome-specific "missing sink" tracers), although for brevity these distributions are not shown here. In general, the higher the latitude of the source region of a tracer, the stronger the seasonal amplitude in concentration of that tracer. Thus the tundra sink (T_{14}) and subarctic Atlantic ocean (T_3) had the strongest seasonal amplitude, and the tropical tracers like T_2 and T_6 had almost no seasonal amplitude in their source regions.

The secondary maximum in seasonal amplitude in the eastern tropics is due to the seasonally-reversing (monsoon) winds in that region which tend to transport tracers across a strong concentration gradient. This pattern was apparent in all tracer that have a strong meridional gradient in the tropics (which is the case for all but the tracers with tropical sources). In the northern summer, the monsoon winds blow *up* the concentration gradient, bringing southern hemisphere air with lower concentration into the Indian Ocean region. In the northern winter, the circulation reverses and the winds carry high-concentration northern air into the southern hemisphere, leading to higher concentrations in the region.

By far the largest seasonal amplitudes simulated in the PBL were for tracers with strongly seasonally varying surface fluxes. Fig. 7.3 shows the amplitude of the simulated seasonal cycle of tracers T_9, T_{15}, and T_{18}, representing the seasonal exchange with the terrestrial biosphere according to the estimates of Fung *et al.* (1987), the CASA model, and SiB2, respectively. All show strong maxima in the regions of strongly seasonal surface fluxes (see section 3.4.4), as expected. The CASA tracer exhibits much weaker seasonal amplitude over the deep continental interiors than either of the other two tracers. The spatial pattern of the seasonal amplitude of tracers T_9 and T_{15} is very similar to that of the annual mean concentrations of these tracers because of the seasonal correlations between fluxes and transport discussed in section Fig. 7.1.1.

The seasonal amplitude of the total CO_2 (Fig. 7.4) as simulated in the three "preferred" scenarios derived in section 6.3.4 is so dominated by the seasonality of the terrestrial biosphere that the maps in Fig. 7.4 are almost identical to those in Fig. 7.3. The

Seasonal Amplitude (ppm)

Seasonal Terrestrial Biosphere

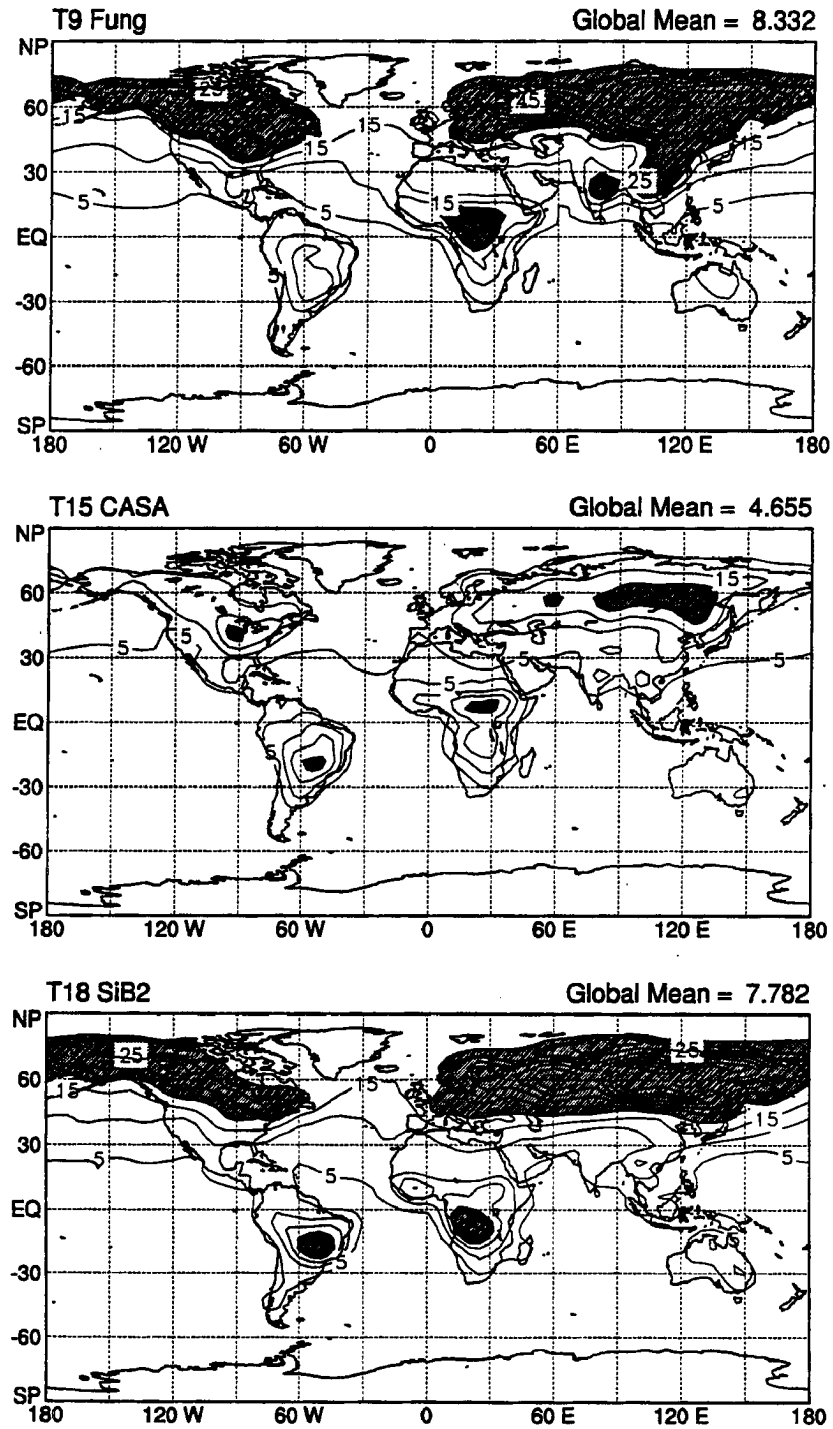

FIGURE 7.3: Peak-to-peak amplitude (ppm) of the seasonal cycle of tracers T_9, T_{15}, and T_{18} in the PBL in the standard experiment. Contour interval in all three panels is 5 ppm. Shaded areas indicate regions of greater than 20 ppm seasonal amplitude.

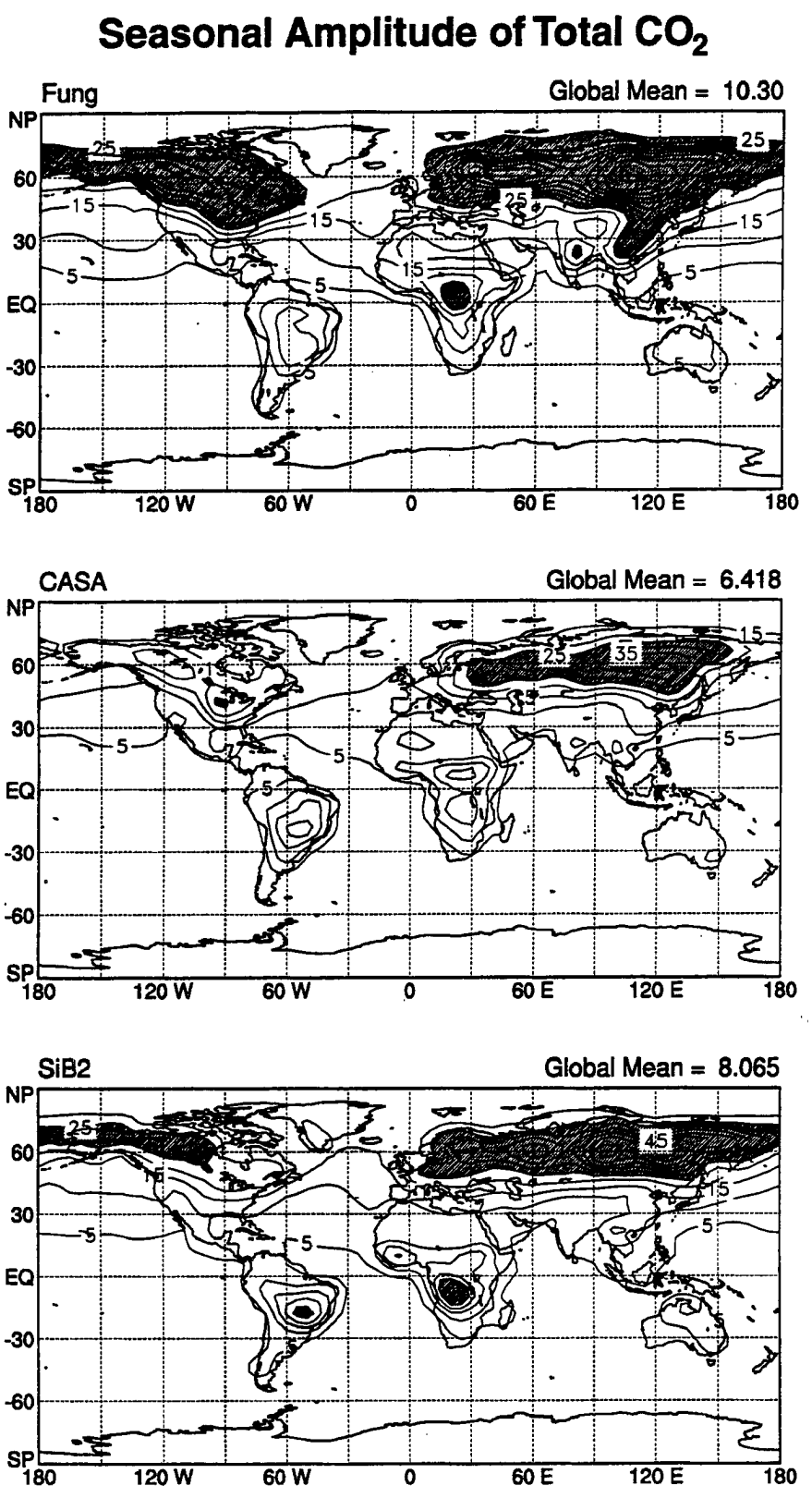

FIGURE 7.4: Peak-to-peak amplitude (ppm) of seasonal variations of total CO_2 in the PBL as simulated by the three "preferred" scenarios derived in section 6.3.4. The contour interval in all three panels is 5 ppm. Areas with greater than 25 ppm seasonal amplitude are shaded.

additional seasonal signal associated with the "missing sink" tracers (T_{13} and T_{14}) and the northern ocean tracers increases the total amplitude in all three scenarios. The maximum amplitude in all three scenarios is over the boreal region of Asia, with values greater than 65 ppm in the Fung scenario, 41 ppm in the CASA scenario, and 55 ppm in the SiB2 scenario.

The simulated seasonal amplitude is much greater over the continental interiors than has been simulated in previous simulations (Fung *et al.*, 1983; Heimann *et al.*, 1986; Fung *et al.*, 1987; Heimann and Keeling, Heimann *et al.*, 1989). Using exactly the same representation of the seasonal exchange with the terrestrial biosphere as tracer T_9 in the present study, Fung *et al.* (1987) obtained amplitudes that were at least a factor of two lower (Fig. 7.5) than those obtained for my tracer T_9. Away from the continents, the am-

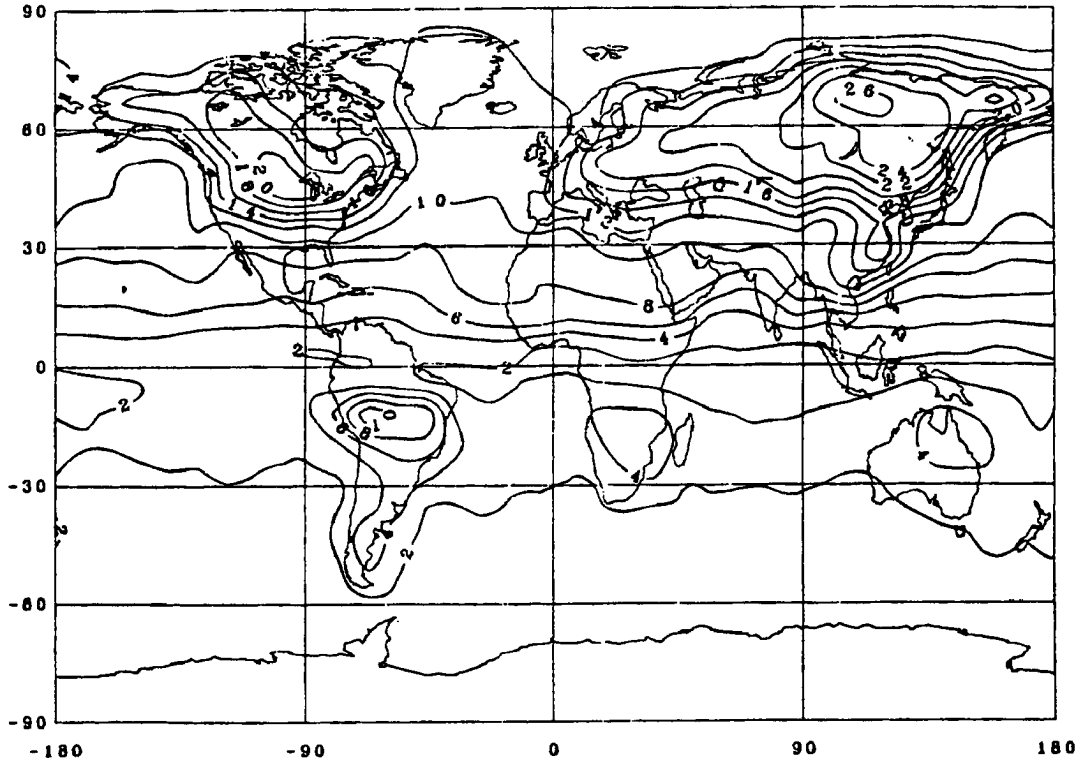

FIGURE 7.5: Peak-to-peak amplitude (ppm) of the seasonal cycle of total CO_2 as simulated by Fung *et al.* (1987). The contour interval is 2 ppm.

plitudes simulated in the present study are quite similar to those of previous studies. Since the NOAA flask stations are intentionally located far from the terrestrial source ar-

eas, they provide little guidance regarding the much stronger continental values obtained here.

The most likely reason for the stronger seasonal amplitude in the present study is the use of a bulk boundary layer parameterization in the CSU GCM. The GISS tracer model has no explicit representation of the PBL, but instead uses layers of constant "sigma" thickness – that is, the layers occupy a constant fraction of the mass above each grid point in the model atmosphere. The lowest layer in the GISS model (as used by Heimann and Keeling, 1989) consists of the lowest 5% of the atmosphere, or about 50 mb. By contrast, the lowest layer in the CSU GCM varies in depth from 10 mb in very stable conditions to about 175 mb in very turbulent conditions. When the PBL is thick, the surface fluxes of the tracers are diluted into a greater mass of air than when it is thin. Lacking this physical process, the GISS model applies the surface fluxes to a lowest layer that is nearly constant in mass. Seasonality in the simulated tracers is therefore driven only by correlations between surface fluxes and cumulus convection and horizontal winds, and is correspondingly weaker than in the CSU GCM.

7.1.2.2 Vertical Structure of Seasonal Amplitude

Above the PBL, the amplitude of the seasonal cycle of CO_2 concentration decreases rapidly as parcels of CO_2-depleted air mix with parcels of CO_2 enhanced air and vice versa. At 500 mb, the amplitude maps (not shown here) look like "zonally smeared" versions of the ones in Fig. 7.4, with very little variation around a latitude circle. A strong meridional gradient is present, with much higher seasonal amplitudes north of about 30° N than elsewhere. The amplitudes in the Fung and SiB2 scenarios are very similar, and the amplitude produced in the CASA scenario is weaker over the northern continents.

Fig. 7.6 shows the ratio of 500 mb amplitude to PBL amplitude for the three preferred scenarios. Over the northern continents, the amplitude is attenuated by a factor of 3 to 4 from the highest values in the PBL in all three scenarios due to the mixing effects of the atmosphere. Over much of the southern hemisphere, the amplitude is greater at 500 mb than at the surface, as was also found by Fung *et al.* (1987) and by Heimann and Keeling (1989) (Fig. 7.6). This probably indicates that the seasonal cycle in the lower and middle southern latitudes is "imposed from above" rather than locally derived, and is dominated by the seasonal signal from the northern biota which is advected into the southern hemisphere via deep tropical convection as discussed in section 6.2.2.

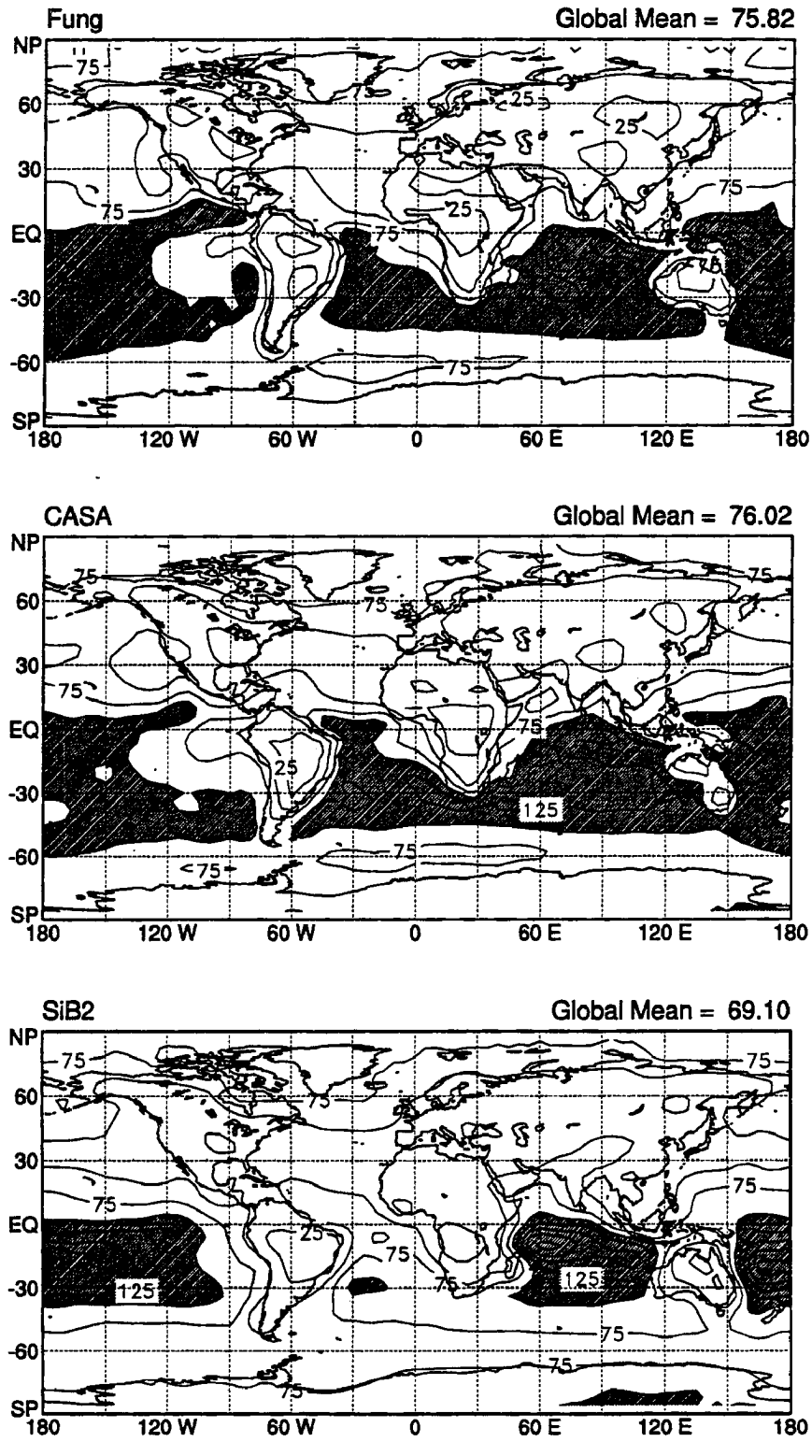

FIGURE 7.6: Ratio of seasonal amplitude of total simulated CO_2 at 500 mb to the amplitude in the PBL for the three preferred scenarios (percent). The contour interval is 25%, and areas with the ratio greater than 100% are shaded.

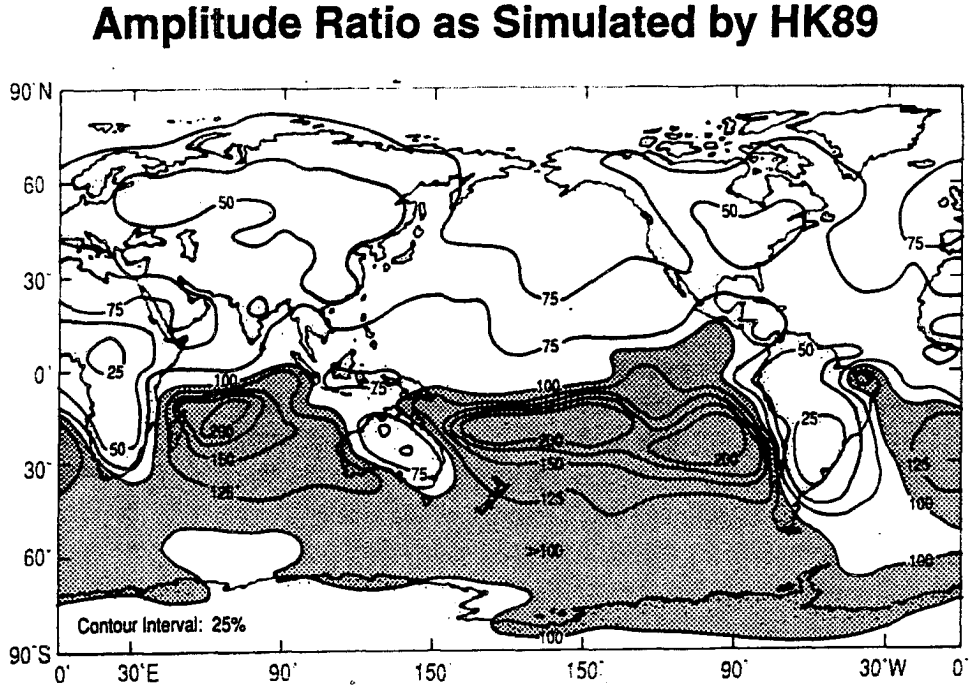

FIGURE 7.7: Ratio of seasonal amplitude of total simulated CO_2 at 500 mb to the amplitude in the lowest model layer (percent) as simulated by Heimann and Keeling (1989). The contour interval is 25%, and areas with the ratio greater than 100% are shaded. Compare to Fig. 7.6.

The spatial patterns of seasonal amplitude in the upper troposphere bear less resemblance to those at the surface (Fig. 7.8). At 200 mb, the major source of seasonal variation in CO_2 concentration is the correlation between surface concentrations and the occurrence of deep cumulus convection. Although all the scenarios considered here share the same cumulus activity, differences in the timing of their seasonal maxima and minima over various regions lead to very different spatial patterns in seasonal amplitude at this level. Unlike the situation in the lower and middle troposphere, at 200 mb the CASA and SiB2 scenarios produce very similar patterns and it is the Fung scenario that is the outlier. All three have regional amplitude maxima over and downwind from the major centers of convective activity in Africa and South America where seasonal rains drive a strong seasonal cycle in terrestrial CO_2 flux. Although deep convection is also very intense over the "warm pool" region of the western Pacific Ocean, the seasonal amplitude of CO_2 in the PBL is weak there so it has little effect on the seasonal cycle aloft. In the Fung scenario, the largest amplitudes are over southeast Asia, and trail northeastward from there into the band of westerly winds associated with the northern hemisphere jet stream. This feature is probably due to a strong drawdown of surface CO_2 over the region during the Indian monsoon in the Fung flux estimates, which is applied during the period

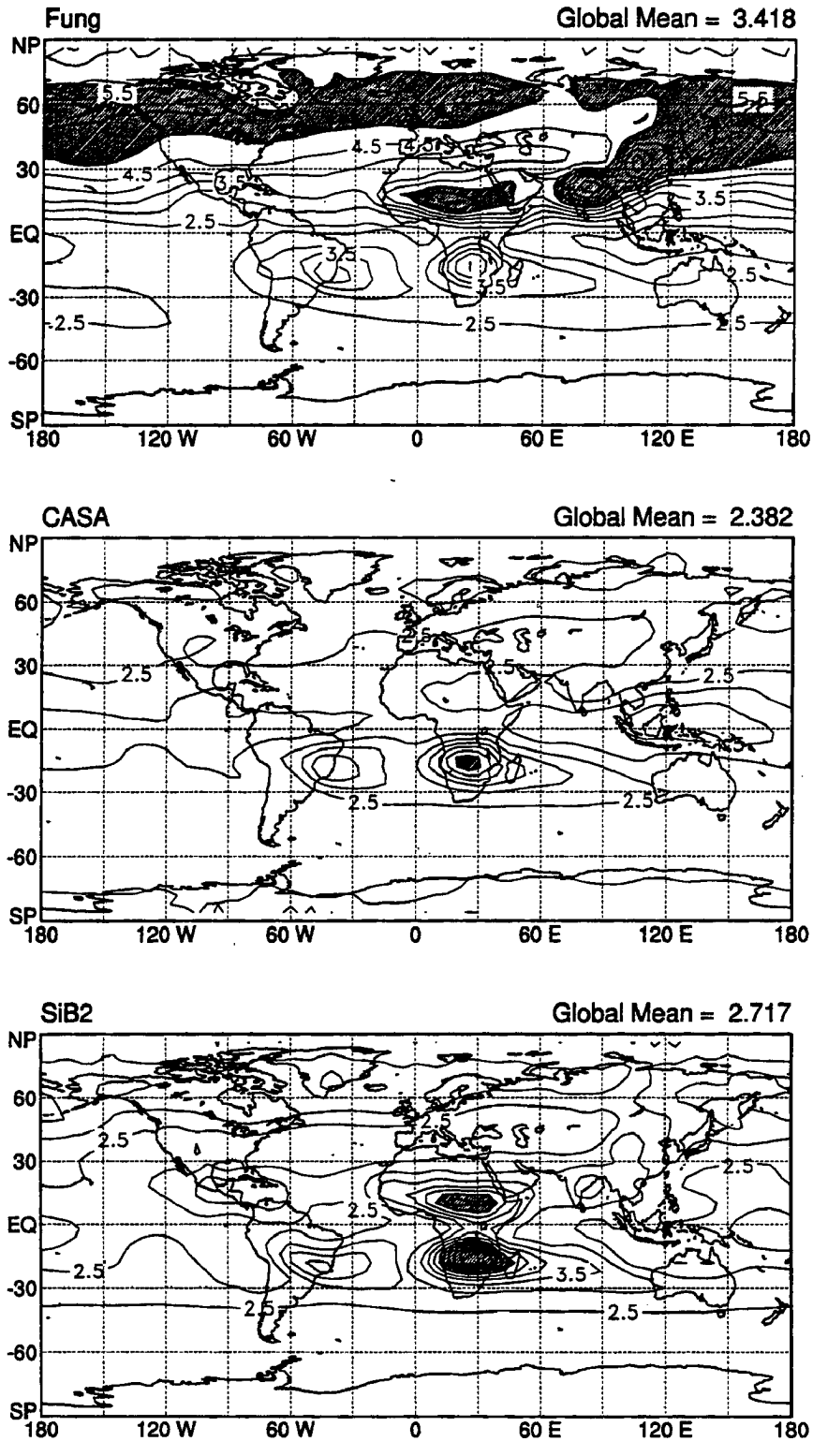

FIGURE 7.8: Peak-to-peak seasonal amplitude (ppm) of total CO_2 at 200 mb as simulated in the three preferred scenarios. The contour interval is 0.5 ppm, and areas with amplitude greater than 5 ppm are shaded.

of most vigorous convective activity. The other two tracers also experience a monsoon season drawdown of surface CO_2, but it is less intense and not as well correlated with the convection.

The variation of amplitude with height integrates information about both the surface fluxes and the model transport of the tracers, so it would be useful to compare the maps presented in the previous several figures with observations. Unfortunately few studies have documented the seasonal variation of CO_2 at high altitude. Bolin and Bischof (1970) analyzed samples collected by commercial aircraft in the 1960's over Scandinavia, and found that the seasonal amplitude decreased from about 6.5 ppm at 2 km to about 3.5 ppm in the upper troposphere, and that the phase of the seasonal cycle at the tropopause lagged that in the lower troposphere by about a month. The amplitude in the lower troposphere as simulated by the CSU GCM is quite variable, depending on the proximity of surface source areas, but in many areas exceeds the 6.5 ppm cited by Bolin and Bischof (1970). In the upper troposphere at 60° N the much more zonally uniform simulated amplitude is about 3 ppm as simulated by the CSU GCM for the CASA and SiB2 scenarios, and about 6 ppm as simulated in the Fung scenario.

Pearman and Beardsmore (1984) conducted an aircraft sampling program over Australia and found that the seasonal amplitude increased with height from about 1.2 ppm in the middle troposphere to about 2 to 3 ppm in the upper troposphere, with the upper level phase leading rather than lagging. This is qualitatively consistent with the results presented above, although in all three scenarios the amplitude at 500 mb over Australia is over 1.7 ppm.

Nakazawa *et al.* (1991) reported on the seasonal cycle of atmospheric CO_2 in the upper troposphere and lower stratosphere at many latitudes over the Pacific, based on samples collected by commercial airliners. They found that the amplitude decreased from about 7 ppm at 36° N to about 2.5 ppm at 30° S across the western Pacific. Only the Fung scenario simulated by the CSU GCM shows anywhere near this much meridional structure at 200 mb in that region. Both the SiB2 and CASA scenarios exhibit an amplitude of about 3 ppm over Japan and 2.5 ppm over southeast Australia, with a minimum of about 1.7 ppm for SiB and 1.4 ppm for CASA over the warm pool region.

Tanaka *et al.* (1987) collected air samples over Japan from 1979 – 1985, and presented mean seasonal cycles for several height intervals. Their results are compared with the three preferred scenarios from the present study in Fig. 7.9 and Table 7.1. They represent-

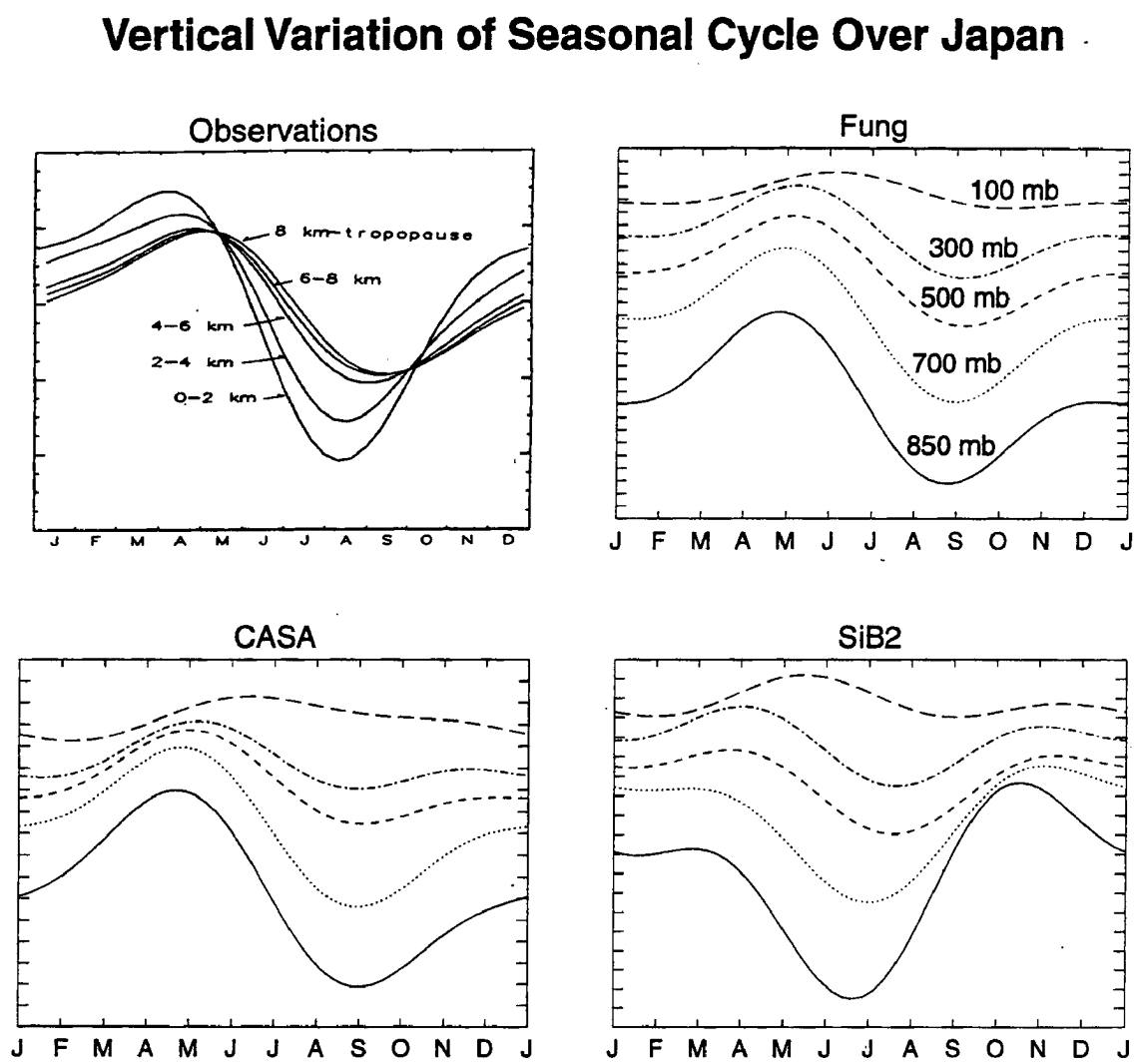

FIGURE 7.9: Monthly variations of the first two harmonics of the seasonal cycle over Japan as observed by Tanaka *et al.* (1987) and as simulated by the three "preferred" scenarios. The tick marks on the ordinate are 1 ppm in all four panels. Month tick marks correspond to the middle of each month for the simulated CO_2, but to the beginning of the month for the observations.

ed the seasonal cycle in terms of just the annual and semiannual Fourier harmonics; for comparison with their results, I have done the same with the last three years of monthly means from the standard experiment in preparing Fig. 7.9 and Table 7.1. Tanaka *et al.* grouped their aircraft samples into five height intervals. For comparison, I have used the constant pressure levels at 850, 700, 500, and 300 mb in the CSU GCM diagnostic output for the single grid cell representing central Japan. During every month included in this analysis, the simulated geopotential height of these pressure levels fell within the height intervals used by Tanaka *et al.* GCM diagnostic output was not saved at 400 mb,

so no data are available for comparison with the observations between 6 and 8 km. The 100 mb level is presented for the GCM data as well, although Tanaka *et al.* show only tropospheric data.

Table 7.1: Seasonal Amplitude (ppm) of CO_2 Over Japan

Height Interval (km)	Pressure Level (mb)	Tanaka *et al.*	GCM Scenario		
			Fung	CASA	SiB2
—	100	—	2.8	2.0	2.2
8 – trop	300	7.6	7.2	3.1	4.1
6 – 8	—	7.6	—	—	—
4 – 6	500	8.0	8.6	4.3	4.3
2 – 4	700	11.0	12.0	7.3	7.0
0 – 2	850	14.5	13.5	9.1	11.2

The aircraft observations show the amplitude of the seasonal cycle of CO_2 decreasing from 14.5 ppm to 7.6 ppm through the depth of the troposphere, with most of the change occurring below about 500 mb. Of the three scenarios tested, the one using the Fung *et al.* fluxes best agrees with these data. None of the three scenarios of simulated CO_2 has amplitudes as high as those of Tanaka *et al.* (1987) at 850 mb, but all three have much higher amplitudes in the PBL (greater than 80 ppm in all three scenarios). Of the three cases, the decrease of amplitude with height is greatest for SiB2 (slightly steeper than observed), and least for Fung (slightly less steep than observed). All three cases simulate a much weaker amplitude in the "stratosphere" at 100 mb. Both the CASA and SiB2 scenarios significantly underestimate the seasonal amplitude in the upper troposphere.

In the observational data, the phase of the seasonal cycle (defined here as the time of minimum CO_2 concentration) lags the phase at the surface by an amount that increases with height to a little over a month in the upper troposphere. The Fung and CASA scenarios do not exhibit such a lag in the troposphere, but the SiB2 scenario does, with the time of minimum CO_2 increasing from about July 1 to about August 1 between 850 and 300 mb. At 100 mb, the shape of the seasonal oscillation is quite different for all three tracers than it is in the troposphere, and is apparently a number of months behind.

The seasonal cycle in the aircraft oscillations is characterized by slowly rising concentrations in the springtime leading to an annual maximum in April, followed by rapidly decreasing concentrations leading to an annual minimum in August and then rapid recovery through the fall. The CASA and Fung scenarios follow this basic pattern well, although their autumn increases are less steep and they have to make up the difference with a stronger springtime peak. The summer minimum in both cases is about a month later than observed. The SiB2 pattern is distinct from the rest however. It lacks a significant springtime peak below about 300 mb, and instead shows maximum concentrations in the autumn in the lower troposphere. The summertime minimum as simulated in the SiB2 scenarios is almost six weeks earlier than in the observations, and about 10 weeks earlier than the other two simulated cases. The reasons for these differences will be explored in section 7.1.4, but at any rate are difficult to understand from the perspective of the single gridpoint analyzed here.

7.1.3 Seasonal Variations of Simulated and Observed CO_2 at the NOAA Flask Stations

Using the monthly mean concentration data at the NOAA flask stations derived for an "average" year in Chapter 4, I subtracted the observed CO_2 concentrations from the total simulated CO_2 using the three "preferred" scenarios of the global carbon budget derived in Chapter 6. Fig. 7.10 shows the difference between the simulated and observed CO_2 at all 40 flask stations, as a function of latitude and month of the year, along with the overall root mean square error for each budget scenario (summed over 40 stations and 12 monthly means for a total of 480 simulated concentrations).

The Fung and CASA scenarios look qualitatively similar in this analysis, while the SiB2 simulation is quite different. Both the Fung and CASA scenarios tend to underestimate the growing season drawdown of CO_2 in the high northern latitudes by several ppm, and to systematically underestimate the CO_2 concentration at high latitudes in fall and winter. Of the three scenarios tested, the one using the CASA model fluxes fits the observations a bit better than the others, with the early northern growing season captured rather well, and with an r.m.s. error of less than 1.7 ppm. All three scenarios agree quite well

Simulated minus Observed CO_2 at Flask Stations

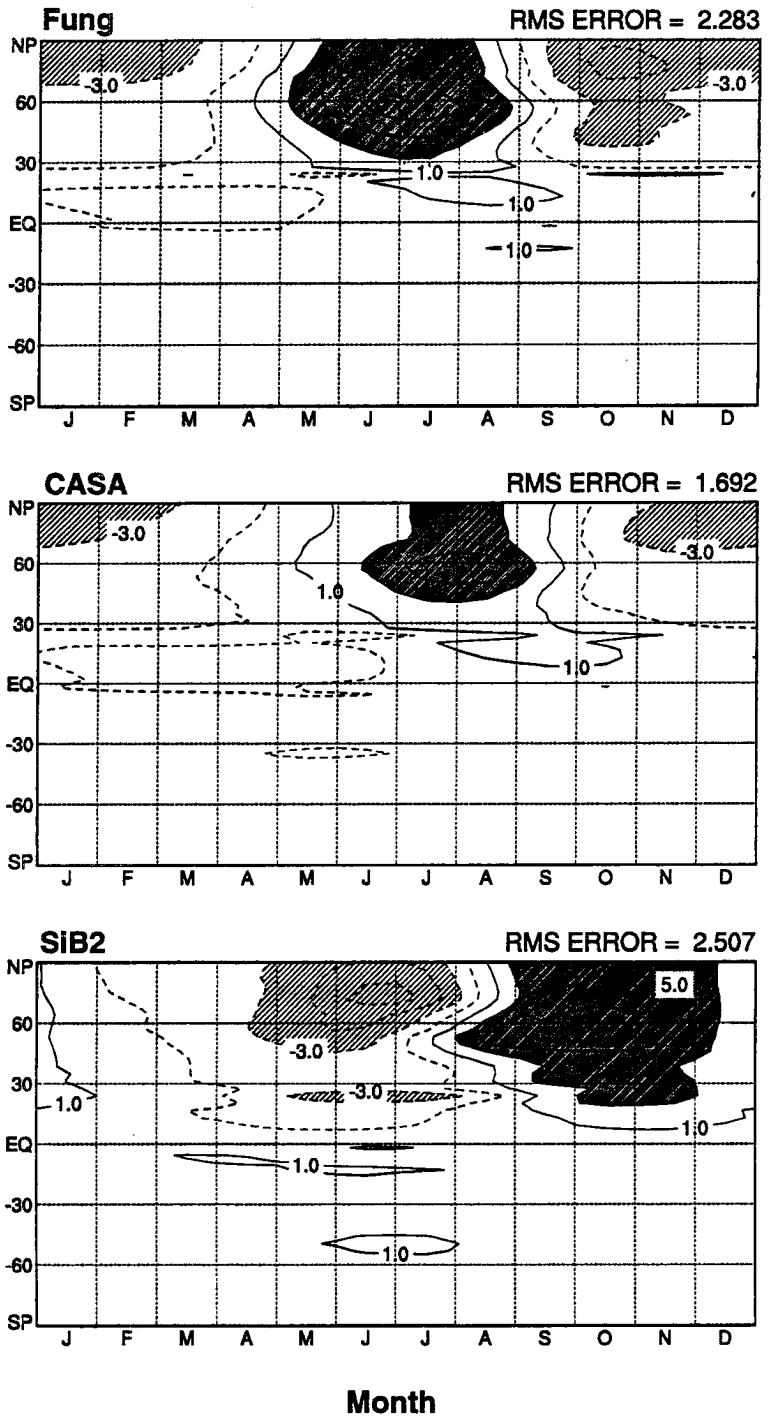

FIGURE 7.10: Comparison of the simulated to observed total CO_2 at the NOAA flask stations using the three "preferred" global budgets derived in Chapter 6. The abscissae are the time of year, and the ordinates are latitude. Smoothed contours of concentration difference are drawn every 2 ppm, and areas above 3 ppm and below -3 ppm are indicated with dark and light shading, respectively.

with the observations at the tropical and southern hemisphere flask stations, but this is not surprising given that the seasonal amplitude is much smaller there.

Unlike the Fung and CASA scenarios, the simulated CO_2 concentration using the SiB2 scenario is less than observed during the northern growing season, and considerably higher than observed in the northern autumn. This suggests an overly vigorous terrestrial exchange of CO_2, or perhaps enhanced horizontal transport of the seasonal signal from the continental interiors to the (mostly mid-ocean) flask stations.

The similarity of the Fung and CASA scenarios (and the fact that the northern seasonal cycle appears to be underestimated in both) is a little surprising given the disparity between the spatial patterns of simulated seasonal amplitude of these two tracers shown in Fig. 7.3. This is because the most prominent areas of difference between the seasonal behavior of these tracers is in the deep continental interiors, which are consciously avoided in selecting flask observation stations which need to be "regionally representative." The fact that very different formulations of tracer fluxes can produce huge differences in simulated concentrations but a similar pattern at the flask stations was noted by TFT90 as a major limitation in our ability to constrain the global carbon budget by using these data, and is emphasized by the results presented here.

More insight into the seasonal behavior of the simulated CO_2 can be obtained by considering the monthly values at individual stations. I selected six flask stations spanning the meridional range of the data, and present the monthly simulated and observed concentrations using each of the budgets in Figs. 7.11 – 7.13. These data were derived from the results of years 2 through 4 of the standard experiment. The concentrations of total simulated CO_2 at each station were set equal to the observed concentrations in January, and then allowed to evolve separately, so that differences in the plots include both seasonal effects and the secular trend.

All three scenarios do rather well at simulating the seasonal variations at the southern hemisphere stations (SPO, CGO), although there is a tendency to underestimate wintertime concentrations there using the CASA and SiB2 data. Since all three scenarios use very similar fluxes for the southern hemisphere oceans, the likely cause of this discrepancy is an insufficiently strong simulated tracer transport into the deep southern hemisphere. This is intriguing, because the interhemispheric mixing of the tracers is a little *too* strong as measured by concentration gradients of ^{85}Kr (see section 5.3). Since the phenomenon is seasonal (the concentrations recover by the following spring), it may sim-

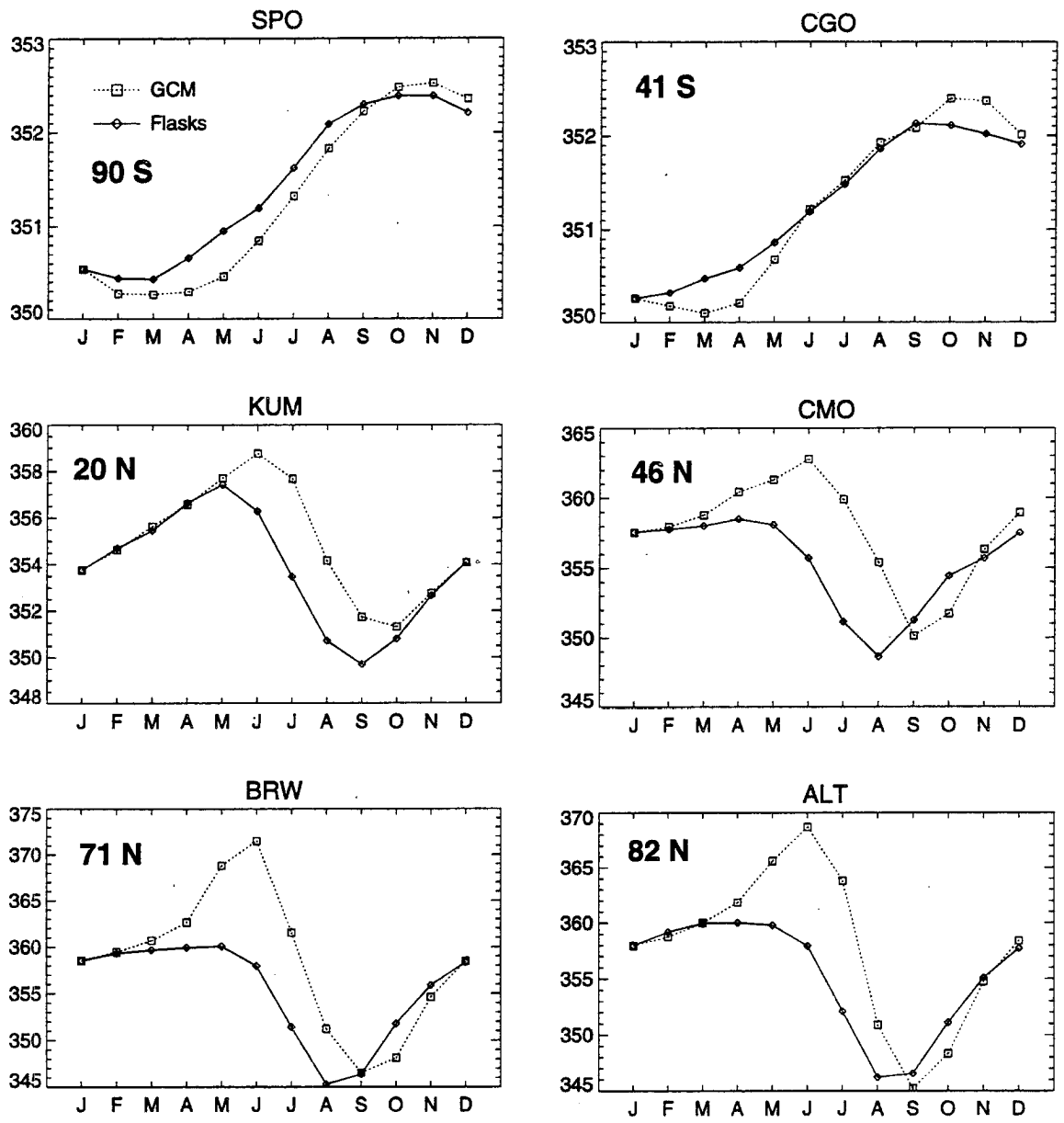

FIGURE 7.11: Monthly mean concentration at six NOAA flask stations for an "average" year as simulated by the CSU GCM using the Fung seasonal biosphere (squares and dashed lines) and as derived from the observational data (diamonds and solid lines). The simulated and observed concentrations at each station have been set equal to one another in January.

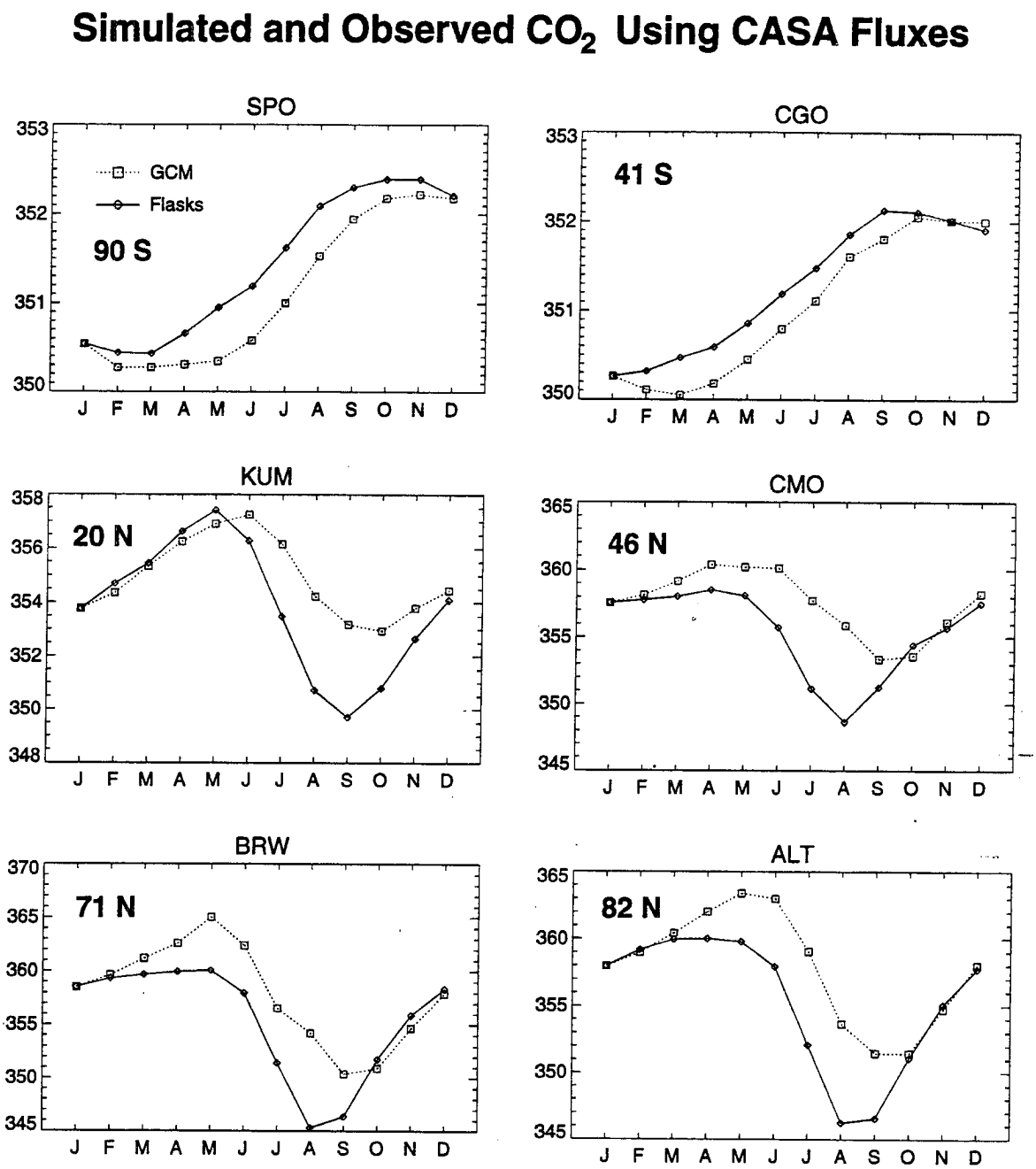

FIGURE 7.12: Monthly mean concentration at six NOAA flask stations for an "average" year as simulated by the CSU GCM using the CASA seasonal biosphere (squares and dashed lines) and as derived from the observational data (diamonds and solid lines). The simulated and observed concentrations at each station have been set equal to one another in January.

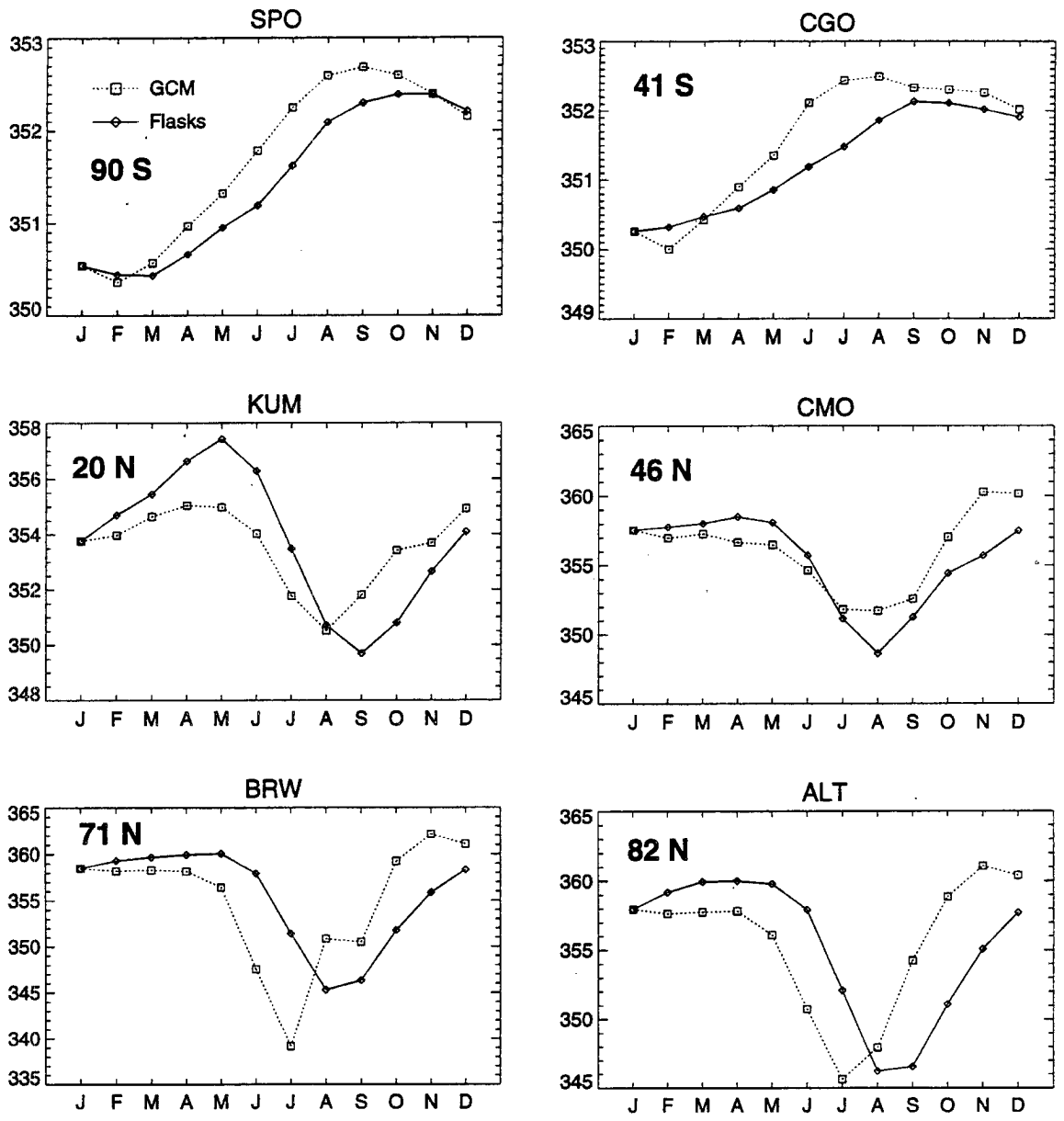

FIGURE 7.13: Monthly mean concentration at six NOAA flask stations for an "average" year as simulated by the CSU GCM using the SiB2 seasonal biosphere (squares and dashed lines) and as derived from the observational data (diamonds and solid lines). The simulated and observed concentrations at each station have been set equal to one another in January.

ply be a result of overly strong seasonal transport in the tropics that influences tracer concentrations several months later in the high southern latitudes.

In the northern hemisphere, the Fung scenario develops erroneously high concentrations in the spring, and concentrations remain too high throughout the growing season. This problem is evident even at the low latitude of KUM, and increases with latitude. Thus although the latitude-time distribution suggested that the growing season drawdown of CO_2 was being underestimated in this scenario, these data suggest rather that release of CO_2 by respiration in the spring may be at fault. This is consistent with the surface flux maps of the Fung *et al.* (1987) tracer presented in Figs. 3.8 – 3.8, which show a substantial amount of net respiration from the temperate and boreal regions in April through June. Over much of the boreal forest region, net release by the land biosphere is higher in May as estimated by Fung *et al.* (1987) than during any other month. The depth of growing season drawdown as simulated by the Fung scenario is actually greater than observed at the flask stations, but because it starts from a higher springtime value, the summer concentrations are overestimated.

The simulated CO_2 at northern hemisphere flask stations also becomes too high in the CASA scenario at the beginning of the growing season, although the problem is not as pronounced as in the Fung scenario. The CASA model also produces a net release of CO_2 from the boreal forest during the springtime, although the magnitude of the flux is quite a bit weaker. At the lower and middle northern latitudes of KUM and CMO, the CASA scenario agrees well with the flask observations until May, but the simulated concentration at the highest latitude stations (BRW, ALT) starts to diverge from the flask curves in April. The depth of growing season drawdown is a bit weaker than observed for these stations in this scenario, and considerably weaker than in the Fung scenario, but because the erroneous springtime peak is also weaker, the agreement is better during the summer months.

The seasonal cycle at these six stations as simulated in the SiB2 scenario is quite different from the other two scenarios considered here. Whereas the Fung and CASA scenarios brought the annual increase in CO_2 to the deep southern hemisphere too late in the year, SiB2 brings it in too early. This probably reflects differences in the seasonal fluxes from the southern hemisphere biota because exchange with the southern oceans is very similar and atmospheric transport is identical in the three scenarios. In the northern hemisphere, the seasonal amplitude is weaker than observed at the lower and middle latitude stations (KUM and CMO), and tends to be too strong at the high latitudes (BRW and

ALT). Moreover, the phase of the seasonal cycle is distinctly shifted in this scenario, both with respect to the flask observations and the other two scenarios. Simulated concentrations are lower than observed in winter and spring, then higher than observed in summer and fall. In sharp contrast to the previously considered scenarios, the growing season drawdown begins about a month too early in the high latitudes, and is over too early as well. At the highest latitudes (ALT), the simulated seasonal cycle has almost the right "shape," but is shifted one month forward in time relative to the flask observations. The phase in the Fung and CASA scenarios more closely resembles that in the "real world," but they suffer from the erroneously high respiration peak in spring, which is completely absent in SiB2.

In general, the amplitude of the seasonal cycle at the high northern latitudes is too large as simulated in the Fung scenario, too small as simulated by CASA, and about right as simulated by on-line SiB2. The SiB2 scenario suffers from significant phase error in simulating the seasonal cycle, however, so the overall agreement with the flask data is not as good as for the other scenarios.

The greatest differences between the simulated CO_2 in the scenarios using prescribed surface fluxes from the terrestrial biosphere (CASA and Fung) and the one in which these fluxes are calculated on-line (SiB2) are in spring and fall. Although it is conceivable that the very different seasonal behavior of the simulated CO_2 in the SiB2 scenario results from differences in the model transport for this tracer, it seems likely that differences in the seasonal distributions of surface fluxes are at least partly responsible. This hypothesis is examined in the next section.

7.1.4 Surface Fluxes of CO_2 as Simulated by SiB2

The meridional and seasonal distributions of the zonal total fluxes of all three of the tracers representing seasonal exchange with the terrestrial biosphere are compared in Fig. 7.14. The upper two panels of this plot were presented in Chapter 3 (Fig. 3.14), but the lower panel could only be estimated since the flux due to SiB2 is calculated prognostically in the CSU GCM. A finer contour interval is used here to emphasize the differences between the three surface flux fields.

The most obvious difference between the SiB2 fluxes and those of the other two tracers is that SiB is characterized by only two prominent features in the northern hemisphere, whereas the other two tracers have three. Respiration in the northern midlatitudes

Zonal Total Carbon Flux from the Terrestrial Biosphere

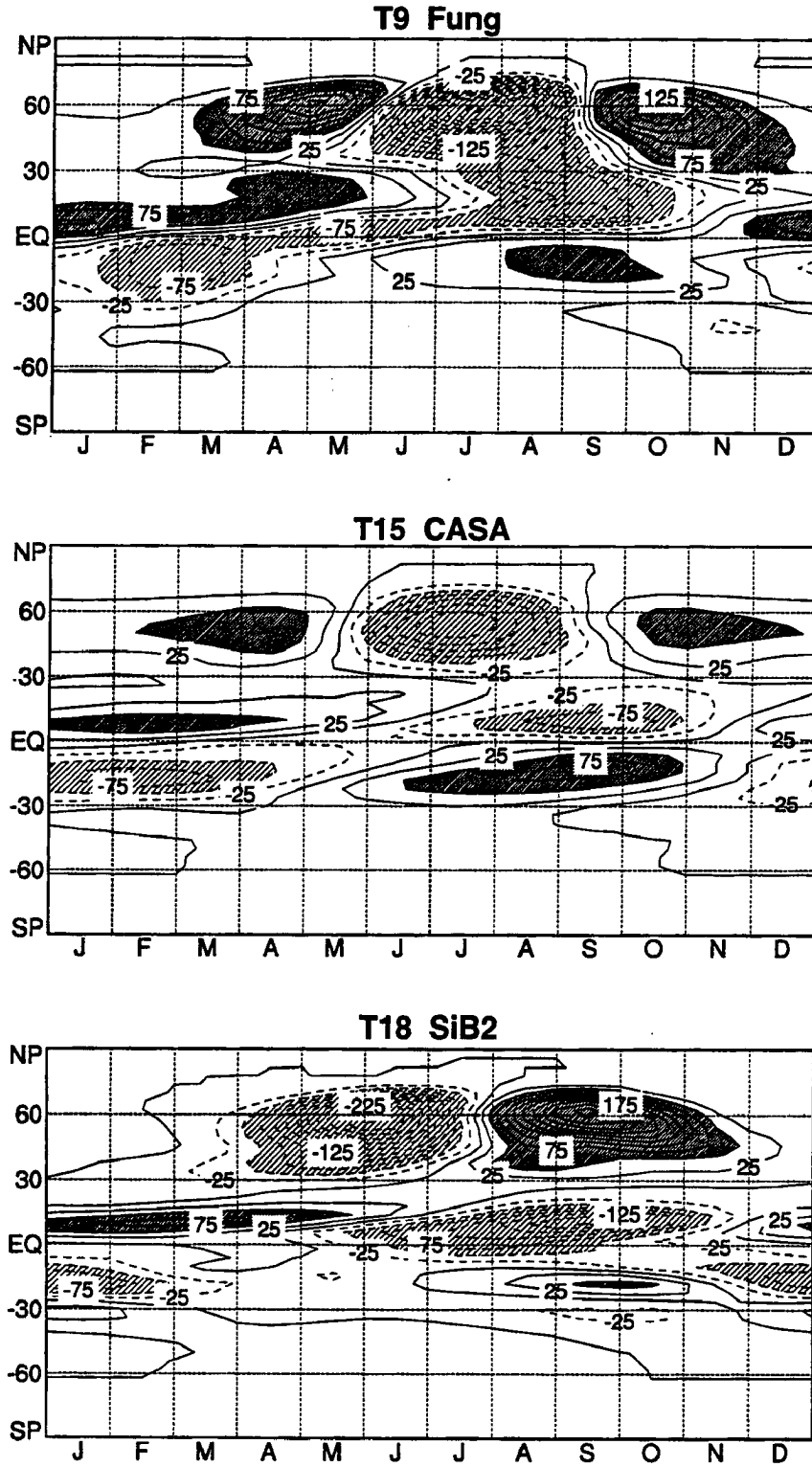

FIGURE 7.14: Zonal total flux of carbon to the atmosphere (10^9 kg C month^{-1} per 4° latitude strip) as represented by tracers T_9, T_{15}, and T_{18}. The contour interval in all three panels is 25, with shading indicating areas of absolute value greater than 50. The ordinates are latitude and the abscissae are month of the year.

in both the Fung and CASA cases is divided approximately evenly between spring and fall, but as represented by SiB2, net release of CO_2 to the atmosphere occurs almost exclusively in the fall north of about 30° N. Furthermore, the growing season drawdown of CO_2 in SiB2 begins between 1.5 and 2 months earlier than as represented in the other two tracers, and is well underway by May while the Fung *et al.* (1987) flux maps show a strong net release of CO_2 to the atmosphere during that month. At the other end of the growing season, SiB2 has become a rather strong net *source* of CO_2 by the middle of August while both T_9 and T_{15} are still being depleted by their respective surface fluxes. Clearly, these differences in the sign of the strong surface fluxes during the boreal growing season can explain much of the difference in the phase and shape of the seasonal cycle discussed in the previous section.

The differences between the surface fluxes noted above are greatest in May and August, near the beginning and end of the northern growing season. Fig. 7.15 shows maps of the surface fluxes of the three tracers for the month of May, and Fig. 7.15 displays the same variables for August. The differences discussed above for the zonal totals are quite obvious in the maps as well, although the CASA fluxes are much weaker than those of the other two tracers. The sign of the CASA fluxes is nearly everywhere the same as the Fung fluxes, however. The biggest differences seem to lie in the boreal forests of Asia, especially in the vicinity of 60° N latitude in both months.

Recall that the surface fluxes of CO_2 reflect an imbalance between carbon assimilation by photosynthesis and release by soil respiration (see sections 3.3.2 and 3.4.4). The tendency of SiB2 to produce large negative fluxes of CO_2 in the boreal spring and large positive fluxes in the fall at first suggests that the northern growing season is starting too soon, apparently before it does in the real world. The assimilation calculation in SiB2 is on much firmer theoretical and empirical ground than the soil respiration calculation, however (section 3.3.2). It is at least as likely that respiration is underestimated in the spring than that assimilation is overestimated.

The Fung *et al.* (1987) fluxes were not available as separate components (assimilation and soil respiration), but only as the net flux of CO_2 at the land surface. The original paper includes monthly time series of the separate components at several grid points representing different biomes, though, and one of these is in the boreal forest (in Canada rather than Siberia, but one would expect similar seasonal behavior). Comparing the components of the Fung *et al.* (1987) fluxes with those simulated in the boreal region by SiB2 (Fig. 7.17), it is clear that the onset of CO_2 release by respiration in SiB2 is delayed

Net Flux from the Terrestrial Biosphere in May

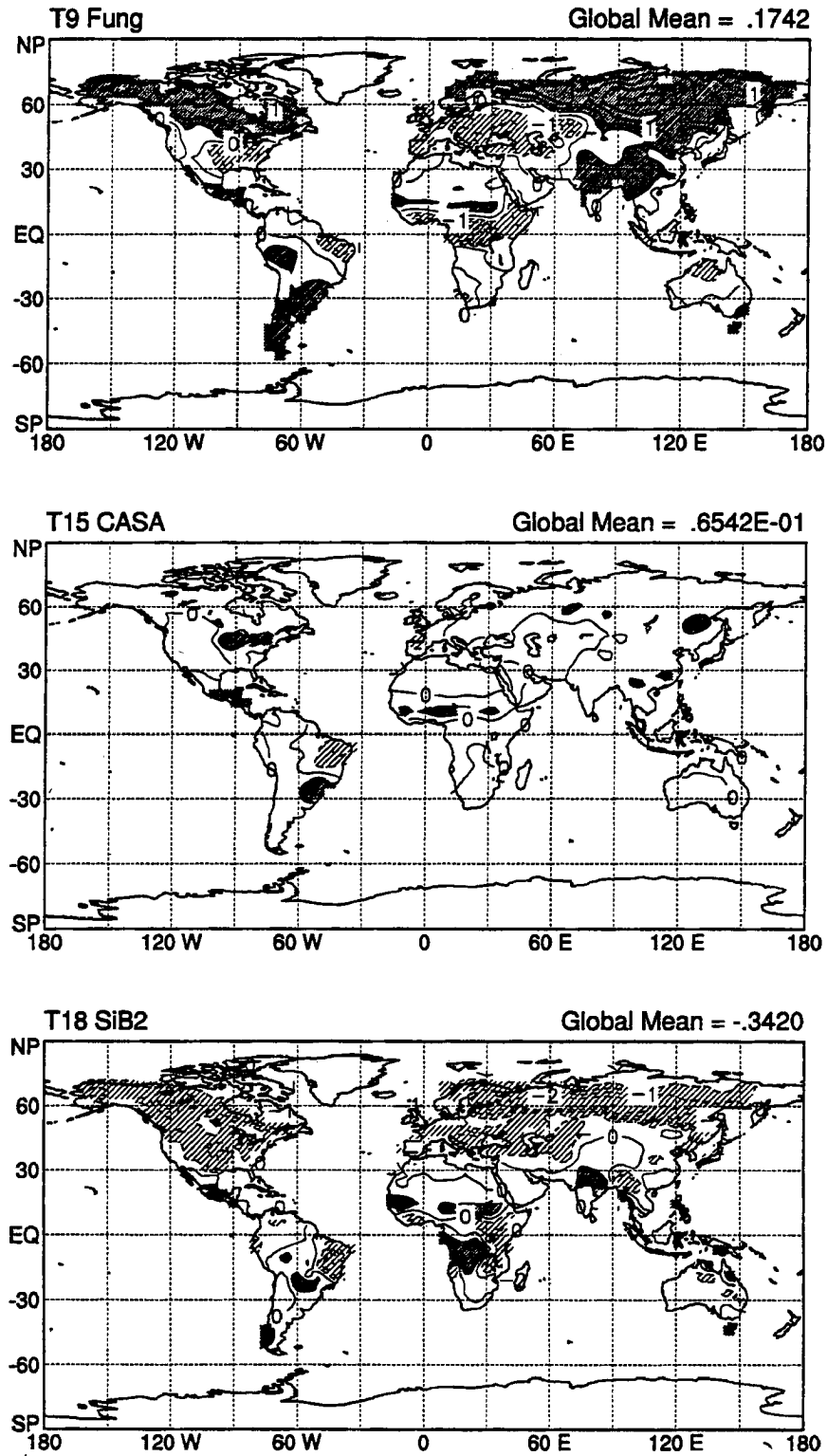

FIGURE 7.15: Comparison of the estimates of net flux to the atmosphere (μMol m^{-2} s^{-1}) of the three tracers used to represent the seasonal terrestrial biota. Contour interval in all three panels is 0.5. Light shading indicates net uptake of greater than 0.5 μMol m^{-2} s^{-1}, and dark shading indicates net release of over 0.5 μMol m^{-2} s^{-1}.

Net Flux from the Terrestrial Biosphere in August

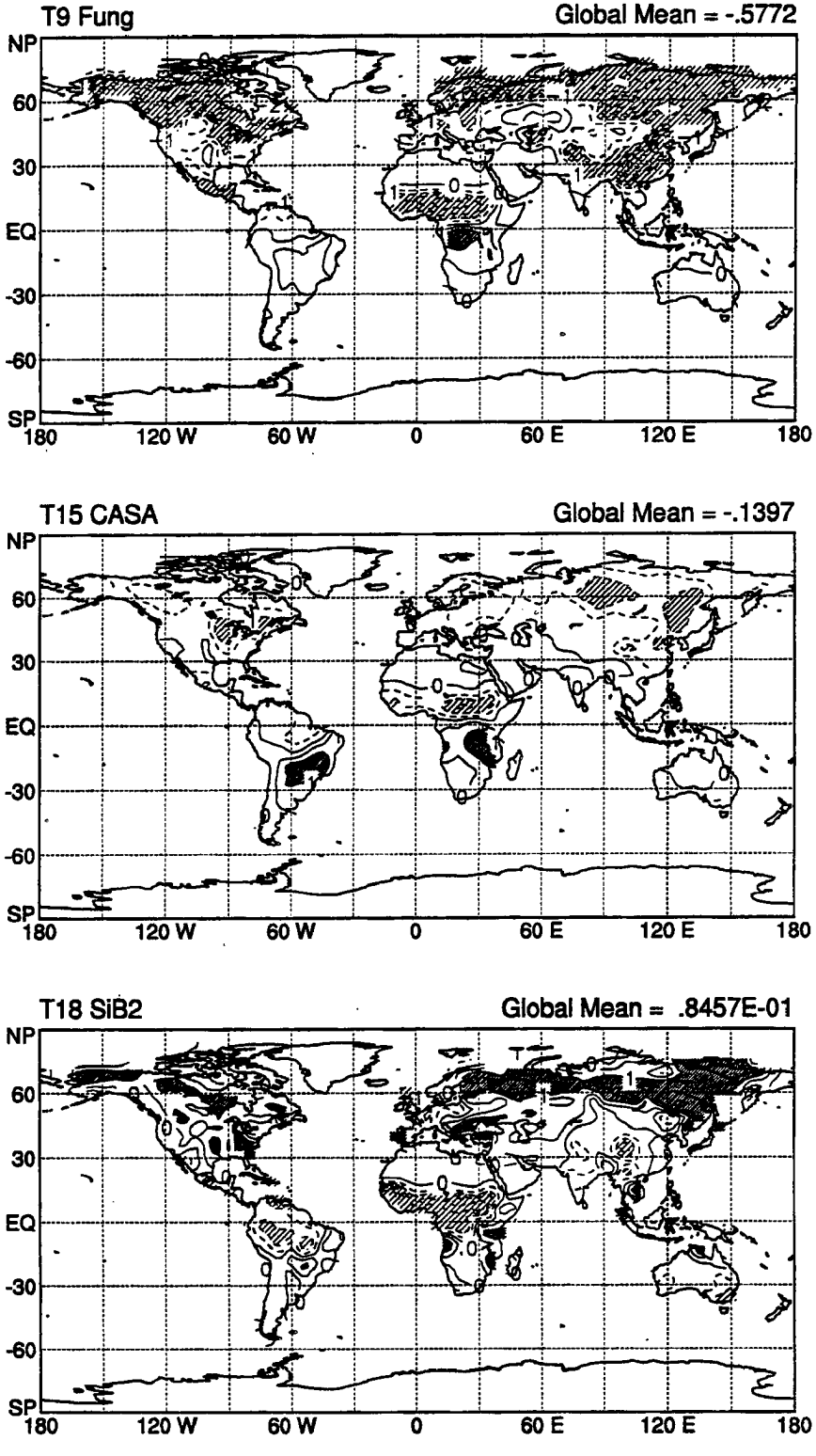

FIGURE 7.16: Comparison of the estimates of net flux to the atmosphere (μMol m^{-2} s^{-1}) of the three tracers used to represent the seasonal terrestrial biota. Contour interval in all three panels is 0.5. Light shading indicates net uptake of greater than 1 μMol m^{-2} s^{-1}, and dark shading indicates net release of over 1 μMol m^{-2} s^{-1}.

Boreal Forest Carbon Flux Components

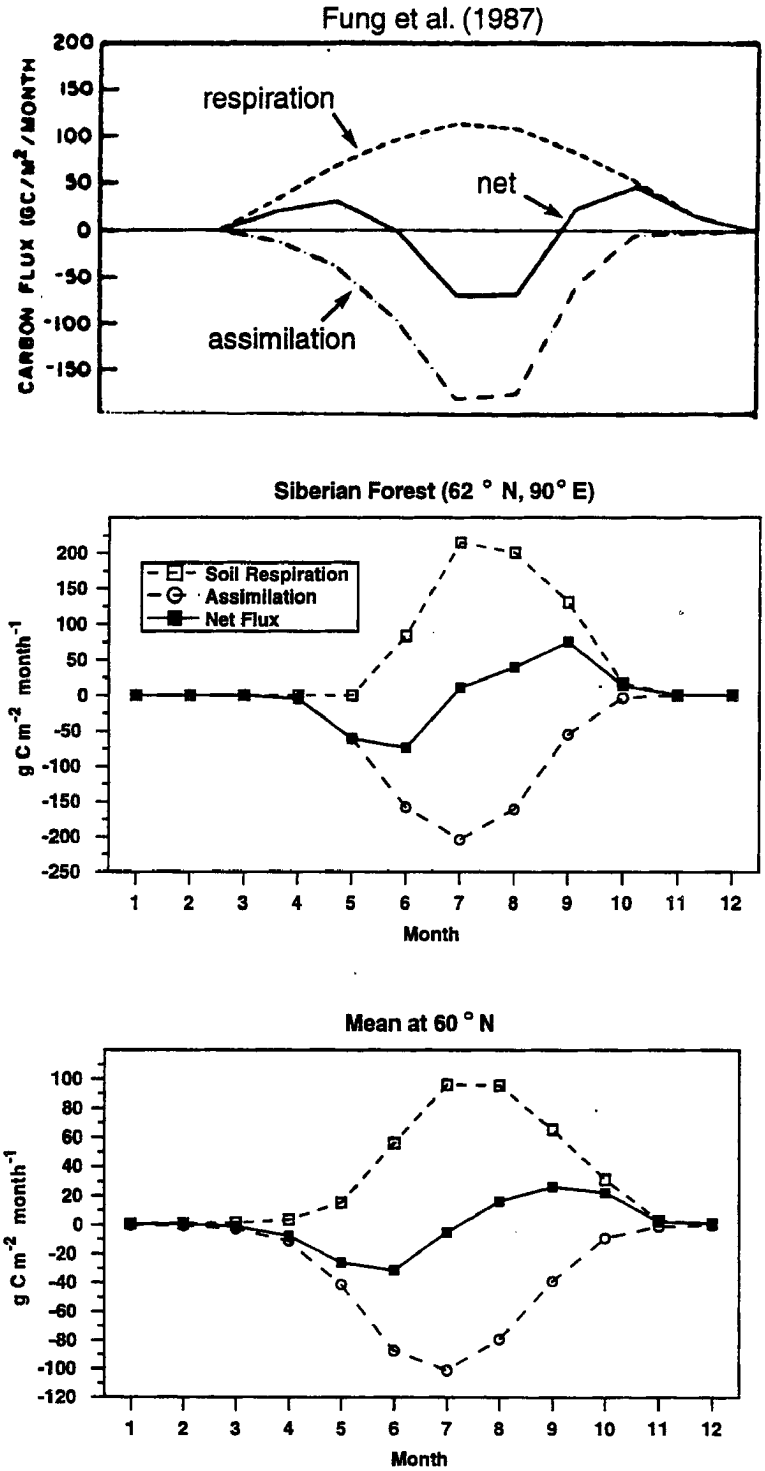

FIGURE 7.17: Components of the surface flux of CO_2 as estimated by Fung *et al.* (1987) from NDVI data and climatological air temperature, and as simulated by SiB2. The Fung data are for coniferous forest at 95° W, 54° N. The middle panel is for SiB2 in central Siberia, and the bottom panel is a zonal mean at 60° N as simulated by SiB2. All values are in grams of carbon m^{-2} per month.

by several months. The Fung *et al.* data show respiration beginning in March, but in central Siberia there is no respiration at all until the end of May in SiB2, and indeed very little respiration in the zonal mean at 60° N.

In the SiB2 simulation, the assimilation rate in May is only 62 g C m^{-2} $month^{-1}$, which is nearly the same as the Fung estimate for the Canadian boreal forest, but in the case of SiB2, assimilation is unopposed by soil respiration at that time, leading to a net uptake of 62 g C m^{-2} $month^{-1}$. By contrast, Fung *et al.* (1987) estimate a net *release* of about 30 g C m^{-2} $month^{-1}$. By July, both scenarios give much larger assimilation rates (SiB2's July estimate exceeds that of Fung *et al.*), and in August, both SiB2 and Fung estimate assimilation at around 150 g C m^{-2} $month^{-1}$. By this time, however, the soil respiration as simulated by SiB2 has increased to the point where it exceeds the assimilation, so that the net flux of CO_2 to the atmosphere is positive in August and still strongly negative as estimated by Fung *et al.* This problem is by no means limited to a few grid cells near the one displayed here; the lower panel of Fig. 7.17 shows that the phenomenon is qualitatively the same in the zonal mean at 60°N although not as intense.

What is wrong? Why does SiB2 fail to simulate any release of CO_2 from the boreal soils by respiration until May or June? Obviously the parameterization of soil respiration is not "turned off," because once it gets going, soil respiration in the boreal region dominates assimilation for the second half of the growing season.

Recall that soil respiration in SiB2 is represented as a simple diagnostic function of soil temperature and soil moisture (see equations (3.25) and (3.26) in section 3.4.4). The function is accumulated throughout the year at each grid point and the soil respiration is then estimated according to the ratio of the instantaneous value of this function and the annual sum for the previous year at that grid point. The annual total respiration is constrained to be equal to the total carbon fixed by assimilation at that grid point in the previous year, so that in the long term no net sources or sinks are expected. The response of soil respiration to soil temperature is simulated as a simple exponential, with a Q_{10} value of 2.0, meaning that the rate of respiration doubles each increase of temperature by 10 K. The temperature used to determine the response is the average temperature between the surface soil and the deep soil layers. When the mean temperature of the soil column falls below the freezing point of water, the diagnostic function is set to zero, and soil respiration in SiB2 stops completely.

The multiyear mean soil temperature for the month of May as simulated by SiB2 is displayed in Fig. 7.18. The soil is still frozen over large areas of Asia and northern Canada, triggering the "switch" that shuts off soil respiration in SiB2 at these grid points. There are no climatological data on soil temperatures at the global scale with which to compare these results, but it seems unlikely that this is a realistic result. The soil at the grid point considered in Fig. 7.17 barely thaws out by June in the multiyear mean, and in fact has snow on the ground in June. The very cold soil temperatures in the boreal forest explain the lack of simulated soil respiration during spring. The assimilation rate is depressed somewhat by the cold temperatures (see equation (3.17) in section 3.3.2), but there is no "switch" at the freezing point for assimilation as there is for soil respiration. Because the annual sum of soil respiration is constrained to equal the annual sum of assimilation, the effect of the lack of respiration in spring is to increase the soil respiration during the warmer months in the boreal forest. Because of the exponential dependence on temperature, the respiration rate in August and September far exceeds the rates first reached upon thawing the soil, and so SiB2 becomes a net source of CO_2 to the boreal atmosphere starting in early August.

The question arises as to why the springtime temperature over Siberia is so cold in the GCM experiment. A full investigation of this phenomenon is beyond the scope of this report, but a few clues are apparent. One might expect the surface to be cold because of erroneous climate forcing from the atmosphere or some regional problem with the radiation budget. The simulated surface air temperature is indeed about 5 K colder than observed (Fig. 7.19) in the region in question (the difference is even greater further to the south).

Another possible explanation for the anomalously cold soil temperatures that produce such unexpected behavior of the simulated CO_2 is suggested by the simulated seasonal dynamics of the snowpack. Dr. Changan Zhang (personal communication) has compared the fractional snow cover as simulated by SiB2 with estimates made from satellite imagery (Dewey and Heim, 1981), and found that the snowmelt in SiB is about 1.5 months later than observed (Fig. 7.20). The presence of snow on the ground dramatically increases the albedo of the land surface, reducing the influence of solar heating, and also insulates the surface from gains of sensible heat from the atmosphere. The latent heat required to melt this late spring snowpack also contributes to the cold temperatures in both the soil and the overlying air.

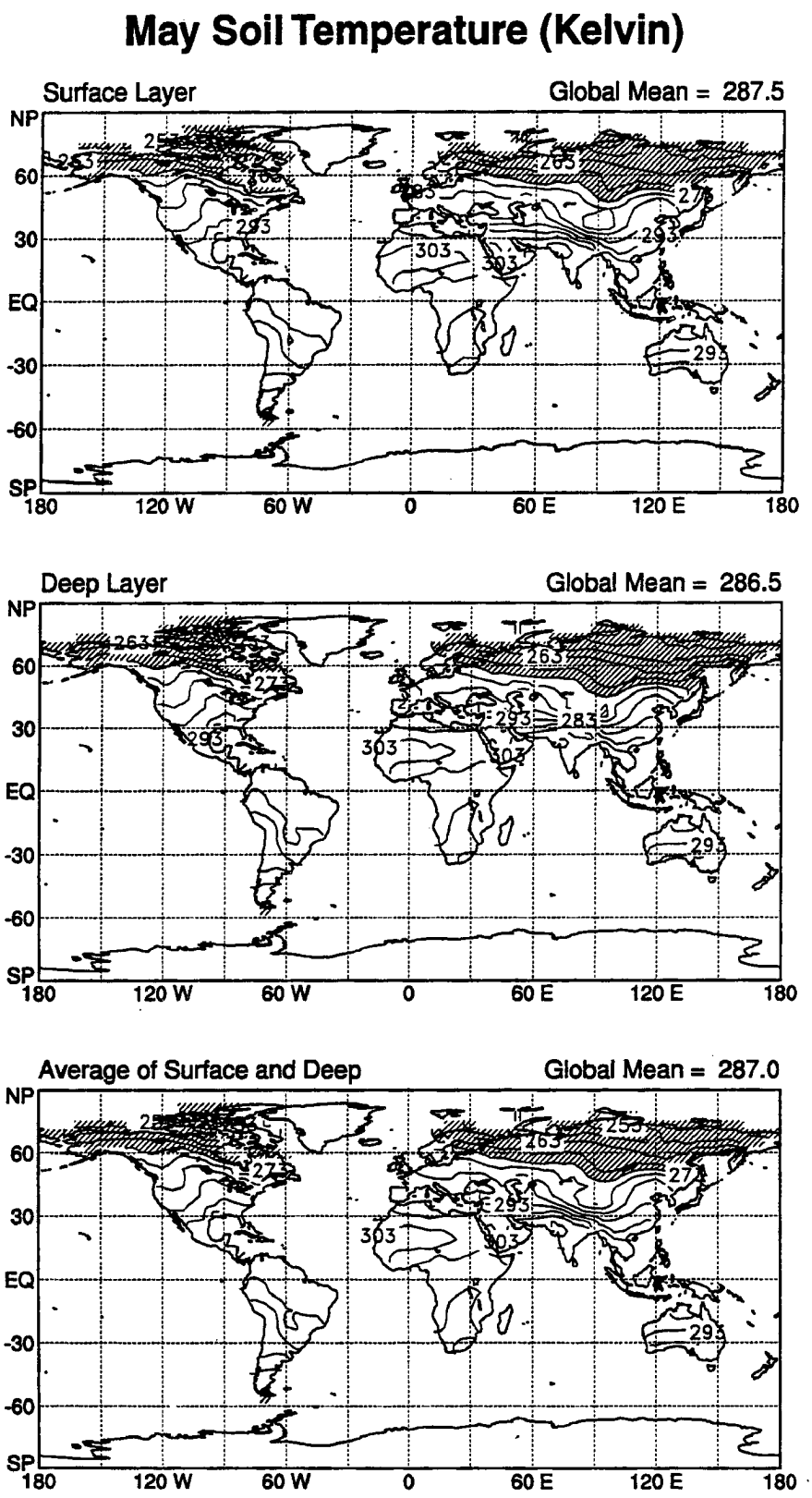

FIGURE 7.18: Soil temperature in May as simulated by SiB2. The contour interval is 5 K in all three panels, and areas below 273 K are shaded.

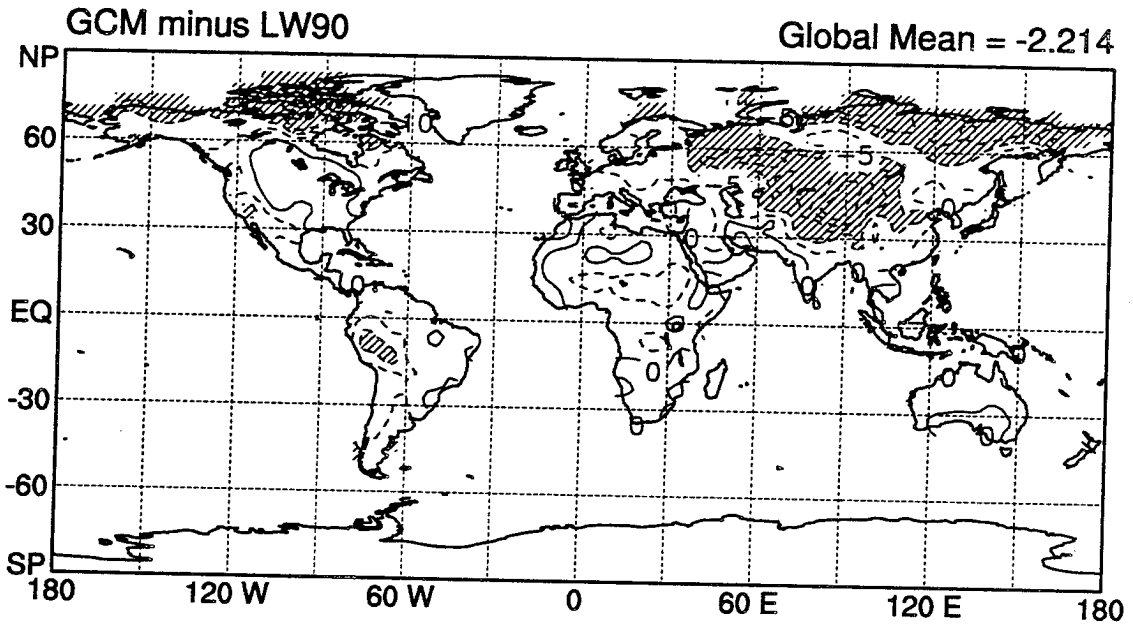

FIGURE 7.19: Difference in surface air temperature for May as simulated by the CSU GCM and estimated from observations by Legates and Willmott (1990). The contour interval is 2.5 K, with shading below -5 K.

Interestingly, the snow is also slow to accumulate in the autumn in the CSU GCM, as compared with the NOAA data. Zhang has also found the same phenomenon when running off-line tests of SiB2 without the parent GCM. In these tests, observed climatological data are used to drive the SiB calculation, so the forcing from above should be more realistic. The fact that the delayed snowmelt and accumulation still occurs in these off-line runs suggests that the problem may lie with SiB rather than the atmospheric climate.

Randall *et al.* (1994) noted that January surface air temperatures in the Siberian region as simulated by SiB2 were substantially *warmer* than observed, and that they were associated with a large upward heat flux from the deep soil. The delay in both snow melt and accumulation in both the full GCM and the off-line tests, and the fact that regional temperatures are too warm in winter and too cold in spring suggests that the heat capacity of the soil is too high. In SiB2, the soil heat capacity is a function of soil moisture content, so diagnosing the precise problem is likely to be complicated, and will require a detailed examination of the model's land surface hydrology as well as the climate of the CSU GCM.

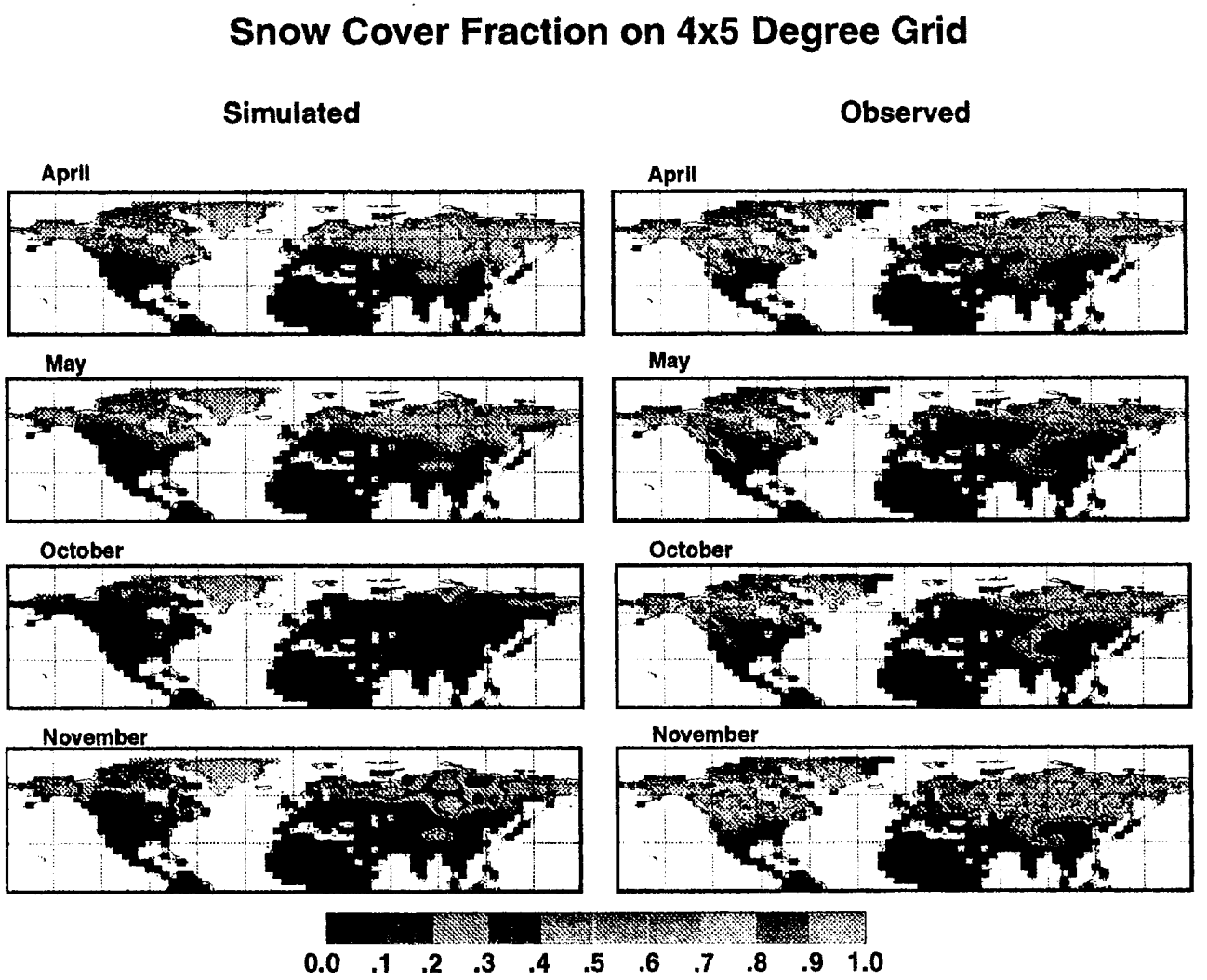

FIGURE 7.20: Comparison of fractional areal coverage of the land surface by snow as simulated by SiB2 in the CSU GCM (left panels) and calculated from visible satellite imagery (Dewey and Heim, 1982) for 1982 – 1991. Changan Zhang (personal communication).

Erroneously high soil heat capacity may result from a tendency for water to accumulate in the deep soil layer of SiB2, where it is unavailable for transpiration because it lies below the root zone. This could result from overestimation of infiltration through the ground, too rapid drainage through the upper two soil layers, too little drainage from the bottom of the deep layer, too little runoff, insufficient upward diffusion of moisture, or any combination of these factors. It is remarkable that unrealistic soil moisture budgets could influence the simulated atmospheric concentration of CO_2 through the heat balance of the soil and thereby the soil respiration, but in such a complicated coupled system, surprises are to be expected.

Ironically, in an earlier simulation a typographical error essentially disabled the freezing point threshold for soil respiration in SiB2, so that the exponential formula (3.25) was applied down to 248 K rather than 273 K, and the resulting simulation of atmospheric CO_2 was much better than the results obtained for the standard experiment (Fig. 7.21).

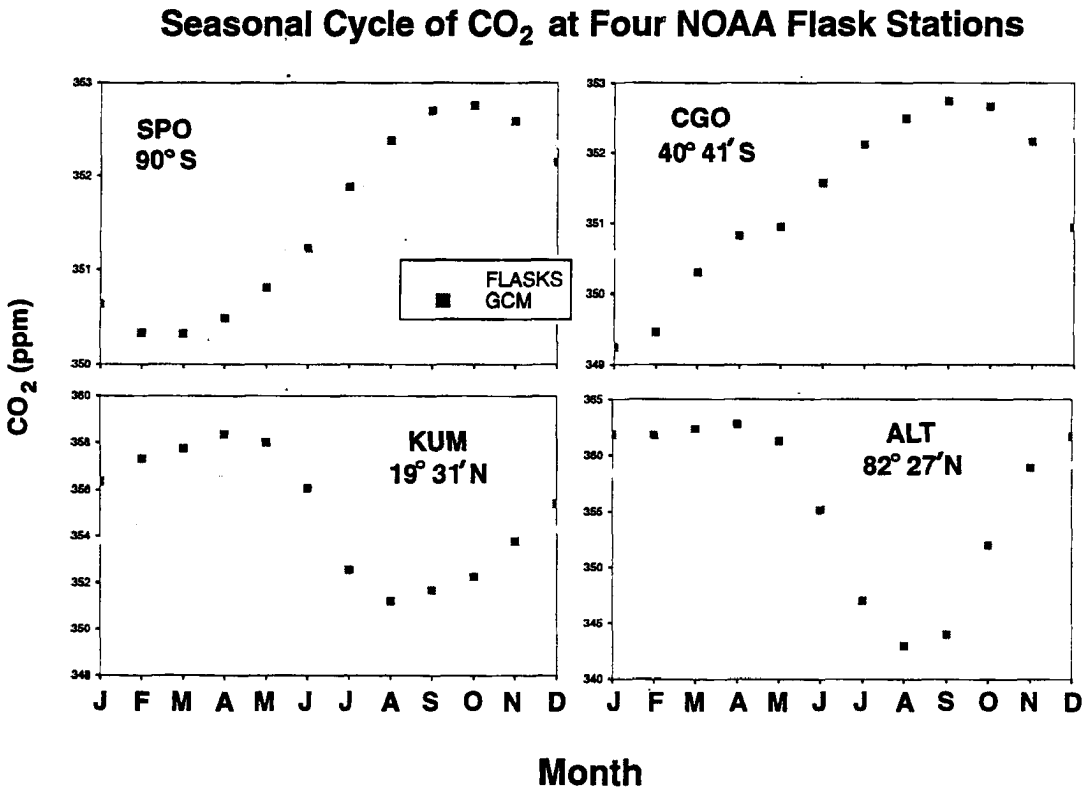

FIGURE 7.21: Simulated and observed CO_2 at four NOAA flask stations in a previous experiment without the low-temperature cutoff for soil respiration.

These results were obtained using the LOWRES mode of the CSU GCM, and also included another coding error which disabled the cumulus transport of all 18 tracers, yet the seasonal fit using SiB2 was better than any of the fits obtained in the standard experiment (including the Fung and CASA scenarios). The error which enabled soil respiration in frozen soils in essence masked the problems with the moisture and heat budgets in the boreal forest, and a very reasonable simulation of atmospheric CO_2 was obtained.

It is clear that SiB2 is quite capable of simulating reasonable carbon fluxes at the land surface, but that the coupled nature of the climate-hydrology-ecology-trace gas system is complicated enough that problems in one component can affect the whole system. The simulation of the surface carbon fluxes and atmospheric CO_2 concentrations has provided valuable information about the other components and highlighted the soil hydrology in a way that was not anticipated at the outset of the study. It is hoped that such coupled modeling can continue to provide insights which lead to improved parameterizations of all the components in the model.

7.2 The Diurnal Cycle

At the local scale, the exchange of carbon between the land surface and the atmosphere is driven by solar radiation, which is absorbed by green plants to allow them to manufacture organic compounds from inorganic CO_2 (see Chapter 1). The diurnal course of incident solar radiation therefore drives a very strong diurnal cycle of photosynthesis, and because decomposition of organic material in the soil is not as sensitive to diurnally varying quantities, the net flux of CO_2 at the land surface changes sign from day to night, producing strong diurnal oscillations in PBL concentrations of CO_2 (Keeling, 1958).

Incident solar radiation is also the primary source of energy that drives the circulation of the atmosphere, from the scale of the Hadley cell down to the scale of small turbulent eddies in the PBL (Peixoto and Oort, 1992). At the local scale, the diurnal course of solar heating at the land surface leads to strong diurnal cycles in surface air temperature and buoyancy, and therefore also in the development of a turbulent boundary layer and cumulus convection.

Because the diurnal variations of surface carbon exchange and atmospheric circulation are each driven by solar radiation, they are strongly correlated in time. Yet in all previous studies of the global carbon cycle using atmospheric tracer transport models, the

diurnal cycle of the surface fluxes has been "averaged out," and prescribed in terms of monthly mean values. Even the diurnal cycle of atmospheric turbulence is only poorly resolved at a time step of four hours (as used by Heimann and Keeling, 1989 and TFT90). Previous studies have represented cumulus convection as a monthly mean mixing frequency, so that vertical tracer transport has no diurnal component either. These idealizations have simplified the tracer transport problem so that the calculations are computationally efficient, but are justified only to the extent that diurnal correlations between the biological exchange of CO_2 and atmospheric circulation do not significantly affect the simulated tracer distribution.

In this section, the diurnal cycle of simulated tracer fluxes, concentrations, and transport are examined. Comparisons with observational data from field studies is made where possible. Because detailed measurements of these parameters has only been done at a handful of locations, the present analysis will focus on three specific grid points in the GCM results: Manaus, Brazil (3° S, 60° W; site of the Amazon Boundary Layer Experiment (ABLE 2), Harriss, *et al.*, 1988); Manhattan, Kansas (39° N, 96.5 ° W; site of the First ISLSCP Field Experiment (FIFE), Sellers *et al.*, 1992*a*); and Harvard Forest (43° N, 72° W), the site of field studies of terrestrial CO_2 exchange (Wofsy, *et al.*, 1993). Because coupled diurnal cycles of CO_2 exchange and atmospheric circulations are most intense at the height of the growing season, only diurnal results for July will be analyzed here. This is also the time of year during which most of the field observations have been taken.

7.2.1 Diurnal Evolution of Terrestrial Carbon Exchange

The net flux of CO_2 from the land surface to the atmosphere is the difference between the uptake of CO_2 by photosynthesizing plants and the release of CO_2 by microbial decomposition in the soil. In SiB2, uptake of CO_2 by plants is represented as the net assimilation rate A_n, which is the rate of photosynthesis minus the autotrophic respiration the plants perform for their own maintenance (see section 3.3.2). Respiration R, is parameterized according to soil temperature and soil moisture, and is constrained to match annual assimilation at each grid point on the multiyear time scale.

Because A_n is very sensitive to incident radiation, it has a much stronger simulated diurnal cycle than does R (Fig. 7.22). At all three locations, the rate of soil respiration increases slightly during the day due to warming of the soil, and the diurnal cycle of the

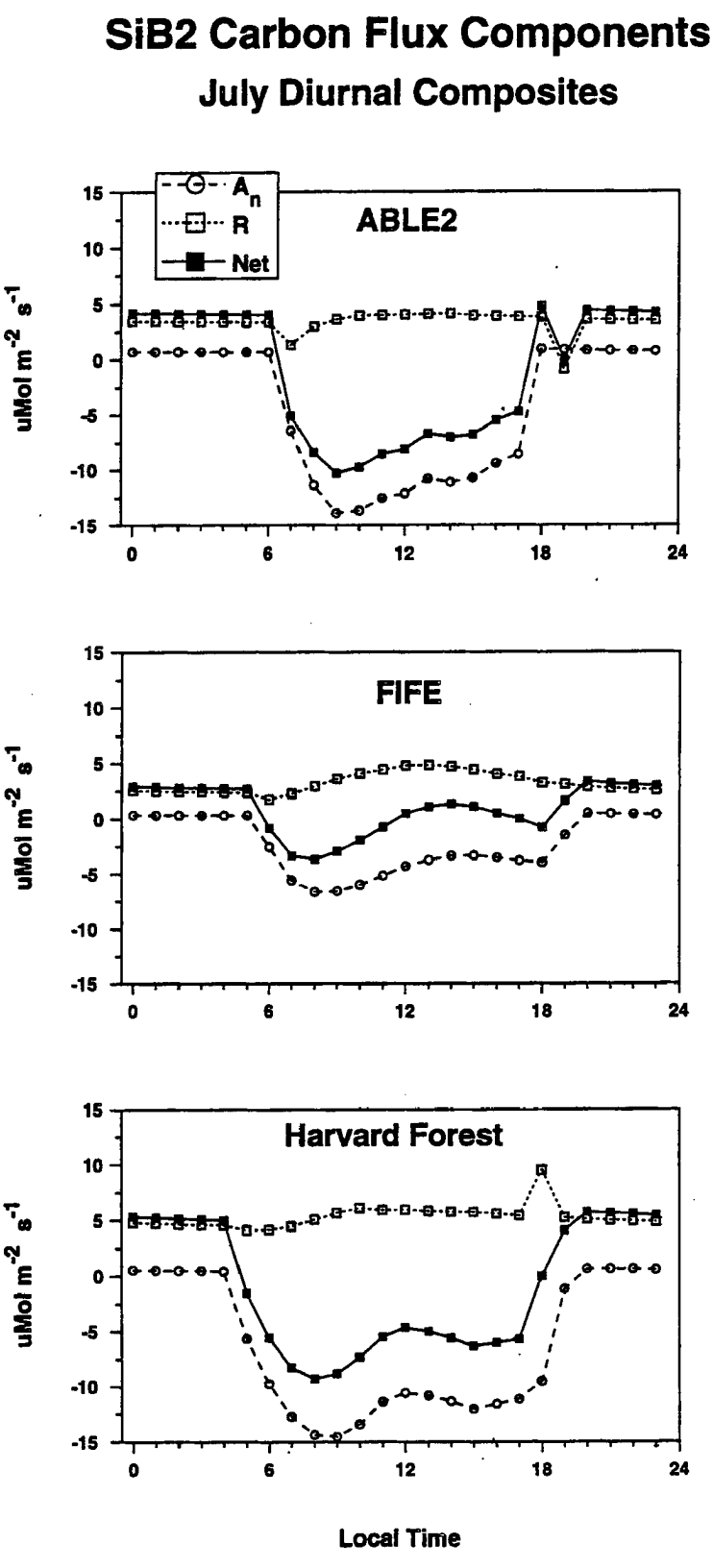

FIGURE 7.22: Mean diurnal cycle of net assimilation, soil respiration, and the net flux of CO_2 in July of year 4 of the standard experiment at the three grid points explained in the text.

net flux is almost entirely driven by diurnal variations in the assimilation rate. All three sites also experience their strongest net uptake in the morning, have somewhat depressed assimilation at mid-day, and have a slightly weaker net flux peak in the afternoon. In the Amazon rainforest, the net flux reaches a maximum of about 10.3 μMol m^{-2} s^{-1}. The peak uptake rate is slightly smaller at Harvard Forest (9.3 μMol m^{-2} s^{-1}), and much smaller at the FIFE site (3.7 μMol m^{-2} s^{-1}). Soil respiration ranges from 3.5 and 4.0 μMol m^{-2} s^{-1} in the Amazon forest, 4.0 to 6.0 μMol m^{-2} s^{-1} in the temperate forest, and 2.5 to 5.0 μMol m^{-2} s^{-1} on the prairie. The larger range at the grassland site is probably due to greater solar warming of the soil there.

The net flux of CO_2 in the PBL was estimated by Fan *et al.* (1990) from eddy correlation measurements near Manaus, Brazil. They found that the highest uptake rates (maximum values were about 22 μMol m^{-2} s^{-1}) occurred in the late morning. Mean daytime fluxes were about 10 μMol m^{-2} s^{-1}, and soil respiration was about 5 μMol m^{-2} s^{-1}, with little diurnal variation. Their measured fluxes were somewhat higher than simulated for the tropical rainforest grid point considered here, but generally consistent with my results in terms of the diurnal cycle.

The simulated net fluxes for the FIFE site are lower than shown by most summertime observations performed there. Verma *et al.* (1989) estimated surface fluxes of CO_2 from eddy correlation measurements (Fig. 7.23), and found peak uptake rates of between 12 and 19 μMol m^{-2} s^{-1}, generally in the late morning hours. The diurnal courses of surface flux varied significantly from day to day, however, due to temperature and moisture stress. The days for which data were reported were all mostly sunny, and so may reflect optimum conditions for photosynthesis. The diurnal composites in Fig. 7.22 include all days in the simulated month and so are expected to fall short of the fluxes that would be obtained in good weather only.

Eddy correlation measurements were used by Wofsy *et al.* (1993) to estimate net carbon exchange between the Harvard Forest and the atmosphere (Fig. 7.24). The data presented in Fig. 7.24 are a composite of two ten day time periods reported by Wofsy *et al.* (1993) in late June and late July. Peak uptake rates are almost twice as strong as those simulated by SiB2 for this grid point, but again the diurnal course is quite well represented by the model. The timing of peak net uptake in the late morning agrees with the simulated fluxes in Fig. 7.22, but the midday dip in the simulated photosynthesis is not evident in the observations. Nighttime fluxes due to soil respiration are somewhat higher in the simulated than the observed data.

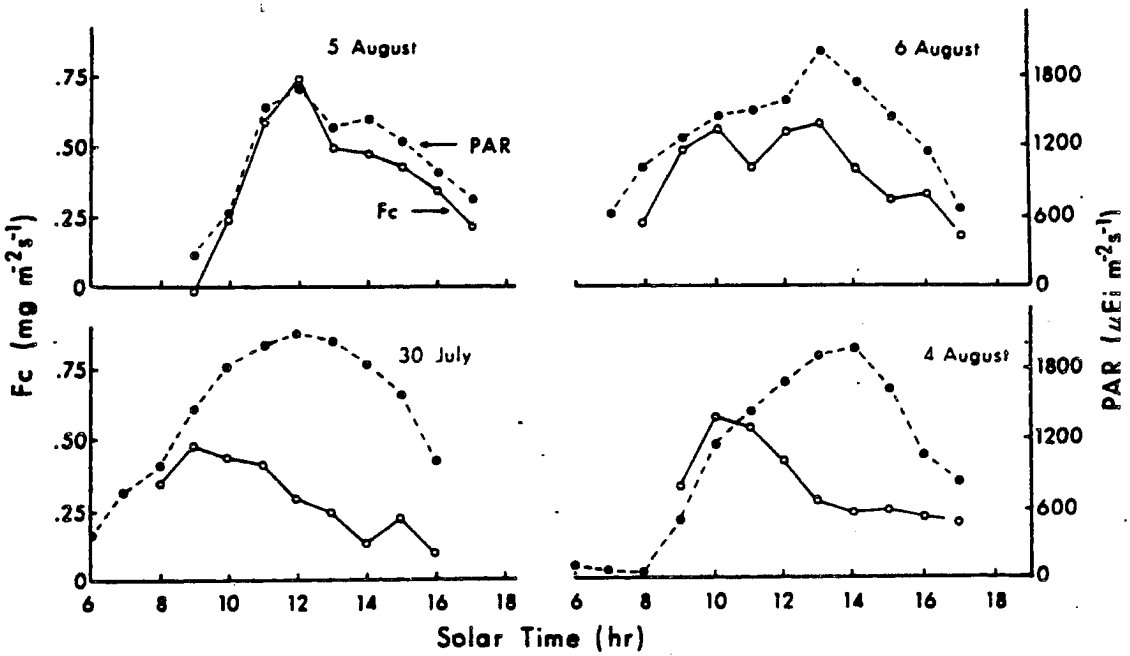

FIGURE 7.23: Diurnal evolution of photosynthetically active radiation (PAR) and net CO_2 flux from the land surface as estimated for four summer days at the FIFE site by Verma *et al.* (1989). The units of carbon flux used here can be converted to μMol m^{-2} s^{-1} by multiplying by 25.

In general, SiB2 captures the diurnal course of July carbon flux at the land surface rather well, although it seems to underestimate the peak rates of assimilation at all three sites. This may reflect a continuing tendency of the model to be overly sensitive to the environmental stresses that lead to a mid-day depression in stomatal conductance in the real world (Randall *et al.*, 1994).

7.2.2 Diurnal Cycles of CO_2 in the PBL

Composite diurnal cycles of simulated PBL depth, cumulus mass flux at the PBL top, and total CO_2 concentration are displayed in Fig. 7.25 for the ABLE 2 site, along with a compilation of observed concentrations for that location based on aircraft measurements taken over a two-week period in July and August 1985 as reported by Wofsy *et al.* (1988). The boundary layer begins to grow by turbulent entrainment in the early morning. This process is accompanied by a mid-morning peak in cumulus convective activity, which removes mass from the PBL and carries it upward. The PBL reaches an average depth of about 100 mb in mid-day, and then begins to contract as the air becomes more

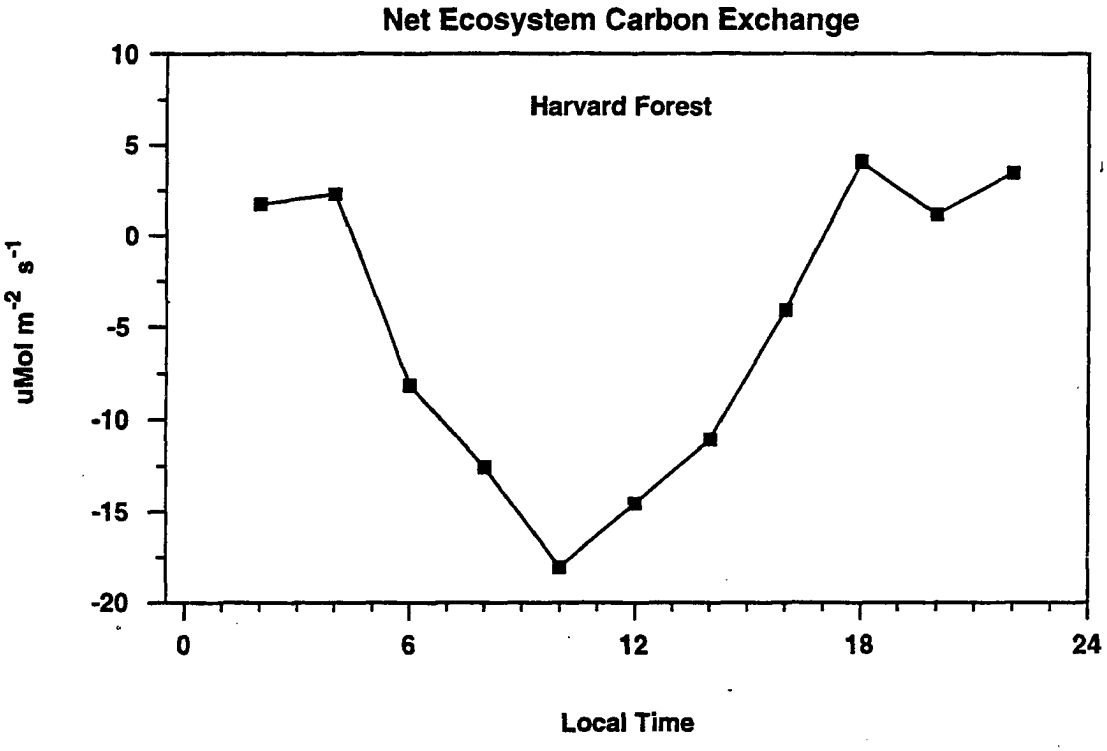

FIGURE 7.24: Net flux of CO_2 to the atmosphere (μMol m^{-2} s^{-1}) due to ecosystem processes in Harvard Forest, as estimated by Wofsy *et al.* (1993) from eddy correlation measurements over two 10 day periods in the summer of 1991

stable in the late afternoon, reaching a nighttime depth of about 20 mb. A second peak in cumulus activity occurs on average at about 1600 local time.

The simulated diurnal course of total CO_2 concentration for the Fung and CASA scenarios follows that of the PBL depth. Because these two scenarios do not include a diurnal cycle in the surface fluxes due to terrestrial biology, the net flux is negative (about 0.1 μMol m^{-2} s^{-1} for T_9 and 0.4 μMol m^{-2} s^{-1} for T_{15}) 24 hours a day. Nighttime "photosynthesis" depletes the PBL of CO_2 disproportionately because it acts on a layer that is only 20 mb thick. In the morning, turbulent entrainment at the PBL top brings in undepleted air, so the concentration rises, reaching a maximum at about the time the PBL stops getting deeper. The concentration in this deeper layer is depleted very slowly by the weak surface fluxes throughout the afternoon, and then more quickly following the collapse of the turbulent PBL in the evening. The peak-to-peak amplitude of the diurnal cycle in total CO_2 in the Fung scenario is less than 1 ppm, and is about 3 ppm using the CASA scenario.

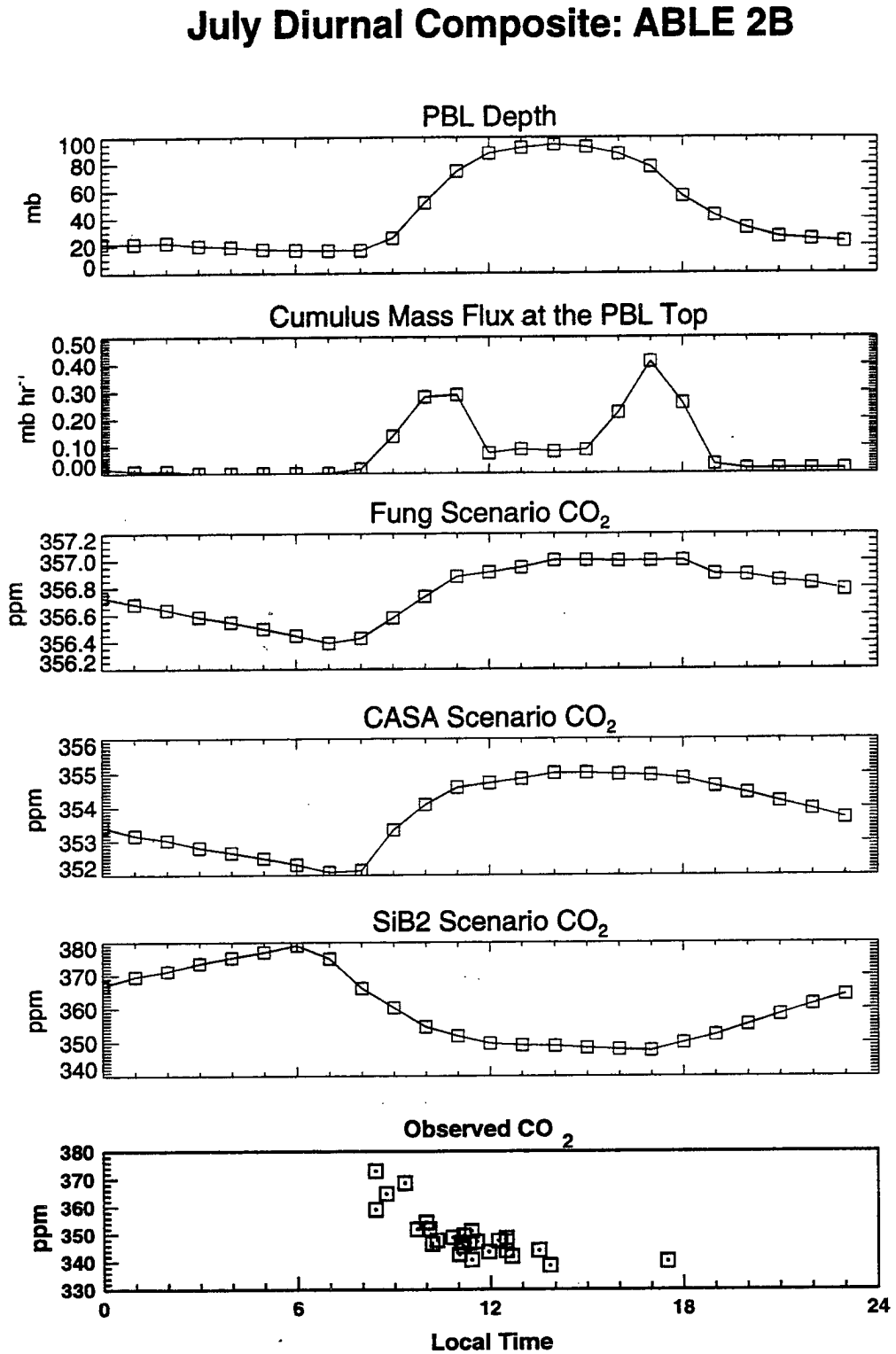

FIGURE 7.25: Boundary layer parameters and total CO_2 as simulated in all three preferred scenarios defined in Chapter 6 for the tropical forest site. The bottom panel is a compilation of aircraft observations reported by Wofsy *et al.* (1988).

By contrast, the total CO_2 as simulated by SiB2 undergoes a diurnal cycle with a peak-to-peak amplitude of about 30 ppm, as does the concentration observed by aircraft. Nighttime soil respiration adds CO_2 to the stable PBL until about 0600 local time, when the sun comes up and photosynthesis begins. Simulated morning concentrations average about 380 ppm. The concentration falls rapidly in the early morning as the uptake acts on a shallow PBL, and then more slowly as the PBL grows and entrains more air from above. By the late afternoon, the simulated concentration has fallen to about 350 ppm on average. The collapse of the turbulence coincides with the cessation of photosynthesis because both are driven by the sun, so the concentration begins to rise again at about 1700 local time.

The diurnal cycles of these variables are qualitatively very similar at the other two field observation sites (FIFE and Harvard Forest), so they will not be presented here.

7.2.3 Vertical Structure of CO_2 in the Lower Troposphere

In the lower troposphere, the simulated vertical structure of the CO_2 concentration undergoes a large diurnal cycle (Fig. 7.26). Early morning concentrations are elevated (to nearly 380 ppm) in the shallow PBL due to stable air and efflux of CO_2 from the soils due to respiration at night. On average, the PBL was less than 200 m deep at 600 local time. By mid-afternoon, the PBL has grown to about 800 m depth by turbulent entrainment, and photosynthetic uptake has depleted this deeper layer of CO_2, reducing its concentration to about 348 ppm by 1600 local time. After sundown, the buoyancy flux at the surface becomes negative and the PBL collapses, and soil respiration once again begins enriching the CO_2 concentration at the surface. A residual layer of air above the PBL top is "left over," with low CO_2 concentrations still reflecting daytime conditions in the PBL. This leads to a very strong nocturnal "CO_2 inversion," characterized by a gradient in CO_2 concentration of nearly 30 ppm across the PBL top by morning. No such "inversion" occurs in the CASA or Fung cases, of course, because they are not subject to diurnally varying surface fluxes.

The vertical structure during July over the Brazilian rainforest as documented by Wofsy *et al.* (1988) underwent a very similar diurnal evolution (Fig. 7.27) as that simulated using SiB2. Note that the mean concentration is different between the observations and the simulation; the simulated concentrations reflect approximately 1990 conditions, whereas the observations were taken in 1985. The aircraft data and the simulation each

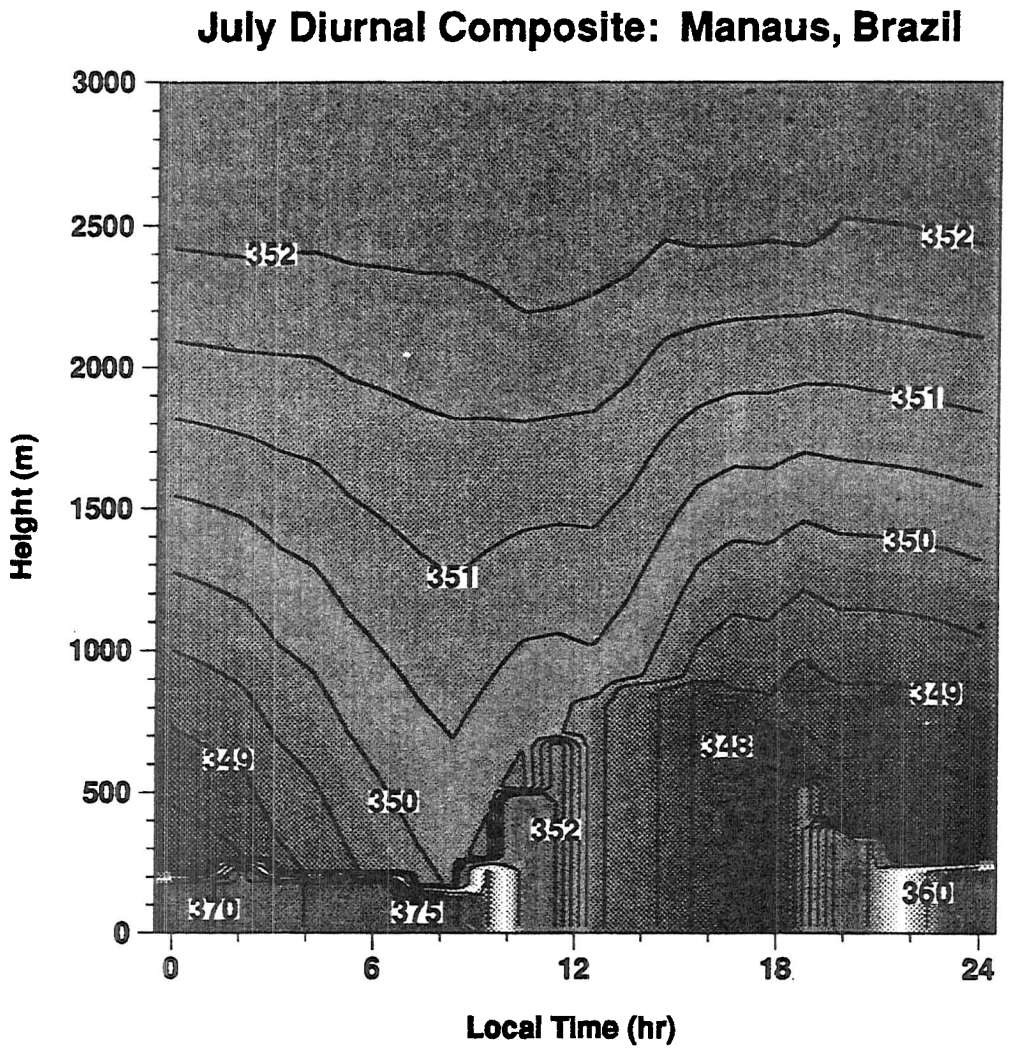

FIGURE 7.26: Concentration of CO_2 *vs.* time of day on the abscissa and height above the ground on the ordinate. Diurnal composite for July at the CSU GCM grid cell corresponding to Manaus, Brazil. Contour interval is 0.5 ppm from 348 to 352 ppm, and 5 ppm from 355 to 380 ppm. Note the diurnal evolution of the PBL.

show a "CO_2 inversion" of about 30 ppm in the early morning. The nighttime aircraft observations do not include data below 300 m (presumably because of the hazards of night flying near the canopy level in the Amazon!), so the surface conditions cannot be compared between the model and observations. Both figures show the "relic" depression in concentration above the nocturnal boundary layer. Small scale turbulent mixing in the relic layer is not resolved by the model, but is quite evident in the observations. The mixing of the CO_2-depleted relic boundary layer air into the free troposphere during the night is likely to be important in controlling the long-range transport and vertical propagation of the signal from daytime photosynthesis throughout the troposphere.

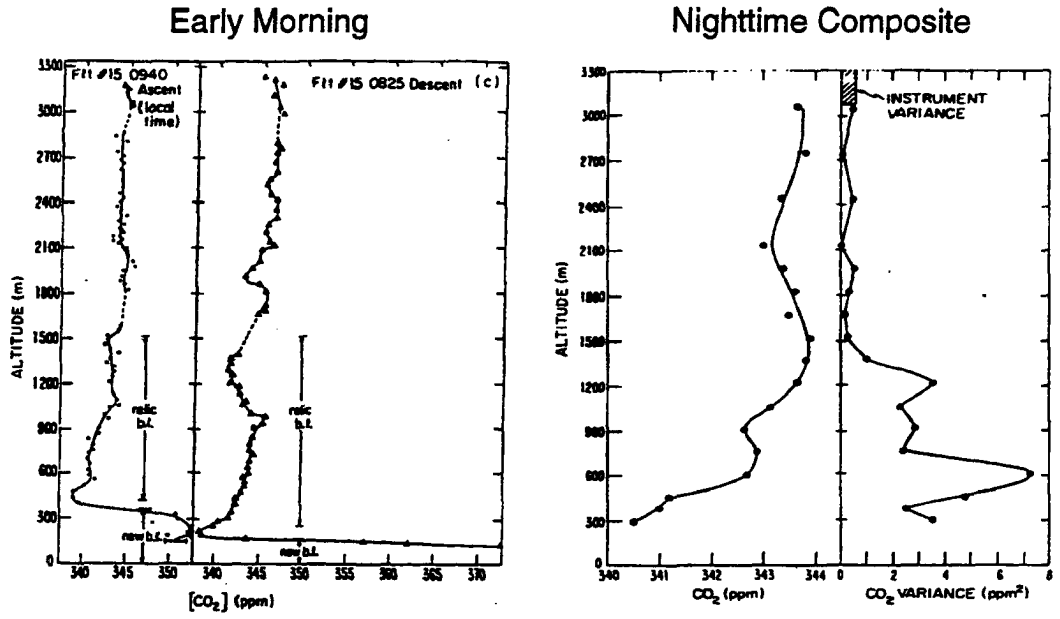

FIGURE 7.27: Vertical profiles of CO_2 concentration measured by aircraft in July, 1985 by Wofsy *et al.* (1988). The left panel shows early morning conditions, and the right panel is a composite of four nighttime profiles. Note that the horizontal scale is quite different in the two panels.

The SiB2 scenario obviously produces much more realistic results for the diurnal evolution of the concentration field in the lower troposphere than either of the other scenarios. The diurnal correlations between atmospheric transport and mixing and surface CO_2 flux account for some of the most striking differences in the seasonal and annual mean distributions of CO_2 in the PBL presented in sections 6.2.1 and 7.1, and based on the results presented in this section, they are probably closer to the true values over the continental interiors than the other scenarios considered. Unfortunately, no long-term monitoring of PBL concentrations on the diurnal time scale has been carried out in these regions, so a rigorous comparison to observations is not possible at this time.

7.3 Summary

The amplitude of the seasonal cycle of atmospheric CO_2 in the PBL is much greater as simulated in this study than has been found by previous studies using off-line tracer transport models. The amplitude is greatest over the northern continents (as high as 60 ppm over parts of Asia), and correlations between the strength of vertical atmospheric

mixing and the surface carbon fluxes in this region lead to strong spatial gradients in CO_2 concentration in the annual mean (section 7.1). The differences between the results of the present experiments and those of previous modeling studies are weaker with increasing distance from areas of strong biological fluxes, but are still evident at the NOAA flask sampling stations. Tracer T_9, with surface fluxes prescribed using the data of Fung *et al.* (1987), had an average concentration at the flask sites in the northern hemisphere that was 0.87 ppm higher than those in the southern hemisphere. In the modeling study of TFT90, this figure was only 0.25 ppm. The stronger affect in the present experiments is due to the use of the prognostic bulk boundary layer in the CSU GCM, which allows much stronger seasonal variations in the strength of vertical mixing in the lower troposphere than is simulated in off-line tracer models.

The amplitude of the seasonal cycle diminishes with height over most of the northern hemisphere, but increases with height over most of the southern hemisphere in all three preferred scenarios tested, reflecting the fact that the seasonal cycle in the southern hemisphere is dominated by transport of the signal from the north. In the upper troposphere, only the Fung scenario reproduces the relatively high seasonal amplitude over Japan documented by Tanaka *et al.* (1987) and the meridional structure of the seasonal amplitude documented by Nakazawa *et al.* (1991). The other scenarios fail to match these features primarily because their surface fluxes are not sufficiently strong during the period of intense vertical transport associated with the Indian summer monsoon

At the NOAA flask stations, the best fit to the seasonal data is produced by the CASA scenario. The seasonal amplitude at the high northern latitudes is a bit too weak in this scenario, but the amplitude in that region is much too strong in the Fung scenario, and although the SiB2 scenario matches the observed amplitudes quite well, it fails to match the phase of the oscillation. Recall that the CASA fluxes were adjusted to better reproduce the expected behavior at high northern latitudes (by decreasing the exponential temperature sensitivity parameter Q_{10}, see section 3.4.4), so the high degree of agreement there should not be too surprising.

The growing season drawdown of CO_2 at high northern latitudes as simulated in the SiB2 scenario begins and ends almost two months too early. The differences between the simulated SiB2 fluxes and the prescribed fluxes of Fung and CASA are greatest over the boreal forest in May and August, and are almost entirely due to differences in soil respiration rather than photosynthesis (section 7.1.4). Simulated soil respiration in SiB2 is very weak to nonexistent in May because the soils over much of the boreal region remain

frozen and snow covered much too late in the season due to unrealistic soil hydrological and thermal properties. Because the annual carbon released by soil respiration must equal the previous year's annual uptake by photosynthesis at every grid cell, unrealistic "extra" respiration occurs in this region when the soil finally warms in August, producing simulated surface fluxes that are much too low in late summer.

The simulated diurnal cycle of surface carbon fluxes, PBL CO_2 concentrations, and vertical gradients and transport is far more realistic as simulated by SiB2 than for the other two scenarios (section 7.2). At the few locations where detailed observations have been collected throughout the PBL, the agreement during the growing season is very good. The simulated diurnal amplitude of CO_2 concentration is between 20 and 30 ppm at the three locations studied. The simulated surface fluxes are a little weaker than observed at mid-day at all three sites, and especially at the temperate grassland site (FIFE). This may reflect continuing hypersensitivity of the model to temperature and drought stress, as was documented in earlier versions of SiB. Alternatively, it may reflect the fact that the model results represent a full month of days and nights whereas the observational data are limited to at most ten-day time series. The diurnally varying vertical structure of CO_2 in the lower troposphere is well simulated for the tropical forest site of the ABLE 2 experiments, and suggests that vertical transport of the diurnal signal due to the growth and decay of the turbulent PBL is an important process for exporting the local signal of biological activity into the free troposphere. This aspect of the atmospheric transport of CO_2 has not been simulated in previous global models.

CHAPTER 8

Conclusions and Recommendations

8.1 Conclusions

The objectives of this study (see section 1.7) were

1) to investigate the surface fluxes and atmospheric transport of CO_2 in order to better understand the global carbon cycle, and

2) to serve as a building block for the integration of models of the atmosphere and the terrestrial biosphere, which will facilitate future work in elucidating the linkages between these components of the Earth system.

In pursuit of objective 1, several multiyear simulations of the global distribution of atmospheric CO_2 were performed, using 18 different tracers representing different aspects of the global carbon cycle. Building the computational machinery necessary for this task directly addressed objective 2 because simulating some of the linkages between the terrestrial biosphere and atmospheric CO_2 was an essential part of the investigation. The two objectives were not pursued separately, but in concert. The results presented in Chapters 5 – 8 directly address objective 1, and were made possible by model developments described in Chapter 3, which address objective 2.

The CSU GCM has been modified to include the prognostic calculation of the concentrations of an arbitrary number of trace gases (sections 3.3 and 3.4). These modifications consist of code to calculate the changes in tracer concentrations due to surface fluxes, advection by the mean atmospheric flow, vertical mixing by dry convection, and vertical transport by penetrative cumulus convection. The tracer code is not in any way restricted to simulating CO_2 – indeed, two radioactive tracers were included in the simulations reported here. Any passive trace gas could be simulated using this code in the future. This

may provide a useful tool for evaluating aspects of the model transport, as was done in the present study using ^{85}Kr and ^{222}Rn. By adding code to calculate changes due to chemical reactions, the transport code for the present study could be used to simulate the concentrations of chemically reactive tracers in the CSU GCM in the future.

Further modifications were made to the CSU GCM to pass information from the land surface parameterization (SiB2) to the trace gas calculation regarding the sources and sinks of CO_2 due to the terrestrial biota (section 3.4.4.3). This is a necessary first step on the road to fully coupled simulations of the interactions between the atmosphere and land biosphere in the carbon cycle. In the past, the assimilation calculation in SiB2 was performed only as part of the determination of stomatal and canopy conductances for use in computing surface fluxes of heat, moisture, and momentum. The use of this information in the trace gas calculation has enabled the carbon exchange at the land surface to be calculated according to variations in environmental forcing at the six minute time step of the CSU GCM. Such a representation allows an investigation of the response of the biota to the diurnal cycle, changing heat and moisture stress, and other physical processes, and is unprecedented in previous global scale carbon cycle modeling. At present, the communication is unidirectional only – the assimilation rate calculated by SiB2 directly affects the concentration of CO_2 in the boundary layer but the simulated CO_2 concentration has no effect on the biochemical calculations in SiB2.

The CSU GCM is successful at reproducing most aspects of tracer distributions which are documented by observational data (sections 5.3 and 5.4). The simulated meridional gradients and interhemispheric exchange of ^{85}Kr agree quite well with the observations of Weiss *et al.* (1983). On the regional scale, simulated concentrations of ^{85}Kr in the PBL suggest that horizontal transport is not well represented in the vicinity of very large point sources. This is an effect of the use of a centered-in-space numerical advection scheme. The simulated vertical concentration profiles of ^{222}Rn reproduce most features of the observational data compiled by Liu *et al.* (1984) over the limited number of locations for which such data are available.

Previous tracer modeling studies (Heimann *et al.*, 1986; Fung *et al.*, 1987; Heimann and Keeling, 1989; TFT90) have required subgrid-scale tracer diffusion to achieve realistic gradients of ^{85}Kr because their interhemispheric exchange was too slow. No such diffusion was used in the present study, yet the interhemispheric exchange was *more* vigorous than reported by most previous studies. Sensitivity experiments using the CSU GCM with a low resolution grid (section 6.1) reveal that the rate of simulated interhemi-

spheric exchange is not limited by horizontal mass flux but rather by vertical mixing due to deep tropical convection which reduces the vertical gradient in tracer concentration. If convective mixing is too strong, southward tracer transport in the upper branch of the Hadley cell is nearly balanced by northward transport near the surface, resulting in very slow interhemispheric mixing. If convective mixing is too weak (as in the LOWRES experiment), the steep vertical gradient in tracer concentrations allow rapid interhemispheric transport and produce unrealistically weak meridional gradients of ^{85}Kr in the tropical lower troposphere.

Multiyear simulations of 18 different tracers were performed with the CSU GCM to investigate hypotheses about sources, sinks, and atmospheric transport of CO_2. The surface fluxes of many of the tracers were defined to be consistent with and allow the results to be compared to those of earlier studies. One tracer (T_{15}) was defined to test the results of a new parameterization (CASA) of seasonal carbon exchange with terrestrial biosphere (Potter *et al.*, 1993) against the observed concentration data.

The simulated tracer concentrations in the annual mean (sections 6.2 and 6.2) were determined by (1) the latitude of the tracer's source region (higher latitude sources produced steeper meridional gradients); (2) the strength of convective mixing in the source region; (3) seasonal correlations between surface fluxes of the tracer and vertical mixing by PBL turbulence and cumulus convection (particularly important for the Fung *et al.* (1987) and CASA tracers); and (4) diurnal correlations between surface fluxes and vertical mixing in the model atmosphere. The last effect was only possible for the SiB2 tracer, and produced very strong concentration maxima in the annual mean in biologically productive regions (see Fig. 6.9).

At the locations of the NOAA flask stations, the meridional gradient simulated by the CSU GCM was about the same as determined in previous studies for tracers without seasonally varying sources (such as T_1, representing the effects of fossil fuel combustion), but was much steeper than previously simulated for strongly seasonal tracers (such as T_9, which used the surface flux data of Fung *et al.*, 1987). The simulated annual mean difference in concentration of T_9 between the northern and southern hemisphere flask stations was 0.87 ppm in this study, compared to 0.25 ppm as simulated by TFT90 using exactly the same fluxes in the GISS tracer model. Two dimensional tracer models produce even weaker annual mean meridional gradients for purely seasonal sources. This difference is due to a more realistic planetary boundary layer in the CSU GCM as compared to the off-

line tracer models, and has a significant effect on the relative strengths of the various components of the global carbon budget that can be inferred from the results.

The meridional profiles of simulated concentration of most of the tracers at the NOAA flask stations fell into a handful of generic categories, and were highly spatially correlated (6.3.1). This made the problem of "inverting" the tracer calculation to deduce the sources and sinks numerically ill-conditioned, and precludes determination of a unique global carbon budget from tracer transport modeling, as was previously found by TFT90. The simulated tracer calculations can be used to evaluate the realism of various scenarios, but because of the spatial correlations between them the selection of the "best" scenario in a numerical sense is not very meaningful (section 6.3.2).

Because of the differences in tracer transport in the CSU GCM, and also because of the different observational data used in the present study, the global carbon budget inferred from the present results not entirely consistent with those produced by earlier studies using off-line tracer models (section 6.3.3). The observational constraints of the meridional gradient and annual growth rate at the NOAA flask stations cannot simultaneously be satisfied if a broadly defined sink due to CO_2 fertilization is used to balance the budget, because such sinks as simulated here (tracers T_{11} and T_{12}) do not produce a steep enough meridional gradient in the northern hemisphere. Sequestration of a significant amount of CO_2 by the temperate forest in the GCM is inconsistent with the relatively high concentrations observed in the tropical Pacific by the NOAA shipboard sampling program. Of the five hypothetical terrestrial sinks tested to balance the carbon budget, only the boreal forest was able to reproduce the meridional structure of observed CO_2 at the flask stations without invoking large compensating sources of other tracers (section 6.3.4). A small to moderate Arctic source is suggested by the concentrations at the northernmost flask stations, and is consistent with some of the scenarios tested. A source of CO_2 in the high latitude southern oceans produces a meridional gradient at the southern hemisphere flask stations that is too weak. This suggests that the global ocean sink is close to 0.8 Gt C yr^{-1}, based on the observations of p_{CO2} at the sea surface compiled by TFT90, and applying a skin temperature correction in the northern hemisphere as suggested by Robertson and Watson (1992).

The differences between the carbon budget scenarios that produce agreement with the observations in the present study and that of TFT90 highlight the role of the simulated tracer transport in such calculations. Most components in the global carbon budget are broadly consistent as deduced in this and previous studies: large anthropogenic emis-

sions in the northern middle latitudes are partly compensated by northern terrestrial sinks, the global oceans are a sink of perhaps 1 Gt C yr^{-1} but not much more, and tropical deforestation is a weaker source than was believed a decade ago. The details of the meridional distributions of the sources and sinks are different enough between the present study and that of TFT90 to place them in different biomes or regions of the ocean, however. This means that such results must be interpreted with caution, and that attention must be paid to other independent validations of the modeled transport such as meteorological fields and radioactive tracers.

The seasonal cycle of simulated CO_2 in the atmosphere is dominated by seasonal exchange of carbon at the land surface. Over land areas with high biological productivity, the amplitude of the simulated seasonal cycle at the surface is nearly twice as strong as that of earlier studies because of the inclusion of a prognostic bulk boundary layer submodel in the CSU GCM. The realism of this enhanced seasonal cycle is not possible to evaluate at this time because long term observational data are not available for the interior regions of the continents, but are concentrated as far away from the large terrestrial fluxes as possible. At the locations of the flask stations, the simulated amplitude of the seasonal cycle is closer to that simulated in previous studies, and agrees fairly well with observations.

The best agreement with the seasonal concentrations at the NOAA flask stations (section 7.1.3) is obtained using the new estimates of net ecosystem production produced by the revised CASA model (Potter *et al.*, 1993). The phase of the seasonal variation of these fluxes is consistent with the earlier estimates of Fung *et al.* (1987) at most locations, but the amplitude is generally weaker. The simulated seasonal amplitude in CO_2 concentration produced using the Fung *et al.* data is greater than observed at most of the flask stations in the northern hemisphere, although the concentrations simulated using these fluxes reproduce the limited observations in the upper troposphere much better than for the CASA scenario. The seasonal variations simulated using the on-line calculation of surface fluxes in SiB2 have about the right amplitude, but their phase leads the observations by 1 to 2 months, especially at high northern latitudes.

The phase error in the seasonal concentrations as simulated by SiB2 is almost entirely due to a shift in the timing of simulated CO_2 release by soil respiration caused by unrealistically low soil temperatures and persistent snow cover in the boreal forests in springtime (section 7.1.4). This problem appears to be caused by unrealistic soil physical properties prescribed as a boundary condition in the affected regions (where very few

field data are available). Because of the assumption that CO_2 released by respiration balances uptake by photosynthesis over a year's time at every grid point, underestimation of soil respiration due to frozen soils in spring requires overestimation at other times of year to preserve the annual integral. The sensitivity of the respiration calculation to soil temperature determines the timing of the "phase shifted" respiration flux, and causes a significant cancelation of the carbon uptake by photosynthesis when soils are warm in late summer. A similar phenomenon greatly reduced the amplitude of the seasonal cycle of NEP in the published version of the CASA model results (Potter *et al.*, 1993). This was corrected by reducing the temperature sensitivity coefficient in the respiration calculation (Q_{10}, see equation 3.23) from 2.0 to 1.5 to make the seasonal amplitude of NEP more closely approximate the earlier estimates of Fung *et al.* (1987). These problems suggest that exponential dependence of soil respiration on temperature may not be as useful in a global model as it is in fitting empirical relationships to field observations.

The use of the on-line surface fluxes from SiB2 produced excellent agreement with the available observational data on the diurnal time scale (section 7.2). The diurnal course of photosynthetic uptake closely matches estimates made from eddy correlation measurements in a tropical forest, a tallgrass prairie, and a temperate forest (section 7.2.1), although its amplitude may be a little too low. The simulated local concentration of CO_2 in the PBL using SiB2 undergoes diurnal oscillations of about 20 – 30 ppm (peak-to-peak), as it does in the observational data. Strong correlations between these oscillations in concentration and PBL turbulence reproduce the very strong vertical gradients in CO_2 concentration observed at the top of the stable nocturnal boundary layer, and result in much more realistic vertical gradients in the lower troposphere than simulated using the prescribed fluxes of Fung *et al.* (1987) or CASA.

8.2 Recommendations for Future Work

This study has successfully addressed the objectives listed in section 1.7, and the results suggest that it would be relatively easy to address several further problems using the framework of the present investigation.

The on-line calculation of carbon exchange at the land surface in SiB2 produces a much greater degree of realism in the diurnal variability of CO_2 concentration in the PBL, and a different vertical structure, especially in the lower troposphere. It would be very instructive to know to what extent these differences affect the long-range atmospher-

ic transport and geographic distribution of CO_2 in the atmosphere. From the present results, it is not possible to attribute the differences in the concentration fields among the different tracers in terms of the diurnal representation, because the behavior of the surface fluxes on longer time scales is also very different. The problems with SiB2's estimates of the seasonal evolution of soil respiration in the boreal forest affect the atmospheric concentrations throughout the northern hemisphere during the summer, and preclude direct comparison with the Fung and CASA tracers.

To evaluate the influence of the coupled diurnal and seasonal cycles of biological activity and atmospheric circulation, a "cleaner" test should be performed in which the effects of such correlations on the transport and distribution of the tracers at the large scale can be isolated from other processes. One such experiment could be performed by repeating the simulation performed here, but prescribing the surface fluxes due to SiB2 as monthly means from the previous model output. This would be analogous to the treatment of the Fung and CASA flux estimates in the present study, but the new tracer would have the same daily and monthly mean surface fluxes as the SiB2 tracer in the standard experiment already performed. Differences in the transport and large scale concentration field between these tracers would be directly attributable to the diurnal cycle of the fluxes.

A more general way to address the influence of coupled diurnal and seasonal cycles would be to perform an experiment in which surface fluxes of a tracer are prescribed to vary in a simple way (for example, with a single harmonic) on both seasonal and diurnal time scales. Four tracers could be simulated: one that includes both the seasonal and diurnal oscillations in surface fluxes, one that is purely seasonal, one that is purely diurnal, and one that reflects only the annual mean of the surface fluxes. Such a calculation would not represent the behavior of any particular aspect of the carbon cycle, but could isolate the effects of correlations between surface exchange and atmospheric transport on multiple time scales.

The problems with high latitude soil respiration as calculated by SiB2 must be addressed if SiB2 is to produce reasonable seasonal behavior in the simulated concentration of CO_2. This will require a careful examination of the hydrologic cycle at the land surface, especially in the boreal forest to determine exactly why the soils stay so cold in spring and so warm in the fall, and why the seasonal accumulation and melting of the snowpack is so slow. Such an examination is necessary in any case, because the regional climate in the boreal forest will not be well simulated in the CSU GCM until this problem is solved. Ultimately, it would be preferable to develop a more robust parameterization of

soil respiration for use with SiB which would be less likely to suffer from these deficiencies. Perhaps a submodel could be developed which would contain the essential elements of the CASA calculation, but could be integrated efficiently at the time step of the GCM. At some point, the assumption of zero net ecosystem production at the annual time scale must be relaxed if the coupled atmosphere-biosphere models are to become useful for estimating long-term changes in the carbon cycle.

The differences between the carbon budget as deduced from the results of this study and those of previous studies emphasize the need to evaluate the transport properties of tracer models carefully. A CO_2 tracer transport model intercomparison project is currently underway (Peter Rayner, personal communication), in which the CSU GCM is participating and which will help to define how much of the current uncertainty in the global carbon budget results from uncertainties in atmospheric transport. The results of the present study suggest that inclusion of a diurnally varying planetary boundary layer will be an important factor in the results of the intercomparison study.

Tracer transport in areas of strong gradients is subject to significant phase error (see section 5.3, especially Fig. 5.12). This problem is much less severe for the simulation of CO_2 than for ^{85}Kr because the fluxes of CO_2 are weak in comparison to the mean concentration, but it reduces the confidence with which some of the results can be interpreted. Concentration differences on the order of 10% of the mean value occur at the top of the nocturnal PBL during the growing season at the land surface, and these may lead to spurious effects. Such problems could be avoided using a more sophisticated numerical advection scheme incorporating the "flux-corrected transport" algorithm of Zalesak (1979; see the recent review of such schemes by Smolarkiewicz and Grabowski, 1990).

Problems with the atmospheric transport of passive tracers in the current CSU GCM are recognized due to the mean meridional circulation, mean zonal winds, and upper level meridional winds being somewhat weaker than observed. These deficiencies may all be related to excessive solar heating in deep tropical clouds, which may result from the relatively low value used for the albedo of ice clouds used in EAULIQ. This possibility should be addressed.

The SiB2 simulation of surface carbon exchange at the land surface produced a very different distribution of CO_2 concentration in the annual mean than the non-diurnally varying flux estimates. By comparison, the changes were rather small at the NOAA flask stations because these were chosen to minimize local or regional effects and emphasize

the background meridional gradient of atmospheric CO_2. Future sites for long-term monitoring of CO_2 concentration should be chosen to try to quantify the variability at continental locations, as has been suggested by TFT90 and Tans (1993). Such observations must resolve both the diurnal and seasonal cycles, and because of the strong vertical gradients over land will require much more elaborate and expensive observing systems than are currently in use in the flask network. Such data would provide a valuable constraint by which the realism of various scenarios of carbon storage on land could be evaluated. The current observational network does not provide a sufficient constraint on the terrestrial exchange of carbon with the atmosphere.

Another important difference between the various scenarios explored in the present study is the meridional gradient of CO_2 in the upper troposphere and its seasonal variation. Because this parameter depends on both the surface fluxes and vertical transport of the model, it can provide valuable information about the realism of both aspects of a simulation. Takakiyo Nakazawa and colleagues at Tohoku University have shown that such information can be obtained relatively cheaply by collecting samples from commercial airliners. Such studies should be expanded to include as much of the world as possible, and should collect data at different seasons of the year.

One aspect of the observational data that was not explored in this study is the isotopic composition of atmospheric CO_2. Stable carbon isotopes are now routinely determined for the NOAA flask samples, and can help in constraining the relative contributions of terrestrial and oceanic sources and sinks Ciais *et al.* (1994). The simulation of ^{13}C has been performed before (Pearman and Hyson, 1986; Gillette and Box, 1986; Heimann and Keeling, 1989), and is quite instructive. Incorporating such a calculation in the CSU GCM would be easy now that the calculation of prognostic tracer concentrations is available. Also, stable oxygen isotopes in CO_2 have been shown by Farquhar *et al.* (1993) to vary dramatically according to their interactions with the biochemical machinery of photosynthesis. Oxygen isotopes are more difficult to include in a tracer simulation because the fractionation of oxygen due to cloud microphysical processes is an important determinant of the background isotopic composition of both CO_2 and H_2O (Jouzel, *et al.*,1987), but could yield very valuable insights about the terrestrial sink. Such a calculation should be attempted in the future.

My results show that the inclusion of diurnal effects of both surface fluxes and atmospheric processes such as boundary layer turbulence in the tracer calculation produce significantly different results than those of off-line tracer calculations that do not include

these processes. Such a calculation is necessarily more computationally expensive than the alternative, but recent developments in the computer technology and economics have made it feasible to perform repeated experiments at low cost. The results shed new light on the importance of transport processes in determining the atmospheric distributions of CO_2, and lead to different interpretations of the sources and sinks at the land surface. Furthermore, the coupling of the calculation of atmospheric and biological processes at the land surface provides an opportunity for better understanding of the linkages between the plant environment and biological influences on radiatively active trace gases. The extra computational investment required for such a calculation is a good one.

References

Aber, J. D., J. M. Melillo, K. J. Nadelhoffer, J. Pastor, and R. D. Boone, 1991: Factors controlling nitrogen cycling and nitrogen saturation in northern temperate forest ecosystems. *Ecological Applications*, **1**, 303-315.

Arakawa, A., and W. H. Schubert, 1974: Interaction of a cumulus cloud ensemble with the large-scale environment, Part I. *J. Atmos. Sci.*, **31**, 674-701.

Arakawa, A. and V. R. Lamb, 1977: Computational design of the basic dynamical processes of the UCLA general circulation model. *Methods in Computational Physics*, **17**, 173-265, Academic Press, New York, 173-265.

Arakawa, A., and V. R. Lamb, 1981: A potential enstrophy and energy conserving scheme for the shallow water equations. *Mon. Wea. Rev.*, **109**, 18-36.

Archer, D., 1990: *Modeling p_{CO2} in the Upper Ocean: a Review of Relevant Physical, Chemical, and Biological Processes*. DOE/RL-01830T-H5, United States Department of Energy, Carbon Dioxide Research Program, Washington, D.C., 63 pp.

Arp, W. J., Effects of source-sink relations on photosynthetic acclimation to elevated CO_2. *Plant Cell Environ.*, **14**, 869-875.

Arrhenius, S., 1896: On the influence of carbonic acid in the air upon the temperature of the ground. *Phil. Mag.*, **41**, 237-276.

Azevedo, A. E., 1982: Atmospheric distribution of CO_2 and its exchange with the biosphere and the oceans, PhD. dissertation, Columbia University, New York.

Baes, C. F., Jr., A. Björkstrom and P. J. Mulholland, 1985: Uptake of carbon dioxide by the oceans. In: J. R. Trabalka and D. E. Reichle (Eds.), *Atmospheric Carbon Dioxide and the Global Carbon Cycle*, DOE/ER-0239, U.S. Department of Energy, Oak Ridge, Tenn., 82-111.

Bacastow, R. B., 1976: Modulation of atmospheric carbon dioxide by the southern oscillation. *Nature*, **261**, 116-118.

Bacastow, R. B., C. D. Keeling and T. P. Whorf, 1985: Seasonal amplitude increase in atmospheric CO_2 concentration at Mauna Loa, Hawaii, 1959-82. *Jour. Geophys. Res.*, **90**, 10529-10540.

Bacastow, R. B. and E. Meier-Reimer, 1990: Ocean circulation model of the carbon cycle. *Clim. Dyn.*, **4**, 95-125.

Ball, J. T., I. E. Woodrow, and J. A. Berry, 1986: A model predicting stomatal conductance and its contribution to the control of photosynthesis under different environmental conditions. In: J. Briggins (Ed.) *Progress in Photosynthesis research*, Martinus Nijhoff, Dordrecht, The Netherlands, **4**, 221-224.

Ball, J. T., 1987: Calculations related to gas exchange. In: E. Zeiger, G. D. Farquhar and I. R. Cowan (Eds.), *Stomatal Function*. Stanford University Press, Stanford, Calif., 446-476.

Ball, J. T., 1988: An analysis of stomatal conductance. Ph.D. Thesis, Stanford University, Stanford, Calif., 89 pp.

Barnola, J. M., D. Raynaud, Y. S. Korotkevitch and C. Lorius, 1987: Vostok ice core: A 160,000 year record of atmospheric CO_2. *Nature*, **329**, 408-414.

Bazazz, F. A. and E. D. Fajer, 1992: Plant life in a CO_2-rich world. *Sci. Amer.*, **Jan.**, 68-74.

Bearman, G., 1989: *Ocean Circulation*. Open University - Pergamon Press, Oxford, 238 pp.

Bischof, W., 1965: Carbon dioxide concentrations in the upper troposphere and lower stratosphere. I. *Tellus*, **17**, 398-402.

Bischof, W., 1966: Space and time variations of the CO_2 content of the troposphere and lower stratosphere. *Tellus*, **18**, 155-158.

Bolin, B. and C. D. Keeling, 1963: Large-scale atmospheric mixing as deduced from the seasonal and meridional variations of carbon dioxide. *Jour. Geophys. Res.*, **68**, 3899-3920.

Bolin, B., and W. Bischof, 1970: Variations of the carbon dioxide content of the atmosphere in the northern hemisphere. *Tellus*, **22**, 431-442.

Bolin, B., 1977: Changes of land biota and their importance for the carbon cycle. *Science*, **196**, 613-615.

Bolin, B. and I. Fung, 1992: The carbon cycle revisited. In D. Ojima (Ed.), *Modeling the Earth System*, University Corporation for Atmospheric Research, Office of Interdisciplinary Earth Studies, Global Change Institute, **3**, Boulder, Colo., 151-164.

Bonan, G. B., 1991: Atmosphere-biosphere exchange of carbon dioxide in boreal forests. *Jour. Geophys. Res.*, **96**, 7301-7312.

Bretherton, F., R. E. Dickinson, I. Fung, B. Moore III, M. Prather, S. Running, and H. Tiessen, 1992: Report: Linkages between terrestrial ecosystems and the atmosphere. In: D. Ojima (Ed.), *Modeling the Earth System*, University Corporation for Atmospheric Research, Office of Interdisciplinary Earth Studies, Global Change Institute, **3**, Boulder, Colo., 181-196.

Briegleb, B. P., P Minnis, V. Ramanathan, and E. Harrison, 1986: Comparison of regional clear-sky albedos inferred from satellite observations and model computations. *J. Clim. Appl. Meteor.*, **25**, 214-226.

Broecker, W. S., 1974: *Chemical Oceanography*, Harcourt Brace Jovanovich, Inc., 214 pp.

Broecker, W. S., T. Takahashi., H. J Simpson and T. - H. Peng, 1979: Fate of fossil fuel carbon dioxide and the global carbon budget. *Science* **206**,409-418.

Broecker, W. S., J. R. Ledwell, T. Takahashi, R. Weiss, L. Merlivat, L. Memery, T. -H. Peng, B. Jahne and K. O. Munnich, 1986. Isotopic versus micrometeorologic ocean CO_2 fluxes: a serious conflict. *Jour. Geophys. Res.*, **91**, 10517-10527.

Broecker, W. S. and T.-H. Peng, 1992: Interhemispheric transport of carbon dioxide by ocean circulation. *Nature*, **356**, 587-589.

Broecker, W. S. and T.-H. Peng, 1993: Evaluation of the ^{13}C constraint on the uptake of fossil fuel CO_2 by the ocean? *Global Biogeochemical Cycles*, **7**, 619-626.

Brown, H. T. and F. Escombe, 1905: On the variations in the amount of carbon dioxide in the air of Kew during the years 1893-1901. *Proc. R. Soc. London (Biol.)*, **76**, 118-121.

Brown, J., A. Colling, D. Park, J. Phillips, D. Rothery and J. Wright, 1989: *Ocean Circulation*, Open University Course, Pergamon Press, Oxford, 238 pp.

Bryan, K., 1984: Accelerating the convergence to equilibrium of ocean climate models. *Jour. Phys. Oceanogr.*, **14**, 666-673.

Buch, K., 1939: Beobachtunge nüber das Kohlensäuregleichgewicht und über den Kohlensaueraustausch zwischen atmosphäre und meer im Nordatantischen Ozean, *Acta Math Phys.*, **11**, 1-32, Academi Abo, Finland.

Budyko, M. I., 1969: The effect of solar radiation variations on the climate of the Earth. *Tellus*, **21**, 611-619.

Callendar, G. S., 1938: The artificial production of carbon dioxide and its influence on temperature. *Quart. Jour. Royal Meteor. Soc.*, **64**, 223-240.

Callendar, G. S., 1940: Variations in the amount of carbon dioxide in different air currents. *Quart. Jour. Royal Meteor. Soc.*, **66**, 395-400.

Callendar, G. S., 1958: On the amount of carbon dioxide in the atmosphere. *Tellus*, **10**, 243-248.

Chamberlain, T. C., 1897: A group of hypotheses bearing on climatic changes. *Jour. Geology*, **5**, 653-683.

Chang, R., 1981: *Chemistry*. Random House, New York. 815 pp.

Cleveland, W. S., A. E. Freeny and T. E. Graedel, 1983: The seasonal component of atmospheric CO_2: information from new approaches to the decomposition of seasonal time series. *Jour. Geophys. Res.*, **88**, 10934-10946.

Collatz, G. J., J. T. Ball, C. Grivet, and J. A. Berry, 1991: Physiological and environmental regulation of stomatal conductance, photosynthesis, and transpiration: a model that includes a laminar boundary layer. *Agric. and Forest Meteorol.*, **54**, 107-136.

Colwell, J. E., 1974: Vegetation canopy reflectance. *Remote Sens. Environ.*, **3**, 174-183.

Conroy, J. P., R. M. Smillie, M. Küppers, B. Küppers, D. I. Bevage, and E. W. Barlow, 1986: Chlorophyll *a* fluorescence and photosynthetic and growth responses of *Pinus radiata* to phosphorus deficiency, drought stress, and high CO_2. *Plant Physiol.*, **81**, 423-429.

Conway, T. J., P. Tans, L. S. Waterman, K. W. Thoning, K. A. Masarie, and R. H. Gammon, 1988: Atmospheric carbon dioxide measurements in the remote global troposphere, 1981-1984. *Tellus*, **40B**, 81-115.

Conway, T. J. and P. P. Tans, 1989: Atmospheric CO_2 concentrations – the NOAA/GMCC flask sampling network (CDIAC NDP-005/R1). Carbon Dioxide Inf. Anal. Cent., Oak Ridge Nat. Lab., Oak Ridge, TN.

Conway, T. J., P. P. Tans, L. S. Waterman, K. Thoning, D. R. Kitzis, K. A. Masarie, and N. Zhang, 1994: Evidence for interannual variability of the carbon cycle from the NOAA/CMDL global air sampling network. *Jour. Geophys. Res.*, (submitted).

Cowan, I. R., 1986: Economics of carbon fixation in higher plants. In: T. J. Givnish (Ed.), *On the Economy of Plant Form and Function*, Cambridge University Press, Cambridge, UK, 133-170.

Craig, H., 1953: The geochemistry of stable carbon isotopes. *Geochim. Cosmochim. Acta*, **3**, 53-92.

Craig, H., 1957: The natural distribution of radiocarbon and the exchange time of carbon dioxide between atmosphere and sea. *Tellus*, **9**, 1-17.

Curtis, P. S., L. M. Balduman, B. G. Drake, and D. F. Whigham, 1990: Elevated atmospheric CO_2 effects on belowground processes in C_3 and C_4 estuarine marsh communities. *Ecology*, **71**, 2001-2006.

Czeplak, G. and C. Junge, 1974: Studies of interhemispheric exchange in the troposphere by a diffusion model. *Adv. Geophys.*, **18B**, 57-72.

Degens, E. T., 1969: Biogeochemistry of stable carbon isotopes. In: G. Eglington and M. T. J. Murphy (Eds.) *Organic Geochemistry, Methods and Results*, Springer-Verlag, New York, 304-329.

Dewey, K. F. and R. Heim, Jr., 1981: Satellite observations of variations in Northern Hemisphere seasonal snow cover. NOAA technical report NESS 87. United States Department of Commerce, Washington, DC., 79 pp.

Dorman, J. L. and P. J. Sellers, 1989: A global climatology of albedo, roughness length and stomatal resistance for atmospheric general circulation models as represented by the Simple Biosphere model (SiB). *Jour. Appl. Meteorol.*, **28**, 833-855.

Drake, B. G., 1992: A field study of the effects of elevated CO_2 on ecosystem processes in a Chesapeake Bay wetland. *Aust. Jour. Bot.*, **40**, 579-595.

Drever, J. I., 1988: *The Geochemistry of Natural Waters,* Prentice Hall, Englewood Cliffs, New Jersey, 437 pp.

Duce, R. A., P. S. Liss, J. T. Merrill, E. L. Atlas, P. Buat-Menard, B. B. Hicks, J. M. Miller, J. M. Prospero, R. Arimoto, T. M. Church, W. Ellis, J. N. Galloway, L. Hansen, T. D. Jickells, A. H. Knap, K. H. Reinhardt, B. Schneider, A. Soudine, J. J. Tokos, S. Tsunogai, R. Wollast, and M. Zhou, 1991: Atmospheric input of trace species to the world oceans. *Global Biogeochem. Cycles*, **5**, 193-259.

Eriksson, E. and P. Welander, 1956: On a mathematical model of the carbon cycle in nature. *Tellus*, **8**, 155-175.

Emanuel, W. R., G. G. Killough, W. M. Post and H. H. Schugart, 1984: Modeling terrestrial ecosystems in the global carbon cycle with shifts in carbon storage capacity by land-use change. *Ecology*, **65**, 970-983.

Enting, I. G., 1985: Principles of constrained inversion in the calibration of carbon cycle models. *Tellus*, **37B**, 7-27.

Enting, I. G., and J. V. Mansbridge, 1987: The incompatibility of ice-core CO_2 data with reconstructions of biotic CO_2 sources. *Tellus*, **39B**, 318-325.

Enting, I. G., and J. V. Mansbridge, 1987: Latitudinal distribution of sources and sinks of CO_2: Results of an inversion study. *Tellus*, **43B**, 156-170.

Enting, I. G., and G. I. Pearman, 1987: Description of a one-dimensional carbon cycle model calibrated using techniques of constrained inversion. *Tellus*, **39B**, 459-476.

Enting, I. G., and J. V. Mansbridge, 1989: Seasonal sources and sinks of atmospheric CO_2. Direct inversion of filtered data. *Tellus*, **39B**, 318-325.

Falkowski, P. G. and C. Wilson, 1992: Phytoplankton productivity in the North Pacific ocean since 1900 and implications for absorption of anthropogenic CO_2. *Nature*, **358**, 741-743.

Fan, S.-M., S. C. Wofsy, P. S. Bakwin, D. J. Jacob, and D. R. Fitzjarrald, 1990: Atmosphere-biosphere exchange of CO_2 and O_3 in the central Amazon forest. *Jour. Geophys. Res.*, **95**, 16851-16864.

Farquhar, G. D., 1979: Models describing the kinetics of ribulose bisphosphate carboxylase-oxygenase. *Arch. Biochem. Biophys.*, **193**, 456-468.

Farquhar, G. D., S. von Caemmerer and J. A. Berry, 1980: A biochemical model of photosynthetic CO_2 assimilation in C_3 plants. *Planta*, **149**, 78-90.

Farquhar, G. D., J. Lloyd, J. A. Taylor, L. B. Flanagan, J. P. Syvertsen, K. T. Hubick, S. C. Wong, and J. R. Ehleringer, 1993: Vegetation effects on the isotope composition of oxygen in atmospheric CO_2. *Nature*, **363**, 439-442.

Faure, G., 1977: *Principles of Isotope Geology.* John Wiley and Sons, New York, 464 pp.

Field, C. and H. A. Mooney, 1986: The photosynthesis-nitrogen relationship in wild plants. In: T. J. Givnish (Ed.), *On the Economy of Plant Form and Function*, Cambridge University Press, Cambridge, UK, 25-55.

Fourier, M., 1827: Mémoire sur les températures du globe terreste et des espaces planétaires. *Mem. de l'Académie Royale des Sciences de l'Institut de France*, **7**, 569-604.

Fowler, L. A., D. A. Randall, and S. A. Rutledge, 1994: Liquid and ice cloud microphysics in the CSU General Circulation Model. Part I: Model description and simulated microphysical processes. Submitted to *Jour. Clim.*

Fowler, L. A. and D. A. Randall 1994: Liquid and ice cloud microphysics in the CSU General Circulation Model. Part II: Impact on cloudiness, the Earth's radiation budget, and the general circulation of the atmosphere. Submitted to *Jour. Clim.*

Francey, R. J., 1985: Cape Grim isotope measurements – A preliminary assessment. *Jour. Atmos. Chem.*, **3**, 247-260.

Francey, R. J., F. J. Robbins, C. E. Allison, and N. G. Richards, 1990. The CSIRO global survey of CO_2 stable isotopes. In: S. R. Wilson and G. P. Ayers, (Eds.), *Baseline Atmospheric Program 1988*, Australian Bureau of Meteorology, 16-27.

Fraser, P. J., G. I. Pearman and P. Hyson, 1983: The global distribution of atmospheric carbon dioxide. 2. A review of provisional background observations, 1978-1980. *Jour. Geophys. Res.*, **88**, 3591-3598.

Fraser, P. J., W. P. Elliot and L. S. Waterman, 1986: Atmospheric CO_2 record from direct chemical measurements during the 19th century. In: J. R. Trabalka and D. E. Reichle (Eds.), *The Changing Carbon Cycle: A Global Analysis*, Springer-Verlag, New York, 66-88.

Friedli, H., H. Loetscher, H. Oeschger, U. Siegenthaler and B. Stauffer, 1986: Ice core record of the $^{13}C/^{12}C$ record of atmospheric CO_2 in the past two centuries. *Nature*, **324**, 237-238.

Fung, I., K. Prentice, E. Matthews, J. Lerner and G. Russell, 1983: Three-dimensional tracer model study of atmospheric CO_2: Response to seasonal exchanges with the terrestrial biosphere. *Jour. Geophys. Res.*, **88**, 1281-1294.

Fung, I. Y., 1986: Analysis of seasonal and geographic patterns of atmospheric CO_2 distributions with a three-dimensional tracer model. In: J. R. Trabalka and D. E. Reichle (Eds.), *The Changing Carbon Cycle: A Global Analysis*, Springer-Verlag, New York, 459-473.

Fung, I. Y., C. J. Tucker and K. C. Prentice, 1987: Application of very high resolution radiometer vegetation index to study atmosphere-biosphere exchange of CO_2. *Jour. Geophys. Res* **92**, 2999-3015.

Gillette, D. A. and E. O. Box, 1986: Modeling seasonal changes of atmospheric carbon dioxide and carbon 13. *Jour. Geophys. Res.*, **91**, 5287-5304.

Givnish, T. J., 1986: Optimal stomatal conductance, allocation of energy between leaves and roots, and the marginal cost of transpiration. In: T. J. Givnish (Ed.), *On the Economy of Plant Form and Function*, Cambridge University Press, Cambridge, UK, 171-213.

Goward, S. N., C. J. Tucker, and D. G. Dye, 1985: North American vegetation patterns observed with the NOAA-7 advanced very high resolution radiometer. *Vegetatio*, **64**, 3-14.

Goward, S. N., A. Kerber, D. G. Dye, and V. Kalb, 1987: Comparison of North and South American biomes from AVHRR observations. *Geocarto*, **2**, 27-40.

Goudriaan, J. and G. L. Atjay, 1977: The possible effects of increased CO_2 on photosynthesis. In: B. Bolin, E. J. Degens, S. Kempe, and P. Ketner (Eds.), *The Global Carbon Cycle*, SCOPE 13, Wiley, New York. 237-249.

Gough, D. O., 1981: Solar interior structure and luminosity variations. *Solar Phys.*, **74**, 21-34.

Graybill, D. A. and S. B. Idso, 1993: Detecting the aerial fertilization effect of atmospheric CO_2 enrichment in tree-ring chronologies. *Global Biogeochem. Cycles*, **7**, 81-95.

Haldane, J. B. S., 1936: Carbon dioxide content of atmospheric air. *Nature*, **137**, 575.

Hall, C. A. S., C. A. Ekdahl and D. E. Wartenberg, 1975: A fifteen-year record of biotic metabolism in the northern hemisphere. *Nature*, **255**, 136-138.

Hall, C. A. S., T. Hanqin, and Y. Qi, 1993: Response of the biosphere to the changing global environment: Evidence from the historic record of biotic metabolism. *World Resource Review*, **5**, 207-213.

Haltiner, G. J. and R. T. Williams, 1980: *Numerical Prediction and Dynamic Meteorology*. J. Wiley and Sons, 477 pp.

Hansen, J., G. Russel, D. Rind, P. Stone, A. Lacis, S. Lebedeff, R. Ruedy and L. Travis, 1983: Efficient three-dimensional global models for climate studies, models I and II. *Mon. Weather Rev.*, **111**, 609-662.

Harmon, M. E., W. K. Ferrell, and J. F. Franklin, 1990: Effects on carbon storage of conversion of old-growth forests to young forests. *Science*, **247**, 699-702.

Harriss, R. C., S. C. Wofsy, M. Garstang, E. V. Browell, L. C. B. Molion, R. J. McNeal, J. M. Hoell, Jr., R. J. Bendura, S. M. Beck, R. L. Navarro, J. T. Riley, and R. L. Snell, 1988: The Amazon Boundary Layer Experiment (ABLE 2A): Dry season, 1985. *Jour. Geophys. Res.*, **93**, 1351-1360.

Harshvardhan, R. Davies, D. A. Randall, and T. G. Corsetti, 1987: A fast radiation parameterization for general circulation models. *J. Geophys. Res.*, **92**, 1009-1016.

Harshvardhan, D. A. Randall, T. G. Corsetti, and D. A. Dazlich, 1989: Earth radiation budget and cloudiness simulations with a general circulation model. *J. Atmos. Sci.*, **46**, 1922-1942.

Heimann, M., C. D Keeling., and I. Y. Fung, 1986: Simulating the atmospheric carbon dioxide distribution with a three-dimensional tracer model. In: J. R. Trabalka and D. E. Reichle (Eds.), *The Changing Carbon Cycle: A Global Analysis*, Springer-Verlag, New York, 16-49.

Heimann, M. and C. D. Keeling, 1989: A three-dimensional model of atmospheric CO_2 transport based on observed winds: 2. Model description and simulated tracer experiments. In: D. H. Peterson (Ed.), *Aspects of Climate Variability in the Pacific and Western Americas, Geophysical Monograph* 55, American Geophysical Union, Washington, DC, 237-275.

Heimann, M., C. D. Keeling and C. J. Tucker, 1989: A three-dimensional model of atmospheric CO_2 transport based on observed winds: Seasonal cycle and synoptic time scale variations. In: D. H. Peterson (Ed.), *Aspects of Climate Variability in the Pacific and*

Western Americas,Geophysical Monograph 55, American Geophysical Union, Washington, DC, 277-303.

Holland, H. D., 1984: *The Chemical Evolution of the Atmosphere and Oceans*. Princeton University Press, Princeton, N. J., 582 pp.

Hollingsworth, A., D. B. Shaw, P. Lonnberg, L. Illari, K. Arpe, and A. J. Simmons, 1986: Monitoring of observation and analysis quality by a data assimilation system. *Monthly Weather Rev.*, **114**, 861-879.

Houghton, J. T., G. J. Jenkins and J. J. Ephraums (Eds.), 1990: *Climate Change. The IPCC Scientific Assessment*. Cambridge University Press.

Houghton, R. A. and G. M. Woodwell, 1983: Effect of increased C, N, P, and S on the global storage of C. In: B. Bolin and R. B. Cook, (Eds.), *The Major Biogeochemical Cycles and Their Interactions*, SCOPE 21, 327-343.

Houghton, R. A., J. E. Hobbie, J. M. Melillo, B. Moore, B. J. Peterson, G. R. Shaver, and G. M. Woodwell, 1983: Changes in the carbon content of terrestrial biota and soils between 1860 and 1980: a net release of CO_2 to the atmosphere. *Ecol. Monogr.*, **53**, 235-262.

Houghton, R. A., R. D. Boone, J. R. Fruci, J. E. Hobbie, J. M. Melillo, C. A. Palm, B. J. Peterson, G. R. Shaver, G. M. Woodwell, B. Moore, D. L. Skole and N. Myers, 1987: The flux of carbon from terrestrial ecosystems to the atmosphere in 1980 due to changes in land use: geographic distribution of the global flux. *Tellus* **39B**, 122-139.

Houghton, R. A., 1989: The long-term flux of carbon to the atmosphere from changes in land use. In: *Proceeding s of the Third International Conference on Analysis and Evaluation of Atmospheric CO_2 Data Present and Past*, Environmental Pollution Monitoring and Research Programme, **59**, World Meteorological Organization, Geneva, Switzerland, 80-85.

Houghton, R. A., 1993: Is carbon accumulating in the northern temperate zone? *Global Biogeochem. Cycles*, **7**, 611-618.

Hyson, P., P. J. Fraser and G. I. Pearman, 1980: A two-dimensional transport simulation model for trace atmospheric constituents. *Jour. Geophys. Res.*, **85**, 4443-4455.

Idso, K. E., 1992: Plant responses to rising levels of atmospheric carbon dioxide: A compilation and analysis of the results of a decade of international research into the direct biological effects of atmospheric CO_2 enrichment. Climatol. Pub. Sci. Paper 23, Office of Climatol., Arizona State Univ., Tempe, Ariz.

Idso, S. B. and B. A. Kimball, 1993: Tree growth in carbon dioxide enriched air and its implications for global carbon cycling and maximum levels of atmospheric CO_2. *Global Biogeochem. Cycles*, **7**, 537-556.

Jacob, D. J., M. J. Prather, S. C. Wofsy and M. B. McElroy, 1987: Atmospheric distribution of ^{85}Kr simulated with a general circulation model. *Jour. Geophys. Res.*, **92**, 6614-6626.

Jouzel, J., G. L. Russell, R. J. Suozzo, R. D. Koster, J. W. C. White, and W. S. Borecker, 1987: Simulations of the HDO and $H_2{}^{18}O$ atmospheric cycles using the NASA GISS general circulation model: The seasonal cycle for present-day conditions. *Jour. Geophys. Res.*, **92**, 14739-14760.

Jarvis, P. G., 1989: Atmospheric carbon dioxide and forests. *Philos. Trans. R. Soc. London, Ser. B*, **324**, 369-392.

Junge, C. E. and G. Czeplak, 1968: Some aspects of the seasonal variation of carbon dioxide and ozone. *Tellus*, **20**, 422-434.

Justice, C., J. Townshend, B. Holben, and C. Tucker, 1985: Analysis of the phenology of global vegetation using meteorological satellite data. *Intern. Jour. Remote Sens.*, **6**, 1271-1318.

Kasting, J. F., O. B. Toon and J. B. Pollack, 1988: How climate evolved on the terrestrial planets. *Scientific American*, **258**, 90-97.

Kauppi, P. E., K. Melikanen and K. Kuusela, 1992: Biomass and carbon budget of European forests, 1971 to 1990. *Science*, **256**, 70-74.

Keeling, C. D., 1958: The concentration and isotopic abundances of atmospheric carbon dioxide in rural areas. *Geochim. Cosmochim. Acta*, **13**, 322-334.

Keeling, C. D., 1960: The concentration and isotopic abundances of carbon dioxide in the atmosphere. *Tellus*, **12**, 200-202.

Keeling, C. D., T. B. Harris and E. M. Wilkins, 1968: Concentration of atmospheric carbon dioxide at 500 and 700 millibars. *Jour. Geophys. Res.*, **73**, 4511-4528.

Keeling, C. D., 1973: Industrial production of carbon dioxide from fossil fuels and limestone. *Tellus*, **25**, 174-198.

Keeling, C. D., 1973: The carbon dioxide cycle: reservoir models to depict the exchange of atmospheric carbon dioxide with the oceans and land plants. In: S. I. Rasool (ed.), *Chemistry of the Lower Atmosphere*, Plenum, New York, 251-329.

Keeling, C. D., R. B. Bacastow, A. E. Bainbridge, C. E. Ekdahl, Jr., P. R. Guenther, L. S. Waterman and J. F. S. Chin, 1976: Atmospheric carbon dioxide variations at Mauna Loa Observatory, Hawaii. *Tellus*, **28**, 538-551.

Keeling, C. D., J. A. Adams, Jr., C. E. Ekdahl, Jr. and P. R. Guenther, 1976: Atmospheric carbon dioxide variations at the South Pole. *Tellus*, **28**, 552-564.

Keeling, C. D., W. G. Mook and P. P. Tans, 1979: Recent trends in the $^{13}C/^{12}C$ ratio of atmospheric carbon dioxide. *Nature*, **277**, 121-123.

Keeling, C. D. and M. Heimann, 1986: Meridional eddy diffusion model of the transport of atmospheric carbon dioxide, 2. Mean annual carbon cycle. *Jour. Geophys. Res.*, **91**, 7782-7796.

Keeling, C. D., R. B. Bacastow, A. F. Carter, S. C. Piper, T. P. Whorf, M. Heimann, W. G. Mook and H. Roeloffzen, 1989: A three-dimensional model of atmospheric CO_2 transport based on observed winds: 1. Analysis of observational data. In: D. H. Peterson (Ed.), *Aspects of Climate Variability in the Pacific and Western Americas*, *Geophysical Monograph* 55, American Geophysical Union, Washington, DC, 165-236.

Keeling, C. D., S. C. Piper and M. Heimann, 1989: A three-dimensional model of atmospheric CO_2 transport based on observed winds: 4. Mean annual gradients and interannual variations. In: D. H. Peterson (Ed.), *Aspects of Climate Variability in the Pacific and Western Americas*, *Geophysical Monograph* 55, American Geophysical Union, Washington, DC, 305-363.

Keeling, R. F., 1988: Measuring correlations between atmospheric oxygen and carbon dioxide mole fractions: A preliminary study in urban air. *Jour. Atmos. Chem.*, **7**, 153-176.

Keeling, R. F. and S. R. Shertz, 1992: Seasonal and interannual variations in atmospheric oxygen and implications for the global carbon cycle. *Nature*, **358**, 723-727.

Keeling, R. F., R. P. Najjar, M. L. Bender and P. P. Tans, 1993: *What atmospheric oxygen measurements can tell us about the global carbon cycle. Global Biogeochem. Cycles*, **7**:37-68.

Kimball, B. A., Carbon dioxide and agricultural yield: An assemblage and analysis of 430 prior observations, *Agron. Jour.*, **75**, 779-788.

Knight, D. H., T. J. Fahey, and S. W. Running, 1985: Factors affecting water and nutrient outflow from lodgepole pine forests in Wyoming. *Ecol. Monogr.*, **55**, 29-48.

Knox, F. and M. McElroy, 1984: Changes in atmospheric CO_2, influence of the marine biota at high latitudes. *Jour. Geophys. Res.*, **89**, 4629-4637.

Kolchugina, T. P. and T. S. Vinson, 1993: Carbon sources and sinks in forest biomes of the former Soviet Union. *Global Biogeochem. Cycles*, **7**, 291-304.

Komhyr, W. D., L. S. Waterman and W. R. Taylor, 1983: Semiautomatic nondispersive infrared analyzer apparatus for CO_2 air sample analyses, *Jour. Geophys. Res.*, **88**, 1315-1322.

Komhyr, W. D., T. B. Harris and L. S. Waterman, 1985: Calibration of nondispersive infrared CO_2 analyzers with CO_2-in-air reference gases, *Jour. Atmos. and Oceanic Technol.*, **2**, 82-88.

Komhyr, W. D., R. H. Gammon, T. B. Harris, L. S. Waterman, T. J. Conway, W. R. Taylor and K. W. Thoning, 1985: Global atmospheric CO_2 distribution and variations from 1968-82 NOAA/GMCC CO_2 flask sample data, *Jour. Geophys. Res.*, **90**, 5567-5596.

Körner, C. and J. A. Arnone, 1992: Responses to elevated carbon dioxide in artificial tropical ecosystems. *Science*, **257**, 1672-1675.

Krauskopf, K. B., 1979: *Introduction to Geochemistry*. McGraw-Hill Book Company, New York, 617 pp.

Legates, D.R. and C.J. Willmott. 1990. Mean seasonal and spatial variability in global surface air temperature. *Theor. Appl. Climatol.* **41**, 11-21.

Legates, D.R. and C.J. Willmott. 1990. Mean seasonal and spatial variability in gauge-corrected global precipitation. *Int. J. Climatology* **10**, 111-127.

Letts, E. A. and R. F. Blake, 1900: The carbonic anhydride of the atmosphere. *R. Dublin Soc. Rep.*, **9**, 107-270.

Lieth, H., 1965: Versuch einer Kartographischen Darstellung der Produktivitat der Pflanzendecke auf der Erde, In: *Geographisches Taschenbuch 1964/1965*, Franz Steiner Verlag Gmbtt., Wiesbaden, 72-80.

Liou, K.-N., 1980: *An Introduction to Atmospheric Radiation*. International Geophysics Series, **26**, Academic Press, San Diego, Calif., 392 pp.

Liss, P. and L. Merlivat, 1986: Air-sea gas exchange rates: Introduction and synthesis. In P. Buat-Menard (Ed.), *The Role of Air-Sea Exchange in Geochemical Cycling*, Adv. Sci. Inst. Ser. 185, Reidel, Hingham, 113-127.

Libby, W. F., 1955: *Radiocarbon Dating*, University of Chicago Press, Chicago, 175 pp.

Liu, S. C., J. R. McAfee, and R. J. Cicerone, 1984: Radon 222 and tropospheric vertical transport. *Jour. Geophys. Res.*, **89**, 7291-7297.

Long, S. P. and B. G. Drake, 1991: Effect of the long-term elevation of CO_2 concentration in the field on the quantum yield of photosynthesis of tthe C_3 sedge, *Scirpus olneyi*. *Plant Physiol.*, **96**, 221-226.

Lord, S. J., 1978: Development and observational verification of a cumulus cloud parameterization. PhD. Dissertation, University of California, Los Angeles, 339 pp.

Lord, S. J., 1982: Interaction of a cumulus cloud ensemble with the large-scale environment. Part III. Semi-prognostic test of the Arakawa-Schubert parameterization. *J. Atmos. Sci.*, **39**, 88-103.

Lord, S. J. and A. Arakawa, 1980: Interaction of a cumulus ensemble with the large-scale environment. Part II. *Jour. Atmos. Sci.*, **37**, 2677-2692.

Lord, S. J., W. C. Chao, and A. Arakawa, 1982: Interaction of a cumulus cloud ensemble with the large-scale environment. Part IV. The discrete model. *J. Atmos. Sci.*, **39**, 104-113.

Lorenc, A. C., 1981: A global three-dimensional multivariate statistical interpolation scheme. *Monthly Weather Rev.*, **109**, 701-721.

Lorimer, G. H., 1981: The carboxylation and oxygenation of ribulose 1,5-bisphosphate: the primary events in photosynthesis and photorespiration. *Ann. Rev. Plant Physiol.*, **32**, 349-383.

Los, S. O., C. O. Justice, and C. J. Tucker, 1994: A global 1° × 1° NDVI data set for climate studies derived from the GIMMS continental NDVI data. *Intern. Jour. Remote Sens.*, in press.

Machta, L., 1974: Global scale atmospheric mixing. *Adv. Geophys.*, **18B**, 33-56.

Maier-Reimer, E. and K. Hasselmann, 1987: Transport and storage of CO_2 in the ocean – An inorganic ocean-circulation cycle model. *Clim. Dyn.*, **2**, 63-90.

Maier-Reimer, E., 1993: Geochemical cycles in an ocean general circulation model. Preindustrial tracer distributions. *Global Biogeochem. Cycles*, **7**, 645-678.

Malanchuk, J. L. and J. Nilsson, Eds., 1989: *The Role of Nitrogen in the Acidification of Soils and Surface Waters*, Nordic Council of Ministers, Stockholm, Sweden.

Manabe, S., and R. Strickler, 1964: Thermal equilibrium of the atmosphere with a convective adjustment. *Jour. Atmos. Sci.*, **21**, 361-385.

Manabe, S., J. Smagorinsky, and R. Strickler, 1965: Simulated climatology of a general circulation model with a hydrologic cycle. *Monthly Weather Review*, **93**, 769-798.

Manabe, S., 1969: Climate and ocean circulation. Part I: The atmospheric radiation and the hydrology of the Earth's surface. *Monthly Weather Review*, **93**, 739-774.

Marland, G. and R. M. Rotty, 1984: Carbon dioxide emissions from fossil fuels: A procedure for estimations and results for 1950-1982. *Tellus*, **36B**, 232-261.

Marland, G., R. M. Rotty and R. L. Treat, 1985: CO_2 from fossil fuel burning: global distributions of emissions. *Tellus*, **37B**, 243-258.

Marland, G., 1989: Fossil fuels CO_2 emissions: Three countries account for 50% in 1988. CDIAC Communications, Winter, 1989, 1-4, Carbon Dioxide Inf. Anal. Cent., Oak Ridge Nat. Lab., Oak Ridge, TN.

Matthews, E., 1983: Global vegetation and land use: New high resolution data bases for climate studies. *J. Clim. Appl. Meteor.*, **22**, 474-487.

McPeters, R. D., D. F. Heath and P. K. Bhartia, 1984: Average ozone profiles for 1979 from the Nimbus-7 SBUV instrument. *J. Geophys. Res.*, **89**, 5199- 5214.

Melillo, J. M., A. D. McGuire, D. W. Kicklighter, B. Moore III, C. J. Vorosmarty, and A. L. Schloss, 1993: Global climate change and terrestrial net primary productivity. *Nature*, **363**, 234-240.

Mintz, Y. and V. Serafini, 1983: Monthly normal global fields of soil moisture and land-surface evapotranspiration. Symposium on variations in the global water budget, Oxford, England, August 10-15, 1981.

Monteith, J. L., 1972: Solar radiation and productivity in tropical ecosystems. *Jour. Appl. Ecol.*, **9**, 747-766.

Mooney, H. A., B. G. Drake, R. J. Luxmore, W. C., Oechel, and L. F. Pielka, 1991: Predicting ecosystem responses to elevated CO_2 concentrations. *BioScience*, **41**, 96-104.

Muntz, A. and E. Aubin, 1886: Mission scientifique du Cap Horn, 1882-1883. *Recherches sur la constitution chimique de l'atmosphere.* Tome III, Les Ministeres de la Marine et de l'Instruction Publique, Paris.

Myers, N., 1980: Report of survey of conversion rates in tropical moist forests. National Research Council, Washington, DC.

Nakazawa, T., K. Miyashita, S. Aoki, and M. Tanaka, 1991: Temporal and spatial variations of upper tropospheric and lower stratospheric carbon dioxide. *Tellus*, **39B**, 106-117.

Nier, A. O. and E. A. Gulbransen, 1939: Variation in the relative abundances of the carbon isotopes. *Jour. Amer. Chem. Soc.*, **61**, 697-698.

Nier, A. O., 1947: A mass spectrometer for isotope and gas analysis. *Rev. Sci. Instr.*, **18**, 398-411.

Neftel, A., E. Moor, H. Oeschger and B. Stauffer, 1985: Evidence from polar ice cores for the increase in atmospheric CO_2 in the past two centuries. *Nature*, **315**, 45-47.

Newell, R. E., D. G. Vincent, and J. W. Kidson, 1969: Interhemispheric mass exchange from meteorological and trace substance observations. *Tellus*, **21**, 641-647.

Nobel, P. S., 1974: *Biophysical Plant Physiology*, Second Edition. W. H. Freeman and Co., San Francisco, 488 pp.

Norby, R. J., C. A. Gunderson, S. D. Wullschleger, E. G. O'Neill, and M. K. McCracken, 1992: Productivity and compensatory responses of yellow-poplar trees in elevated CO_2. *Nature*, **357**, 322-324.

Oeschger, H., U. Siegenthaler, U. Schotterer and A. Gugelmann, 1975: A box diffusion model to study the carbon dioxide exchange in nature. *Tellus*, **27**, 168-192.

Olson, J. S., R. M. Garrels, R. A. Berner, T. V. Armentano, M. I. Dyer and D. H. Yaalon, 1985: The natural carbon cycle. In: J. R. Trabalka and D. E. Reichle (Eds.), *Atmospheric Carbon Dioxide and the Global Carbon Cycle*, DOE/ER-0239, U.S. Department of Energy, Oak Ridge, Tenn.,175-213.

Oort, A. H. and E. M. Rasmussen, 1971: *Atmospheric Circulation Statistics*. Professional Paper 5, National Oceanic and Atmospheric Administration, Rockland, MD, 323 pp.

Pales, J. C. and C. D. Keeling, 1965: The concentration of atmospheric carbon dioxide in Hawaii. *Jour. Geophys. Res.*, **24**, 6053-6076.

Palmer, T. N., G. J. Shutts, and R. Swinbank, 1986: Alleviation of a systematic westerly bias in general circulation and numerical weather prediction models through an orographic gravity wave parameterization. *Quart. J. Roy. Meteor. Soc.*, **112**, 1001-1039.

Parton, W. J., D. S. Schimel, C. V. Cole, and D. S. Ojima, 1987: Analysis of factors controlling soil organic matter levels in Great Plains grasslands. *Soil Sci. Am. Jour.*, **51**, 1173-1179.

W. J. Parton, J. M. O. Scurlock, D. S. Ojima, T. G. Gilmanov, R. J. Scholes, D. S. Schimel, T. Kirchner, J.-C. Menaut, T. Seastedt, E. Garcia Moya, A. Kamnalrut, and J. I. Kinyamario, 1993: Observations and modeling of biomass and soil organic matter dynamics for the grassland biome worldwide. *Global Biogeochem. Cycles*, **7**, 785-810.

Payne, R. E., 1972: Albedo of the sea surface. *J. Atmos. Sci.*, **29**, 959-970.

Pearman, G. I., 1980: Atmospheric CO_2 concentration measurements: A review of methodologies, existing programmes, and available data. *Rep. 3*, WMO Proj. on Res. and Monit. of Atmos. CO_2, Geneva.

Pearman, G. I. and P. Hyson, 1980: Activities of the global biosphere as reflected in atmospheric CO_2 records. *Jour. Geophys. Res.*, **85**, 4468-4474.

Pearman, G. I. and P. Hyson, 1981: The annual variation of atmospheric CO_2 concentration observed in the northern hemisphere. *Jour. Geophys. Res.*, **86**, 9839-9843.

Pearman, G. I., P. Hyson and P. J. Fraser, 1983: The global distribution of atmospheric carbon dioxide: 1. Aspects of observations and modeling. *Jour. Geophys. Res.*, **88**, 3581-3590.

Pearman, G. I., and D. J. Beardsmore, 1984: Atmospheric carbon dioxide measurements in the Australian region: Ten years of aircraft data. *Tellus*, **36B**, 1-24.

Pearman, G. I., D. Etheridge, F. deSilva and P. J. Fraser, 1986: Evidence of changing concentrations of atmospheric CO_2, N_2O, and CH_4 from air bubbles in Antarctic ice. *Nature*, **320**, 248-250.

Pearman, G.I., and Hyson, P., 1986. Global transport and inter-reservoir exchange of carbon dioxide with particular reference to stable isotopic distributions. *Jour. Atmos. Chem.*, **4**, 81-124.

Peixoto, J. P. and A. H. Oort, 1992: *Physics of Climate*. Amer. Inst. Physics, New York, 520 pp.

Peng, T.-H. and T. Takahashi, 1989: In: M. P. Farrell (Ed.), *Biogeochemistry of CO_2 and the Greenhouse Effect.* Am. Chem. Soc. Symp., CRC/Lewis, Boca Raton, Florida.

Peng, T.-H. and W. S. Broecker, 1991: Dynamical limitations on the Antarctic iron fertilization strategy. *Nature*, **349**, 227-229.

Petermann, A. and J. Graftiau, 1892-1893: Recherches sur la composition de l'atmosphere, Premiere partie, Acide carbonique contenu dans l'air atmospherique. *Bruxelles Mem. Couronn.*, **47**, 1-79.

Peterson and Melillo, 1985: The potential storage of carbon caused by eutrophication of the biosphere. *Tellus*, **37B**, 117-127.

Plass, G. N., 1956: The carbon dioxide theory of climatic change. *Trans. Amer. Geophys. Union*, **34**, 332.

Plass, G. N., 1956: The carbon dioxide theory of climate change. *Tellus*, **8**, 140-154.

Plumb, R. A., and D. D. McConalogue, 1988: On the meridional structure of long-lived tropospheric constituents. *Jour. Geophys. Res.*, **93**, 15897-15913.

Post, W. M., T.-H. Peng, W. R. Emanuel, A. W. King, V. H. Dale and D. L. DeAngelis, 1990: The global carbon cycle. *Amer. Scientist*, **78**, 310-326.

Potter, C. S., J. T. Randerson, C. B. Field, P. A. Matson, P. M. Vitousek, H. A. Mooney, and S. A. Klooster, 1993: Terrestrial ecosystem production: A process-oriented model based on global satellite and surface data. *Global Biogeochem. Cycles*, **7**, 811-842.

Prather, M. J., 1986: Numerical advection by conservation of second-order moments. *Jour. Geophys. Res.*, **91**, 6671-6681.

Prather, M., M. McElroy, S. Wofsy, G. Russel and D. Rind, 1987: Chemistry of the global troposphere: Fluorocarbons as tracers of air motion. *Jour. Geophys. Res.*, **92**, 6579-6613.

Press, F. and R. Siever, 1978: *Earth*, Second Edition. W. H. Freeman and Co., San Francisco, Calif., 649 pp.

Prinn, R. G., P. G. Simmonds, R. A. Rasmussen, R. D. Rosen, F. N. Alyea, C. A. Cardelino, A. J. Crawford, D. M. Cunnold, P. J. Fraser and J. E. Lovelock, 1983: The atmospheric lifetime experiment 1. Introduction, instrumentation and overview. *Jour. Geophys. Res.*, **88**, 8353-8367.

Quay, P. D., B. Tilbrook and C. S. Wong, 1992: Oceanic uptake of fossil fuel CO_2: Carbon-13 evidence. *Science*, **256**, 74-78.

Raich, J. W., E. B. Rastetter, J. M. Melillo, D. W. Kicklighter, P. A. Steudler, and B. J. Peterson, 1991: Potential net primary productivity of South America: Application of a global model. *Ecol. Applications*, **1**, 399-429.

Randall, D. A., 1980: Entrainment into a stratocumulus layer with distributed radiative cooling. *J. Atmos. Sci.*, **37**, 148-159.

Randall, D. A., 1984: Buoyant production and consumption of turbulence kinetic energy in cloud-topped mixed layers. *J. Atmos. Sci.*, **41**, 402-413.

Randall, D. A., J. A. Abeles, and T. G. Corsetti, 1985: Seasonal simulations of the planetary boundary layer and boundary-layer stratocumulus clouds with a general circulation model. *J. Atmos. Sci.*, **42**, 641-676.

Randall, D. A., 1987: Turbulent fluxes of liquid water and buoyancy in partly cloudy layers. *J. Atmos. Sci.*, **44**, 850-858.

Randall, D. A., Harshvardhan, D. A. Dazlich, and T. G. Corsetti, 1989: Interactions Among Radiation, Convection, and Large-Scale Dynamics in a General Circulation Model. *J. Atmos. Sci.*, **46**, 1943-1970.

Randall, D. A., Harshvardhan, and D. A. Dazlich, 1991: Diurnal variability of the hydrologic cycle in a general circulation model. *Jour. Atmos. Sci.*, **48**, 40-62.

Randall, D. A., Q. Shao and C.-H. Moeng, 1992: A second-order bulk boundary-layer model. *Jour. Atmos. Sci.*, **49**, 1903-1923.

Randall, D. A. and D.-M. Pan, 1993: Implementation of the Arakawa-Schubert parameterization with a prognostic closure. In: K. Emanuel and D. Raymond (Eds.), *The Representation of Cumulus Convection in Numerical Models*, a Meteorological Monograph, American Meterological Society, 246 pp.

Randall, D. R., P. J. Sellers, J. A. Berry, D. A. Dazlich, C. Zhang, J. A. Collatz, A. S. Denning, S. O. Los, C. B. Field, I. Fung, C. O. Justice, and C. J. Tucker, 1994: A revised land-surface parameterization (SiB2) for GCMs. Part 3: The greening of the Colorado State University General Circulation Model. Submitted to *Jour. Clim.*

Randel, W. J., 1992: *Global Atmospheric Circulation Statistics, 1000 - 1 mb*. NCAR Technical Note TN-366+STR, National Center for Atmospheric Research, Boulder, CO 256 pp.

Rasmussen, E. and T. Carpenter, 1982: Variations in tropical sea surface temperature and surface wind fields associated with the Southern Oscillation/El Niño. *Mon. Weather. Rev.*, **110**, 354-384.

Reiset, J. A., 1882: Recherches sur la proportion de l'acide carbonique dans l'air. *Ann. Chim. Phys.*, **26**, 145-221.

Revelle, R., and H. S. Suess, 1957: Carbon dioxide exchange between the atmosphere and ocean and the question of an increase of atmospheric CO_2 during the past decades. *Tellus*, **9**, 18-27.

Richardson, A. J. and C. L. Wiegand, 1977: Distinguishing vegetation from soil background information. *Photogramm. Eng. Remote Sens.*, **43**, 1541-1522.

Riebesell, U., D. A. Wolf-Gladrow, and V. Smetacek, 1993: Carbon dioxide limitation of marine phytoplankton growth rates. *Nature*, **361**, 249-251.

Rintoul, S. R., 1992: Towards coupled physical-biogeochemical models of the ocean carbon cycle. In: D. Ojima (Ed.), *Modeling the Earth System*, University Corporation for Atmospheric Research, Office of Interdisciplinary Earth Studies, Global Change Institute, **3**, Boulder, Colo., 39-76.

Robertson, J. E. and A. J. Watson, 1992: Thermal skin effect of the surface ocean and its implications for CO_2 uptake. *Nature*, **358**, 738-740.

Rogers, H. H., C. M. Peterson, J. N. McCrimmon, and J. D. Cure, 1992: Response of plant roots to elevated atmospheric carbon dioxide. *Plant Cell Environ.*, **15**, 749-752.

Rood, R. B., 1987: Numerical advection algorithms and their role in atmospheric transport and chemistry models. *Rev. Geophys.*, **25**, 71-100.

Rotty, R. M., 1973: Commentary on and extension of calculative procedure for CO_2 production. *Tellus*, **25**, 508-517.

Running, S. W. and J. C. Coughlan, 1988: A general model of forest ecosystem processes for regional applications. I. Hydrologic balance, canopy gas exchange and primary production processes. *Ecol. Modeling*, **42**, 125-154.

Running, S. W., R. R. nemani, D. L. Peterson, L. E. Band, D. F. Potts, L. L. Pierce, and M. A. Spanner, 1989: Mapping regional forest evapotranspiration and photosynthesis by coupling satellite data with ecosystem simulation modeling. *Ecology*, **70**, 1090-1101.

Running, S. W., 1992: A bottom-up evolution of terrestrial ecosystem modeling theory, and ideas toward global vegetation modeling. In: D. Ojima (ed.), *Modeling the Earth System*, University Corporation for Atmospheric Research, Office of Interdisciplinary Earth Studies, Global Change Institute, **3**, Boulder, Colo., 263-280.

Running, S. W. and E. R. Hunt, Jr., 1993: Generalization of a forest ecosystem process model for other biomes, BIOME-BGC, and an application for global-scale models. In: J. R. Ehleringer and C. B. Field (Eds.), *Scaling Physiological Processes: Leaf to Globe*, Academic Press, San Diego, 141-158.

Russel, G. L. and J. A. Lerner, 1981: A new finite-differencing for the tracer transport equation. *Jour. Appl. Meteor.*, **20**, 1483-1498.

Sagan, C. and G. Mullen, 1972: Earth and Mars: Evolution of atmospheres and surface temperatures. *Science*, **177**, 52-56.

Sanford, R. L., W. J. Parton, D. S. Ojima, and D. J. Lodge, 1991: Hurricane effects on soil organic matter dynamics and forest production in the Luquillo Experimental Forest, Puerto Rico: Results of simulation modeling. *Biotropica*, **23**, 364-373.

Sarmiento, J. L., J. C. Orr and U. Siegenthaler, 1992: A perturbation simulation of CO_2 uptake in an ocean general circulation model. *Jour. Geophys. Res.*, **97**, 3621-3645.

Sarmiento, J. L. and E. T. Sundquist, 1992: Revised budget for the oceanic uptake of anthropogenic carbon dioxide. *Nature*, **356**, 589-593.

Sato, N., Sellers, P.J., Randall, D.A., Schneider, E.K., Shukla, J., Kinter, J.L., Hou, Y-T., Albertazzi, E. 1989. Effects of implementing the simple biosphere model (SiB) in a general circulation model. *J. Atmos. Sci.*, **46**, 2757-2782.

Saxton, K. E., W. J. Rawls, J. S. Romberger, and R. I. Papendick, 1986: Estimating generalized soil-water characteristics from texture. *Soil Sci. Soc. Amer. Jour.*, **50**, 1031-1036.

Schiffman, P. M. and W. C. Johnson, 1989: Phytomass and detrital carbon storage during regrowth in the southeastern United States Piedmont. *Can. Jour. For. Res.*, **19**, 69-78.

Schindler, D. W. and S. E. Bayley, 1993: The biosphere as an in creasing sink for atmospheric carbon: Estimates from increased nitrogen deposition. *Global Biogeochem. Cycles*, **7**, 717-734.

Schlesinger, W. H., 1984: Soil organic matter: A source of atmospheric CO_2. In: G. M. Woodwell (Ed.), *The Role of Terrestrial Vegetation in the Global Carbon Cycle*, SCOPE 23, John Wiley and Sons, New York, 111-127.

Schlesinger, W. H., 1991: *Biogeochemistry: An Analysis of Global Change*. Academic Press, New York, 443 pp.

Schubert, S., S. Moorthi, C.-K. Park, M. Suarez, and W. Higgins, 1990: *An Atlas of ECMWF Analyses (1980-87)*. NASA Technical Memorandum 100747, National Aeronautic and Space Administration, Goddard Space Flight Center, Greenbelt, MD, 262 pp.

Schultze, F., 1871: Tägliche Beobachtungen über den Kohlensäureghalt der Atmosphäre zu Rostokvom 18 October 1868 bis 31 Juli 1871. *Landwirtscha Vers. Stn.*, **14**, 366-388.

Siegenthaler, U., 1983: Uptake of atmospheric CO_2 by an outcrop-diffusion model of the ocean. *Jour. Geophys. Res.*, **88**, 3599-3608.

Siegenthaler, U. and T. Wenk, 1984: Rapid atmospheric CO_2 variations and ocean circulation. *Nature*, **308**, 624-625.

Siegenthaler, U. and H. Oeschger, 1987: Biospheric CO_2 emissions during the past 200 years reconstructed by deconvolution of ice core data. *Tellus*, **39B**, 140-154.

Sedjo, R. A., 1992: Temperate forest ecosystems in the global carbon cycle. *Ambio*, **21**, 274-277.

Sellers, P. J., 1985: Canopy reflectance, photosynthesis, and transpiration. *Intern. Jour. Remote Sens.*, **6**, 1335-1371.

Sellers, P. J., 1987: Canopy reflectance, photosynthesis, and transpiration, II. The role of biophysics in the linearity of their interdependence. *Remote Sens. Environ.*, **21**, 143-183.

Sellers, P. J., Y. Mintz, Y. C. Sud, and A. Dalcher, 1986: A simple biosphere model (SiB) for use within general circulation models. *J. Atmos. Sci.*, **43**, 505-531.

Sellers, P. J., J. A. Berry, G. J. Collatz, C. B. Field, and F. G. Hall, 1992: Canopy reflectance, photosynthesis, and transpiration. III. A reanalysis using enzyme kinetics - electron transfer models of leaf physiology. *Remote Sens. Environ.*, **42**, 1-20.

Sellers, P. J., F. G. Hall, G. Asrar, D. E. Strebel, and R. E. Murphy, 1992: An overview of the First International Satellite Land Surface Climatology Project (ISLSCP) Field Experiment (FIFE). *Jour. Geophys. Res.*, **97**, 18345-18371.

Sellers, P. J., M. D. Heiser, and F. G. Hall, 1992: Relations between surface conductance and spectral vegetation indices at intermediate (100 m^2 to 15 km^2) length scales. *Jour. Geophys. Res.*, **97**, 19033-19059.

Sellers, P. J, D. R. Randall, J. A. Collatz, J. A. Berry, C. B. Field, D. A. Dazlich, and G. D. Collelo, 1994: A revised land-surface parameterization (SiB2) for GCMs. Part 1: Model formulation. Submitted to *Jour. Clim.*

Sellers, P. J., S. O. Los, C. J. Tucker, C. O. Justice, D. A. Dazlich, G. J. Collatz, and D. A. Randall, 1994: A revised land surface parameterization (SiB2) for atmospheric GCMs. Part 2: The generation of global fields of terrestrial biophysical parameters from satellite data. Submitted to *Jour. Clim.*

Smith, V. N., 1953: A recording infrared analyser. *Instruments*, **26**, 421-427.

Smolarkieicz, P. K. and W. W. Grabowski, 1990: The multidimensional positive definite advection transport algorithm: nonoscillatory option. *Jour. Comp. Phys.*, **86**, 355-375.

Solomons, T. W. G., 1980: *Organic Chemistry.* Wiley, New York. 1131 pp.

Stephens, G. L., D. A. Randall, S. J. Tjemkes, I. M. Wittmeyer, and D. A. Dazlich, 1993: The Earth's radiation budget in relation to the hydrologic cycle. Part III. Comparison of observations with a GCM. *Jour. Geophys. Res.*, **98**, 4931-4950.

Stryer, L., 1981: *Biochemistry*, Second Edition. W. H. Freeman and Co., San Francisco, 949 pp.

Suarez, M. J., A. Arakawa, and D. A. Randall, 1983: Parameterization of the planetary boundary layer in the UCLA general circulation model: Formulation and results. *Mon Wea. Rev,* **111**, 2224-2243.

Tanaka, M., T. Nakazawa and A. Aoki, 1987: Time and space variations of tropospheric carbon dioxide over Japan. *Tellus*, **39B**, 3-12.

Tans, P. P., T. J. Conway, and T. Nakazawa, 1989: Latitudinal distribution of the sources and sinks of atmospheric carbon dioxide derived from surface observations and an atmospheric transport model. *Jour. Geophys. Res.*, **94**, 5151-5172.

Tans, P. P., I. Y. Fung and T. Takahashi, 1990: Observational constraints on the global atmospheric CO_2 budget. *Science* **247**,1431-1438.

Tans, P. P., J. A. Berry and R. F. Keeling, 1993: Oceanic $^{13}C/^{12}C$ observations: a new window on ocean CO_2 uptake. *Global Biogeochemical Cycles*, **7**, 353-368.

Tans, P. P., 1993: Observational strategy for assessing the role of terrestrial ecosystems in the global carbon cycle: Scaling down to regional levels. In: J. R. Ehleringer and C. B. Field, (Eds.), *Scaling Physiological Processes: Leaf to Globe*, Academic Press, San Diego, 179-190.

Tans, P. P., 1994: Why carbon dioxide from fossil fuel burning won't go away. In: J. Birks, A. Elterman, D. Macalady, and T. Wildeman (Eds.), *Advances in Environmental Chemistry*, Lewis Publishing (In Press).

Tans, P. P., I. Y. Fung, and I. G. Enting, 1994: Storage versus flux budgets: The terrestrial uptake of CO_2 during the 1980's. In: G. M. Woodwell and F. T. Mackenzie (Eds.), *Biotic Feedbacks in the Global Climatic System; Will the Warming Feed the Warming?* Oxford University Press (In Press).

Thomas, R. B. and B. R. Strain, 1991: Root restriction as a factor in photosynthetic acclimation of cotton seedlings grown in elevated carbon dioxide. *Plant Physiol.*, **96**, 627-634.

Thompson, M. L., I. G. Enting, G. I. Pearman, and P. Hyson, 1986: Interannual variations of atmospheric CO_2 concentration. *Jour. Atmos. Chem.*, **4**, 125-155.

Thoning, K. W., P. Tans, T. J. Conway, and L. S. Waterman, 1987: NOAA/GMCC calibrations of CO_2-in-air reference gases: 1979-85, NOAA Tech. Memo. (ERL ARL-150), Environ. Res. Lab., Boulder, Colo., 63 pp.

Thoning, K. W, T. J. Conway, N. Zhang, and D. Kitzis, 1994: Ana;ysis system for measurement of the CO_2 mixing ratio in flask air samples. *Jour. Geophys. Res.*, (submitted).

Thornthwaite, C. W., 1948: An approach toward rational classification of climate. *Geogr. Rev.*, **38**, 55-94.

Thorpe, T. E., 1867: On the amount of carbonic acid contained in sea-air. *Jour. Chem. Soc. London*, **5** (complete series **20**), 189-201.

Toggweiler, J. R., K. Dixon and K. Bryan, 1989: Simulations of radiocarbon in a coarse-resolution world ocean model, I, Steady-state, pre-bomb distributions. *Jour. Geophys. Res.*, **94**, 8217-8242.

Toggweiler, J. R., K. Dixon and K. Bryan, 1989: Simulations of radiocarbon in a coarse-resolution world ocean model, II, Distributions of bomb-produced ^{14}C. *Jour. Geophys. Res.*, **94**, 8243-8264.

Trenberth, K. E., and J. G. Olson, 1988: An evaluation and intercomparison of global analyses from the National Meteorological Center and the European Centre for Medium Range Weather Forecasts. *Bull. Amer. Meteor. Soc.*, **69**, 1047-1057.

Tucker, C. J., 1979: Red and photographic infrared linear combinations for monitoring vegetation. *Remote Sens. Environ.*, **8**, 127-150.

Tucker, C. J., 1980: A critical review of remote sensing and other methods for non-destructive estimation of standing crop biomass. *Grass Forage Sci.*, **35**, 177-182.

Tucker, C. J., I. Y. Fung, C. D. Keeling and R. H. Gammon, 1986: Relationship between atmospheric CO_2 variations and a satellite-derived vegetation index. *Nature*, **319**, 195-199.

Tyndall, J., 1861: On the absorption and radiation of heat by gases and vapors, and the physical connection of radiation, absorption, and conduction. *Phil. Mag*, **22**, 169-194.

Verma, S. B., J. Kim, and R. J. Clement, 1989: Carbon dioxide, water vapor, and sensible heat fluxes over a tallgrass prairie. *Boudary-Layer Meteorol.*, **46**, 53-67.

Vitousek, P. M. and W. A. Reiners, 1975: Ecosystem succession and nutrient retention: A hypothesis. *BioScience*, **25**, 376-381.

Walker, J. G. C., 1977: *Evolution of the Atmosphere*, Macmillan, New York.

Wallace, J. M. and P. V. Hobbs, 1977: *Atmospheric Science: An Introductory Survey*. Academic Press, Orlando, Florida, 467 pp.

Weiss, R. F., 1974: Carbon dioxide in water and seawater: The solubility of a non-ideal gas. *Marine Chemistry*, **2**, 203-215.

Weiss, W., A. Sittkus, H. Stockburger, and H. Sartorius, 1983: Large-scale atmospheric mixing derived from meridional profiles of Krypton 85. *Jour. Geophys. Res.*, **88**, 8574-8578.

Whittaker, R. H. and G. E. Likens, 1975: The biosphere and man. In: H. Lieth and R. H. Whittaker (Eds.), *Primary Productivity of the Biosphere, Ecological Studies*, **14**, Springer-Verlag, New York, 305-328.

Williams, W. E., K. Garbutt, F. A. Bazzaz, and P. M. Vitousek, 1986: *Oecologia*, **69**, 454.

Wilson, C. A., and J. F. B. Mitchell, 1986: Diurnal variation and cloud in a general circulation model. *Quart. J. Roy. Meteor. Soc.*, **112**, 347-409.

Wofsy, S.C., Harriss, R.C., Kaplan, W.A., 1988. Carbon dioxide in the atmosphere over the Amazon Basin. *Jour. Geophys. Res.*, **93**, 1377-1387.

Wofsy, S. C., M. L. Goulden, J. W. Munger, S.-M. Fan, P. S. Bakwin, B. C. Daube, S. L. Bassow, and F. A. Bazzaz, 1993: Net exchange of CO_2 in a mid-latitude forest. *Science*, **260**, 1314-1316.

Woodwell, G. M., J. E. Hobbie, R. A. Houghton, J. M. Melillo, B. Moore, B. J. Peterson, and G. R. Shaver, 1983: Global deforestation: Contribution to atmospheric carbon dioxide. *Science*, **222**, 1081-1086.

Worsley, T. R., and R. D. Nance, 1989. Carbon redox and climate control through Earth history: A speculative reconstruction. *Paleogeog., Paleoclim., Paleoecol. (Global and Planetary Change Section)*, **75**, 259-282.

Zalesak, S. T., 1979: Fully multidimensional flux-corrected transport algorithms for fluids. *Jour. Comp. Phys.*, **31**, 335-362.

Appendix

Derivation of Global Carbon Budget Terms by Fitting Simulated Tracers to Observed CO_2 Concentrations

The object of this appendix is to derive an expression which can be solved for the coefficients α_i such that the linear combination of tracer concentrations

$$C_{Tn} = \sum_{i=1}^{N_T} \alpha_i C_{in} \qquad \text{(F.1)}$$

best fits the observed concentrations obs_n. In (A.1), C_{in} represents the concentration of tracer T_i at station n ($i = 1, \ldots, M$), and C_{Tn} is the "total" CO_2 concentration at station n, which is to be compared with the observed annual mean concentration at the same station obs_n ($n = 1, \ldots, N$). Because of the linear nature of the tracer calculation (see the discussion in section 3.2), determination of the coefficients α_i for the best fit of tracer *concentrations* (C_i) is equivalent to finding the best map of the tracer *fluxes* (F_i) which describe the CO_2 budget of the Earth's atmosphere in a manner consistent with both the observed annual mean concentration field and the simulated transport. The total surface flux of CO_2 at each grid point x on the planet is therefore given by

$$F(x) = \sum_{i=1}^{N_T} \alpha_i F_i(x) \,. \qquad \text{(F.2)}$$

Considering the constraints outlined on page 229 in section 6.3.2, we make the following definitions:

$$C_{Tn} = C_{\text{fix},\,n} + \alpha_2 C_{\text{def},\,n} + C_{\text{resid},\,n} \qquad \text{(F.3)}$$

where C_{Tn} is the total simulated CO_2 at station n as before, and

$$C_{\text{fix},n} \equiv C_1 + C_6 + C_9$$

$$C_{\text{def},n} \equiv C_2 \quad , \tag{F.4}$$

$$C_{\text{resid},n} \equiv \sum_{i=1}^{M} \beta_i C'_i$$

where M is the number of "free" or "fitted" tracers, which are designated as C'_i since their indices are different from the original C_i. The coefficients β_i will be fit by a least squares technique below, and are equivalent to some of the α_i above, but apply only to the "free" tracers. Constraint 4 above is expressed by

$$F_{\text{fix}} + \alpha_2 F_{\text{def}} + \sum_{i=1}^{M} \alpha_i F'_i = S \tag{F.5}$$

where

$$F_{\text{fix}} \equiv F_1 + F_6 + F_9 = 7.0 \text{ Gt C yr}^{-1}$$
$$F_{\text{def}} \equiv F_2 = 1.0 \text{ Gt C yr}^{-1} \tag{F.6}$$

From (F.5),

$$\alpha_2 = \frac{S - F_{\text{fix}} - \sum_{i=1}^{M} \alpha_i F'_i}{F_{\text{def}}}. \tag{F.7}$$

There remain M unknown coefficients α_i to be determined by fitting the C_{Tn} to the obs_n.

Substituting from (F.7) and (F.4) into (F.3), the total simulated CO_2 concentration at each flask station is given by

$$C_{Tn} = C_{\text{fix},n} + \frac{1}{F_{\text{def}}}\left(S - F_{\text{fix}} - \sum_{i=1}^{M} \beta_i F'_i\right) C_{\text{def},n} + \sum_{i=1}^{M} \beta_i C'_{in} \qquad \text{(F.8)}$$

The sum of the squared differences between the observed and combined simulated concentrations is defined as

$$SSD \equiv \sum_{n=1}^{N} (C_{Tn} - obs_n)^2. \qquad \text{(F.9)}$$

The "best" combination of tracers C_T is defined to be the one for which *SSD* is minimized. This occurs when the partial derivative of *SSD* with respect to each coefficient is zero, that is, when

$$\frac{\partial}{\partial \beta_i}(SSD) = 0 \qquad \text{for each } i, \quad 1 \le i \le M. \qquad \text{(F.10)}$$

For a given tracer, say $i=k$,

$$\begin{aligned} \frac{\partial}{\partial \beta_k}(SSD) &= \frac{\partial}{\partial \beta_k}\left[\sum_{n=1}^{N} (C_{Tn} - obs_n)^2\right] \\ &= 2\sum_{n=1}^{N} (C_{Tn} - obs_n)\frac{\partial C_{Tn}}{\partial \beta_k} \end{aligned} \qquad \text{(F.11)}$$

The derivative in the right-hand-side of (F.11) can be evaluated directly from (F.8):

$$\frac{\partial C_{Tn}}{\partial \beta_k} = C_{in} - \frac{F'_i}{F_{\text{def}}} C_{\text{def},n}. \qquad \text{(F.12)}$$

Substituting (F.12) into (F.11), the minimum of *SSD* is given when

$$\frac{\partial}{\partial \beta_k}(SSD) = 2\sum_{n=1}^{N}\left[(C_{Tn} - obs_n)\left(C'_{in} - \frac{F'_i}{F_{\text{def}}}C_{\text{def},n}\right)\right] = 0. \qquad \text{(F.13)}$$

Dividing (F.13) by 2 and substituting from (F.8) for C_{Tn}, the condition we wish to enforce is given by

$$\sum_{j=1}^{N_S}\left(C'_{in} - \frac{F'_i}{F_{\text{def}}}C_{\text{def},n}\right)$$

$$\left(C_{\text{fix},n} + \frac{1}{F_{\text{def}}}\left(S - F_{\text{fix}} - \sum_{i=1}^{M}\beta_i F'_i\right)C_{\text{def},n} + \sum_{i=1}^{M}\beta_i C'_{in} - \text{obs}_n\right) = 0 \qquad \text{(F.14)}$$

Grouping terms containing β_i, (F.14) may be rewritten as

$$\sum_{i=3}^{M}\left[\beta_i\sum_{n=1}^{N}\left(C'_{kn} - \frac{F_k}{F_{\text{def}}}C_{\text{def},n}\right)\left(C'_{in} - \frac{F_i}{F_{\text{def}}}C_{\text{def},n}\right)\right] =$$

$$-\sum_{n=1}^{N}\left[\left(C'_{kn} - \frac{F_k}{F_{\text{def}}}C_{\text{def},n}\right)\left(C_{\text{fix},n} + \frac{1}{F_{\text{def}}}(S - F_{\text{fix}})\,C_{\text{def},n} - \text{obs}_n\right)\right] \qquad \text{(F.15)}$$

The complete system of M equations can be written much more conveniently in matrix form as

$$A\ \beta = b. \qquad \text{(F.16)}$$

From (F.15), the elements of **A** are given by

$$a_{ki} = \sum_{n=1}^{N} \left(C'_{kn} - \frac{F_k}{F_{\text{def}}} C_{\text{def},n} \right) \left(C'_{in} - \frac{F_i}{F_{\text{def}}} C_{\text{def},n} \right), \tag{F.17}$$

and the elements of the right-hand side vector **b** are

$$b_k = -\sum_{n=1}^{N} \left[\left(C'_{kn} - \frac{F_k}{F_{\text{def}}} C_{\text{def},n} \right) \left(C_{\text{fix},n} + \frac{1}{F_{\text{def}}} (S - F_{\text{fix}}) C_{\text{def},n} - \text{obs}_n \right) \right]. \tag{F.18}$$

The rows of A are numbered $k = 1, M$ and the columns are numbered $i = 1, M$.

List of Abbreviations

^{85}Kr	Krypton-85
^{222}Rn	Radon-222
ABLE	Amazon Boundary-Layer Experiment
BATS	Biosphere-Atmosphere Transfer Scheme
CASA	Carnegie-Ames-Stanford Approach (terrestrial ecosystem carbon cycle model)
CFC	Chlorofluorocarbon
CO_2	Carbon dioxide
CSU	Colorado State University
EAULIQ	Cloud microphysics parameterization (Fowler *et al.*,1994)
ECMWF	European Center for Medium-Range Weather Forecasting
FIFE	First ISLSCP Field Experiment
GCM	General Circulation Model
GISS	Goddard Institute for Space Studies
HK89	Heimann and Keeling (1989)
ISLSCP	International Satellite Land-Surface Climatology Project
ITCZ	Intertropical convergence zone
LW90	Legates and Willmott (1990*a*, *b*)
µMol	micromole
NASA	National Areonautic and Space Adminsistration

NCAR	National Center for Atmospheric Research
NOAA	National Oceanic and Atmospheric Admisnistration
NEP	Net ecosystem production
NPP	Net primary production (or productivity)
PAR	Photosynthetically active radiation
PBL	Planetary Boundary Layer
pCi	picocurie (unit of radioactive decay)
SiB	Simple Biosphere model
STP	Standard temperature and pressure
SVD	Sigular-Value Decomposition
TEM	Terrestrial Ecosystem Model
TFT90	Pieter Tans, Inez Fung, and Taro Takahashi, 1990